eman ta zabal zazu

Universidad del País Vasco
Euskal Herriko Unibertsitatea

Symmetry-breaking and topology in correlated and amorphous matter

A PhD thesis submitted to the University of the Basque Country by

Daniel Muñoz Segovia

Supervised by

Fernando de Juan

Adolfo G. Grushin

November 2023

Contents

Acknowledgements

Bueno, por fin ha llegado este momento. Aunque para vosotros sea el principio, escribo esto el día anterior a depositar, con todas las prisas y los nervios, aunque esto no será una sorpresa para quienes me conozcáis. Aunque esta época ha tenido sus altibajos, siento que ha sido muy positiva, sobre todo a nivel personal. Y esto es gracias a todas las personas que me habéis rodeado a lo largo de estos años. Creo que no solo salgo de aquí como mejor investigador, sino también como mejor persona, gracias a vosotros.

En primer lugar, quiero agradecer enormemente a mis directores de tesis, Fernando y Fito, mi "caring father" y mi "cool uncle" (aunque los dos sois cool y caring). No estaría aquí si no fuera por vosotros. Me habéis enseñado dos estilos diferentes de hacer física, siempre transmitiéndome confianza y motivación. Gracias por vuestra paciencia ante mi testarudez cuando no entiendo algo. Discutir con vosotros en la pizarra son de los mejores momentos que me llevo. En particular, guardo especial cariño a cuando, hace ya tres años, pudimos reunirnos los tres juntos en Donosti. Ojalá podamos repetirlo algún día. Más allá de la física per se, sobre todo quiero agradeceros que siempre me habéis apoyado. No puedo expresar todo lo que significáis personalmente para mí, sois mucho más que mis directores de tesis. Me habéis enseñado a que también se puede y se debe desconectar y disfrutar de la vida en investigación. Me habéis dedicado tiempo cuando yo no estaba bien y con mis inseguridades, me habéis escuchado, me habéis aconsejado, y os habéis esforzado para que todo me fuera lo mejor posible. Gracias.

También quiero agradecer al DIPC su apoyo durante estos años. Ojalá volvamos a cruzar nuestros caminos en algún momento. Gracias también a la gente con la que he discutido sobre física. Thanks to you and your group, Miguel, it is always a pleasure to work with you.

I would also like to thank all the people I have met in my stays in Grenoble: Katee, Miguel Ángel, Quentin, Richard, Ángel, Serguei, Laura, Leon, Antonia, Selma, Justin, Simone... I have always felt welcome and enjoyed so much there. Thanks again Fito and Katee. I hope we can hike and climb together soon again, and, why not, also have some gin tonics. Thanks Richard for the incredible hangovers after these parties. And thanks to all the people at Néel for the interesting physics discussions, I have learned a lot from you. Aunque no hayamos coincidido tanto como me gustaría, gracias Miguel Ángel por apoyarme tanto, y por las infinitas risas. I would also like to thank Paul. Working with you has been great, I have really had a good time despite the struggles trying to make the spillage work.

I am also grateful to Asier, Nish, Peter, Héctor, Raquel... You have made my visit to NY much more enjoyable with your kindness and physics insight. Gracias Asier por apoyarme, no olvidaré esas noches de la ruina, cerve y helado, ni nuestra aventura andando por el polígono desértico. Y gracias Héctor por tus interesantes conversaciones, por hacerme ver las cosas de otra forma, y por

apoyarme. Hablar de física contigo me ha ayudado mucho a motivarme en mis momentos bajos, y el salseo tampoco está mal. Thanks Jörn for your hospitality, it is always a pleasure discussing with you.

Volviendo a Donosti, esta etapa no hubiera sido lo mismo sin vosotros. Gracias Dani, Sara y Rodrigo. Si me preguntan por una imagen que describa the good old times de mi tesis, sin duda sería nosotros cuatro comiendo en las estrellas de cemento. No os imagináis en lo importantes que os habéis convertido para mi, y todo lo que me habéis apoyado. Ojalá la historia se repita, ya sea en Donosti, en Rosario, en NY o donde sea. Gracias también a Lucía, y perdón por mis chistes malos... aunque ya sabes que mi maestro es Rodrigo. Os llevo en mi corazón, que es más grande que una manzana. Gracias Matteo, Giovanni, Marcos, Lurdes... por acogerme desde el principio. Sarai sempre il pubblico migliore, Matteo, grazie per tutto. Gracias Irián, Óscar, Fernando y María por escucharme y aconsejarme. Gracias a Laura por esas conversaciones de apoyo, y por enseñarme que no puedo seguirte el ritmo a cervezas. Gracias a mis compañeros de piso, María, Camil, Paco, Miguel y Henrique, por las conversaciones del día a día, el apoyo y, sobre todo, por aceptar mi rutina nocturna. Si algo me ha caracterizado durante esta etapa ha sido el pelo largo, y vosotros sois los causantes. Gracias al resto de gente del DIPC y de Donosti, Xabi, Pina, Leire, Francisco, Jorge, Coco, Iñigo, Mikel, Nicol, y un largo etcétera donde me dejo muchas personas.

Gracias también a la gente maravillosa que conocí en el máster, Jaime, Inés, Laura, Carmen... Me habéis hecho mejor persona, y me siento muy orgulloso que seamos amigos. También quiero agradecer a Alberto por el trabajo que hicimos juntos y por la pasión y conocimiento que me transmitiste.

Volviendo a Valladolid, me gustaría agradecer a los que siempre habéis estado ahí, Soraya, Sergio, Adrián y Elena. Siempre que nos juntamos me siento como si el tiempo no hubiera pasado, es genial que sigamos creciendo juntos. Gracias también a todos mis amigos de la carrera, Donís, Paquique, Camilo, Santi, Amezua, Sandra, Hernández, Marina, Laura, Carlota, Maralla, Sofía, Marta, ... Esas casas rurales son purificantes, ojalá nunca dejemos de hacerlas (pero la sidra con moderación). Gracias también a Isma, por ser mi amigo desde que no tengo memoria. También quiero agradecer a Rosa haberme abierto las puertas al mundo de la física.

Por supuesto, gracias a mi familia. Siempre me habéis apoyado en cada una de mis decisiones, y sobre todo ante el agobio que me surge en cada una de ellas. Gracias mamá, papá, Moni, Aghy, abuela, abuelo, tata, tío... No estaría aquí sin vosotros. Gracias por entenderme y por tener el tacto y la paciencia que tenéis conmigo. Voglio anche ringraziare la mia famiglia in Italia, Max, Maria Lisa, Giuliano, Alfonso e Silvana, tutti siete molto importanti per me. Sempre che vado a Brosso mi sento come a casa. Y, aunque quizás todavía no sepáis cuánto significáis para mí, gracias a mis hermanos Alex, Raúl, Diego y Jaime. Cada vez que volvía a Valladolid, daba igual el trabajo y

la ansiedad que tuviera en Donosti, disfrutaba a tope con vosotros. Me hacéis ver las cosas que realmente importan en la vida. Me encanta veros crecer, y a la vez ser el más niño de vosotros para jugar y aprender de vosotros. Estoy super orgulloso de ser vuestro hermano.

Finalmente, quiero agradecer a una de las sorpresas más bonitas de este último año. Gracias por aparecer Nuria. Este año ha sido muy duro para mi por muchos, o no tantos, motivos. Tú me has apoyado desde el principio, y has hecho de lo que pensaba que iba a ser un año horrible una experiencia maravillosa. Gracias por entenderme a mí y a mis circunstancias, y por superar juntos las adversidades. Tengo muchas ganas de seguir en esta aventura juntos.

A todos, gracias.

Para mi abuelo Mariano
Siempre confiaste en mí

List of Publications

- *Nematic and stripe orders within the charge density wave state of doped $TiSe_2$.*
  Daniel Muñoz-Segovia, Jörn W. F. Venderbos, Adolfo G. Grushin, and Fernando de Juan.
  arXiv:2308.15541 (2023). Under review in Physical Review Letters.

- *Observation of Superconducting Collective Modes from Competing Pairing Instabilities in Single-Layer $NbSe_2$.*
  Wen Wan, Paul Dreher, **Daniel Muñoz-Segovia**, Rishav Harsh, Haojie Guo, Antonio J. Martínez-Galera, Francisco Guinea, Fernando de Juan, and Miguel M. Ugeda.
  Adv. Mater. **34**, 2206078 (2022).

- *Structural spillage: An efficient method to identify noncrystalline topological materials.*
  Daniel Muñoz-Segovia, Paul Corbae, Dániel Varjas, Frances Hellman, Sinéad M. Griffin, and Adolfo G. Grushin.
  Phys. Rev. Research **5**, L042011 (2023).

- *Amorphous topological matter: Theory and experiment.*
  Paul Corbae, Julia D. Hannukainen, Quentin Marsal, **Daniel Muñoz-Segovia**, and Adolfo G. Grushin.
  EPL **142**, 16001 (2023).

Introduction

One of the frontiers of modern condensed matter physics is the study of the exotic quantum phases arising from electronic correlations, which are further enriched by their interplay with topology and disorder. In this Thesis, we study a variety of properties of several such phases. First, we analyze the symmetry of the charge density wave state of 1T-$TiSe_2$ [1]. Then, we examine the collective modes appearing in the superconducting phase of monolayer 2H-$NbSe_2$ [2]. Finally, we propose an indicator to identify nontrivial topological phases in noncrystalline systems [3, 4]. In this chapter, we provide an overview of the general context and relevance of each of these topics.

There are several approaches to classify and characterize the phases of matter and the transitions between them. Symmetry is a crucial tool for this purpose. Indeed, each phase can be associated to a group of preserved spatial and local symmetries. Within the Landau theory [5, 6], phase transitions are understood as spontaneous symmetry breaking: the change in certain parameters induces a different phase which breaks more, or different, symmetries. Importantly, this occurs spontaneously due to the internal interactions of the system, in the absence of any external source that explicitly breaks the symmetries. Symmetry breaking can be monitored by a local order parameter, the expectation value of an operator that transforms as a representation of the symmetry group and becomes nonzero only in the broken-symmetry phase. The dynamics of this order parameter gives rise to collective modes, which can be important in the low-energy physics of the system [7].

An ubiquitous broken-symmetry phase is the so-called charge density wave (CDW) state [8, 9], which appears in a variety of correlated systems, from Copper oxides [10, 11] to transition metal dichalcogenides [12–16]. In a CDW transition, the electronic charge distribution acquires a modulation with a different periodicity from the normal state, breaking a subgroup of the translational symmetry. The order parameter is therefore related to the expectation value of the charge density at the wavevector $\boldsymbol{Q}$ of the new modulation. As a consequence of the charge modulation, the electronic structure is reconstructed. If the normal state is metallic, partial or full gaps are opened in the Fermi surface, which reduces the total electronic energy in the CDW state. Due to the electron-phonon coupling, phonons are also affected by the CDW instability [17],

and the electronic charge density modulation is accompanied by a lattice distortion with the same symmetry.

CDW materials display a variety of properties and phenomenology. Part of the richness comes from the modulation wavevector $\boldsymbol{Q}$, which allows to distinguish CDWs in terms of the commensuration between the original lattice periodicity and the new modulation of the charge density. Within this scheme, commensurate CDWs still preserve a subset of the translations, and therefore a real-space periodic supercell can be defined. On the other hand, no translational symmetry is exactly preserved in an incommensurate CDW. External parameters, such as temperature, doping or pressure, might drive a crossover between commensurate and incommensurate phases, as in transition metal dichalcogenides [13, 18]. In Chapter 1, we focus on the commensurate CDW phase of 1T-$TiSe_2$. Besides transitions between different CDWs, the phase diagrams of CDW materials typically show other correlated phases nearby that break different symmetries, such as superconductivity and magnetism [19]. The study of the interplay and coexistence of these orders, ranging from competition to even cooperation, is at the forefront of research in condensed matter physics, and remains an open problem in general [20]. This motivates the study of the properties and origin of CDWs. Two of the materials studied in this Thesis, 1T-$TiSe_2$ and 2H-$NbSe_2$, display coexisting CDW and superconducting phases for certain parameter ranges [21–33].

The microscopic mechanism driving the CDW is a persistent source of controversies [34–38]. Depending on the dimensionality of the system and the strength of the interactions, the ordering wavevector $\boldsymbol{Q}$ might be mainly set by Fermi surface nesting [39, 40], electron-phonon coupling [8, 34] or electron-electron interactions [41–45]. While the microscopic origin of the CDW is a relevant question that has implications in several aspects, such as the interplay with competing phases, important information can also be extracted regardless of its origin, such as the symmetry of the CDW.

Indeed, while the breaking of translational symmetry is its defining property, a CDW might break further spatial symmetries [46, 47]. This might generically occur in 2D and 3D systems, where multiple modulation wavevectors $\boldsymbol{Q}$ might be related by point-group symmetries. The stripe CDW order in cuprates is an example of such a scenario, where the unidirectional CDW modulation breaks the fourfold rotational symmetry of the underlying lattice [10, 11]. A special case that has attracted attention in recent years occurs when the rotational symmetries are broken only after a secondary nematic instability within the CDW state. For instance, a transition to a nematic CDW has ben identified in in kagome AV_3Sb_5 metals [48–51]. The case of 1T-$TiSe_2$ is particularly intriguing, since similar signatures have been found [52–56], but the symmetry of its CDW remains a source of controversy. Chapter 1 of this Thesis is devoted to this problem.

Another emblematic collective phase of matter is superconductivity, which is a special case

of spontaneous symmetry breaking. Phenomenologically, superconductors are defined by the ability to support persistent supercurrents in their ground state [57], which leads to a vanishing resistance and the expulsion of magnetic fields, known as Meissner effect [58]. Microscopically, superconductors can be regarded as charged superfluids, where bosonic pairs of electrons, known as Cooper pairs [59], condense into a phase coherent state, driven by an effective electron-electron attraction at low energies. Neutral superfluids break the continuous $U(1)$ symmetry related to particle number conservation, and therefore constitute well-defined broken-symmetry states in the grand-canonical ensemble. On the other hand, Cooper pairs are charged, and therefore couple to the electromagnetic field. The $U(1)$ symmetry in superconductors is therefore linked to the local gauge invariance, which cannot be broken since it is just a redundancy in our physical description [60]. Therefore, there are no local gauge-invariant observables associated with superconductivity that exhibit long-range order [61–63]. While this is a fundamental aspect of superconductivity, the analogy with superfluids can be applied to determine several ground state properties, such as the superconducting gap, without considering the gauge invariance issue.

Within this formalism, the order parameter of a superconductor describes the Cooper pair wavefunction, and can be classified according to the spatial and spin symmetries of this pairing. In the simplest case, no further symmetries are broken, which is described by a s-wave spin-singlet pairing. The most common origin for the attractive interaction in these superconductors is the electron-phonon interaction [64–66]. Electron-phonon driven s-wave spin-singlet superconductivity is called conventional superconductivity. The pairing interaction in the majority of the rest of superconductors, dubbed unconventional, is thought to originate from electron-electron interactions [67] or their collective modes, such as spin fluctuations [68], skyrmions [69] or plasmons [70]. Moreover, local repulsion tends to be large in unconventional superconductors, which suppresses the s-wave spin-singlet channel with no sign changes of the superconducting gap, thus favouring a different pairing symmetry [71, 72]. Consequently, unconventional superconductors typically break additional symmetries. The d-wave spin-singlet superconducting pairing in tetragonal cuprate superconductors is a paradigmatic case where the superconducting order parameter breaks the fourfold rotational symmetry of the underlying lattice [10, 73]. Iron-based superconductors [74] and heavy fermion systems [75] are other examples of unconventional superconductors. The thorough understanding of unconventional superconductivity and the development of a consistent and complete microscopic theory for it remains one of the paramount challenges of condensed matter physics [71, 72].

Interestingly, collective modes in a superconductor can provide valuable information about the pairing [68, 76]. This has been traditionally exploited in conventional superconductors, where phonons leave signatures in the tunneling current which allow to quantify the electron-phonon coupling [76]. Spin fluctuations also impact the electronic spectral function in unconventional

superconductors [68]. The amplitude and phase dynamics of the superconducting order parameter itself also describes collective modes [77–79]. A special case occurs when several pairing channels compete, where the fluctuations towards the subleading channels define new superconducting collective modes [80, 81], as in iron-based superconductors [82, 83]. In Chapter 2, we will show that monolayer 2H-$NbSe_2$ is a surprising example of this scenario.

Despite its success, the theory of spontaneous symmetry breaking does not provide a complete classification of quantum phases and phase transitions. There are phase transitions between phases with the same symmetry that cannot be differentiated by any local order parameter. This is where the field of topology becomes useful in condensed matter physics. This was first manifested with the discovery of the quantum Hall effect [84]: 2D electron gases under large magnetic fields exhibit quantized Hall conductivity while remaining insulators with a vanishing longitudinal conductivity. Systems with an integer number of filled Landau levels are insulators with the same symmetries, but they have different quantized Hall conductivities, associated to a different Chern numbers [85–89]. The Chern number is an integer topological invariant related to the change of the phase of the wavefunction around the magnetic Brillouin zone, which can only change in a topological phase transition where the mobility gap closes [85–89].

As exemplified by the Chern number, topology deals with global properties of the wavefunctions, which define different topological invariants. Symmetry is also crucial in this field, since topological classes are defined with respect to an equivalence relation consisting of adiabatic transformations that respect the underlying symmetries. In this sense, topological phases are protected by the symmetries that, if removed, would change the topology. Their nonlocal character grants topologically nontrivial phases with a notion of robustness against local symmetry-preserving perturbations. In general, this is related to certain quantized responses, such as the Hall conductivity in Chern insulators [90] and the Faraday and Kerr rotation in 3D strong topological insulators [91–93]. Moreover, when interfaced with topologically different systems, topological phases usually display anomalous boundary states which cannot be removed if the boundary itself respects the protecting symmetries.

Depending on their protecting symmetries, topological phases are classified as strong, if the protecting symmetries are only the local time-reversal, particle-hole, or chiral symmetries [94–98], or crystalline, if they also require translational or other spatial symmetries [99, 100]. Regardless of whether the symmetries are needed for the protection, they greatly facilitate the topological characterization. This is especially the case for translational invariance in crystals, which has been traditionally exploited by topology. In noninteracting systems, Bloch's theorem allows to define a crystal momentum in the Brillouin zone. This simplifies the topological characterization, since topological invariants can be expressed as integrals over the Brillouin zone of certain geometric quantities. For instance, the integral of the Berry curvature gives the Chern number. However,

this computation is still hard in general. In conjunction with translational symmetry, point-group symmetries can notably simplify this task even more via the so-called symmetry indicators [101–107]. Symmetry indicators partially determine topological invariants based on the symmetry eigenvalues of the occupied bands at high symmetry points in the Brillouin zone. Due to their role in topological protection and characterization, crystalline symmetries have a crucial role in the understanding of topological phases.

Nevertheless, topological phases can also exist in the absence of translational symmetry, extending the field of topological phases to amorphous, disordered, quasicrystalline and nanocrystalline materials. For instance, this is clear for strong topological insulators, which are only protected by local symmetries and a mobility gap [94–98]. Actually, the presence of plateaus of quantized Hall conductivity over ranges of magnetic field in a quantum Hall insulator relies on certain amount of disorder to localize all states but one in each Landau level. Furthermore, disorder can even induce topological phases starting from trivial crystals, as in the so-called topological Anderson insulators [108, 109]. Moreover, new topological phenomena can arise in noncrystalline systems. Quasicrystals can host topological phases protected by rotational symmetries incompatible with translational symmetry [110–112]. Amorphous systems lack exact spatial symmetries, but they can be preserved on average, which leads to the so-called statistical topological insulators [113]. However, identifying topological phases in noncrystalline systems is harder due to the absence of exact translational symmetry and, consequently, of a Brillouin zone. While several topological markers have been recently proposed, there is no generic and efficient method to characterize topological phases in noncrystalline solids. We will address this issue in Chapter 3.

This Thesis involves three of the topics described above. It is divided in three chapters. The first chapter deals with different secondary instabilities within an already broken-symmetry ground state. In particular, we study 1T-$TiSe_2$, a transition metal dichalcogenide that displays a commensurate $2 \times 2 \times 2$ CDW. Motivated by the diverging conclusions of different experiments regarding the symmetry of the CDW state [52–54, 56, 114], we develop a theory where electron doping drives two transitions to nematic and stripe CDWs where the threefold symmetry of the underlying lattice is spontaneously broken [1].

The second chapter concerns the study of the collective modes of the superconducting order parameter in a multiband system. Here, we consider another transition metal dichalcogenide, monolayer 2H-$NbSe_2$. At low temperature, $NbSe_2$ becomes superconducting, with a ground state which is likely a conventional s-wave spin-singlet superconductor. Motivated by the recent experimental results from the group of Miguel Ugeda [2], together with other unconventional features in the critical field [115, 116], we study the superconducting collective modes in the presence of a subleading unconventional pairing. We find that the fluctuations towards this subleading pairing define a Leggett mode, which leaves signatures in the tunneling spectrum.

Finally, the third chapter is devoted to the topic of topological states in noncrystalline systems [4]. In particular, we address the problem of signaling nontrivial topological phases in such systems. We introduce the structural spillage, a new topological indicator applicable to noncrystalline solids, which measures the band inversions between the noncrystalline system and a known reference crystal, and is readily compatible with *ab initio* calculations [3]. The application of this method to amorphous bilayer Bismuth predicts it to be a topological insulator.

Resumen en castellano

Una de las fronteras de la física de la materia condensada es el estudio de las fases cuánticas exóticas que surgen de la interacción entre correlaciones electrónicas, topología y desorden. En esta Tesis, hemos estudiado diversas propiedades de varias de estas fases. En primer lugar, hemos analizado la simetría del estado de onda de densidad de carga de 1T-$TiSe_2$ [1]. Luego, hemos examinado los modos colectivos que aparecen en la fase superconductora de la monocapa de 2H-$NbSe_2$ [2]. Finalmente, hemos propuesto un indicador para identificar fases topológicas no triviales en sistemas amorfos [3, 4]. Este capítulo proporciona un breve resumen del contexto general de cada uno de estos temas, así como de los resultados particulares que hemos obetenido.

Existen varios enfoques para clasificar y caracterizar las fases de la materia y las transiciones entre ellas. La simetría es una herramienta crucial para este propósito. De hecho, cada fase puede ser asignado un grupo de simetrías espaciales y locales preservadas. En la teoría de Landau [5, 6], las transiciones de fase se entienden como ruptura espontánea de simetría: cambiar ciertos parámetros induce una fase diferente que rompe más, o diferentes, simetrías. Esto ocurre de manera espontánea debido a las interacciones internas del sistema, en ausencia de cualquier fuente externa que rompa explícitamente las simetrías. La ruptura de simetría puede ser indicada por un parámetro de orden local, el valor esperado de un operador que se transforma como una representación del grupo de simetría y que es distinto de cero sólo en la fase con la simetría rota. La dinámica de este parámetro de orden da lugar a modos colectivos, que pueden ser importantes en la física de baja energía del sistema [7].

Una conocida fase de ruptura de simetría es el estado de onda de densidad de carga (CDW, por sus siglas en inglés) [8, 9], que aparece en numerosos sistemas correlacionados, desde los óxidos de cobre [10, 11] hasta los dicalcogenuros de metales de transición [12–16]. En una transición CDW, la distribución de carga electrónica adquiere una modulación con una periodicidad diferente a la del estado normal, rompiendo un subgrupo de la simetría de translación. El parámetro de orden está relacionado con el valor esperado de la densidad de carga con el vector de onda $\boldsymbol{Q}$ correspondiente a la nueva modulación. Como consecuencia de la modulación de carga, la estructura electrónica se reconstruye. Si el estado normal es metálico, se abren brechas (gaps) parciales o completas en la superficie de Fermi, lo que reduce la energía electrónica total en el estado CDW. Debido a la

interacción electrón-fonón, los fonones también se ven afectados por la inestabilidad CDW [17], y la modulación de la densidad de carga electrónica va acompañada de una distorsión de la red con la misma simetría.

Los materiales CDW muestran una rica variedad de propiedades y fenomenología. Parte de la riqueza proviene del vector de onda $\boldsymbol{Q}$ de la modulación, que permite distinguir las CDWs en términos de la conmensuración entre la periodicidad original de la red y la nueva modulación de la densidad de carga. En este esquema, las CDWs conmensuradas preservan un subgrupo de las translaciones, y por lo tanto se puede definir una supercelda periódica en el espacio real. Por otro lado, ninguna simetría de translación se preserva exactamente en una CDW inconmensurada. Parámetros externos, como la temperatura, el dopaje o la presión, pueden inducir una transición entre fases conmensuradas e inconmensuradas, como en los dicalcogenuros de metales de transición [13, 18]. En el Capítulo 1, nos centraremos en la fase CDW conmensurada de 1T-$TiSe_2$. Además de las transiciones entre diferentes CDWs, los diagramas de fase de los materiales CDW suelen mostrar otras fases correlacionadas cercanas que rompen simetrías diferentes, como la superconductividad y el magnetismo [19]. El estudio de la interacción y coexistencia de estos estados, que va desde la competición hasta la cooperación, se encuentra en la vanguardia de la investigación en física de la materia condensada y sigue siendo un problema sin resolver en muchos casos [20]. Esto motiva el estudio de las propiedades y el origen de las CDWs. Dos de los materiales estudiados en esta Tesis, 1T-$TiSe_2$ y 2H-$NbSe_2$, muestran fases CDW y superconductoras que coexisten para ciertos rangos de parámetros [21–33].

El mecanismo microscópico que origina las CDWs es una continua fuente de controversias [34–38]. Dependiendo de la dimensionalidad del sistema y la fuerza de las interacciones, el vector de onda $\boldsymbol{Q}$ de la CDW puede estar principalmente determinado por el anidamiento (nesting) de la superficie de Fermi [39, 40], la interacción electrón-fonón [8, 34] o las interacciones electrón-electrón [41–45]. Mientras que el origen microscópico de la CDW es una pregunta relevante con implicaciones en varios aspectos, como la interacción con fases competidoras, también se puede extraer información importante independientemente de su origen, como la simetría de la CDW.

De hecho, aunque la ruptura de la simetría de translación es su propiedad definitoria, una CDW podría romper más simetrías espaciales [46, 47]. Esto puede ocurrir genéricamente en sistemas 2D y 3D, donde múltiples vectores de onda $\boldsymbol{Q}$ pueden estar relacionados por simetrías del grupo puntual. La CDW de rayas (stripe) en los cupratos es un ejemplo donde la modulación unidireccional CDW rompe la simetría de rotación cuártica C_4 de la red subyacente [10, 11]. Un caso especial que ha atraído la atención en los últimos años ocurre cuando las simetrías de rotación sólo se rompen después de una segunda inestabilidad a una fase nemática dentro del estado CDW. Por ejemplo, se ha identificado una transición a una CDW nemática en los metales kagome AV_3Sb_5 [48–51]. El caso de 1T-$TiSe_2$ es particularmente intrigante, ya que se han encontrado

señales similares [52–56], pero la simetría de su CDW sigue siendo motivo de controversia. El Capítulo 1 de esta Tesis está dedicado a este problema.

Otra fase colectiva emblemática es la superconductividad, que es un caso especial de ruptura espontánea de simetría. Fenomenológicamente, los superconductores se definen por su capacidad para mantener supercorrientes persistentes en su estado fundamental [57], lo que conduce a una resistencia nula y a la expulsión de campos magnéticos, conocida como efecto Meissner [58]. Microscópicamente, los superconductores pueden considerarse como superfluidos cargados, donde pares de electrones, conocidos como pares de Cooper [59], condensan en un estado coherente, causado por una atracción efectiva entre electrones a bajas energías. Los superfluidos no cargados rompen la simetría continua $U(1)$ relacionada con la conservación del número de partículas, y por lo tanto constituyen estados de ruptura de simetría bien definidos en la colectividad macrocanónica. Por otro lado, los pares de Cooper están cargados y, por lo tanto, se acoplan al campo electromagnético. La simetría $U(1)$ en los superconductores está vinculada a la invariancia gauge local, que no puede romperse, ya que sólo es una redundancia en nuestra descripción física [60]. Por lo tanto, no existen observables locales invariantes gauge asociados a la superconductividad que exhiban orden de largo alcance [61–63]. Si bien este es un aspecto fundamental de la superconductividad, la analogía con los superfluidos se puede aplicar para determinar varias propiedades del estado fundamental, como el gap superconductor, sin considerar el problema de la invariancia gauge.

En este formalismo, el parámetro de orden de un superconductor describe la función de onda de los pares de Cooper y puede clasificarse según las simetrías espaciales y de espín de este apareamiento. En el caso más simple, la superconductividad no rompe más simetrías, y está descrita por un apareamiento de onda s y singlete de espín. El origen más común para la interacción atractiva en estos superconductores es la interacción electrón-fonón [64–66]. La superconductividad de onda s y singlete de espín originada por la interacción electrón-fonón se llama superconductividad convencional. La interacción atractiva en la mayoría del resto de superconductores, denominados no convencionales, se cree que proviene de las interacciones electrón-electrón [67] o de sus modos colectivos, como las fluctuaciones de espín [68], los esquirmiones (skyrmions) [69] o los plasmones [70]. Además, en los superconductores no convencionales, la repulsión local tiende a ser grande, lo que suprime el canal de onda s y singlete de espín que no presenta cambios de signo del gap superconductor, favoreciendo así una simetría de apareamiento diferente [71, 72]. En consecuencia, los superconductores no convencionales suelen romper simetrías espaciales. El apareamiento de onda d y singlete de espín en cupratos tetragonales superconductores es un caso paradigmático en el que el parámetro de orden superconductor rompe la simetría de rotación cuártica C_4 de la red subyacente [10, 73]. Los superconductores basados en hierro [74] y los sistemas de fermiones pesados [75] son otros ejemplos de superconductores no convencionales. La comprensión detallada de la superconductividad no convencional y el desarrollo de una teoría

microscópica coherente y completa para ésta siguen siendo uno de los principales desafíos en física de la materia condensada [71, 72].

Es interesante señalar que los modos colectivos en un superconductor pueden proporcionar información valiosa sobre el apareamiento [68, 76]. Tradicionalmente, esto se ha aprovechado en superconductores convencionales, donde los fonones dejan señales en la corriente túnel que permiten cuantificar la interacción electrón-fonón [76]. Las fluctuaciones de espín también afectan a la función espectral electrónica en superconductores no convencionales [68]. La dinámica de amplitud y fase del propio parámetro de orden superconductor también describe modos colectivos [77–79]. Un caso especial ocurre cuando varios canales de apareamiento compiten, donde las fluctuaciones hacia los canales secundarios definen nuevos modos colectivos superconductores [80, 81], como en los superconductores basados en hierro [82, 83]. En el Capítulo 2, mostraremos que la monocapa de 2H-$NbSe_2$ es un ejemplo sorprendente de este escenario.

A pesar de su éxito, la teoría de la ruptura espontánea de simetría no proporciona una clasificación completa de las fases cuánticas y sus transiciones. Existen transiciones de fase entre fases con la misma simetría que no pueden diferenciarse por ningún parámetro de orden local. Aquí es donde el campo de la topología se vuelve útil en física de la materia condensada. Esto se manifestó por primera vez con el descubrimiento del efecto Hall cuántico [84]: los gases de electrones 2D en un campo magnético fuerte muestran una conductividad Hall cuantizada y, al mismo tiempo, son aislantes con conductividad longitudinal nula. Los sistemas con un número entero de niveles de Landau llenos son aislantes con las mismas simetrías, pero tienen diferentes conductividades Hall cuantizadas, asociadas a diferentes números de Chern [85–89]. El número de Chern es un invariante topológico entero relacionado con el cambio de fase de la función de onda alrededor de la zona de Brillouin magnética, que sólo puede cambiar en una transición de fase topológica donde el gap de movilidad se cierra [85–89].

Como ejemplifica el número de Chern, la topología trata sobre propiedades globales de las funciones de onda, que definen diferentes invariantes topológicos. La simetría también es crucial en este campo, ya que las clases topológicas se definen con respecto a una relación de equivalencia que consiste en transformaciones adiabáticas que respetan las simetrías subyacentes. En este sentido, las fases topológicas están protegidas por las simetrías que, si se eliminan, cambiarían la topología. Su carácter no local otorga a las fases topológicamente no triviales una noción de robustez contra perturbaciones locales que preservan la simetría. En general, esto está relacionado con ciertas respuestas cuantizadas, como la conductividad Hall en aislantes de Chern [90] y las rotaciones de Faraday y de Kerr en aislantes topológicos fuertes en 3D [91–93]. Además, en la interfaz entre sistemas topológicamente diferentes, suelen aparecer estados de borde anómalos que no se pueden eliminar si la propia interfaz respeta las simetrías que protegen las fases topológicas.

Dependiendo de las simetrías que las protegen, las fases topológicas se clasifican como fuertes, si sólo están protegidas por las simetrías locales de inversión temporal, partícula-hueco o quiral [94–98], o cristalinas, si también requieren simetrías de traslación u otras simetrías espaciales [99, 100]. Independientemente de si son necesarias para la protección, las simetrías facilitan en gran medida la caracterización topológica. Esto es especialmente relevante para la invariancia de traslación en cristales, que ha sido tradicionalmente aprovechada por la topología. En sistemas no interactuantes, el teorema de Bloch permite definir un momento cristalino en la zona de Brillouin. Esto simplifica la caracterización topológica, ya que los invariantes topológicos se pueden expresar como integrales sobre la zona de Brillouin de ciertas cantidades geométricas. Por ejemplo, la integral de la curvatura de Berry proporciona el número de Chern. Sin embargo, este cálculo sigue siendo difícil en general. Junto con la simetría de traslación, las simetrías del grupo puntual pueden simplificar notablemente esta tarea gracias a los llamados indicadores de simetría [101–107]. Los indicadores de simetría determinan parcialmente los invariantes topológicos dependiendo de los valores propios de las simetrías de las bandas ocupadas en los puntos de alta simetría de la zona de Brillouin. Debido a su función en la protección y caracterización topológica, las simetrías cristalinas desempeñan un papel crucial en la comprensión de las fases topológicas.

Sin embargo, las fases topológicas también pueden existir en ausencia de simetría de traslación, lo que extiende el campo de las fases topológicas a materiales amorfos, desordenados, cuasicristalinos y nanocristalinos. Por ejemplo, esto es evidente para aislantes topológicos fuertes, que sólo están protegidos por simetrías locales y un gap de movilidad [94–98]. De hecho, la presencia de mesetas (plateaus) de conductividad Hall cuantizada durante rangos de campo magnético en un aislante Hall cuántico necesita de cierta cantidad de desorden para localizar todos los estados excepto uno en cada nivel de Landau. Además, el desorden puede incluso inducir fases topológicas partiendo de cristales triviales, como en los llamados aislantes topológicos de Anderson [108, 109]. Es más, nuevos fenómenos topológicos pueden surgir en sistemas no cristalinos. Los cuasicristales pueden albergar fases topológicas protegidas por simetrías rotacionales incompatibles con la simetría de traslación [110–112]. Los sistemas amorfos carecen de simetrías espaciales exactas, pero pueden preservarse en promedio, lo que lleva a los llamados aislantes topológicos estadísticos [113]. Sin embargo, identificar las fases topológicas en sistemas no cristalinos es más difícil debido a la ausencia de simetría de traslación exacta y, en consecuencia, de una zona de Brillouin. Aunque se han propuesto varios marcadores topológicos recientemente, no existe un método genérico y eficiente para caracterizar fases topológicas en sólidos no cristalinos. Abordaremos este problema en el Capítulo 3.

Esta Tesis abarca tres de los temas descritos anteriormente. Está dividida en tres capítulos. El primer capítulo trata sobre diferentes inestabilidades secundarias dentro de un estado fundamental que ya ha roto la simetría. En particular, hemos estudido el 1T-$TiSe_2$, un dicalcogenuro de metal de

transición que muestra una CDW commensurada $2 \times 2 \times 2$. Motivados por las observaciones de distintas simetrías de la fase CDW en experimentos de microscopía de efecto túnel [52–54, 56, 114], hemos desarrollado una teoría en la que el dopaje provoca dos transiciones a CDWs nemáticos y de rayas, donde la simetría de rotación C_3 de la red subyacente se rompe espontáneamente [1]. Primero, hemos realizado el análisis de simetrías del sistema para construir un modelo $\boldsymbol{k} \cdot \boldsymbol{p}$ acoplado al parámetro de orden de la CDW. El estado fundamental a dopaje cero es simétrico bajo C_3, caracterizado por un parámetro de orden con tres componentes iguales $\vec{\Delta} = (\Delta, \Delta, \Delta)$. Cuando el dopaje aumenta hasta cruzar unas singularidades de van Hove incipientes, hay una transición a una CDW nemática con parámetro de orden $\vec{\Delta} = (\Delta_1, \Delta_2, \Delta_2)$. Si el dopaje se incrementa aún más, la energía electrónica se minimiza para una CDW de rayas, caracterizada por un parámetro de orden $\vec{\Delta} = (\Delta, 0, 0)$. Tambien hemos demostrado que dichas CDWs aparecen en un modelo de ligaduras fuertes mínimo, que hemos resuelto en la aproximación del campo medio autoconsistente. Dado que el dopaje no se puede controlar precisamente en los experimentos, nuestra teoría puede resolver el problema de la simetría de la CDW, reconciliando todos los experimentos.

El segundo capítulo está dedicado al estudio de los modos colectivos del parámetro de orden superconductor en un sistema multibanda. En particular, hemos considerado otro dicalcogenuro de metales de transición, la monocapa de 2H-$NbSe_2$. A bajas temperaturas, el $NbSe_2$ se vuelve superconductor, con un estado fundamental que probablemente es un superconductor convencional de onda *s* y singlete de espín. Motivados por la observación de resonancias bosónicas en el espectro de túnel del estado superconductor de la monocapa de 2H-$NbSe_2$ por el grupo de Miguel Ugeda [2], junto con otras características no convencionales en el campo magnético crítico [115, 116], hemos estudiado los modos colectivos superconductores en presencia de una interacción atractiva en un canal de apareamiento secundario no convencional. Hemos encontrado que las fluctuaciones hacia este apareamiento secundario, junto con el acoplo espín-órbita (SOC) en ausencia de inversión espacial, definen un modo de Leggett, que consiste en la fluctuación de la fase relativa entre los parámetros de orden de las bandas separadas por el SOC. Hemos calculado que su energía es menor que el gap de las cuasipartículas en el superconductor, por lo que el modo de Leggett está bien definido y no puede decaer. Además, hemos determinado que deja señales en la función espectral de los electrones, y por lo tanto podría ser detectado en experimentos que midan el espectro túnel. Finalmente, hemos discutido cómo el modo de Leggett es compatible con las resonancias bosónicas observadas en [2]. En conclusión, es necesario considerar los modos colectivos superconductores para analizar las resonancias que aparecen en la corriente túnel.

Finalmente, el tercer capítulo involucra el tema de los estados topológicos en sistemas no cristalinos [4]. En particular, hemos abordado el problema de cómo señalar fases topológicas no triviales en tales sistemas, donde no hay métodos simultáneamente genéricos y eficientes. En este capítulo, hemos introducido el "structural spillage" (derrame estructural), un nuevo indicador

topológico aplicable a sólidos amorfos, que mide las inversiones de bandas entre el sistema no cristalino y un cristal de referencia conocido, y es directamente compatible con cálculos *ab initio* [3]. Debido a las analogías con el “spin-orbit spillage" [117], los correladores extraños [118, 119], y los indicadores de simetrías en promedio [120], el structural spillage puede indicar el estado topológico de un material no cristalino, tal y como demostramos en nuestros cálculos de ligaduras fuertes en modelos basados en Bismuto amorfo. Así, el structural spillage abre la puerta a la clasificación sistemática de sistemas no cristalinos topológicos.

Chapter 1

Nematic charge density wave in 1T-TiSe2

In this chapter, we study the charge density wave (CDW) state in the transition metal dichalcogenide 1T-$TiSe_2$. We present a theory to reconcile conflicting experimental claims regarding the nature of the CDW state in $TiSe_2$, including whether there is a single or multiple CDW transitions and the occasional observation of rotation symmetry breaking. Using a $\boldsymbol{k} \cdot \boldsymbol{p}$ model for monolayer $TiSe_2$ coupled to the CDW order parameter, we show how commonplace electron doping x drives two transitions to threefold (C_3) symmetry breaking states within the CDW. First, for sufficient ellipticity of the conduction bands, as displayed by the realistic band structure of $TiSe_2$, incipient van Hove singularities appear in the CDW conduction bands. Therefore, starting from a C_3-symmetric $3Q$ CDW at low doping, the system is driven to a nematic $3Q$ CDW when the chemical potential crosses the incipient van Hove singularities. Upon further increasing the doping, we find a transition to a $1Q$ stripe state due to the gain of electronic energy. We then show how both stripe and nematic states emerge from a minimal interacting tight-binding model, for both positive and negative initial gaps. Since the doping of most experimental samples cannot be precisely controlled, our theory provides a coherent picture for the long-standing puzzle of the symmetry of the CDW. Finally, we discuss several experimental techniques that could verify our predictions, such as transport, photoemission and tunneling measurements.

1.1 Introduction

In this section, we will first describe CDWs in a general setting, highlighting the role of the charge susceptibility, electron-phonon coupling and electron-electron interactions, as well as the possibility of breaking further spatial symmetries. We will then introduce the general family of transition metal dichalcogenide materials and their different stackings, which lead to a variety of correlated physics. Focusing on 1T-$TiSe_2$ in particular, we will describe the properties of its normal state as well as its CDW, emphasizing the different controversies that have been brought about in this material. Particular attention is paid to the apparently contradictory signatures of the symmetry of the CDW. Motivated by these, we will describe our model and calculations in the next sections.

1.1.1 Charge density waves

CDWs are correlated states where the electronic charge density spontaneously breaks translational symmetry [8, 9]. CDWs were first proposed by Peierls for a quasi-1D 1-band metallic electron system, interacting only via a with weak electron-phonon coupling [39, 40]. If c_k are the electron annihilation operators at momentum $\boldsymbol{k}$, and b_q are the phonon annihilation operators at momentum $\boldsymbol{q}$, the Hamiltonian reads

$$H = H_e + H_{ph} + H_{e-ph} = \sum_k \varepsilon_k c_k^\dagger c_k + \sum_q \Omega_q b_q^\dagger b_q + \sum_{kq} g_{k,k+q} c_k^\dagger c_{k+q} (b_q^\dagger + b_{-q}), \tag{1.1}$$

where ε_k and Ω_q are the electron and phonon dispersions, respectively, and $g_{k,k+q}$ is the electron-phonon coupling. For simplicity, we have left the spin index of the fermion operators implicit.

In a quasi-1D metal, the Fermi surface has large parallel patches connected by twice the Fermi momentum, $\boldsymbol{Q} = 2\boldsymbol{k}_F$. This property, known as Fermi surface nesting, indicates that the system has a tendency towards instabilities with a spatial modulation with wavevector $\boldsymbol{Q}$, since these modulations can open gaps and gain electronic energy. Quantitatively, this tendency is indicated by the electronic charge susceptibility of the system, which measures the energy cost of charge fluctuations around equilibrium. For the noninteracting electronic Hamiltonian H_e, the bare electronic susceptibility reads

$$\chi_0(\boldsymbol{q}, \Omega) = \sum_k \sum_{i\omega} \mathrm{tr}[G_0(\boldsymbol{k}, i\omega) G_0(\boldsymbol{k}+\boldsymbol{q}, i\omega + \Omega)] = \sum_k \frac{f(\varepsilon_{k+q}) - f(\varepsilon_k)}{\Omega - (\varepsilon_{k+q} - \varepsilon_k) + i\eta}, \tag{1.2}$$

where $G_0(\boldsymbol{k}, i\omega) = [i\omega - \epsilon_k]^{-1}$ is the bare electronic Matsubara-Green's function, $f(\varepsilon) = [1 + e^{\epsilon/k_B T}]^{-1}$ is the Fermi function, T is the temperature, $\eta \to 0^+$, and the trace in the first equality is over the internal spin degrees of freedom. The tendency towards charge modulation

of H_e is reflected in the divergence of $\chi_0(\boldsymbol{q},\Omega)$ for $\Omega \to 0$ at the momentum $\boldsymbol{Q} = 2\boldsymbol{k}_F$ at zero temperature. For an infinitesimal electron-phonon interaction $g_{k,k+Q}$ coupling these states, the system undergoes the so-called Peierls instability to a CDW with a charge density[1]

$$\rho(\boldsymbol{r}) = \rho_0(\boldsymbol{r}) + \mathrm{Re}\left[\Delta e^{i\boldsymbol{Q}\cdot\boldsymbol{r}}\right], \tag{1.3}$$

where $\rho_0(\boldsymbol{r})$ is the bare charge density of H_e and $\Delta = \sum_{\boldsymbol{k}} \langle c^\dagger_{\boldsymbol{k}} c_{\boldsymbol{k}+\boldsymbol{Q}} \rangle$ is the order parameter of the CDW. The order parameter Δ is complex in general, indicating the amplitude and the phase of the modulation. Equivalently, its real and imaginary parts correspond to modulations $\cos(\boldsymbol{Q}\cdot\boldsymbol{r})$ and $\sin(\boldsymbol{Q}\cdot\boldsymbol{r})$, respectively, which have a $\frac{\pi}{2}$ phase difference. In certain situations, such as in the presence of inversion symmetry in our example, the real and imaginary parts might transform differently under point group symmetries, and therefore only one of them might be realized. Note that in our quasi-1D scenario with Fermi surface nesting, the modulation wavevector $\boldsymbol{Q} = 2\boldsymbol{k}_F$ is generally incommensurate with the original lattice periodicity.

As a consequence of the charge modulation, a gap is opened in the electronic spectrum rendering the system insulating, and the electron-phonon coupling drives a periodic lattice distortion to screen the charge. The divergent electronic susceptibility guarantees that the gain in electronic energy is always greater than the elastic energy cost of the lattice displacements. In this weak coupling picture, lattice distortion is a byproduct of the electronic charge modulation, which would occur irrespective of the presence of the lattice distortion. The divergence is gradually smoothed with increasing temperature, which defines a critical temperature T_{CDW} above which the CDW is no longer stable. Above T_{CDW}, due to the electron-phonon coupling, the frequency Ω_q of the phonon mode that freezes in the CDW is renormalized around the momentum $\boldsymbol{Q}$, exhibiting a minimum known as Kohn anomaly [17]. At T_{CDW}, $\Omega_{\boldsymbol{Q}}$ vanishes, giving rise to the static lattice distortion in the CDW.

CDWs have signatures in several experimentally observable quantities. The real-space charge modulation can be directly measured with scanning tunneling microscopy (STM). New Bragg peaks at $\boldsymbol{Q}$ appear in neutron and X-ray diffraction, as well as in the Fourier transform of STM maps [121]. The change in the electronic spectrum and the transfer of spectral weight between states separated by momentum $\boldsymbol{Q}$ can be observed with angle-resolved photoemission spectroscopy (ARPES) [122–127]. The softening of the phonon mode can be observed by X-ray scattering [128] and Raman spectroscopy [129]. Furthermore, the CDW transition can leave fingerprints in the transport properties of the system, such as a change in the slope of the temperature-dependent electrical resistivity [130, 131].

[1] Eq. (1.3) only displays the modulation with the lowest order harmonic $\boldsymbol{Q}$, but modulations with $\boldsymbol{Q} + \boldsymbol{G}$ will appear for the reciprocal lattice vectors $\boldsymbol{G}$ of the original unit cell.

In practice, the idealized divergence of the electronic susceptibility in a 1D crystal is smoothed by several effects beyond temperature, such as deviation from perfect nesting, disorder-induced scattering, electron-electron interactions, etc. [34]. This is the case of 2D and 3D systems, where Fermi surface nesting is much weaker. For a CDW to occur in these cases, the electron-phonon coupling has to be greater than a given value. Therefore, away from the ideal weak-coupling limit, the states far from the Fermi level and the momentum dependence of the electron-phonon coupling become important [34, 35, 132]. The relative importance of the Fermi surface drops compared to the whole band contribution, and the nesting of the Fermi surface is no longer a good indicator of the presence of a CDW instability nor predictive of its wavevector $\boldsymbol{Q}$. Indeed, the nesting of the Fermi surface only measures the peaking of the imaginary part of the static susceptibility

$$\lim_{\Omega\to 0}\frac{1}{\Omega}\chi''(\boldsymbol{q},\Omega) = \pi\sum_{\boldsymbol{k}}\delta\left(E_F-\varepsilon_{\boldsymbol{k}}\right)\delta\left(E_F-\varepsilon_{\boldsymbol{k}+\boldsymbol{q}}\right), \tag{1.4}$$

where E_F is the Fermi energy. However, what determines the instability is the real part of the static susceptibility $\chi'(\boldsymbol{q},\Omega=0)$ [34], which involves the energy differences $\varepsilon_{\boldsymbol{k}+\boldsymbol{q}}-\varepsilon_{\boldsymbol{k}}$ (see Eq. (1.2)). This becomes even more important in multiband systems due to the interband transitions[2]. Furthermore, in the strong-coupling case, where the instability is of the electron-phonon-coupling driven Jahn-Teller type, nonlinear lattice effects become important [132]. Above the critical temperature, fluctuation-induced short-range order is established, which already affects the electronic spectrum; for example, partial gaps open [35]. The long-range coherence is only reached at T_{CDW}. Moreover, strong-coupling CDWs tend to lock into the lattice and be commensurate [35].

Besides electron-phonon coupling, electron-electron interactions can also drive a CDW. The paradigmatic model is the excitonic insulator instability of semiconducting or semimetallic systems with a small indirect bandgap or overlap, respectively [43–45]. In this case, interband Coulomb interaction might be attractive in the CDW channel at the momentum $\boldsymbol{Q}$ connecting the electron and hole pockets. This scenario shares analogies with the BCS theory of superconductivity that will be described in Chapter 2, where the two components of the Nambu spinors are the electron and hole bands here. Consequently, in general there is no particle-hole symmetry, since the masses and anisotropies of the electron and hole bands can be different, nor $U(1)$ symmetry, which would represent an artificial charge conservation in the electron and hole pockets separately. Therefore, under realistic conditions the instability is no longer weak-coupling as in the BCS theory, since there is no divergent susceptibility. Nevertheless, an analogous gap equation can still be written down. Instead of Cooper pairs, it is electron-hole pairs, or excitons, which condense in a coherent state. While in simple models a collective mode of excitonic or plasmonic nature is predicted to

[2]Furthermore, in multiband systems, matrix elements of the overlap between states enter in the susceptibility.

soften in the transition [45, 133], this mode can be Landau damped if decay into single-particle excitations is allowed [134, 135]. Nevertheless, electron-phonon coupling hybridizes this mode with a certain phonon, which should indeed become soft [35, 133].

Finding excitonic insulators in real materials is hard since there is no symmetry distinction with an electron-phonon driven CDW [35]. Indeed, since electron-phonon coupling is always present, pure excitonic insulators are arguably thought experiments [34]. Nevertheless, the question of the contribution of electron-electron interactions to the stability of a CDW is well-defined. Other examples where electron-electron interactions drive CDWs are Wigner crystals [41, 42, 136] and 2D metals with van Hove singularities close to the Fermi level [137–139].

Regardless of their origin, a new feature appears in CDWs in 2D and 3D. Due to the point group symmetries, there might be several symmetry-equivalent momenta $\boldsymbol{Q}$ corresponding to a given charge modulation. For instance, we will see that the CDW in monolayer 1T-$TiSe_2$ corresponds to a modulation with momenta $\boldsymbol{Q}_i = \Gamma M_i$, and there are three M_i points in its hexagonal Brillouin zone related by threefold (C_3) symmetry. The same scenario applies to the CDW in kagome AV_3Sb_5 metals [48–50]. In these cases, the CDW has a multicomponent order parameter, where each component is related to the amplitude of the modulation in each of the symmetry-equivalent $\boldsymbol{Q}$. The new degrees of freedom in multi-Q CDWs associated to the relative values of the amplitudes at the different $\boldsymbol{Q}$ allow the CDW to break additional spatial symmetries beyond the translational symmetry. In the case of monolayer 1T-$TiSe_2$, when the amplitudes of the three modulations are the same, the C_3 symmetry is preserved. When any of the amplitudes becomes inequivalent, the C_3 symmetry is broken in the CDW state. In this Chapter, we will study how electron doping induces transitions from the symmetric CDW to C_3-symmetry-broken CDWs. This situation is reminiscent of the kagome AV_3Sb_5 metals, where a nematic CDW has also recently been discovered [48–50].

1.1.2 Transition metal dichalcogenides

The material we focus on this Chapter, $TiSe_2$, is an example of a transition metal dichalcogenide (TMD). TMDs are layered materials with chemical formula MX_2, where M is a transition metal and X is a chalcogen, typically S, Se or Te [15, 16]. The transition metal commonly belongs to the groups IV (e.g. Ti), V (e.g. Nb, Ta) or VI (e.g. Mo, W). Each "unit" Van der Waals layer is formed by a layer of the transition metal sandwiched between two layers of the chalcogen. Typically, the individual layers of each element form a triangular lattice with threefold rotational symmetry, although they can also be distorted. Depending on the relative positions of the individual layers inside the unit layer and the stacking of different unit layers, TMDs display different polytypes [140] (see Fig. 1.1). For example, in the octahedral 1T polytype the atoms in the three individual layers are located in the three different Wyckoff positions forming a triangular lattice (see Fig. 1.2(a)). Namely, if we label these three positions as a, b, c, and we use lowercase letters for the chalcogens and capital

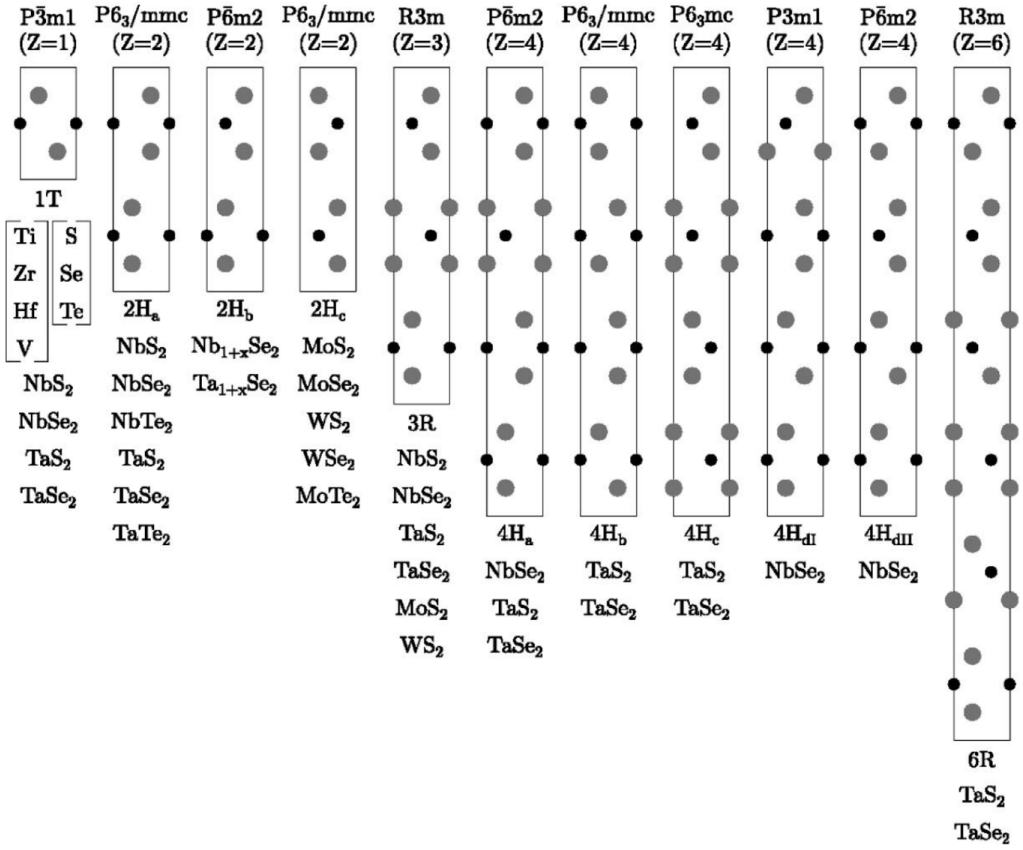

FIGURE 1.1: Schematic stackings of distinct TMD polytypes, indicating their space group, number of layers in the unit cell, and representative TMDs crystallizing in each polytype. Extracted from Ref. [140].

letters for the transition metal, the stacking is *aBc*. The bulk unit cell consists of one layer. $TiSe_2$ crystallizes in the 1T polytype. Another polytype that we will study throughout this thesis is the trigonal prismatic $2H_a$ polytype, which is the most stable polytype of $NbSe_2$ and has two layers per unit cell in the bulk, whose stacking is *aBa cBc* (see Fig. 1.2(b)).

The different combinations of transition metals and polytypes give rise to a variety of correlated states, such as CDWs, superconductivity, Mott insulators, etc., which have been under scrutiny for decades [12–16, 35]. Moreover, their study in the 2D limit has also been allowed thanks to the development of a variety of synthesis methods [15, 16]. This Chapter is devoted to the study of the CDW in $TiSe_2$, while Chapter 2 will analyze the superconductivity in monolayer $NbSe_2$.

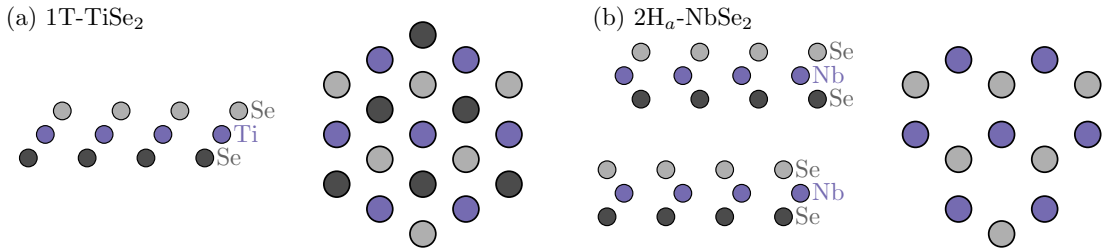

FIGURE 1.2: Side and top views of the lattices of (a) 1T-$TiSe_2$ and (b) $2H_a$-$NbSe_2$. Only the top view of the top layer of $2H_a$-$NbSe_2$ is shown for visualization purposes.

1.1.3 $TiSe_2$: state of the art

Normal state

The transition metal dichalcogenide $TiSe_2$ crystallizes in the octahedral 1T polytype (see Fig. 1.2(a)). It has space group $P\bar{3}m1$ (#164) and point group D_{3d} in both monolayer and bulk samples, whose generators are the out-of-plane threefold rotational symmetry C_3, the in-plane twofold rotational symmetry C_{2x}, and the intralayer inversion symmetry i (see Appendix 1.A for the group theory analysis). The band structure near the Fermi level of monolayer $TiSe_2$ features an electron pocket at the three M points and two hole pockets located at Γ [141], as shown in Fig. 1.3. The electron pockets derive from Ti d orbitals and have M_1^+ symmetry, so they are even under i and C_{2x}. The hole pockets derive from Se p orbitals and transform as Γ_3^-, which is odd under the intralayer inversion. Spin-orbit coupling (SOC) splits the two valence bands at Γ, where they are degenerate in its absence (see Fig. 1.3(c,d)). The electron and hole pockets are nearly energetically aligned, but the presence of a small indirect gap ($E_g > 0$) or overlap ($E_g < 0$) is still debated, especially in the bulk [126, 127, 142–144]. Bulk $TiSe_2$ displays a similar band structure, with the lowest-lying electron pockets located at the L points and having L_1^+ symmetry instead [145, 146]. Below but close to the Γ_3^- valence bands, bulk $TiSe_2$ also features Γ_2^- and A_3^- hole pockets at the Γ and A points, respectively. While in principle these bands only play a spectator role in the CDW, they might be have an effect in certain experiments.

Several reasons lie behind the semiconductor versus semimetal controversy. First of all, uncontrolled electron doping is ubiquitously found in $TiSe_2$ samples due to Se vacancies and Ti interstitials [131, 147, 148]. Consequently, the bottom of the conduction bands is usually slightly filled, and can be observed in ARPES. Together with the thermal broadening, which is unavoidable when measuring the high-temperature normal state, this makes the gap or overlap difficult to resolve. Moreover, due to the strong-coupling nature of the CDW, the gapped spectrum of the CDW phase can extend above T_{CDW} [144, 149, 150]. Finally, band structure calculations cannot help to solve this issue, since the significant correlations make the computed gap strongly depend

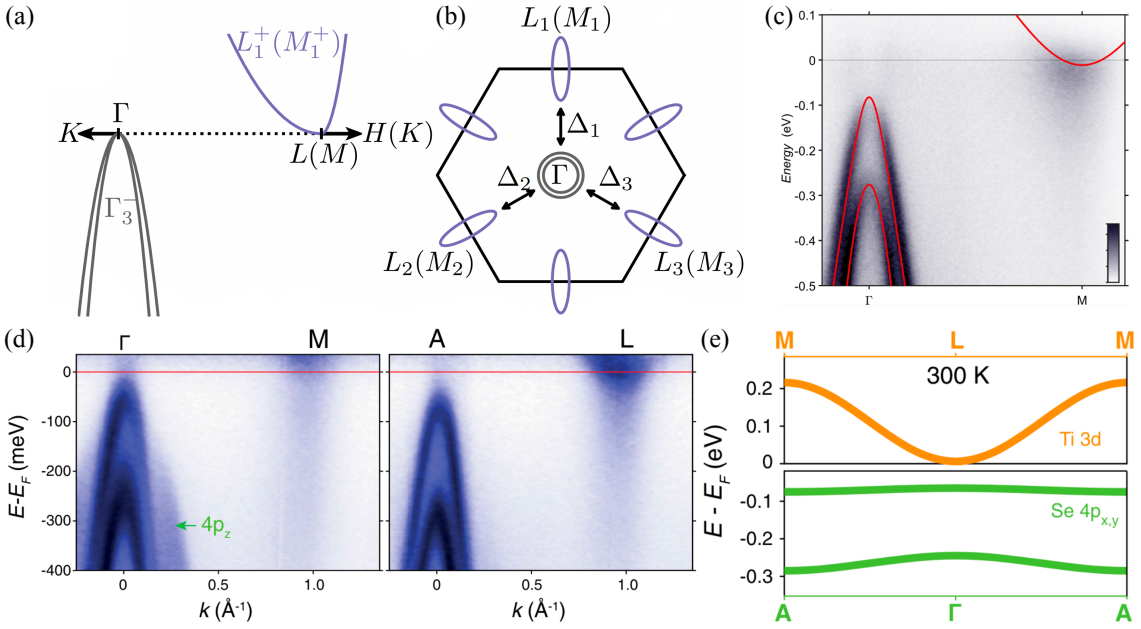

FIGURE 1.3: (a) Low energy band structure without SOC and symmetry labels for the bands for the bulk (notation in parenthesis for the monolayer) (obtained with model (1.26)). (b) Fermi surface sketch of the normal state in the semimetallic case without SOC. The order parameter $\vec{\Delta}$ coupling conduction and valence bands is also shown. (c) ARPES band structure of monolayer $TiSe_2$ in the normal state at $T = 265$K (extracted from Ref. [127]). (d) ARPES band structure of bulk $TiSe_2$ in the normal state at $T = 300$K (extracted from Ref. [126]). (e) Sketch of the k_z dispersion in the normal state of bulk $TiSe_2$ (extracted from Ref. [126]).

on the exchange-correlation functional used in density functional theory (DFT) calculations [146], or other details in GW extensions [151–153]. Nevertheless, recent ARPES experiments, which have simultaneously measured the Γ and L bands at room temperature, have concluded that, when appropriately accounting for the thermal broadening, $TiSe_2$ is semiconducting with an indirect gap of $E_{\text{gap}} \sim 80$meV in both bulk and monolayer [126, 127] (see Figs. 1.3(c,d)). This is consistent with Ref. [142], which further electron doped the system to fully resolve the conduction band and determined an indirect gap as long as the doping does not strongly renormalize the gap. The narrow gap scenario is also supported by the fit to the temperature-dependent resistivity [131]. Nevertheless, given that the debate remains unresolved [144], in this chapter we will consider both positive and negative gaps in the normal state, and show that this does not qualitatively change our conclusions.

Charge density wave state

As the temperature is decreased, the L_1^- phonon of bulk $TiSe_2$ softens [128], and a commensurate $2 \times 2 \times 2$ CDW develops below $T_{\text{CDW}}^{3D} \sim 200$K [35, 154] (see Fig. 1.4). The charge

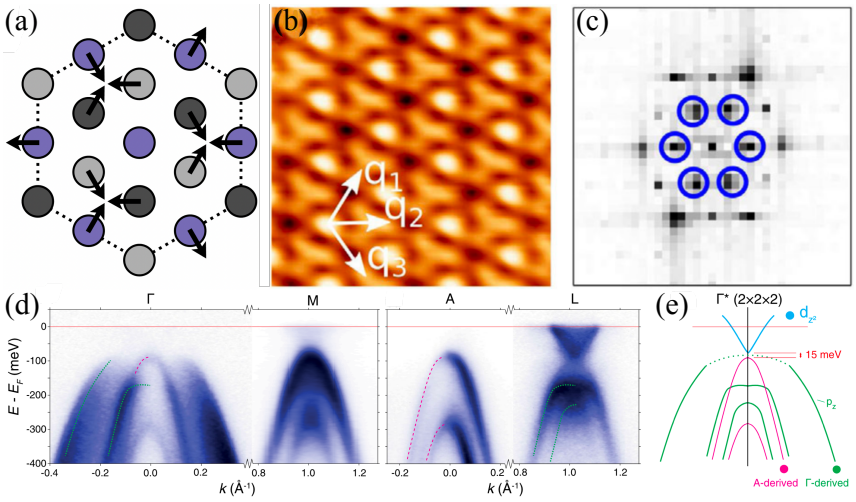

FIGURE 1.4: (a) Sketch of the in-plane atomic displacements involved in the $TiSe_2$ CDW. (b) Real space STM image of the surface of bulk $TiSe_2$ in the CDW state (adapted from Ref. [114]). (c) Fourier transform of (b) highlighting the Bragg peaks associated to the CDW (adapted from Ref. [114]). (d) ARPES band structure of bulk $TiSe_2$ in the CDW state (extracted from Ref. [126]). (e) Sketch of the low-energy band structure in the CDW state of bulk $TiSe_2$ (extracted from Ref. [126]).

modulation can be observed in STM as a pattern where charge is concentrated in one of each four top Se atoms (see Figs. 1.4(b,c)). This distortion, with momenta $\boldsymbol{Q} = \Gamma L_i$ and symmetry L_1^-, couples the Γ_3^- and L_1^+ hole and electron pockets, causing a repulsion between them that can be observed in ARPES (see Figs. 1.4(d,e)). In the CDW, the L point backfolds to Γ, as evidenced by the observation of the valence band replica at L in ARPES (see Fig. 1.4(d)). Analogously, in monolayer $TiSe_2$, it is the M_1^- phonon coupling the Γ_3^- and M_1^+ bands that condenses. The critical temperature in the monolayer depends on the substrate [155], likely due to Ti-Se bond length and Se vacancy concentration differences [156], but is typically $T_{\mathrm{CDW}}^{2D} \sim 230$K.

Electron doping and pressure undermine the commensurate CDW, decreasing its critical temperature until it dies in a putative quantum critical point at $x_{\mathrm{CDW}} \sim 0.06\mathrm{e/f.u.}$ or $p_{\mathrm{CDW}} \sim 3\mathrm{GPa}$ [21–25, 141, 156–159]. Before the commensurate CDW is completely suppressed, there appears an incommensurate CDW phase at intermediate temperature, which smoothly transitions to the commensurate phase at lower temperature [23, 25, 156, 157]. Interestingly, a superconducting dome is found close to the putative quantum critical point, where the discommensurations appear at low temperature [21–25, 27, 28] (see Fig. 1.5). As predicted by Mcmillan [8, 13, 18], the incommensurate CDW forms commensurate domains separated by sharp domain walls where electrons tend to accumulate, which can drive the superconductivity [23, 24, 26, 156, 157, 160, 161]. In order to fully understand these interesting phases, first it is necessary to study the parent commensurate CDW state, which, as we discuss below, is the source of several unresolved debates.

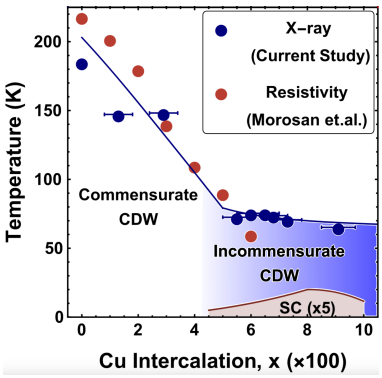

FIGURE 1.5: Sketch of the temperature-doping phase diagram of bulk $TiSe_2$. Extracted from Ref. [25].

To this end, in this Thesis we focus on the zero-pressure, low-doping ($x < x_{\mathrm{CDW}}$) regime, where the CDW is commensurate.

Due to the band structure reminiscent of a model excitonic insulator, the microscopic mechanism driving the CDW has been discussed at length, but lacks an agreed solution up to date. Both the strong electron-phonon coupling Jahn-Teller-like picture [128, 162–164] and the excitonic insulator scenario [123, 133, 159, 165] have been proposed. Both interactions are sizeable and could in principle drive the CDW separately or jointly [166, 167]. As explained in Section 1.1.1, differentiating between both mechanisms is hard, since the majority of ground state observables are analogous in both. Moreover, due to the mentioned difficulties in appropriately modeling the normal state, the quantitative agreement between a given theory and experiment, for example in the critical temperature or doping, cannot be taken as definitive proof of any scenario. Nevertheless, due to the different timescales associated with the dynamics of phonons and excitons, out-of-equilibrium experiments point to a sizeable contribution of both interactions [168–172]. These experiments indicate that the strong electron-phonon coupling governs the in-plane short-range order, whereas excitonic correlations set the out-of-plane long-range coherence. Indeed, this is consistent with the fact that, in bulk $TiSe_2$, in-plane order sets at a temperature $\sim T^{2D}_{\mathrm{CDW}}$, and out-of-plane coherence is then developed at T^{3D}_{CDW} [173].

Several other controversies regarding the CDW properties of $TiSe_2$ have arisen. Two puzzles originated from the temperature-dependent electrical resistivity ρ. Traditionally grown samples using the chemical vapor transport method usually display a resistivity as the black line in Fig. 1.6(a), with a low-temperature resistivity saturating at a finite value and with a positive slope $\left(\frac{d\rho}{dT}(T \to 0) > 0\right)$, typical of a metallic ground state [131, 147, 154, 174]. However, this arises from the native electron doping induced in this growth process [131, 147, 174]. Indeed,

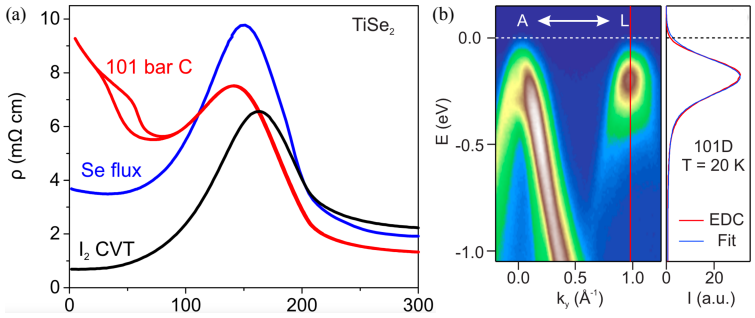

FIGURE 1.6: (a) Resistivity as a function of temperature for bulk $TiSe_2$ grown by three different techniques. (b) ARPES spectrum of pressure-grown bulk $TiSe_2$ (correspoding to the red line in (a)) in the CDW state at $T = 20$K, showing the backfolded valence band in L but without sign of the electron pocket. Extracted from Ref. [147].

Ref. [147] has recently achieved stoichiometric samples with insulating low-temperature resistivity $\left(\frac{d\rho}{dT}(T \to 0) < 0\right)$ (red line in Fig. 1.6(a)) and, correspondingly, with the conduction band unoccupied, as in Fig. 1.6(b). ARPES also resolves a gap in the low-temperature CDW, with the smallest gap now occurring between the L and A points [126] (see Figs. 1.4(d,e)). Surprisingly, while the latter is uncoupled to the CDW, this gap is smaller than the normal state gap at room temperature [126]. The reason might be a trivial temperature renormalization of the gap due to charge transfer between Ti and Se. The second question posed by the resistivity was the origin of the peak in the resistivity at $T^* \sim 150 - 165$K. It is now understood as arising from a crossover from electron-dominated transport at low-temperature, to a high-temperature regime ruled by thermally-activated holes [131]. Moreover, the mobility of the carriers increases as going away from T_{CDW}, where the scattering with CDW fluctuations is the strongest [174]. Actually, both the peak height and T^* tend to anticorrelate with the a amount of extrinsic doping [131, 154].

Symmetry of the CDW

An arguably more fundamental controversy still unresolved up to date involves the symmetry of the CDW. As explained above, the primary CDW order parameter $\vec{\Delta}$ is agreed to have L_1^- symmetry, as established by neutron diffraction [154] and X-ray [175] experiments (in the monolayer, the symmetry is M_1^- [176]). This modulation has momenta $\boldsymbol{Q}_i = \Gamma L_i$ in the bulk ($\boldsymbol{Q}_i = \Gamma M_i$ in the monolayer). Since there are three inequivalent L (M) points, $\vec{\Delta} = (\Delta_1, \Delta_2, \Delta_3)$ has three components representing the amplitudes for the three $\boldsymbol{Q}_i$ modulation vectors. These experiments are compatible with a C_3-symmetric $3Q$ configuration of $\vec{\Delta}$, with the three components having equal magnitude, $\vec{\Delta} = (\Delta, \Delta, \Delta)$. This configuration agrees with DFT results at stoichiometry [141, 177].

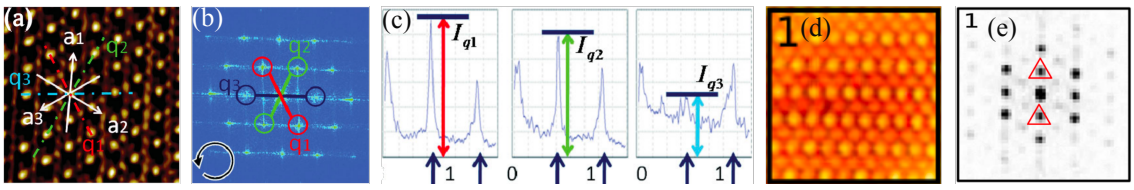

FIGURE 1.7: (a) Real space STM image of the surface of bulk $TiSe_2$ in the CDW state (extracted from Ref. [53]). (b) Fourier transform of (a) highlighting the Bragg peaks associated to the CDW (extracted from Ref. [53]). (b) Fourier transform of (a) along the three $\Gamma\bar{M}$ directions, highlighting the different intensity of the three CDW Bragg peaks indicating broken C_3 symmetry (extracted from Ref. [53]). (d) Real space STM image of the surface of bulk Cu-doped $TiSe_2$ in the CDW state (extracted from Ref. [56]). (e) Fourier transform of (d) highlighting the only nonzero CDW Bragg, which indicates a $1Q$ stripe CDW (extracted from Ref. [56]).

However, a few STM experiments in the surface of bulk $TiSe_2$ are incompatible with this C_3-symmetric $3Q$ state [52–54]. Indeed, Refs. [52–54] observed domains where the charge modulation has a preferred direction, which is clearly revealed in the different intensity of the three CDW Bragg peaks at the $\Gamma\overline{M}_i$ momenta of the surface Brillouin zone (see Figs. 1.7(a-c)). Two of the intensities of the Bragg peaks are similar, and the other is significantly smaller ($\Delta_1 \ll \Delta_2 \sim \Delta_3$). Therefore, the C_3 symmetry is broken in the CDW state of these samples, at least on the surface. This contrasts with other STM experiments, where C_3 symmetry is preserved [114]. The situation was further complicated by the STM report of coexisting domains of C_3-symmetric $3Q$ CDW and $1Q$ stripe CDW in Cu doped samples [56], the latter having only one nonzero CDW Bragg peak (see Figs. 1.7(d-e)).

A possible explanation of Refs. [52–55] proposed by Refs. [178–182] was a second transition to a chiral CDW with space group $C2$, breaking all mirrors, inversion and C_3 symmetries. If only the L_1^- order parameter $\vec{\Delta}$ condenses, an interlayer inversion symmetry is always present. Therefore, the chiral CDW needs the condensation of two phonons, which Refs. [55, 178–182] propose to be the L_1^- and L_2^+ phonons. While Refs. [55, 182] provided X-ray and thermodynamic signatures of a second transition to a chiral CDW, the X-ray evidence has been contested and argued to be compatible with the achiral C_3-symmetric $3Q$ CDW [183, 184]. Moreover, the temperature where the transition to the chiral CDW was proposed coincides with the onset of a symmetry-preserving out-of-plane displacement of the Se atoms [184], which could explain the thermodynamic anomalies. Also, since the STM experiments [52–54] probe the surface, they are insensitive to the presence or absence of bulk inversion symmetry, and can only establish the breaking of the rotational symmetry. An alternative proposal of a chiral and C_3-symmetry breaking CDW was put forward by Ref. [185], whose DFT calculations for pristine bulk $TiSe_2$ predict the mixing of L_1^- and M_1^- phonons, leading to a space group $C2$. Explaining the variability of the CDW symmetry observed in STM remains a challenge. We point out that the debate regarding

the breaking of inversion symmetry only applies to bulk $TiSe_2$. The C_3-symmetric $3Q$ CDW in monolayer $TiSe_2$ already breaks inversion and mirror symmetries due to the order parameter being M_1^-.

Recently, Refs. [186, 187] have measured the circular photogalvanic effect (CPGE) in bulk $TiSe_2$. CPGE is a nonlinear optical effect where a different DC current is generated by right and left circularly polarized light. It is useful to probe the symmetries of the system, since the CPGE is nonzero only in gyrotropic systems, which are noncentrosymmetric. In particular, the longitudinal CPGE is finite only in chiral materials, while a nonzero transverse CPGE requires the breaking of C_3 symmetry. As other techniques, the CPGE can only probe the average symmetry of the region spanned by the laser spot; if smaller domains break the symmetry but restore it on average, the CPGE is blind to the symmetry breaking. With this in mind, we now describe the experiments of Refs. [186, 187]. In the absence of training, the longitudinal CPGE vanishes in both the normal and the CDW states of $TiSe_2$, indicating the presence of inversion symmetry on average. Refs. [186, 187] have also measured the CPGE in trained samples. For that, starting at high temperature in the normal state, they train the system with circular light above a threshold intensity while cooling to low temperatures. Then, after removing the training light, the longitudinal CPGE is nonzero, indicating a chiral state. Indeed, the sign of the CPGE current can be controlled by the left or right-handed helicity of the training light. Moreover, when heating the system, the nonzero CPGE persists until a temperature T_{CPGE} about 20K lower than T_{CDW}. On the other hand, the transverse CPGE always vanishes, which indicates the presence of C_3 symmetry on average. The resulting CDW state after training is thus chiral, but preserves C_3 symmetry, which points out that the physics behind the CPGE experiments [186, 187] with training is different than that of the STM experiments [52–54, 56]. There have been a few proposals to explain the CPGE experiments [186, 187], but no consensus has been reached. We will shortly discuss these and propose a new interpretation of the CPGE results in the discussion Section 1.6.3.

In this thesis we focus on the equilibrium CDW of $TiSe_2$ and the C_3-symmetry breaking observed in STM. We provide an alternative explanation for the C_3-symmetry breaking which requires only the standard L_1^- order parameter $\vec{\Delta}$ and does not necessarily involve the breaking of inversion symmetry. Such an spontaneous electronic nematic order has also been observed with STM in kagome AV_3Sb_5 metals [48–50] and moiré heterostructures [188, 189]. In particular, we show that electron doping of the CDW of monolayer $TiSe_2$ drives further electronic instabilities to C_3-breaking states, first in the form nematic $3Q/2Q$ CDW states consistent with Refs. [52–54], and then as a $1Q$ stripe CDW at further doping, reminiscent of Ref. [56]. The uncontrolled native doping ubiquitously found in $TiSe_2$ samples can therefore explain the variability of symmetries observed. Our theory pertains to the low-doping case only, $x < x_{\text{CDW}} \sim 0.06\text{e/f.u.}$, where the CDW remains commensurate. We will discuss how our theory could be generalized to address

bulk $TiSe_2$ and the coupling to circularly polarized light.

1.2 k.p model

In this section, we construct a continuum $\boldsymbol{k}\cdot\boldsymbol{p}$ model that reproduces the low-energy valence and conduction bands of $TiSe_2$, constrained by the symmetries of the high temperature phase (space group $P\bar{3}m1$, point group D_{3d}). The group-theoretical analysis needed to construct the model can be found in Appendix 1.A. Then, we add the symmetry-allowed coupling to the mean-field order parameter of the CDW, and analyze the ground state as a function of different parameters.

1.2.1 Monolayer model

p hole bands at Γ

We begin by considering the continuum $\boldsymbol{k}\cdot\boldsymbol{p}$ model for monolayer $TiSe_2$. Its low-energy band structure is sketched in Fig. 1.3. The two band eigenstates at Γ transform as Γ_3^-, which corresponds to the E_u irreducible representation (irrep) of the little group D_{3d}. We define their annihilation operators $p=\{p_x,p_y\}$. We can now classify their Hermitian fermion bilinears $p^\dagger p$ according to symmetry as :

$$\Gamma_1^+\ (A_{1g}) \to p_x^\dagger p_x + p_y^\dagger p_y, \tag{1.5}$$

$$\Gamma_2^+\ (A_{2g}) \to -i\left(p_x^\dagger p_y - p_y^\dagger p_x\right), \tag{1.6}$$

$$\Gamma_3^+\ (E_g) \to \left\{p_x^\dagger p_x - p_y^\dagger p_y, -\left(p_x^\dagger p_y + p_y^\dagger p_x\right)\right\}, \tag{1.7}$$

where the notation in parenthesis corresponds to the little group irreps. Now, crystal momentum $\boldsymbol{k}=(k_x,k_y)$ transforms as E_u in D_{3d}, and therefore its quadratic combinations transform as:

$$A_{1g} \to k_x^2+k_y^2 := k^2, \tag{1.8}$$

$$E_g \to \left\{k_x^2-k_y^2, -2k_xk_y\right\}, \tag{1.9}$$

where the A_{2g} combination $k_xk_y - k_yk_x$ vanishes since it is antisymmetric. Using the multiplication rules of Appendix 1.A.2, the second quantized Hamiltonian $\hat{H}^0_{pp} = \sum_k p^\dagger H^0_{pp}(\boldsymbol{k}) p$ to quadratic order in momentum reads as:

$$H^0_{pp}(\boldsymbol{k}) = \begin{pmatrix} a_p k^2 + b_p(k_x^2-k_y^2) & b_p 2k_xk_y \\ b_p 2k_xk_y & a_p k^2 - b_p(k_x^2-k_y^2) \end{pmatrix}, \tag{1.10}$$

where b_p induces a splitting between the two isotropic hole bands at nonzero momentum:

$$\varepsilon^0_{p\pm}(\boldsymbol{k}) = (a_p \pm b_p)k^2, \tag{1.11}$$

and parametrizes the orbital texture of their eigenvectors:

$$p^0_+(\boldsymbol{k}) = \frac{k_x}{k}p_x + \frac{k_y}{k}p_y, \tag{1.12}$$

$$p^0_-(\boldsymbol{k}) = -\frac{k_y}{k}p_x + \frac{k_x}{k}p_y. \tag{1.13}$$

Ab initio calculations [145] show that the top valence band has p_x character along the ΓM line, i.e., it is odd under the mirror m_x along $k_x = 0$ and becomes M_1^- at M, which sets $b_p < 0$. We take the value $b_p/a_p = 0.25$ from Refs. [125, 141]. While we will not consider SOC in our calculations, here we write the hole Hamiltonian with SOC for completeness. The Pauli matrices σ corresponding to the spin degree of freedom transform as $\sigma_0 \to A_{1g}$, $\sigma_z \to A_{2g}$, $\{\sigma_x, \sigma_y\} \to E_g$, with the latter two being time-reversal odd. To lowest order in momentum, the SOC between the hole bands is therefore $\lambda\tau_y\sigma_z$, where τ_y is the Pauli matrix in the orbital $\{p_x, p_y\}$ space corresponding to the combination (1.6). The Hamiltonian with SOC can thus be separated in spin up and down components with opposite coupling $\pm\lambda$, giving rise to a splitting between the two valence bands:

$$\varepsilon^{0\lambda}_{p\pm\sigma}(\boldsymbol{k}) = a_p k^2 \mp \sigma\sqrt{\left(b_p k^2\right)^2 + \lambda^2}, \tag{1.14}$$

with $\sigma = \pm$ for spin up/down.

d electron bands at *M*

Now, we derive the Hamiltonian of the three electron pockets at the M points, which transform as M_1^+ (A_{1g} of the little group C_{2h}). We define their annihilation operators $d = \{d_1, d_2, d_3\}$, where d_i represents the band at $\boldsymbol{M}_i$, with (see Fig. 1.3(b)):

$$\boldsymbol{M}_1 = \tfrac{2\pi}{\sqrt{3}}(0, 1), \tag{1.15}$$

$$\boldsymbol{M}_2 = \tfrac{2\pi}{\sqrt{3}}(-\tfrac{\sqrt{3}}{2}, -\tfrac{1}{2}), \tag{1.16}$$

$$\boldsymbol{M}_3 = \tfrac{2\pi}{\sqrt{3}}(\tfrac{\sqrt{3}}{2}, -\tfrac{1}{2}). \tag{1.17}$$

In the normal state, the three electron bands are uncoupled. Therefore, we can derive the energy of, for example, d_1, and then obtain the dispersions of d_2 and d_3 by applying the threefold rotational symmetry connecting the three M points. The little group C_{2h} of $\boldsymbol{M}_1$ is generated by $\{C_{2x}, i\}$,

with irreps $\{A_{1g}, A_{1u}, A_{2g}, A_{2u}\}$. The bilinear $d_1^\dagger d_1$ transforms as A_{1g}. The crystal momenta transform as $k_x \to A_{1u}$ and $k_y \to A_{2u}$, and therefore their quadratic combinations can be classified as $k_x^2 \to A_{1g}$, $k_y^2 \to A_{1g}$, and $k_x k_y \to A_{2g}$, all of them being even under time-reversal symmetry (TRS). Therefore, the dispersion of the d electron bands reads:

$$\varepsilon_{d1}(\boldsymbol{k}) = a_{d\perp}k_x^2 + a_{d\parallel}k_y^2 = a_d(k_x^2 + k_y^2) + b_d(k_x^2 - k_y^2), \tag{1.18}$$

$$\varepsilon_{d2}(\boldsymbol{k}) = a_d(k_x^2 + k_y^2) + b_d[-\tfrac{1}{2}(k_x^2 - k_y^2) - \sqrt{3}k_x k_y], \tag{1.19}$$

$$\varepsilon_{d3}(\boldsymbol{k}) = a_d(k_x^2 + k_y^2) + b_d[-\tfrac{1}{2}(k_x^2 - k_y^2) + \sqrt{3}k_x k_y], \tag{1.20}$$

where we have defined the average curvature $a_d = \frac{1}{2}(a_{d\perp} + a_{d\parallel})$ and the ellipticity $b_d = \frac{1}{2}(a_{d\perp} - a_{d\parallel})$. Since the electron pockets have the long axis along the ΓM direction, $b_d > 0$. DFT calculations predict a large ellipticity value, $b_d/a_d \sim 0.87$ [141, 149, 159], which we take as the realistic value for the rest of this work. This value is also within the range of the experimentally reported conduction band masses (see Table 1.C.1). The second quantized Hamiltonian $\hat{H}^0_{dd} = \sum_{\boldsymbol{k}} d^\dagger H^0_{dd}(\boldsymbol{k}) d$ corresponding to the d electron pockets is then:

$$H^0_{dd}(\boldsymbol{k}) = \mathrm{diag}\left[\varepsilon_{d,1}(\boldsymbol{k}), \varepsilon_{d,2}(\boldsymbol{k}), \varepsilon_{d,3}(\boldsymbol{k})\right]. \tag{1.21}$$

The Hamiltonian H^0_{dd} could have also been easily obtained using the multiplication rules in the extended point group of Appendix 1.A.2. The extended point group is a convenient approach to deal with the symmetry properties of CDWs [190–192]. The extended point group is the symmetry group that includes the original point group of the normal state and the translations that are broken by the CDW. For monolayer $TiSe_2$, the extended point group is the symmetry group of a 2×2 supercell in the normal state. It has irreps $\Gamma_1^\pm$, $\Gamma_2^\pm$ and $\Gamma_3^\pm$ that do not involve translations, and irreps $M_1^\pm$ and $M_2^\pm$ that characterize the observables with a $\boldsymbol{Q} = \Gamma M$ modulation. See Appendix 1.A.2 for more details. To rederive the conduction band Hamiltonian H^0_{dd}, we use the fact that the $d^\dagger d$ bilinears transform under the symmetry of the extended point group as

$$\Gamma_1^+ \left(A_{1g}\right) \to d_1^\dagger d_1 + d_2^\dagger d_2 + d_3^\dagger d_3, \tag{1.22}$$

$$\Gamma_3^+ \left(E_g\right) \to \left\{ d_1^\dagger d_1 - \frac{1}{2}d_2^\dagger d_2 - \frac{1}{2}d_3^\dagger d_3, \frac{\sqrt{3}}{2}\left(d_2^\dagger d_2 - d_3^\dagger d_3\right) \right\}, \tag{1.23}$$

$$M_1^+ \to \left\{ d_2^\dagger d_3 + d_3^\dagger d_2, d_3^\dagger d_1 + d_3^\dagger d_1, d_1^\dagger d_2 + d_2^\dagger d_1 \right\}, \tag{1.24}$$

$$M_2^+ \to i\left\{ d_2^\dagger d_3 - d_3^\dagger d_2, d_3^\dagger d_1 - d_3^\dagger d_1, d_1^\dagger d_2 - d_2^\dagger d_1 \right\}. \tag{1.25}$$

The combinations of (1.22) and (1.23) with the crystal momentum terms (1.8) and (1.9), respectively, lead to the Hamiltonian H^0_{dd} (1.21). We note that a $\boldsymbol{k}$-independent SOC does not affect the

electron pockets in the $\boldsymbol{k}\cdot\boldsymbol{p}$ model.

Anticipating the 2×2 CDW phase transition, we work in the folded Brillouin zone where the M point is folded to Γ. In the basis $\{d_1, d_2, d_3, p_x, p_y\}$, the bare $\boldsymbol{k}\cdot\boldsymbol{p}$ Hamiltonian is

$$H^0(\boldsymbol{k}) = \begin{pmatrix} \frac{E_g}{2} + H^0_{dd}(\boldsymbol{k}) & 0 \\ 0 & -\frac{E_g}{2} + H^0_{pp}(\boldsymbol{k}) \end{pmatrix}, \tag{1.26}$$

where E_g is the gap in the normal state, which is at most $|E_g| < 100$ meV. . The presence of a small indirect gap ($E_g > 0$) or overlap ($E_g < 0$) is still debated [126, 127, 142–144], but our conclusions remain qualitatively the same in both cases. We stress again that we do not consider SOC, since it does not qualitatively affect the CDW [146]. The bands of the model (1.26) are displayed as grey dotted lines in Fig. 1.8(a-c).

Coupling to the CDW

Next, we consider the CDW order parameter with M_1^- symmetry and even under time-reversal symmetry, denoted $\vec{\Delta} = (\Delta_1, \Delta_2, \Delta_3)$, which hybridizes the valence and conduction bands. The order parameter $\vec{\Delta}$ can be thought of as the amplitude of the condensed M_1^- phonon displacement in normal coordinates after a Hubbard-Stratonovich transformation, or as the excitonic order parameter of the same symmetry obtained from a mean-field decoupling. In order to derive the form of the coupling, we need the symmetry classification of the $d^\dagger p$ bilinears in the extended point group:

$$M_1^- \to \left\{ d_1^\dagger p_x, d_2^\dagger \left(-\frac{1}{2}p_x + \frac{\sqrt{3}}{2}p_y\right), d_3^\dagger \left(-\frac{1}{2}p_x - \frac{\sqrt{3}}{2}p_y\right) \right\}, \tag{1.27}$$

$$M_2^- \to \left\{ d_1^\dagger p_y, d_2^\dagger \left(-\frac{1}{2}p_y - \frac{\sqrt{3}}{2}p_x\right), d_3^\dagger \left(-\frac{1}{2}p_y + \frac{\sqrt{3}}{2}p_x\right) \right\}. \tag{1.28}$$

Each M_i^- bilinear allows for two Hermitian combinations: the time-reversal even $(d^\dagger p)_{M_i^-} + \text{h.c.}$, and the time-reversal odd $i[(d^\dagger p)_{M_i^-} - \text{h.c.}]$.

The time-reversal-symmetric M_1^- order parameter $\vec{\Delta}$ couples to the time-reversal even (1.27). To lowest order in $|\vec{\Delta}| = \sqrt{\Delta_1^2 + \Delta_2^2 + \Delta_3^2}$ and $\boldsymbol{k}$, the symmetry-allowed coupling to $\vec{\Delta}$ is therefore described by the following total Hamiltonian:

$$H = \begin{pmatrix} \frac{E_g}{2} + H^0_{dd}(\boldsymbol{k}) & H_{dp}(\vec{\Delta}) \\ H^\dagger_{dp}(\vec{\Delta}) & -\frac{E_g}{2} + H^0_{pp}(\boldsymbol{k}) \end{pmatrix}, \tag{1.29}$$

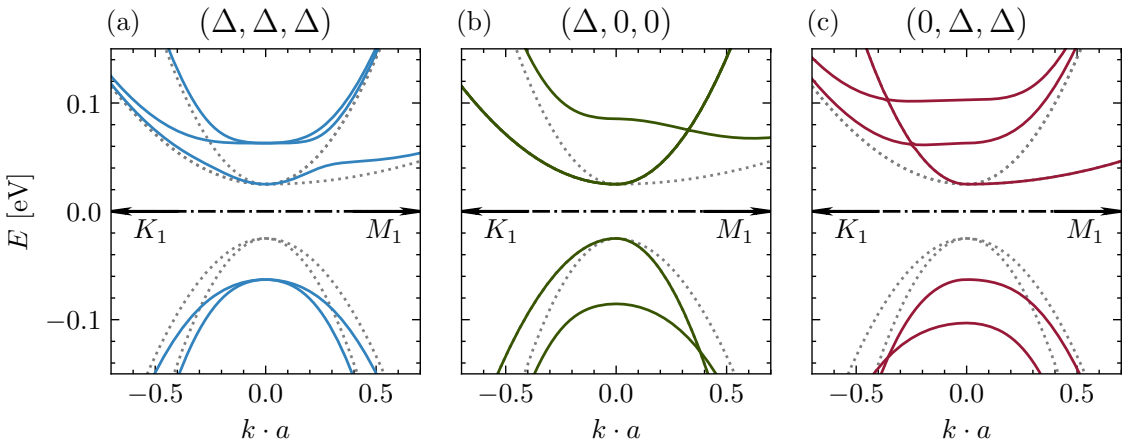

FIGURE 1.8: Folded bands in the presence of the order parameter $\vec{\Delta}$ in the momentum directions ΓK_1 and ΓM_1. The configurations of $\vec{\Delta}$ are (a) (Δ, Δ, Δ), (b) $(\Delta, 0, 0)$, and (c) $(0, \Delta, \Delta)$. The lowest conduction band for (c) $(0, \Delta, \Delta)$ is twofold degenerate in the ΓK_1 and ΓM_1 directions. Grey dashed lines show the bands for $\vec{\Delta} = 0$.

where

$$H_{dp}^{\dagger}(\vec{\Delta}) = \begin{pmatrix} \sqrt{\frac{2}{3}}\Delta_1 & -\frac{1}{\sqrt{6}}\Delta_2 & -\frac{1}{\sqrt{6}}\Delta_3 \\ 0 & \frac{1}{\sqrt{2}}\Delta_2 & -\frac{1}{\sqrt{2}}\Delta_3 \end{pmatrix}. \tag{1.30}$$

As deduced from Eqs. (1.27), three other order parameters would also couple the electron and hole pockets: a TRS odd M_1^-, and a TRS even and odd M_2^-. In the isotropic $b_p = b_d = 0$ case, the four order parameters have exactly the same effect on the band eigenvalues. Away from this limit, the M_1^- and M_2^- order parameters differ, but the time reversal even and odd combinations are still degenerate. As we will discuss in Section 1.4.1, this degeneracy arises due to the artificial $U(1)$ symmetry of the $\boldsymbol{k} \cdot \boldsymbol{p}$ model representing the separate charge conservation in the valence and conduction bands in the normal state. In the $\boldsymbol{k} \cdot \boldsymbol{p}$ model, this degeneracy can only be broken by adding umklapp interactions [193], but it is naturally lifted in a tight-binding model. Here we consider only the coupling to the time-reversal even M_1^- order parameter, which is the only one of the four that condenses in $TiSe_2$.

With the $\boldsymbol{k} \cdot \boldsymbol{p}$ Hamiltonian H of Eq. (1.29), we can study the resulting bands from the condensation of different configurations of $\vec{\Delta}$. The C_3-symmetric $3Q$ state [154] is represented by $\vec{\Delta} = \frac{|\vec{\Delta}|}{\sqrt{3}}(1, 1, 1)$. This order parameter causes a repulsion between the doublet of valence bands and a doublet of conduction bands (see Fig. 1.8(a)), leaving the band edge of the third conduction band unaffected by the CDW transition, as seen in ARPES [126, 127]. Figs. 1.8(b,c) show the bands for the $1Q$ $\vec{\Delta} = |\vec{\Delta}|(1, 0, 0)$ and $2Q$ $\vec{\Delta} = \frac{|\vec{\Delta}|}{\sqrt{2}}(0, 1, 1)$ states, respectively. In the $1Q$ case, only one conduction band is repelled to high energies, and one of the valence bands is left unaffected.

1.2.2 Bulk model

In bulk $TiSe_2$, the electron pockets occur at the L points and have L_1^+ symmetry, resulting in an order parameter with L_1^- symmetry. The bulk $\boldsymbol{k}\cdot\boldsymbol{p}$ model follows from replacing these labels in the monolayer model, and adding the k_z dispersion. The momentum k_z transforms as A_{2u} in the point group D_{3d}, and the quadratic combinations as $k_z^2 \to A_{1g}$ and $\{-k_zk_y, k_zk_x\} \to E_g$. The bare Hamiltonian is then modified as

$$\varepsilon_{d1}^{k_z}(\boldsymbol{k}) = \varepsilon_{d1}(\boldsymbol{k}) + c_d k_z^2 - d_d k_z k_y, \tag{1.31}$$

$$\varepsilon_{d2}^{k_z}(\boldsymbol{k}) = \varepsilon_{d2}(\boldsymbol{k}) + c_d k_z^2 + d_d\left(\frac{1}{2}k_zk_y + \frac{\sqrt{3}}{2}k_zk_x\right), \tag{1.32}$$

$$\varepsilon_{d3}^{k_z}(\boldsymbol{k}) = \varepsilon_{d3}(\boldsymbol{k}) + c_d k_z^2 + d_d\left(\frac{1}{2}k_zk_y - \frac{\sqrt{3}}{2}k_zk_x\right), \tag{1.33}$$

$$H_{pp}^{0k_z}(\boldsymbol{k}) = H_{pp}^{0}(\boldsymbol{k}) + \begin{pmatrix} c_p k_z^2 - d_p k_z k_y & -d_p k_z k_x \\ -d_p k_z k_x & c_p k_z^2 + d_p k_z k_y \end{pmatrix}, \tag{1.34}$$

Our proposed mechanism for rotation symmetry breaking in principle applies to both monolayer and bulk samples with the corresponding replacement of the symmetry labels, so for simplicity we now focus on the monolayer.

1.2.3 k.p ground state

The M_1^- CDW order parameter $\vec{\Delta} = (\Delta_1, \Delta_2, \Delta_3)$ has three symmetry-related components, allowing for distinct ground states. Depending on the resulting symmetry group of the CDW, five cases can be distinguished in the monolayer:

$\vec{\Delta}$		Space group	Point group
C_3-symmetric $3Q$	(Δ, Δ, Δ)	P321 (#149)	D_3
Stripe $1Q$	$(\Delta, 0, 0)$	C2/c (#15)	C_{2h}
Nematic $2Q$	$(0, \Delta, \Delta)$	C2/m (#12)	C_{2h}
Nematic $3Q$	$(\Delta_1, \Delta_2, \Delta_2)$	C2 (#5)	C_2
Generic	$(\Delta_1, \Delta_2, \Delta_3)$	P1 (#1)	1

While all components of the M_1^- order parameter $\vec{\Delta}$ are odd under inversion with respect to the Ti sites, there is another inversion center on the bond connecting Ti sites. Both $\vec{\Delta} = (\Delta, 0, 0)$ and $\vec{\Delta} = (0, \Delta, \Delta)$ preserve at least one such inversion center, so they are achiral. States $\vec{\Delta} = (\Delta, \Delta, \Delta)$ and $\vec{\Delta} = (\Delta_1, \Delta_2, \Delta_2)$, however, do break all inversion centers in the monolayer and they are chiral. In bulk $TiSe_2$, the order parameter $\vec{\Delta}$ transforms as L_1^- and all ordered phases are achiral, since an interlayer inversion symmetry is always preserved. Chiral structures could be obtained with an M_1^-

order parameter, which is not the leading bulk instability [194]. Alternatively, the simultaneous condensation of both L_1^- and L_2^+ order parameters also gives rise to a chiral CDW [178–182].

Motivated by the contradictory experimental evidence [52, 54, 114, 154, 178–182], we now focus on the problem of the symmetry of the ground state in monolayer $TiSe_2$ and its stability upon doping. These questions can be partially addressed within the continuum $\boldsymbol{k}\cdot\boldsymbol{p}$ model without knowledge of the precise nature or structure of the interaction that gives rise to $\vec{\Delta}$. The direction of $\vec{\Delta}$ for fixed magnitude $|\vec{\Delta}|$ can be obtained at zero temperature by minimizing the total energy of the occupied bands $E = \int \frac{d^2k}{(2\pi)^2} \sum_n \varepsilon_n(\boldsymbol{k})\theta[\mu - \varepsilon_n(\boldsymbol{k})]$ where $H\psi_n(\boldsymbol{k}) = \varepsilon_n(\boldsymbol{k})\psi_n(\boldsymbol{k})$. This approximate method can be applied if the interaction giving rise to the CDW only depends on $|\vec{\Delta}|^2 = \Delta_1^2 + \Delta_2^2 + \Delta_3^2$, which holds when any local four-fermion interaction is decoupled only in the chosen channel. Note that nothing can be said about the magnitude $|\vec{\Delta}|$ with this approach, since the interaction energy cost cannot be considered. Therefore, the results of this section should be interpreted as the preferred direction of $\vec{\Delta}$ assuming that the interactions are such that the CDW condenses with the magnitude $|\vec{\Delta}|$. Phase diagrams should therefore not be thought of as the experimental phase diagrams obtained by varying the corresponding parameters: for instance, the change in $|\vec{\Delta}|$ and eventual disappearance of the CDW with doping cannot be captured. This physics can only be captured with a self-consistent calculation of $\vec{\Delta}$, assuming a given microscopic interaction, as we will describe in Section 1.4. Nevertheless, the advantage of the approximate method is that no particular interaction is assumed, and that it allows for an easier interpretation of the origin of the different phases.

We have identified the electron doping x and the conduction band ellipticity b_d/a_d as the crucial parameters determining the symmetry of the ground state. Fig. 1.9(a) shows a phase diagram for fixed $|\vec{\Delta}|$ and $E_g = +50\text{meV}$, as a function of x and b_d/a_d. The bare density of states (DOS) $\rho = 1/(4\pi\sqrt{a_d^2 - b_d^2})$ is kept constant by varying a_d, to emphasize the role of the ellipticity. The phase diagram reveals the appearance of four different phases. At stoichiometry and low doping, the ground state is the C_3-symmetric $3Q$ phase for any b_d, as expected from DFT calculations [141, 177]. Below certain ellipticities, $b_d/a_d < 0.7$, there is a sharp $3Q$ to $1Q$ transition at a critical doping x_{1Q}. Additionally, at higher values of b_d/a_d, a nematic $3Q$ phase emerges where $|\vec{\Delta}| = (\Delta_1, \Delta_2, \Delta_2)$, with $|\Delta_1| \neq |\Delta_2|$. Further increasing b_d/a_d, Δ_1 vanishes and the nematic phase becomes $2Q$ with $|\vec{\Delta}| = (0, \Delta, \Delta)$. As explained above, this $2Q$ state differs from the nematic $3Q$ phase in an extra inversion symmetry centered in the Ti-Ti bond.

The $3Q$ to $1Q$ transition can be understood most clearly in the isotropic case $b_p = b_d = 0$, for which the energies of the two phases can be computed and integrated analytically. The analytical derivation of the total energy of each state can be found in Appendix 1.B. At charge neutrality, if there is a gap between valence and conduction bands in the CDW state, only the valence bands are

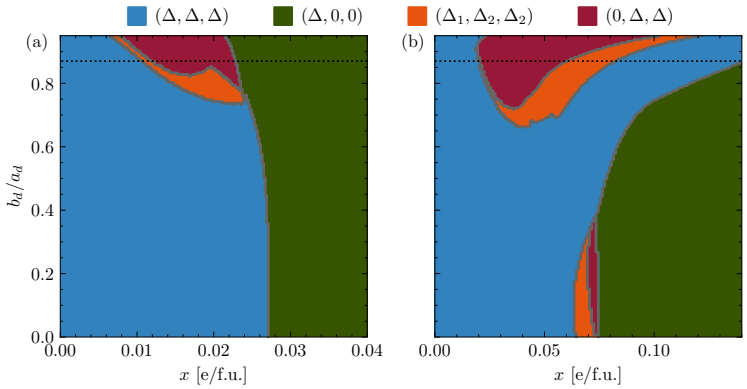

FIGURE 1.9: (a) Constant $|\vec{\Delta}|\ \boldsymbol{k}\cdot\boldsymbol{p}$ phase diagram for $E_g = +50$meV and $|\vec{\Delta}| = 100$meV as a function of electron doping x and ellipticity of the conduction bands b_d/a_d. The black dotted line indicates the realistic ellipticity $b_d/a_d = 0.87$. (b) The same as (a) but with $E_g = -100$meV and on a larger x range.

filled. The C_3-symmetric $3Q$ state has the minimum total energy in this case since in this phase both valence bands are pushed downwards in energy the most (see Fig. 1.8). When adding carriers, the chemical potential in the $1Q$ state is lower than in the $3Q$ phase, since the lowest conduction band is twofold degenerate only in the $1Q$ case (see Fig. 1.8(b)). Consequently, the energy of the $3Q$ phase increases faster relative to the $1Q$ state, eventually making the latter lower in energy at a critical doping x_{1Q}, which in the $E_g = 0$ limit takes the simple form $n_{1Q} = \frac{|\vec{\Delta}|}{\pi}\sqrt{\frac{\log 2}{3a_d(a_d-a_p)}}$, with $n_{1Q} = x_{1Q}/V_{\text{unit cell}}$ the electron density. This mechanism is still at work at finite b_d, as we observe numerically in Fig. 1.9.

The $3Q/2Q$ nematic phase has a different origin. Fig. 1.10(a) shows a close up of the dispersion of the lowest-lying conduction band ε_{c1} along ΓM as a function of b_d for fixed a_d and $\vec{\Delta} = \frac{|\vec{\Delta}|}{\sqrt{3}}(1,1,1)$. Fig. 1.10(b) shows the corresponding DOS. Increasing the ellipticity first produces a kink in the dispersion (a relative minimum of $\frac{d\varepsilon_{c1}}{dk_y}$), which eventually gives rise to a van Hove singularity with diverging DOS. When the filling is close to that of the six symmetry-equivalent incipient van Hove singularities, breaking the C_3 symmetry can lower the energy by splitting these saddle points in energy, a known mechanism for nematicity in the doped honeycomb lattice [138] and in Kagome superconductors [139]. Indeed, such splitting is observed in Fig. 1.10(c,d) in the nematic state, explaining its origin. In Fig. 1.9(a), this $3Q/2Q$ nematic phase develops even at values of b_d where the van Hove singularities are not fully developed and there is only a finite but sizable DOS peak. Eventually, for higher doping, the $1Q$ stripe phase always develops.

Fig. 1.9(b) shows the phase diagram for the semimetallic case with $E_g = -100$meV, which displays the following differences with respect to $E_g > 0$. First, there is an intermediate nematic $3Q/2Q$ state also at small ellipticity, which occurs at fillings where the second conduction band, of

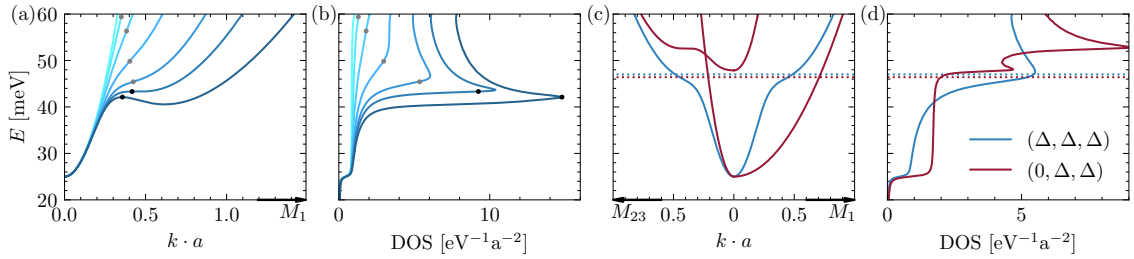

FIGURE 1.10: (a) Lowest conduction band along the ΓM direction and corresponding DOS in the C_3-symmetric $3Q$ phase with $E_g = +50$meV and $|\vec{\Delta}| = 100$meV for constant a_d and ellipticities $b_d/a_d = 0, 0.39, 0.60, 0.78, 0.88, 0.92, 0.95$. A kink in the band is signaled by gray dots, and a van Hove singularity by black dots. (b) Corresponding DOS for each band in (a). (c) Conduction bands along the ΓM_1 and ΓM_2 directions (ΓM_3 is equivalent to ΓM_2) in the C_3-symmetric $3Q$ (blue) and nematic $2Q$ (red) phases with $E_g = +50$meV, $|\vec{\Delta}| = 100$meV and $b_d/a_d = 0.87$. Horizontal dotted lines indicate the chemical potentials for $x = 0.0182$, where the C_3-symmetric $3Q$ phase is unstable towards the $2Q$ state. (d) Corresponding DOS for each band in (c). The three equivalent incipient van Hove singularities of the lowest conduction band in the symmetric $3Q$ state disappear in the $2Q$ state, which has higher DOS at lower energy and therefore lower total energy.

approximate mexican hat shape for $\vec{\Delta} = \frac{|\vec{\Delta}|}{\sqrt{3}}(1,1,1)$, begins to be populated. Since the DOS is also large there, a similar mechanism as the one for large ellipticity drives the transition to the nematic $3Q/2Q$ phase. Furthermore, at high ellipticity, including the realistic value $b_d/a_d \sim 0.87$, a reentrant C_3-symmetric $3Q$ phase appears between the nematic $3Q$ state and the $1Q$ stripe phase. In this region, the doping is well above the incipient van Hove singularities, so that no nematic instability occurs, but the $1Q$ state energy is still higher. This reentrant phase shows that the mechanisms for the $1Q$ and $2Q/3Q$ nematic states are indeed different.

Finally, we mention that the particular ratio $\frac{\Delta_1}{\Delta_2}$ in the $2Q/3Q$ nematic phase is likely dependent on the higher order terms in crystal momentum beyond our $\boldsymbol{k} \cdot \boldsymbol{p}$. Nevertheless, the instability towards a nematic phase is a strong prediction of our theory. Indeed, we will show in Section 1.4.1 that it is reproduced by our self-consistent mean-field calculations in a lattice model.

1.3 Ginzburg-Landau theory

In this section, we write down the uniform Ginzburg-Landau free-energy functional of the M_1^- order parameter $\vec{\Delta}$ to grasp a complementary understanding of the nematic and stripe CDWs. The Ginzburg-Landau functional is an expansion of the microscopic free-energy in powers of the order parameter. Therefore, it is strictly applicable when $\vec{\Delta}$ is small, which typically occurs close to the CDW transition, although qualitative information can be also extrapolated to lower temperatures. The Ginzburg-Landau theory is useful for predicting the configuration of $\vec{\Delta}$ that condenses at

T_{CDW}. Here, we show that, while the $3Q$ to $1Q$ transition can be captured within this framework, the nematic $2Q/3Q$ phase cannot be obtained from this approach.

The uniform Ginzburg-Landau free-energy density up to fourth order in $\vec{\Delta}$ reads

$$F_\Delta = a_\Delta|\vec{\Delta}|^2 + b_\Delta|\vec{\Delta}|^4 + c_\Delta(\Delta_1^4 + \Delta_2^4 + \Delta_3^4), \tag{1.35}$$

where $b_\Delta > 0$ and $b_\Delta > -c_\Delta$ for F_Δ to be well-defined in the limit of large $\vec{\Delta}$. When $a_\Delta < 0$, $\vec{\Delta}$ condenses into a state determined by the sign of c_Δ. For $c_\Delta > 0$ we have the $3Q$ C_3-symmetric ground state $\Delta = \Delta_0\frac{1}{\sqrt{3}}(1,1,1)$, while for $c_\Delta < 0$ we have the $1Q$ stripe phase $\Delta = \Delta_0(0,0,1)$. Therefore, the $\boldsymbol{k}\cdot\boldsymbol{p}$ results would correspond to starting from $c_\Delta > 0$ at stoichiometry, with electron doping changing the sign of c_Δ at x_{1Q}. We emphasize that this analysis is phenomenological and only valid close to the critical temperature, where $|\vec{\Delta}|$ is small, as opposed to our $\boldsymbol{k}\cdot\boldsymbol{p}$ analysis. Other perspective from this observation is that the fact that both C_3-symmetric $3Q$ and $1Q$ stripe phases can be obtained from this Ginzburg-Landau functional to fourth order suggests that the critical temperatures of both phases should be similar. While we have not explicitly computed the Ginzburg-Landau coefficients from a microscopic model to prove that, our self-consistent microscopic calculations of Section 1.4.2 will show that this is indeed the case.

The $2Q/3Q$ nematic phase cannot be obtained from the free energy (1.35). Indeed, this is in agreement with the fact that a perturbation series in $\vec{\Delta}$ is not able to properly reproduce the saddle point in the dispersion of the C_3-symmetric $3Q$ CDW state[3]. This suggests that the instability towards the $2Q/3Q$ nematic CDW might occur at a lower temperature than that of the C_3-symmetric $3Q$ and stripe $1Q$ states. In Section 1.4.2, we will show that our self-consistent microscopic calculations reproduce this prediction. Moreover, in Section 1.5 we will explain an additional mechanism favouring a nematic CDW based on the coupling of $\vec{\Delta}$ to another order parameter.

1.4 Tight-binding model

The continuum $\boldsymbol{k}\cdot\boldsymbol{p}$ model provides a compelling basic understanding of the CDW phase diagram as a function of doping, purely based on energetic considerations. To obtain a more refined understanding based on a model which includes microscopic interactions, in this section we develop an effective tight-binding lattice model and study its ground state phase diagram within self-consistent Hartree-Fock theory. We construct a minimal tight-binding model that accurately

[3]Including sixth-order terms in the Ginzburg-Landau functional could give rise to a $2Q/3Q$ nematic CDW for appropriately chosen coefficients. However, since $\vec{\Delta}$ is nonperturbative in this phase, as exhibited also by the considerably lower critical temperature in the self-consistent calculations of Section 1.4.2, this mechanism for nematicity might be different than the one we have demonstrated here.

captures the band dispersion and eigenstate symmetry near the Fermi level and reproduces the low-energy $\boldsymbol{k}\cdot\boldsymbol{p}$ model when expanded near Γ and M. By considering quasi-local interactions that induce the CDW of appropriate symmetry, we show that the mean-field calculations support the doping-induced nematic and stripe CDWs predicted by the $\boldsymbol{k}\cdot\boldsymbol{p}$ model.

1.4.1 Construction of the model

Realistic tight-binding model

The lattice of 1T-$TiSe_2$ has lattice vectors

$$\boldsymbol{a}_1 = a\,(1,0,0)\,, \tag{1.36}$$

$$\boldsymbol{a}_2 = a\left(\tfrac{1}{2},\tfrac{\sqrt{3}}{2},0\right), \tag{1.37}$$

$$\boldsymbol{a}_3 = c\,(0,0,1)\,, \tag{1.38}$$

with $a \simeq 3.54$ Å and $c \simeq 6.00$ Å the lattice parameters [195], and consists of three atoms per unit cell:

- One Ti atom at the $1a$ Wyckoff position $\boldsymbol{r}_{\mathrm{Ti}} = (0,0,0)$,
- Two Se atoms at the $2d$ Wyckoff position $\left\{\boldsymbol{r}_{\mathrm{Se}_1} = \left(\frac{a}{\sqrt{3}}\frac{\sqrt{3}}{2}, \frac{a}{\sqrt{3}}\frac{1}{2}, -z_{\mathrm{Se}}\right),\right.$ $\left.\boldsymbol{r}_{\mathrm{Se}_2} = \left(\frac{a}{\sqrt{3}}\frac{\sqrt{3}}{2}, -\frac{a}{\sqrt{3}}\frac{1}{2}, z_{\mathrm{Se}}\right)\right\}$,

with $z_{\mathrm{Se}} \simeq 1.55$ Å. Although the overall symmetry is trigonal, the environment of the Ti atoms is approximately cubic ($z_{\mathrm{Se}}^{\mathrm{cubic}} = \frac{a}{\sqrt{6}} \simeq 1.45$ Å).

A realistic tight-binding model of $TiSe_2$ representing the low-energy bands with the atomic orbitals that contribute the most would consist of at least 7 orbitals per unit cell [196]:

- The approximate t_{2g} triplet of Ti d orbitals $\{d_{ab}, d_{ca}, d_{bc}\}$, with a, b, c the approximately cubic directions, which are actually split in a singlet $d_{2z^2-x^2-y^2} \rightarrow A_{1g}$ and a doublet $\sim \{\frac{\sqrt{2}}{\sqrt{3}}d_{x^2-y^2} + \frac{1}{\sqrt{3}}d_{zy}, -(\frac{\sqrt{2}}{\sqrt{3}}d_{xy} + \frac{1}{\sqrt{3}}d_{zx})\} \rightarrow E_g$ in the point group D_{3d};
- The doublet of $\{p_x, p_y\}$ orbitals per each Se atom, which transform as the E representations of the site symmetry group C_{3v} of the Se site.

In 2D and in the absence of SOC, the low-energy physics is dominated by the antibonding-like combination of Se-p orbitals transforming as Γ_3^- at Γ, and a mixture of the Ti-d orbitals transforming as M_1^+ at the three M points. In bulk $TiSe_2$, a p_z orbital per each Se atom should be included, since its antibonding-like combination Γ_2^- at Γ lies close to the Γ_3^- pocket [28, 145]. This set of 7 (or 9) bands are isolated and can be Wannierized [145, 196].

Effective lattice model

Here we have considered instead an effective lattice model for monolayer $TiSe_2$ with the same space group $P\bar{3}m1$ that reproduces the band dispersion and eigenstate symmetry of the electron and hole pockets near the Fermi level. Our tight-binding model can thus be regarded as a lattice regularization of the $\boldsymbol{k}\cdot\boldsymbol{p}$ model. We have chosen a regularization with 3 orbitals per unit cell, all of them sitting at the same $1a$ Wyckoff position $\boldsymbol{r} = (0,0,0)$ of a triangular lattice (see Fig. 1.11(a)):

- One orbital, denoted d_{z^2}, transforms as A_{1g} and gives rise to the conduction band M_1^+ at M;
- A doublet, called $\{p_x, p_y\}$, transforms as E_u and reproduces the valence bands Γ_3^- at Γ.

We stress that these orbitals should not be thought of the real atomic orbitals, but rather as appropriate combinations of them. As such, the d_{z^2} and the $\{p_x, p_y\}$ orbitals can be regarded as Wannier orbitals fitting the band structure close to M and Γ, respectively. Far from these points, however, these bands would mix with the ones coming from the other combinations of orbitals in the realistic model. For instance, the lowest lying conduction band at Γ, which is higher than the M conduction pockets and does not play a role in the CDW, is a Γ_3^+ in reality, while our conduction band is always totally symmetric by construction and thus Γ_1^+. However, since the low-energy pockets close to the Fermi level play the major role in the physics of the CDW, this will not affect our conclusions. Finally, although formally our model also has a m_z mirror symmetry, it plays no role, since all orbitals are located at $z = 0$ and belong to the m_z even sector.

We include 8 symmetry-allowed parameters in our effective 2D lattice model: onsite energies ε_p and ε_d, hoppings up to third nearest neighbours $t_{dd}^{(n)}$ for the d_{z^2} orbital, nearest-neighbour σ and π hoppings for the $\{p_x, p_y\}$ orbitals, and an interorbital nearest-neighbour hopping t_{dp}:

$$\begin{aligned} H_0 = &\sum_i \left(\varepsilon_d d_i^\dagger d_i + \varepsilon_p \boldsymbol{p}_i^\dagger \cdot \boldsymbol{p}_i\right) + \sum_{n=1}^{3} \sum_{\langle ij\rangle_n} t_{dd}^{(n)} d_i^\dagger d_j - \sum_{\langle ij\rangle_1} i t_{dp} \left(d_i^\dagger \hat{\boldsymbol{r}}_{ij} \cdot \boldsymbol{p}_j - h.c.\right) \\ &- \sum_{\langle ij\rangle_1} \Big[\left(t_{pp\sigma} + t_{pp\pi}\right) \left(\boldsymbol{p}_i^\dagger \cdot \hat{\boldsymbol{r}}_{ij}\right)\left(\hat{\boldsymbol{r}}_{ij} \cdot \boldsymbol{p}_j\right) - t_{pp\pi} \boldsymbol{p}_i^\dagger \cdot \boldsymbol{p}_j \Big] . \end{aligned} \tag{1.39}$$

Here $\langle ij\rangle_n$ are the n^{th} nearest neighbours, $\boldsymbol{p}_i = \left(p_{xi}, p_{yi}\right)$ is the vector of p orbitals, and $\hat{\boldsymbol{r}}_{ij} = (\boldsymbol{r}_j - \boldsymbol{r}_i)/|\boldsymbol{r}_j - \boldsymbol{r}_i|$ is the unit vector from site i to site j. As in the $\boldsymbol{k}\cdot\boldsymbol{p}$ model, in the Hamiltonian (1.39) we have neglected SOC. While this can quantitatively change the critical temperature and related quantities, we expect that the qualitative picture remains the same [146].

The Hamiltonian parameters are chosen to reproduce the gap and masses of the bands near the Fermi level. In particular, we solve for the noninteracting gap E_g, the masses m_{v1}, m_{v2} of the two valence bands at Γ, the masses m_{cx}, m_{cy} of the conduction bands at M perpendicular and

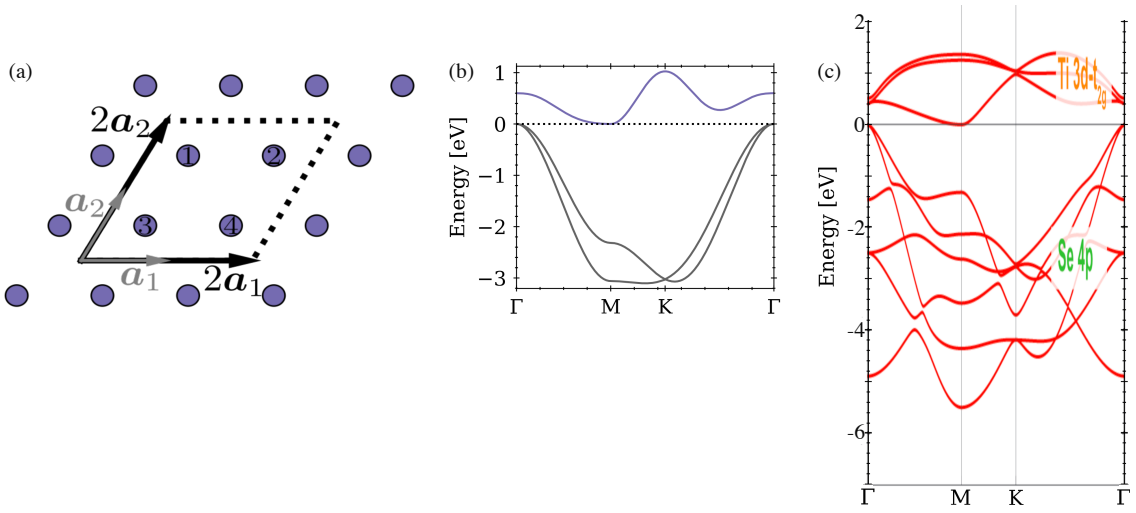

FIGURE 1.11: (a) Triangular lattice of the effective tight-binding model with our choice of lattice vectors and supercell. (b) Band structure of the effective lattice model (1.39) for $E_g = 0$. Purple (grey) indicate the conduction (valence) bands, which are mainly composed of d (p) orbitals. (c) Band structure of the realistic tight-binding model of Ref. [126]. Adapted from Ref. [126], scaling the energy and momentum axes to be equal to (b).

parallel to the ΓM direction, and the energy $\varepsilon_{c\Gamma}$ of the conduction band at Γ. The resulting system of equations would be underconstrained, so we choose to leave t_{dp} as a free parameter. Since the valence bands are of p character while the conduction bands are of d character, t_{dp} only affects the band curvatures to second order with an energy denominator dominated by $\varepsilon_d - \varepsilon_p$, so its influence on the bands is almost negligible (see Appendix 1.C.1). Nevertheless, we choose to keep it finite because it breaks the artificial $U(1)$ gauge symmetry representing the separate charge conservation in the conduction and valence bands. This artificial symmetry is present in the $\boldsymbol{k}\cdot\boldsymbol{p}$ model and can give rise to spurious results in a self-consistent mean-field calculation. The subtle but important role of t_{dp} in selecting a mean-field solution is further explained below in Section 1.4.1. The relationships between the Hamiltonian parameters and the gap and masses are displayed in Eqs. (1.90)-(1.102) in Appendix 1.C.1. Here we take the gap and masses from Ref. [125] based on ARPES measurements on monolayer $TiSe_2$: $m_{v1} = -0.7m_e$, $m_{v2} = (50/3)m_{v2} = -0.42m_e$, $m_{cy} = 10m_{v1} = 7m_e$, $m_{cx} = m_{cy}/14 = 0.5m_e$ (see table 1.C.1 for a comparison of these values with other works). The resulting band structure for $E_g = 0$ is shown in Fig. 1.11(b), compared to the bands of the tight-binding model of Ref. [126] in Fig. 1.11(c).

Interactions and CDW

To account for the CDW, we consider a supercell with superlattice vectors $2\boldsymbol{a}_i$, with $\boldsymbol{a}_1 = a(1,0)$ and $\boldsymbol{a}_2 = a(\frac{1}{2}, \frac{\sqrt{3}}{2})$ and label the supercell sites by $j = 1,2,3,4$, as in Fig. 1.11(a). Without

loss of generality, we choose the origin of coordinates of a cell at $\boldsymbol{r}_1 = (0,0)$, so $\boldsymbol{r}_2 = a(1,0)$, $\boldsymbol{r}_3 = a(-\frac{1}{2}, -\frac{\sqrt{3}}{2})$, and $\boldsymbol{r}_4 = a(\frac{1}{2}, -\frac{\sqrt{3}}{2})$.

We choose the CDW order in the effective lattice model to be represented by the local p-d hybridization, encoded in the fermion bilinear $\langle d_j^\dagger p_{\alpha j}\rangle$, with $j = 1,...,4$ running over the sites of the 2x2 supercell (see Fig. 1.11(a)). There are eight $\langle d_j^\dagger p_{\alpha j}\rangle$, which represent an onsite orbital order and transform under symmetry as $\Gamma_3^- \oplus M_1^- \oplus M_2^-$, with the real and imaginary parts being even and odd under TRS, respectively. The symmetry adapted operators read

$$\langle d^\dagger p\rangle^{\alpha}_{\Gamma_3^-} = \frac{1}{2}\sum_j \langle d_j^\dagger p_{\alpha j}\rangle, \tag{1.40}$$

$$\langle d^\dagger p\rangle^{a}_{M_1^-} = \frac{1}{2}\sum_j e^{i\boldsymbol{M}_a\cdot\boldsymbol{r}_j}\langle d_j^\dagger \boldsymbol{p}_j\rangle \times \hat{\boldsymbol{M}}_a, \tag{1.41}$$

$$\langle d^\dagger p\rangle^{a}_{M_2^-} = \frac{1}{2}\sum_j e^{i\boldsymbol{M}_a\cdot\boldsymbol{r}_j}\langle d_j^\dagger \boldsymbol{p}_j\rangle \cdot \hat{\boldsymbol{M}}_a, \tag{1.42}$$

where the subindices label the irrep of the extended point group according to which the operators transform, and the superindices $\alpha = 1,2$ and $a = 1,2,3$ label the different components of the multidimensional irreps. We have defined $\boldsymbol{v}\times\boldsymbol{w} = v_x w_y - v_y w_x$, and $\hat{\boldsymbol{M}}_a = \frac{\boldsymbol{M}_a}{|\boldsymbol{M}_a|}$, with the momenta $\boldsymbol{M}_a$ defined in Eqs. (1.15)-(1.17).

We complete the model with the most local interaction that is attractive only for the M_1^- channel, which is

$$H_{dp1} = V_{dp}\sum_{\langle ij\rangle_1}\left(d_i^\dagger \boldsymbol{p}_i\right)^\dagger \cdot \left(1 - 2\hat{\boldsymbol{r}}_{ij}\otimes\hat{\boldsymbol{r}}_{ij}\right)\cdot\left(d_j^\dagger \boldsymbol{p}_j\right), \tag{1.43}$$

with $V_{dp} > 0$. We have defined the rank-two tensor $T = \boldsymbol{v}\otimes\boldsymbol{w}$ with components $T_{\alpha\beta} = v_\alpha w_\beta$. We now show that, at the mean-field level, H_{dp1} is attractive with coupling $-2V_{dp}$ for the M_1^- channel, whereas it is repulsive with $+2V_{dp}$ for the M_2^- channel, and it does not couple to the Γ_3^- channel.

The mean-field Hamiltonian H_{MF} in real-space is obtained by decoupling the Hamiltonian $H_0 + H_{dp1}$ of Eqs. (1.39), (1.43) in the onsite orbital order $\langle d_j^\dagger p_{\alpha j}\rangle$ channel, which corresponds to the Fock channel of the V_{dp} interaction. We obtain $H_{\mathrm{MF}} = H_0 + H_{dp1}^{\mathrm{MF}}$, with

$$\begin{aligned} H_{dp1}^{\mathrm{MF}} = V_{dp}\sum_{\langle ij\rangle}\Big\{&\Big[\langle d_i^\dagger \boldsymbol{p}_i\rangle^*\cdot\left(2\hat{\boldsymbol{r}}_{ij}\otimes\hat{\boldsymbol{r}}_{ij} - 1\right)\cdot\left(d_j^\dagger \boldsymbol{p}_j\right) + \mathrm{h.c.}\Big] - \\ &- \langle d_i^\dagger \boldsymbol{p}_i\rangle^*\cdot\left(2\hat{\boldsymbol{r}}_{ij}\otimes\hat{\boldsymbol{r}}_{ij} - 1\right)\cdot\langle d_j^\dagger \boldsymbol{p}_j\rangle\Big\}, \end{aligned} \tag{1.44}$$

with the expectation values taken in the self-consistent mean-field ground state. We can write this mean-field interaction as a matrix in the basis $\{d_1^\dagger p_{x1}, d_1^\dagger p_{y1}, d_2^\dagger p_{x2}, d_2^\dagger p_{y2}, d_3^\dagger p_{x3}, d_3^\dagger p_{y3}, d_4^\dagger p_{x4}, d_4^\dagger p_{y4}\}$:

$$V_{dp}\langle d^\dagger p\rangle^* \cdot \begin{pmatrix} 0 & 0 & 1 & 0 & -\frac{1}{2} & \frac{\sqrt{3}}{2} & -\frac{1}{2} & -\frac{\sqrt{3}}{2} \\ 0 & 0 & 0 & -1 & \frac{\sqrt{3}}{2} & \frac{1}{2} & -\frac{\sqrt{3}}{2} & \frac{1}{2} \\ 1 & 0 & 0 & 0 & -\frac{1}{2} & -\frac{\sqrt{3}}{2} & -\frac{1}{2} & \frac{\sqrt{3}}{2} \\ 0 & -1 & 0 & 0 & -\frac{\sqrt{3}}{2} & \frac{1}{2} & \frac{\sqrt{3}}{2} & \frac{1}{2} \\ -\frac{1}{2} & \frac{\sqrt{3}}{2} & -\frac{1}{2} & -\frac{\sqrt{3}}{2} & 0 & 0 & 1 & 0 \\ \frac{\sqrt{3}}{2} & \frac{1}{2} & -\frac{\sqrt{3}}{2} & \frac{1}{2} & 0 & 0 & 0 & -1 \\ -\frac{1}{2} & -\frac{\sqrt{3}}{2} & -\frac{1}{2} & \frac{\sqrt{3}}{2} & 1 & 0 & 0 & 0 \\ -\frac{\sqrt{3}}{2} & \frac{1}{2} & \frac{\sqrt{3}}{2} & \frac{1}{2} & 0 & -1 & 0 & 0 \end{pmatrix} \cdot d^\dagger p \tag{1.45}$$

Diagonalizing this matrix, we get eigenvalue -2 for the eigenvectors $\langle d^\dagger p\rangle_{M_1^-}$ (1.41), $+2$ for $\langle d^\dagger p\rangle_{M_2^-}$ (1.42), and 0 for $\langle d^\dagger p\rangle_{\Gamma_3^-}$ (1.42). Consequently, we can recast H_{dp1}^{MF} in Eq. (1.44) as

$$\begin{aligned} H_{dp1}^{\mathrm{MF}} = \sum_{\text{supercells}} \Big\{ & -2V_{dp}\left(\langle d^\dagger p\rangle_{M_1^-}^* \left[d^\dagger p\right]_{M_1^-} + \text{h.c.} - \left|\langle d^\dagger p\rangle_{M_1^-}\right|^2\right) + \\ & +2V_{dp}\left(\langle d^\dagger p\rangle_{M_2^-}^* \left[d^\dagger p\right]_{M_2^-} + \text{h.c.} - \left|\langle d^\dagger p\rangle_{M_2^-}\right|^2\right)\Big\}. \end{aligned} \tag{1.46}$$

As we anticipated, the mean-field Hamiltonian (1.44) is only attractive in the M_1^- channel.

The last step to write the explicit expression of the order parameter $\vec{\Delta}$ is to determine its normalization so that it couples to the $\boldsymbol{k}\cdot\boldsymbol{p}$ at $\boldsymbol{k}=0$ as in $H_{dp}(\vec{\Delta})$ of Eq. (1.29). For that, we express the low-energy $\boldsymbol{k}\cdot\boldsymbol{p}$ eigenfunctions $\{d_1^{kp}, d_2^{kp}, d_3^{kp}, p_x^{kp}, p_y^{kp}\}$ in the basis of tight-binding orbitals $\{d_j, p_{xj}, p_{yj}\}_{j=1}^4$ in the 2×2 supercell. Taking into account that d_a^{kp} have momentum ΓM and p_α^{kp} have zero momentum, and that the eigenfunctions at Γ and M are purely p and purely d in the tight binding, respectively, we obtain:

$$d_a^{kp} = \frac{1}{2}\sum_j e^{i\boldsymbol{M}_a\cdot\boldsymbol{r}_j} d_j, \tag{1.47}$$

$$p_\alpha^{kp} = \frac{1}{2}\sum_j p_\alpha, \tag{1.48}$$

The projection of the time-reversal symmetric M_1^- component of H_{dp1}^{MF} onto the $\boldsymbol{k}\cdot\boldsymbol{p}$ bands at momentum $\boldsymbol{k}=0$ of the CDW Brillouin zone is therefore as in Eq. (1.29) with

$$H_{dp}^{\dagger}=\frac{1}{2}\left(-2V_{dp}\right)\mathrm{Re}\begin{pmatrix}\langle d^{\dagger}p\rangle^{1}_{M_1^-} & -\frac{1}{2}\langle d^{\dagger}p\rangle^{2}_{M_1^-} & -\frac{1}{2}\langle d^{\dagger}p\rangle^{3}_{M_1^-}\\ 0 & \frac{\sqrt{3}}{2}\langle d^{\dagger}p\rangle^{2}_{M_1^-} & -\frac{\sqrt{3}}{2}\langle d^{\dagger}p\rangle^{3}_{M_1^-}\end{pmatrix}. \tag{1.49}$$

Comparing this expression to Eq. (1.30), we conclude that the explicit expression of the time-reversal symmetric M_1^- CDW order parameter $\vec{\Delta}$ in the tight binding is

$$\Delta_a=\sqrt{\frac{3}{8}}\left(-2V_{dp}\right)\mathrm{Re}\langle d_j^{\dagger}\boldsymbol{p}_j\rangle^{a}_{M_1^-}=-\sqrt{\frac{3}{8}}V_{dp}\sum_j e^{i\boldsymbol{M}_a\cdot\boldsymbol{r}_j}\mathrm{Re}\langle d_j^{\dagger}\boldsymbol{p}_j\rangle\times\hat{\boldsymbol{M}}_a, \tag{1.50}$$

Our mean-field decoupling (1.44) allows for another three order parameters. One is the TRS odd M_1^- counterpart of $\vec{\Delta}$, which corresponds to taking the imaginary part instead of the real part in Eq. (1.50). In the presence of separate charge conservation for the p and d orbitals, the time-reversal even and odd M_1^- order parameters would be degenerate [193]. However, the presence of a small t_{dp} hopping breaks their degeneracy in favor of the real part $\vec{\Delta}$ in all cases. Indeed, the TRS odd M_1^- order parameter is identically zero in our calculations. The other two order parameters transform as TRS even and odd M_2^-, $\Psi_{a\pm}=+\sqrt{\frac{3}{8}}V_{dp}\sum_j\frac{1}{2}(e^{i\boldsymbol{M}_a\cdot\boldsymbol{r}_j}\langle d_j^{\dagger}\boldsymbol{p}_j\rangle\cdot\hat{\boldsymbol{M}}_a\pm\mathrm{h.c.})$, and the interaction is repulsive for both[4]. $\vec{\Psi}_+$ is nonzero but small only in the nematic phase, where it is symmetry allowed, with $\vec{\Delta}=(\Delta_1,\Delta_2,\Delta_2)$ and $\vec{\Psi}_+=(0,\Psi_+,-\Psi_+)$. Therefore, our interacting tight-binding model only favors time-reversal even M_1^- instabilities, as required. Our interacting tight-binding Hamiltonian therefore serves as a minimal model to analyze the energetics of the M_1^- CDW order.

1.4.2 Self-consistent mean-field calculations

In this section, we discuss the mean-field T-x phase diagrams obtained by self-consistently solving the Hamiltonian H_{MF} (1.44) for different values of the initial gap E_g. These calculations corroborate that the existence of C_3-breaking phases is qualitatively robust.

For each E_g, we choose V_{dp} such that the critical doping for the disappearance of the commensurate CDW is $x_{\mathrm{CDW}}\sim 0.06\mathrm{e}/\mathrm{f.u.}$, as determined experimentally [24, 25, 127, 197]. Indeed, in our simplified effective model with a given initial gap E_g, it is not generically possible to choose a value of the interaction that reproduces both the critical temperature T_{CDW} and the critical doping x_{CDW} for the disappearance of the CDW. Our aim is not to reproduce these values quantitatively,

[4] Curiously, if the interaction were attractive in the M_2^- channel, the t_{dp} would favor the time-reversal breaking CDW.

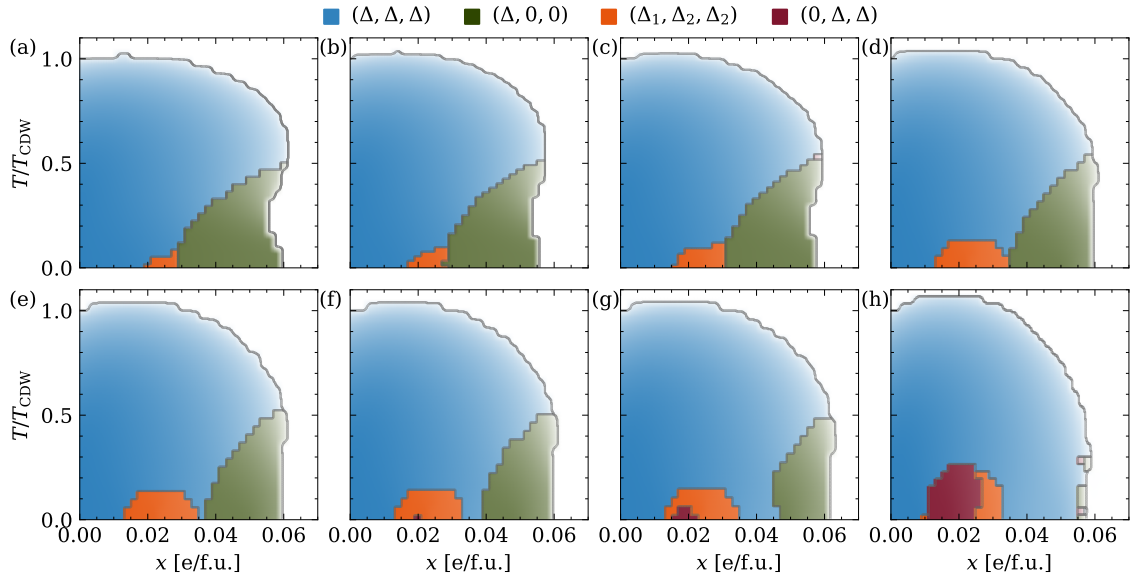

FIGURE 1.12: Temperature-doping phase diagrams obtained by self-consistently solving the mean-field Hamiltonian of Eq. (1.44) for different gaps, and thus, as explained, different interaction strengths and critical temperatures. The intensity of the color of each phase is proportional to $|\vec{\Delta}|$. T_{CDW} is the critical temperature at stoichiometry.

(a) $E_g = +50\mathrm{meV}$, $V_{dp} = 890\mathrm{meV}$, $T_{\mathrm{CDW}} = 576\mathrm{K}$;
(b) $E_g = +25\mathrm{meV}$, $V_{dp} = 845\mathrm{meV}$, $T_{\mathrm{CDW}} = 459\mathrm{K}$;
(c) $E_g = 0$, $V_{dp} = 800\mathrm{meV}$, $T_{\mathrm{CDW}} = 378\mathrm{K}$;
(d) $E_g = -25\mathrm{meV}$, $V_{dp} = 740\mathrm{meV}$, $T_{\mathrm{CDW}} = 269\mathrm{K}$;
(e) $E_g = -27.5\mathrm{meV}$, $V_{dp} = 733\mathrm{meV}$, $T_{\mathrm{CDW}} = 259\mathrm{K}$;
(f) $E_g = -30\mathrm{meV}$, $V_{dp} = 725\mathrm{meV}$, $T_{\mathrm{CDW}} = 249\mathrm{K}$;
(g) $E_g = -35\mathrm{meV}$, $V_{dp} = 716.5\mathrm{meV}$, $T_{\mathrm{CDW}} = 239\mathrm{K}$;
(h) $E_g = -50\mathrm{meV}$, $V_{dp} = 650\mathrm{meV}$, $T_{\mathrm{CDW}} = 145\mathrm{K}$;

which would require including physics well beyond our model like electron-phonon coupling, lattice anharmonicity [198], doping-dependent screening, the effect of the substrate [125, 199], fluctuation corrections to mean field [200], etc., but rather to show the generic existence of C_3-breaking phases. Because of this, we choose interaction strengths to match the critical doping above which the commensurate CDW dies and present the phase diagrams as a function of T/T_{CDW}, noting that the critical temperature at charge neutrality T_{CDW} generally changes for different values of E_g. The critical doping we take, $x_{\mathrm{CDW}} \sim 0.06\mathrm{e/f.u.}$ [24, 25, 127, 197], is only an approximate estimate, since at this doping there is a crossover to an incommensurate CDW, where the ground state consists of commensurate domains separated by domain walls [13, 18, 25, 157].

Fig. 1.12 displays the resulting phase T-x diagrams for decreasing gap from $E_g = +50\mathrm{meV}$ to $E_g = -50\mathrm{meV}$. States (Δ,Δ,Δ), $(\Delta_1,\Delta_2,\Delta_2)$, and $(\Delta,0,0)$ appear in all cases, while a $2Q$ $(0,\Delta,\Delta)$ phase develops only for a sufficiently negative gap ($E_g \lesssim -30\mathrm{meV}$). At zero temperature,

the C_3-symmetric $3Q$ phase (Δ, Δ, Δ) is the most stable at low doping, while the $1Q$-stripe order only develops at high doping, with the nematic $3Q/2Q$ phase developing in between, in agreement with our $\boldsymbol{k} \cdot \boldsymbol{p}$ predictions of Fig. 1.9. While the $3Q$ nematic and the $1Q$ stripe phases share a boundary for positive gaps, they separate for sufficiently negative gaps ($E_g \lesssim -25\text{meV}$), where the reentrant C_3-symmetric $3Q$ phase is also observed between the nematic $3Q$ and the $1Q$ phases. This clearly indicates that the origin of these two phases is different, in agreement with our theory. Starting from high temperature, the first transition is always to the C_3-symmetric $3Q$ phase. At high doping, the $1Q$ phase develops at a lower but comparable temperature, as expected from the Ginzburg-Landau analysis of Section 1.3. On the other hand, the nematic $3Q/2Q$ phase only appears at low temperature ($T_{\text{nematic}} \sim 0.2\ T_{\text{CDW}}$), which is expected for a secondary instability of the $3Q$ CDW state. Regarding the dependence of the phase diagram on the gap, the most prominent feature is the shift of the $1Q$ stripe phase to higher doping for decreasing gap, until this phase disappears. This is consistent with the $\boldsymbol{k} \cdot \boldsymbol{p}$ predictions of Fig. 1.9, which show that the doping above which the $1Q$ solution is more stable than the $3Q$ increases with decreasing gap. Finally, the relative extension of the $2Q$ phase with respect to the $3Q$ nematic phase increases with decreasing gap. Nevertheless, we stress again that the actual nematic state, i.e., the ratio Δ_1/Δ_2, might depend on details beyond our model, such as anharmonic effects.

1.5 Robustness of the nematic state and secondary order parameter

Recent bulk X-ray diffraction experiments have identified a secondary order parameter [184], in the form of out-of-plane Se displacements with symmetry M_1^+ in bulk samples, which was also found in *ab initio* calculations [177]. This M_1^+ order parameter $\vec{\Phi} = (\Phi_1, \Phi_2, \Phi_3)$ is symmetry allowed in the CDW produced by $\vec{\Delta}$ in both bulk and monolayer, as it breaks no further symmetries. Indeed, it develops at T_{CDW} and linearly but slowly increases with decreasing temperature. Remarkably, below a given $T^* \sim 165\text{K}$, its associated X-ray diffraction peak undergoes a sharp increase, indicating that below this temperature $\vec{\Phi}$ is not only symmetry-induced but its condensation is energetically favorable. Incidentally, T^* coincides with the maximum of the electrical resistivity discussed in Section 1.1.3, although whether these two features are actually connected remains unknown.

In this section, we discuss the effect of $\vec{\Phi}$ in the bands of the $\boldsymbol{k} \cdot \boldsymbol{p}$ model, and show that it can enhance the DOS peak associated to the incipient saddle point in the CDW conduction band. By adding further interactions to the effective lattice model that decouple in the $\vec{\Phi}$ channel, we demonstrate that the nematic CDW is robust and even enhanced.

1.5.1 k.p model

By symmetry, to linear order, $\vec{\Phi}$ can only couple the Ti d bands with themselves as

$$H_{dd}^{\Phi}(\vec{\Phi}) = \begin{pmatrix} 0 & \Phi_3 & \Phi_2 \\ \Phi_3 & 0 & \Phi_1 \\ \Phi_2 & \Phi_1 & 0 \end{pmatrix}. \tag{1.51}$$

We note that the coupling is the same in the bulk, since the three electron pockets are separated by the momentum $\boldsymbol{M}$; for example, $\boldsymbol{L}_1 + \boldsymbol{L}_2 = -\boldsymbol{M}_3 + \boldsymbol{G}_z$, with $\boldsymbol{G}_z = (0, 0, 2\pi/c)$ a reciprocal lattice vector. The total Hamiltonian can be obtained by adding Eqs. (1.29) and (1.51):

$$H = \begin{pmatrix} \frac{E_g}{2} + H_{dd}^0(\boldsymbol{k}) + H_{dd}^{\Phi}(\vec{\Phi}) & H_{dp}(\vec{\Delta}) \\ H_{dp}^{\dagger}(\vec{\Delta}) & -\frac{E_g}{2} + H_{pp}^0(\boldsymbol{k}) \end{pmatrix}, \tag{1.52}$$

It is useful to define the "sign" of $\vec{\Phi}$ as $\mathrm{sign}(\Phi_1\Phi_2\Phi_3)$. As opposed to $\vec{\Delta}$, which produces the same band structure for either sign, the bands are sensitive to the sign of $\vec{\Phi}$. Indeed, when $\vec{\Delta} = 0$, a C_3-symmetric $3Q$ $\vec{\Phi} = (\Phi, \Phi, \Phi)$ splits the three electron pockets in a singlet with band edge at energy $\frac{E_g}{2} + 2\Phi$ and a doublet at $\frac{E_g}{2} - \Phi$ (see Figs. 1.13(a,b)). Therefore, $\Phi > 0$ *raises* the singlet conduction band with respect to the doublet, while $\Phi < 0$ *lowers* it. In the presence of a finite $\vec{\Delta} = (\Delta, \Delta, \Delta)$, the sign of $\vec{\Phi}$ has the same effect. In this case, the electron pockets are already split in singlet and doublet by $\vec{\Delta}$, and $\vec{\Phi}$ shifts them depending on its sign, as shown in Figs. 1.13(c-f). Moreover, via the finite p-d coupling induced by $\vec{\Delta}$, $\vec{\Phi}$ also affects the valence bands. Indeed, the conduction and valence band edges at $\boldsymbol{k} = 0$ for $\vec{\Delta} = (\Delta, \Delta, \Delta)$ and $\vec{\Phi} = (\Phi, \Phi, \Phi)$ are:

$$\varepsilon_c^{\text{singlet}}(\boldsymbol{k} = 0) = \frac{E_g}{2} + 2\Phi, \tag{1.53}$$

$$\varepsilon_c^{\text{doublet}}(\boldsymbol{k} = 0) = -\frac{\Phi}{2} + \sqrt{\left(\frac{E_g - \Phi}{2}\right)^2 + \Delta^2}, \tag{1.54}$$

$$\varepsilon_v^{\text{doublet}}(\boldsymbol{k} = 0) = -\frac{1}{2}\Phi - \sqrt{\left(\frac{E_g - \Phi}{2}\right)^2 + \Delta^2}, \tag{1.55}$$

With this in mind, we now analyze which sign of $\vec{\Phi}$ is energetically favorable. At stoichiometry and for a positive gap, only the energies of the filled valence bands matter. $\vec{\Phi}$ couples to the valence bands only indirectly via $\vec{\Delta}$. It shifts them downward when $\Phi > 0$, which is thus the preferred state at charge neutrality. For finite electron doping, this effect competes against the energy gain coming from the direct $\vec{\Phi}$ coupling of conduction bands when the singlet is shifted to lower energies instead (see Appendix 1.D.1, where we analytically and numerically determine this energy gain from the

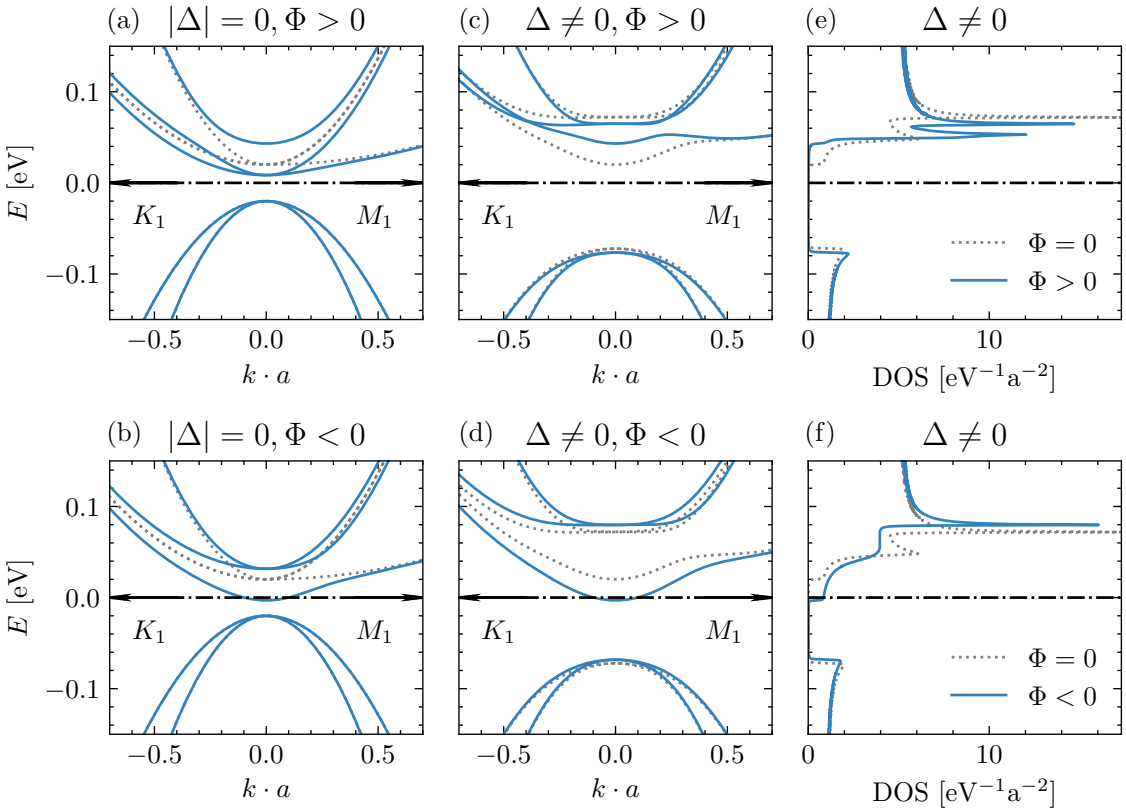

FIGURE 1.13: $\boldsymbol{k} \cdot \boldsymbol{p}$ bands in the C_3-symmetric $3Q$ state with $\vec{\Delta} = (\Delta, \Delta, \Delta)$ and $\vec{\Phi} = (\Phi, \Phi, \Phi)$. The $\boldsymbol{k} \cdot \boldsymbol{p}$ parameters are $E_g = 40\text{meV}$, $a_d = 0.33\text{eV}/a$, $b_d/a_d = 0.87$, $a_p = -0.58\text{eV}/a$, $b_p/a_p = 0.25$, $|\vec{\Delta}| = 120\text{meV}$, $|\vec{\Phi}| = 20\text{meV}$. (a) $\Delta = 0$ and $\Phi > 0$. (b) $\Delta = 0$ and $\Phi < 0$. The grey dotted lines in (a) and (b) are the noninteracting bands with $\Delta = 0$ and $\Phi = 0$. (c) $\Delta \neq 0$ and $\Phi > 0$. (d) $\Delta \neq 0$ and $\Phi < 0$. (e) DOS corresponding to the bands at (c) with $\Delta \neq 0$ and $\Phi > 0$. (f) DOS corresponding to the bands at (d) with $\Delta \neq 0$ and $\Phi < 0$. The grey dotted lines in (c), (d), (e), (f) correspond to the case $\Delta \neq 0$ and $\Phi = 0$.

conduction bands). As we will show in our effective lattice model, this competition induces a sign change of $\vec{\Phi}$ at a finite doping.

The conduction band singlet displays an incipient saddle point in the presence of $\vec{\Delta}$, which drives the nematic state, as explained in Section 1.2. When $\Phi > 0$, which is the preferred sign at low doping, this band is shifted to higher energies. This shift is $\boldsymbol{k}$-dependent, being larger at $\boldsymbol{k} = 0$ (see Fig. 1.13(c)). This effect enhances the peak in the DOS associated to the incipient van Hove singularity, as shown in Fig. 1.13(e). Indeed, for the parameters used in this figure, the saddle point is not fully developed for $\Phi = 0$, so there is just a finite peak in the DOS. $\Phi > 0$ induces a real van Hove singularity. This enhancement of the DOS peak can enhance the nematic instability. Our self-consistent mean-field calculations in the effective lattice model of Section 1.5.3 confirm

this prediction. On the other hand, $\Phi < 0$ has the opposite effect: it weakens the peak in the DOS.

1.5.2 Ginzburg-Landau theory

Before moving on to the mean-field calculations in the lattice model, we analyze how $\vec{\Phi}$ enters in the Ginzburg-Landau theory, and show that it couples to the primary order parameter $\vec{\Delta}$. The Ginzburg-Landau free-energy functional of $\vec{\Phi}$ alone is similar to that of $\vec{\Delta}$ of Eq. (1.35), but it allows for an additional cubic term, which is even under inversion for $\vec{\Phi}$:

$$F_\Phi = a_\Phi|\vec{\Phi}|^2 + d_\Phi\Phi_1\Phi_2\Phi_3 + b_\Phi|\vec{\Phi}|^4 + c_\Phi(\Phi_1^4+\Phi_2^4+\Phi_3^4). \tag{1.56}$$

This manifests that $\mathrm{sign}(\Phi_1\Phi_2\Phi_3)$ has physical meaning, as shown in the $\boldsymbol{k}\cdot\boldsymbol{p}$ model. As we discussed in the previous section, for $\vec{\Delta}=0$, $\vec{\Phi}$ prefers $\Phi_1\Phi_2\Phi_3<0$, which determines that $d_\Phi>0$ in the Ginzburg-Landau free-energy.

Now, $\vec{\Delta}$ and $\vec{\Phi}$ are also coupled in the free-energy density. The coupling of lowest order reads

$$F^{(3)}_{\Delta\Phi} = d_{\Delta\Phi}(\Phi_1\Delta_2\Delta_3 + \Phi_2\Delta_3\Delta_1 + \Phi_3\Delta_1\Delta_2). \tag{1.57}$$

The sign of the coefficient $d_{\Delta\Phi}$, at least close to stoichiometry, can be determined from the fact that the total energy is reduced when $\vec{\Phi}$ pushes the valence bands to lower energies via $\vec{\Delta}$. In this case, $\Phi_1\Phi_2\Phi_3>0$, which indicates that $d_{\Delta\Phi}<0$ (see Appendix 1.D.2).

The cubic coupling $F^{(3)}_{\Delta\Phi}$ illustrates that $\vec{\Phi}$ is induced as soon as $\vec{\Delta}$ condenses. Indeed, for finite $\vec{\Delta}$, $F^{(3)}_{\Delta\Phi}$ is linear in $\vec{\Phi}$, making $\vec{\Phi}$ finite even if its quadratic coefficient a_Φ is positive. This is consistent with the X-ray observation of a small linear increase of the Se displacements with M_1^+ below T_{CDW} [184]. The change of slope at T^* might originate from the quadratic coefficient a_Φ becoming negative at this temperature, which increases $\vec{\Phi}$.

Finally, we mention a complementary mechanism by which the nematic CDW can be enhanced due to the coupling with the secondary order parameter $\vec{\Phi}$. The cubic term $F^{(3)}_\Phi = d_\Phi\Phi_1\Phi_2\Phi_3$ has coefficient $d_\Phi>0$, which, in the C_3-symmetric $3Q$ state $\vec{\Delta}=(\Delta,\Delta,\Delta)$, $\vec{\Phi}=(\Phi,\Phi,\Phi)$, favours $\Phi<0$. On the other hand, the cubic coupling $F^{(3)}_{\Delta\Phi}$ has coefficient $d_{\Delta\Phi}<0$, which favours $\Phi>0$ instead. At low doping, $F^{(3)}_{\Delta\Phi}$ dominates and $\Phi>0$. Instead, at moderate doping, before the transition to the $1Q$ stripe phase, it is $F^{(3)}_\Phi$ that dominates and $\Phi<0$, since d_Φ increases with doping (see Appendix 1.D.2). In the intermediate region, both terms compete, and can enhance the nematic state. Indeed, the change of sign of $\vec{\Phi}$ in our self-consistent mean-field calculations in the lattice model occurs within the nematic phase, as we show in Appendix 1.D.3. Besides the shift of the incipient saddle point by $\vec{\Phi}$ explained in the previous section, this cubic term competition might further favour nematiciy. We thoroughly describe this mechanism in Appendix 1.D.2.

1.5.3 Effective lattice model: additional interactions

In this section we include further interactions in the effective lattice model of Eqs. (1.39) and (1.43), and show that the nematic and stripe phases are robust. Indeed, the new interactions give rise to the secondary order parameter $\vec{\Phi}$, and the nematic dome is slightly enlarged, likely due to the change in the incipient saddle point and the competition of the Ginzburg-Landau cubic terms.

Defining the additional interactions and order parameters

We include two new interactions: an onsite density-density d-p interaction

$$H_{dp0} = U_{dp} \sum_i \left(d_i^\dagger d_i - n_{d0} \right) \left(\boldsymbol{p}_i^\dagger \cdot \boldsymbol{p}_i - n_{p0} \right) \tag{1.58}$$

and a nearest-neighbour density-density d-d interaction

$$H_{dd1} = V_{dd} \sum_{\langle ij \rangle_1} \left(d_i^\dagger d_i - n_{d0} \right) \left(d_j^\dagger d_j - n_{d0} \right), \tag{1.59}$$

where $n_{d0} = \langle d_i^\dagger d_i \rangle_0 (T=0)$ and $n_{p0} = \langle \boldsymbol{p}_i^\dagger \cdot \boldsymbol{p}_i \rangle_0 (T=0)$ are the densities at zero temperature computed in the ground state of the initial noninteracting Hamiltonian H_0 of Eq. (1.39). We subtract these noninteracting densities n_{d0} and n_{d+p0} to exclude renormalizations of the bands and, in particular, of the gap, that would arise due to double-counting of the interactions and doping[5]. That way, we isolate the effect of the CDW. The total interaction Hamiltonian becomes $H_{\text{int}} = H_{dp1} + H_{dp0} + H_{dd1}$.

To find a mean-field solution, we consider the decoupling in the onsite orbital order $\langle d_j^\dagger p_{\alpha j} \rangle$, as well as in the onsite charge densities $n_{di} = \langle d_i^\dagger d_i \rangle$ and $n_{pi} = \langle \boldsymbol{p}_i^\dagger \cdot \boldsymbol{p}_i \rangle$. This corresponds to the Fock channel of H_{dp1} (H_{dp1}^{MF} in Eq. (1.43)), the Hartree and Fock channels of H_{dp0}, and the Hartree channel of H_{dd1}. The total mean-field Hamiltonian is $H_{\text{MF}} = H_0 + H_{dp1}^{\text{MF}} + H_{dp0}^{\text{MF}} + H_{dd1}^{\text{MF}}$, with

$$\begin{aligned} H_{dp0}^{\text{MF}} =& U_{dp} \sum_i \left\{ n_{p,i} \left(d_i^\dagger d_i - n_{d0} \right) + n_{d,i} \left(\boldsymbol{p}_i^\dagger \cdot \boldsymbol{p}_i - n_{p0} \right) - n_{d,i} n_{p,i} \right\} - \\ & - U_{dp} \sum_i \left\{ \left[\langle d_i^\dagger \boldsymbol{p}_i \rangle^* \cdot \left(d_i^\dagger \boldsymbol{p}_i \right) + \text{h.c.} \right] - \langle d_i^\dagger \boldsymbol{p}_i \rangle^* \cdot \langle d_i^\dagger \boldsymbol{p}_i \rangle \right\}, \end{aligned} \tag{1.60}$$

$$H_{dd1}^{\text{MF}} = V_{dd} \sum_{\langle ij \rangle_1} \left\{ n_{d,j} \left(d_i^\dagger d_i - n_{d0} \right) + n_{d,i} \left(d_j^\dagger d_j - n_{d0} \right) - n_{d,i} n_{d,j} \right\}, \tag{1.61}$$

[5] In reality, doping might induce a band renormalization. However, since our lattice model has effective orbitals and interactions, it does not accurately capture it. Therefore, the phase diagrams we present should be interpreted as providing the phases that would appear at a given doping if the normal state gap at this doping is E_g.

where $n_{d,i} = \langle d_i^\dagger d_i \rangle - n_{d0}$ and $n_{p,i} = \langle \boldsymbol{p}_i^\dagger \cdot \boldsymbol{p}_i \rangle - n_{p0}$ are the excess charge densities with respect to the noninteracting system at zero temperature, with the expectation values taken in the mean-field ground state.

Now, we perform the symmetry analysis of the new order parameters involved in the total mean field Hamiltonian. As described in Section 1.4.1, the onsite orbital orders $\langle d_j^\dagger p_{\alpha j} \rangle$ transform as $\Gamma_3^- \oplus M_1^- \oplus M_2^-$ (see Eqs. (1.40)-(1.42)). The onsite charge orders $n_{d,j}$ and $n_{p,j}$ transform as time-reversal even $\Gamma_1^+ \oplus M_1^+$. The symmetry adapted expressions read as

$$n_{c,\Gamma_1^+} = \frac{1}{2} \sum_j n_{c,j}, \tag{1.62}$$

$$n^a_{c,M_1^+} = \frac{1}{2} \sum_j e^{i\boldsymbol{M}_a \cdot \boldsymbol{r}_j} n_{c,j}, \tag{1.63}$$

where $c = d, p$. The Γ_1^+ components are just the normalized total excess charge in the supercell with respect to the noninteracting value, which are therefore subject to the charge conservation law $n_{d,\Gamma_1^+} + n_{p,\Gamma_1^+} = 0$; note that we defined $n_{c,j} = \langle c_j^\dagger c_j \rangle - \langle c_i^\dagger c_i \rangle_0 (T = 0)$. The M_1^+ channels correspond to a CDW, and will compose the secondary order parameter $\vec{\Phi}$.

The next step is writing down the expressions for the order parameters that enter in the mean-field Hamiltonian H_{MF}. As worked out in Section 1.4.1, H^{MF}_{dp1} has an attractive coupling $-2V_{dp}$ in the $\langle d^\dagger p \rangle_{M_1^-}$ channel and a repulsion $+2V_{dp}$ for $\langle d^\dagger p \rangle_{M_2^-}$. Now, the Fock term of H^{MF}_{dp0} can be rewritten as

$$\left[H^{\mathrm{MF}}_{dp0} \right]_{\mathrm{Fock}} = -U_{dp} \sum_{\text{supercells}} \sum_{\gamma = M_1^-, M_2^-, \Gamma_3^-} \left(\langle d^\dagger p \rangle^*_\gamma \left[d^\dagger p \right]_\gamma + \text{h.c.} - \left| \langle d^\dagger p \rangle_\gamma \right|^2 \right). \tag{1.64}$$

Therefore, it is attractive with coupling $-U_{dp}$ in all the $\langle d^\dagger p \rangle_{M_1^-}$, $\langle d^\dagger p \rangle_{M_2^-}$, and $\langle d^\dagger p \rangle_{\Gamma_3^-}$ channels. In the onsite charge sector, the Hartree term of H^{MF}_{dp0} can be rewritten as

$$\left[H^{\mathrm{MF}}_{dp0} \right]_{\mathrm{Hartree}} = U_{dp} \sum_{\text{supercells}} \sum_{\gamma = \Gamma_1^+, M_1^+} \left\{ n_{d,\gamma} \left(\left[p^\dagger p \right]_\gamma - n_{p0} \right) + n_{p,\gamma} \left(\left[d^\dagger d \right]_\gamma - n_{d0} \right) - n_{d,\gamma} n_{p,\gamma} \right\}. \tag{1.65}$$

Finally, in the basis $\{d_1^\dagger d_1, d_2^\dagger d_2, d_3^\dagger d_3, d_4^\dagger d_4\}$, H_{dd1}^{MF} can be recast as

$$H_{dd1}^{\mathrm{MF}} = \sum_{\text{supercells}} \{2V_{dd} n_d \cdot \begin{pmatrix} 0 & 1 & 1 & 1 \\ 1 & 0 & 1 & 1 \\ 1 & 1 & 0 & 1 \\ 1 & 1 & 1 & 0 \end{pmatrix} \cdot \left(d^\dagger d - n_{d0}\right) - V_{dd} n_d \cdot \begin{pmatrix} 0 & 1 & 1 & 1 \\ 1 & 0 & 1 & 1 \\ 1 & 1 & 0 & 1 \\ 1 & 1 & 1 & 0 \end{pmatrix} \cdot n_d \}. \tag{1.66}$$

The eigenvalues of this matrix are $+3$ and -1 for the $\left[d^\dagger d\right]_{\Gamma_1^+}$ and $\left[d^\dagger d\right]_{M_1^+}$ eigenvectors, respectively. Therefore, H_{dd1}^{MF} can be expressed as

$$\begin{aligned} H_{dd1}^{\mathrm{MF}} = \sum_{\text{supercells}} \Bigg\{ & 6V_{dd} \left[n_{d,\Gamma_1^+} \left(\left[d^\dagger d\right]_{\Gamma_1^+} - n_{d0} \right) - \frac{1}{2} n_{d,\Gamma_1^+}^2 \right] \\ & -2V_{dd} \left[n_{d,M_1^+} \left(\left[d^\dagger d\right]_{M_1^+} - n_{d0} \right) - \frac{1}{2} n_{d,M_1^+}^2 \right] \Bigg\}, \end{aligned} \tag{1.67}$$

showing that it has a repulsive coupling $+6V_{dd}$ in the Γ_1^+ channel and an attraction $-2V_{dd}$ in the M_1^+ CDW.

With this information, we can write down the explicit expressions for the primary M_1^- $\vec{\Delta}$ and secondary M_1^+ $\vec{\Phi}$ order parameters:

$$\Delta_a = -\sqrt{\frac{3}{8}} \left(U_{dp} + 2V_{dp}\right) \frac{1}{2} \sum_j e^{i\boldsymbol{M}_a \cdot \boldsymbol{r}_j} \mathrm{Re}\langle d_j^\dagger \boldsymbol{p}_j \rangle \times \hat{\boldsymbol{M}}_a, \tag{1.68}$$

$$\Phi_a = \frac{1}{4} \sum_j e^{i\boldsymbol{M}_a \cdot \boldsymbol{r}_j} \left(-2V_{dd} n_{d,j} + U_{dp} n_{p,j}\right), \tag{1.69}$$

which couple to the low-energy electron and hole pockets as described in the $\boldsymbol{k} \cdot \boldsymbol{p}$ model in Eqs. (1.30) and (1.51), respectively.

Besides these two order parameters, which dominate the CDW physics, our mean-field decoupling H_{MF} allows for other 8 mean-field terms in the Hamiltonian:

- The TRS even M_2^- CDW orbital order discussed in Section 1.4.1, which is only nonzero but small in the nematic phase, where it is symmetry allowed.
- The TRS odd M_1^- and M_2^- CDW orbital orders discussed in Section 1.4.1, which always vanish in our calculations.
- The TRS even and odd Γ_3^- nematic orbital orders now have an attraction due to the onsite interaction U_{dp}. However, they are highly unfavorable from the kinetic band energy perspective, since they couple the valence bands with the conduction band at the same $\boldsymbol{k}$, where

the direct gap is large. Therefore, they vanish in our calculations.

- The Γ_1^+ terms coming from the total charge for the valence and conduction bands. They induce a rigid shift of the conduction and valence bands separately, and therefore renormalize the gap, but without breaking any symmetry. Indeed, the d band shifts by and amount $\rho_d = (6V_{dd}n_{d\Gamma_1^+} + U_{dp}n_{p\Gamma_1^+})$, and the p band by $\rho_p = U_{dp}n_{d\Gamma_1^+}$. Charge conservation implies that $n_{p\Gamma_1^+} = -n_{d\Gamma_1^+}$, so the gap is renormalized as $E_g \to E_g + (\rho_d - \rho_p) = E_g + 2(3V_{dd} - U_{dp})n_{d\Gamma_1^+}$. Since $n_{d\Gamma_1^+}$ is the excess charge with respect to the zero-temperature value in the normal state H_0 for each doping, only temperature renormalizes the gap via this mechanism. Since the DOS of the conduction bands is larger than that of the valence bands, we always have $n_{d\Gamma_1^+} \geq 0$ and increasing with temperature, so the gap increases with increasing temperature if $3V_{dd} > U_{dp}$, and it decreases otherwise.
- The M_1^+ CDW charge order of the p bands. It does not directly couple the low-energy valence bands, but it is symmetry-induced in the M_1^- CDW state due to an indirect energy gain via $\vec{\Delta}$ involving higher energy bands. However, it is smaller than the M_1^+ order parameter $\vec{\Phi}$ of the d band.

Self-consistent mean-field calculations

Fig. 1.14 shows T-x phase diagrams for gaps $E_g = +50, 0, -25, -30, -50$meV. We compare the results with finite V_{dp}, U_{dp} and V_{dd} interactions (Eqs. (1.43), (1.58) and (1.59)) in the top row, to those with only V_{dp} in the bottom row. The nematic and stripe CDWs are robust against the new interactions, and the phase diagrams remain qualitatively the same as with only V_{dp}. Moreover, the $2Q/3Q$ nematic dome is expanded, with T_{nematic} reaching up to $0.3T_{\text{CDW}}$. Within the nematic dome, the relative extension of the $2Q$ phase with respect to the $3Q$ nematic state also increases when including the U_{dp} and V_{dd} interactions. On the other hand, the $1Q$ stripe phase is slightly suppressed and pushed to higher dopings.

Now, the C_3-symmetric $3Q$ and nematic phases also have a symmetry allowed $\vec{\Phi}$ component. The C_3-symmetric $3Q$ phase is $\vec{\Delta} = (\Delta, \Delta, \Delta)$, $\vec{\Phi} = (\Phi, \Phi, \Phi)$, the nematic $3Q$ state is $\vec{\Delta} = (\Delta_1, \Delta_2, \Delta_2)$, $\vec{\Phi} = (\Phi_1, \Phi_2, \Phi_2)$, and the $2Q$ phase is $\vec{\Delta} = (0, \Delta, \Delta)$, $\vec{\Phi} = (\Phi, 0, 0)$. The enhanced nematic phase is consistent with the enhanced DOS peak of to the incipient conduction band saddle point by $\vec{\Phi}$, as well as with the competition of the Ginzburg-Landau cubic terms (see Appendix 1.D.3). Instead, $\vec{\Phi}$ vanishes in the $1Q$ stripe phase, since it is not allowed by symmetry there. This could be deduced from the cubic Ginzburg-Landau coupling of Eq. (1.57), which vanishes in the stripe phase. Since a finite $\vec{\Phi}$ contributes to the energy gain, the vanishing $\vec{\Phi}$ in the stripe phase might explain why it is suppressed.

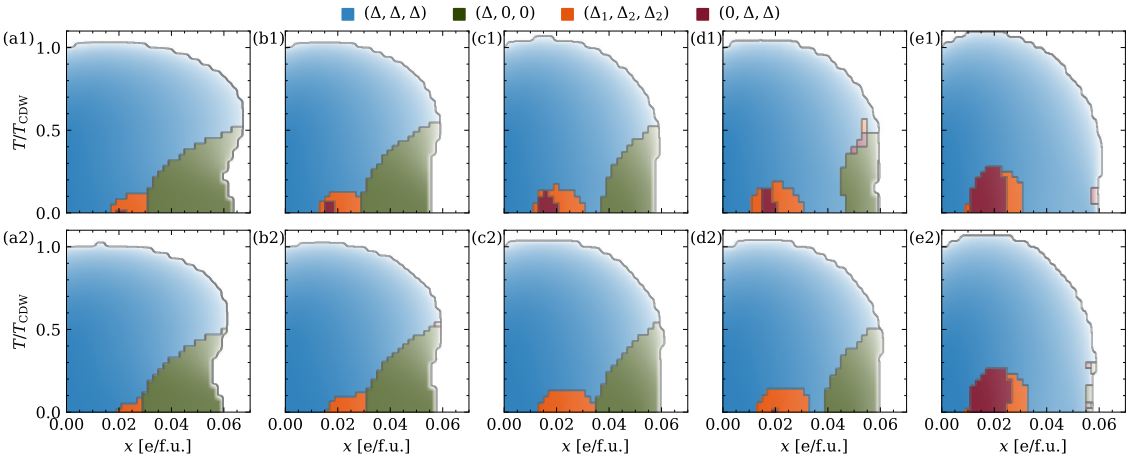

FIGURE 1.14: Temperature-doping phase diagrams obtained by self-consistently solving the mean-field Hamiltonian H_{MF} of Eqs. (1.44), (1.60), (1.61) for different gaps and interaction strengths. The intensity of the color of each phase is proportional to $|\vec{\Delta}|$. The first row displays the results for finite V_{dp}, U_{dp}, and V_{dd} interactions, which are compared to the results with only finite V_{dp} in the second row. T_{CDW} is the critical temperature at stoichiometry.

(a1)	$E_g = +50$meV,	$V_{dp} = 450$meV,	$U_{dp} = 900$meV,	$V_{dd} = 400$meV,	$T_{\mathrm{CDW}} = 596$K;
(a2)	$E_g = +50$meV,	$V_{dp} = 890$meV,	$U_{dp} = 0$,	$V_{dd} = 0$,	$T_{\mathrm{CDW}} = 576$K;
(b1)	$E_g = 0$,	$V_{dp} = 400$meV,	$U_{dp} = 800$meV,	$V_{dd} = 400$meV,	$T_{\mathrm{CDW}} = 358$K;
(b2)	$E_g = 0$,	$V_{dp} = 800$meV,	$U_{dp} = 0$,	$V_{dd} = 0$,	$T_{\mathrm{CDW}} = 378$K;
(c1)	$E_g = -25$meV,	$V_{dp} = 400$meV,	$U_{dp} = 680$meV,	$V_{dd} = 400$meV,	$T_{\mathrm{CDW}} = 259$K;
(c2)	$E_g = -25$meV,	$V_{dp} = 740$meV,	$U_{dp} = 0$,	$V_{dd} = 0$,	$T_{\mathrm{CDW}} = 269$K;
(d1)	$E_g = -30$meV,	$V_{dp} = 400$meV,	$U_{dp} = 650$meV,	$V_{dd} = 400$meV,	$T_{\mathrm{CDW}} = 239$K;
(d2)	$E_g = -30$meV,	$V_{dp} = 725$meV,	$U_{dp} = 0$,	$V_{dd} = 0$,	$T_{\mathrm{CDW}} = 249$K;
(e1)	$E_g = -50$meV,	$V_{dp} = 400$meV,	$U_{dp} = 520$meV,	$V_{dd} = 400$meV,	$T_{\mathrm{CDW}} = 155$K;
(e2)	$E_g = -50$meV,	$V_{dp} = 650$meV,	$U_{dp} = 0$,	$V_{dd} = 0$,	$T_{\mathrm{CDW}} = 145$K;

1.6 Discussion

Motivated by the contradictory STM experiments of refs. [52–54, 56, 114], we have analyzed the doping dependence of the symmetry of the commensurate CDW in monolayer $TiSe_2$. Based on general arguments from the $\boldsymbol{k} \cdot \boldsymbol{p}$ model and on self-consistent mean-field calculations in a minimal tight-binding model, we have established that electron doping drives two transitions to C_3-symmetry-broken phases within the CDW. As typically predicted by DFT calculations [141, 177], the CDW is a C_3-symmetric $3Q$ state at stoichiometry. The lowest conduction band in the CDW develops an incipient saddle point with a high DOS. When the electron doping is close to this van Hove filling, the system undergoes a nematic instability towards a nematic $3Q/2Q$ CDW. Further increasing the doping, there is a transition to a $1Q$ stripe CDW driven by the gain in electronic energy.

We now discuss whether this picture can be translated to bulk $TiSe_2$, and propose other experimental techniques to probe the nematic and stripe states. We also propose a new interpretation

for the light-induced chiral state in bulk $TiSe_2$ [186, 187], whose origin is different from the C_3-broken states observed in STM [52–54, 56, 114]. We close this Chapter with a discussion of the open problems in the field.

1.6.1 Bulk $TiSe_2$: comparison to STM experiments

Our calculations assume a monolayer for simplicity, but we expect the existence of doping-induced transitions to carry over to the bulk limit, because $TiSe_2$ is a quasi 2D van der Waals material with weak band dispersion in the k_z direction. In the bulk, the primary order parameter has L_1^- symmetry, and the secondary order parameter transforms as M_1^+, which preserves all the symmetries of the L_1^-.

Our mechanism driving the nematic phase relies on the DOS peak associated to the incipient saddle point in the lowest conduction band. While the DOS will never be divergent in $3D$, it is also not divergent for realistic parameters in the monolayer, and yet the nematic phase appears, due to the strong-coupling character of the CDW in $TiSe_2$. The DOS peak will be reduced in the bulk, but our $\boldsymbol{k}\cdot\boldsymbol{p}$ calculations predict a nematic dome for considerably smaller conduction band ellipticity, and thus DOS peak (see Fig. 1.8). This suggests that our proposal for nematic states is compatible with the C_3-breaking states observed in STM [52–54], where one CDW Bragg peak is much smaller than the other two. The uncontrolled native doping ubiquitously present in $TiSe_2$ samples can then explain the variability of the ground state symmetry observed [114].

Remarkably, the L_1^- order parameter preserves the inversion center between layers, and therefore none of the bulk versions of our proposed states is chiral. This differentiates our theory from previous proposals [178–181], which require the condensation of an additional L_2^+ phonon. It is also worth noting that the DFT calculations of Ref. [185] predict a chiral CDW at stoichiometry with two condensed phonons: the L_1^- in a $(0,\Delta,\Delta)$ configuration plus the M_1^- in a $(\Psi,0,0)$ state. This predicted structure has space group $C2$ and therefore breaks C_3 symmetry, so it is a candidate for the STM experiments of Refs. [52–54]. The change of this state with doping and temperature should be studied to analyze whether it could also explain the variability of the ground state symmetry. Its robustness against different exchange-correlation functionals [146] should also be evaluated.

Regarding our predicted $1Q$ stripe phase, Ref. [56] reported STM measurements on Cu-doped $TiSe_2$ showing the coexistence of short-range domains of the C_3-symmetric $3Q$ CDW and the $1Q$ stripe CDW at intermediate dopings. Further doping renders the CDW incommensurate, where all the domains become $3Q$ again. Modeling phase coexistence in such inhomogeneous states is beyond the scope of this Thesis, but our predicted $1Q$ stripe phase at high doping is a good starting

point. The fact that the $3Q$ to $1Q$ transition is first order is also compatible with the observed phase separation.

Finally, we caution however that, since STM is a surface probe and doping need not be homogeneous, the bulk and surface CDW states need not be the same. Furthermore, the effect of a surface termination might favor the rotational symmetry breaking (see Appendix 1.D.2).

1.6.2 Experimental signatures of the nematic and stripe states

Our prediction of a robust, doping-induced C_3-breaking phase in $TiSe_2$, motivated by different STM experiments, can solve the long-standing puzzle of the symmetry of the CDW. Our theory can be further confirmed with several other probes. The existence of a nematic transition can be quantified by elastoresistance measurements, which directly measure the nematic susceptibility. An early experiment [201] indeed detected a sharp change in elastoresistance below 200K. This signature has also been recently found in kagome AV_3Sb_5 metals [50], which display a nematic CDW too [48–50].

C_3-symmetry breaking can also be detected in low frequency Raman spectroscopy, as observed in 2H-$TaSe_2$ [202]. For instance, the broken C_3 symmetry would split the E CDW phonon mode, which would be twofold degenerate otherwise. ARPES experiments may also detect different intensity for the three conduction band pockets in the C_3 breaking states, due to the different backfolded spectral weight. Another unique set of techniques sensitive to the symmetry of the ground state relies on nonlinear optics or transport. In particular, the existence of the nematic state in monolayer samples could be demonstrated by the nonlinear Hall effect [203], which vanishes for D_3 symmetry but becomes possible once it is broken.

1.6.3 Bulk $TiSe_2$: light-induced CPGE

Bulk samples cooled in the presence of circularly polarized light display a longitudinal circular photogalvanic effect (CPGE) below $T_{\mathrm{CPGE}} < T_{\mathrm{CDW}}$, which is consistent with C_3 symmetry [186, 187]. We emphasize that this light-induced chiral state is unrelated to the one observed in STM. The interpretation of Ref. [186] of this light-induced chiral state is based on the secondary transition at T_{CPGE} to the chiral CDW of Refs. [55, 178–182]. In particular, Ref. [186] proposes that, without training, domains of opposite chirality coexist so that inversion symmetry is present on average, but the training favors one chirality via the coupling to the circularly polarized light. However, the presence of C_3 symmetry discards the chiral CDW proposed by Refs. [178–182] generated by the condensation of L_1^- and L_2^+ phonons, as well as the chiral CDW determined by Ref. [185] with $L_1^-(0,\Delta,\Delta) + M_1^-(\Psi,0,0)$.

Instead, this light-induced chiral state is likely induced by the condensation of phonons with M_1^- symmetry [194] aided by the presence of circular light. Indeed, a C_3-symmetric $3Q$ CDW with order parameter M_1^-, as in the monolayer, has space group $P321$ and point group D_3, and is therefore chiral, C_3-symmetric and compatible with the experiments [186, 187]. Note that the M_1^- is not the leading bulk instability, so the interpretation in terms of chiral domains does not apply, and an alternative explanation is required. Ref. [194] suggested that the M_1^- state could be stabilized in the nonequilibrium situation where the electronic temperature is increased by the training light. This is consistent with the fact that the in-plane order is set at a higher temperature $T_{\text{in-plane}}$, and the long-range order in the out-of-plane stacking direction is only set at $T_{\text{CDW}} < T_{\text{in-plane}}$ [173]. This means that between $T_{\text{in-plane}}$ and T_{CDW} the CDW can be regarded as an incoherent superposition of the L_1^- and the M_1^- order parameters. Moreover, this goes also along the lines of the out-of-equilibrium experiment of Ref. [171], where light first suppresses the long-range out-of-plane order, since this is set by the excitonic correlations, which have a much faster timescale than phonons. However, we note that since the training light is removed once low temperatures are reached and the M_1^- is not the leading bulk instability, this explanation is not complete.

Instead, we propose that the chiral state M_1^- in this theory has to be metastable, although sufficiently close in energy to the centrosymmetric CDW ground state so that it has a long lifetime. By applying the training light in the normal state and cooling, the metastable chiral state might become the lowest energy stationary state due to coupling to the light. When the training light is removed at low temperature, the system can be trapped in the local minimum of the chiral state, and thermal fluctuations might drive the system to the achiral ground state only above T_{CPGE}. In Appendix 1.E, we analyze the possible existence of a metastable chiral state within a Ginzburg-Landau functional coupling the time-reversal symmetric L_1^- and M_1^- order parameters. We conclude that a metastable M_1^- state can indeed exist if the coupling between both order parameters is strong.

Finally, we suggest an additional mechanism via which the light might favour the M_1^- state beyond the higher electronic temperature. The circularly polarized light in normal incidence can be effectively represented by a coupling $\Lambda = [\boldsymbol{E} \times \boldsymbol{E}^*]_z$, where $\boldsymbol{E}$ is the in-plane electric field. Λ transforms as the time-reversal odd A_{2g} irrep of the $TiSe_2$ point group D_{3d}. Therefore, time-reversal symmetry prevents terms linear in Λ in the Ginzburg-Landau functional. Since Λ^2 transforms as time-reversal even A_{1g}, the coefficients of $F_{\Delta\Psi}$ can be renormalized by the circularly polarized light to order Λ^2. In the microscopic $\boldsymbol{k}\cdot\boldsymbol{p}$ or tight-binding models, Λ couples linearly to the time-reversal odd A_{2g} combination of the valence bands at Γ of Eq. (1.6), $-i\left(p_x^\dagger p_y - p_y^\dagger p_x\right)$. Physically, this coupling can be thought to arise from a Floquet-like effective picture. This coupling effectively splits the valence bands, and might also favour the metastable M_1^- CDW in the stationary

state. Studying whether this is actually the case is an interesting problem for the future.

1.6.4 Outlook

We have developed a theory that predicts a nematic CDW arising from an incipient saddle point in the CDW conduction band, and a stripe CDW coming from the electronic energy gain when doping the CDW, and we have discussed their applicability to different experiments.

Our theory opens up a number of avenues for further work. The most direct follow-up would be improving our effective lattice model by adding, for example, SOC. While the incipient saddle point would still be present with SOC, whether the SOC quantitatively enhances or shrinks the nematic and stripe states remains to be settled. Our understanding of the effect of the normal state gap, together with the impact of SOC, can allow us to compare $TiSe_2$ to other isostructural materials, which might display a wider nematic region. For instance, 1T-$ZrTe_2$ is semimetallic and has higher SOC [204, 205]. While a few experiments have focused on the role of excitonic correlations in its CDW [204, 205], the presence of nematicity has not been tackled yet.

Extending the effective lattice model to bulk 3D $TiSe_2$ is also straightforward by adding an interlayer hopping for the d and p orbitals. This would allow to quantify the persistence of the nematic states. Simulating a surface or a substrate is also possible by adding hoppings with the appropriate A_{2u} symmetry, which become allowed once that inversion and C_{2x} symmetries are broken. This would enable us to resolve whether the nematic phases are a bulk phase or live only on the surface in certain regions of the parameter space. Analogously, as discussed before, an effective coupling to the light could be added to evaluate whether the chiral metastable scenario is applicable to the experiments [186, 187].

The impact of disorder and defects on the CDW local symmetry is also crucial. A first approach to this problem could use perturbation theory in the $\boldsymbol{k} \cdot \boldsymbol{p}$ model coupled to a given impurity potential. A more accurate modelling would require solving the mean-field equations in real space with the realistic tight-binding model. Defects might strongly affect the local symmetry of the CDW. For instance, they could drive an inhomogeneous solution with domains with different symmetry nucleating from regions close or far from the defects. This becomes even more pressing at high doping, where the discommensurations appear. Also at high doping, while several studies have pointed to the relation of the network of commensurate domains and domain walls to superconductivity [23, 24, 26, 156, 157, 160, 161], there is still room for further study. For instance, superconductivity appears when doping is close to filling the second conduction band, where the DOS is enhanced. Whether these two observations are related is not known yet.

Despite their different band structure, $TiSe_2$ shares several analogies with the kagome AV_3Sb_5 metals, which have recently attracted considerable attention. Kagome AV_3Sb_5 metals have

$P6/mmm$ space group and D_{6h} point group, which is just the D_{3d} point group of $TiSe_2$ with an additional m_z mirror symmetry [51]. They exhibit van Hove singularities close to the Fermi level and support a $2 \times 2 \times 2$ CDW phase, where the Ginzburg-Landau functional describing the CDW order parameters is analogous to the one discussed here for $TiSe_2$ (see Eq. (1.110)) [51]. Remarkably, they undergo a second transition to a nematic CDW at lower temperatures [48–50], and they also become superconducting. A thorough investigation of their analogies could allow to apply some of the theories developed for these materials to $TiSe_2$, and vice versa.

We believe that our theory sets the foundation to understand the symmetry of the CDW in $TiSe_2$. In conjunction with new experiments, we hope that it will finally serve to settle this long-standing problem.

Appendices

1.A Group theory: extended point group and symmetries of the different ground states

In this Appendix, we describe the space group of the normal state of $TiSe_2$, we introduce its extended point group to study its CDW. This group-theoretical analysis is used to construct the $\boldsymbol{k}\cdot\boldsymbol{p}$ and tight-binding models, and classify their ground states.

1.A.1 Space group

The normal state of $TiSe_2$ has the symmorphic space group $P\bar{3}m1$ (#164), with point group D_{3d}. We will only consider the symmetry groups without spin. The generators of D_{3d} are $\{C_{3z}, C_{2x}, i\}$, with the center located in a Ti site. Its irreducible representations (irreps) are $\{A_{1g}, A_{2g}, E_g, A_{1u}, A_{2u}, E_u\}$ (see Ref. [206] for the character table). The subindex $1/2$ in the A irreps indicates the parity under C_{2x}, and the subindex g/u refers to the parity under the intralayer inversion i.

The little group of the Γ point, under which Γ remains invariant, is also D_{3d}. Its irreps, in space group notation, are $\{A_{1g}\equiv\Gamma_1^+, A_{2g}\equiv\Gamma_2^+, E_g\equiv\Gamma_3^+, A_{1u}\equiv\Gamma_1^-, A_{2u}\equiv\Gamma_2^-, E_u\equiv\Gamma_3^-\}$. On the other hand, the commensurate CDW has wavevector L in the bulk and M in the monolayer. Their little cogroup, which leaves the wavevector invariant, is C_{2h}. For instance, with the choice of the three $\boldsymbol{Q}=\Gamma L, \Gamma M$ of Fig. 1.3,

$$\boldsymbol{Q}_1 = (0, \frac{2\pi}{\sqrt{3}}, Q_z), \tag{1.70}$$

$$\boldsymbol{Q}_2 = (-\frac{\sqrt{3}}{2}\frac{2\pi}{\sqrt{3}}, -\frac{1}{2}\frac{2\pi}{\sqrt{3}}, Q_z), \tag{1.71}$$

$$\boldsymbol{Q}_3 = (\frac{\sqrt{3}}{2}\frac{2\pi}{\sqrt{3}}, -\frac{1}{2}\frac{2\pi}{\sqrt{3}}, Q_z), \tag{1.72}$$

with $Q_z=\pi, 0$ for L, M, the little cogroup of $\boldsymbol{Q}_1$ has generators $\{C_{2x}, i\}$. Their irreps are $\{Q_{1/2}^{\pm}\}$, which are all one-dimensional, where the superindex $\pm$ indicates the parity under the intralayer

inversion i, and the subindex $1/2$ refers to the parity under C_{2x}. We will take the irreps $\{Q^{\pm}_{1/2}\}$ to mean the irreps of the space group. Since there are three symmetry-equivalent $\boldsymbol{Q}$ points in the star, $\{Q^{\pm}_{1/2}\}$ are three-dimensional.

1.A.2 Extended point group

A convenient approach to deal with the symmetry classification of $\boldsymbol{Q} = \Gamma L, \Gamma M$ instabilities is the so-called extended point group [190–192], where the translations that are broken by the CDW are included in the point group. This approach consists of determining the symmetry group of the $2 \times 2(\times 2)$ supercell, and classifying the observables according to the irreps of this extended point group. The extended point group approach reorganizes the division of the space group S as the semidirect product of the point group P with the translation group T, $S = P \wedge T$, by defining the extended point group $\tilde{P} = P \wedge T_1$, where T_1 is the subgroup of translations broken in the CDW, so that $S = \tilde{P} \wedge T_2$, with $T = T_1 \times T_2$.

For monolayer $TiSe_2$, where $\boldsymbol{Q} = \Gamma M$, we perform group multiplication of the original point group D_{3d} with the group $\{E, t_1, t_2, t_3\}$, where t_1 represents the translation by $\boldsymbol{a}_1 = a(1,0)$, t_2 by $\boldsymbol{a}_2 - \boldsymbol{a}_1 = a(-\frac{1}{2}, \frac{\sqrt{3}}{2})$, and t_3 by $-\boldsymbol{a}_2 = a(-\frac{1}{2}, -\frac{\sqrt{3}}{2})$. Due to the imposed translational symmetry with a 2×2 unit cell, the group multiplication rules are $t_i t_i = E$ and $t_i t_j = t_k$, with $i \neq j \neq k$. The extended point group in the monolayer, $D^{(M)}_{3d} = D_{3d} \wedge \{E, t_1, t_2, t_3\}$, turns out to be isomorphic to the cubic point group O_h. We label the irreps of the extended point group $D^{(M)}_{3d}$ with the space group notation, $\{\Gamma^{\pm}_1, \Gamma^{\pm}_2, \Gamma^{\pm}_3, M^{\pm}_1, M^{\pm}_2\}$. which are in one-to-one correspondence to the irreps od O_h, $\{A_{1g/u}, A_{2g/u}, E_{g/u}, T_{2g/u}, T_{1g/u}\}$. The generators of $D^{(M)}_{3d}$ are $\{C_{3z}, C_{2x}, i, t_1, t_2\}$, which are related to the generators $\{C_{3[111]}, C_{2[1-10]}, i, C_{2[001]}, C_{2[100]}\}$ of O_h via the isomorphism. The character table of $D^{(M)}_3$ (from which $D^{(M)}_{3d}$ is obtained by the direct product with the intralayer inversion i) and its correspondence with the point group O is shown in table 1.A.1. The classes are $3t = \{t_1, t_2, t_3\}$, $6C_2 = \{C_{2l}, t_l C_{2l}\}$ (C_2 rotations and products of translations along axis l times C_2 rotations with the same axis l), $8C_3 = \{C^{\pm}_{3z}, t_l C^{\pm}_{3z}\}$, and $6tC_2 = \{t_l C_{2m}\}$ (products of translations along axis l times C_2 rotations with different axis m). The representation matrices of the generators of $D^{(M)}_3$ are shown in table 1.A.2.

In the bulk, $\boldsymbol{Q} = \Gamma L$, and the extended point group $D^{(L)}_{3d}$ is the direct product of $D^{(M)}_{3d}$ with the out-of-plane translation t_z by one unit cell $(0,0,c)$, which commutes with all the other symmetry operations. Correspondingly, the irreps of $D^{(L)}_{3d}$ just carry an additional label $\pm$ indicating whether the irrep is even (the same in consecutive layers) or odd (opposite in consecutive layers) under t_z. Alternatively, the product of t_z with the intralayer inversion i gives an interlayer inversion symmetry I, with center in the midpoint between two Ti sites in adyacent layers, which also commute with all the other symmetry operations. Therefore, the additional label can be chosen to indicate the parity under this interlayer inversion instead.

	$1E$	$3t(\equiv 3C_{2[100]})$	$6C_2(\equiv 6C_{2[1-10]})$	$8C_3$	$6tC_2(\equiv 6C_4)$
$\Gamma_1(\equiv A_1)$	1	1	1	1	1
$\Gamma_2(\equiv A_2)$	1	1	-1	1	-1
$\Gamma_3(\equiv E)$	2	2	0	-1	0
$M_1(\equiv T_2)$	3	-1	1	0	-1
$M_2(\equiv T_1)$	3	-1	-1	0	1

TABLE 1.A.1: Character table of the extended point group $D_3^{(M)}$, and one-to-one correspondence with the cubic point group O.

	t_1	t_2	C_{3z}	C_{2x}
Γ_1	1	1	1	1
Γ_2	1	1	1	-1
Γ_3	$\begin{pmatrix} 1 & 0 \\ 0 & 1 \end{pmatrix}$	$\begin{pmatrix} 1 & 0 \\ 0 & 1 \end{pmatrix}$	$\begin{pmatrix} -\frac{1}{2} & -\frac{\sqrt{3}}{2} \\ \frac{\sqrt{3}}{2} & -\frac{1}{2} \end{pmatrix}$	$\begin{pmatrix} 1 & 0 \\ 0 & -1 \end{pmatrix}$
M_1	$\begin{pmatrix} 1 & 0 & 0 \\ 0 & -1 & 0 \\ 0 & 0 & -1 \end{pmatrix}$	$\begin{pmatrix} -1 & 0 & 0 \\ 0 & 1 & 0 \\ 0 & 0 & -1 \end{pmatrix}$	$\begin{pmatrix} 0 & 0 & 1 \\ 1 & 0 & 0 \\ 0 & 1 & 0 \end{pmatrix}$	$\begin{pmatrix} 1 & 0 & 0 \\ 0 & 0 & 1 \\ 0 & 1 & 0 \end{pmatrix}$
M_2	$\begin{pmatrix} 1 & 0 & 0 \\ 0 & -1 & 0 \\ 0 & 0 & -1 \end{pmatrix}$	$\begin{pmatrix} -1 & 0 & 0 \\ 0 & 1 & 0 \\ 0 & 0 & -1 \end{pmatrix}$	$\begin{pmatrix} 0 & 0 & 1 \\ 1 & 0 & 0 \\ 0 & 1 & 0 \end{pmatrix}$	$\begin{pmatrix} -1 & 0 & 0 \\ 0 & 0 & -1 \\ 0 & -1 & 0 \end{pmatrix}$

TABLE 1.A.2: Representation matrices of the generators of the extended point group $D_3^{(M)}$.

Now, we provide the multiplication rules for the irreps in the extended point group $D_3^{(M)}$, which can be obtained from the character table and representation matrices. Adding the parity under intralayer and interlayer inversion symmetries follows straightforwardly. Let the basis of the irreps be $\Gamma_2, \Gamma_3 \to (\Gamma_3^1, \Gamma_3^2)$, $M_1 \to (M_1^1, M_1^2, M_1^3)$, and $M_2 \to (M_2^1, M_2^2, M_2^3)$. Then:

- $\Gamma_2 \otimes \Gamma_3 = \Gamma_3$
  - $\square$ $[\Gamma_2 \otimes \Gamma_3]_{\Gamma_3} \to \left(-\Gamma_2\Gamma_3^2\,,\; +\Gamma_2\Gamma_3^1\right)$
- $\Gamma_2 \otimes M_{1/2} = M_{2/1}$
  - $\square$ $[\Gamma_2 \otimes M_{1/2}]_{M_{2/1}} \to \left(\Gamma_2 M_{1/2}^1\,,\; \Gamma_2 M_{1/2}^2\,,\; \Gamma_2 M_{1/2}^3\right)$
- $\Gamma_3 \otimes \Gamma'_3 = \Gamma_1 \oplus \Gamma_2 \oplus \Gamma_3$
  - $\square$ $[\Gamma_3 \otimes \Gamma'_3]_{\Gamma_1} \to \Gamma_3^1\Gamma'^1_3 + \Gamma_3^2\Gamma'^2_3$
  - $\square$ $[\Gamma_3 \otimes \Gamma'_3]_{\Gamma_2} \to \Gamma_3^1\Gamma'^2_3 - \Gamma_3^2\Gamma'^1_3$
  - $\square$ $[\Gamma_3 \otimes \Gamma'_3]_{\Gamma_3} \to \left(\Gamma_3^1\Gamma'^1_3 - \Gamma_3^2\Gamma'^2_3\,,\; -(\Gamma_3^1\Gamma'^2_3 + \Gamma_3^2\Gamma'^1_3)\right)$

- $\Gamma_3 \otimes M_1 = M_1 \oplus M_2$
  - $[\Gamma_3 \otimes M_1]_{M_1} \to \left(M_1^1\Gamma_3^1\,,\; M_1^2\left(-\frac{1}{2}\Gamma_3^1+\frac{\sqrt{3}}{2}\Gamma_3^2\right)\,,\; M_1^3\left(-\frac{1}{2}\Gamma_3^1-\frac{\sqrt{3}}{2}\Gamma_3^2\right)\right)$
  - $[\Gamma_3 \otimes M_1]_{M_2} \to \left(M_1^1\Gamma_3^2\,,\; M_1^2\left(-\frac{\sqrt{3}}{2}\Gamma_3^1-\frac{1}{2}\Gamma_3^2\right)\,,\; M_1^3\left(\frac{\sqrt{3}}{2}\Gamma_3^1-\frac{1}{2}\Gamma_3^2\right)\right)$
- $\Gamma_3 \otimes M_2 = M_1 \oplus M_2$
  - $[\Gamma_3 \otimes M_2]_{M_1} \to \left(M_2^1\Gamma_3^2\,,\; M_2^2\left(-\frac{\sqrt{3}}{2}\Gamma_3^1-\frac{1}{2}\Gamma_3^2\right)\,,\; M_2^3\left(\frac{\sqrt{3}}{2}\Gamma_3^1-\frac{1}{2}\Gamma_3^2\right)\right)$
  - $[\Gamma_3 \otimes M_2]_{M_2} \to \left(M_2^1\Gamma_3^1\,,\; M_2^2\left(-\frac{1}{2}\Gamma_3^1+\frac{\sqrt{3}}{2}\Gamma_3^2\right)\,,\; M_2^3\left(-\frac{1}{2}\Gamma_3^1-\frac{\sqrt{3}}{2}\Gamma_3^2\right)\right)$
- $M_i \otimes M'_i = \Gamma_1 \oplus \Gamma_3 \oplus M_1 \oplus M_2$ $(i = 1, 2)$
  - $[M_i \otimes M'_i]_{\Gamma_1} \to \frac{1}{\sqrt{3}}\left(M_i^1 M'^1_i + M_i^2 M'^2_i + M_i^3 M'^3_i\right)$
  - $[M_i \otimes M'_i]_{\Gamma_3} \to \sqrt{\frac{2}{3}}\left(M_i^1 M'^1_i - \frac{1}{2}M_i^2 M'^2_i - \frac{1}{2}M_i^3 M'^3_i\,,\; \frac{\sqrt{3}}{2}(M_i^2 M'^2_i - M_i^3 M'^3_i)\right)$
  - $[M_i \otimes M'_i]_{M_1} \to \frac{1}{\sqrt{2}}\left(M_i^2 M'^3_i + M_i^3 M'^2_i\,,\; M_i^3 M'^1_i + M_i^1 M'^3_i\,,\; M_i^1 M'^2_i + M_i^2 M'^1_i\right)$
  - $[M_i \otimes M'_i]_{M_2} \to \frac{1}{\sqrt{2}}\left(M_i^2 M'^3_i - M_i^3 M'^2_i\,,\; M_i^3 M'^1_i - M_i^1 M'^3_i\,,\; M_i^1 M'^2_i - M_i^2 M'^1_i\right)$
- $M_1 \otimes M_2 = \Gamma_2 \oplus \Gamma_3 \oplus M_1 \oplus M_2$
  - $[M_1 \otimes M_2]_{\Gamma_2} \to \frac{1}{\sqrt{3}}\left(M_1^1 M_2^1 + M_1^2 M_2^2 + M_1^3 M_2^3\right)$
  - $[M_1 \otimes M_2]_{\Gamma_3} \to \sqrt{\frac{2}{3}}\left(M_1^1 M_2^1 - \frac{1}{2}M_1^2 M_2^2 - \frac{1}{2}M_1^3 M_2^3\,,\; \frac{\sqrt{3}}{2}(M_1^2 M_2^2 - M_1^3 M_2^3)\right)$
  - $[M_1 \otimes M_2]_{M_1} \to \frac{1}{\sqrt{2}}\left(M_1^2 M_2^3 - M_1^3 M_2^2\,,\; M_1^3 M_2^1 - M_1^1 M_2^3\,,\; M_1^1 M_2^2 - M_1^2 M_2^1\right)$
  - $[M_1 \otimes M_2]_{M_2} \to \frac{1}{\sqrt{2}}\left(M_1^2 M_2^3 + M_1^3 M_2^2\,,\; M_1^3 M_2^1 + M_1^1 M_2^3\,,\; M_1^1 M_2^2 + M_1^2 M_2^1\right)$

The character table, representation matrices and multiplication rules allow us to build the symmetry constrained $\boldsymbol{k}\cdot\boldsymbol{p}$ Hamiltonian and its coupling to any order parameter. To do this, we remind that the momentum transforms as an E_u irrep $\{k_x, k_y\}$, the fermionic states transform as M_1^+ $\{d_1, d_2, d_3\}$ for the conduction bands and as Γ_3^- $\{p_x, p_y\}$ for the valence bands, and the order parameter $\vec{\Delta} = (\Delta_1, \Delta_2, \Delta_3)$ transforms as M_1^-. By multiplying irreps as desired and demanding that the total Hamiltonian be a scalar Γ_1^+, all terms in Sections 1.2 and 1.5.1 can be derived.

1.B k.p model: analytical solution for the $3Q$-$1Q$ critical doping x_{1Q}

The existence of a critical doping x_{1Q} above which a $1Q$ solution for $\vec{\Delta}$ is obtained can be shown analytically in the $\boldsymbol{k}\cdot\boldsymbol{p}$ model in the simplified case where $b_p = b_d = 0$. Consider a generic

state $\vec{\Delta} = (\Delta_1, \Delta_2, \Delta_3)$ parametrized as

$$\vec{\Delta} = |\vec{\Delta}|[\cos(\theta), \sin(\theta)\cos(\varphi), \sin(\theta)\sin(\varphi)], \tag{1.73}$$

with $|\vec{\Delta}| = \sqrt{\Delta_1^2 + \Delta_2^2 + \Delta_3^2}$, $\theta \in [0, \pi]$, and $\varphi \in [0, 2\pi]$. The eigenvalues of the $\boldsymbol{k} \cdot \boldsymbol{p}$ Hamiltonian of Eq.(1.29) for $b_p = b_d = 0$ are:

$$\varepsilon_{c0}(\boldsymbol{k}) = \frac{E_g}{2} + a_d k^2, \tag{1.74}$$

$$\varepsilon_{c\pm}(\boldsymbol{k}) = \frac{1}{2}\left[(a_d + a_p)k^2 + \sqrt{\left[E_g + (a_d - a_p)k^2\right]^2 + \tfrac{4}{3}\left(|\vec{\Delta}|^2 \pm \sqrt{\tfrac{3}{2}(\Delta_1^4 + \Delta_2^4 + \Delta_3^4) - \tfrac{1}{2}|\vec{\Delta}|^4}\right)}\right] =$$
$$= \frac{1}{2}\left[(a_d + a_p)k^2 + \sqrt{\left[E_g + (a_d - a_p)k^2\right]^2 + \tfrac{4}{3}|\vec{\Delta}|^2 f_{\pm}(\theta, \varphi)}\right], \tag{1.75}$$

$$\varepsilon_{v\pm}(\boldsymbol{k}) = \frac{1}{2}\left[(a_d + a_p)k^2 - \sqrt{\left[E_g + (a_d - a_p)k^2\right]^2 + \tfrac{4}{3}\left(|\vec{\Delta}|^2 \pm \sqrt{\tfrac{3}{2}(\Delta_1^4 + \Delta_2^4 + \Delta_3^4) - \tfrac{1}{2}|\vec{\Delta}|^4}\right)}\right] =$$
$$= \frac{1}{2}\left[(a_d + a_p)k^2 - \sqrt{\left[E_g + (a_d - a_p)k^2\right]^2 + \tfrac{4}{3}|\vec{\Delta}|^2 f_{\pm}(\theta, \varphi)}\right], \tag{1.76}$$

where $k = |\boldsymbol{k}|$ and we have defined

$$f_{\pm}(\theta, \varphi) = 1 \pm \sqrt{\tfrac{3}{2}(\cos^4(\theta) + \sin^4(\theta)\cos^4(\varphi) + \sin^4(\theta)\sin^4(\varphi)) - \tfrac{1}{2}}. \tag{1.77}$$

$\varepsilon_{v\pm}$ are the two valence bands, ε_{c0} is the lowest conduction band, which always remains uncoupled, and $\varepsilon_{c\pm}$ are the two highest conduction bands.

The energies only depend on the direction of $\vec{\Delta}$ via the quartic invariant $(\Delta_1^4 + \Delta_2^4 + \Delta_3^4)$, which, for a given modulus $|\vec{\Delta}|$, is minimum for $\vec{\Delta} = \frac{|\vec{\Delta}|}{\sqrt{3}}(1,1,1)$, and maximum for $\vec{\Delta} = |\vec{\Delta}|(1,0,0)$. We assume that the CDW phase displays a gap between valence and conduction bands so that the valence bands are fully filled at stoichiometry $x = 0$, for which $E_g > 0$ is a sufficient condition. Then the ground state in the undoped case $x = 0$ has to be either the 3Q C_3-symmetric state $\vec{\Delta} = \frac{|\vec{\Delta}|}{\sqrt{3}}(1,1,1)$ or the 1Q stripe state $\vec{\Delta} = |\vec{\Delta}|(1,0,0)$. For the 3$Q$ C_3-symmetric state, two pairs of valence and conduction bands are repelled and remain degenerate:

$$\varepsilon_{c+}^{3Q}(\boldsymbol{k}) = \varepsilon_{c-}^{3Q}(\boldsymbol{k}) = \varepsilon_{c}^{3Q}(\boldsymbol{k}) = \frac{1}{2}\left[(a_d + a_p)k^2 + \sqrt{\left[E_g + (a_d - a_p)k^2\right]^2 + \tfrac{4}{3}|\vec{\Delta}|^2}\right], \tag{1.78}$$

$$\varepsilon_{v+}^{3Q}(\boldsymbol{k}) = \varepsilon_{v-}^{3Q}(\boldsymbol{k}) = \varepsilon_{v}^{3Q}(\boldsymbol{k}) = \frac{1}{2}\left[(a_d + a_p)k^2 - \sqrt{\left[E_g + (a_d - a_p)k^2\right]^2 + \tfrac{4}{3}|\vec{\Delta}|^2}\right], \tag{1.79}$$

while for the $1Q$ stripe state, only one pair of valence and conduction bands is repelled:

$$\varepsilon^{1Q}_{c+}(\boldsymbol{k}) = \frac{1}{2}\left[(a_d+a_p)k^2 + \sqrt{\left[E_g+(a_d-a_p)k^2\right]^2 + \tfrac{8}{3}|\vec{\Delta}|^2}\right], \tag{1.80}$$

$$\varepsilon^{1Q}_{c-}(\boldsymbol{k}) = \varepsilon_{c0}(\boldsymbol{k}), \tag{1.81}$$

$$\varepsilon^{1Q}_{v+}(\boldsymbol{k}) = \frac{1}{2}\left[(a_d+a_p)k^2 - \sqrt{\left[E_g+(a_d-a_p)k^2\right]^2 + \tfrac{8}{3}|\vec{\Delta}|^2}\right], \tag{1.82}$$

$$\varepsilon^{1Q}_{v-}(\boldsymbol{k}) = -\frac{E_g}{2} + a_p k^2, \tag{1.83}$$

In order to determine the ground state, we compute the difference in total energy density at zero temperature $\delta E = E - E^{3Q}$ between a generic state $\vec{\Delta} = (\Delta_1, \Delta_2, \Delta_3)$ and the $\vec{\Delta} = \frac{|\vec{\Delta}|}{\sqrt{3}}(1,1,1)$ phase. At stoichiometry $x = 0$,

$$\begin{aligned}
\delta E(x=0) = &\int \frac{d^2k}{(2\pi)^2}\left[\varepsilon_{v+}(\boldsymbol{k}) + \varepsilon_{v-}(\boldsymbol{k}) - 2\varepsilon^{3Q}_v(\boldsymbol{k})\right] = \\
=&\frac{1}{8\pi(a_d-a_p)}\left\{\frac{E_g}{2}\left[\sqrt{E_g^2 + \tfrac{4}{3}|\vec{\Delta}|^2 f_+(\theta,\varphi)} + \sqrt{E_g^2 + \tfrac{4}{3}|\vec{\Delta}|^2 f_-(\theta,\varphi)} - 2\sqrt{E_g^2+\tfrac{4}{3}|\vec{\Delta}|^2}\right] + \right. \\
&+\frac{4}{3}|\vec{\Delta}|^2\left[\log\left(-E_g + \sqrt{E_g^2+\tfrac{4}{3}|\vec{\Delta}|^2}\right) - \right. \\
&-\frac{1}{2}f_+(\theta,\varphi)\log\left(\frac{-E_g+\sqrt{E_g^2+\tfrac{4}{3}|\vec{\Delta}|^2 f_+(\theta,\varphi)}}{f_+(\theta,\varphi)}\right) - \\
&\left.\left.-\frac{1}{2}f_-(\theta,\varphi)\log\left(\frac{-E_g+\sqrt{E_g^2+\tfrac{4}{3}|\vec{\Delta}|^2 f_-(\theta,\varphi)}}{f_-(\theta,\varphi)}\right)\right]\right\}.
\end{aligned} \tag{1.84}$$

$\delta E(x=0)$ is always a non-negative quantity, and it is equal to zero only if $\vec{\Delta} = \frac{|\vec{\Delta}|}{\sqrt{3}}(1,1,1)$, when $f_\pm(\theta,\varphi) = 1$. Therefore, the ground state at charge neutrality is the $3Q$ C_3-symmetric state, and the $1Q$ stripe state has the highest energy:

$$\begin{aligned}
\delta E^{1Q}(x=0) = &\frac{1}{8\pi(a_d-a_p)}\left[\frac{E_g}{2}\left(\sqrt{E_g^2+\tfrac{8}{3}|\vec{\Delta}|^2} + E_g - 2\sqrt{E_g^2+\tfrac{4}{3}|\vec{\Delta}|^2}\right) + \right. \\
&\left. + \frac{4}{3}|\vec{\Delta}|^2\log\left(2\frac{-E_g+\sqrt{E_g^2+\tfrac{4}{3}|\vec{\Delta}|^2}}{-E_g+\sqrt{E_g^2+\tfrac{8}{3}|\vec{\Delta}|^2}}\right)\right].
\end{aligned} \tag{1.85}$$

In the limit $E_g \to 0$ we have simply $\delta E(x=0) = \frac{|\vec{\Delta}|^2}{24\pi(a_d-a_p)}[f_+\log(f_+) + f_-\log(f_-)]$, and $\delta E^{1Q}(x=0) = \frac{|\vec{\Delta}|^2}{12\pi(a_d-a_p)}\log 2$. For finite E_g, $\delta E(x=0)$ decreases with increasing E_g for fixed $|\vec{\Delta}|$.

Now consider doping a small carrier density $n = x/V_{\text{unit cell}}$ such that only the lowest conduction band ε_{c0} is populated. This assumption holds in the majority of the $\boldsymbol{k}\cdot\boldsymbol{p}$ phase diagrams of Fig. 1.9, except for a small region in the case of large negative gap and small ellipticity where a nematic phase appears, as explained in Section 1.2.3. This assumption is also verified in all the self-consistent mean-field calculations. Except for the 1Q phase, the lowest conduction band is non-degenerate and equal for all $|\vec{\Delta}|$, so that the total energy difference $\delta E(x)$ remains the same as $\delta E(x=0)$.

However, the 1Q stripe phase displays a doubly-degenerate lowest conduction band. In this case, for a given carrier density n, the chemical potential is lower for the 1Q state than for the 3Q one, which allows the possibility of a transition to the 1Q phase at a critical doping, as we show below. The lowest conduction band is uncoupled by the order parameter, and thus remains parabolic with constant DOS $1/(4\pi a_d)$. The chemical potential is set by the carrier density:

$$n = \int_0^{\mu^{3Q}} d\varepsilon \frac{1}{4\pi a_d}\theta(\varepsilon - E_g/2) = \frac{\mu^{3Q} - E_g/2}{4\pi a_d} \tag{1.86}$$

$$n = \int_0^{\mu^{1Q}} d\varepsilon \frac{2}{4\pi a_d}\theta(\varepsilon - E_g/2) = \frac{\mu^{1Q} - E_g/2}{2\pi a_d} \tag{1.87}$$

And the total energy density difference is

$$\begin{aligned}\delta E^{1Q}(x) - \delta E^{1Q}(x=0) &= \int_0^{\mu^{1Q}} d\varepsilon \frac{\varepsilon}{2\pi a_d}\theta(\varepsilon - E_g/2) - \int_0^{\mu^{3Q}} d\varepsilon \frac{\varepsilon}{4\pi a_d}\theta(\varepsilon - E_g/2) = \\ &= \frac{1}{8\pi a_d}\left[2(2\pi a_d n)^2 - (4\pi a_d n)^2\right] = -\pi a_d n^2\end{aligned} \tag{1.88}$$

The transition to the 1Q state occurs at the x_{1Q} such that $\delta E^{1Q}(x_{1Q}) = 0$, so

$$n_{1Q} = 2\sqrt{\frac{\delta E^{1Q}(x=0)}{\pi a_d}}, \tag{1.89}$$

where we have added a factor 2 to take into account the spin degeneracy. In the limit $E_g \to 0$, we have $n_{1Q} = \frac{|\vec{\Delta}|}{\pi}\sqrt{\frac{\log 2}{3a_d(a_d - a_p)}}$.

We can estimate x_{1Q} from this calculation taking $a_p = -0.89\hbar^2/m_e$ and $a_d = 0.27\hbar^2/m_e$, with m_e the electron mass, which reproduce the same normal-state DOS as the realistic values $a_p = -0.95\hbar^2/m_e$, $b_p = -0.24\hbar^2/m_e$, $a_d = 0.54\hbar^2/m_e$ and $b_d = 0.46\hbar^2/m_e$ used in our effective tight-binding model. From the ARPES experiment on monolayer $TiSe_2$ of Ref. [127], where the normal-state gap is $E_g \sim 80$meV and the low-temperature gap is $E_g/2 + \sqrt{(E_g/2)^2 + 4|\vec{\Delta}|^2/3} \sim 180$meV, one obtains an order parameter $|\vec{\Delta}| \sim 230$meV in the low-doping case. Using these

numerical values, we can estimate the critical doping for the transition from the $3Q$ to the $1Q$ states to be $x_{1Q} \sim 0.07\mathrm{e/f.u.}$. Despite neglecting b_p and b_d, this value is of the order of magnitude of that obtained in the self-consistent mean-field calculations. The quantitative agreement is even better for a smaller $|\vec{\Delta}|$, which accounts for its decrease with increasing doping. The numerical results for x_{1Q} for $E_g > 0$ and nonzero b_p and b_d are displayed in Fig. 1.9(a), which demonstrates that if the CDW survives at high enough doping, a $1Q$ phase universally appears for any ellipticity and gap.

1.C Tight-binding model and mean-field theory

Here we describe the choice of the parameters of the effective tight-binding model, and the details of the self-consistent mean-field calculations.

1.C.1 Effective lattice model: choice of parameters

The Hamiltonian of our three-orbital triangular lattice model is given by Eq. (1.39). Its parameters are the onsite energies ε_p and ε_d, the hoppings up to third nearest neighbours $t_{dd}^{(n)}$ for the d_{z^2} orbital, the σ and π nearest-neighbour hoppings $t_{pp\sigma}$ and $t_{pp\pi}$ for the p orbitals, and the nearest-neighbour interorbital hopping t_{dp}. We choose these Hamiltonian parameters by solving for the noninteracting gap E_g, the masses m_{v1}, m_{v2} of the two valence bands at Γ, the masses m_{cx}, m_{cy} of the conduction bands at M perpendicular and parallel to the ΓM direction, and the energy $\varepsilon_{c\Gamma}$ of the conduction band at Γ, leaving t_{dp} as a free parameter. The gap, the masses and $\varepsilon_{c\Gamma}$ depend on the hoppings as:

$$E_g = \varepsilon_d - \varepsilon_p - \left[2t_{dd}^{(1)} + 2t_{dd}^{(2)} - 6t_{dd}^{(3)} - 3t_{pp\sigma} + 3t_{pp\pi}\right] \tag{1.90}$$

$$\varepsilon_{c\Gamma} = \varepsilon_d + 6\left[t_{dd}^{(1)} + t_{dd}^{(2)} + t_{dd}^{(3)}\right] \tag{1.91}$$

$$\widetilde{m}_{v1}^{-1} = \frac{3}{4}\left[t_{pp\sigma} - 3t_{pp\pi}\right] \tag{1.92}$$

$$\widetilde{m}_{v2}^{-1} = -\frac{3}{4}\left[-3t_{pp\sigma} + t_{pp\pi} + \frac{24t_{dp}^2}{\varepsilon_d - \varepsilon_p + 3\left(2t_{dd}^{(1)} + 2t_{dd}^{(2)} + 2t_{dd}^{(3)} + t_{pp\sigma} - t_{pp\pi}\right)}\right] \tag{1.93}$$

$$\widetilde{m}_{cy}^{-1} = 3\left[t_{dd}^{(1)} - t_{dd}^{(2)} - 4t_{dd}^{(3)} + \frac{6t_{dp}^2}{\varepsilon_d - \varepsilon_p - \left(2t_{dd}^{(1)} + 2t_{dd}^{(2)} - 6t_{dd}^{(3)} + 3t_{pp\sigma} + t_{pp\pi}\right)}\right] \tag{1.94}$$

$$\widetilde{m}_{cx}^{-1} = -t_{dd}^{(1)} + 9t_{dd}^{(2)} - 12t_{dd}^{(3)} + \frac{2t_{dp}^2}{\varepsilon_d - \varepsilon_p - \left(2t_{dd}^{(1)} + 2t_{dd}^{(2)} - 6t_{dd}^{(3)} - t_{pp\sigma} - 3t_{pp\pi}\right)} \tag{1.95}$$

where we have defined $\widetilde{m} = ma^2/\hbar^2$, where a is the lattice constant. Inverting these relationships, we find that the hoppings as a function of the gap, the masses, $\varepsilon_{c\Gamma}$ and t_{dp} can be expressed as:

$$\begin{aligned}\varepsilon_d =&\frac{1}{256}\left(48\widetilde{m}_{cx}^{-1}+80\widetilde{m}_{cy}^{-1}+\frac{288t_{dp}^2}{8\widetilde{m}_{v1}^{-1}-3E_g}-\right.\\&\left.-\frac{15(8\widetilde{m}_{v2}^{-1}-3E_g)(2\varepsilon_{c\Gamma}+E_g)^2}{(8\widetilde{m}_{v2}^{-1}-3E_g)(2\varepsilon_{c\Gamma}+E_g)+288t_{dp}^2}+70\varepsilon_{c\Gamma}+123E_g\right)\end{aligned} \tag{1.96}$$

$$\varepsilon_p = \widetilde{m}_{v1}^{-1}+\widetilde{m}_{v2}^{-1}+\frac{36t_{dp}^2}{2\varepsilon_{c\Gamma}+E_g}-\frac{E_g}{2} \tag{1.97}$$

$$\begin{aligned}t_{dd}^{(1)} =&\frac{1}{256}\left(16(\widetilde{m}_{cy}^{-1}-\widetilde{m}_{cx}^{-1})+\frac{96t_{dp}^2}{3E_g-8\widetilde{m}_{v1}^{-1}}-\right.\\&\left.-\frac{3(8\widetilde{m}_{v2}^{-1}-3E_g)(2\varepsilon_{c\Gamma}+E_g)^2}{(8\widetilde{m}_{v2}^{-1}-3E_g)(2\varepsilon_{c\Gamma}+E_g)+288t_{dp}^2}+30\varepsilon_{c\Gamma}-9E_g\right)\end{aligned} \tag{1.98}$$

$$t_{pp\sigma} = -\frac{\widetilde{m}_{v1}^{-1}}{6}+\frac{\widetilde{m}_{v2}^{-1}}{2}+\frac{18t_{dp}^2}{2\varepsilon_{c\Gamma}+E_g} \tag{1.99}$$

$$t_{pp\pi} = -\frac{\widetilde{m}_{v1}^{-1}}{2}+\frac{\widetilde{m}_{v2}^{-1}}{6}+\frac{6t_{dp}^2}{2\varepsilon_{c\Gamma}+E_g} \tag{1.100}$$

$$\begin{aligned}t_{dd}^{(2)} =&\frac{1}{256}\left(16(\widetilde{m}_{cx}^{-1}-\widetilde{m}_{cy}^{-1})+\frac{96t_{dp}^2}{8\widetilde{m}_{v1}^{-1}-3E_g}-\right.\\&\left.-\frac{3(3E_g-8\widetilde{m}_{v2}^{-1})(2\varepsilon_{c\Gamma}+E_g)^2}{(8\widetilde{m}_{v2}^{-1}-3E_g)(2\varepsilon_{c\Gamma}+E_g)+288t_{dp}^2}+2\varepsilon_{c\Gamma}-7E_g\right)\end{aligned} \tag{1.101}$$

$$\begin{aligned}t_{dd}^{(3)} =&\frac{1}{1536}\left(-48\widetilde{m}_{cx}^{-1}-80\widetilde{m}_{cy}^{-1}+\frac{288t_{dp}^2}{3E_g-8\widetilde{m}_{v1}^{-1}}-\right.\\&\left.-\frac{15(3E_g-8\widetilde{m}_{v2}^{-1})(2\varepsilon_{c\Gamma}+E_g)^2}{(8\widetilde{m}_{v2}^{-1}-3E_g)(2\varepsilon_{c\Gamma}+E_g)+288t_{dp}^2}-6\varepsilon_{c\Gamma}-27E_g\right)\end{aligned} \tag{1.102}$$

When inverting Eqs. (1.90)-(1.95), we have chosen the Eqs. (1.96)-(1.102) that give $t_{pp\sigma}+t_{pp\pi}<0$, which sets the correct p_x character for the top valence band along the ΓM line. This choice implies that, for equal attraction in M_1^- and M_2^- channels, the M_1^- is preferred, since its repels more the top p_x band. The interorbital hopping t_{dp} also favors the time-reversal even M_1^- with respect to the M_2^- order parameter[6].

Table 1.C.1 shows different values of the masses of the bands extracted from previous works.

[6] Above a certain value of t_{dp}, the time-reversal odd M_2^- becomes more favored by t_{dp}. However, in our calculations, we will always set a larger attraction in the M_2^- channel.

Reference	Technique	$\frac{m_{v1}}{m_e}$	$\frac{m_{v2}}{m_e}$	$\frac{m_{cy}}{m_e}$	$\frac{m_{cx}}{m_e}$	$\frac{m_{v2}}{m_{v1}}$	$-\frac{m_{cy}}{m_{v2}}$	$\frac{m_{cy}}{m_{cx}}$
[125]	ARPES 2D	-0.7	-0.45	7.1	?	0.64	16	?
[122, 123]	ARPES 3D	?	-0.23	5.5	2.2	?	24	2.5
[124]	ARPES 3D	?	?	6	0.5	?	?	12
[159]	DFT 2D	?	-0.19	3.46	0.22	?	18	16
[141]	DFT 2D	-0.25	-0.15	5.6	0.4	0.60	37	14
[149]	DFT 3D	?	-0.22	4.3	0.29	?	20	15

TABLE 1.C.1: Values of the masses of the valence and conduction bands obtained in previous works.

Here, we choose the values of Ref. [125] based on ARPES measurements on monolayer $TiSe_2$: $m_{v1} = -0.7m_e, m_{v2} = (50/3)m_{v2} = -0.42m_e, m_{cy} = 10m_{v1} = 7m_e, m_{cx} = m_{cy}/14 = 0.5m_e$. Then, for gap $E_g = 0$, as shown in Fig. 1.12, the hopping parameters are $\varepsilon_d \simeq 0.329$eV, $\varepsilon_p \simeq -2.016$eV, $t_{dd}^{(1)} \simeq -0.017$eV, $t_{dd}^{(2)} \simeq 0.092$eV, $t_{dd}^{(3)} \simeq -0.030$eV, $t_{pp\sigma} \simeq -0.429$eV, $t_{pp\pi} \simeq 0.243$eV, and $t_{dp} \simeq 0.1$eV.

1.C.2 Mean-field theory: calculation details

We perform self-consistent mean-field calculations on the Hamiltonian H_{MF} of Eq. (1.44) in the 2×2 supercell defined in Fig. 1.11(a). We introduce a initial seed for the order parameters, and recompute them iteratively until convergence is reached, defined as $\sqrt{\sum |\langle c^\dagger c\rangle_{n+1} - \langle c^\dagger c\rangle_n|} < \epsilon_0$. Since we work in the canonical ensemble, in each iteration we set the chemical potential to keep the number of particles fixed.

In order to find the ground state which minimizes the free energy, we initialize the self-consistent loop with different seeds: $\vec{\Delta} = (\Delta, \Delta, \Delta)$, $\vec{\Delta} = (\Delta, 0, 0)$, $\vec{\Delta} = (0, \Delta, \Delta)$, and $\vec{\Delta} = (\Delta_1, \Delta_2, \Delta_2)$. To guarantee that each seed converges to the phase that we want, we first run the self-consistent loop by symmetry-restricting the mean-field parameters to have the symmetry they initially have. Once convergence has been reached, we run unrestricted self-consistent loops whose seeds are the solutions of the restricted loops.

1.D Secondary order parameter

In this Appendix, we first compute the energy of the conduction bands in the $\boldsymbol{k} \cdot \boldsymbol{p}$ model and show that the sign $\Phi_1\Phi_2\Phi_3 < 0$ is always preferred by $\vec{\Phi}$ alone. Then we explain the complementary mechanism where the coupling to the secondary M_1^+ order parameter $\vec{\Phi}$ can enhance the nematic CDW based on the competition of the Ginzburg-Landau cubic terms.

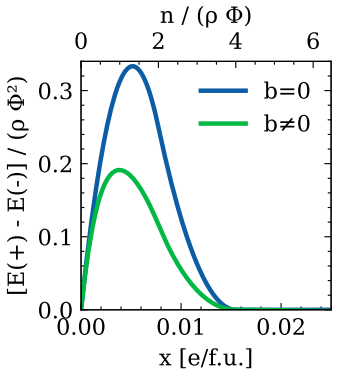

FIGURE 1.D.1: Difference of total energy of the $\boldsymbol{k}\cdot\boldsymbol{p}$ conduction bands between the states $\Phi = +|\Phi|$ and $\Phi = -|\Phi|$ for $\vec{\Delta} = 0$ and $\vec{\Phi} = (\Phi,\Phi,\Phi)$. Both the realistic case with $b_d/a_d = 0.87$ and the isotropic case with $b_d = 0$ are shown.

1.D.1 k.p model: total energy of the $\Phi > 0$ and $\Phi < 0$ states

As discussed in Section 1.5.1, the sign of $\vec{\Phi}$, defined as $\text{sign}(\Phi_1\Phi_2\Phi_3)$, has a different effect on the bands. In a C_3-symmetric $3Q$ configuration with $\vec{\Phi} = (\Phi,\Phi,\Phi)$, $\Phi > 0$ raises the singlet conduction band with respect to the doublet, while $\Phi < 0$ lowers it (see Fig. 1.13). To analyze which case is favored by $\vec{\Phi}$, we compute the total energy of the conduction bands as a function of doping x for $\vec{\Delta} = 0$. In this case, $\vec{\Phi}$ only couples the conduction bands with themselves, and therefore only affects the energetics at finite doping. Numerically, we have determined that, for $\vec{\Delta} = 0$ and $\vec{\Phi} = (\Phi,\Phi,\Phi)$ at finite doping x, lowering the singlet has the lowest energy regardless of x (see Fig. 1.D.1). Therefore, $\vec{\Phi}$ favors $\Phi_1\Phi_2\Phi_3 < 0$. Fig. 1.D.1 shows that the energy difference between $\Phi_1\Phi_2\Phi_3 > 0$ and $\Phi_1\Phi_2\Phi_3 < 0$ increases until the doublet of conduction bands begins to be populated in the $\Phi_1\Phi_2\Phi_3 < 0$ case. From then on, it decreases until the three conduction band edges are populated in both cases, where the energy difference becomes zero.

The total energy of the conduction bands for $\vec{\Delta} = 0$ can indeed be computed analytically in the isotropic $b_d = 0$ case. The starting point is the Hamiltonian for the 3 conduction bands alone in 2D, given by Eqs.(1.21) and (1.51):

$$H_{dd}(\boldsymbol{k}) = \begin{pmatrix} a_d k^2 + b_d\left[k_x^2 - k_y^2\right] & \Phi_3 & \Phi_2 \\ \Phi_3 & a_d k^2 + b_d\left[-\frac{1}{2}\left(k_x^2 - k_y^2\right) - \sqrt{3}k_x k_y\right] & \Phi_1 \\ \Phi_2 & \Phi_1 & a_d k^2 + b_d\left[-\frac{1}{2}\left(k_x^2 - k_y^2\right) + \sqrt{3}k_x k_y\right] \end{pmatrix}, \tag{1.103}$$

with $k^2 = k_x^2 + k_y^2$. The energies can be obtained analytically as

$$\varepsilon_n(\boldsymbol{k}) = a_d k^2 + \sqrt{b_d^2 k^4 + \frac{4}{3}|\vec{\Phi}|^2}\cos\left[\theta_n(\boldsymbol{k},\vec{\Phi})\right], \tag{1.104}$$

where

$$\theta_n(\boldsymbol{k},\vec{\Phi}) = \frac{1}{3}\arccos\left(\frac{b_d^3 k^{(6)} + 8\Phi_A - 2b_d[(k_x^2-k_y^2)\Phi_x - 2k_x k_y \Phi_y]}{(b_d^2 k^4 + \frac{4}{3}|\vec{\Phi}|^2)^{3/2}}\right) - \frac{2\pi}{3}(n-1), \tag{1.105}$$

with $\Phi_A = \Phi_1\Phi_2\Phi_3$, $\{\Phi_x,\Phi_y\} = \{2\Phi_1^2 - \Phi_2^2 - \Phi_3^2, +\sqrt{3}(\Phi_2^2 - \Phi_3^2)\}$, $k^{(6)} = k_x^6 - 15k_x^4k_y^2 + 15k_x^2k_y^4 - k_y^6 = k^6\cos(6\varphi)$, and φ the azimuthal angle between $\boldsymbol{k}$ ad the x axis. Remarkably, the only $\vec{\Phi}$-dependent terms entering the single-particle energies are $|\vec{\Phi}|$, $\{\Phi_x,\Phi_y\}$ and $\Phi_1\Phi_2\Phi_3$. This means that the Ginzburg-Landau free-energy density can only depend on functions of these. In particular, the direction dependence is set by $\{\Phi_x,\Phi_y\}$ and $\Phi_1\Phi_2\Phi_3$, the latter term being the same as the cubic term in Eq. (1.56).

In order to treat the problem analytically, we consider the case with $b_d = 0$. In this case, $\vec{\Phi}$ only acts as a rigid shift of the bands, whose dispersion becomes:

$$\varepsilon_n(\boldsymbol{k}) = a_d k^2 + \frac{2}{\sqrt{3}}|\vec{\Phi}|\cos\left[\frac{1}{3}\arccos\left(\frac{8\Phi_1\Phi_2\Phi_3}{(\frac{2}{\sqrt{3}}|\vec{\Phi}|)^3}\right) - \frac{2\pi}{3}(n-1)\right]. \tag{1.106}$$

In this case, the direction dependence of the free energy has to be $\sim \Phi_1\Phi_2\Phi_3$, i.e., the same as the cubic term in Eq. (1.56).

In particular, we compute the zero-temperature free-energy densities for the C_3-symmetric order parameters $\vec{\Phi} = (\Phi,\Phi,\Phi)$, with $\Phi > 0$ and $\Phi < 0$. As explained in Section 1.5.1, the bands in these cases are split into a singlet at energy 2Φ and a doublet at energy $-\Phi$. For a given $|\Phi|$, there exist two regimes for the electron density n: either only the lower set of bands (doublet for $\Phi > 0$ and singlet for $\Phi < 0$) is occupied, or the three bands have a nonzero filling. The total energy densities E_+ and E_- for $\Phi > 0$ and $\Phi < 0$, respectively, with respect to the normal-state energy $E_0 = n^2/(2\rho)$ for $\Phi = 0$, are:

$$E_+ - E_0 = \begin{cases} \frac{1}{4}\frac{n^2}{\rho} - n\Phi, & \text{if } n < 2\rho\Phi, \\ -\rho\Phi^2, & \text{if } n > 2\rho\Phi, \end{cases} \tag{1.107}$$

$$E_- - E_0 = \begin{cases} \frac{n^2}{\rho} - 2n|\Phi|, & \text{if } n < \rho|\Phi|, \\ -\rho|\Phi|^2, & \text{if } n > \rho|\Phi|, \end{cases} \tag{1.108}$$

where $\rho = 3/(4\pi\sqrt{a_d^2 - b_d^2})$ is the total density of states (DOS) of the three bands. Therefore, the difference between them is

$$E_+ - E_- = \begin{cases} -\frac{3}{4}\frac{n^2}{\rho} + n|\Phi|, & \text{if } n < \rho|\Phi|, \\ \frac{1}{4}\frac{n^2}{\rho} - n|\Phi| + \rho|\Phi|^2, & \text{if } \rho|\Phi| < n < 2\rho|\Phi|, \\ 0, & \text{if } n > 2\rho|\Phi|. \end{cases} \tag{1.109}$$

As anticipated, the energy of the $\Phi < 0$ state is lower than that of the $\Phi > 0$, and the energy difference increases with the electron density for small enough n filling just the lower set of bands, which is the only region where the self-consistent Hartree-Fock calculations predict a charge-density wave instability. This analytical result for $b_d = 0$ is shown in Fig. 1.D.1, which also shows that the numerical result for $b_d \neq 0$ has the same qualitative features.

1.D.2 Ginzburg-Landau theory: complementary nematic mechanism and nonanalyticities

In this section, we write down the full symmetry-derived Ginzburg-Landau free-energy density coupling the L_{1-} and M_1^+ order parameters, $\vec{\Delta}$ and $\vec{\Phi}$, respectively, up to fourth order. We thoroughly explain the complementary mechanism that can enhance the nematicity based on the competition between the two cubic terms of Eqs. (1.56) and (1.57). Finally, we comment on the possible nonanaliticities of the Ginzburg-Landau functional at zero temperature, and their role in the nematic enhancement.

Ginzburg-Landau functional up to fourth order

Using group theory, the Ginzburg-Landau free-energy density coupling $\vec{\Delta}$ and $\vec{\Phi}$ up to fourth order is

$$F_{\Delta\Phi} = F_\Delta + F_\Phi + F_{\Delta\Phi}^{(3)} + F_{\Delta\Phi}^{(4)}, \tag{1.110}$$

where F_Δ, F_Φ and $F_{\Delta\Phi}^{(3)}$ are defined in Eqs. (1.35),(1.56),(1.57) and $F_{\Delta\Phi}^{(4)}$ is the fourth order coupling:

$$F_\Delta = a_\Delta|\vec{\Delta}|^2 + b_\Delta|\vec{\Delta}|^4 + c_\Delta\left(\Delta_1^4 + \Delta_2^4 + \Delta_3^4\right), \tag{1.111}$$

$$F_\Phi = a_\Phi|\vec{\Phi}|^2 + d_\Phi\Phi_1\Phi_2\Phi_3 + b_\Phi|\vec{\Phi}|^4 + c_\Phi\left(\Phi_1^4 + \Phi_2^4 + \Phi_3^4\right), \tag{1.112}$$

$$F_{\Delta\Phi}^{(3)} = d_{\Delta\Phi}\left(\Phi_1\Delta_2\Delta_3 + \Phi_2\Delta_3\Delta_1 + \Phi_3\Delta_1\Delta_2\right), \tag{1.113}$$

$$F_{\Delta\Phi}^{(4)} = e_{\Delta\Phi}|\vec{\Delta}|^2|\vec{\Phi}|^2 + g_{\Delta\Phi}|\vec{\Delta}\cdot\vec{\Phi}|^2 + h_{\Delta\Phi}\left(\Delta_1\Delta_2\Phi_1\Phi_2 + \Delta_1\Delta_3\Phi_1\Phi_3 + \Delta_2\Delta_3\Phi_2\Phi_3\right). \tag{1.114}$$

Incidentally, since they share the same point group and 2×2 nature of the CDW, this Ginzburg-Landau functional is analogous to the one of kagome AV_3Sb_5 metals [51], where a nematic CDW has also been found.

Cubic competition and nematicity

As discussed in Section 1.5.2, the signs of the cubic coefficients are $d_\Phi > 0$, since, for $\vec{\Delta} = 0$, $\vec{\Phi}$ favors $\Phi_1\Phi_2\Phi_3 < 0$, and $d_{\Delta\Phi} < 0$, since for $\vec{\Delta} \neq 0$, $\Phi_1\Phi_2\Phi_3 > 0$ decreases the energy of the valence bands. At finite doping, these two cubic terms, $f_\Phi^{(3)} = \Phi_1\Phi_2\Phi_3$ and $f_{\Delta\Phi}^{(3)} = \Phi_1\Delta_2\Delta_3 + \Phi_2\Delta_3\Delta_1 + \Phi_3\Delta_1\Delta_2$, are therefore frustrated. Close to stoichiometry, $d_{\Delta\Phi}$ dominates and the ground state is C_3 symmetric with $\Phi_1\Phi_2\Phi_3 > 0$. At high doping (but before the transition to the $1Q$ stripe phase), it is d_Φ that dominates instead (as we will discuss in Appendix 1.D.2, $d_\Phi \propto x$), so $\Phi_1\Phi_2\Phi_3 < 0$. At intermediate doping where both cubic terms are of the same order, the frustration can be relieved by breaking C_3 symmetry, with a nematic solution $\Delta = (\Delta_1, \Delta_2, \Delta_2)$ and $\Phi = (\Phi_1, \Phi_2, \Phi_2)$ (see Appendix 1.D.2). This solution can lower the energy penalty $d_\Phi\Phi_1\Phi_2\Phi_3$ while maintaining $\Phi_1\Phi_2\Phi_3 > 0$. This mechanism can therefore enhance the nematic CDW in $TiSe_2$.

While the main role in this nematic scenario is played by the cubic terms, the last quartic coupling of Eq. (1.114), $f_{\Delta\Phi}^{(4)} = \Delta_1\Delta_2\Phi_1\Phi_2 + \Delta_3\Delta_1\Phi_3\Phi_1 + \Delta_2\Delta_3\Phi_2\Phi_3$, which depends on the relative signs between $\vec{\Delta}$ and $\vec{\Phi}$, might also have an effect. To show this explicitly, we assume a $3Q$ C_3-symmetric solution with $\vec{\Delta} = |\Delta_0|(1,1,1)$ and $\vec{\Phi} = |\Phi_0|(x_1, x_2, x_3)$, where $x_i = \pm 1$. Depending on the relative signs between $\vec{\Delta}$ and $\vec{\Phi}$, the Ginzburg-Landau terms can take four different combinations of values:

$\frac{\vec{\Phi}}{\lvert\Phi_0\rvert}$	$\frac{f_\Phi^{(3)}}{\lvert\Phi_0\rvert^3}$	$\frac{f_{\Delta\Phi}^{(3)}}{\lvert\Delta_0\rvert^2\lvert\Phi_0\rvert}$	$\frac{f_{\Delta\Phi}^{(4)}}{\lvert\Delta_0\rvert^2\lvert\Phi_0\rvert^2}$
$(+1,+1,+1)$	$+1$	$+3$	$+3$
$(-1,+1,+1)$	-1	$+1$	-1
$(+1,-1,-1)$	$+1$	-1	-1
$(-1,-1,-1)$	-1	-3	$+3$

(1.115)

Considering just the cubic terms, the solution $\vec{\Phi} = |\Phi_0|(1,1,-1)$ satisfies the sign requirements preferred by both cubic terms. One could then expect this solution in the intermediate regime where both cubic terms are of the same order, instead of the $3Q$ nematic phase. However, if the quartic coefficient $h_{\Delta\Phi}$ is large, it can restrict the possible solutions to those with $f_{\Delta\Phi}^{(4)} \gtrless 0$ depending on $h_{\Delta\Phi} \lessgtr 0$.

In Appendix 1.D.3, we will discuss how the self-consistent mean-field calculations in the effective lattice model with $\vec{\Phi}$ are compatible with the proposal of the competition of the cubic

terms.

Effect of a surface or a substrate

In the presence of a surface for the bulk, or a substrate for the monolayer, inversion and C_{2x} symmetries are broken and the point group becomes C_{3v}, so two new terms are allowed in the Ginzburg-Landau free energy density coupling the M_1^- and the M_1^+ order parameters:

$$\begin{aligned} F_{\Delta\Phi}^{\text{surf}} = l_{\Delta\Phi}[\Delta_1\Phi_1(\Phi_2^2-\Phi_3^2)+\Delta_2\Phi_2(\Phi_3^2-\Phi_1^2)+\Delta_3\Phi_3(\Phi_1^2-\Phi_2^2)]+ \\ + m_{\Delta\Phi}[\Phi_1\Delta_1(\Delta_2^2-\Delta_3^2)+\Phi_2\Delta_2(\Delta_3^2-\Delta_1^2)+\Phi_3\Delta_3(\Delta_1^2-\Delta_2^2)]. \end{aligned} \tag{1.116}$$

These new terms also have a direction dependence of the order parameters, and are not minimized by the C_3-symmetric $3Q$ solution. Indeed, for generic parameters within the $3Q$ region ($c_\Delta > 0$, $c_\Phi > 0$), in Appendix 1.D.2 we numerically find that increasing the coefficients $l_{\Delta\Phi}$ and $m_{\Delta\Phi}$ favors the nematic $3Q$ phase, which is now symmetry-equivalent to the $2Q$ phase, since the inversion symmetry differing them is now broken (see Section 1.2.3). Therefore, it is possible that the C_3 symmetry is broken at a higher temperature in the surface.

Ginzburg-Landau phase diagrams

In this section we study the ground state of the Ginzburg-Landau free-energy functional $F_{\Delta\Phi}$ of Eqs. (1.110) and (1.116) coupling the M_1^- $\vec{\Delta}$ and M_1^+ $\vec{\Phi}$ order parameters. We show that nematicity can indeed emerge from the competition of the cubic terms, and it is enhanced by a surface or a substrate. We remark that, since $F_{\Delta\Phi}$ is perturbative in $\vec{\Delta}$, it does not capture the nematicity from the conduction band incipient saddle point, which is the main mechanism for nematicity in realistic $TiSe_2$. Therefore, the results in this section should be interpreted as a signature that the nematic state induced by the incipient saddle point can be enhanced by the order parameter $\vec{\Phi}$ via this competition of cubic terms.

We have not determined the values of the Ginzburg-Landau coefficients from the microscopic theory, and we set them to arbitrary values, with the following considerations. First, the quadratic coefficients a_Δ, a_Φ are related to the difference between the actual temperature and the critical temperature, being negative below T_{CDW}. Since $\vec{\Delta}$ condenses first and $\vec{\Phi}$ only onsets at a lower temperature, we take $a_\Delta < a_\Phi$. The isotropic quadratic coefficients b_Δ, b_Φ have to be positive so that $F_{\Delta\Phi}$ goes to infinity as $|\vec{\Delta}|$ and $|\vec{\Phi}|$ go to infinity. We are interested in the study of the nematic $\vec{\Delta} = (\Delta_1, \Delta_2, \Delta_2)$ state, which appears as an instability within the region where the $3Q$ phase is more stable, so we choose the quartic coefficients c_Δ, c_Φ positive to favor the $3Q$ versus the $1Q$ state. We set the cubic term of $|\vec{\Phi}|$ $d_\Phi > 0$ as determined from the $\boldsymbol{k}\cdot\boldsymbol{p}$ model. With these

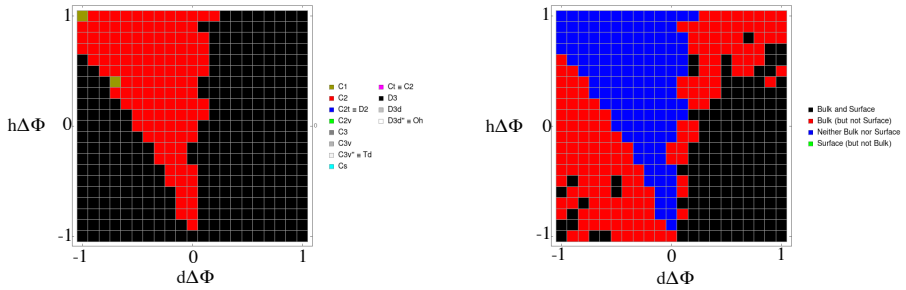

FIGURE 1.D.2: Phase diagram obtained solving the global minimum of the Ginzburg-Landau functional of Eq. (1.110). (a) Resulting point groups in the monolayer. The C_3-symmetric $3Q$ phase, with point group D_3, is represented in black. The $3Q$ nematic phase, with point group C_2, is plotted in red. (b) Phase diagrams indicating where the threefold rotational symmetry is present. Black indicates that both bulk and surface are C_3-symmetric, blue signals the regions where C_3 is broken in both the bulk and the surface, and red represents the regions where the bulk is C_3-symmetric but the surface is nematic. The red regions, where C_3 is preserved in the bulk but broken in the surface, grow with decreasing temperature. We have chosen the following values for the coefficients: $a_\Delta = -0.3$, $a_\Phi = -0.1$, $c_\Delta = 0.5$, $d_\Phi = 0.5$, $c_\Phi = 0.5$, $e_{\Delta\Phi} = -0.5$, $g_{\Delta\Phi} = 0.5$. The surface in (b) is simulated using $l_{\Delta\Phi} = 2$ of Eq. (1.116).

considerations, we fix the coefficients and study the phase diagram as a function of the cubic $d_{\Delta\Phi}$ and quartic $h_{\Delta\Phi}$ couplings, which play an important role in the nematic mechanism.

Fig. 1.D.2(a) shows such a phase diagram in the CDW state ($a_\Delta < a_\Phi < 0$). Black indicates the C_3-symmetric $3Q$ CDW, while red signals the nematic $\vec{\Delta} = (\Delta_1, \Delta_2, \Delta_2)$ state. As required by the cubic-competition mecahnism, the nematicity only occurs when $d_{\Delta\Phi} < 0$, and when both cubic terms are of the same order, $d_{\Delta\Phi} \sim d_\Phi$. The quartic term $h_{\Delta\Phi}$ also plays a crucial role, since it favors nematicity when it is positive.

Fig. 1.D.2(b) shows the comparison of the same phase diagram with and without a large surface term $l_{\Delta\Phi} > 0$. Blue represents the regions where the state is nematic in both cases. Interestingly, red indicates the regions where the surface term induces a nematic state from an otherwise rotationally symmetric phase in the bulk.

nonanalyticity in the zero-temperature free energy

Strictly speaking, the Ginzburg-Landau free-energy density of Eq. (1.110) is only valid when both $\vec{\Delta}$ and $\vec{\Phi}$ order parameters are small, i.e., close to the transition temperature or close to the critical doping. At low temperatures and dopings, the full series should be considered, which can result in some of the coefficients being nonanalytic if computed at zero temperature. For instance, a typical temperature dependence is $\propto 1/T$. Indeed, we will show that the cubic term $d_\Phi \Phi_1 \Phi_2 \Phi_3$ becomes nonanalytic at zero temperature, which can be easily understood from dimensional analysis. Nevertheless, our intuitive explanation for the enhancement of the $3Q$

nematic state still applies, since it only relies on the competition between the different relative signs of the order parameters, and the nonanalyticity changes the dependence on the modulus of the order parameters, but the sign dependence is set by symmetry. Importantly, we will not only show that there exists a nonanalytic linear-in-$\vec{\Phi}$ term in the free-energy density, but that the coefficient of this term increases with electron doping, as mentioned in Section 1.5.2.

The fact that the cubic term is actually nonanalytic can be derived from dimensional analysis of the possible terms that might enter in the free energy density of the order parameter $\vec{\Phi}$ coupling the conduction bands. At zero temperature, the only dimensional parameters in the $\boldsymbol{k}\cdot\boldsymbol{p}$ Hamiltonian are the effective masses m or the density of states ρ, with dimensions $[m] = [1/\rho] = EL^2$, the electron density $[n] = 1/L^2$, and the order parameter $[\Phi] = [E]$[7]. The free-energy density has dimensions $[F] = [E/L^2]$. The units of the coefficient of the l^{th} term, $c_l|\vec{\Phi}|^l$, are $[c_l] = E^{1-l}/L^2$, so $c_l \propto n(\rho/n)^{l-1}$. In particular, $c_1 \propto n$, $c_2 \propto \rho$, and $c_{l+2} = \rho^{l+1}/n^l$. The free energy should vanish for zero electron doping $n = 0$, since, in the absence of Δ, $\vec{\Phi}$ only modifies the dispersion of the conduction bands, which are empty in this case. Therefore, at zero temperature, the free-energy density has to depend on $|\vec{\Phi}|$ as

$$F_\Phi = \alpha\frac{n^2}{\rho} + \beta n|\vec{\Phi}| + \gamma\rho|\vec{\Phi}|^2. \tag{1.117}$$

The dimensionless coefficients α, β and γ could also have a nonanalytic $\vec{\Phi}$ dependence as a dimensionless function, such as a $\Phi_1\Phi_2\Phi_3/|\vec{\Phi}|^3$. The linear term is nonanalytic, but a part of it should have a direction dependence as the cubic term of Eq. (1.56), i.e., $\sim \Phi_1\Phi_2\Phi_3/|\vec{\Phi}|^2$. Importantly, the linear term increases with the electron doping. We note that, at finite temperatures, the additional parameter $[T] = E$ allows $c_l \propto n/T^{l-1}$ or $c_l \propto \rho/T^{l-2}$.

Indeed, starting from the $\boldsymbol{k}\cdot\boldsymbol{p}$ model in the isotropic $b_d = 0$ limit, in Appendix 1.D.1 we have determined analytically the exact form of Eq. (1.117) for $\vec{\Phi} = \pm|\vec{\Phi}|(1,1,1)$. Equations (1.107) and (1.108) confirm that indeed the zero-temperature free energy has a linear-in-$|\vec{\Phi}|$ term which is linear in the electron density n, and a quadratic-in-$|\vec{\Phi}|$ term which is proportional to the DOS.

The nonanalyticity is crucial for the possibility of enhancing the nematic phase. First, since the term with the $\Phi_1\Phi_2\Phi_3$ direction dependence is linear in $|\vec{\Phi}|$, and not cubic, it is of the same order in $|\vec{\Phi}|$ as the cubic coupling $F^{(3)}_{\Delta\Phi}$, which allows their competition. It is also key for this scenario that the coefficient multiplying the term $\sim \Phi_1\Phi_2\Phi_3$ increases with the electron doping, so that at intermediate doping there is frustration with the cubic coupling $F^{(3)}_{\Delta\Phi}$.

[7] An additional parameter with units of energy is the attraction g in the $\vec{\Phi}$ channel. This would enter in the mean-field energy cost to develop order, which is proportional to $|\vec{\Phi}|^2/g$.

1.D.3 Self-consistent calculations in the effective lattice model

The self-consistent mean-field calculations in the effective lattice model with $\vec{\Phi}$ are compatible with the proposal of the competition of the cubic terms. Fig. 1.D.3 shows the $T-x$ phase diagrams with nonzero V_{dp}, U_{dp} and V_{dd} interactions, together with the values of the cubic and quartic terms

$$f_{\Phi}^{(3)} = \Phi_1\Phi_2\Phi_3, \tag{1.118}$$

$$f_{\Delta\Phi}^{(3)} = \Phi_1\Delta_2\Delta_3 + \Phi_2\Delta_3\Delta_1 + \Phi_3\Delta_1\Delta_2, \tag{1.119}$$

$$f_{\Delta\Phi}^{(4)} = \Delta_1\Delta_2\Phi_1\Phi_2 + \Delta_1\Delta_3\Phi_1\Phi_3 + \Delta_2\Delta_3\Phi_2\Phi_3. \tag{1.120}$$

For all the parameters studied, we find that the quartic term $f_{\Delta\Phi}^{(4)} \geq 0$. Within the C_3-symmetric $3Q$ CDW, this is only compatible with $\vec{\Phi} = \pm|\Phi_0|(1,1,1)$ (see Table (1.115)). This suggests that the quartic coupling constant $h_{\Delta\Phi}$ of Eq. 1.114 is large and negative. The cubic terms choose $\vec{\Phi} = |\Phi_0|(1,1,1)$ for low doping, where $d_{\Delta\Phi}$ dominates, and $\vec{\Phi} = -|\Phi_0|(1,1,1)$ for high doping, where d_{Φ} dominates instead. The intermediate region where both cubic terms are of the same order and $\Phi_1\Phi_2\Phi_3$ changes sign occurs around the same doping as the nematic dome driven by the conduction band incipient saddle point. In Section 1.5.3, we showed that this nematic dome is enhanced by the U_{dp} and V_{dd} interactions, and we discussed how this can be related to the effect of $\vec{\Phi}$ in the incipient saddle point. Now, the agreement with the cubic term competition picture suggests that also this mechanism might further promote the nematicity. Finally, we note that the nematic phase appears first as a $3Q/2Q$ nematic state with $f_{\Phi}^{(3)} \leq 0, f_{\Delta\Phi}^{(3)} < 0$ and $f_{\Delta\Phi}^{(4)} \geq 0$, and then the cubic signs change giving rise to a $3Q$ nematic phase with $f_{\Phi}^{(3)} > 0, f_{\Delta\Phi}^{(3)} > 0$ and $f_{\Delta\Phi}^{(4)} > 0$.

1.E Light-induced gyrotropic state: Ginzburg-Landau theory

In this Appendix, we study the Ginzburg-Landau functional coupling the time-reversal symmetric L_1^- ($\vec{\Delta}$) and M_1^- ($\vec{\Psi}$) order parameters, and analyze the conditions under which a metastable chiral minimum exists. The Ginzburg-Landau functional $F_{\Delta\Psi}$ reads

$$F_{\Delta\Psi} = F_{\Delta} + F_{\Psi} + F_{\Delta\Psi}^{(4)}, \tag{1.121}$$

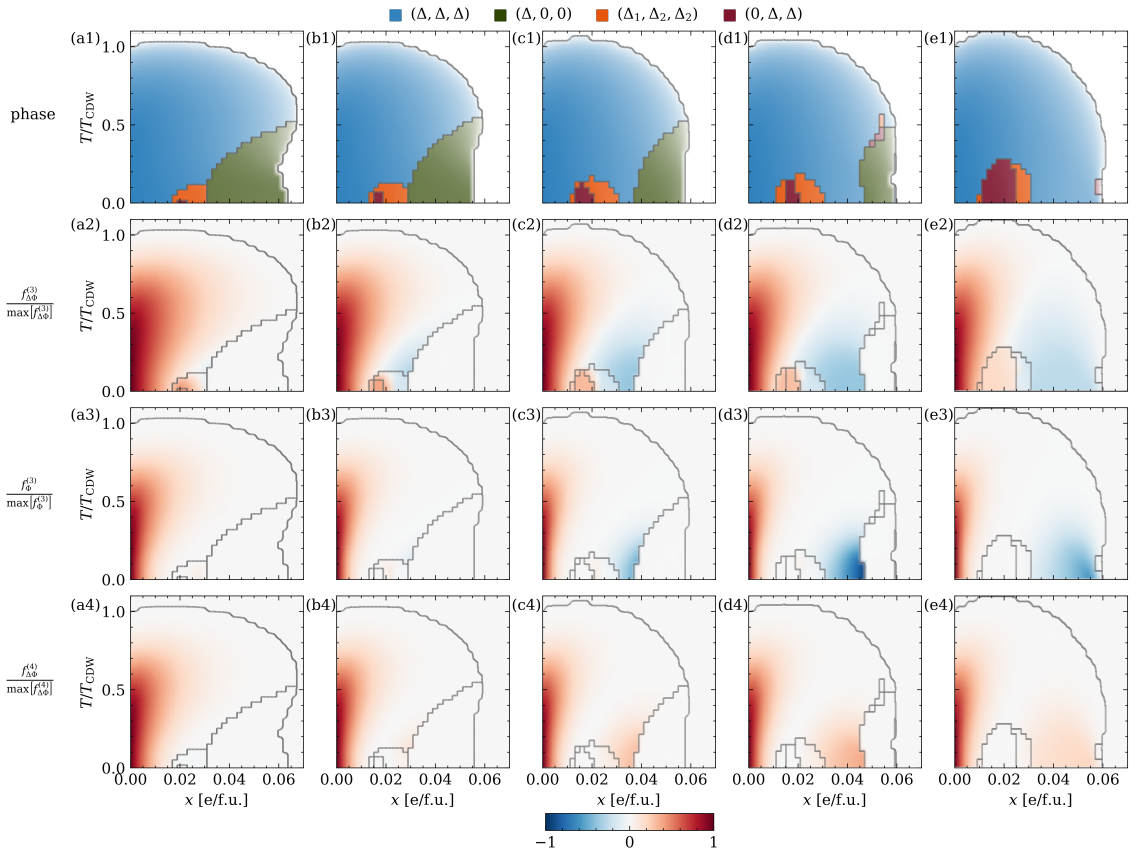

FIGURE 1.D.3: Temperature-doping phase diagrams obtained by self-consistently solving the mean-field Hamiltonian of Eqs. (1.44), (1.60), (1.61) for different gaps, using the same V_{dp}, U_{dp} and V_{dd} interactions as in the first row of Fig. 1.14:

(a) $E_g = +50\text{meV}$, $V_{dp} = 450\text{meV}$, $U_{dp} = 900\text{meV}$, $V_{dd} = 400\text{meV}$, $T_{\text{CDW}} = 596\text{K}$;
(b) $E_g = 0$, $V_{dp} = 400\text{meV}$, $U_{dp} = 800\text{meV}$, $V_{dd} = 400\text{meV}$, $T_{\text{CDW}} = 358\text{K}$;
(c) $E_g = -25\text{meV}$, $V_{dp} = 400\text{meV}$, $U_{dp} = 680\text{meV}$, $V_{dd} = 400\text{meV}$, $T_{\text{CDW}} = 259\text{K}$;
(d) $E_g = -30\text{meV}$, $V_{dp} = 400\text{meV}$, $U_{dp} = 650\text{meV}$, $V_{dd} = 400\text{meV}$, $T_{\text{CDW}} = 239\text{K}$;
(e) $E_g = -50\text{meV}$, $V_{dp} = 400\text{meV}$, $U_{dp} = 520\text{meV}$, $V_{dd} = 400\text{meV}$, $T_{\text{CDW}} = 155\text{K}$.

T_{CDW} is the critical temperature at stoichiometry. The first row indicates the symmetry of the CDW: C_3-symmetric $3Q$, $1Q$ stripe or $3Q/2Q$ nematic. The intensity of the color of each phase is proportional to $|\vec{\Delta}|$. The second, third and four rows display the combinations of order parameters $f^{(3)}_{\Delta\Phi}$ (1.119), $f^{(3)}_{\Phi}$ (1.118) and $f^{(4)}_{\Delta\Phi}$ (1.120), respectively, normalized by their corresponding maximum value in each plot. Within the C_3-symmetric $3Q$ state, the sign of both cubic terms changes when crossing the nematic $3Q/2Q$ dome, while the quartic term remains always positive.

where F_Δ and F_Ψ are the individual free energies given by Eq. (1.35), $F^{(4)}_{\Delta\Psi}$ is the coupling between them in the absence of light, whose lowest order is quartic:

$$F_\Delta = a_\Delta|\vec{\Delta}|^2 + b_\Delta|\vec{\Delta}|^4 + c_\Delta\left(\Delta_1^4 + \Delta_2^4 + \Delta_3^4\right), \tag{1.122}$$

$$F_\Psi = a_\Psi|\vec{\Psi}|^2 + b_\Psi|\vec{\Psi}|^4 + c_\Psi\left(\Psi_1^4 + \Psi_2^4 + \Psi_3^4\right), \tag{1.123}$$

$$F^{(4)}_{\Delta\Psi} = e_{\Delta\Psi}|\vec{\Delta}|^2|\vec{\Psi}|^2 + g_{\Delta\Psi}|\vec{\Delta}\cdot\vec{\Psi}|^2 + h_{\Delta\Psi}\left(\Delta_1\Delta_2\Psi_1\Psi_2 + \Delta_1\Delta_3\Psi_1\Psi_3 + \Delta_2\Delta_3\Psi_2\Psi_3\right). \tag{1.124}$$

The circularly polarized light in normal incidence can be effectively represented by a coupling $\Lambda = [\boldsymbol{E} \times \boldsymbol{E}^*]_z$, where $\boldsymbol{E}$ is the electric field in the plane. Λ transforms as the time-reversal odd A_{2g} irrep of the $TiSe_2$ point group D_{3d}. Therefore, time-reversal symmetry prevents terms linear in Λ in the Ginzburg-Landau functional. Since Λ^2 transforms as time-reversal even A_{1g}, the coefficients of $F_{\Delta\Psi}$ can be renormalized by the circularly polarized light to order Λ^2. The electronic temperature might also renormalize the coefficients. We mention that Ref. [186] proposed that the coupling to the circularly polarized light is via $\tilde{\Lambda} = [\boldsymbol{E} \times \frac{\partial \boldsymbol{E}^*}{\partial z}]_z$, which depends on the electric field gradient along the out-of-plane direction in the sample. While $\tilde{\Lambda}$ is time-reversal even A_{1g} and therefore can couple linearly to the order parameters, the dispersive effects, i.e., the optical effects depending on the gradient of the electric field, or equivalent on a nonzero momentum of the light, are typically weaker.

With this in mind, we now analyze the relative minima of $F_{\Delta\Psi}$ to study whether a metastable chiral phase with partial or full M_1^- order parameter exists. Given the presence of C_3 symmetry in the CPGE experiments [186, 187], we consider the particular case with $\vec{\Delta} = (\Delta, \Delta, \Delta)$ and $\vec{\Psi} = (\Psi, \Psi, \Psi)$. $F_{\Delta\Psi}$ reduces to:

$$F_{\Delta\Psi}^{C_3} = t_\Delta \Delta^2 + v_\Delta \Delta^4 + t_\Psi \Psi^2 + v_\Psi \Psi^4 + u_{\Delta\Psi} \Delta^2 \Psi^2, \tag{1.125}$$

where

$$t_\Delta = 3a_\Delta, \tag{1.126}$$
$$v_\Delta = 9b_\Delta + 3c_\Delta, \tag{1.127}$$
$$t_\Psi = 3a_\Psi, \tag{1.128}$$
$$v_\Psi = 9b_\Psi + 3c_\Psi, \tag{1.129}$$
$$u_{\Delta\Psi} = 9e_{\Delta\Psi} + 3g_{\Delta\Psi} + 3h_{\Delta\Psi}. \tag{1.130}$$

For the free energy $F_{\Delta\Psi}^{C_3}$ to be well defined, $v_\Delta > 0$, $v_\Psi > 0$, and $u_{\Delta\Psi} > -2\sqrt{v_\Delta v_\Psi}$.

There are four relative extremal solutions:

- No CDW (0):

$$(0) \begin{cases} \Delta = 0 \\ \Psi = 0 \\ F_{\Delta\Psi}^{C_3} = 0 \end{cases} \tag{1.131}$$

- Single order parameter (α), with $\alpha = \Delta, \Psi$ and $\beta = \Psi, \Delta$:

$$(\alpha) \begin{cases} \alpha^2 = -\frac{t_\alpha}{2v_\alpha} \\ \beta = 0 \\ F^{C_3}_{\Delta\Psi} = -\frac{t_\alpha^2}{4v_\alpha} \end{cases} \tag{1.132}$$

- Coexistence $(\Delta\Psi)$:

$$(\Delta\Psi) \begin{cases} \Delta^2 = -\frac{2v_\Psi t_\Delta - u_{\Delta\Psi} t_\Psi}{4v_\Delta v_\Psi - u^2_{\Delta\Psi}} \\ \Psi^2 = -\frac{2v_\Delta t_\Psi - u_{\Delta\Psi} t_\Delta}{4v_\Delta v_\Psi - u^2_{\Delta\Psi}} \\ F^{C_3}_{\Delta\Psi} = -\frac{v_\Delta t_\Psi^2 + v_\Psi t_\Delta^2 - u_{\Delta\Psi} t_\Psi t_\Delta}{4v_\Delta v_\Psi - u^2_{\Delta\Psi}} \end{cases} \tag{1.133}$$

Assuming both quadratic coefficients to be negative, $t_\alpha < 0$ and $t_\beta < 0$, and defining the order α such that $2v_\alpha \frac{t_\beta}{t_\alpha} < 2v_\beta \frac{t_\alpha}{t_\beta}$, as a function of the coupling $u_{\Delta\Psi}$ we have the following minima:

- One minimum with coexistence for $u_{\Delta\Psi} < 2v_\alpha \frac{t_\beta}{t_\alpha}$
- One minimum with a single order α for $2v_\alpha \frac{t_\beta}{t_\alpha} < u_{\Delta\Psi} < 2v_\beta \frac{t_\alpha}{t_\beta}$
- Two relative minima with a single order each (with that of α being the ground state) for $u_{\Delta\Psi} > 2v_\beta \frac{t_\alpha}{t_\beta}$

For a metastable state to exist, strong coupling $u_{\Delta\Psi} > 2v_\beta \frac{t_\alpha}{t_\beta}$ is required. In the absence of light, we have $\alpha = \Delta$. If the system is in the regime with a metastable minimum, and light renormalizes the coefficients such that $2v_\Psi \frac{t_\Delta}{t_\Psi}$ becomes smaller than $2v_\Delta \frac{t_\Psi}{t_\Delta}$ (if v_Ψ decreases and t_Ψ increases faster than the corresponding Δ quantities), then the explanation based on the light-induced metastable M_1^- state might apply.

Chapter 2

Superconducting collective modes in 1H-NbSe2

Superconductivity is the emblematic example of a collective emergent phenomenon in condensed matter physics. Understanding unconventional superconductivity beyond the electron-phonon driven s-wave spin-singlet pairing is one of the main ongoing challenges in the field. In this Chapter, we study the superconducting transition metal dichalcogenide 2H-$NbSe_2$ in its monolayer form. While its ground state is likely a conventional superconductor, it also displays unconventional features. Indeed, the in-plane critical magnetic field displays several signatures pointing to the presence of a subleading f-wave spin-triplet pairing. Motivated by the recent observation of satellite peaks in the scanning tunneling microscopy (STM) experiments performed by our collaborators [2], in this Chapter we analyze the effect of the subleading f-wave spin-triplet pairing on the collective mode spectrum of the superconducting state of monolayer $NbSe_2$. In particular, in combination with the spin-orbit coupling and the absence of inversion symmetry, we show that the subleading pairing leads to a Leggett mode, consisting of the fluctuation of the relative phase between the pairings in the spin-split bands of monolayer $NbSe_2$. We determine its energy, and show that it is undamped and well-defined as long as the interaction remains attractive in the subleading pairing channel. We also demonstrate that it leaves fingerprints in the electron spectral function, and could thus be detected in tunneling experiments. Finally, we discuss the possible interpretation of the STM resonances of Ref. [2] in terms of the Leggett mode.

2.1 Introduction

In this section, we present an overview of the field of superconductivity. After explaining the defining properties of a superconductor, we focus on general aspects relevant to our study of the superconducting state of monolayer $NbSe_2$. We first discuss the subtleties appearing in defining superconductivity in 2D. We then move on to describe the microscopic BCS theory of superconductivity. We provide a general formulation, defining the pairing operators and order parameters for a general interaction, which will be useful for the analysis of $NbSe_2$ in Section 2.2.2 and in Appendix 2.B. We also pay special attention to the symmetry classification of the superconducting pairings. With a view to interpreting the STM resonances of Ref. [2], we introduce the collective modes that might appear in a superconductor in a general setting. We then describe the particular features of monolayer 2H-$NbSe_2$, comparing it to its bulk counterpart. We describe its band structure and symmetry properties, as well as its CDW and superconducting instabilities. We conclude this section by thoroughly describing the recent experiments uncovering unconventional signatures in the superconducting state of monolayer $NbSe_2$, including the twofold-anisotropic in-plane critical magnetic field [115, 116] and the bosonic resonances observed in STM [2]. In subsequent sections, we introduce a simple $\boldsymbol{k}\cdot\boldsymbol{p}$ model for monolayer $NbSe_2$, and study its possible superconducting instabilities within BCS theory, as well as its collective mode spectrum.

2.1.1 Superconductivity

Definition and macroscopic effective description

Superfluidity and its charged counterpart, superconductivity, are ordered phases consisting of a coherent state made of bosonic quasiparticles. In the case of superconductors, which can be regarded as charged superfluids, these bosonic quasiparticles are Cooper pairs of two electrons [59] (or higher even numbers [207]). The broken symmetry of the coherent state in superfluids is the particle number conservation, which is well-defined in the grand canonical ensemble, when the system can interchange particles with a bath. This symmetry is associated with the $\mathcal{U}(1)$ complex phase of their order parameter, which in the simplest case is a scalar complex quantity $\Delta(\boldsymbol{r}) = |\Delta(\boldsymbol{r})|e^{i\varphi(\boldsymbol{r})}$, which can be interpreted as the expectation value of the appropriate field operator $\hat{\Delta}(\boldsymbol{r})$. Indeed, the particle number N and the phase φ are conjugate variables, and thus they obey the uncertainty relation $(\delta\varphi)(\delta N) \gtrsim 1$ [57]. In a coherent state, the phase is well-defined, and therefore the particle number is strictly ill-defined. However, in the canonical ensemble, where the particle number is fixed, such an expectation value with a defined phase can never develop. Nevertheless, the order parameter and broken symmetry manifest in the correlation functions at long distances:

$$\langle\hat{\Delta}^\dagger(\boldsymbol{r}')\hat{\Delta}(\boldsymbol{r})\rangle \xrightarrow[|\boldsymbol{r}'-\boldsymbol{r}|\gg]{\text{ODLRO}} \Delta^*(\boldsymbol{r}')\Delta(\boldsymbol{r}) = \text{constant}. \tag{2.1}$$

This is the defining property of off-diagonal long-range order (ODLRO) [57, 208], of which superfluidity and superconductivity are the paradigmatic examples. In the thermodynamic limit, the canonical and grand-canonical ensembles become equivalent, since the uncertainty in the phase and the relative uncertainty in the particle number $\frac{(\delta N)}{N}$ can be both made negligible, given that $(\delta\varphi)\frac{(\delta N)}{N} \gtrsim \frac{1}{N} \to 0$. Therefore, from now on, we will work in the grand-canonical ensemble for simplicity.

The defining properties of a superconductor are the persistent current superflow in equilibrium, with its associated zero resistance, and the Meissner effect, which stands for the full expulsion of magnetic fields by the superconductor. In order to describe them, the Ginzburg-Landau theory is effective. A phenomenological Ginzburg-Landau free-energy functional can be written on the basis of symmetry, without having to resort to the particular microscopic theory from which it is derived. We start by considering a s-wave spin-singlet pairing of a neutral superfluid with full rotational invariance, whose Ginzburg-Landau functional reads

$$F[\Delta] = \int d^d\boldsymbol{r} \left[\frac{\hbar^2}{2m^*} |\boldsymbol{\nabla}\Delta|^2 + r|\Delta|^2 + \frac{1}{2}u|\Delta|^4 \right], \tag{2.2}$$

where m^* is the mass of the bosonic quasiparticles that condense, $u > 0$, and, in a homogeneous system, r changes sign at the mean-field transition temperature T_{MF}, so it is conventional to write $r = a(T - T_{\mathrm{MF}})$ with $a > 0$. The Ginzburg-Landau theory is valid to describe the low-energy phenomenology at length scales larger than the coherence length $\xi_0 = \sqrt{\frac{\hbar^2}{2am^*T_{MF}}}$. In particular, the Ginzburg-Landau theory describes this low-energy physics by the spatial fluctuations of the collective order parameter $\Delta(\boldsymbol{r}) = |\Delta(\boldsymbol{r})|e^{i\varphi(\boldsymbol{r})}$.

Within this effective description, we first review the persistent superflow in the context of neutral superfluids. A twist in the condensate phase φ gives rise to a coherent particle current density, $\boldsymbol{J}_n = n_s\frac{\hbar}{m^*}\boldsymbol{\nabla}\varphi$, where $n_s \propto |\Delta|^2$ is the superfluid density, which measures the rigidity of the phase, i.e., the cost of spatial fluctuations of the phase, and therefore controls the phase coherence. This expression can be rewritten as $\boldsymbol{J}_n = n_s\boldsymbol{v}_s$, where $\boldsymbol{v}_s = \frac{\hbar}{m^*}\boldsymbol{\nabla}\varphi$ is the superfluid velocity. This superflow is topologically stable due to the topology associated with the winding number of the order parameter (technically, its first homotopy group π_1) [57, 209]. A conventional s-wave spin-singlet order parameter, whose manifold under which it is invariant is $U(1)$, has winding $\pi_1[U(1)] = \mathbb{Z}$, which means that the circulation of the phase of the order parameter around the sample is an integer multiple of 2π, $\oint d\boldsymbol{r}\cdot\boldsymbol{\nabla}\varphi = 2\pi n_\varphi$. The number of twists n_φ is a topological invariant, since it cannot be changed by continuous deformations of the phase. As long as $n_s > 0$, it can only change by creating domain walls with vanishing amplitude, $|\Delta| = 0$, whose energetic cost is exponentially large in the thermodynamic limit. Since the superfluid velocity is proportional to the phase gradient, $\boldsymbol{v}_s = \frac{\hbar}{m^*}\boldsymbol{\nabla}\varphi$, the superflow is topologically protected. More

concretely, the circulation of the velocity around the sample, or vorticity, is quantized

$$\oint d\boldsymbol{r} \cdot \boldsymbol{v}_s = \tfrac{h}{m^*} n_\varphi \tag{2.3}$$

Eq. (2.3) is called Onsager-Feynman quantization. Similar reasoning allows to regard vortices, which are singular lines in the superfluid around which the phase winds an integer multiple of 2π, as topological defects. For completeness, we mention that other order parameter manifolds have a winding different from $\mathbb{Z}$, and their superflow can therefore decay through continuous reduction of the winding number [209]. These order parameters arise from the condensation of bosons with finite angular momentum, such as the complex vector order parameter of the A phase of ^{3}He with manifold $SO(3)$ [209].

Until now, we have discussed the persistent superflow in the case of neutral superfluids. We now consider superconductors, where the charged Cooper pairs couple to the electromagnetic field, so that the changes in the phase of the order parameter are linked to the gauge vector potential $\boldsymbol{A}$. Their Ginzburg-Landau functional has to consider the coupling to the electromagnetic field too. For a s-wave spin-singlet rotationally-invariant superconductor, the Ginzburg-Landau free energy reads

$$F[\Delta, \boldsymbol{A}] = \int d^d\boldsymbol{r} \left[\frac{\hbar^2}{2m^*} \left| \left(\boldsymbol{\nabla} - i\frac{e^*}{\hbar}\boldsymbol{A} \right) \Delta \right|^2 + r|\Delta|^2 + \frac{1}{2}u|\Delta|^4 + \frac{1}{2\mu_0} (\boldsymbol{\nabla} \times \boldsymbol{A})^2 \right], \tag{2.4}$$

where $e^* = 2e$ is the charge of the Cooper pairs, with e the electron charge, and μ_0 the vacuum magnetic permeability. The Ginzburg-Landau functional (2.4) is explicitly gauge invariant, since gauge transformations act as $\Delta(\boldsymbol{r}) \to \Delta(\boldsymbol{r})e^{i\alpha(\boldsymbol{r})}$, $\boldsymbol{A}(\boldsymbol{r}) \to \boldsymbol{A}(\boldsymbol{r}) + \frac{\hbar}{e^*}\boldsymbol{\nabla}\alpha(\boldsymbol{r})$. Although a gauge choice for $\Delta(\boldsymbol{r})$ has to be selected for explicit calculations, observables are gauge invariant. Indeed, the $U(1)$ local gauge invariance in superconductors cannot be broken [60], and consequently no local gauge-invariant observable associated with superconductivity exhibits long-range order [61–63]. An alternative understanding of superconductivity where gauge invariance is always explicitly preserved describes superconductivity as topological order [61–63]. As such, it displays a ground-state degeneracy dependent on the genus of the manifold where the superconductor lives, as well as fractionalization of excitations [61–63]. Nevertheless, here we will consider their pragmatic description as charged superfluids with an order parameter $\Delta(\boldsymbol{r})$.

From the Ginzburg-Landau functional (2.4), we can derive the charge current density $\boldsymbol{J}_c = e^* n_s \boldsymbol{v}_s$, where $\boldsymbol{v}_s = \frac{\hbar}{m^*}(\boldsymbol{\nabla}\varphi - \frac{e^*}{\hbar}\boldsymbol{A})$ is the superfluid velocity. The superflow in a superconductor is also topologically protected against phase deformations, and we will later show that its decay into single-particle excitations is protected by the gap in the spectrum. Cooper pairs in solid-state superconductors might also condense with a finite relative orbital angular momentum. Nevertheless,

unlike in rotationally invariant superfluids, crystal fields and spin-orbit coupling usually reduce the continuum symmetry to be $U(1)$ always, which guarantees the topological protection of the supercurrent. Due to the coupling to the electromagnetic field, the quantization of the circulation implies the quantization of the magnetic flux $\Phi = n_\varphi \Phi$ in the vortices. Finally, we note that, while a consequence of the persistent superflow is a vanishing longitudinal resistance, the latter is not unique to superconductors. For instance, the longitudinal resistance also vanishes in the quantum Hall effect (see Chapter 3).

Besides the persistent superflow, superconductors are characterized by the Meissner effect, which also naturally arises due to the coupling between Cooper pairs and the electromagnetic field. By minimizing the Ginzburg-Landau functional (2.4), one can derive that the magnetic field verifies that $\nabla^2 \boldsymbol{B} = \frac{1}{\lambda_L^2}\boldsymbol{B}$, where $\lambda_L^2 = \frac{m^*}{\mu_0 n_s e^{*2}}$ is the London penetration depth [57, 210]. The only uniform solution in the superconducting state, where $n_s > 0$, is $\boldsymbol{B} = 0$. In the presence of an external magnetic field, the magnetic field near the surface or around the vortices decays exponentially within a distance λ_L, $\boldsymbol{B} \sim e^{-|\boldsymbol{r}|/\lambda_L}$. Beyond a certain critical external field H_c, the uniform Meissner effect is no longer stable, and the system transitions to the normal state. Depending on the ratio $\frac{\lambda_L}{\xi_0}$ between the London penetration depth λ_L and the coherence length ξ_0, which determines the surface energy of a superconductor-normal state interface, two types of superconductors can be distinguished. In type I superconductors, the coherence length is larger that the penetration depth, $\xi_0 > \lambda_L$, the interface energy is positive, and there is a first-order transition to the normal state at H_c. On the other hand, the coherence length is smaller that the penetration depth in type II superconductors, $\xi_0 < \lambda_L$, which implies a negative interface energy. Type II superconductors exhibit two critical fields, $H_{c1} < H_{c2}$. Below the lower critical field H_{c1}, the homogeneous Meissner effect completely expels the magnetic field. Between H_{c1} and the upper critical field H_{c2}, the magnetic field partially penetrates the bulk in the form of vortices, which form an Abrikosov flux lattice.

Superconductivity in 2D

The Ginzburg-Landau theory, within a mean-field treatment, has allowed us to explain the two defining properties of superconductivity, namely the persistent supercurrent and the Meissner effect. Before concluding this section, it is worth discussing the subtleties that arise in 2D superconductivity, where fluctuations beyond mean-field theory have a crucial effect. The main message of this discussion will be that superconductivity exists in 2D at finite temperatures, it has been experimentally observed in thin films and 2D materials, and several of its features, especially those related to symmetries, are accurately described within the mean-field BCS theory explained in the next section.

The first aspect to consider is Mermin-Wagner(-Hohenberg-Wegner) theorem [211–214], which states that no long-range order spontaneously breaking a continuous symmetry can develop in 2D systems with sufficiently short-range interactions at finite temperature in the thermodynamic limit. It applies to the particular case of the $U(1)$ symmetry in superfluids [212], but also to the $O(2)$ symmetry of magnetic XY models [211, 213] and 2D crystals [214]. The reason is that the long-wavelength soft phase fluctuations renormalize the correlation function of Eq. (2.1) so that it decays as a power law at long distances:

$$\langle \hat{\Delta}^\dagger(\boldsymbol{r}')\hat{\Delta}(\boldsymbol{r})\rangle \xrightarrow[|\boldsymbol{r}'-\boldsymbol{r}|\gg]{\text{2D}} |\Delta_0|^2 \left(\frac{\xi}{|\boldsymbol{r}'-\boldsymbol{r}|}\right)^{\eta}, \tag{2.5}$$

where ξ is an appropriate correlation length and Δ_0 is an appropriate amplitude. In 1D, the situation is even worse and the correlation function decays exponentially:

$$\langle \hat{\Delta}^\dagger(\boldsymbol{r}')\hat{\Delta}(\boldsymbol{r})\rangle \xrightarrow[|\boldsymbol{r}'-\boldsymbol{r}|\gg]{\text{1D}} |\Delta_0|^2 \exp\left(-\frac{|\boldsymbol{r}'-\boldsymbol{r}|}{\xi}\right). \tag{2.6}$$

There are certain roundabouts around Mermin-Wagner theorem. For quasi-2D systems, such as the layered superconducting cuprates, a small interlayer coupling stabilizes long-range order[1] [215]. In the case of purely 2D superconductors, the key observation is that Mermin-Wagner theorem is strictly valid only in the thermodynamic limit, for a sufficiently large system. For realistic parameters, the length scale above which Mermin-Wagner theorem would apply is larger than typical system sizes [215–217], so effectively long-range order can develop in a finite purely 2D sample below a nonzero temperature. All these ideas can be applied to superconductivity even if the local $U(1)$ gauge symmetry is never broken [215].

A different crucial aspect to be considered in 2D is that, even in the thermodynamic limit, there is a finite temperature phase transition between a disordered state and the quasi-long-range ordered state with power-law correlations (2.5), known as Berezinskii-Kosterlitz-Thouless (BKT) transition [215, 218–222]. All derivatives of the thermodynamic potential are continuous across the transition, but the superfluid density n_s abruptly drops to zero at the transition. The physical picture is that below the transition temperature T_{BKT}, vortices of opposite winding are paired due to energetic reasons, and do not destroy the superflow, at least for a small $\boldsymbol{v}_s$ and for a T_{BKT} rather small compared to the mean-field transition temperature T_{MF}. Above T_{BKT}, entropy allows the proliferation of unpaired vortices, which can move across the supercurrent and damp it. This effect applies to superfluids as well as superconductors, although several subtleties appear for the latter

[1] While the minimum interlayer coupling allowing long-range order is infinitesimally small for a exponent $\eta < 2$ in Eq. (2.5), the case $\eta > 2$ requires an interlayer coupling larger than a finite but small cutoff [215].

due to the coupling with the electromagnetic field [215, 222–224].

In summary, 2D superconductivity can exist below T_{BKT} for realistic finite sample sizes. At low enough temperatures, where fluctuations are suppressed, mean-field theory should correctly describe different properties, such as the magnitude of the superconducting order parameter, and especially the features associated with the symmetry of the order parameter. Indeed, in this work we will use mean-field theory to describe a 2D superconductor. In the following section we describe the microscopic mean-field theory of superconductivity.

Microscopic description of superconductivity: BCS theory

Until now we have described superconductivity within the effective Ginzburg-Landau formalism, where the free-energy functional can be phenomenologically derived from the symmetries of the problem. However, to describe certain features, a microscopic theory becomes necessary. The first and simplest microscopic theory of superconductivity was developed by Bardeen, Cooper and Schrieffer (BCS) [64]. It is based on the observation by Cooper that, starting from a filled Fermi sea, an infinitesimally weak electron-electron attraction induces a two-particle bound state [59], now called Cooper pair. If $c^\dagger_\alpha(\boldsymbol{r})$ is the electron creation operator at position $\boldsymbol{r}$ and with internal degrees of freedom α (e.g., spin), we define the two particle operator

$$\hat{\Phi}^\dagger_{\alpha\beta}(\boldsymbol{r},\boldsymbol{R}) = c^\dagger_\alpha(\boldsymbol{R}+\tfrac{1}{2}\boldsymbol{r})c^\dagger_\beta(\boldsymbol{R}-\tfrac{1}{2}\boldsymbol{r}), \tag{2.7}$$

where $\boldsymbol{r}$ is the relative coordinate and $\boldsymbol{R}$ is the center of mass position. In momentum space,

$$\hat{\Phi}^\dagger_{\alpha\beta}(\boldsymbol{k},\boldsymbol{q}) = c^\dagger_\alpha(\boldsymbol{k}+\tfrac{1}{2}\boldsymbol{q})c^\dagger_\beta(-\boldsymbol{k}+\tfrac{1}{2}\boldsymbol{q}), \tag{2.8}$$

where $\boldsymbol{q}$ is the total momentum of the pair, and $\boldsymbol{k}$ is the relative momentum of the electrons forming the pair. The Cooper pair creation operator with pair wavefunction $\phi_{\alpha\beta}(\boldsymbol{r},\boldsymbol{R})$ thus reads

$$\hat{\Phi}^\dagger = \int d^d\boldsymbol{R}\int d^d\boldsymbol{r}\sum_{\alpha\beta}\phi_{\alpha\beta}(\boldsymbol{r},\boldsymbol{R})\hat{\Phi}^\dagger_{\alpha\beta}(\boldsymbol{r},\boldsymbol{R}) = \sum_{\boldsymbol{q}}\sum_{\boldsymbol{k}}\sum_{\alpha\beta}\phi_{\alpha\beta}(\boldsymbol{k},\boldsymbol{q})\hat{\Phi}^\dagger_{\alpha\beta}(\boldsymbol{k},\boldsymbol{q}), \tag{2.9}$$

where $\phi_{\alpha\beta}(\boldsymbol{k},\boldsymbol{q})$ is the Fourier transformed Cooper pair wavefunction.

Before explaining the BCS theory, we mention that the dependence on the total momentum $\boldsymbol{q}$, or equivalently on the center of mass position $\boldsymbol{R}$, characterizes the spatial modulation of the pairing. Unless otherwise stated, we will focus on homogeneous superconductors, where the pairing $\phi_{\alpha\beta}$ does not depend on $\boldsymbol{R}$ and therefore the total momentum $\boldsymbol{q}$ vanishes. We will set $\phi_{\alpha\beta}(\boldsymbol{k}) = \phi_{\alpha\beta}(\boldsymbol{k},\boldsymbol{q}=0)$. Superconductors whose order parameter has $\boldsymbol{q}\neq 0$ are called pair

density waves (PDWs) or Fulde-Ferrell-Larkin-Ovchinnikov (FFLO) states [225–227], and break translational symmetry, analogously to the charge density waves studied in Chapter 1.

Inspired by the Cooper pair instability, the BCS theory describes a superconductor as a coherent condensate of Cooper pairs, whose wavefunction is $|\mathrm{BCS}\rangle = \exp[\hat{\Phi}^\dagger]|0\rangle$, with $|0\rangle$ the electron vacuum. This ground state is the static mean-field solution of a microscopic Hamiltonian, whose key ingredient is a frequency-independent attractive electron-electron interaction V. Originally, the BCS theory was applied to conventional superconductors, where this attraction is mediated by the phonons and induces an isotropic s-wave spin-singlet order parameter [64]. BCS theory has been generalized to account for anisotropic pairings, and it works irrespective of the source of the attraction. However, it is only accurate within the weak-coupling regime, where the attraction V is small, and when the dynamical effects of the frequency-dependent interaction are not relevant. Since, as we will see, the critical temperature T_c depends on the magnitude of V, its quantitative validity is restricted to low-T_c superconductors. Nevertheless, it can also capture certain qualitative features of high-T_c superconductors, such as the d-wave pairing symmetry of cuprate superconductors [10].

Explicitly, the static BCS Hamiltonian in momentum space with an attraction V reads:

$$\begin{aligned} H_{\mathrm{BCS}} &= H_0 + \sum_{\boldsymbol{k}\boldsymbol{k}'\boldsymbol{q}} \sum_{\alpha\beta,\gamma\delta} V_{\alpha\beta,\delta\gamma}(\boldsymbol{k},\boldsymbol{k}',\boldsymbol{q}) c^\dagger_\alpha(\boldsymbol{k}+\tfrac{1}{2}\boldsymbol{q}) c^\dagger_\beta(-\boldsymbol{k}+\tfrac{1}{2}\boldsymbol{q}) c_\gamma(-\boldsymbol{k}'+\tfrac{1}{2}\boldsymbol{q}) c_\delta(\boldsymbol{k}'+\tfrac{1}{2}\boldsymbol{q}) = \\ &= H_0 + \sum_{\boldsymbol{k}\boldsymbol{k}'\boldsymbol{q}} \sum_{\alpha\beta,\gamma\delta} \hat{\Phi}^\dagger_{\alpha\beta}(\boldsymbol{k},\boldsymbol{q}) V_{\alpha\beta,\delta\gamma}(\boldsymbol{k},\boldsymbol{k}',\boldsymbol{q}) \hat{\Phi}_{\delta\gamma}(\boldsymbol{k}',\boldsymbol{q}), \end{aligned} \tag{2.10}$$

where in the second line we have used the two-particle operators defined in Eq. (2.8), and H_0 is the single-particle Hamiltonian

$$H_0 = \sum_{\boldsymbol{k}} \sum_{\alpha\beta} c^\dagger_\alpha(\boldsymbol{k}) h_{0,\alpha\beta}(\boldsymbol{k}) c_\beta(\boldsymbol{k}). \tag{2.11}$$

According to our sign convention, V is attractive where it is negative. Hermiticity requires that $V_{\alpha\beta,\delta\gamma}(\boldsymbol{k},\boldsymbol{k}',\boldsymbol{q}) = V^*_{\delta\gamma,\beta\alpha}(\boldsymbol{k}',\boldsymbol{k},\boldsymbol{q})$, which allows to regard it as a $\boldsymbol{q}$-dependent Hermitian matrix $V(\boldsymbol{q})$ with rows labelled by $\alpha,\beta,\boldsymbol{k}$. Until now, this Hamiltonian is a general static interacting Hamiltonian, and the second row is just an appropriate rewriting for taking the mean-field solution. For instance, the long-range density-density Coulomb interaction for a spinful band in 3D would read $V_{\alpha\beta,\delta\gamma}(\boldsymbol{k},\boldsymbol{k}',\boldsymbol{q}) = \frac{e^2}{\varepsilon_0|\boldsymbol{k}'-\boldsymbol{k}|^2}\delta_{\alpha\delta}\delta_{\beta\gamma}\delta_{\boldsymbol{q},0}$. Originally, the BCS theory was applied to a one-band system with full rotational and inversion symmetries, and without spin-orbit coupling. The attraction was assumed to be constant in momentum space for the spin-singlet channel: $V_{\alpha\beta,\delta\gamma}(\boldsymbol{k},\boldsymbol{k}',\boldsymbol{q}) = -\frac{g}{V_{\mathrm{syst}}}[-i\sigma_y]_{\alpha\beta}[i\sigma_y]_{\gamma\delta}\delta_{\boldsymbol{q},0}$. As we will show below, the artificially assumed

constant attraction leads to a divergence in the integrals that determine the order parameter of the theory. This issue is solved by restricting the attraction to electrons with energy below a cutoff Λ. Physically, in the case of phonon-mediated superconductors, this energy cutoff Λ corresponds to the Debye energy, which determines the onset of the low-energy attractive interaction.

The BCS wavefunction is the mean-field ground state of the BCS Hamiltonian (2.10) when decoupled in the Cooper channel, which corresponds to considering only the expectation values of the particle-particle operators $\hat{\Phi}^\dagger_{\alpha\beta}(\boldsymbol{k},\boldsymbol{q})$, but not of the particle-hole operators (i.e., neglecting the Hartree and Fock channels). In particular, the pairing order parameters read:

$$\bar{\Delta}_{\delta\gamma}(\boldsymbol{k}',\boldsymbol{q}) = -\sum_{\boldsymbol{k}}\sum_{\alpha\beta}\langle\hat{\Phi}^\dagger_{\alpha\beta}(\boldsymbol{k},\boldsymbol{q})\rangle V_{\alpha\beta,\delta\gamma}(\boldsymbol{k},\boldsymbol{k}',\boldsymbol{q}), \tag{2.12}$$

$$\Delta_{\alpha\beta}(\boldsymbol{k},\boldsymbol{q}) = -\sum_{\boldsymbol{k}'}\sum_{\gamma\delta} V_{\alpha\beta,\delta\gamma}(\boldsymbol{k},\boldsymbol{k}',\boldsymbol{q})\langle\hat{\Phi}_{\delta\gamma}(\boldsymbol{k}',\boldsymbol{q})\rangle = \bar{\Delta}^*_{\beta\alpha}(\boldsymbol{k},\boldsymbol{q}). \tag{2.13}$$

The pairings Δ are the order parameters of superconductivity. Their transformations under symmetries determine the symmetries broken in the superconductor. They can be classified according to the irreps of the symmetry group of the system. For instance, for a system without spin-orbit coupling and therefore with $SU(2)$ spin rotation symmetry, the pairing can be differentiated in spin-singlet, with zero total spin $S = 0$, and spin-triplet, with $S = 1$ and $S_z = 1, 0, -1$. In particular, writing explicitly the spin degree of freedom, and taking $\boldsymbol{q} = 0$ for simplicity, we can separate

$$\Delta(\boldsymbol{k}) = \left[\Delta_S(\boldsymbol{k})\sigma_0 + \vec{\Delta}_T(\boldsymbol{k})\cdot\vec{\sigma}\right] i\sigma_y, \tag{2.14}$$

where σ_μ are the spin Pauli matrices, $\Delta_S(\boldsymbol{k})$ is a complex function representing the spin-singlet pairing, and $\vec{\Delta}_T(\boldsymbol{k})$ are the spin-triplet pairings. If there are additional orbital degrees or freedom, $\Delta_S(\boldsymbol{k})$ and $\Delta^\mu_T(\boldsymbol{k})$ are matrices. The fermion anticommutation forces $\Delta_S(\boldsymbol{k})$ to be a even function of $\boldsymbol{k}$, $\Delta_S(\boldsymbol{k}) = \Delta_S(-\boldsymbol{k})$, and $\vec{\Delta}_T(\boldsymbol{k})$ to be an odd function of $\boldsymbol{k}$, $\vec{\Delta}_T(\boldsymbol{k}) = -\vec{\Delta}_T(-\boldsymbol{k})$. The singlet and triplet components can be further classified according to the irreps of the point group, which allows to analyze the spatial symmetries broken by the order parameter. For example, with full rotational invariance, $\Delta_S(\boldsymbol{k})$ and $\Delta^\mu_T(\boldsymbol{k})$ can be decomposed in spherical harmonics. In this case, depending on their orbital angular momentum L, which is encoded in their $\boldsymbol{k}$ dependence and orbital structure, the pairings are called s-wave ($L = 0$), p-wave ($L = 1$), d-wave ($L = 2$), f-wave ($L = 3$), etc. Fermion anticommutation forces even orbital angular momenta to be spin-singlet, and odd orbital angular momenta to be spin-triplet.

In a crystalline lattice, rotational symmetries are reduced, and the pairings can only be classified according to the irreps of the point group. In other words, the pairing multiplets corresponding to an orbital angular momentum split into different components, which transform according to the irreps

of the point group, and no longer have degenerate critical temperatures. Nevertheless, the L-wave notation is still conventionally used, with the meaning that an L-wave irrep with full rotational symmetry would reduce to the corresponding irrep of the actual point group, and that the pairing has the same nodal structure as a function of $\boldsymbol{k}$ as an L-wave pairing with full rotational symmetry. As an example, we consider a 2D triangular lattice with point group D_{3h} (see the the character table in Appendix 2.A), which applies to monolayer 2H-$NbSe_2$ (see Sections 2.1.4 and 2.2). The s-wave spin-singlet pairing is always symmetric under all the operations of the point group. Certain components of other multiplets, such as the $d_{3z^2-x^2-y^2}$ spin-singlet pairing, are also invariant under all the symmetries, and are therefore called s-wave too since they are indistinguishable in terms of symmetry. The other four components of the d-wave spin-singlet pairing transform as the 2D irreps $\{d_{x^2-y^2}, -d_{xy}\}$ and $\{d_{xz}, d_{yz}\}$, but are still dubbed d-wave. To refer to one of the two irreps, the L-wave notation is not enough and one has to further specify. For instance, in our example, the two irreps differ by the parity under the out-of-plane mirror symmetry m_z. Alternatively, the $\{d_{x^2-y^2}, -d_{xy}\}$ pairings have 4 sign changes when going around the Brillouin zone in 2D, while $\{d_{xz}, d_{yz}\}$ only have 2. When spin-orbit coupling is nonzero, the spin-singlet and spin-triplet labels are no longer applicable, since the orbital and spin parts of the pairing become intertwined. The full pairing should be labelled as the irreps of the corresponding point group. Again, the spin-singlet and spin-triplet notation is still used, referring to the corresponding pairing that would be obtained for vanishing SOC. This is illustrated by the f-wave spin-triplet pairing in our example with point group D_{3h}. In particular, we focus on the $f_{x(x^2-3y^2)}$ component that has 6 sign changes and spatial dependence $\cos(3\theta)$ in the Brillouin zone, and transforms as a 1D irrep of D_{3h} with well-defined spin-triplet in the absence of SOC. With SOC, it splits into two irreps. The f-wave opposite-spin pairing, which has total spin $S_z = 0$ and is characterized by an out-of-plane vector $\vec{\Delta}_T^{S_z=0}(\boldsymbol{k}) = (0, 0, \Delta_T^z)$, is symmetric under all point group operations, and therefore can mix with the s-wave spin-singlet; this is a consequence of the absence of inversion symmetry that will be further explained in Sections 2.1.4 and 2.2. The f-wave equal-spin pairing components, with total spin $S_z = \pm 1$ and in-plane vector $\vec{\Delta}_T^{S_z=\pm 1}(\boldsymbol{k}) = (\Delta_T^x, \Delta_T^y, 0)$, transform as a different 2D irrep.

To conclude the discussion about the symmetry transformation properties of the superconducting pairing, we mention the case of time-reversal symmetry. Due to the gauge freedom in choosing its global phase, the superconducting order parameter cannot be directly assigned a parity under time-reversal symmetry (see more details in Section 3.1.1 of Chapter 3). Instead, only relative phases have physical meaning. Consequently, time-reversal symmetry can only be broken when the superconducting order parameter has several components that condense with a complex relative phase distinct from 0 or π. Usually, the components are associated with a multidimensional irrep, as in the long-sought $p + ip$ superconductor, but they can belong to different irreps that are almost degenerate accidentally, as in a $s + id$ state [228].

With the aid of symmetries, we can separate the pairing in different components. We now show, in the general case, how to self-consistently determine each component and their effect in the electronic dispersion. The BCS theory is the mean-field theory of the static Hamiltonian (2.10) when decoupled only in the Cooper or superconducting channel, i.e., neglecting the Hartree and Fock decouplings, which would give rise to electron-hole order parameters of the form $\sim \langle c^\dagger c \rangle$. With this in mind, the mean-field BCS Hamiltonian in terms of the superconducting order parameters Δ of Eqs. (2.12-2.13) reads:

$$\begin{aligned} H_{\text{BCS}}^{\text{MF}} = H_0 - \sum_{\boldsymbol{k}\boldsymbol{q}} \sum_{\alpha\beta} \left[\bar{\Delta}_{\alpha\beta}(\boldsymbol{k},\boldsymbol{q}) \hat{\Phi}_{\alpha\beta}(\boldsymbol{k},\boldsymbol{q}) + \hat{\Phi}^\dagger_{\alpha\beta}(\boldsymbol{k},\boldsymbol{q}) \Delta_{\alpha\beta}(\boldsymbol{k},\boldsymbol{q}) \right] - \\ - \sum_{\boldsymbol{k}\boldsymbol{k}'\boldsymbol{q}} \sum_{\alpha\beta\gamma\delta} \bar{\Delta}_{\alpha\beta}(\boldsymbol{k},\boldsymbol{q}) \left[V^{-1}(\boldsymbol{q}) \right]_{\alpha\beta,\delta\gamma} (\boldsymbol{k},\boldsymbol{k}') \Delta_{\delta\gamma}(\boldsymbol{k}',\boldsymbol{q}), \end{aligned} \tag{2.15}$$

where $V^{-1}(\boldsymbol{q})$ is the inverse of $V(\boldsymbol{q})$, defined as $\sum_{\mu\nu\boldsymbol{p}} V_{\alpha\beta,\mu\nu}(\boldsymbol{k},\boldsymbol{p},\boldsymbol{q}) \left[V^{-1}(\boldsymbol{q})\right]_{\mu\nu,\delta\gamma} (\boldsymbol{p},\boldsymbol{k}') = \delta_{\alpha\delta}\delta_{\beta\gamma}\delta_{\boldsymbol{k}\boldsymbol{k}'}$. From now on, we will focus on homogeneous superconductors, where $\boldsymbol{q} = 0$.

The order parameter Δ is obtained by self-consistently solving the mean-field BCS Hamiltonian $H_{\text{BCS}}^{\text{MF}}$. While $H_{\text{BCS}}^{\text{MF}}$ is quadratic, it is not number conserving. A useful approach to solve the problem is to transform it to a usual $\psi^\dagger\psi$ bilinear form by doubling the degrees of freedom in Nambu space. Nambu spinors are combinations of electron and hole operators

$$\psi^\dagger(\boldsymbol{k}) = \left[c^\dagger(\boldsymbol{k}), c(-\boldsymbol{k}) \right] = \left[c^\dagger_\uparrow(\boldsymbol{k}), c^\dagger_\downarrow(\boldsymbol{k}), c_\uparrow(-\boldsymbol{k}), c_\downarrow(-\boldsymbol{k}) \right], \tag{2.16}$$

where $c^\dagger(\boldsymbol{k})$ is a vector of creation operators running over the internal degrees of freedom, and in the second equality we have explicitly written down the spin degree of freedom. Nambu spinors fulfill the fermionic anticommutation relation $\{\psi_\alpha(\boldsymbol{k}), \psi^\dagger_\beta(\boldsymbol{k})\} = \delta_{\alpha\beta}\delta_{\boldsymbol{k}\boldsymbol{k}'}$, where now α, β label the internal degrees of freedom as well as the Nambu electron/hole degree of freedom. In Nambu space, the mean-field BCS Hamiltonian becomes

$$H_{\text{BCS}}^{\text{MF}} = \frac{1}{2} \sum_{\boldsymbol{k}} \psi^\dagger(\boldsymbol{k}) \cdot H_{\text{BdG}}(\boldsymbol{k}) \cdot \psi(\boldsymbol{k}) - \sum_{\boldsymbol{k}\boldsymbol{k}'} \bar{\Delta}(\boldsymbol{k}) \cdot V^{-1}(\boldsymbol{k},\boldsymbol{k}') \cdot \Delta(\boldsymbol{k}') + C, \tag{2.17}$$

where $C = \frac{1}{2}\sum_{\boldsymbol{k}} \text{tr}\left[h_0(\boldsymbol{k})\right]$ is a constant independent of the Nambu spinors and of the order parameter, and the Bogoliubov-de-Gennes Hamiltonian $H_{\text{BdG}}(\boldsymbol{k})$ is

$$H_{\text{BdG}}(\boldsymbol{k}) = \begin{pmatrix} h_0(\boldsymbol{k}) & -\Delta(\boldsymbol{k}) \\ -\bar{\Delta}(\boldsymbol{k}) & -h_0^T(-\boldsymbol{k}) \end{pmatrix}, \tag{2.18}$$

where now we regard the order parameter $\Delta(\boldsymbol{k})$ as a matrix in the spin-orbital space and, from Eqs. (2.12-2.13), $\bar{\Delta}_{\alpha\beta}(\boldsymbol{k}) = \Delta^*_{\beta\alpha}(\boldsymbol{k})$ is the Hermitian conjugate of $\Delta_{\alpha\beta}(\boldsymbol{k})$. We note that $h_0^T(-\boldsymbol{k}) =$

$h_0^*(-\boldsymbol{k})$ is the time-reversal conjugate of the noninteracting Hamiltonian (see Chapter 3). Assuming time-reversal invariance in the normal state, $h_0^T(-\boldsymbol{k}) = h_0(\boldsymbol{k})$.

H_{BdG} is a quadratic Hamiltonian which can be diagonalized, and therefore allows to self-consistently solve for $\Delta_{\alpha\beta}(\boldsymbol{k})$ defined in Eqs. (2.12-2.13). The self-consistent equation for $\Delta_{\alpha\beta}(\boldsymbol{k})$ is called gap equation. If a nontrivial self-consistent solution with $\Delta_{\alpha\beta}(\boldsymbol{k}) \neq 0$ is found, a gap is opened at all $\boldsymbol{k}$ in the Fermi surface where $\Delta_{\alpha\beta}(\boldsymbol{k}) \neq 0$. Pairings transforming according to different irreps of the point groups have separate gap equations and do not couple with each other. The pairing that condenses is the one that has a higher critical temperature T_c, which can be obtained from the gap equation in the limit $\Delta(\boldsymbol{k}, T \to T_c^-) \to 0$. In Section 2.2.2, we will determine the gap equations for the relevant pairings in monolayer $NbSe_2$ using the functional integral formalism [57], which is more convenient than diagonalizing H_{BdG} in multiband cases.

In the BCS theory, the particular value of T_c and of the zero-temperature order parameter Δ depend on nonuniversal parameters. Nevertheless, for a constant effective attraction $V = -\frac{g}{V_{\text{syst}}}$, with V_{syst} the volume of the system, they both display the same exponential dependence with the effective attraction, $\propto \exp(-\frac{1}{N_0 g})$, with N_0 the density of states (DOS) in the normal state, and their ratio is a universal prediction of BCS theory

$$\frac{2\Delta}{k_B T_c} \simeq 2\pi e^{-\gamma_E} \simeq 3.53, \tag{2.19}$$

with $\gamma_E \simeq 0.577$ the Euler-Mascheroni constant. Another defining property of the weak-coupling BCS theory is that the superfluid weight, which controls the phase coherence, is set at the same T_c as the one where the gap develops.

These predictions are verified by a variety of weak-coupling superconductors. However, as the interaction becomes stronger, the properties of superconductors depart from the BCS theory, even in the case of conventional phonon-mediated superconductors. One reason is that, in these cases, the frequency-dependence of the effective electron-electron attraction becomes crucial. The mean-field theory that properly considers these dynamical effects is called Migdal-Eliashberg theory [65, 66]. Generalizations of Migdal-Eliashberg theory apply to any type of boson mediating the interaction, as in the case of quantum critical fluctuations close to magnetic or nematic phase transitions. The main requirement of Migdal-Eliashberg theory is that the dynamics of the mediating boson is much slower than that of the electrons, which typically means that the characteristic energy scale of the boson Λ is much smaller than the Fermi energy, $\Lambda \ll E_F$ [229]. As for the BCS theory formulation above, this prevents its direct applicability to low-density systems. Another property of strong-coupling superconductors is that the temperatures where the superconducting gap and the superfluid weight onset are not generally the same. First, an incoherent Δ becomes nonzero, leading to a pseudogap phase, and the phase coherence is only reached at a lower T_c.

Before concluding this section, we mention that the pair-breaking effect of a magnetic field previously explained in the context of the Meissner effect can be divided in two contributions within the microscopic theory. In 3D, the strongest contribution which determines the critical magnetic field is called orbital effect, and is due to the minimal coupling to the electromagnetic gauge potential, as in Eq. (2.4). Intuitively, the orbital effect describes the tendency of the magnetic field to localize the electron motion in cyclotron orbits. The other pair-breaking contribution is the Zeeman spin splitting of the bands. The Zeeman field breaks time-reversal symmetry, and therefore the Kramers pairs $c_{k\uparrow}$ and $c_{-k\downarrow}$ are no longer degenerate. This introduces an energy cost for homogeneously pairing opposite spins, suppressing spin-singlet and $S_z = 0$ spin-triplet pairings. In 2D, due to the confined motion in the out-of-plane direction, the Zeeman effect is the main mechanism determining the in-plane critical magnetic field.

2.1.2 Collective modes in a superconductor

Collective modes are excitations related to the dynamical fluctuations of bosonic modes which are sufficiently long-lived. Depending on the nature of the bosonic mode, two types of collective modes can be distinguished. Particle-hole collective modes are related to fluctuations of the form $\sim \langle c^\dagger c \rangle$, such as phonons [76], spin resonances [230, 231] or nematic fluctuations [232]. In superconductors, collective modes also emerge in the particle-particle channel $\sim \langle c^\dagger c \rangle$, as we will describe below. In order to describe collective modes, one needs an action decoupled in the desired channels. It is worth pointing out that several collective modes are directly related to spontaneously broken-symmetry phases. For instance, within the broken-symmetry state, the fluctuations of the order parameter around the mean-field configuration define collective modes. Moreover, collective modes also arise if there is a tendency towards a subleading broken-symmetry phase. Examples of both cases are magnons in magnetically-ordered states and paramagnons in metals close to a magnetic instability. While collective modes are generically gapped, if a continuous global symmetry is broken, Goldstone theorem guarantees the presence of certain gapless collective modes, the so-called Goldstone modes [7]. In this section, we study collective modes appearing in superconductors. It is worth mentioning that, while particle-hole collective modes are not necessarily linked to superconductivity, their features might only appear in the superconducting state, where the gap opening reduces the Landau damping, i.e., their decay into quasiparticles. In the following we focus on the particle-particle channel. In Section 2.3, we will show that particle-particle collective modes might leave signatures in the tunneling spectrum of $NbSe_2$ [2].

In the simplest single-band s-wave spin-singlet scenario in 3D, superfluids and superconductors are characterized by a complex order parameter Δ, with an amplitude $|\Delta|$ and a phase φ. We assume a homogeneous mean-field configuration, where Δ is position independent. The long-wavelength spatial fluctuations of Δ in a neutral superfluid are described by the Ginzburg-Landau functional

of Eq. (2.2). A simple way to understand the emergence of collective modes is constructing an action from this free energy, by adding a dynamical term involving the time derivative of the order parameter

$$S[\Delta] = \int dt \int d^d\boldsymbol{r} \left[\hbar^2 \left(|\partial_t \Delta|^2 - \frac{1}{2m^*}|\boldsymbol{\nabla}\Delta|^2\right) - r|\Delta|^2 - \frac{1}{2}u|\Delta|^4\right]. \tag{2.20}$$

For simplicity, we have included only the second derivative in time, which renders the theory Lorentz invariant, but a first time derivative, related to damping, generically appears [233]. There are two collective modes associated with the dynamics of $\Delta = |\Delta|e^{i\varphi}$, resulting from the fluctuations of the amplitude $|\Delta|$ and the phase φ, respectively [234]. Their propagators can be obtained by expanding the action to quadratic order in the fluctuations around the mean-field solution, and their energy dispersion is given by the poles of their propagators. In this case, if $\Delta = (|\Delta| + a)e^{i(\varphi+\theta)}$, one expands in a and θ. The resulting collective modes occur in the particle-particle channel, since the superconducting order parameter is a particle-particle expectation value $\bar{\Delta} \sim \langle c^\dagger c^\dagger \rangle$.

The amplitude fluctuations a define the Higgs mode, which is gapped [234]. The Higgs mode is challenging to observe experimentally, since it does not directly couple to external probes. Moreover, in a single-band s-wave singlet BCS superconductor, the gap of the Higgs mode coincides exactly with the quasiparticle gap $2|\Delta|$, and therefore the Higgs mode can decay into quasiparticle pairs and is damped. This might be circumvented when a particle-hole collective mode couples to the Higgs mode. In this case, the resulting hybrid mode might have an energy smaller than $2|\Delta|$, and therefore it can be long-lived. This scenario has been proposed in bulk $NbSe_2$, where the Higgs mode couples to the CDW amplitude phonon mode [235–239].

On the other hand, the phase fluctuations θ give rise to a gapless Goldstone mode, associated with the broken continuous $U(1)$ symmetry [7, 234]. Phase fluctuations are soft in the long-wavelength limit, $\Omega \to 0$ as $\boldsymbol{q} \to 0$, since the action is invariant under a homogeneous shift of the phase. In a neutral superfluid, the Goldstone mode has linear dispersion, $\Omega \propto |\boldsymbol{q}|$.

In a superconductor, the charged Cooper pairs couple to the electromagnetic field. Then, gauge invariance requires adapting the action with the minimal coupling

$$\begin{aligned} S[\Delta, A] = \int dt \int d^d\boldsymbol{r} \Bigg[\hbar^2 \left(\left|\left(\partial_t + i\frac{e^*}{\hbar}A_0\right)\Delta\right|^2 - \frac{1}{2m^*}\left|\left(\boldsymbol{\nabla} - i\frac{e^*}{\hbar}\boldsymbol{A}\right)\Delta\right|^2\right) - \\ -r|\Delta|^2 - \frac{1}{2}u|\Delta|^4 - \frac{1}{2\mu_0}(\boldsymbol{\nabla}\times\boldsymbol{A})^2\Bigg], \end{aligned} \tag{2.21}$$

Now, while the Higgs mode can be determined analogously to that of a neutral superfluid, the phase mode is radically different. The $U(1)$ symmetry relevant in a superconductor is the local gauge

redundancy, which cannot be broken. Therefore, Goldstone theorem does not apply, and there is no protected gapless mode. Indeed, due to the coupling with the electromagnetic field, the phase mode, which is associated with the longitudinal fluctuations of the electromagnetic field, becomes gapped in 3D via the so-called Anderson-Higgs mechanism [77–79]. Indeed, due to its direct link to the plasmon, the mass of the phase mode becomes the plasma frequency. The transverse fluctuations of the electromagnetic field are also gapped, which gives rise to the Meissner effect, with the gap being related to the London penetration depth.

The above discussion only applies to 3D, where actual long-range order exist. As we mentioned before, only quasi-long-range order can develop in 2D in the thermodynamic limit, and no continuous symmetry can be explicitly broken. In 2D, the phase mode of both superfluids and superconductors is gapless, but its dispersion is renormalized, $\Omega \propto \sqrt{|\boldsymbol{q}|}$. Again, in superconductors, this reflects the connection between the phase mode and the plasmon, which also shows this dispersion in 2D metals.

Additional particle-particle collective modes can be defined when we consider further degrees of freedom. In a single-band system, they generally occur when a subleading superconducting instability in a channel with different symmetry from the ground state appears near in energy. The subleading superconducting pairings are self-consistent solutions of the gap equation with a lower T_c than the ground state, and correspond to extrema (relative minima or saddle points) of the free energy. The fluctuation from the ground state towards these channels, with a given relative phase, constitutes collective modes called Bardasis-Schrieffer modes [80]. Bardasis and Schrieffer studied such collective modes in the case of a s-wave spin-singlet ground state fluctuating towards higher angular momentum pairings, but they can be generalized to a nontrivial ground state [228, 240]. Usually, the fluctuation with $\pi/2$ relative phase with respect to the ground state, or imaginary fluctuation, is lower in energy, while that with 0 relative phase, or real fluctuation, does not usually show a pole [80, 233]. For a gapped superconducting ground state, as long as there is an attraction in a subleading channel, the energy of the Bardasis-Schrieffer mode is lower than the quasiparticle gap 2Δ, and therefore it is a well-defined collective mode. Importantly, the mass of Bardasis-Schrieffer modes is not renormalized by the Anderson-Higgs mechanism. Signatures of a Bardasis-Schrieffer mode have been proposed and observed in the Raman spectra of iron-based superconductors [83, 241–245], where the s-wave and d-wave pairings compete. Bardasis-Schrieffer modes can also leave fingerprints in other optical responses, such as the near-field terahertz response [233] and nonlinear optics [246]. An important point to note is that Bardasis-Schrieffer modes, and in general collective modes in the particle-particle channel, can couple and hybridize with particle-hole collective modes with the same symmetry. This has been proposed to occur in iron-based superconductors, where nematic fluctuations can couple to the Bardasis-Schrieffer mode associated with the fluctuation to the subleading d-wave pairing [247].

In multiband systems, besides the Bardasis-Schrieffer modes, another type of superconducting collective modes emerges, the so-called Leggett modes [81]. In this case, an order parameter $\Delta_n = |\Delta_n| e^{i\varphi_n}$ can be associated with each band, whose relative phase $\varphi_n - \varphi_{n'}$ is fixed by the interband coupling in the ground state. The Leggett modes are associated with the fluctuation of the relative phases, i.e., with the phases fluctuating out of phase, towards the π-shifted state. For instance, Leggett considered a 2-band system, with amplitude and phase fluctuations in both bands, $\Delta_1 = (|\Delta_1| + a_1) e^{i(\varphi_1 + \theta_1)}$ and $\Delta_2 = (|\Delta_2| + a_2) e^{i(\varphi_2 + \theta_2)}$. These fluctuations are generally coupled to each other, defining a 4×4 matrix, whose eigenmodes are the total amplitude $(a_1 + a_2)$ Higgs mode, the total phase $(\theta_1 + \theta_2)$ Goldstone mode, the relative phase $(\theta_1 - \theta_2)$ Leggett mode, and the relative amplitude $(a_1 - a_2)$ mode. Only one of the two latter modes displays an actual pole; the Leggett mode is well-defined as long as the intraband pairing interaction is larger than the interband one [248–251], so that the state with π shift in the relative phase is an extremum, which is the usual case [81]. If the interband pairing interaction vanishes, there is no preferred relative phase difference, and the Leggett mode is gapless. Increasing the interband pairing interactions gaps the Leggett mode, but its mass is smaller than 2Δ as long as the interband pairing interaction remains smaller than the intraband one, and therefore the Leggett mode is a well-defined, undamped collective mode. As the Bardasis-Schrieffer mode, the Leggett mode mass is not renormalized by Coulomb interactions [81, 250–252]. Indeed, the Leggett mode can be regarded as a Bardasis-Schrieffer-like mode involving the fluctuation from the ground state (e.g. s_{++}) to an excited state with the same symmetry but opposite relative superconducting phase (e.g. s_{+-}). In more complicated situations with several order parameters and spin-orbit coupling, a collective mode might fit into more than one of these categories [253].

A particular scenario for the emergence of a Leggett mode, relevant to the case of monolayer $NbSe_2$ analyzed in this Chapter, is when the two bands stem from the spin-orbit splitting of a band in a noncentrosymmetric system [252]. In systems with more than two bands, several Leggett modes can be defined [254–257]. Leggett modes leave fingerprints in Raman spectroscopy [258, 259], linear [260] and nonlinear optics [261, 262], ARPES [263], and Josephson junctions [264, 265]. The prototypical material where Leggett modes have been observed is the two-band superconductor MgB_2 [263, 266, 267], but they have also been proposed in iron-based superconductors [268, 269] and in Sr_2RuO_4 [270]. Additionally, analogous collective modes can be realized in other broken symmetry phases, such as magnetic systems [271] and structural transitions [272].

When a multicomponent order parameter condenses in the ground state, as in time-reversal symmetry breaking superconductors, more particle-particle collective modes emerge. They are generically called clapping modes [273, 274], and they are generalizations of the Bardasis-Schrieffer and Leggett modes involving relative phase or amplitude fluctuations. A particular

example are the spin-wave-like modes in time-reversal breaking spin-triplet (e.g. $p+ip$) superconductors [275].

For completeness, we enumerate other collective modes that can appear in superconductors. Carlson-Goldman modes [276] are charge-neutral gapless collective modes that arise in the presence of normal quasiparticles (e.g. close to T_c), and consist of the out-of-phase oscillation of the superfluid and normal densities. Although not a collective mode, we also mention Mcmillan-Rowell oscillations, which are oscillations in the tunneling spectrum when tunneling to a thin metallic film on a superconductor [277], or to a superconducting film on a metal [278, 279], arising from the interference of Andreev-reflected quasiparticles within the film.

2.1.3 2H transition metal dichalcogenides

In Chapter 2, we have analyzed 1T-$TiSe_2$, a transition metal dichalcogenide (TMD) with the octahedral 1T polytype. In this Chapter, we will focus on 2H-$NbSe_2$, a different TMD with the trigonal prismatic $2H_a$ polytype (see Fig. 1). The bulk unit cell of 2H TMDs consists of two unit layers, with each monolayer displaying the chalcogens one on top of the other, unlike in the 1T structure. While the monolayer, usually denoted 1H, is noncentrosymmetric, the 3D bulk stackings $2H_a$ and $2H_c$ restore an interlayer inversion symmetry (see Fig. 1.1). Commonly used transition metals are Nb and Ta in group V, whose band structure is metallic with a half-filled band coming from the metal d orbitals, as well as Mo and W in group VI, which are insulators with this d band completely filled. The insulating group VI 2H-TMDs, such as WSe_2, $MoSe_2$ and $MoTe_2$, have been widely studied due to their optical properties. Moreover, electron or hole doping has been proposed to drive interesting correlated phases in these materials, such as magnetic states [280] or topological superconductivity [281]. The metallic group V 2H-TMDs, such as $NbSe_2$, $TaSe_2$, NbS_2 and TaS_2, usually display a 3×3 CDW instability in their bulk or monolayer form. However, the CDW does not completely gap the Fermi surface, and most of them become superconducting at lower temperatures. In the following, we will focus on $NbSe_2$, although we will also comment a few features of the related compounds $TaSe_2$, NbS_2 and TaS_2, which share an almost analogous band structure.

2.1.4 2H-$NbSe_2$: state of the art

In this section, we will describe the electronic structure and instabilities of $NbSe_2$. We will mainly focus on monolayer 1H-$NbSe_2$, since, besides having simpler electronic structure and symmetries, our contribution applies to the monolayer. Nevertheless, we will also mention the differences with bulk 2H-$NbSe_2$, which has been widely studied.

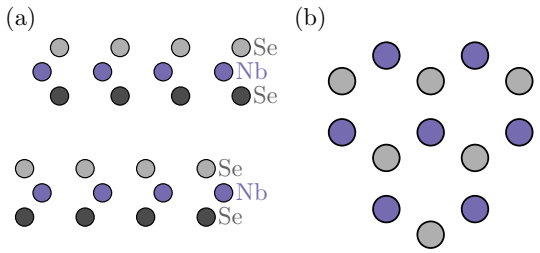

FIGURE 1: (a) Side and (b) top views of the lattice of $2H_a$-$NbSe_2$. Only the top view of the top layer is shown in (b) for visualization purposes.

Normal state

Monolayer 1H-$NbSe_2$ crystallizes in the symmorphic space group $P\bar{6}m2$ (#187), with point group D_{3h}, whose generators are the out-of-plane threefold symmetry C_{3z}, the in-plane mirror symmetry m_x, and the out-of-plane mirror symmetry m_z [282] (see Appendix 2.A for the character table). Crucially, it is non-centrosymmetric, which provides 1H-$NbSe_2$ with several interesting properties. Its electronic band structure shows a half-filled band crossing the Fermi level, with large hole pockets around Γ and around $K_\pm := \pm K = \frac{4\pi}{3a}(\pm 1, 0)$ (see Figs. 2(a,b)). This band mainly derives from the Nb d orbitals. In particular, at Γ the band has d_{z^2} character and symmetry Γ_1 (A_1' of the little group), while the orbital character is $d_\pm = d_{x^2-y^2} \mp i d_{xy}$ at the $K_\pm$ points, and therefore have symmetry K_3 (${}^{+1}E'$) and K_5 (${}^{-1}E'$), respectively. At the Fermi level, where the hole pockets lie away from the Γ and $K_\pm$ points, the orbitals slightly mix, but the dominant character remains the same. There is a gap to the other d-derived bands, which lie at higher energies. Incidentally, the inversion of orbital character between the Γ and K points implies that the band crossing the Fermi level is obstructed, with the Wannier functions centered at the triangular lattice not occupied by neither Nb or Se (see Chapter 3) [283].

Due to the absence of inversion symmetry, SOC breaks the spin-degeneracy of the bands. The stronger SOC is local, which only couples the $d_\pm$ states inducing a rigid energy shift, but leaves the d_{z^2} unaffected. Consequently, the SOC splitting is stronger in the K pockets, and almost negligible in the Γ pocket, where moreover vanishes in the ΓM direction due to symmetry. In the absence of a substrate, the out-of-plane mirror symmetry m_z imposes that S_z is a good quantum number, which gives rise to the so-called Ising SOC. Each state can therefore be labelled with the actual spin up or down (see Fig. 2(b)). Moreover, time-reversal symmetry induces a spin-valley coupling: the top band at valley K_+ has spin down ($d_{+\downarrow}$), while the top band at valley K_- has spin up ($d_{-\uparrow}$). This special type of SOC grants interesting properties to the superconducting state, as we will describe below. Finally, we note that the substrate-induced Rashba SOC breaks the m_z mirror symmetry, reducing the point group to C_{3v}, and breaking the conservation of the spin S_z.

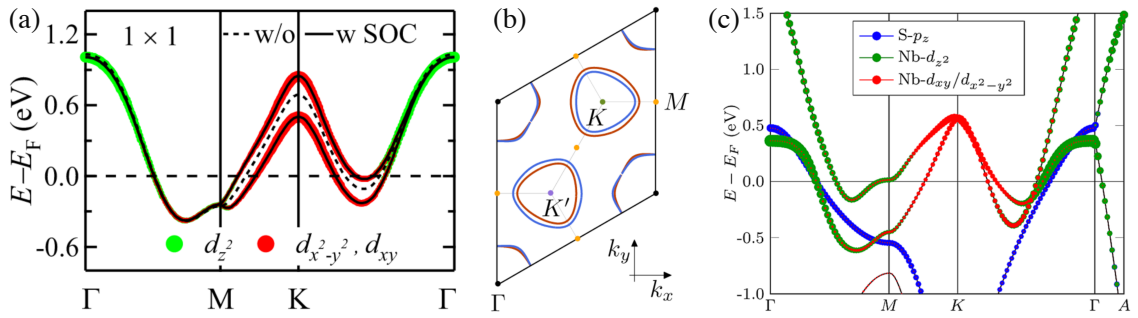

FIGURE 2: Electronic band structure of the normal state of $NbSe_2$ (or related compounds). (a) Bands of monolayer TaS_2 with and without Ising SOC. The color and line width indicate the main orbital composition at each $\boldsymbol{k}$. Extracted from Ref. [284]. (b) Fermi surface of monolayer $NbSe_2$ with Ising SOC. The color indicates spin up (blue) and spin down (red). Extracted from Ref. [285]. (c) Bands of bulk NbS_2 without SOC. The color and line width indicate the main orbital composition at each $\boldsymbol{k}$. Note the additional 3D band around Γ coming from the Se p_z orbital. Extracted from Ref. [286].

It is worth highlighting the differences with bulk 2H-$NbSe_2$, whose unit cell is doubled in the z direction and is now composed of two layers, with an additional interlayer inversion symmetry (space group $P6_3/mmc$, #194, point group D_{6h}) [282]. Due to the inversion symmetry, the bands are spin-degenerate in the bulk. However, the bands are doubled due to the layer degree of freedom. The qualitative shape of the bands remains the same, with quasi-2D $d_\pm$ and d_{z^2} hole pockets around the $K_\pm$ and Γ points, respectively (see Fig. 2(c)). The main difference is the appearance of a new 3D band around the Γ point with Se p_z character.

Charge density wave state

Irrespective of the number of layers, $NbSe_2$ undergoes a transition to a quasi-commensurate 3×3 CDW state, driven by the strong anisotropic electron-phonon coupling [12, 31, 287–291]. In the CDW, a longitudinal phonon with symmetry Σ_1 (A_1') condenses at momentum $\boldsymbol{Q} = \frac{2}{3}\Gamma M$, mainly involving the in-plane displacement of Nb atoms. The transition temperature $T_{\mathrm{CDW}} \simeq 33$K is similar in both bulk and monolayer samples [12, 287, 288, 290], although in the monolayer it can depend on substrate and synthesis conditions [289, 290, 292]. Nevertheless, a significant difference between the CDW in bulk and monolayer $NbSe_2$ is the energy of the CDW amplitude phonon mode, which is quite higher in the monolayer, as displayed in its Raman spectrum [289, 293].

While the quasi-commensurate 3×3 periodicity has been established, the exact atomic arrangement has not been fully settled. There are several almost-degenerate structural distortions due to a phase degree of freedom related to the center of the modulation [294]. Indeed, distinct structures have been experimentally observed to coexist in STM experiments [294, 295] (see Fig 3(a)),

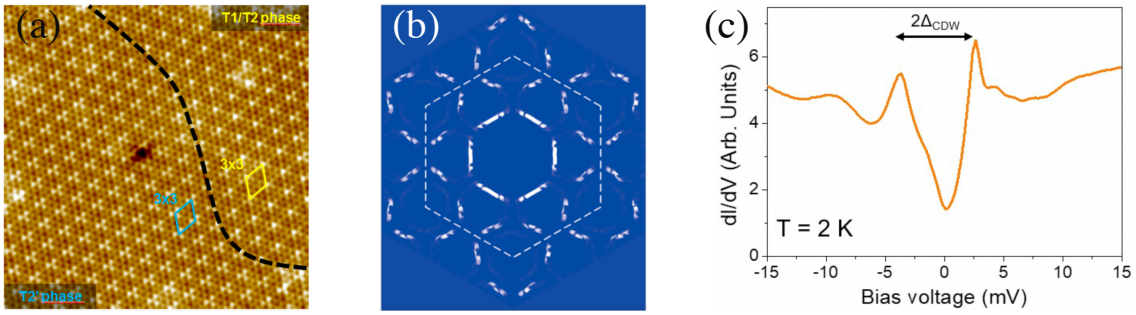

FIGURE 3: Charge density wave of $NbSe_2$. (a) Real space STM map of bulk $NbSe_2$ showing two domains with different atomic arrangements within the 3×3 CDW. Extracted from Ref. [294]. (b) Reconstructed Fermi surface of one CDW state of monolayer $NbSe_2$ without SOC. Extracted from Ref. [297]. (c) STM spectrum of monolayer $NbSe_2$ showing the V-shaped feature of the CDW. Extracted from Ref. [2].

which naturally arise from the incommensurate nature of the CDW [32]. Moreover, a different distortion was proposed based on X-ray diffraction of the bulk material [296].

The effect of the CDW on the electronic bands is qualitatively the same for all distortions: it opens partial gaps at the Fermi surface, especially at the K pockets, where there are hot spots of the electron-phonon coupling connected by the CDW wavevectors [31, 297] (see Fig 3(b)). While this reduces the DOS at the Fermi level, the system remains metallic. The DOS becomes V-shaped, with coherence peaks at $\sim \pm 4$meV, arising from the partial gaps [290] (see Fig 3(c)).

It is also instructive to discuss the effect of the CDW on the spin fluctuations, which are predicted to be strong in monolayer $NbSe_2$ [33, 297–299]. Indeed, in the absence of CDW, DFT calculations predict that the spin fluctuations would drive the system to an antiferromagnetic state [297], with a competing ferromagnetic phase near in energy too [300, 301]. However, by reducing the DOS, the CDW suppresses the spin fluctuations, and the CDW state remains nonmagnetic [297, 301]. Nevertheless, accurately determining the spin fluctuations in the presence of the CDW remains an open problem.

Superconducting state

Further lowering the temperature drives both bulk and monolayer $NbSe_2$ to a superconducting state [29], coexisting with the CDW. The superconductivity is usually accepted to occur in a conventional s-wave channel, which fully gaps the Fermi surface. The general belief is that superconductivity is driven by the same phonons responsible for the CDW transition [31–33, 286] (see however [30]). The coexistence between CDW and superconductivity is allowed since the CDW only partially gaps the Fermi surface. Nonetheless, both ordered states compete, and

superconductivity is enhanced when the CDW is suppressed due to the increased DOS and electron-phonon coupling [31]. Experimental signatures of this competition appear when suppressing the CDW with pressure [302, 303] or disorder [304, 305].

Unlike the CDW, the superconducting critical temperature significantly decreases from the bulk ($T_{\mathrm{CDW}}^{3D} \simeq 7$K) to the monolayer ($T_{\mathrm{CDW}}^{2D} \simeq 2$K) [290]. One of the factors contributing to this suppression might be the lower DOS in the CDW state of monolayer $NbSe_2$. Surface effects, weaker screening and enhanced spin fluctuations might also play a role [33, 298]. Indeed, since Coulomb interactions are stronger in the monolayer, the superconducting pairing induced by repulsive interactions in the absence of electron-phonon coupling has been studied, obtaining an extended s_{+-}-wave spin-singlet state with the gap changing sign between the Γ and K pockets [306], or an $S_z = 0$ f-wave spin-triplet state, with gap changing sign from K_+ to K_- [285, 306].

The single- or multi-gap nature of $NbSe_2$ has been a source of discussion. While tunneling spectra of the monolayer are consistent with a single gap [307], bulk samples show signatures of two-gap superconductivity [308]. On the other hand, *ab initio* Migdal-Eliashberg calculations show a quite anisotropic s-wave gap, whose distribution exhibits the maximum gaps at hot spots in the K pockets [31, 33]. It is therefore generally believed that the two-gap superconductivity in the bulk comes from a large gap arising from these hot spots in the K pockets and a smaller gap mainly coming from the Γ bands. Although it remains not completely settled, several arguments have been proposed to explain why only one gap is observed in single- and few-layer samples. One proposal is that the stronger CDW in the monolayer gaps the hot spots which would have the larger superconducting gap [31]. On the other hand, the fact that the bulk has the additional Se p_z band at Γ points to the importance of tunneling selectivity [33]. Indeed, tunneling is naturally more sensitive to the Se p_z orbitals, and, besides the 3D Se p_z band at Γ in the bulk, the weight of the Se p_z orbitals also peaks at certain hot spots of the K pockets. It is tempting then to associate the two gaps in the bulk to the Γ Se p_z pocket and to the K pockets, and the single gap in the monolayer to the K pockets. Nevertheless, to explain the shape of the tunneling spectrum of the whole band in the monolayer, a higher sensitivity to the Γ Nb pocket compared to the K pockets is required [309]. We also mention that the CDW backfolds the K points to Γ, and thus their tunneling sensitivity could be comparable at low energies [308].

Even if the ground state has a conventional s-wave pairing, the superconductivity in monolayer $NbSe_2$ displays unusual features. First of all, due to the band splitting induced by Ising SOC in the noncentrosymmetric structure, only opposite-spin Cooper pairs can form as weak-coupling instabilities with zero total momentum. This feature is called Ising superconductivity. Of these pairings, two are momentum independent, and correspond to the fully-gapped s-wave spin-singlet state, and the out-of-plane f-wave spin-triplet state with $S_z = 0$, which is gapped at the $K_\pm$ pockets but has six nodes at the Γ pocket. We will explicitly define them in Section 2.2.1. In conventional

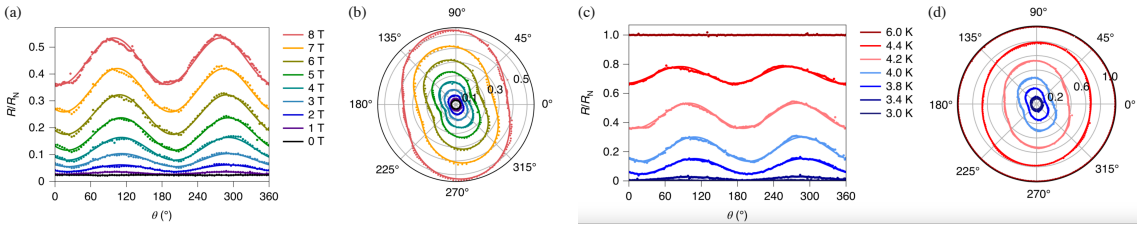

FIGURE 4: Magnetoresistance of few-layer $NbSe_2$ in the superconducting transition. Extracted from Ref. [115]. (a) Magnetoresistance, in units of the normal state resistance, as a function of the azimuthal angle of the in-plane magnetic field at $T \simeq 4.2$K, for different magnitudes of the field. (b) Polar plot of (a). (c) Magnetoresistance as a function of the azimuthal angle of the in-plane magnetic field at $H \simeq 8$T, for different temperatures. (d) Polar plot of (c).

centrosymmetric 2D superconductors, the critical in-plane field is determined by the competition between the pairing and the Zeeman field, which tends to align spins parallel to it and therefore suppresses the s-wave spin-singlet state, giving rise to the Pauli paramagnetic limit. On the other hand, the strong out-of-plane locking of the spins by the Ising SOC protects the superconductivity against in-plane magnetic fields, endowing monolayer $NbSe_2$ with a high in-plane critical field way beyond the Pauli limit [310–313]. We note that few-layer samples also show an enhanced critical field due to the same mechanism, which still applies there thanks to the fact that interlayer coupling is small and the pairing is mainly intralayer. Incidentally, for a s-wave or $S_z = 0$ f-wave state, a high in-plane magnetic above the Pauli limit but below the critical field can drive a topological superconductor with nodes at the momenta in the Γ pocket where the Ising SOC vanishes [306, 314].

Another unusual property, generic to noncentrosymmetric superconductors with SOC [315, 316], is that the labels spin-singlet and spin-triplet are no longer good quantum numbers. In other words, spin-singlet and spin-triplet pairings are symmetry-allowed to mix in the ground state. In monolayer $NbSe_2$, this mixing occurs between the s-wave spin-singlet and the $S_z = 0$ f-wave spin-triplet pairings [317]. In the absence of SOC, the orbital part of the s-wave singlet transforms according to the A_1' irrep of D_{3h}, while the one of the f-wave triplet is actually an A_2', whose angular dependence is like $\cos(3\theta)$. Spin bilinears transform as $S_z \to A_2'$ and $\{S_x, S_y\} \to E''$ in D_{3h}. Therefore, with Ising SOC, while the s-wave singlet Δ_S still transforms as A_1', the f-wave triplet splits, with the out-of-plane, opposite spin $S_z = 0$ triplet Δ_T^z transforming as A_1', and the in-plane, equal-spin $S_z = \pm 1$ triplets $\mathbf{\Delta}_T^{xy}$ transforming as E''. The symmetry-allowed mixing is reflected in the fact that Δ_S and Δ_T^z belong to the same A_1' irrep. In monolayer $NbSe_2$, however, the mixing is thought to be small, with a dominant Δ_S and about 10% Δ_T^z contribution.

Unconventional features in the superconducting state of single- and few-layer $NbSe_2$

More recently, despite its assumed conventional pairing, Refs. [115, 116] have found that the superconducting state of monolayer and few-layer $NbSe_2$ exhibits twofold-symmetric magnetotransport, breaking the underlying threefold symmetry of the lattice (see Fig. 4). In particular, the in-plane critical magnetic field and the trace of the magnetoconductivity in the superconducting transition region are twofold anisotropic [115, 116]. Importantly, the twofold anisotropy disappears in the normal state, where the magnetotransport recovers the expected threefold symmetry. The twofold-anisotropic magnetotransport requires the coupling of the superconducting order parameter to a tensorial quantity [318], for which several microscopic mechanisms have been proposed. A possible explanation relies on the presence of a component of a nematic superconducting pairing, which spontaneously breaks the rotational symmetry of the lattice, similar to the nematic CDW discussed in Chapter 1. Candidates for the nematic pairings include a d-wave spin-singlet pairing (E' irrep of D_{3h}; see Appendix 2.A), which would couple to strain [115], or the in-plane, equal-spin $S_z = \pm 1$ f-wave spin-triplet pairing (E''), which couples to the magnetic field [116]. Even if the ground state is the conventional s-wave spin-singlet, these nematic pairings can be induced by strain or the in-plane magnetic field as long as they are subleading instabilities [115, 319, 320]. We note that, in the presence of substrate-induced Rashba SOC, the d-wave spin-singlet and in-plane f-wave spin-triplet nematic pairings have the same symmetry. The scenario involving a subleading in-plane f-wave spin-triplet nematic pairing is further supported by the tunneling spectroscopy experiments of Ref. [313]. In particular, to fit the temperature-dependent in-plane critical magnetic field, Ref. [313] needs to consider an in-plane f-wave component induced by the field [319, 320]. Ref. [321] has proposed an alternative scenario, also based on $NbSe_2$/ferromagnet tunnel junction experiments [322], where the nematic magnetoresistance originates from the magnetic exchange of intrinsic defects in $NbSe_2$.

Another unconventional feature of monolayer $NbSe_2$ reveals in the local tunneling spectroscopy experiments performed by our collaborators [2]. In the superconducting state, the STM spectra display resonances beyond the superconducting coherence peak (see Fig 5(a)). These resonances, observed as dip-hump satellite features usually symmetrically with respect to the Fermi level, have been confirmed for several samples, tips, sample locations and substrates, and they only appear in the monolayer, but not in the bulk. In particular, three resonances are observed, whose energies nearly coincide with a resonance and their higher harmonics. Indeed, measured from the coherence peaks, their average energies are $\Omega_n \simeq n0.53\text{meV}$ (see Fig 5(b)). Substrate effects are discarded, since the same phenomenology appears both in a metallic substrate (bilayer graphene on SiC(0001)) and an insulating one (hBN on Ir(111)), with the average superconducting gap $\Delta \simeq 0.4\text{meV}$ being the same in both substrates. Tip artifacts can also be ruled out, since several tips are used and calibrated in known materials. Band structure effects can also be discarded, since

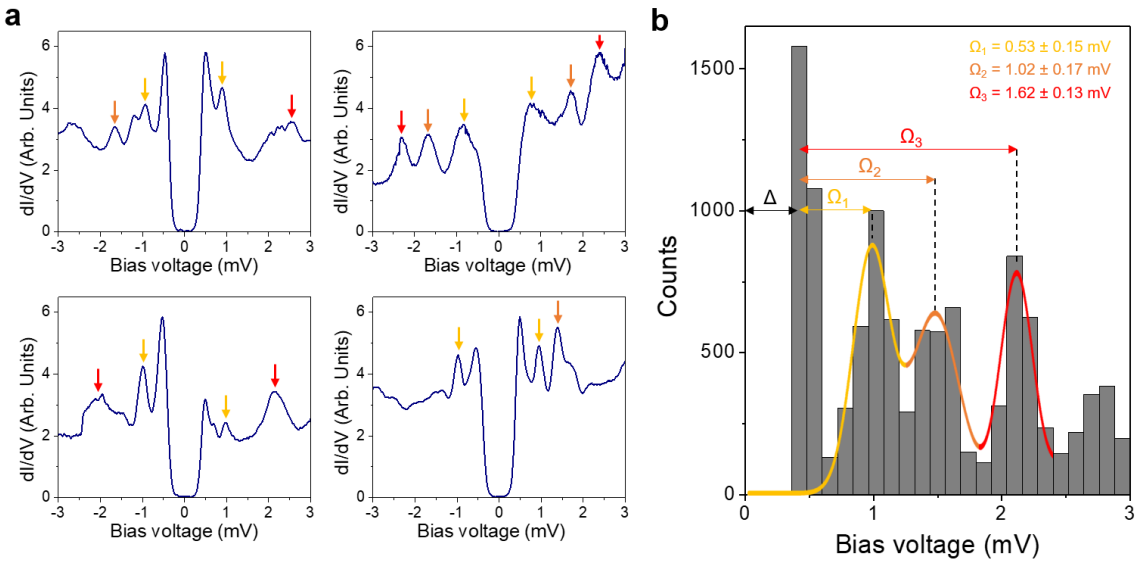

FIGURE 5: STM spectra and statistics of resonances on a graphene substrate. Extracted from Ref. [2]. (a) Four representative dI/dV curves acquired in monolayer $NbSe_2$ at $T = 0.34$K. The arrows identify the fundamental Ω_1 mode (yellow) and the harmonics Ω_2 (orange) and Ω_3 (red). (b) Histogram of the resonance energies from 2855 dI/dV curves acquired on different locations, and using different samples and tips. Three clear peaks can be identified for energies larger than the superconducting gap (Δ). A Gaussian fit to the peaks yield the following values: $\Omega_1 = 0.53$meV, $\Omega_2 = 1.02$meV and $\Omega_3 = 1.62$meV.

there are no features at these energies. We therefore interpret the resonances as signatures of a collective bosonic mode and its harmonics. We highlight that the first resonance lies below the quasiparticle edge, $\Omega_1 < 2\Delta$, indicating that it is undamped, since it cannot decay into fermionic quasiparticles. However, the energies of the higher harmonics are greater than 2Δ. A microscopic calculation would be required to determine whether higher harmonics are overdamped, which might depend on the boson-boson interactions.

The resonances are intrinsically related to superconductivity. Indeed, when increasing the temperature, they fade out at ~ 1.4K, below the critical temperature $T_c \simeq 2$K (see Fig. 6(a)). As shown in Fig. 6(b), the amplitude of the peaks decays faster than thermal broadening, and therefore their decay is correlated to the weakening of superconductivity. Their disappearance with temperature also discards band structure and extrinsic effects. Furthermore, the resonances also gradually smear out with increasing out-of-plane magnetic field, and disappear within the vortex state (see Fig. 6(c)). Fig. 6(d) shows that the normalized energy of the resonances $\frac{\Omega_n}{2\Delta}$ increases nonlinearly with magnetic field. When represented versus Δ, $\frac{\Omega_n}{2\Delta}$ anticorrelates with Δ, with an approximately linear dependence. Note that the resonances disappear soon after the energy of the first resonance Ω_1 surpasses the quasiparticle edge 2Δ. The energy of the higher resonances, however, always remains above 2Δ.

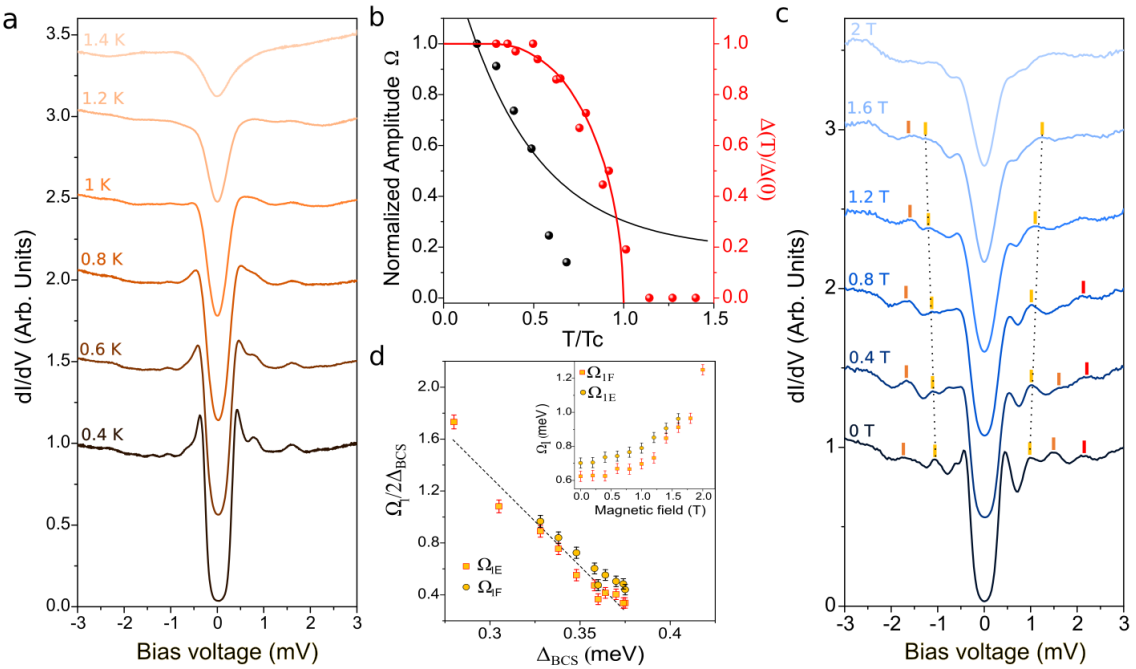

FIGURE 6: Temperature and magnetic field dependence of the dip-hump features on a graphene substrate. Extracted from Ref. [2]. (a) Evolution of the resonances with temperature from 0.4K up to 1.4K. (b) Normalized amplitude of the Ω_2 mode for empty states in (a) as a function of the temperature T (black dots). This amplitude decays faster than thermal broadening (black curve). The superconducting gap Δ (red circles) and its BCS fit (red line) are also shown. (c) Evolution of the resonances with perpendicular magnetic field $B_\perp$ up to 2T. The energies of the resonances are marked, as well as dashed lines connecting the energies of the fundamental mode Ω_1. (d) Ratio $\frac{\Omega_1}{2\Delta}$ versus Δ extracted from the $B_\perp$-evolution in (c), for both filled (Ω_{1F}, circles) and empty (Ω_{1E}, squares) states. A linear fit is shown as a dashed line. The inset represents the nonlinear energy dependence of the fundamental mode Ω_1 with the magnetic field.

The anticorrelation between $\frac{\Omega_n}{2\Delta}$ and Δ does not only occur when they change under a magnetic field, but also for their local values taken at different positions of a sample. Indeed, Fig. 7 shows such an anticorrelation, with the three modes Ω_n displaying similar slope. Crucially, the energy Ω_1 of the fundamental mode is smaller than the quasiparticle edge 2Δ, indicating that this bosonic mode cannot decay into Bogoliubov quasiparticles and is thus undamped.

In summary, the STM experiment of Ref. [2] on monolayer $NbSe_2$ displays three satellite peaks at energies $\Delta + n\Omega_1$, with $\Omega_1 < 2\Delta$. These resonances gradually disappear with temperature and out-of-plane magnetic field before the superconductivity dies. The energies $\frac{\Omega_1}{2\Delta}$ are anticorrelated with the gap Δ. We can discard tip and band structure effects at these small energy scales. We will interpret them as a collective bosonic mode Ω_1 and its harmonics, which couple to the fermionic quasiparticles and renormalize their tunneling spectrum. The purpose of this chapter is to decide what is the most likely collective mode. Three classes of candidates might be considered:

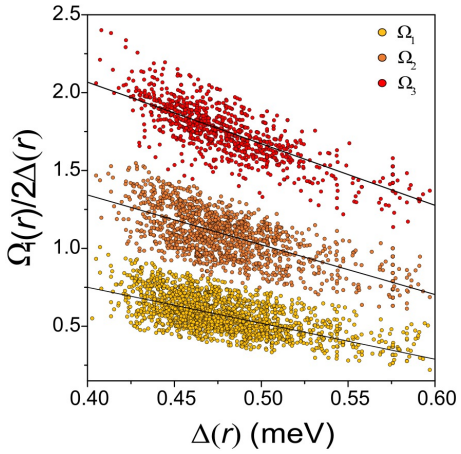

FIGURE 7: Anticorrelation of the local $\frac{\Omega_n(\boldsymbol{r})}{2\Delta(\boldsymbol{r})}$ as a function of $\Delta(\boldsymbol{r})$. Results from 1974 dI/dV curves measured at $T = 0.34$K in several samples and with several tips on a graphene substrate are provided. Black lines are linear fits for each mode. Extracted from Ref. [2].

phonons, particle-hole modes such as spin fluctuations, and superconducting collective modes. First, according to Raman experiments [289, 293] and to DFT calculations [31, 32, 323], there are no relevant phonon features below $\sim$ 3meV, neither in the normal or in the CDW state. In particular, the energy of the CDW amplitude mode is noticeably raised from the bulk to the monolayer (8.6meV). Secondly, enhanced spin fluctuations have been predicted in monolayer $NbSe_2$ due to the weaker screening. Indeed, in the absence of the CDW, the system is close to an instability towards an antiferromagnetic state [33, 297–299], with a competing ferromagnetic state near in energy too [300, 301]. Spin fluctuations can indeed give rise to resonances in the spectral function [324], and they would also disappear with temperature and magnetic field within the superconducting state. However, spin fluctuations are suppressed by the CDW, and the magnetic instabilities are killed [297]. Nevertheless, properly studying the spin fluctuations in the CDW remains an open problem. Finally, superconducting collective modes in the particle-particle channel could also describe the phenomenology. The Goldstone mode, which is gapless in 2D, and the Higgs mode, which lies at 2Δ and cannot couple to the CDW phonon mode in the monolayer due to its higher energy, can be discarded. On the other hand, the twofold nematic magnetotransport in the superconducting state suggests the possibility of a competition between pairing channels, which naturally gives rise to Bardasis-Schrieffer-like or Leggett-like modes. In the rest of the Chapter, we present a simple microscopic model of monolayer $NbSe_2$, where such a competition appears naturally. We compute the energy of the Bardasis-Schrieffer/Leggett mode, and demonstrate that it gives rise to features in the spectral function. Finally, we compare these predictions to the STM experiment.

2.2 Microscopic k.p model

In this section, we will introduce a minimal model for monolayer $NbSe_2$, and discuss the different interactions and pairing channels. We will also determine its superconducting ground state, on top of which we will study the collective fluctuations in the next section.

2.2.1 Definition of the model

A $\boldsymbol{k}\cdot\boldsymbol{p}$ model considering the three hole pockets at Γ, K_+, and K_- of monolayer $NbSe_2$ was introduced by Ref. [306]. Here we consider instead a minimal model with two bands, representing the hole pockets at $K_\pm$. To justify why we neglect the Γ pocket, we need to analyze the possible pairing channels of this multiband superconductor, which have been discussed by Refs. [300, 306]. It is instructive to start the discussion without SOC, and for simplicity to restrict to momentum-independent pairing within each band. In this case, the Γ pocket can only have spin-singlet pairing with s-wave orbital symmetry, which transforms as the A_1' irrep of the point group D_{3h}. However, the $K_\pm$ valleys might support two different pairings: either spin-singlet pairing with s-wave symmetry (A_1'), which has the same gap in the two valleys (see Fig. 8(a)), or spin-triplet pairing with f-wave orbital symmetry (A_2'), which has gap of opposite sign in the two valleys (see Fig. 8(b)). When Ising SOC is included, pairing channels cannot be classified independently by orbital and spin symmetry. Indeed, the spin $c^\dagger c$ bilinears transform according to the point group irreps as $c^\dagger\sigma_0 c \to A_1'$, $c^\dagger\sigma_z c \to A_2'$, and $\{c^\dagger\sigma_x c, c^\dagger\sigma_y c\} \to E''$, where σ_μ are the Pauli matrices acting on the spin degree of freedom. Then, the spin cc bilinears transform as $c\sigma_0 i\sigma_y c \to A_1'$, $c\sigma_z i\sigma_y c \to A_2'$, and $\{c\sigma_x i\sigma_y c, c\sigma_y i\sigma_y c\} \to E''$. Multiplying the orbital and spin symmetry transformation properties, we obtain that the f-wave spin-triplet splits into the opposite-spin pairing, with spin $S_z = 0$ and spin vector $\vec{\Delta}_T^{S_z=0}(\boldsymbol{k}) = (0,0,\Delta_T^z)$ pointing in the out-of-plane direction, which transforms as an A_1' irrep, and the equal-spin pairing, with spin $S_z = \pm 1$ and in-plane $\vec{\Delta}_T^{S_z=\pm1}(\boldsymbol{k}) = (\Delta_T^x, \Delta_T^y, 0)$ vector, corresponding to an E'' irrep. As mentioned in section 2.1.4, the out-of-plane triplet has the same symmetry as the standard s-wave singlet and can therefore mix with it in the ground state. Indeed, Figs. 8(c,d) show that the out-of-plane triplet can be regarded as an extended s-wave pairing with opposite sign in the spin-split bands. According to the Migdal-Eliashberg calculations of phonon-mediated superconductivity [30–33], the ground state is mainly composed by the standard s-wave spin-singlet. Moreover, based on the enhanced electronic correlations and spin fluctuations, and on the nematic magnetotransport experiments, we assume the f-wave triplet to be a close subleading competitor. In this picture, the superconducting pairing in the Γ pocket is a spectator, since it just assumes a s-wave symmetric gap, with the same sign as the $K_\pm$ pockets due to the interband coupling. This justifies our model neglecting the Γ pocket to simplify the discussion.

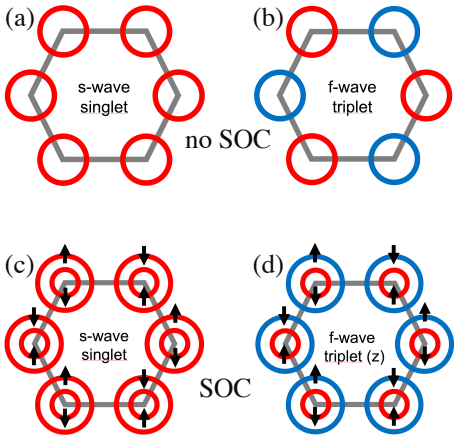

FIGURE 8: Sketch of the s-wave spin-singlet and f-wave spin-triplet pairings in the K pockets. Colors indicate the sign of the gap: red is positive and blue is negative. (a) Singlet (A_1') and (b) triplet (A_2') in the absence of SOC. (c) Singlet (A_1') and (d) out-of-plane triplet (A_1') with SOC. In (c,d), we define the gap as the pertinent expectation value in the order spin-up spin-down, $\langle d_\uparrow d_\downarrow \rangle$. For the outer pocket, this corresponds to $\Delta = \langle d_{K_+\uparrow} d_{K_-\downarrow} \rangle$ at both $K_\pm$ valleys. Instead, for the inner pocket, this corresponds to $\Delta = \langle d_{K_-\uparrow} d_{K_+\downarrow} \rangle$ at both $K_\pm$ valleys. The choice of the absolute phase is arbitrary.

With this in mind, we now construct our minimal model for the $K_\pm$ valleys. We define the fermionic operators in the band basis as $\psi = (d_{K_+\uparrow}, d_{K_+\downarrow}, d_{K_-\uparrow}, d_{K_-\downarrow})$ for the two valleys and spins. To a first approximation, the operators $d_{K_\pm\sigma}$ in the band basis can be thought of combinations of the orbitals $\{d_{x^2-y^2}, d_{xy}\}$. Indeed, if the Fermi surface lied exactly at the $K_\pm$ points, $d_{K_\pm\sigma} = d_{\pm\sigma} = d_{x^2-y^2} \mp i d_{xy}$. We consider a non-interacting Hamiltonian $H_0 = \sum_{\boldsymbol{k}} \psi^\dagger(\boldsymbol{k}) H_0(\boldsymbol{k}) \psi(\boldsymbol{k})$ with isotropic parabolic dispersion and constant Ising SOC:

$$H_0(\boldsymbol{k}) = \xi(\boldsymbol{k})\tau_0\sigma_0 + \lambda\tau_z\sigma_z, \tag{2.22}$$

where τ_μ are the Pauli matrices acting on the valley index $\{d_{K_+}, d_{K_-}\}$, $\xi(\boldsymbol{k}) = -\frac{k^2}{2m} - \mu$ is the single-particle energy without SOC with μ the chemical potential, and λ is the constant Ising SOC. Throughout this work, we will use bold symbols to denote two-dimensional vectors like the momentum $\boldsymbol{k} = (k_x, k_y)$, and arrows to denote three-dimensional vectors like the spin $\vec{S} = (S_x, S_y, S_z)$.

The eigenvalues of $H_0(\boldsymbol{k})$ are just the original dispersion rigidly shifted by the constant Ising SOC λ, $\varepsilon_\pm(\boldsymbol{k}) = \xi(\boldsymbol{k}) \pm \lambda$, where the $+$ corresponds to $K_+ \uparrow$ and $K_- \downarrow$, while the $-$ applies to $K_+ \downarrow$ and $K_- \uparrow$. In particular, the DOS remains unchanged by the $\boldsymbol{k}$-independent Ising SOC, and the spin-split bands have the same constant DOS $N_{01} = \frac{m}{2\pi}$ associated with a 2D parabolic band of mass m. Therefore, the symmetry-allowed singlet-triplet mixing in the superconducting state, which is proportional to the difference between the DOS of the spin-split bands [316], vanishes

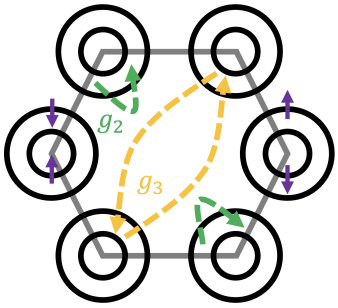

FIGURE 9: Sketch of the intraband density-density g_2 and interband pair-hopping g_3 interactions in our model of the K pockets of $NbSe_2$.

identically in this model. In Appendix 2.B, we will introduce a different DOS via a $\boldsymbol{k}$-dependent Ising SOC. Given that it does not qualitatively modify the superconducting collective modes, we will first neglect it for simplicity.

Interactions

Ref. [306] considered all symmetry-allowed momentum-independent spin-symmetric interactions in their 3-band model. Following their notation, the momentum-independent interactions that respect the $SU(2)$ spin symmetry in our 2-band model read

$$H_{\text{int}} = \frac{1}{V_{\text{syst}}} \Bigg\{ g_5 \sum_{\boldsymbol{Q}\tau} \left[n_{\tau\uparrow}(\boldsymbol{Q}) n_{\tau\downarrow}(-\boldsymbol{Q}) \right] + g_2 \sum_{\boldsymbol{Q}} \left[n_{K_+}(\boldsymbol{Q}) n_{K_-}(-\boldsymbol{Q}) \right] + \\ + g_3 \sum_{\boldsymbol{k}\boldsymbol{k}'\boldsymbol{q}} \sum_{\sigma\sigma'} \left[d^\dagger_{K_+\sigma}(\boldsymbol{k}) d^\dagger_{K_-\sigma'}(-\boldsymbol{k}+\boldsymbol{q}) d_{K_+\sigma'}(-\boldsymbol{k}'+\boldsymbol{q}) d_{K_-\sigma}(\boldsymbol{k}') \right] \Bigg\}, \tag{2.23}$$

where $\tau = K_\pm$, $n_\tau = n_{\tau\uparrow} + n_{\tau\downarrow}$, $n_{\tau\sigma}(\boldsymbol{Q}) = \sum_{\boldsymbol{k}} d^\dagger_{\tau\sigma}(\boldsymbol{k}) d_{\tau\sigma}(\boldsymbol{k}+\boldsymbol{Q})$, g_2 is an intervalley intraband density-density interaction involving the $K_\pm$ valleys, g_3 is an intervalley interband pair-hopping interaction between the K_+ and K_- pockets, g_5 is the intravalley intraband Hubbard-like repulsion, and V_{syst} is the volume of the system (see Fig. 9). From now on, we omit the momentum labels for simplicity, as well as the factor $1/V_{\text{syst}}$, which will indeed cancel out when we take the homogeneous mean-field approximation. In this shorthand notation, Eq. (2.23) reads

$$H_{\text{int}} = g_5 \sum_{\tau} n_{\tau\uparrow} n_{\tau\downarrow} + g_2 n_{K_+} n_{K_-} + g_3 \sum_{\sigma\sigma'} (d^\dagger_{K_+\sigma} d^\dagger_{K_-\sigma'} d_{K_+\sigma'} d_{K_-\sigma}). \tag{2.24}$$

Ref. [300] has also classified the interactions between the bands at the $K_\pm$ valleys, expressing them in terms of spin operators $\vec{S}_\tau = d^\dagger_\tau \vec{\sigma} d_\tau$. Rewriting our interaction Hamiltonian (2.24) in this

notation, we arrive to

$$H_{\text{int}} = g_5 \sum_{\tau} n_{\tau\uparrow} n_{\tau\downarrow} + \left(g_2 - \frac{1}{2} g_3 \right) n_{K_+} n_{K_-} - g_3 \vec{S}_{K_+} \cdot \vec{S}_{K_-}, \tag{2.25}$$

which reflects that the spin-spin interaction comes from the intervalley pair-hopping interaction g_3. As discussed in Refs. [300, 306], the microscopic origin of these couplings might be a combination of electron-phonon interactions, Coulomb interactions, or spin fluctuations, the latter especially in the case of g_3. In our sign convention, repulsive interactions would be positive, $g_i > 0$, and attractive interactions negative, $g_i < 0$. Finally, we mention that a similar model has been considered by Ref. [325] in the context of exciton-mediated spin-triplet superconductivity in lightly-doped semiconductors (in their notation, $g_5 \to g_0$, $(g_2 - \frac{1}{2} g_3) \to g_1$, $g_3 \to g_2$).

To further illuminate the microscopic origin of the different interactions, it is illustrative to consider a microscopic model for the local Coulomb repulsion. As mentioned before, in the limit of a small Fermi surface, the bands have an approximately constant orbital character, with $d_{K_\pm \sigma} = d_{\pm\sigma} = d_{x^2-y^2} \mp i d_{xy}$. Therefore, we consider the two-orbital Slater-Kanamori Hamiltonian [326], which includes all the allowed interactions between orbital and spin degrees of freedom:

$$H_{\text{int}}^{SK} = U \sum_{\gamma} n_{\gamma\uparrow} n_{\gamma\downarrow} + \sum_{\sigma\sigma'} \sum_{\gamma \neq \gamma'} \left[\frac{U'}{2} n_{\gamma\sigma} n_{\gamma'\sigma'} + \frac{J}{2} d^\dagger_{\gamma\sigma} d^\dagger_{\gamma'\sigma'} d_{\gamma\sigma'} d_{\gamma'\sigma} + \frac{J'}{2} d^\dagger_{\gamma\sigma} d^\dagger_{\gamma\sigma'} d_{\gamma'\sigma'} d_{\gamma'\sigma} \right], \tag{2.26}$$

where $\sigma = \uparrow, \downarrow$ labels the spin and $\gamma = x^2 - y^2, xy$ runs through the d orbitals. U is the intraorbital Hubbard repulsion, U' is the interorbital Hubbard interaction, J is the Hund exchange coupling, and J' is the pair hopping interaction. The combination of D_{3h} orbital symmetry and $SU(2)$ spin rotation symmetry of the interactions forces $J' = U - U' - J$, which we assume from now on (full rotational invariance would also add the constrain $U - U' = 2J$). Using the approximate change from the orbital to the band basis, $d_{K_\pm \sigma} = d_{\pm\sigma} = d_{x^2-y^2} \pm i d_{xy}$, we find that the interactions in the band basis are related to the Slater-Kanamori interactions as:

$$g_2 = U - J, \tag{2.27}$$

$$g_3 = U - U', \tag{2.28}$$

$$g_5 = U' + J. \tag{2.29}$$

Superconducting pairings and interactions

In this work, we only focus on instabilities in the particle-particle channel. While monolayer $NbSe_2$ displays coexisting CDW order and superconductivity, we do not consider the CDW. This approximation is justified since the CDW only partially gaps the Fermi surface, quantitatively changing the DOS and the electron-phonon coupling strength, but it does not qualitatively affect superconductivity [31, 33]. With this in mind, it is useful to rewrite the interaction Hamiltonian of Eqs. (2.24) and (2.25) in terms of pairing operators:

$$H_{\text{int}} = (g_2 + g_3)\hat{\Phi}_S^\dagger \hat{\Phi}_S + g_5 \hat{\mathbf{\Phi}}_{S'}^\dagger \cdot \hat{\mathbf{\Phi}}_{S'} + (g_2 - g_3)\vec{\hat{\Phi}}_T^\dagger \cdot \vec{\hat{\Phi}}_T, \tag{2.30}$$

where

$$\hat{\Phi}_S(\boldsymbol{k}) = \tfrac{1}{2}\psi(-\boldsymbol{k})\tau_x i\sigma_y \psi(\boldsymbol{k}), \tag{2.31}$$

$$\hat{\mathbf{\Phi}}_{S'}(\boldsymbol{k}) = \tfrac{1}{2}\psi(-\boldsymbol{k})\{\tau_0, i\tau_z\} i\sigma_y \psi(\boldsymbol{k}), \tag{2.32}$$

$$\vec{\hat{\Phi}}_T(\boldsymbol{k}) = \tfrac{1}{2}\psi(-\boldsymbol{k}) i\tau_y \vec{\sigma} i\sigma_y \psi(\boldsymbol{k}) = \tfrac{1}{2}\psi(-\boldsymbol{k}) i\tau_y \{-\sigma_z, i\sigma_0, \sigma_x\}\psi(\boldsymbol{k}), \tag{2.33}$$

Here, $\hat{\Phi}_S$ is the spin-singlet s-wave (A_1') channel, $\hat{\mathbf{\Phi}}_{S'}$ is a spin-singlet d-wave (E') channel, and $\vec{\hat{\Phi}}_T$ is the spin-triplet f-wave pairing. We have implicitly dropped the sum over the total Cooper pair momentum $\boldsymbol{Q}$ in Eq. (2.23). Since $\hat{\mathbf{\Phi}}_{S'}$ couples electrons within the same valley, it can only lead to a pair density wave with nonzero total momentum, so we neglect it; in any case, we assume $g_5 > 0$ to be repulsive. Indeed, for simplicity we will omit g_5 in our calculations.

Regarding the values of the interactions, we assume that the intervalley density-density interaction is attractive, $g_2 < 0$, which favors both the s-wave and f-wave channels. Microscopically this can arise from the electron-phonon interaction. Crucially, we also assume that $|g_2| > |g_3|$, so that the interaction is attractive in both channels. The choice between the two is made by the sign of g_3. When $g_3 = 0$ both channels have the same attraction, while the s-wave singlet ground state is favoured when $g_3 < 0$. For convenience, we define the attraction in the singlet and triplet channels as $g_S = g_2 + g_3 = 2U - U' - J$ and $g_T = g_2 - g_3 = U' - J$, respectively. The fact that $g_3 < 0$ favors interorbital triplet pairing is consistent with the observation made for several other multiorbital systems that the repulsive Hund coupling J can lead to triplet superconductivity if it can overcome the interorbital Hubbard U' [327–330]. While microscopically $U' > J$, this can change when these values are renormalized as high-energy degrees of freedom are integrated out in a low-energy model. Here we assume $g_3 < 0$ instead, so that the ground state is the s-wave spin-singlet, as predicted by *ab initio* calculations [30–33]. In summary, the interaction

Hamiltonian that we will use to compute the superconducting collective modes becomes

$$H_{\text{int}} = g_S \hat{\Phi}_S^\dagger \hat{\Phi}_S + g_T \vec{\hat{\Phi}}_T^\dagger \cdot \vec{\hat{\Phi}}_T, \tag{2.34}$$

with $g_S < g_T < 0$.

We remark that we consider interactions that respect the $SU(2)$ spin rotation symmetry. However, in the presence of SOC, interactions only need to fulfill the double point group of the system. Indeed, interactions are affected by Ising SOC in two ways. On the one hand, the triplet coupling g_T becomes different for the out-of-plane triplet $\hat{\Phi}_T^z = \frac{1}{2}\psi i\tau_y\sigma_x\psi$ with A_1' symmetry ($g_T \to g_T^z$) and for the in-plane triplet $\hat{\boldsymbol{\Phi}}_{\boldsymbol{T}}^{\boldsymbol{xy}} = \frac{1}{2}\psi i\tau_y\{i\sigma_0, -\sigma_z\}\psi$ with E'' symmetry ($g_T \to g_T^{xy}$). This effect can be easily taken into account in our model just by substituting $g_T \to g_T^z$ and $g_T \to g_T^{xy}$ in the Leggett and Bardasis-Schrieffer energy expressions given below, respectively. On the other hand, a new interaction $\left(\hat{\Phi}_S^\dagger \hat{\Phi}_T^z + \text{h.c.}\right)$ mixing the A_1' singlet with the A_1' out-of-plane triplet is allowed to appear, which also induces a singlet-triplet mixed ground state. We will now omit this term for simplicity, and discuss its effects in Appendix 2.B.

Tendency towards magnetism

Before moving on to determining the superconducting ground state, it is instructive to discuss the possible magnetic instabilities of our model. For that, we need to reinsert the intraband Hubbard-like repulsion g_5. We define the magnetizations in the z direction M_τ of valley $\tau = K_\pm$ by expressing the densities as $n_{\tau\uparrow} = \frac{1}{2}(n_\tau + M_\tau)$, $n_{\tau\downarrow} = \frac{1}{2}(n_\tau - M_\tau)$. Within the Stoner picture, assuming that spins polarize in the z direction, the interaction becomes

$$H_{\text{int}} \approx \frac{g_5}{4}\left(n_{K_+}^2 + n_{K_-}^2 - M_{K_+}^2 - M_{K_-}^2\right) + \left(g_2 - \frac{g_3}{2}\right) n_{K_+} n_{K_-} - \frac{g_3}{2} M_{K_+} M_{K_-}, \tag{2.35}$$

As usual, the Hubbard like repulsion $g_5 > 0$ favors the independent spin polarization of each band. But the existence of ferromagnetism is decided by g_3, where $g_3 > 0$ favors it, while $g_3 < 0$ simply favors a renormalization of the Ising SOC ($M_{K_+} = -M_{K_-}$). Since we always assume that $g_3 < 0$, ferromagnetism is not favored in this simple picture.

More realistic calculations predict monolayer $NbSe_2$ to be close to a ferromagnetic instability. Our model is too simple to capture the simultaneous leading attraction in the s-wave spin-singlet channel, subleading attraction in the f-wave spin-triplet channel, and tendency towards ferromagnetism. These three conditions can be fulfilled when including the Γ pocket. The important ingredient is the interpocket pair-hopping interaction between the Γ and $K_\pm$ pockets, named g_4 in Ref. [306]. If this coupling is large, the s-wave spin-singlet channel can be the leading attraction even if $g_3 > 0$, so that the f-wave spin-triplet channel is subleading (see Eqs. (23-25) of Ref.

[306]), and ferromagnetism is preferred compared to the SOC renormalization. Nevertheless, it is worth highlighting that the interactions we consider apply to low energies. In particular, the signs of g_2 and g_3 at higher energies might change, and a ferromagnetic instability coming from the whole band might still occur even if $g_3 < 0$ at low energies.

2.2.2 Superconducting gap equations

In summary, our model consists of the single-particle Hamiltonian (2.22), with the interactions (2.34) in the s-wave spin-singlet $\hat{\Phi}_S$ and in the f-wave spin-triplet $\vec{\hat{\Phi}}_T$ channels, which can be thought to be local in real space:

$$H = \sum_{\boldsymbol{k}} \psi^\dagger(\boldsymbol{k}) \left[\xi(\boldsymbol{k})\tau_0\sigma_0 + \lambda\tau_z\sigma_z\right] \psi(\boldsymbol{k}) + \sum_{\boldsymbol{r}} \left[g_S \hat{\Phi}_S^\dagger(\boldsymbol{r})\hat{\Phi}_S(\boldsymbol{r}) + g_T \vec{\hat{\Phi}}_T^\dagger(\boldsymbol{r}) \cdot \vec{\hat{\Phi}}_T(\boldsymbol{r})\right], \quad (2.36)$$

where

$$\hat{\Phi}_S(\boldsymbol{r}) = \tfrac{1}{2}\psi(\boldsymbol{r})\tau_x i\sigma_y \psi(\boldsymbol{r}), \quad (2.37)$$

$$\vec{\hat{\Phi}}_T(\boldsymbol{r}) = \tfrac{1}{2}\psi(\boldsymbol{r}) i\tau_y \vec{\sigma} i\sigma_y \psi(\boldsymbol{r}). \quad (2.38)$$

Ising SOC splits the triplet in the out-of-plane A_1' and in-plane E'' components:

$$\hat{\Phi}_T^z(\boldsymbol{r}) = \frac{1}{2}\psi(\boldsymbol{r}) i\tau_y\sigma_z i\sigma_y \psi(\boldsymbol{r}), \quad (2.39)$$

$$\hat{\boldsymbol{\Phi}}_{\boldsymbol{T}}^{\boldsymbol{xy}}(\boldsymbol{r}) = \frac{1}{2}\psi(\boldsymbol{r}) i\tau_y\{\sigma_x, \sigma_y\} i\sigma_y \psi(\boldsymbol{r}), \quad (2.40)$$

which can be easily accommodated in the interaction by assigning these components different interactions g_T^z and g_T^{xy}.

Hubbard-Stratonovich transformation

The next step towards modeling the collective modes in $NbSe_2$ is to determine and solve the gap equation for the Hamiltonian H of Eq. (2.36). In the introduction, we have shown how to derive the gap equation by performing a mean-field approximation of H in the Cooper channel $\Delta_i = -g_i\langle\hat{\Phi}_i\rangle$, $i = S, Tz, Tx, Ty$, transforming to Nambu space, and diagonalizing the resulting BdG Hamiltonian. Here, due to the Hamiltonian being a larger matrix, it is simpler to work in the functional integral formalism, which is also convenient to determine the collective mode fluctuations. For that, the fermion operators with canonical anticommutation relations $\{\psi_\alpha^\dagger, \psi_\beta\} = \delta_{\alpha\beta}$ are replaced by fermion fields that anticommute $\{\bar{\psi}_\alpha, \psi_\beta\} = 0$. We will apply the imaginary time Matsubara formalism to account for the finite temperature. Within this formalism,

the inverse bare electron and hole Matsubara Green's functions read

$$\left[G_0^{(p)}\right]^{-1}(k) = i\omega_n\tau_0\sigma_0 - H_0(\boldsymbol{k}) = i\omega_n\tau_0\sigma_0 - \left[\xi(\boldsymbol{k})\tau_0\sigma_0 + \lambda\tau_z\sigma_z\right], \tag{2.41}$$

$$\left[G_0^{(h)}\right]^{-1}(k) = i\omega_n\tau_0\sigma_0 + H_0^*(-\boldsymbol{k}) = i\omega_n\tau_0\sigma_0 + \left[\xi(\boldsymbol{k})\tau_0\sigma_0 + \lambda\tau_z\sigma_z\right], \tag{2.42}$$

where $i\omega_n = \frac{2\pi}{\beta}(n+\frac{1}{2})$ are the fermionic Matsubara frequencies, with $n \in \mathbb{Z}$, $\beta = (k_B T)^{-1}$ and T the temperature. The action in imaginary time τ for the fermions $\mathcal{S} = \left[\int_x \bar{\psi}(x)\partial_\tau\psi(x) + H\right]$ reads

$$\mathcal{S}[\bar{\psi},\psi] = -\int_k \bar{\psi}(k)\left[G_0^{(p)}\right]^{-1}(k)\psi(k) + g_S\int_x \bar{\Phi}_S(x)\Phi_S(x) + g_T\int_x \vec{\bar{\Phi}}_T(x)\cdot\vec{\Phi}_T(x), \tag{2.43}$$

where the pairing operators Φ_S and $\vec{\Phi}_T$ are given by Eqs. (2.37) and (2.38) in terms of fermion fields, and we have used the shorthand notations $x \equiv (\tau, \boldsymbol{r})$, $k \equiv (i\omega_n, \boldsymbol{k})$, $\int_x \equiv \int_0^\beta d\tau \int d^2r$, and $\int_k \equiv \frac{1}{\beta}\sum_{i\omega_n}\int \frac{d^2k}{(2\pi)^2}$.

Since we have assumed attractive interactions in both singlet Φ_S and triplet $\vec{\Phi}_T$ pairing channels, $g_S < g_T < 0$, we can perform a Hubbard-Stratonovich transformation in both channels[2]. This transformation amounts to introducing the new bosonic fields $\Delta_i(x) \sim -g_i\Phi_i(x)$ to rewrite the partition function Z in terms of a new action $\tilde{\mathcal{S}}$ which depends on the new bosons Δ and only quadratically on the fermions ψ:

$$Z = \int D\bar{\psi}D\psi e^{-\mathcal{S}[\bar{\psi},\psi]} = \int D\bar{\psi}D\psi\prod_i D\bar{\Delta}_i D\Delta_i e^{-\tilde{\mathcal{S}}[\bar{\psi},\psi,\bar{\Delta},\Delta]}, \tag{2.44}$$

where $i = S, Tz, Tx, Ty$. Using the following identity derived from Gaussian integrations [332]

$$\begin{aligned}&\exp\left[-g_i\int_x \bar{\Phi}_i(x)\Phi_i(x)\right] = \\ &= \int D\bar{\Delta}_i D\Delta_i \exp\left[-\int_x\left(-\bar{\Delta}_i(x)\Phi_i(x) - \bar{\Phi}_i(x)\Delta_i(x) - \frac{1}{g_i}\bar{\Delta}_i(x)\Delta_i(x)\right)\right],\end{aligned} \tag{2.45}$$

we obtain the new action

$$\begin{aligned}\tilde{\mathcal{S}}[\bar{\psi},\psi,\bar{\Delta},\Delta] = &-\int_k \bar{\psi}(k)\left[G_0^{(p)}\right]^{-1}(k)\psi(k) - \\ &-\int_x\sum_i\left[\bar{\Delta}_i(x)\Phi_i(x) + \bar{\Phi}_i(x)\Delta_i(x) + \frac{1}{g_i}\bar{\Delta}_i(x)\Delta_i(x)\right],\end{aligned} \tag{2.46}$$

[2] If the interaction were repulsive in a given channel, a modified Hubbard-Stratonovich procedure would be required; see e.g. Appendix A of Ref. [331] and references therein.

which is quadratic in the fermion fields ψ.

With a view to deriving the gap equation, it is useful to write the action (2.46) fully in real space. We define the matrices M_i of the pairing operators as $\Phi_i = \frac{1}{2}\psi M_i \psi$, so from Eqs. (2.37-2.40) we get

$$M_S = \tau_x i\sigma_y, \tag{2.47}$$
$$M_T^z = i\tau_y\sigma_z i\sigma_y, \tag{2.48}$$
$$M_T^x = i\tau_y\sigma_x i\sigma_y, \tag{2.49}$$
$$M_T^y = i\tau_y\sigma_y i\sigma_y. \tag{2.50}$$

We also define the matrix pairing fields

$$\hat{\Delta}_i = M_i^\dagger \Delta_i. \tag{2.51}$$

In real space, the inverse Matsubara Green's function, which only depends on the relative position of the fermions, reads

$$\left[G_0^{(p)}\right]^{-1}(x,x') = \left[G_0^{(p)}\right]^{-1}(x'-x) = \int_k e^{-ik(x'-x)}\left[G_0^{(p)}\right]^{-1}(k), \tag{2.52}$$

while the local superconducting pairings are $\Delta_i(x,x') = \Delta(\frac{x+x'}{2})\delta(x-x')$. The new action in real space, using matrix notation in both internal and spatial indices and the Einstein summation convention, becomes

$$\tilde{S}[\bar{\psi},\psi,\bar{\Delta},\Delta] = -\bar{\psi}\left[G_0^{(p)}\right]^{-1}\psi - \sum_i\left(\frac{1}{2}\psi^T\hat{\bar{\Delta}}_i\psi + \frac{1}{2}\bar{\psi}\hat{\Delta}_i\bar{\psi}^T + \frac{1}{4}\mathrm{Tr}\left[\hat{\bar{\Delta}}_i g_i^{-1}\hat{\Delta}_i\right]\right). \tag{2.53}$$

Nambu space

In order to integrate out the fermion fields of the new action (2.53), it is useful to introduce the Nambu spinor fields $\Psi = (\psi, \bar{\psi}^T)^T = (d_{K_+\uparrow}, d_{K_+\downarrow}, d_{K_-\uparrow}, d_{K_-\downarrow}, \bar{d}_{K_+\uparrow}, \bar{d}_{K_+\downarrow}, \bar{d}_{K_-\uparrow}, \bar{d}_{K_-\downarrow})$. We will use the notation ρ_μ to denote the Pauli matrices in Nambu space. Particle and hole Matsubara Green's functions are related by[3]:

$$\bar{\psi}[G_0^{(p)}]^{-1}\psi = \psi^T[G_0^{(h)}]^{-1}\bar{\psi}^T. \tag{2.54}$$

[3]The identity 2.54 is true for fields due to the equivalence between partition functions up to a numerical constant. For operators, one should add the term $-\frac{1}{2}\mathrm{tr}[H_0(\boldsymbol{k})]$ arising from the anticommutation relation of a creation and an annihilation operator of the same state; see Eq. (2.17).

The normal term in the action (2.53) can be rewritten as:

$$\bar{\psi}\left[G_0^{(p)}\right]^{-1}\psi = \frac{1}{2}\left\{\bar{\psi}\left[G_0^{(p)}\right]^{-1}\psi + \psi^T\left[G_0^{(h)}\right]^{-1}\bar{\psi}^T\right\} = \frac{1}{2}\bar{\Psi}G_0^{-1}\Psi, \tag{2.55}$$

where we have defined the inverse normal bare Gorkov Green's function in Nambu space G_0^{-1} as

$$G_0^{-1} = \begin{pmatrix}\left[G_0^{(p)}\right]^{-1} & 0\\ 0 & \left[G_0^{(h)}\right]^{-1}\end{pmatrix} \Rightarrow G_0^{-1}(k) = i\omega_n\rho_0 - H_0(\boldsymbol{k})\rho_z. \tag{2.56}$$

The anomalous terms can also be reexpressed as:

$$\frac{1}{2}\psi^T\hat{\bar{\Delta}}_i\psi + \frac{1}{2}\bar{\psi}\hat{\Delta}_i\bar{\psi}^T = \frac{1}{2}\bar{\Psi}\left(\hat{\bar{\Delta}}_i\frac{1}{2}\rho_- + \hat{\Delta}_i\frac{1}{2}\rho_+\right)\Psi. \tag{2.57}$$

Inserting the identities (2.55) and (2.57) in the action (2.53), the action in Nambu space reads

$$\tilde{\mathcal{S}}[\bar{\Psi},\Psi,\bar{\Delta},\Delta] = -\left\{\frac{1}{2}\bar{\Psi}G^{-1}\Psi + \sum_i\frac{1}{4}\mathrm{Tr}\left[\hat{\bar{\Delta}}_i g_i^{-1}\hat{\Delta}_i\right]\right\}, \tag{2.58}$$

where the inverse full Gorkov BdG Green's function is:

$$G^{-1} = G_0^{-1} + \sum_i\left(\hat{\bar{\Delta}}_i\frac{1}{2}\rho_- + \hat{\Delta}_i\frac{1}{2}\rho_+\right) = \begin{pmatrix}\left[G_0^{(p)}\right]^{-1} & \sum_i\hat{\Delta}_i\\ \sum_i\hat{\bar{\Delta}}_i & \left[G_0^{(h)}\right]^{-1}\end{pmatrix}. \tag{2.59}$$

Effective action and gap equation

The final step to derive the gap equation is integrating out the fermions in the action (2.58), which gives rise to the following effective action for the superconducting fields:

$$\begin{aligned}\mathcal{S}_{\mathrm{eff}}[\bar{\Delta},\Delta] &= -\sum_i\frac{1}{4}\mathrm{Tr}\left[\hat{\bar{\Delta}}_i g_i^{-1}\hat{\Delta}_i\right] - \mathrm{Tr}\left[\log G^{-1}\right] = \\ &= -\int_x\left[\frac{1}{g_S}\bar{\Delta}_S(x)\Delta_S(x) + \frac{1}{g_T}\vec{\bar{\Delta}}_T(x)\cdot\vec{\Delta}_T(x)\right] - \mathrm{Tr}\left[\log G^{-1}\right],\end{aligned} \tag{2.60}$$

where the functional trace is defined as

$$\mathrm{Tr}\left[\log G^{-1}\right] = \int_x \mathrm{tr}\left\{\left[\log G^{-1}\right](x,x)\right\}. \tag{2.61}$$

The gap equation can be obtained as the saddle point of the effective action with respect to the Hubbard-Stratonovich fields Δ_i, $\frac{\delta \mathcal{S}_{\text{eff}}[\bar{\Delta},\Delta]}{\delta \bar{\Delta}_i(x)} = 0$:

$$\frac{1}{g_i}\Delta_i(x) = -\text{tr}\left[G(x,x)M_i\rho_-\right]. \tag{2.62}$$

We will assume that the superconducting pairing fields Δ_i are spatially-homogeneous, so that $\Delta_i(x) = \Delta_i$, or equivalently $\Delta_i(q) = (2\pi)^2\beta\delta(q)\Delta_i$. In this case, the Gorkov BdG Green's function depends just on the relative momentum k, $G^{-1}(k,q) = (2\pi)^2\beta\delta(q)G^{-1}(k)$, with

$$G^{-1}(k) = \begin{pmatrix} i\omega_n\tau_0\sigma_0 - H_0(\boldsymbol{k}) & -\Delta_S\tau_x i\sigma_y - \vec{\Delta}_T\cdot i\tau_y(\sigma_x,-\sigma_y,\sigma_z)i\sigma_y \\ \bar{\Delta}_S\tau_x i\sigma_y + \vec{\bar{\Delta}}_T\cdot i\tau_y(\sigma_x,\sigma_y,\sigma_z)i\sigma_y & i\omega_n\tau_0\sigma_0 + H_0(\boldsymbol{k}) \end{pmatrix}. \tag{2.63}$$

Applying this ansatz to the gap equation (2.62), using the fact that $G(x,x) = \int_k G(k)$, we arrive at the following gap equation in momentum space:

$$\frac{1}{g_i}\Delta_i = -\int_k \text{tr}\left[G(k)M_i\rho_-\right]. \tag{2.64}$$

Ground state

We now determine the superconducting ground state of our model by solving the gap equation. The gap equation (2.64) is general for the interactions of the form (2.36). In particular, it allows for singlet-triplet mixing between Δ_S and Δ_T^z in principle. However, we now explicitly show, as we advanced, that the mixing vanishes in our model since the DOS of the spin-split bands is the same. We assume that either only an A_1' potentially singlet-triplet mixed state of Δ_S and Δ_T^z condenses, or only one component of the E'' in-plane triplet $\boldsymbol{\Delta}_T^{xy}$ condenses. The quasiparticle energies in the superconducting state with SOC are, for the A_1' potentially singlet-triplet mixed state:

$$E_\pm(\boldsymbol{k}) = \sqrt{\varepsilon_\pm^2(\boldsymbol{k}) + |\Delta_S \pm \Delta_T^z|^2} = \sqrt{\varepsilon_\pm^2(\boldsymbol{k}) + |\Delta_\pm|^2}, \tag{2.65}$$

with $\Delta_\pm = \Delta_S \pm \Delta_T^z$, and for a component of the E'' triplet:

$$E_\pm^{xy}(\boldsymbol{k}) = \sqrt{\varepsilon_\pm^2(\boldsymbol{k}) + |\Delta_i|^2}, \tag{2.66}$$

with $i = Tx, Ty$, and the band energies with SOC are $\varepsilon_\pm(\boldsymbol{k}) = \xi(\boldsymbol{k}) \pm \lambda$. In the absence of SOC, there is no singlet-triplet mixing, and the quasiparticle energies in this case are

$$E(\boldsymbol{k}) = \sqrt{\xi^2(\boldsymbol{k}) + |\Delta_i|^2}, \tag{2.67}$$

for $i = S, Tz, Tx, Ty$.

After performing the sum over Matsubara frequencies, we obtain the following gap equations for the A_1' singlet Δ_S and triplet Δ_T^z and for the E'' triplet $\mathbf{\Delta}_T^{xy}$:

$$\begin{aligned} -\frac{1}{g_S}\Delta_S = \Delta_S \int \frac{d^2k}{(2\pi)^2} \left\{ \frac{\tanh\left[\frac{\beta}{2}E_+(\boldsymbol{k})\right]}{E_+(\boldsymbol{k})} + \frac{\tanh\left[\frac{\beta}{2}E_-(\boldsymbol{k})\right]}{E_-(\boldsymbol{k})} \right\} + \\ + \Delta_T^z \int \frac{d^2k}{(2\pi)^2} \left\{ \frac{\tanh\left[\frac{\beta}{2}E_+(\boldsymbol{k})\right]}{E_+(\boldsymbol{k})} - \frac{\tanh\left[\frac{\beta}{2}E_-(\boldsymbol{k})\right]}{E_-(\boldsymbol{k})} \right\}, \end{aligned} \tag{2.68}$$

$$\begin{aligned} -\frac{1}{g_T}\Delta_T^z = \Delta_T^z \int \frac{d^2k}{(2\pi)^2} \left\{ \frac{\tanh\left[\frac{\beta}{2}E_+(\boldsymbol{k})\right]}{E_+(\boldsymbol{k})} + \frac{\tanh\left[\frac{\beta}{2}E_-(\boldsymbol{k})\right]}{E_-(\boldsymbol{k})} \right\} + \\ + \Delta_S \int \frac{d^2k}{(2\pi)^2} \left\{ \frac{\tanh\left[\frac{\beta}{2}E_+(\boldsymbol{k})\right]}{E_+(\boldsymbol{k})} - \frac{\tanh\left[\frac{\beta}{2}E_-(\boldsymbol{k})\right]}{E_-(\boldsymbol{k})} \right\}, \end{aligned} \tag{2.69}$$

$$-\frac{1}{g_T}\mathbf{\Delta}_T^{xy} = \mathbf{\Delta}_T^{xy} \int \frac{d^2k}{(2\pi)^2} \frac{\tanh\left[\frac{\beta}{2}(E(\boldsymbol{k})+\lambda)\right] + \tanh\left[\frac{\beta}{2}(E(\boldsymbol{k})-\lambda)\right]}{E(\boldsymbol{k})}. \tag{2.70}$$

In general, the gap equations (2.68) and (2.69) of Δ_S and Δ_T^z are coupled, giving rise to singlet-triplet mixing. However, we now show that, in the presence of just constant Ising SOC, these gap equations become decoupled. For that, we change the momentum integration by an energy integration with an energy cutoff Λ[4], $\int \frac{d^2k}{(2\pi)^2} \to N_\pm \int_{-\Lambda}^{\Lambda} d\varepsilon_\pm$, where $N_+ = N_- = \frac{m}{2\pi}$ is the DOS of each spin-split band in the normal state. First, the mixing term vanishes at T_c, since the linearized gap equations are analogous to Eqs. (2.68) and (2.69) but with the quasiparticle energies $E_\pm$ substituted by the energies in the normal state $\varepsilon_\pm$, and the energy integrations over ε_+ and ε_- are exactly equal. The singlet-triplet mixing also vanishes at lower temperatures. In particular, at $T = 0$, we arrive to the following gap equations for $\Delta_\pm = \Delta_S \pm \Delta_T^z$ in the A_1' channel:

$$-\Delta_+ = 2(g_S + g_T)\Delta_+ N_+ \text{argsinh}\left(\frac{\Lambda}{|\Delta_+|}\right) + 2(g_S - g_T)\Delta_- N_- \text{argsinh}\left(\frac{\Lambda}{|\Delta_-|}\right), \tag{2.71}$$

$$-\Delta_- = 2(g_S + g_T)\Delta_- N_- \text{argsinh}\left(\frac{\Lambda}{|\Delta_-|}\right) + 2(g_S - g_T)\Delta_+ N_+ \text{argsinh}\left(\frac{\Lambda}{|\Delta_+|}\right). \tag{2.72}$$

Since $N_+ = N_-$ for momentum-independent Ising SOC, the solutions of these equations are $\Delta_+ = \Delta_- = \Delta_S$, $\Delta_T^z = 0$, and $\Delta_+ = -\Delta_- = \Delta_T^z$, $\Delta_S = 0$. The superconducting gaps in these

[4]The same high-energy cutoff Λ applies to both spin-split bands as long as the chemical potential μ is much larger than Λ, which is of the order of the Debye frequency. Indeed, this is the relevant situation for $NbSe_2$, where $\mu \sim 500\text{meV} \gg \Lambda \sim 20\text{meV}$.

cases are, respectively,

$$\Delta_S = \frac{\Lambda}{\sinh\left[-\frac{1}{\bar{g}_S}\right]} \simeq 2\Lambda \exp\left[-\frac{1}{\bar{g}_S}\right], \tag{2.73}$$

$$\Delta_T^z = \frac{\Lambda}{\sinh\left[-\frac{1}{\bar{g}_T}\right]} \simeq 2\Lambda \exp\left[-\frac{1}{\bar{g}_T}\right], \tag{2.74}$$

where we have defined the dimensionless coupling constants $\bar{g}_i$ as

$$\bar{g}_i = N_0 g_i \tag{2.75}$$

with $N_0 = 2N_+ + 2N_- = 4\frac{m}{2\pi}$ the total DOS in the normal state. Therefore, effectively the gap equations (2.68) and (2.69) become decoupled for constant Ising SOC, and we could rewrite them as

$$\begin{aligned} -\frac{1}{g_i}\Delta_i = \Delta_i \int \frac{d^2k}{(2\pi)^2} \frac{\tanh\left[\frac{\beta}{2}E_+(\boldsymbol{k})\right]}{E_+(\boldsymbol{k})} + \frac{\tanh\left[\frac{\beta}{2}E_-(\boldsymbol{k})\right]}{E_-(\boldsymbol{k})} = \\ = N_0\Delta_i \int_{-\Lambda}^{\Lambda} d\varepsilon \frac{\tanh\left[\frac{\beta}{2}\sqrt{\varepsilon^2+\Delta_i^2}\right]}{2\sqrt{\varepsilon^2+\Delta_i^2}}, \end{aligned} \tag{2.76}$$

with $E_\pm(\boldsymbol{k}) = \sqrt{\varepsilon_\pm^2(\boldsymbol{k}) + \Delta_i^2}$ as in Eq. (2.66), and $i = S, Tz$. In particular, both gap equations are identical and unaffected by the Ising SOC. Again, this is a consequence of the fact that the A_1' singlet Δ_S and the A_1' triplet Δ_T^z pair electrons with opposite spins, which are those available at the Fermi level with zero momentum pairing.

On the other hand, the gap equation (2.70) for the E'' in-plane triplet $\boldsymbol{\Delta}_T^{xy}$ shows that it is suppressed by Ising SOC, and eventually killed when the Ising SOC λ becomes bigger than the energy cutoff Λ, which is the situation in $NbSe_2$. This is due to the fact that the E'' triplet $\boldsymbol{\Delta}_T^{xy}$ involves pairing between equal-spin states, but zero momentum Cooper pairs at the Fermi level can only be made with opposite spins. Therefore, in the absence of a substrate or an in-plane magnetic field, the E'' in-plane triplet $\boldsymbol{\Delta}_T^{xy}$ cannot be the ground state. Nevertheless, if the attraction g_T in the f-wave spin-triplet channel is sizable, the E'' in-plane part $\boldsymbol{\Delta}_T^{xy}$ could be induced with an in-plane magnetic field $B_\parallel$, which also transforms as an E'' irrep of the point group. This could explain the previous magnetotransport experiments displaying signatures of a nematic pairing [115, 116]. Another observation in this direction is that the Rashba SOC $\propto (k_x\sigma_y - k_y\sigma_x)\tau_0$ induced by the breaking of the out-of-plane mirror symmetry by a substrate would suppress the A_1' singlet and the A_1' triplet, while not affecting the E'' triplet [306]. However, we will not consider substrate or

in-plane magnetic field effects here.

In summary, assuming $|g_S| > |g_T|$, the ground state is a conventional s-wave spin-singlet superconductor with order parameter given by the usual expression (2.73) at zero temperature. The ground state is described by the following effective action:

$$\mathcal{S}^{(0)}_{\text{eff}}[\bar{\Delta},\Delta] = -\int_x \left[\frac{1}{g_S}\bar{\Delta}_S(x)\Delta_S(x)\right] - \text{Tr}\left[\log G_0^{-1}\right], \tag{2.77}$$

where, choosing a real positive gap $\Delta_S(x) = \Delta$, with $\Delta > 0$ given by Eq. (2.73), the ground state bare inverse Gorkov BdG Green's function is:

$$G_0^{-1}(i\omega_n, \boldsymbol{k}) = i\omega_n \tau_0\sigma_0\rho_0 - \xi(\boldsymbol{k})\tau_0\sigma_0\rho_z - \lambda\tau_z\sigma_z\rho_z + \Delta\tau_x\sigma_y\rho_y. \tag{2.78}$$

Inverting it explicitly,

$$\begin{aligned}
G_0(i\omega_n, \boldsymbol{k}) = &\frac{1}{2}\left[\frac{i\omega_n}{(i\omega_n)^2 - E_+^2(\boldsymbol{k})} + \frac{i\omega_n}{(i\omega_n)^2 - E_-^2(\boldsymbol{k})}\right]\tau_0\sigma_0\rho_0 + \\
&+\frac{1}{2}\left[\frac{\varepsilon_+(\boldsymbol{k})}{(i\omega_n)^2 - E_+^2(\boldsymbol{k})} + \frac{\varepsilon_-(\boldsymbol{k})}{(i\omega_n)^2 - E_-^2(\boldsymbol{k})}\right]\tau_0\sigma_0\rho_z + \\
&+\frac{1}{2}\left[\frac{i\omega_n}{(i\omega_n)^2 - E_+^2(\boldsymbol{k})} - \frac{i\omega_n}{(i\omega_n)^2 - E_-^2(\boldsymbol{k})}\right]\tau_z\sigma_z\rho_0 + \\
&+\frac{1}{2}\left[\frac{\varepsilon_+(\boldsymbol{k})}{(i\omega_n)^2 - E_+^2(\boldsymbol{k})} - \frac{\varepsilon_-(\boldsymbol{k})}{(i\omega_n)^2 - E_-^2(\boldsymbol{k})}\right]\tau_z\sigma_z\rho_z - \\
&-\frac{1}{2}\left[\frac{\Delta}{(i\omega_n)^2 - E_+^2(\boldsymbol{k})} + \frac{\Delta}{(i\omega_n)^2 - E_-^2(\boldsymbol{k})}\right]\tau_x\sigma_y\rho_y - \\
&-\frac{1}{2}\left[\frac{\Delta}{(i\omega_n)^2 - E_+^2(\boldsymbol{k})} - \frac{\Delta}{(i\omega_n)^2 - E_-^2(\boldsymbol{k})}\right]\tau_y\sigma_x\rho_y,
\end{aligned} \tag{2.79}$$

with $E_\pm(\boldsymbol{k}) = \sqrt{\varepsilon_\pm^2(\boldsymbol{k}) + \Delta^2}$. Crucially, since $g_T < 0$ too, the out-of-plane f-wave triplet Δ_T^z is subleading, meaning that it represents a self-consistent solution of the gap equation characterized by a relative minimum in the free-energy functional. This is essential for the collective fluctuations described in the next section.

2.3 Particle-particle collective modes

Particle-particle collective modes in superconductors might occur when there is a subleading attraction in a pairing channel besides the ground state. Our model has an A_1' ground state, which is fully s-wave spin-singlet for constant Ising SOC, and, crucially, an attractive interaction in the f-wave spin-triplet channels. Therefore, in principle, we have two possible collective modes in

our model, defined by the fluctuations toward the imaginary part of the out-of-plane A_1' and the in-plane E'' f-wave triplets. In the absence of singlet-triplet mixing in the ground state, both correspond to Bardasis-Schrieffer collective modes. For the former A_1' mode, the attraction in the triplet channel guarantees that it is well-defined, with energy $\Omega_L < 2\Delta$ [251]. However, due to the Ising SOC suppression of the E'' channel, the E'' mode is likely pushed to higher energies and damped, and therefore unobservable. We note that, for a general singlet-triplet mixed ground state, the former A_1' mode can be better described as a Leggett mode. In this case, the spin-split pockets have gaps in the band basis $\Delta_\pm = \Delta_S \pm \Delta_T^z$, and the collective mode corresponds to the relative phase fluctuation of these two gaps. Henceforth, we refer to the A_1' mode as the Leggett (L) mode and to the E'' mode as the Bardasis-Schrieffer (BS) mode. We note that, in the absence of Ising SOC, where $SU(2)$ spin rotation symmetry is recovered, both modes become the same, since both components of the triplet are degenerate.

From a computational point of view, collective modes are defined whenever their corresponding propagator displays a pole (or strong enough divergence) with vanishing imaginary part at zero temperature. This requires the energy of the collective mode to be below the quasiparticle edge, $\Omega < 2\Delta$. We will show that the Leggett mode fulfills that and is indeed well-defined. We will determine the propagators at the random phase approximation (RPA) level in the long-wavelength limit, by expanding the effective action of (2.60) to quadratic order in the fluctuating fields [233]. The coefficients multiplying these fluctuating fields define their corresponding propagators, whose poles determine the energies of the collective modes. We will also show that the Leggett and Bardasis-Schrieffer modes couple to the fermionic degrees of freedom, modifying their spectral function and therefore leaving signatures detectable in tunneling experiments. We will eventually discuss how an anticorrelation between the mode energy and the superconducting gap, as observed in the STM experiments of Ref. [2], is compatible with the Leggett mode. We therefore propose the Leggett mode as a possible candidate for explaining the resonances in the STM experiments [2], which constitutes a further signature for the subleading f-wave spin-triplet pairing in monolayer $NbSe_2$.

2.3.1 Collective mode energies with constant Ising SOC

In the case of vanishing singlet-triplet mixing with a real positive s-wave singlet gap, the fluctuating bosonic fields ϕ_L and $\boldsymbol{\phi}_{BS}$ correspond to the imaginary parts $\Delta_T^z = i\phi_L$ and $\boldsymbol{\Delta}_T^{xy} = i\boldsymbol{\phi}_{BS}$ of the f-wave spin-triplet pairings. From the Gorkov BdG Green's function (2.63), we obtain that the Leggett and Bardasis-Schrieffer fluctuations couple to the ground state Gorkov BdG Green's

function via the matrices:

$$M_L = \tau_y \sigma_x \rho_x, \tag{2.80}$$

$$\boldsymbol{M}_{BS} = \left(-\tau_y \sigma_z \rho_x, \tau_y \sigma_0 \rho_y\right). \tag{2.81}$$

Note that, since the chosen ground state gap Δ couples to Nambu space via ρ_y, then the ρ_x in M_L and M^x_{BS} indicates that the fluctuations have a $\frac{\pi}{2}$ phase shift with respect to the ground state, as required. M^y_{BS} also has a $\frac{\pi}{2}$ phase shift, but it corresponds to ρ_y due to the additional $-$ sign of Δ^y_T in the Gorkov BdG Green's function (2.63). Now, we expand the total effective action (2.60) to quadratic order in the fluctuating fields Φ_i, $i = L, BS$, obtaining:

$$\mathcal{S}_{\text{eff}}[\Delta, \phi_i] - \mathcal{S}^{(0)}_{\text{eff}}[\Delta] = \int_q D_i^{-1}(q)\phi_i(q)\phi_i(-q), \tag{2.82}$$

where $\mathcal{S}^{(0)}_{\text{eff}}[\Delta]$ is the effective action (2.77) of the ground state with no fluctuating fields, and $D_i^{-1}(q)$ is the inverse propagator of the Leggett ($i = L$) or Bardasis-Schrieffer ($i = BS$) collective mode. This inverse propagator $D_i^{-1}(q)$ is related to the RPA susceptibility $\chi_i(q)$ in the corresponding channel via:

$$D_i^{-1}(q) = -\frac{1}{g_T} + \chi_i(q), \tag{2.83}$$

where the susceptibility is given by:

$$\chi_i(q) = \frac{1}{2}\int_k \text{tr}[G_0(k) M_i G_0(k+q) M_i], \tag{2.84}$$

with $G_0(k)$ the ground state bare Gorkov BdG Green's function (2.79), and M_i the coupling matrices defined in Eqs. (2.80) and (2.81).

Performing the traces, we obtain the following Leggett and Bardasis-Schrieffer susceptibilities:

$$\begin{aligned}\chi_L(i\Omega_m, \boldsymbol{q}) = 2\int_k \Bigg\{ &\frac{i\omega_n(i\Omega_m + i\omega_n) - [\varepsilon_+(\boldsymbol{k})\varepsilon_+(\boldsymbol{k}+\boldsymbol{q}) + \Delta^2]}{[(i\omega_n)^2 - E^2_+(\boldsymbol{k})][(i\omega_n + i\Omega_m)^2 - E^2_+(\boldsymbol{k}+\boldsymbol{q})]} + \\ &+ \frac{i\omega_n(i\Omega_m + i\omega_n) - [\varepsilon_-(\boldsymbol{k})\varepsilon_-(\boldsymbol{k}+\boldsymbol{q}) + \Delta^2]}{[(i\omega_n)^2 - E^2_-(\boldsymbol{k})][(i\omega_n + i\Omega_m)^2 - E^2_-(\boldsymbol{k}+\boldsymbol{q})]} \Bigg\},\end{aligned} \tag{2.85}$$

$$\begin{aligned}\chi_{BS}(i\Omega_m, \boldsymbol{q}) = 2\int_k \Bigg\{ &\frac{i\omega_n(i\Omega_m + i\omega_n) - [\varepsilon_+(\boldsymbol{k})\varepsilon_-(\boldsymbol{k}+\boldsymbol{q}) + \Delta^2]}{[(i\omega_n)^2 - E^2_+(\boldsymbol{k})][(i\omega_n + i\Omega_m)^2 - E^2_-(\boldsymbol{k}+\boldsymbol{q})]} + \\ &+ \frac{i\omega_n(i\Omega_m + i\omega_n) - [\varepsilon_-(\boldsymbol{k})\varepsilon_+(\boldsymbol{k}+\boldsymbol{q}) + \Delta^2]}{[(i\omega_n)^2 - E^2_-(\boldsymbol{k})][(i\omega_n + i\Omega_m)^2 - E^2_+(\boldsymbol{k}+\boldsymbol{q})]} \Bigg\}.\end{aligned} \tag{2.86}$$

First, as expected, in the limit of vanishing Ising SOC, where $\varepsilon_{\pm}(\boldsymbol{k}) \to \xi(\boldsymbol{k})$ and $E_{\pm}(\boldsymbol{k}) \to E(\boldsymbol{k})$, both susceptibilities are identical

$$\chi_0(i\Omega_m, \boldsymbol{q}) = 4 \int_k \frac{i\omega_n(i\Omega_m + i\omega_n) - [\xi(\boldsymbol{k})\xi(\boldsymbol{k}+\boldsymbol{q}) + \Delta^2]}{[(i\omega_n)^2 - E^2(\boldsymbol{k})][(i\omega_n + i\Omega_m)^2 - E^2(\boldsymbol{k}+\boldsymbol{q})]}, \tag{2.87}$$

confirming that the Leggett and Bardasis-Schrieffer modes become degenerate in this case. In the presence of Ising SOC, the Leggett mode to the A_1' triplet has two contributions, one from each spin-split band $\varepsilon_{\pm}$, indicating that it does not mix the bands with opposite SOC splitting. Moreover, we will show that the Leggett mode is unaffected by the constant Ising SOC, and $\chi_L(i\Omega_m, \boldsymbol{q}) = \chi_0(i\Omega_m, \boldsymbol{q})$, implying that its energy is independent of the constant Ising SOC[5]. On the other hand, the Bardasis-Schrieffer mode to the E'' triplet does mix them, as illustrated by the terms mixing ε_+ and ε_-. Consequently, the constant single-particle SOC λ will affect the Bardasis-Schrieffer mode by increasing its energy with respect to the spinless case, while the Leggett mode energy will be independent of λ, as expected.

After performing the sums over the fermionic Matsubara frequency $i\omega_n$, the susceptibilities in the long-wavelength limit $\boldsymbol{q} \to 0$ read as:

$$\begin{aligned}\chi_L(i\Omega_m) = -\int \frac{d^2k}{(2\pi)^2} \Bigg[&\frac{\tanh\left[\frac{\beta}{2}E_+(\boldsymbol{k})\right]}{E_+(\boldsymbol{k})} \left\{1 + \frac{(i\Omega_m)^2}{[2E_+(\boldsymbol{k})]^2 - (i\Omega_m)^2}\right\} + \\ &+ \frac{\tanh\left[\frac{\beta}{2}E_-(\boldsymbol{k})\right]}{E_-(\boldsymbol{k})} \left\{1 + \frac{(i\Omega_m)^2}{[2E_-(\boldsymbol{k})]^2 - (i\Omega_m)^2}\right\} \Bigg],\end{aligned} \tag{2.88}$$

$$\begin{aligned}\chi_{BS}(i\Omega_m) = -\int \frac{d^2k}{(2\pi)^2} \Bigg[&\frac{\tanh\left[\frac{\beta}{2}E_+(\boldsymbol{k})\right]}{E_+(\boldsymbol{k})} \{1 + B_+(i\Omega_m, \boldsymbol{k})\} + \\ &+ \frac{\tanh\left[\frac{\beta}{2}E_-(\boldsymbol{k})\right]}{E_-(\boldsymbol{k})} \{1 + B_-(i\Omega_m, \boldsymbol{k})\} \Bigg],\end{aligned} \tag{2.89}$$

[5]For a $\boldsymbol{k}$-dependent Ising SOC, the superconducting gap is modified due to the singlet-triplet mixing, and thus the energy of the Leggett mode depends on the $\boldsymbol{k}$-dependent part of the Ising SOC (see Appendix 2.B).

where we have defined the quantities:

$$B_+(i\Omega_m,\boldsymbol{k}) = \frac{\left[\varepsilon_+^2-\varepsilon_-^2+(i\Omega_m)^2\right]\left[(\varepsilon_+-\varepsilon_-)^2-(i\Omega_m)^2\right]}{[i\Omega_m+E_++E_-][i\Omega_m+E_+-E_-][i\Omega_m-E_++E_-][i\Omega_m-E_+-E_-]}, \tag{2.90}$$

$$B_-(i\Omega_m,\boldsymbol{k}) = \frac{\left[\varepsilon_-^2-\varepsilon_+^2+(i\Omega_m)^2\right]\left[(\varepsilon_+-\varepsilon_-)^2-(i\Omega_m)^2\right]}{[i\Omega_m+E_++E_-][i\Omega_m+E_+-E_-][i\Omega_m-E_++E_-][i\Omega_m-E_+-E_-]}, \tag{2.91}$$

We have omitted the explicit $\boldsymbol{k}$-dependence of the energies for simplicity. Note that, in the limit of vanishing SOC, $B_\pm(i\Omega_m,\boldsymbol{k}) \to \frac{(i\Omega_m)^2}{[2E(\boldsymbol{k})]^2-(i\Omega_m)^2}$. Using the gap equation (2.76) and defining the following functions:

$$F_L^\pm(i\Omega_m) = \frac{1}{N_0}\int\frac{d^2k}{(2\pi)^2}\frac{\tanh\left[\frac{\beta}{2}E_\pm(\boldsymbol{k})\right]}{E_\pm(\boldsymbol{k})}\frac{(i\Omega_m)^2}{[2E_\pm(\boldsymbol{k})]^2-(i\Omega_m)^2}, \tag{2.92}$$

$$F_{BS}^\pm(i\Omega_m) = \frac{1}{N_0}\int\frac{d^2k}{(2\pi)^2}\frac{\tanh\left[\frac{\beta}{2}E_\pm(\boldsymbol{k})\right]}{E_\pm(\boldsymbol{k})}B_\pm(i\Omega_m,\boldsymbol{k}), \tag{2.93}$$

$$F_i(i\Omega_m) = F_i^+(i\Omega_m)+F_i^-(i\Omega_m), \tag{2.94}$$

we obtain the following collective mode propagators:

$$D_i^{-1}(i\Omega_m) = -\frac{1}{g_T}+\frac{1}{g_S}-N_0F_i(i\Omega_m) = N_0\left\{\left(\frac{1}{|\bar{g}_T|}-\frac{1}{|\bar{g}_S|}\right)-F_i(i\Omega_m)\right\}, \tag{2.95}$$

where we have used the assumption $g_S, g_T < 0$. The collective mode energies are given by the solution Ω_i of:

$$D_i^{-1}\left(i\Omega_m\to\Omega_i+i0^+\right)=0 \Rightarrow F_i\left(\Omega_i\right)=\left(\frac{1}{|\bar{g}_T|}-\frac{1}{|\bar{g}_S|}\right). \tag{2.96}$$

We will first consider the zero-temperature limit of the momentum integrations in $F_{i\pm}(\Omega)$, where $\tanh\left[\frac{\beta}{2}E_\pm(\boldsymbol{k})\right]\to 1$. We define the dimensionless energy of the collective mode $\bar{\Omega}_i$ as its energy normalized by twice the superconducting gap

$$\bar{\Omega}_i = \frac{\Omega_i}{2\Delta}. \tag{2.97}$$

When $\bar{\Omega}_i < 1$ the collective mode is undamped due to the absence of a quasiparticle decay channel, while for $\bar{\Omega}_i > 1$ damping becomes possible.

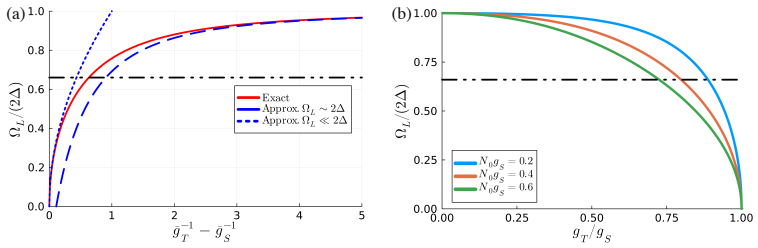

FIGURE 10: Normalized energy of the Leggett mode $\bar{\Omega}_L = \frac{\Omega_L}{2\Delta}$ at zero temperature. (a) As a function of the difference $\left(|\bar{g}_T|^{-1} - |\bar{g}_S|^{-1}\right)$. The red solid line corresponds to the exact numerical solution of Eq. (2.99), while the blue dotted and dashed lines are the approximate analytical expressions given in Eq. (2.100). (b) As a function of the ratio of triplet-to-singlet attraction g_T/g_S, for several values of the attraction in the s-wave singlet channel g_S. The horizontal black dashed-dotted lines indicates the experimental expectation value $\frac{\Omega_1}{2\Delta} = 0.66$ of the resonance observed in STM in Ref. [2].

Leggett mode energy at zero temperature

First, we compute the energy of the Leggett mode. The functions $F_{L\pm}(\Omega)$ relevant for this mode can be computed analytically by changing variables to $x = \varepsilon_\pm/\Delta$:

$$F_L(\Omega) = \frac{1}{2}\int_{-\infty}^{\infty} dx \frac{1}{\sqrt{1+x^2}} \frac{\bar{\Omega}^2}{1+x^2-\bar{\Omega}^2} = \begin{cases} \frac{\bar{\Omega}\arcsin(\bar{\Omega})}{\sqrt{1-\bar{\Omega}^2}} & , \text{if } |\bar{\Omega}| < 1, \\ \frac{|\bar{\Omega}|\left[-\text{argsinh}\left(\sqrt{\bar{\Omega}^2-1}\right)+i\frac{\pi}{2}\text{sign}(\bar{\Omega})\right]}{\sqrt{\bar{\Omega}^2-1}} & , \text{if } |\bar{\Omega}| > 1. \end{cases} \tag{2.98}$$

Note that the integral converges, so we do not need to invoke a high-energy cutoff. For $g_S < g_T < 0$, $-\frac{1}{g_T} + \frac{1}{g_S} = \frac{1}{|g_T|} - \frac{1}{|g_S|} > 0$, and thus the only solution of the real part of Eq. (2.96) lies in the region $\Omega_L < 2\Delta$, where the Leggett mode is undamped. Therefore, the energy of the Leggett mode is the solution of:

$$\left(\frac{1}{|\bar{g}_T|} - \frac{1}{|\bar{g}_S|}\right) = \frac{\bar{\Omega}_L \arcsin(\bar{\Omega}_L)}{\sqrt{1-(\bar{\Omega}_L)^2}}. \tag{2.99}$$

The exact numerical solution for $\bar{\Omega}_L$ is plotted in Fig. 10(a) as a function of the combination of the couplings $\left(|\bar{g}_T|^{-1} - |\bar{g}_S|^{-1}\right)$, and in Fig. 10(b) as a function of the triplet-to-singlet ratio g_T/g_S. Analytically, we can obtain the energy in the limits of small energy, where $|\Omega_L| \ll 2\Delta$ and $\left(|\bar{g}_T|^{-1} - |\bar{g}_S|^{-1}\right) \ll 1$, and large energy, where $|\Omega_L| \sim 2\Delta$ and $\left(|\bar{g}_T|^{-1} - |\bar{g}_S|^{-1}\right) \gg 1$ [233]:

$$\bar{\Omega}_L \simeq \begin{cases} \sqrt{\frac{1}{|\bar{g}_T|} - \frac{1}{|\bar{g}_S|}} & , \text{if } |\bar{\Omega}_L| \ll 1, \\ 1 - \frac{\pi^2}{8[1+(|\bar{g}_T|^{-1}-|\bar{g}_S|^{-1})]^2} & , \text{if } |\bar{\Omega}_L| \sim 1. \end{cases} \tag{2.100}$$

The Leggett mode energy is $\Omega_L < 2\Delta$ as long as there is attraction in the out-of-plane f-wave

triplet channel, $g_T < 0$. When this attraction goes to zero ($g_T \to 0 \Rightarrow \frac{1}{|\bar{g}_T|} - \frac{1}{|\bar{g}_S|} \to \infty$), Ω_L approaches the quasiparticle edge 2Δ, and becomes ill-defined for $g_T > 0$[6]. In the opposite limit, when $g_T \to g_S$, the Leggett mode becomes gapless, signaling the degenerate singlet and out-of-plane triplet channels in the $g_T = g_S$ limit. For $g_T < g_S < 0$, the out-of-plane triplet becomes the ground state, and the Leggett mode would consist of the imaginary fluctuation towards the s-wave singlet.

It is insightful to compare the energy of the Leggett mode with that of the resonance observed in the STM experiments of our collaborators [2]. Assuming that the resonance is indeed a manifestation of the Leggett mode, from the experimentally measured average value of $\frac{\Omega_L}{2\Delta} = 0.66$ we can estimate the ratio g_T/g_S and hence how close the triplet state is. This first requires an estimate of the dimensionless coupling $\bar{g}_S = N_0 g_S$. Using our weak coupling BCS limit with a superconducting gap of $\Delta \sim 0.4$meV and a Debye frequency cutoff in the range of bulk estimates $\Lambda \sim 20$meV [333], this corresponds to $\bar{g}_S \sim 0.2$. However, the ratio $2\Delta/k_B T_c \sim 4.9$ in our experiment indicates moderate to strong coupling, so the value of $\bar{g}_S$ is likely larger. From the energy of the Leggett mode $\bar{\Omega}_L$ as a function of g_T/g_S for $\bar{g}_T = 0.2 - 0.6$ displayed Fig. 10(b), we can estimate that setting $\bar{\Omega}_L \sim 0.66$ produces a sizable triplet attraction in the range $g_T/g_S \sim 0.7 - 0.9$.

Bardasis-Schrieffer mode at zero temperature

We now turn to the Bardasis-Schrieffer mode. We have not been able to obtain analytical expressions for the functions $F_{BS\pm}(\Omega)$ relevant for the Bardasis-Schrieffer mode for a general Ising SOC λ. Nevertheless, based on the suppression of the E'' triplet pairing by the Ising SOC (in the absence of Rashba SOC), we expect a damped Bardasis-Schrieffer mode with energy $\Omega_{BS} > 2\Delta$, i.e., an ill-defined mode. What we can compute analytically is the series expansion of $F_{BS\pm}(\Omega)$ in small $\lambda/\Delta \ll 1$. Indeed, after the change of variables $\boldsymbol{k} \to x = \xi(\boldsymbol{k})/\Delta$, we obtain:

$$\begin{aligned} F_{BS\pm}(\Omega) &= -\frac{1}{4}\int_{-\infty}^{\infty} dx \frac{1}{\sqrt{1+\left(x \pm \frac{\lambda}{\Delta}\right)^2}} \frac{\left(\bar{\Omega}^2 \pm x\frac{\lambda}{\Delta}\right)\left(\bar{\Omega}^2 - \frac{\lambda^2}{\Delta^2}\right)}{\bar{\Omega}^4 - \bar{\Omega}^2\left(1 + x^2 + \frac{\lambda^2}{\Delta^2}\right) + x^2\frac{\lambda^2}{\Delta^2}} = \\ &= \frac{1}{2}\left\{F_L(\Omega) + \frac{1}{2}\left(\frac{\lambda}{\Delta}\right)^2 \frac{1}{\bar{\Omega}^2 - 1}\left[1 + \frac{F_L(\Omega)}{\bar{\Omega}^2}\right] + \mathcal{O}\left[\left(\frac{\lambda}{\Delta}\right)^4\right]\right\}. \end{aligned} \tag{2.101}$$

[6] Indeed, our whole theory breaks down in the $g_T > 0$ regime, since the Hubbard-Stratonovich transformation in the triplet channel is only valid for attractive g_T

Despite not representing the experimentally relevant situation, this approximation predicts the expected increase of the energy of the Bardasis-Schrieffer mode with the Ising SOC:

$$\bar{\Omega}_{BS} \simeq \begin{cases} \sqrt{\left(\bar{\Omega}_L\right)^2 + \left(\frac{\lambda}{\Delta}\right)^2 + \mathcal{O}\left[\left(\frac{\lambda}{\Delta}\right)^4, \left(\frac{\lambda}{\Delta}\right)^2 \left(\bar{\Omega}_L\right)^2\right]} & \text{, when } |\bar{\Omega}_{BS}| \ll 1, \\ \bar{\Omega}_L + \frac{1}{2}\left(\frac{\lambda}{\Delta}\right)^2 + \mathcal{O}\left[\left(\frac{\lambda}{\Delta}\right)^3, \left(\frac{\lambda}{\Delta}\right)^2 \left(1 - \bar{\Omega}_L\right)\right] & \text{, when } |\bar{\Omega}_{BS}| \sim 1. \end{cases} \tag{2.102}$$

Leggett mode at low temperature

Going back to the Leggett mode, we now estimate the temperature dependence of its energy in the $T \ll \Delta$ limit, with Δ the zero temperature gap. We will show that, as long as the temperature is low, the energy of the Leggett mode is only slightly shifted upwards, with the same exponential temperature dependence $\sim e^{-\beta\Delta}$ as the gap. This increase of the normalized energy with temperature is expected, since the collective mode should be overdamped (i.e., $\Omega_1 \geq 2\Delta$) at the critical temperature [233]. Moreover, we would expect that it becomes overdamped at a lower temperature, corresponding to the critical temperature where the out-of-plane f-wave triplet pairing would condense in the absence of s-wave singlet. Indeed, this temperature sets the onset of a relative minimum for the out-of-plane f-wave triplet solution in the free-energy functional.

We first determine the temperature dependence of the gap. Assuming also that $T \ll \Delta(T)$, then we can make the following approximation to leading order in temperature:

$$\tanh\left[\frac{\beta\Delta(T)}{2}\sqrt{x^2+1}\right] \simeq 1 - 2\exp\left(-\beta\Delta\sqrt{x^2+1}\right). \tag{2.103}$$

Then, the solution of the gap equation (2.76) gives the usual exponentially small correction to the gap at low temperatures:

$$\Delta(T) \simeq \left(1 - e^{-\beta\Delta}\sqrt{\frac{2\pi}{\beta\Delta}}\right)\Delta. \tag{2.104}$$

We now derive the temperature dependence of the Leggett mode energy. After the change of variables $x = \xi(\boldsymbol{k})/\Delta(T)$, we obtain that F_L takes on the form:

$$\begin{aligned} F_L(\Omega, T) &= \frac{1}{2}\int_{-\infty}^{\infty} dx \frac{1}{x^2 + 1 - \bar{\Omega}^2} \frac{\tanh\left[\frac{\beta\Delta(T)}{2}\sqrt{x^2+1}\right]}{\sqrt{x^2+1}} \simeq \\ &\simeq F_L(\Omega) - \int_{-\infty}^{\infty} dx \frac{1}{x^2 + 1 - \bar{\Omega}^2} \frac{\exp\left(-\beta\Delta\sqrt{x^2+1}\right)}{\sqrt{x^2+1}}. \end{aligned} \tag{2.105}$$

While the last integration cannot be performed analytically, we can deduce that its temperature dependence will be exponential, as in the case of the gap. Indeed, we can estimate it to be:

$$F_L(\Omega, T) \simeq F_L(\Omega)\left[1 - 2\gamma(\Omega)e^{-\beta\Delta}\right], \tag{2.106}$$

where $\gamma(\Omega)$ is a positive function of Ω of order 1. We mention here that $\gamma(\Omega)$ might also be slightly temperature dependent, but its temperature dependence is polynomial at most. Therefore, the inverse propagator of the Leggett mode at small T gets a exponential temperature correction:

$$D_L^{-1}(\Omega) = N_0\left\{\left(\frac{1}{|\bar{g}_T|} - \frac{1}{|\bar{g}_S|}\right) - F_L(\Omega)\left[1 - 2\gamma(\Omega)e^{-\beta\Delta}\right]\right\}, \tag{2.107}$$

This positive correction increases the dimensionless Leggett mode energy $\bar{\Omega}_L(T) = \frac{\Omega_L(T)}{2\Delta(T)}$, as expected. Indeed, since $\bar{\Omega}_L(T)$ will be exponentially similar to $\bar{\Omega}_L(T=0)$, to leading order in temperature we can write that $\gamma\left[\Omega_L(T)\right]e^{-\beta\Delta} \simeq \gamma_L e^{-\beta\Delta}$, where we have defined $\gamma_L = \gamma\left[\Omega_L(T=0)\right] \sim 1$. Therefore $\bar{\Omega}_L(T)$ can be obtained from $\bar{\Omega}_L(T=0)$ simply rescaling $\left(|\bar{g}_T|^{-1} - |\bar{g}_S|^{-1}\right)$ to $\left(|\bar{g}_T|^{-1} - |\bar{g}_S|^{-1}\right)\left(1 + 2\gamma_L e^{-\beta\Delta}\right)$, i.e.,

$$\bar{\Omega}_L\left[T, \left(\frac{1}{|\bar{g}_T|} - \frac{1}{|\bar{g}_S|}\right)\right] = \bar{\Omega}_L\left[T=0, \left(\frac{1}{|\bar{g}_T|} - \frac{1}{|\bar{g}_S|}\right)\left(1 + 2\gamma_L e^{-\beta\Delta}\right)\right]. \tag{2.108}$$

The same argument would apply to the energy of the Bardasis-Schrieffer mode in the case of small Ising SOC, and therefore its normalized energy would also be exponentially increased by temperature in the $T \ll \Delta$ limit.

2.3.2 Tunneling current and coupling to the fermionic self-energy

Until now, we have determined that, in the presence of constant Ising SOC, the Leggett mode consisting of the fluctuation from the s-wave spin-singlet ground state to the out-of-plane f-wave spin-triplet subleading channel is well-defined with energy $\Omega_L < 2\Delta$ given by Eq. (2.99) and displayed in Fig. 10. The pertinent question to determine whether the Leggett mode might explain the STM experiment [2] is whether it couples to the electron spectral function, which is the quantity measured in tunneling experiments. Most works to date have attributed satellite peaks to particle-hole excitations like spin waves, which become undamped in the presence of superconductivity due to the gap opening and consequent decrease of the possible decay channels. However, we now show that particle-particle collective modes, and in particular the Leggett and the Bardasis-Schrieffer modes, should also leave fingerprints in the spectral function, in particular peaks at the energies $\Delta + \Omega_i$. This is consistent with the paradigmatic two-band superconductor MgB_2, where the Leggett mode has been observed in Raman [266] and terahertz spectroscopy [267], and a signature at the same energies also appears in ARPES [263] and tunneling experiments [334].

We now present a simplified calculation along the lines of Ref. [335] to show how coupling to a particle-particle collective mode leads to peaks in the STM tunneling current.

Collective mode propagator

Bosonic excitations have elastic and inelastic contributions to the tunneling spectrum [336, 337]. The elastic contribution describes the self-energy corrections to the fermionic spectral function due to the exchange of virtual bosons, in a process that conserves the energy of the electron. The inelastic contribution refers to the excitation of real bosons in the tunneling process, changing the energy of the electron. Both leave features in the tunneling current of superconductors, with the elastic part producing more peak-like features, and the inelastic part giving rise to more onset-like shoulder-dip features. The inelastic contribution is sizable when tunneling is effective at all momenta, since there is a large phase space for the boson in tunneling [336, 337]. Conversely, the inelastic tunneling contribution can be neglected when tunneling is dominated by small momenta. The peak-like shape of the resonances observed in the STM experiment [2], as well as the fact that a dominant tunneling selectivity at small momenta is required to reproduce the normal state tunneling [309], suggest that it is the elastic contribution that dominates in monolayer $NbSe_2$. Therefore, we will not consider the inelastic contribution in this work, and will only determine the elastic renormalization of the fermionic spectral function by the Leggett and Bardasis-Schrieffer modes following the lines of Ref. [335].

The bare Gorkov BdG Green's function unrenormalized by the boson is given in Eq. (2.79). On the other hand, in the previous subsection we have obtained the collective mode propagator at zero momentum to be:

$$D_i^{-1}(i\Omega_m) = N_0 \left[\left(\frac{1}{|\bar{g}_T|} - \frac{1}{|\bar{g}_S|} \right) - F_i(i\Omega_m) \right] = N_0 \left[F_i\left(\Omega_i\right) - F_i(i\Omega_m) \right], \tag{2.109}$$

where we have used the fact that $D_i^{-1}(i\Omega_m \to \Omega_i + i0^+) = 0$. In order to simplify the calculations, we expand the propagator about its poles at $i\Omega = \pm\Omega_i$ to leading order:

$$D_i(i\Omega_m) \simeq \frac{Z_i}{\left(\Omega_i\right)^2 - (i\Omega_m)^2}, \tag{2.110}$$

where we have defined the residues of the Leggett and Bardasis-Schrieffer propagators

$$Z_L = \frac{8\Delta^2}{N_0}\frac{1-\left(\bar{\Omega}_{1L}\right)^2}{1+\frac{\left(|\bar{g}_T|^{-1}-|\bar{g}_S|^{-1}\right)}{\left(\bar{\Omega}_{1L}\right)^2}}, \tag{2.111}$$

$$Z_{BS} \simeq \frac{8\Delta^2}{N_0}\left\{\frac{1-\left(\bar{\Omega}_{1BS}\right)^2}{1+\frac{\left(|\bar{g}_T|^{-1}-|\bar{g}_S|^{-1}\right)}{\left(\bar{\Omega}_{1BS}\right)^2}}+ \right. \\ \left. +\left[1-\frac{\left(|\bar{g}_T|^{-1}-|\bar{g}_S|^{-1}\right)\left[1+\left(|\bar{g}_T|^{-1}-|\bar{g}_S|^{-1}\right)\right]}{\left[\left(|\bar{g}_T|^{-1}-|\bar{g}_S|^{-1}\right)+\left(\bar{\Omega}_{1BS}\right)^2\right]^2}\right]\left(\frac{\lambda}{\Delta}\right)^2+\mathcal{O}\left[\left(\frac{\lambda}{\Delta}\right)^4\right]\right\}, \tag{2.112}$$

where we have applied the low SOC λ/Δ expansion to the Bardasis-Schrieffer mode. We observe that the residues of the propagators scale with Δ^2, reflecting that the weights of these bosons are suppressed as $\Delta \to 0$. Moreover, the dimensionless function $\frac{N_0 Z_L}{4\Delta^2}$, which is only a function of $\bar{\Omega}_L$,

$$\frac{N_0 Z_L}{4\Delta^2} = 2\frac{1-\bar{\Omega}_L^2}{1+\frac{\arcsin\left(\bar{\Omega}_L\right)}{\bar{\Omega}_L\sqrt{1-\bar{\Omega}_L^2}}}, \tag{2.113}$$

varies from 1 for $\bar{\Omega}_L = 0$, to 0 for $\bar{\Omega}_L = 1$, indicating that the weight of the propagator is greater the smaller $\bar{\Omega}_L$, or, equivalently, the greater the triplet attraction.

Boson-fermion effective action and fermionic self-energy

Particle-particle collective modes are formed by the fermions, glued by their interactions. The renormalizations of the fermionic spectral function due to these collective modes should therefore be fully included by solving the microscopic model of interacting fermions. Here, we take a simplified approach inspired by the spin-fermion model [338]. We assume that the collective mode is an efficient independent bosonic degree of freedom at low energies, which couples to the low-energy fermions. Despite this approximation, we expect that the qualitative features, and particularly the fact that the Leggett mode renormalizes the fermionic spectral function, still apply. We therefore propose the following phenomenological action coupling the fermions Ψ to the collective boson ϕ_i in Nambu space, which can be thought of as integrating out the high-energy fermionic degrees of freedom from action (2.58):

$$\mathcal{S} = -\frac{1}{2}\int_k \Psi^\dagger(k)G_0^{-1}(k)\Psi(k) + \int_q \phi_i(q)D^{-1}(q)\phi_i(-q) - \frac{\alpha_i}{\sqrt{2}}\int_k\int_q \Psi^\dagger(k)\phi_i(q)M_i\Psi(k+q), \tag{2.114}$$

where the matrices M_i via which the Leggett and Bardasis-Schrieffer modes couple to the fermions were defined in Eqs. (2.80)-(2.81). The coupling strengths α_i should be computed from the microscopic interacting fermion model, and it will depend on the interaction g_T. Here, we take it as a parameter.

The coupling of the fermions to the collective mode induces a quasiparticle self-energy[7] $\Xi(i\omega_n)$, which consists of a normal part $\tilde{\Sigma}(i\omega_n)$ in the ρ_0 channel including lifetime effects, and an anomalous part $\tilde{\Phi}(i\omega_n)$ in the ρ_y channel modeling the effect of superconducting pairing. To one loop, the self-energy reads:

$$\begin{aligned}\Xi_i(i\omega_n) = \quad &\overset{k-p}{\overset{\frown}{\underset{k \qquad p \qquad k}{\rightarrow\!\bullet\!\rightarrow}}} \quad = \alpha_i^2 \int_p M_i G_0(p) M_i D_i(k-p) = \\ &= \alpha_i^2 \frac{1}{\beta} \sum_{i\nu_m} \int \frac{d^2p}{(2\pi)^2} M_i G_0(i\nu_m, \boldsymbol{p}) M_i D_i(i\omega_n - i\nu_m).\end{aligned} \tag{2.115}$$

As we will see below, we can parametrize this self-energy as:

$$\Xi_i(i\omega_n) = \tilde{\Sigma}_i(i\omega_n)\tau_0\sigma_0\rho_0 + \tilde{\Phi}_i(i\omega_n)\tau_x\sigma_y\rho_y. \tag{2.116}$$

Therefore, the renormalized inverse Green's function becomes:

$$\begin{aligned}G_i^{-1}(i\omega_n, \boldsymbol{k}) &= G_0^{-1}(i\omega_n, \boldsymbol{k}) + \Xi_i(i\omega_n) = \\ &= \Sigma_i(i\omega_n)\tau_0\sigma_0\rho_0 - \xi(\boldsymbol{k})\tau_0\sigma_0\rho_z - \lambda\tau_z\sigma_z\rho_z + \Phi_i(i\omega_n)\tau_x\sigma_y\rho_y,\end{aligned} \tag{2.117}$$

where, for convenience, we have redefined Σ_i and Φ_i by introducing the frequency $i\omega_n$ and the gap Δ, respectively, i.e.:

$$\Sigma_i(i\omega_n) = i\omega_n + \tilde{\Sigma}_i(i\omega_n), \tag{2.118}$$

$$\Phi_i(i\omega_n) = \Delta + \tilde{\Phi}_i(i\omega_n). \tag{2.119}$$

[7] Due to our assumption of a non-dispersive boson propagator, the self-energy is also momentum-independent

Thus, we arrive at the following renormalized Matsubara Green's function:

$$\begin{aligned}
G_i(i\omega_n,\boldsymbol{k}) = &\frac{1}{2}\left[\frac{\Sigma_i(i\omega_n)}{\Sigma_i(i\omega_n)^2-\Phi_i(i\omega_n)^2-\varepsilon_+^2(\boldsymbol{k})}+\frac{\Sigma_i(i\omega_n)}{\Sigma_i(i\omega_n)^2-\Phi_i(i\omega_n)^2-\varepsilon_-^2(\boldsymbol{k})}\right]\tau_0\sigma_0\rho_0+\\
&+\frac{1}{2}\left[\frac{\varepsilon_+(\boldsymbol{k})}{\Sigma_i(i\omega_n)^2-\Phi_i(i\omega_n)^2-\varepsilon_+^2(\boldsymbol{k})}+\frac{\varepsilon_-(\boldsymbol{k})}{\Sigma_i(i\omega_n)^2-\Phi_i(i\omega_n)^2-\varepsilon_-^2(\boldsymbol{k})}\right]\tau_0\sigma_0\rho_z+\\
&+\frac{1}{2}\left[\frac{\Sigma_i(i\omega_n)}{\Sigma_i(i\omega_n)^2-\Phi_i(i\omega_n)^2-\varepsilon_+^2(\boldsymbol{k})}-\frac{\Sigma_i(i\omega_n)}{\Sigma_i(i\omega_n)^2-\Phi_i(i\omega_n)^2-\varepsilon_-^2(\boldsymbol{k})}\right]\tau_z\sigma_z\rho_0+\\
&+\frac{1}{2}\left[\frac{\varepsilon_+(\boldsymbol{k})}{\Sigma_i(i\omega_n)^2-\Phi_i(i\omega_n)^2-\varepsilon_+^2(\boldsymbol{k})}-\frac{\varepsilon_-(\boldsymbol{k})}{\Sigma_i(i\omega_n)^2-\Phi_i(i\omega_n)^2-\varepsilon_-^2(\boldsymbol{k})}\right]\tau_z\sigma_z\rho_z-\\
&-\frac{1}{2}\left[\frac{\Phi_i(i\omega_n)}{\Sigma_i(i\omega_n)^2-\Phi_i(i\omega_n)^2-\varepsilon_+^2(\boldsymbol{k})}+\frac{\Phi_i(i\omega_n)}{\Sigma_i(i\omega_n)^2-\Phi_i(i\omega_n)^2-\varepsilon_-^2(\boldsymbol{k})}\right]\tau_x\sigma_y\rho_y-\\
&-\frac{1}{2}\left[\frac{\Phi_i(i\omega_n)}{\Sigma_i(i\omega_n)^2-\Phi_i(i\omega_n)^2-\varepsilon_+^2(\boldsymbol{k})}-\frac{\Phi_i(i\omega_n)}{\Sigma_i(i\omega_n)^2-\Phi_i(i\omega_n)^2-\varepsilon_-^2(\boldsymbol{k})}\right]\tau_y\sigma_x\rho_y.
\end{aligned} \tag{2.120}$$

Tunneling DOS: general case

To obtain the tunneling DOS $N_i(\omega)$, we first define the integration over momenta of the spectral function $A_i(\omega)$:

$$A_i(\omega) = -\frac{1}{\pi}\int\frac{d^2k}{(2\pi)^2}G_i''(i\omega_n\to\omega+i0^+,\boldsymbol{k}), \tag{2.121}$$

where $f''(x) = \mathrm{Im}\,[f(x)]$. $N_i(\omega)$ is then obtained from the upper left block $(\rho_0+\rho_z)$ as

$$N_i(\omega) = \mathrm{tr}\left[\left(\frac{\rho_0+\rho_z}{2}\right)A_i(\omega)\right]. \tag{2.122}$$

Transforming the momentum integration into an energy integration, $\int\frac{d^2k}{(2\pi)^2}\to\frac{N_0}{4}\int_{-\infty}^{\infty}d\varepsilon_\pm$, we obtain the general expression

$$N_i(\omega) = N_0\mathrm{Im}\left[\frac{\Sigma_i(\omega)}{\sqrt{\Phi_i(\omega)^2-\Sigma_i(\omega)^2}}\right]. \tag{2.123}$$

Tunneling DOS: bare case without collective modes

In the bare case without the boson renormalization ($\Sigma_i(\omega)=\omega+i\delta$, $\Phi_i(\omega)=\Delta$) we find:

$$A_0(\omega) = \frac{N_0}{4}\left[\frac{|\omega|}{\sqrt{\omega^2-\Delta^2}}\tau_0\sigma_0\rho_0-\frac{\Delta\mathrm{sign}(\omega)}{\sqrt{\omega^2-\Delta^2}}\tau_x\sigma_y\rho_y\right]\Theta(\omega^2-\Delta^2), \tag{2.124}$$

where $\Theta(x)$ is the Heaviside step function, and thus we obtain

$$N_0(\omega) = N_0 \frac{|\omega|}{\sqrt{\omega^2 - \Delta^2}} \Theta(\omega^2 - \Delta^2), \tag{2.125}$$

so the DOS is zero for $\omega < \Delta$, displays the usual square-root-singular coherence peak at $\omega = \Delta$, and decays to the normal DOS at large ω (see the dashed blue line in Fig. 11).

Tunneling DOS: effect of the Leggett or Bardasis-Schrieffer mode

Extra structure in the ω dependence of the DOS can appear when there is structure in $\Sigma_i(\omega)$ and $\Phi_i(\omega)$. Now, we will show that, in the presence of a boson with gap Ω_i, both self energies develop a singularity at $\omega = \Delta + \Omega_i$, when fermionic quasiparticles can decay into the boson. In particular, we compute the self-energy to one loop in order to derive the renormalized DOS. Applying the spectral representation to the Matsubara Green's functions of both electrons and bosons, and performing the sum over Matsubara frequencies using the standard procedure, the imaginary part of the self-energy can be written as:

$$\Xi_i''(\omega) = \alpha_i^2 \int_{-\infty}^{\infty} d\epsilon M_i A_0(\epsilon) M_i D_i''(\omega - \epsilon) \left[1 + n_B(\omega - \epsilon) - n_F(\epsilon)\right], \tag{2.126}$$

where n_B and n_F are the Bose-Einstein and Fermi-Dirac distribution functions, respectively.

Now, substituting the particular form of the approximate boson propagator that we are considering, $D_i''(\epsilon) = \frac{\pi Z_i}{2\Omega_i} \left[\delta(\epsilon - \Omega_i) - \delta(\epsilon + \Omega_i)\right]$, the imaginary part of the self-energy becomes:

$$\begin{aligned} \Xi_i''(\omega) = \frac{\pi \alpha_i^2 Z_i}{2\Omega_i} M_i \{ & A_0(\omega - \Omega_i) \left[n_B(\Omega_i) + 1 - n_F(\omega - \Omega_i)\right] + \\ & + A_0(\omega + \Omega_i) \left[n_B(\Omega_i) + n_F(\omega + \Omega_i)\right] \} M_i. \end{aligned} \tag{2.127}$$

At zero temperature, the previous expression simplifies to:

$$\Xi_i''(\omega) = \frac{\pi \alpha_i^2 Z_i}{2\Omega_i} M_i \left\{ A_0(\omega - \Omega_i) \Theta(\omega - \Omega_i) + A_0(\omega + \Omega_i) \Theta(-\omega - \Omega_i) \right\} M_i, \tag{2.128}$$

and we see that in this approximation the self-energy simply gets at copy of $A_0(\omega)$ shifted by Ω_i. For $\omega > 0$, this further reduces to:

$$\begin{aligned} \Xi_i''(\omega > 0) = & \frac{\pi \alpha_i^2 Z_i N_0}{8\Omega_i} \Theta(\omega - \Delta - \Omega_i) \cdot \\ & \cdot \left[\frac{|\omega - \Omega_i|}{\sqrt{(\omega - \Omega_i)^2 - \Delta^2}} \tau_0 \sigma_0 \rho_0 + \frac{\Delta}{\sqrt{(\omega - \Omega_i)^2 - \Delta^2}} \tau_x \sigma_y \rho_y \right]. \end{aligned} \tag{2.129}$$

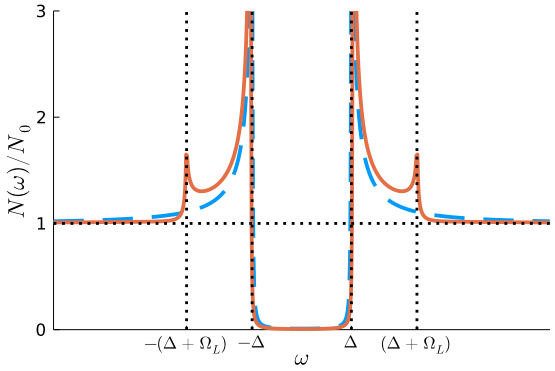

FIGURE 11: Density of states as a function of energy in the superconducting state. Blue dashed line: bare DOS $N_0(\omega)$ without coupling to the Leggett mode (2.125). Red solid line: DOS renormalized by the Leggett mode to first order computed using Eqs. (2.123), (2.130), (2.131). We have used a coupling $\alpha_L^2 = \frac{16\Omega_L}{\pi Z_L N_0^2}$, and we have added a finite broadening via a constant imaginary part $\eta = 10^{-2}\Delta$ in the frequency, $\omega \to \omega + i\eta$.

Therefore, the zero-temperature imaginary parts of the normal and anomalous self-energies read as:

$$\tilde{\Sigma}_i''(\omega > 0) = \frac{\pi\alpha_i^2 Z_i N_0}{8\Omega_i} \frac{|\omega - \Omega_i|}{\sqrt{(\omega - \Omega_i)^2 - \Delta^2}} \Theta(\omega - \Delta - \Omega_i), \tag{2.130}$$

$$\tilde{\Phi}_i''(\omega > 0) = \frac{\pi\alpha_i^2 Z_i N_0}{8\Omega_i} \frac{\Delta}{\sqrt{(\omega - \Omega_i)^2 - \Delta^2}} \Theta(\omega - \Delta - \Omega_i). \tag{2.131}$$

The nonzero imaginary part of the self-energy means that there is a finite lifetime due to the coupling to the boson. In particular, the imaginary part of both the normal $\tilde{\Sigma}_i''(\omega)$ and the anomalous $\tilde{\Phi}_i''(\omega)$ self-energies have a square-root singularity at $|\omega| = \Delta + \Omega_1$, and are zero below it. By the Kramers-Kronig relation, the real parts must also display the same singularity.

We can then go back to Eq. (2.123) to compute the DOS, and the peaks in the self-energies will lead to a peak in the DOS at $\Delta + \Omega_i$. Despite the different matrix structure of our problem, the analytical expressions for the self-energy we have obtained are exactly the same as in Ref. [335], and therefore the functional form of $N(\omega)$ is that of Fig. 13(a) of Ref. [335], displaying the mentioned peak at $\Delta + \Omega_i$, as we also show in Fig. 11. When computing the self-energy to higher orders, further satellites at $|\omega| = \Delta + n\Omega_i$ are expected to appear in the DOS.

2.3.3 Comparison with the STM resonances

The Leggett mode, which for constant Ising SOC corresponds to the fluctuation from the s-wave spin-singlet ground state to the out-of-plane f-wave spin-triplet subleading channel, is

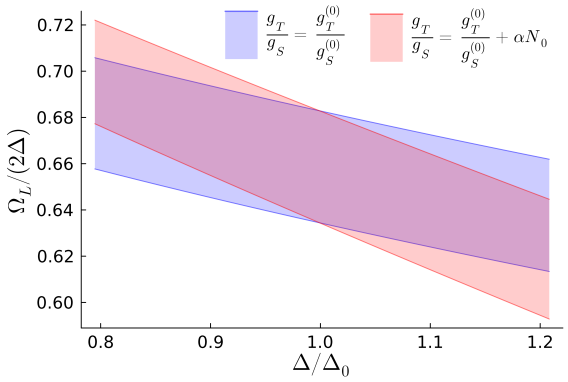

FIGURE 12: Allowed values of the energy of the Leggett mode $\bar{\Omega}_L = \frac{\Omega_L}{2\Delta}$ as a function of the superconducting gap Δ normalized to a given value Δ_0. The blue lines are obtained when the DOS N_0 changes over a range of values for a fixed triplet to singlet interaction ratio $g_T/g_S = g_T^{(0)}/g_S^{(0)}$. The blue band is then obtained by allowing a set of interaction ratios. The red lines and band are obtained analogously, but for an interaction ratio that correlates with the DOS, $g_T/g_S = g_T^{(0)}/g_S^{(0)} + \alpha N_0$, with $\alpha > 0$.

well-defined with energy $\Omega_L < 2\Delta$ as long as there is an attraction in the triplet channel, and leaves signatures in the electron spectral function at $\Delta + \Omega_L$ and higher harmonics. We now discuss whether it might be responsible for the STM resonances [2].

With increasing temperature, while their energy remains approximately the same, the amplitude of the STM resonances is suppressed near but below T_c. These facts are consistent with the small exponential dependence on temperature of Ω_L (see Eq. (2.108)), and with the residue of the Leggett propagator scaling as Δ^2 (see Eq. (2.111)). On the other hand, the energy of the resonances significantly increases with the out-of-plane magnetic field, surpassing 2Δ at moderate fields. A precise modeling of this situation would require considering the vortex mixed state. Nevertheless, the changes in the energy likely do not originate just from variations of the gap, and the effect of the magnetic field might be reducing the triplet attraction g_T, by, for instance, hardening spin fluctuations.

What we can address is the anticorrelation between the local normalized resonance energy and the local gap. For that, we analyze a simplified situation where local variations of the model parameters, in particular g_S, g_T and the DOS N_0, induce changes in the local gap and local Leggett mode energy analogous to changing the parameters in Eqs. (2.73) and (2.99), respectively. If we assume that N_0 varies spatially, while the interaction ratio $g_T/g_S = g_T^{(0)}/g_S^{(0)}$ is kept homogeneous, then both Δ and $\bar{\Omega}_L$ change. In particular, increasing the DOS increases the gap Δ but decreases $\bar{\Omega}_L$, leading to a moderate anticorrelation. Fig. 12 shows such an anticorrelation in blue, where we have also included a range of possible values of $g_T^{(0)}$, which gives rise to an

anticorrelated "band". Alternatively, we can additionally let g_T depend on the DOS, for instance linearly, so that $g_T/g_S = g_T^{(0)}/g_S^{(0)} + \alpha N_0$. In this case, assuming a positive coefficient $\alpha > 0$, $\bar{\Omega}_L$ is further decreased by increasing the DOS, inducing a larger anticorrelation (see red band in Fig. 12). The analysis of other possible local variations suggests that the anticorrelation is a quite generic feature of the Leggett mode. While more detailed calculations with actual local variations of the parameters should be carried out, our simple modelling indicates that the Leggett mode is compatible with the anticorrelation.

In conclusion, we believe that the Leggett mode, which we have derived in a simple model, might be compatible with the STM experiment [2]. This suggests that the presence of the subleading f-wave spin-triplet channel is a coherent picture to explain both the STM resonances and the nematic magnetotransport [115, 116] in the superconducting state of monolayer $NbSe_2$.

2.4 Discussion and conclusions

We have analyzed the superconducting collective modes of a model of the hole pockets at the K points of monolayer $NbSe_2$. In the presence of a subleading spin-triplet superconducting pairing, a Leggett mode naturally arises. We have determined that its energy Ω_L is smaller than twice the superconducting gap 2Δ, which allows the Leggett mode to be well-defined and long-lived. We have also shown that it renormalizes the electron spectral function, leading to peaks at energies $\Delta + \Omega_L$ in the tunneling spectrum. We have also discussed the possible interpretation of the resonances observed in STM by Ref. [2] in terms of the Leggett mode. The suppression of the resonances with temperature and magnetic field within the superconducting state, as well as the anticorrelation of their energy with the superconducting gap are compatible with the Leggett mode. The presence of a subleading spin-triplet pairing thus provides a coherent picture for monolayer $NbSe_2$, capable of explaining the STM resonances along with the twofold anisotropy of the in-plane critical magnetic field [115, 116]. While other explanations remain possible, we believe this is the most likely one. Our general message is therefore that one should also consider superconducting collective modes in the particle-particle channel when interpreting tunneling experiments.

The main ingredients of our model are Ising SOC, which splits the bands with a spin-valley locking, and static local interactions g_S and g_T that decouple into a s-wave spin-singlet Δ_S and a f-wave spin-triplet $\vec{\Delta}_T$ superconducting pairing. The latter is split by the Ising SOC in out-of-plane opposite-spin Δ_T^z and in-plane equal-spin $\mathbf{\Delta}_T^{xy}$ pairings. Assuming a s-wave ground state and a subleading attractive interaction in the f-wave channel naturally gives rise to the Leggett collective mode, which consists of the fluctuation of the relative phase between the spin-split bands. In the absence of singlet-triplet mixing, the Leggett mode reduces to a Bardasis-Schrieffer fluctuation towards the out-of-plane f-wave spin-triplet Δ_T^z state with $\frac{\pi}{2}$ relative phase with respect to the

s-wave Δ_S ground state. Within the functional integral formalism, its propagator is given by the expansion of the effective action to quadratic order in the field associated with Δ_T^z. The pole of its propagator in the long-wavelength limit defines its energy, which is always $\Omega_L < 2\Delta$ as long as the interaction in the Δ_T^z channel is attractive. Slightly increasing the temperature only slightly increases its energy, but the quasiparticle residue of its propagator scales with Δ^2, so its amplitude decays below T_c. Considering elastic scattering only, and using a low-energy effective action coupling the fermions in the superconductor with the Leggett mode, we have determined the renormalized electron spectral function to first order in perturbation theory due to the coupling to the Leggett mode. As we show in Appendix 2.B, this picture is robust to singlet-triplet mixing in the ground state, and the energy of the Leggett mode is only slightly decreased.

As long as there is an attraction in the f-wave channel, we expect the Leggett mode to survive against including more realistic features to the model, such as the hole pocket at Γ or gap anisotropies along the pockets. The same applies to the effect of the CDW, which we have ignored in our work since it only opens partial gaps in the Fermi surface. Regarding the effect of disorder, Refs. [317, 320] have determined that, in a singlet-triplet mixed ground state, the triplet component is rapidly suppressed. Nevertheless, the Leggett mode is defined also for a pure s-wave ground state, which is robust to disorder, so we expect a certain robustness again disorder as long as the triplet interaction remains attractive. The challenge in all these cases is determining the interaction in the f-wave channel, and analyzing whether it remains attractive.

It is worth discussing the Migdal-Eliashberg calculations of monolayer $NbSe_2$ performed by Ref. [33] after the publication of our work [2]. By including electron-phonon interactions determined *ab initio*, and adding spin fluctuations, they obtained an s-wave ground state with small singlet-triplet mixing, but with a repulsive effective interaction in the f-wave channel. They instead found a different subleading $s_\pm$ state, whose gap has opposite sign in the Γ and K pockets, but the same sign in the inner and outer pockets at K. Incidentally, this $s_\pm$ state has been proposed to arise from purely repulsive interactions if the interband coupling between Γ and K dominates [306]. A Leggett mode would also arise from their calculation, but consisting of the relative phase fluctuation between the Γ and K bands. We mention that the CDW was ignored in this prediction, which might significantly affect both the electron-phonon coupling and the spin fluctuations [297].

It is interesting to analyze whether the Leggett mode carries on to isostructural transition metal dichalcogenides, such as monolayer NbS_2, $TaSe_2$ and TaS_2. Ref. [339] has observed dip-hump features in the STM spectrum of monolayer 1H-TaS_2. 1H-TaS_2 displays similar CDW and superconducting instabilities to 1H-$NbSe_2$. However, the STM features in 1H-TaS_2 have energies $\Omega \gg 2\Delta$, and they survive to high magnetic fields beyond the critical field. This discards the Leggett mode as a possible explanation in 1H-TaS_2, and suggests a different origin. While Ref. [339] speculated with a magnetic fluctuation responsible for the f-wave pairing interaction, the

robustness against magnetic field remains to be explained. Moreover, in spin-fluctuation-mediated superconductors, the gap opening strongly renormalizes the spin fluctuations, which acquire a gap and become undamped only below T_c [335, 338]. Ref. [340] has also detected features in the STM spectrum of the CDW state of monolayer 1H-NbS_2, at energies $\gtrsim 2.5$meV. However, monolayer 1H-NbS_2 does not become superconducting, and therefore the features have to originate from a mechanism unrelated to superconductivity. Based on DFT calculations, Ref. [340] has proposed the STM features to originate from inelastic scattering of the phase and amplitude CDW modes. The temperature dependence of the resonances, whose energy should decrease with increasing temperature in the case of CDW modes, might constitute a test for this interpretation.

2.4.1 Outlook

Several avenues remain open in $NbSe_2$ and similar compounds, both on the theory side and in the interpretation of the experiments. It would be interesting to determine the microscopic interactions and the superconductivity in the presence of the CDW, and analyze whether a Leggett mode survives. If the f-wave state is not subleading, a coherent picture for the experimental evidence is lacking. This evidence is: twofold-anisotropic in-plane critical magnetic field in few-layer $NbSe_2$ [115, 116], enhanced in-plane critical magnetic field beyond Ising protection in few-layer $NbSe_2$ [313], and STM resonances within the superconducting state of monolayer $NbSe_2$ with energy $\Omega < 2\Delta$ [2]. The nematic magnetotransport could also arise from a d-wave order parameter that couples to strain [115], or from other tensor perturbation not necessarily involving a subleading superconducting pairing [318, 321]. In view of the TaS_2 [339] and NbS_2 [340] STM resonances, which are not directly related to superconductivity, it would be interesting to reevaluate the role of phonons in $NbSe_2$. While the phonon energies in both the normal state and the commensurate CDW are considerably higher than the resonance energy in $NbSe_2$, the effect of the slight incommensuration present in real samples has not been studied yet, and could give rise to lower-energy CDW phonons. In summary, the next step in the theory side might need to consider the effects of the CDW and its incommensuration in the superconducting pairings and the collective modes.

On the experimental side, it would be desirable to further analyze the resonances observed in STM. Raman spectroscopy and nonlinear optics are promising tools [258–262, 267], since they can provide information on the symmetry of the bosonic mode. The Leggett mode is totally symmetric (A_1'), so these techniques could verify this prediction or disprove the Leggett mode interpretation. It would also be interesting to study other aspects that we have not explicitly mentioned so far, namely the spatial distribution and amplitudes of the resonances. First, in individual spectra, the amplitudes of the three resonances, which we have interpreted as harmonics, are not always in descending order from the first the the third harmonic, as a perturbative calculation involving

higher-order scattering processes would predict. For individual spectra, this might be related to matrix elements and spatial fluctuations, but we would expect the average spectrum over the CDW unit cell to have this monotonous decrease of the amplitudes. Further analysis of the experimental data is needed to analyze this hypothesis. A more intriguing, perhaps related, observation is that in a few individual spectra the third resonance appears when the second does not. Studying the spatial distribution of these events might also shed light on their origin.

Other related TMDs where the ideas and models discussed in this chapter could be applied are the $4H_b$ polytypes, whose stacking consist of alternating T and H layers (see Fig. 1.1). In particular, $4H_b$-TaS_2 has raised a lot of attention due to signatures of two-component topological superconductivity and time-reversal symmetry breaking [341–350], as well as twofold-anisotropic critical field [346]. The superconductivity is thought to arise mainly from the H layer, analogous to the one studied in this chapter. The study of the subleading pairings in H monolayers is therefore relevant for $4H_b$-TaS_2, where an unconventional pairing might be stabilized. Indeed, the role of the interlayer coupling to the T layer, which isolated supports a Mott insulating state, is unclear yet.

To sum up, we believe that out theory puts forward the investigation of potential superconducting collective modes in 2D transition metal dichalcogenides, which should be considered when interpreting tunneling experiments. The potential presence of a subleading unconventional pairing leads to interesting properties, and, under the right circumstances, could lead to unconventional superconductivity in transition metal dichalcogenides, such as the $4H_b$ polytype.

Appendices

2.A Group theory: point group of monolayer $NbSe_2$

In this Appendix, we describe the space group $P\bar{6}m2$ and point group D_{3h} characterizing the normal state of monolayer $NbSe_2$. This group-theoretical analysis is used to construct the $\boldsymbol{k}\cdot\boldsymbol{p}$ model, and classify the pairing symmetries.

The space group $P\bar{6}m2$ is symmorphic. The Γ point has little group D_{3h} with time reversal symmetry $\mathcal{T}$, whereas the K points are invariant under C_{3h} and the anti-unitary combination $m_x\mathcal{T}$.

The point group D_{3h} is generated by the out-of-plane threefold symmetry C_{3z}, the in-plane mirror symmetry m_x, and the out-of-plane mirror symmetry m_z [282]. Its character table is given in Table 2.A.1. It has irreps $A_1^{m_z}, A_2^{m_z}, E^{m_z}$, where $m_z = ',''$ indicates the parity under m_z, and we have chosen the subindices $1,2$ to indicate the parity under the in-plane mirrors with a view to easily including Rashba SOC. Indeed, Rashba SOC breaks the m_z symmetry but preserves the in-plane mirrors, rendering the point group C_{3v}, with irreps A_1, A_2, E. For completeness, we also present the character table of C_{3h} in Table 2.A.2, which is isomorphic to the little group at the K points.

D_{3h}	$1\ E$	$2\ C_{3z}$	$3\ m_x$	$1\ m_z$	$2\ m_zC_{3z}$	$3\ C_{2y}$
$A_1' \equiv \Gamma_1$	1	1	1	1	1	1
$A_2' \equiv \Gamma_2$	1	1	-1	1	1	-1
$E' \equiv \Gamma_5$	2	-1	0	2	-1	0
$A_1'' \equiv \Gamma_3$	1	1	1	-1	-1	-1
$A_2'' \equiv \Gamma_4$	1	1	-1	-1	-1	1
$E'' \equiv \Gamma_6$	2	-1	0	-2	1	0

TABLE 2.A.1: Character table of the D_{3h} point group. The labels for the little group at Γ are also provided. The superindices $'$ and $''$ indicate even and odd under m_z, respectively. The subindices $_1$ and $_2$ indicate even and odd under m_x.

C_{3h}	$1\ E$	$1\ C_{3z}$	$1\ C_{3z}^{-1}$	$1\ m_z$	$1\ m_z C_{3z}$	$1\ m_z C_{3z}^{-1}$
$A' \equiv K_1$	1	1	1	1	1	1
$A'' \equiv K_2$	1	1	-1	-1	1	1
${}^{+1}E' \equiv K_3$	1	$e^{+i2\pi/3}$	$e^{-i2\pi/3}$	1	$e^{+i2\pi/3}$	$e^{-i2\pi/3}$
${}^{-1}E' \equiv K_5$	1	$e^{-i2\pi/3}$	$e^{+i2\pi/3}$	1	$e^{-i2\pi/3}$	$e^{+i2\pi/3}$
${}^{+1}E'' \equiv K_4$	1	$e^{+i2\pi/3}$	$e^{-i2\pi/3}$	-1	$-e^{+i2\pi/3}$	$-e^{-i2\pi/3}$
${}^{-1}E'' \equiv K_6$	1	$e^{-i2\pi/3}$	$e^{+i2\pi/3}$	-1	$-e^{-i2\pi/3}$	$-e^{+i2\pi/3}$

TABLE 2.A.2: Character table of the C_{3h} point group. The labels for the little group at K are also provided. The superindices $'$ and $''$ indicate even and odd under m_z, respectively.

2.B Effect of singlet-triplet mixing in the Leggett mode

In this Appendix, we consider a ground state with mixed s-wave spin-singlet Δ_S and out-of-plane f-wave spin-triplet Δ_T^z, and show that the Leggett mode remains qualitatively the same. As we mentioned in Section 2.2.1, there are two ways of introducing this mixing: including a $\boldsymbol{k}$-dependent Ising SOC that makes the DOS of the spin-split bands different, and adding a symmetry-allowed interaction that explicitly mixes Δ_S and Δ_T^z. The general model $H = H_0 + H_{\text{int}}$ is therefore

$$H_0(\boldsymbol{k}) = \xi(\boldsymbol{k})\tau_0\sigma_0 + \lambda(\boldsymbol{k})\tau_z\sigma_z, \tag{2.132}$$

$$H_{\text{int}} = g_S\hat{\Phi}_S^\dagger\hat{\Phi}_S + g_T^z\hat{\Phi}_T^{z\dagger}\hat{\Phi}_T^z + g_{ST}\left(\hat{\Phi}_T^{z\dagger}\hat{\Phi}_S + \hat{\Phi}_S^\dagger\hat{\Phi}_T^z\right) + g_T^{xy}\hat{\boldsymbol{\Phi}}_T^{xy\dagger}\cdot\hat{\boldsymbol{\Phi}}_T^{xy}, \tag{2.133}$$

where, to leading order in $\boldsymbol{k}$, the Ising SOC is

$$\lambda(\boldsymbol{k}) = \lambda - \eta\frac{\boldsymbol{k}^2}{2m}, \tag{2.134}$$

with $\eta > 0$ a dimensionless parameter, which we will show to be $\eta = (N_- - N_+)/(N_- + N_+)$ the relative difference of DOS of the spin-split bands. Physically, the η term arises due to the fact that the atomic SOC only affects the $d_\pm$ orbitals, whose weight in the bands is exactly 1 in the K points, but it decays to about 0.8 at the Fermi level due to mixing with the d_{z^2} orbital [351]. Defining the Ising SOC at the Fermi level $\lambda_F = \lambda(\boldsymbol{k} = k_F) = \lambda - \eta|\mu|$, we can estimate that $\eta = (\lambda - \lambda_F)/|\mu| \sim 0.2\lambda/|\mu| \sim 0.03$. The singlet-triplet mixing due to this term will therefore be small, as concluded by Ref. [306]. Regarding the interaction term, we will omit the in-plane triplet, which is suppressed by SOC, and call $g_T^z = g_T$.

The single-particle energies are

$$\varepsilon_\pm(\boldsymbol{k}) = \xi(\boldsymbol{k}) \pm \lambda(\boldsymbol{k}) = -\frac{\boldsymbol{k}^2 - k_{F\pm}^2}{2m_\pm}, \tag{2.135}$$

where the new masses are $m_\pm = \frac{m}{1\pm\eta}$ and the Fermi momenta are $\frac{k_{F\pm}^2}{2m_\pm} = -\mu \pm \lambda$. We highlight that the $\pm$ labels refer to the spin-split pocket shifted up and down by SOC, respectively. Correspondingly, $+$ is the outer pocket $(d_{K_+\uparrow}, d_{K_-\downarrow})$ and $-$ is the inner pocket $(d_{K_+\downarrow}, d_{K_-\uparrow})$. The DOS of these spinful bands is $N_\pm = \frac{m_\pm}{2\pi} = \frac{N_{01}}{1\pm\eta}$, where $N_{01} = \frac{m}{2\pi} = \frac{N_0}{4}$ is the DOS of each band in the absence of SOC. The DOS difference between the spin-split bands is $N_- - N_+ = N_{01}\frac{2\eta}{1-\eta^2} \sim 0.06 N_{01}$. Note that the inner pocket has a higher DOS.

Due to the singlet-triplet mixing, the outer and inner pockets develop different superconducting gaps $\Delta_\pm$, which we will define later. We assume a ground state with dominant s-wave spin-singlet, where both $\Delta_\pm$ have the same sign, which can be realized if $g_S < g_T < -|g_{ST}| < 0$. In particular, we choose $\Delta_\pm > 0$. The Bogoliubov quasiparticle energies are

$$E_\pm(\boldsymbol{k}) = \sqrt{\varepsilon_\pm^2(\boldsymbol{k}) + \Delta_\pm^2}. \tag{2.136}$$

In the following, we determine the gap equation to see the relation between the outer and inner gaps $\Delta_\pm$ and the mixing of singlet and triplet order parameters. We will then determine the Leggett mode energy following the steps of section 2.3.1. The Leggett mode consists of the relative phase fluctuation between the outer and inner pockets. In the general case with singlet-triplet mixing, this no longer coincides with the Bardasis-Schrieffer mode related to the out-of-plane triplet, which complicates the calculations, but the result remains analogous.

2.B.1 Gap equation and ground state

If $g_{ST} = 0$ and the mixing originates only from the single-particle η SOC, then the gap equations for the coupled singlet $\Delta_S = -g_S\langle\hat{\Phi}_S\rangle$ and triplet $\Delta_T^z = -g_T\langle\hat{\Phi}_T^z\rangle$ channels are given by Eqs. (2.68) and (2.69). In this case, $\Delta_\pm = \Delta_S \pm \Delta_T^z$, and the gap equations in terms of $\Delta_\pm$ read

$$-\Delta_+ = 2(g_S + g_T)\Delta_+ f_+(T) + 2(g_S - g_T)\Delta_- f_-(T), \tag{2.137}$$
$$-\Delta_- = 2(g_S + g_T)\Delta_- f_-(T) + 2(g_S - g_T)\Delta_+ f_+(T), \tag{2.138}$$

where we have defined

$$f_\pm(T) = \int \frac{d^2k}{(2\pi)^2}\frac{\tanh\left[\frac{\beta}{2}E_\pm(\boldsymbol{k})\right]}{E_\pm(\boldsymbol{k})} = N_\pm\int_{-\Lambda}^{\Lambda} d\varepsilon \frac{\tanh\left[\frac{\beta}{2}\sqrt{\varepsilon^2+\Delta_\pm^2}\right]}{2\sqrt{\varepsilon^2+\Delta_\pm^2}}, \tag{2.139}$$

In particular, $f_\pm(T=0) = N_\pm \mathrm{argsinh}\left(\frac{\Lambda}{|\Delta_\pm|}\right)$. The gap equations (2.137) and (2.138) can be decoupled, giving rise to separate equations for Δ_+ and Δ_-.

If $g_{ST} \neq 0$, however, the previous gap equations are no longer applicable. More dramatically, $\Delta_S = -g_S\langle\hat{\Phi}_S\rangle$ and $\Delta_T^z = -g_T\langle\hat{\Phi}_T^z\rangle$ no longer couple to the Gorkov Green's function (2.63) via the matrices $M_S = \tau_x i\sigma_y$ and $M_T^z = y\tau_y\sigma_z i\sigma_y$ of Eqs. (2.47) and (2.48), respectively. Instead, following the generalized BCS theory outlined in the Introduction, we define the interaction matrix

$$g = \begin{pmatrix} g_S & g_{ST} \\ g_{ST} & g_T \end{pmatrix}. \tag{2.140}$$

The adequate pairings Δ_s and Δ_t^z, that indeed couple to the fermions with M_S and M_T^z, are defined as

$$\mathbf{\Delta}_{st} = \begin{pmatrix} \Delta_s \\ \Delta_t^z \end{pmatrix} = -g \begin{pmatrix} \langle\hat{\Phi}_S\rangle \\ \langle\hat{\Phi}_T^z\rangle \end{pmatrix} = \begin{pmatrix} -g_S\langle\hat{\Phi}_S\rangle - g_{ST}\langle\hat{\Phi}_T^z\rangle \\ -g_T\langle\hat{\Phi}_T^z\rangle - g_{ST}\langle\hat{\Phi}_S\rangle \end{pmatrix}. \tag{2.141}$$

We stress that, while Δ_s is mainly singlet and Δ_t^z is mainly out-of-plane triplet, they are different from the pure singlet $\Delta_S = -g_S\langle\hat{\Phi}_S\rangle$ and pure out-of-plane triplet $\Delta_T^z = -g_T\langle\hat{\Phi}_T^z\rangle$ pairings, and they only become equivalent in the limit $g_{ST} = 0$. Indeed,

$$\Delta_s = \Delta_S + \frac{g_{ST}}{g_T}\Delta_T^z, \tag{2.142}$$

$$\Delta_t = \Delta_T^z + \frac{g_{ST}}{g_S}\Delta_S, \tag{2.143}$$

The effective action in terms of the new pairings Δ_s and Δ_t^z reads

$$\mathcal{S}_{\text{eff}}[\bar{\Delta}, \Delta] = -\int_x \left[\bar{\mathbf{\Delta}}_{st} \cdot g^{-1} \cdot \mathbf{\Delta}_{st}\right] - \text{Tr}\left[\log G^{-1}\right], \tag{2.144}$$

where the Gorkov BdG Green's function reads

$$G^{-1}(k) = \begin{pmatrix} i\omega_n\tau_0\sigma_0 - H_0(\boldsymbol{k}) & -\Delta_s\tau_x i\sigma_y - \Delta_t^z i\tau_y\sigma_z i\sigma_y \\ \bar{\Delta}_s\tau_x i\sigma_y + \bar{\Delta}_t i\tau_y\sigma_z i\sigma_y & i\omega_n\tau_0\sigma_0 + H_0(\boldsymbol{k}) \end{pmatrix}, \tag{2.145}$$

which is analogous to Eq. (2.63) by replacing Δ_S and Δ_T^z by Δ_s and Δ_t^z, respectively. Here we have also omitted the in-plane triplet, which remains unchanged by the singlet-triplet mixing. Consequently, assuming real pairing, the outer and inner gaps are now

$$\Delta_\pm = \Delta_s \pm \Delta_t^z. \tag{2.146}$$

It is useful to define the gap Δ and mixing angle θ by

$$\Delta_s = \Delta\cos(\theta), \tag{2.147}$$

$$\Delta_t^z = -\Delta\sin(\theta). \tag{2.148}$$

In the limit $g_{ST} = 0$, θ is the singlet-triplet mixing angle: if $\theta = 0$, the state is pure singlet, in which case Δ is the gap. We have chosen a minus sign in the second equation since $\Delta_t^z < 0$ for $\eta > 0$. For $g_{ST} \neq 0$, θ indicates the mixing between Δ_s and Δ_t^z. The outer and inner gaps in terms of Δ and θ read:

$$\Delta_\pm = \Delta\left[\cos(\theta) \mp \sin(\theta)\right], \tag{2.149}$$

so

$$\Delta = \sqrt{\frac{1}{2}\left(\Delta_+^2 + \Delta_-^2\right)}. \tag{2.150}$$

The effective action (2.144) is thus similar to (2.60), but now the inverse interaction matrix g^{-1} is not diagonal:

$$g^{-1} = \frac{1}{\det(g)}\begin{pmatrix} g_T & -g_{ST} \\ -g_{ST} & g_S \end{pmatrix}, \tag{2.151}$$

where $\det(g) = g_S g_T - g_{ST}^2$. This leads to the following modified gap equations for the outer and inner pockets:

$$-\Delta_+ = 2(g_S + g_T + 2g_{ST})\Delta_+ f_+(T) + 2(g_S - g_T)\Delta_- f_-(T), \tag{2.152}$$

$$-\Delta_- = 2(g_S + g_T - 2g_{ST})\Delta_- f_-(T) + 2(g_S - g_T)\Delta_+ f_+(T), \tag{2.153}$$

which are similar to the gap equations but with the additional factors $\pm 2g_{ST}$, which tend to make the inner or outer pocket larger, depending on the sign of g_{ST}. The numerical solution of the gap equations indicates that $\eta > 0$ and $g_{ST} > 0$ lead to a larger gap in the inner pocket, which has a higher DOS, whereas $g_{ST} < 0$ has the opposite effect. Correspondingly, $\eta > 0$ and $g_{ST} > 0$ favour $\Delta_T^z < 0$ and $\Delta_t^z < 0$, and the opposite for $g_{ST} < 0$. The bare ground state action and Gorkov BdG Green's function read:

$$\begin{aligned}\mathcal{S}_{\text{eff}}^{(0)}[\bar{\Delta}, \Delta] = &-\int_x \left[\frac{g_T}{\det(g)}\cos^2(\theta) + \frac{g_S}{\det(g)}\sin^2(\theta) + 2\frac{g_{ST}}{\det(g)}\sin(\theta)\cos(\theta)\right]\bar{\Delta}(x)\Delta(x) - \\ &- \text{Tr}\left[\log G_0^{-1}\right],\end{aligned} \tag{2.154}$$

$$G_0^{-1}(k) = i\omega_n \tau_0\sigma_0\rho_0 - \xi(\boldsymbol{k})\tau_0\sigma_0\rho_z - \lambda(\boldsymbol{k})\tau_z\sigma_z\rho_z + \Delta_s\tau_x\sigma_y\rho_y + \Delta_t^z\tau_y\sigma_x\rho_y, \tag{2.155}$$

2.B.2 Leggett mode energy

Now, the Leggett mode is the relative phase fluctuation between the outer and inner pockets. The fluctuating field corresponds to the phase φ such that $\Delta'_\pm = \Delta_\pm e^{i\pm\varphi} \simeq \Delta_\pm \pm i\varphi\Delta_\pm$. In terms

of the s, tz basis, this becomes

$$\Delta_s' = \Delta_s + i\Delta_t^z \varphi = \Delta\cos(\theta) - i\sin(\theta)\phi_L, \tag{2.156}$$

$$\Delta_t^{z\prime} = \Delta_t^z + i\Delta_s \varphi = -\Delta\sin(\theta) + i\cos(\theta)\phi_L, \tag{2.157}$$

where we have defined the Leggett bosonic field in terms of the gap Δ and the phase fluctuation φ as $\phi_L = \Delta\varphi$. In the absence of singlet-triplet mixing. this recovers that the Leggett mode is the fluctuation of the out-of-plane triplet with imaginary phase. In the general case, to compute the Leggett mode propagator, we substitute Δ_s and Δ_t^z in the action (2.144) by Δ_s' and $\Delta_t^{z\prime}$, and expand to quadratic order in ϕ_L. We obtain:

$$\mathcal{S}_{\text{eff}}[\Delta, \phi_L] - \mathcal{S}_{\text{eff}}^{(0)}[\Delta] = \int_q D_L^{-1}(q)\phi_L(q)\phi_L(-q), \tag{2.158}$$

where $D_L^{-1}(q)$ is the inverse Leggett propagator:

$$D_L^{-1}(q) = -\left[\frac{g_T}{\det(g)}\sin^2(\theta) + \frac{g_S}{\det(g)}\cos^2(\theta) + 2\frac{g_{ST}}{\det(g)}\sin(\theta)\cos(\theta)\right] + \chi_L(q), \tag{2.159}$$

with the susceptibility:

$$\chi_L(q) = \frac{1}{2}\int_k \text{tr}[G_0(k)M_L G_0(k+q)M_L]. \tag{2.160}$$

The coupling matrix of the Leggett mode to the fermions is now

$$M_L = \tau_y\sigma_x\rho_x\cos(\theta) - \tau_y\sigma_y\rho_x\sin(\theta). \tag{2.161}$$

The susceptibility in the long-wavelength limit is similar to Eq. (2.88) but with an additional factor depending on the mixing angle:

$$\chi_L(i\Omega_m) = \chi_L^+(i\Omega_m) + \chi_L^-(i\Omega_m), \tag{2.162}$$

$$\chi_L^\pm(i\Omega_m) = -\left[1 \mp \sin(2\theta)\right]\int \frac{d^2k}{(2\pi)^2}\frac{\tanh\left[\frac{\beta}{2}E_+(\boldsymbol{k})\right]}{E_+(\boldsymbol{k})}\left\{1 + \frac{(i\Omega_m)^2}{[2E_+(\boldsymbol{k})]^2 - (i\Omega_m)^2}\right\}. \tag{2.163}$$

We can identify the second term of (2.163) with the $F_L^\pm(i\Omega_m)$ function that we defined in Eq. (2.92), but now with the appropriate gaps and dispersion $E_\pm(\boldsymbol{k}) = \sqrt{\varepsilon_\pm^2(\boldsymbol{k}) + \Delta_\pm^2}$. This allows

to define two normalized Leggett energies, one for each gap:

$$\bar{\Omega}_L^{\pm} = \frac{\Omega_L}{2\Delta_{\pm}}. \tag{2.164}$$

Inserting the gap equation to simplify the first term of Eq. (2.163), after a few manipulations we arrive at the following Leggett propagator

$$\begin{aligned} D_L^{-1}(\Omega) = N_0 \cos(2\theta) \Bigg[\frac{|\bar{g}_S| - |\bar{g}_T|}{\det(\bar{g})} - \frac{1}{2}\frac{\cos(\theta) - \sin(\theta)}{\cos(\theta) + \sin(\theta)} \frac{1}{1+\eta} F_L(\bar{\Omega}_+) - \\ - \frac{1}{2}\frac{\cos(\theta) + \sin(\theta)}{\cos(\theta) - \sin(\theta)} \frac{1}{1-\eta} F_L(\bar{\Omega}_-) \Bigg], \end{aligned} \tag{2.165}$$

where $\det(\bar{g}) = N_0^2 \det(g)$, and $F_L(\bar{\Omega})$ was defined in Eq. (2.94), whose analytical expression at zero temperature is given by Eq. (2.98). The zeros of the inverse propagator (2.165) define the energy of the Leggett mode. To compare it to the case without singlet-triplet mixing, it is illustrative to analyze the low-energy limit $\Omega_L \ll \Delta_{\pm}$, where

$$\bar{\Omega}_L = \frac{\Omega_L}{2\Delta} = \sqrt{\frac{|\bar{g}_S| - |\bar{g}_T|}{|\bar{g}_S||\bar{g}_T| - \bar{g}_{ST}^2} (1-\eta^2)\cos(2\theta)}, \tag{2.166}$$

where $\cos(2\theta) = \frac{\Delta_+\Delta_-}{\Delta^2}$. Comparing this expression to Eq. (2.100), we conclude that in the realistic case with small mixing, i.e., small g_{ST} and η, the Leggett mode energy remains approximately the same. Moreover, the mixing tends to decrease the Leggett energy, especially by the $\boldsymbol{k}$-dependent SOC.

Chapter 3

Topological amorphous matter

The field of topology in condensed matter physics has allowed us to better understand and classify quantum phases and phase transitions. This field has traditionally focused on crystalline materials, where the translational and point-group symmetries simplify the classification and characterization of topological phases. While the robustness against disorder has been studied since the beginning of the field, only recently progress has been made in defining and characterizing topological phases in noncrystalline systems, such as amorphous and quasicrystalline materials. Despite the variety of phases and diagnostic tools in amorphous topological matter, there is no generic and efficient method to characterize topology in noncrystalline solids. Here, we introduce the structural spillage, a new indicator that predicts the unknown topological phase of a noncrystalline solid, which is readily compatible with first-principles calculations. In particular, the structural spillage compares the occupied states of a noncrystalline solid to its crystalline counterpart, and provides a quantitative measure of the band inversions differentiating them. We also adapt its formulation to tight-binding calculations, and illustrate its potential using 2D amorphous bismuth models, predicting the bilayer to be a new topologically nontrivial material. Finally, we present the density functional theory calculations implemented by our collaborators [3], which demonstrate the suitability of the structural spillage.

3.1 Introduction

In this section, we present an overview of the field of topological quantum matter. Focusing on translationally-invariant crystals, we first describe the twofold role of symmetries in topological matter: not only do they protect topological phases, but they also facilitate their classification. We then briefly depict the basic structural properties of noncrystalline systems, mainly focusing on amorphous materials. Finally, we describe the recent advances in realizing topological phases in amorphous systems, paying special attention to the topological indicators available in the absence of translational symmetry.

3.1.1 Topology in crystals

There are phase transitions which lie beyond the Landau paradigm of spontaneous symmetry breaking. The emblematic case is that of topological phase transitions, where it is a topological index, and not symmetry, what changes in the transition. Here, we will only focus on the topological phases that can be described by quadratic noninteracting or mean-field Hamiltonians, and mainly on gapped states. These are a subset of the so-called symmetry-protected topological (SPT) phases[1] [353, 354]. Unlike intrinsic topological order [352, 355], characteristic of fractional quantum Hall phases [356, 357] and certain quantum spin liquids [358–361], topological properties of SPTs are not stable against arbitrary strong interactions, but they are protected by certain symmetries. In SPT phases, topological quantities are related to global properties of the occupied wavefunctions, which cannot be differentiated by any measurement of the expectation value of a local operator. States belonging to different topological classes cannot be connected to each other by local adiabatic transformations of the Hamiltonian respecting the underlying symmetries[2]. In particular, topologically trivial systems are those which can be smoothly connected to an atomic insulator. The absence of adiabatic continuity between topologically distinct phases leads to the bulk-boundary correspondence: an anomalous gapless boundary state should appear in the boundary between two topologically distinct phases if the boundary respects the protecting symmetries. Here, anomalous has a twofold meaning. First, anomalous boundary states cannot be realized in a well-defined system in the dimensions of the boundary; they can only exist in the boundary of the higher dimensional topological phase. For instance, 1D anomalous edge states of a 2D topological phase cannot be realized in purely 1D systems. Second, anomalous boundary

[1] According to certain definitions of topological order [352], the integer quantum Hall state and the chiral topological superconductor are topologically ordered, even if they can be described by quadratic Hamiltonians. However, a more restrictive notion of topological order that requires nontrivial topological excitations excludes these phases from the definition of topological order.

[2] If we include the requirement of preserving the number of occupied and/or unoccupied orbitals, two new types of unstable topology appear, deemed delicate and fragile topology [362]. Unstable topological phases do not display anomalous boundary states. Here, we will only consider stable topology.

states cannot be removed by local symmetry-preserving perturbations at the boundary [362]. In particular, anomalous boundary states are robust to Anderson localization, if the disorder preserves the protecting symmetries[3].

In this section we highlight the twofold role of symmetry within topological states of matter. On the one hand, the possible topological phases depend on the symmetries present. In this sense, symmetries can protect topological phases. On the other hand, even if certain symmetries are not necessary for topological protection, they can greatly facilitate the topological classification in practice by simplifying the expressions of the topological invariants.

Symmetries are transformations which leave the Hamiltonian invariant [98, 364, 365]. We consider the second-quantized Hamiltonian of a free-fermion system $\hat{H} = \sum c^\dagger \cdot H \cdot c$, where c are a basis of annihilation operators of the Hilbert space of interest. The matrix representation H of the Hamiltonian is called the first-quantized Hamiltonian. The operator $\hat{S}$ associated to a symmetry commutes with the second-quantized Hamiltonian, $\hat{S}\hat{H}\hat{S}^{-1} = \hat{H}$, and leaves the canonical anticommutation relations invariant, $\hat{S}\{c_a, c_b^\dagger\}\hat{S}^{-1} = \{c_i, c_j^\dagger\}$. Depending on their matrix representation S, symmetries can be classified as linear and unitary, or anti-linear and anti-unitary. While $\hat{S}$ always commutes with the second-quantized Hamiltonian $\hat{H}$, S can commute or anti-commute with the first-quantized Hamiltonian H. Therefore, four types of symmetry can be distinguished based on the unitarity of S and its commutation with H:

- Unitary symmetries are represented by a unitary matrix U, and commute with H, $UHU^{-1} = H$. Unitary symmetries are the only ones where H and U can be simultaneously block-diagonalized, with each block transforming as an irreducible representation of the symmetry. Spatial symmetries, such as translations and rotations, are unitary symmetries. Certain local symmetries, such as rotations in the spin or orbital space, are also unitary.

- Anti-unitary symmetries are also known as time-reversal-like symmetries $\hat{T}$, since time-reversal symmetry (TRS) is their representative example. They are represented by the product of a unitary matrix and complex conjugation $T = U_T\mathcal{K}$, and commute with H, $U_T H^* U_T^{-1} = H$. Applying this relation twice and the unitarity of U_T, we obtain that $T^2 = \pm 1$. Physical TRS can be represented as $T = e^{-i\pi S_y}\mathcal{K}$, with S_y the spin projected to the y direction. Therefore, $T^2 = +1$ corresponds to spinless or integer spin particles, and $T^2 = -1$ to half-odd-integer spin particles. In the latter case, Kramers theorem applies, which implies that time-reversed states are degenerate. Finally, we mention that only operators with the same number of creation and annihilation operators, such as electron-hole bilinears of the form $c^\dagger c$, can be classified as TRS even or odd, while the single-particle

[3] This view has been recently challenged [363].

operators c cannot be labelled this way due to the gauge freedom in choosing the phase of the state.

- Anti-unitary anti-symmetries $\hat{P}$, also called particle-hole- or charge-conjugation-like symmetries after their archetypical example, are also represented by the product of a unitary matrix and complex conjugation $P = U_P\mathcal{K}$, but anti-commute with H, $U_P H^* U_P^{-1} = -H$, and impose that $\mathrm{Tr}[H] = 0$. Again, $P^2 = \pm 1$. Now, P relates a single-particle state with energy E to other with energy $-E$. By construction, mean-field Bogoliubov-de Gennes (BdG) Hamiltonians of superconductors have particle-hole symmetry (PHS).

- Unitary anti-symmetries $\hat{C}$, also known as chiral symmetries, are represented by a unitary matrix U_C, but anti-commute with H, $U_C H U_C^{-1} = -H$. They can be regarded as the product of a TRS and a PHS, $\hat{C} = \hat{T} \cdot \hat{P}$, so $U_C = U_T U_P^*$. The chiral symmetry always squares to $+1$, so it has eigenvalues ± 1. As PHS, it relates single-particle states with opposite energies. Finally, not only does chiral symmetry impose that $\mathrm{Tr}[H] = 0$, but in the eigenbasis of U_C, H is block off-diagonal:

$$H = \begin{pmatrix} 0 & h \\ h^\dagger & 0 \end{pmatrix} \tag{3.1}$$

  Within this context, a chiral system is defined as a system invariant under a chiral symmetry. This should not be confused with the concept of chiral structure introduced in Chapter 1, which referred to the absence of any inversion, mirror or rotoinversion symmetry. Yet another meaning of the term chiral is used in the field of superconductivity, where a chiral superconductor is a time-reversal breaking topological superconductor whose pairing winds in momentum space and has a finite orbital angular momentum. Moreover, edge states are also dubbed chiral when they disperse only in one direction. For example, integer quantum Hall states and 2D chiral topological superconductors display chiral edge states.

Depending on the nature of the protecting symmetries, topological phases have been traditionally given different names. If the protecting symmetries are only combinations of the local TRS, PHS and chiral symmetries, the phases are termed strong topological [95–98]. Other topological phases require spatial symmetries for their protection as well, such as translational, rotational and mirror symmetries. Since the field of topology has traditionally focused on translationally-invariant crystals, these phases are known as weak or crystalline topological phases [99, 100].

The combinations of the TRS, PHS and chiral symmetries protecting strong topological phases give rise to the ten Altland-Zirnbauer symmetry classes [94, 366], which are known as the tenfold way. By including PHS and chiral symmetry, this classification extends the three Wigner-Dyson classes [367] for TRS: the complex unitary class A with no symmetries, the real orthogonal class

Class	T	P	C	d	0	1	2	3	4	5	6	7
A	0	0	0		$\mathbb{Z}$	0	$\mathbb{Z}$	0	$\mathbb{Z}$	0	$\mathbb{Z}$	0
AIII	0	0	1		0	$\mathbb{Z}$	0	$\mathbb{Z}$	0	$\mathbb{Z}$	0	$\mathbb{Z}$
AI	+	0	0		$\mathbb{Z}$	0	0	0	$2\mathbb{Z}$	0	$\mathbb{Z}_2$	$\mathbb{Z}_2$
BDI	+	+	1		$\mathbb{Z}_2$	$\mathbb{Z}$	0	0	0	$2\mathbb{Z}$	0	$\mathbb{Z}_2$
D	0	+	0		$\mathbb{Z}_2$	$\mathbb{Z}_2$	$\mathbb{Z}$	0	0	0	$2\mathbb{Z}$	0
DIII	−	+	1		0	$\mathbb{Z}_2$	$\mathbb{Z}_2$	$\mathbb{Z}$	0	0	0	$2\mathbb{Z}$
AII	−	0	0		$2\mathbb{Z}$	0	$\mathbb{Z}_2$	$\mathbb{Z}_2$	$\mathbb{Z}$	0	0	0
CII	−	−	1		0	$2\mathbb{Z}$	0	$\mathbb{Z}_2$	$\mathbb{Z}_2$	$\mathbb{Z}$	0	0
C	0	−	0		0	0	$2\mathbb{Z}$	0	$\mathbb{Z}_2$	$\mathbb{Z}_2$	$\mathbb{Z}$	0
CI	+	−	1		0	0	0	$2\mathbb{Z}$	0	$\mathbb{Z}_2$	$\mathbb{Z}_2$	$\mathbb{Z}$

TABLE 1: Periodic table of strong topological gapped phases. d is the space dimension. If TRS or PHS is present, the sign of its square is written. The possible topological phases can have an integer ($\mathbb{Z}$), even-integer ($2\mathbb{Z}$), or $\mathbb{Z}_2$ topological index. 0 indicates absence of topological phases.

AI with TRS squaring to $T^2 = +1$, and the real symplectic class AII with TRS squaring to $T^2 = -1$. Strong topological phases are classified in the so-called periodic table (see table 1), which determines the possible topological classes depending on the Altland-Zirnbauer symmetry class and the dimensionality of the system [95–98, 368]. The possible topological invariants can be either integer-valued[4], such as the Chern and winding numbers, or $\mathbb{Z}_2$, like the Chern-Simons and Fu-Kane invariants. Since TRS, PHS and chiral symmetry are local, strong topological phases do not require spatial symmetries to be defined. Therefore, they are robust to disorder, as long as it preserves the symmetry class and does not close the bulk mobility gap. Furthermore, all the boundaries display anomalous boundary states, characterized by the so-called Anderson delocalization, i.e., they cannot be localized by any amount of symmetry-preserving disorder on the boundary. The number of anomalous boundary states is related to the value of the topological invariants.

Spatial symmetries can enrich the topological classification and give rise to new phases [100]. For instance, weak topological phases are protected by translational symmetry. In particular, a 3D weak topological insulator can be regarded as a stack of 2D topological insulators along a given direction, and the $\mathbb{Z}_2$ invariant can still be defined in 3D thanks to the translational invariance along this direction [372]. Anomalous boundary states only appear in the surfaces parallel to this direction, since translational symmetry is only preserved there. Other crystalline topological phases are protected by point-group symmetries, such as rotational symmetry [99], mirror symmetry [373], and nonsymmorphic symmetries [374]. The general idea is that topological invariants can

[4]When adding many-body interactions, certain $\mathbb{Z}$ invariants become $\mathbb{Z}_8$ [369–371].

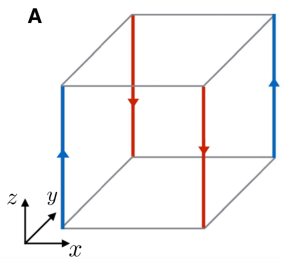

FIGURE 1: Sketch of the chiral hinge states of a 3D HOTI protected by the combination $C_{4z}T$ of fourfold rotational symmetry and time-reversal symmetry. Extracted from [375]

be defined at the subspaces of the Brillouin zone (BZ) which are invariant under the symmetry. Anomalous boundary states only appear at the boundaries that respect the protecting symmetries. This idea lead to the introduction of higher order topological insulators (HOTIs) [375]. For a d-dimensional system, we define its n^{th} order boundaries as the $d-n$ dimensional boundaries. For instance, the first order boundaries of a 3D system are its 2D surfaces, and its higher order boundaries are its 1D hinges and 0D corners. The first order boundaries of a HOTI do not respect the protecting symmetries and are therefore gapped, but some of its higher order boundaries are gapless. In particular, the anomalous boundary states appear in higher order boundaries that are the intersection of boundaries related by the protecting symmetries (see e.g. Fig. 1). Indeed, the mass term in the symmetry-related boundaries has opposite sign, so it is forced to vanish in their intersection, giving rise to the higher order boundary state. Even if the intersection is not perfectly sharp, as in, e.g., a round corner, the previous argument guarantees that the boundary state appears somewhere in this region.

Even if spatial symmetries are not required for their protection, they simplify the identification and classification of topological phases. First of all, translational symmetry has been traditionally assumed in the field of topological phases. For instance, the periodic table of strong topological phases 1 was derived for Bloch Hamiltonians [95–98], taking advantage of the fact that the Brillouin zone has the topology of a torus. The expressions of the topological invariants are also routinely given in terms of integrations over the whole Brillouin zone, or a subspace of it in the case of crystalline topological insulators. The Chern number C of a 2D system, for example, is the integral of the Berry curvature $\Omega^z_{nm}(\boldsymbol{k})$ over the Brillouin zone:

$$C = \frac{1}{2\pi}\int_{BZ} d^2k \,\mathrm{Tr}\left[\Omega^z(\boldsymbol{k})\right], \tag{3.2}$$

where the Berry curvature is a gauge-invariant geometrical quantity defined in terms of the Berry connection $A^{\alpha}_{nm}(\boldsymbol{k})$:

$$A^{\alpha}_{nm}(\boldsymbol{k}) = i\langle u_{n\boldsymbol{k}}|\partial^{\alpha}u_{m\boldsymbol{k}}\rangle, \tag{3.3}$$

$$\Omega^{z}(\boldsymbol{k}) = \epsilon^{z\alpha\beta}\frac{1}{2}\left(\partial^{\alpha}A^{\beta} - \partial^{\alpha}A^{\beta} + [A^{\alpha}, A^{\beta}]\right), \tag{3.4}$$

with $|u_{m\boldsymbol{k}}\rangle$ the cell-periodic Bloch eigenstates, $\partial^{\alpha} := \frac{\partial}{\partial k_{\alpha}}$, $\alpha = x, y$, and $\epsilon^{\gamma\alpha\beta}$ the completely antisymmetric tensor.

Even with the help of translational symmetry, computing the topological invariants is, in general, computationally expensive, since it requires the knowledge of the Bloch wavefunctions over the entire Brillouin zone with sufficient resolution. Space group symmetries remarkably simplify this task thanks to the theories of symmetry indicators and topological quantum chemistry [102–107]. Symmetry indicators provide a sufficient, but not necessary, condition for a set of Bloch bands to be topological, based on its symmetry representations at the high symmetry points of the Brillouin zone. Note that this assumes a noninteracting and translationally invariant Hamiltonian. The sufficient criterion for topology of symmetry indicators is based on the fact that, by definition, trivial atomic insulators can be described by fully-filled orbitals localized in real-space. Therefore, all the possible sets of symmetry representations of bands that can be derived from atomic insulators can be determined by Fourier transforming all the possible combinations of lattices and orbitals. If a set of bands cannot be described in this way, it is topological. Furthermore, symmetry indicators allow to partially determine the topological invariants [105, 376–378]. The paradigmatic example is that of inversion symmetric topological insulators, where the strong and weak $\mathbb{Z}_2$ indices can be determined from the parity under inversion symmetry of the eigenfunctions at the time-reversal invariant momenta [101, 372].

The approach of topological quantum chemistry is therefore based on the obstruction to Wannierize topological insulators [379–382]. For a given set of bands, Wannier functions are real-space wavefunctions, labelled by a unit cell index and a band-like internal index, obtained by a unitary transformation of the Bloch eigenstates. The Wannier obstruction refers to the impossibility of finding exponentially-localized symmetry-preserving Wannier functions for the occupied states of a topological insulator. Indeed, this feature is now taken as the definition of topological insulators.

The viewpoint of topological quantum chemistry and symmetry indicators allows to differentiate obstructed atomic insulators [383–385]. Two atomic limits can be topologically different, and thus a bulk gap closing has to occur to transition between them while respecting the symmetries. Obstructed atomic insulators are atomic limits which are not adiabatically connected to the atomic

insulator with all the Wannier functions localized in the positions of the physical atoms. A subset of them is symmetry-indicated [386]. Although they do not display anomalous boundary states, generically they retain certain boundary signature, such as fractional corner charges and, typically, gapped surface states within the bulk gap [385].

For completeness, we mention that there are also gapless topological materials [98, 387]. These materials display nodal points, lines or surfaces which cannot be fully gapped by small perturbations local in momentum space and that respect the protecting symmetries, so that the bulk gap is not affected far from the nodes. Therefore, even if topological nodes are defined using lattice or continuous translations, they are robust against smooth perturbations in real space which vary slowly on the lattice scale. A topological invariant can be associated to each node separately, which is given as an integral over a submanifold of the Brillouin zone. However, the sum of topological invariants over the Brillouin zone vanishes [388–390]. For instance, Weyl semimetals display an even number of twofold crossings, each with an associated Chern number. A tenfold classification analogous to that of topological gapped phases has been derived for gapless systems [98]. Further spatial symmetries enrich the possible gapless topological phases, allowing for Dirac semimetals [387], nodal line semimetals [391], multifold fermions [392], etc. Several topological semimetals also display boundary states, such as Fermi arcs in the case of Weyl semimetals. The theory of topological quantum chemistry is also useful to identify symmetry-enforced crossings, based on the possible connectivities of the symmetry representations at the high symmetry points.

Finally, we review other methods that have been used to diagnose and characterize topological phases beyond topological invariants and symmetry indicators. A defining property of topological phases that has been used with this aim is the presence of quantized responses. For instance, the Hall conductivity for Chern insulators [86, 87, 90], the thermal Hall conductivity for chiral topological superconductors [393], the Witten effect for axion topological insulators [394–396], the longitudinal electrical conductance for chiral edge states [397], and the longitudinal electrical conductance for helical edge states in the absence of dephasing and inelastic interactions [398]. Related to this conductance quantization, the scattering matrix can be used to determine the topological invariants [399]. The presence of boundary states is also a signature of topological phases. The topology also manifests in the entanglement spectrum [400], whose trace has discontinuities as a consequence of the spectral flow in topological insulators. Another topological indicator is the spin-orbit spillage [117], which will be described in Section 3.2.1.

3.1.2 Lack of translational symmetry

Condensed matter physics has commonly focused on the study of translationally-invariant crystalline systems, with the preconception that disorder is generally detrimental to the development of exotic states of matter, as well as to the performance of devices. Here, we confute this view

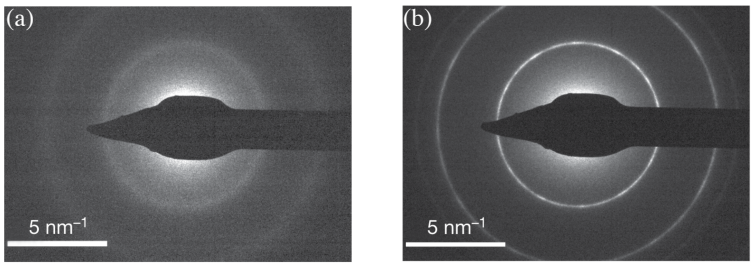

FIGURE 2: (a) Electron diffraction pattern of monolayer amorphous carbon showing broad Bragg rings. (b) Electron diffraction pattern of nanocrystalline graphene. The well-defined Bragg rings arise from the angle-average of the Bragg peaks of graphene single-crystalline domains, but they are not broaden due to the well-defined atomic distances. Extracted from Ref. [411].

and discuss that not only can known topological phases be realized in noncrystalline systems, but also that new phenomenology appears. In particular, we will mainly concentrate on the recent developments on topological amorphous matter. In this section, we describe the basic characteristics of amorphous and structurally disordered systems, while next section will be devoted to the description of topological phases in such systems.

Amorphous and glassy materials are defined by an atomic structure without long-range order [401]. However, they typically deviate from just an uncorrelated random distribution of atoms [402–405]. Indeed, the local environments around the atoms, encoded in their coordination numbers, bond lengths and angles, are determined by the chemistry of the atoms, i.e., their electronic configuration. For instance, covalently-bonded solids display short-range order, with approximately constant coordination number and well-defined nearest neighbour distances peaked around the values of their crystalline counterparts [401–406].

The atomic structure of amorphous solids is revealed in their diffraction pattern [402–405, 407]. Since they are isotropic on average, the sharp Bragg peaks characteristic of crystalline materials are replaced by rings (see Fig. 2(a)). These rings are broadened due to the fluctuations of the bond lengths (compare Figs. 2(a) and (b)). The radii, width and intensity of the diffraction rings can be used to determine the structure factor and estimate an average bond distance and coordination number of the amorphous structure [408, 409]. The short-range order with its characteristic length scales is also manifested in ARPES [410], where features reminiscent to Brillouin zone repetitions appear.

The limited experimental data characterizing the complex structural motifs present in amorphous materials complicates the construction of phenomenological models. A paradigmatic class of such models is based on continuous random networks [403, 404, 407], which, in the simplest case, exhibit constant coordination numbers with no dangling bonds and a narrow distribution of

bond lengths [401]. These continuous random network models have been applied to covalently-bonded amorphous solids, such as amorphous silicon [405, 406, 412, 413]. On the other hand, realistically modeling amorphous materials is challenging due to the large systems sizes required. The standard method relies on *ab initio* molecular dynamics [414–416], where an initial crystalline structure is melted, and then quenched to low temperatures and annealed. In 2D amorphous materials, an *ab initio* bond-flipping method has also been proposed [417, 418], which iteratively distorts randomly selected bonds and then relaxes the structure.

Similarly to crystals, amorphous materials display a variety of electronic properties. From a transport perspective, they range from insulators and semiconductors to metals. Thanks to their short-range order, the density of states (DOS) of amorphous solids might show features reminiscent to crystals [406, 412, 413, 419], such as spectral gaps. Amorphous materials are an interesting playground to study the physics of Anderson localization, and they can display exotic magnetic textures [420]. Despite the disorder, amorphous superconductors have also been synthesized [421, 422]. Indeed, to a first approximation, the isotropic superconducting gap in conventional superconductors is unaffected by dilute disorder, a statement known as Anderson's theorem [423–425]. While stronger disorder usually suppresses the critical temperature T_c, in certain cases the disorder-induced multifractality and rare regions might even give rise to an enhancement of T_c [426–428]. Due to this mechanism or to the suppression of other non-superconducting instabilities by the disorder, several amorphous materials display a higher T_c than their crystalline counterparts. For example, amorphous Bismuth is a metal that becomes superconducting at $\sim$ 6K [429], while its crystalline counterpart is a low-density compensated semimetal which only undergoes a superconducting transition below $\sim$ 0.5mK [430].

Besides their interesting physical properties, the growth of several amorphous materials requires less stringent conditions than single crystals, and allows for a range of compositions. This makes amorphous materials useful for several technological applications [401], from window glass to computer memories and solar cells [431, 432]. For instance, phase-change materials, which can transition between the amorphous and crystalline states in a controlled and reversible manner by applying current or laser pulses [433], are used in computer memory-storage devices [431, 432].

Before concluding this section, it is worth mentioning quasicrystals [434–436], which lie between the amorphous and crystalline limits. Quasicrystalline lattices are ordered, in the sense that they are constructed from a set of composition rules using a given unit block called tile, but they lack translational periodicity. They typically feature long-range rotational order [437], which gives rise to sharp diffraction peaks [438–441]. Their energy spectrum shows interesting fractal and localization properties [442]. A simple 1D example is given by an atomic chain with an incommensurate potential, as in an incommensurate CDW [443]. In higher dimensions,

the absence of perfect translational invariance in quasicrystals allows rotational symmetries not compatible with crystals [435], including fivefold or eightfold rotations [444].

3.1.3 Topology in amorphous systems

The robustness of topological phases against disorder has been studied since the beginning of the field with the integer quantum Hall effect [445–447]. In this case, not only are topological properties robust, but a modest amount of disorder is crucial for the quantization of the conductivity away from integer filling of a Landau level [445–447] (see however Ref. [448]). Indeed, for symmetry class A in 2D, which applies to the quantum Hall effect, states at any energy are localized by any amount of disorder except at a set of discrete energies, where a delocalized state can appear [447, 449]. These are the energies where the topological transitions between phases with different Chern numbers occur.

In lattice systems, disorder has been usually modelled by disordering the onsite energies, and typically uncorrelated between different sites [450]. We will refer to this kind of disorder as Anderson disorder. Within this point of view, the disordered energies are sampled from a probability distribution characterized by an energy scale W. In the limit of infinite disorder, $W \to \infty$, all noninteracting systems are trivial localized Anderson insulators. However, topological insulators are robust against moderate disorder preserving the protecting symmetries, as long as it does not close the mobility gap. This especially applies to strong topological phases, which are only protected by local non-spatial symmetries. Moreover, moderate disorder can renormalize the parameters of the low-energy effective theory and favour and even induce a topological phase from an otherwise trivial state [108, 109]. This so-called topological Anderson insulator [108, 109] or superconductor [451] is adiabatically connected to the disorder-free topological state. The robustness against disorder extends to spatial-symmetry-protected topological phases, as long as the disorder preserves the protecting symmetry on average [113, 452–457]. This protection is related to the so-called statistical topological insulators [113], which are spectral insulators displaying gapless boundary states. The symmetry class of d-dimensional statistical topological insulators has to allow a topological phase in the $(d-n)$-dimensional boundary. Then, the gapless boundary states are pinned to the critical point of a topological phase transition. Consequently, they behave as critical $(d-n)$-dimensional states, and not like topological boundary states: for instance, the conductance of a 1D critical state scales polynomially with size, instead of being constant. Certain crystalline topological insulators might become statistical topological insulators when disorder is added.

In this Thesis, we will focus on systems with structural disorder, i.e., disorder in the geometry of the lattice itself. Although physical amorphous materials present both structural and Anderson disorder, it is worth studying the former for several reasons. First of all, contrary to a random

potential, structural disorder leads to a continuum low-energy theory where the metric is also disordered [458], as in quenched quantum gravity, which can lead to a different localization length critical exponent in a topological phase transition [458]. Secondly, identifying a characteristic energy scale for structural disorder is not always obvious. Moreover, some of the methods to study Anderson disorder in regular lattices, such as the transfer matrix method, can no longer be applied with structural disorder, which calls for the development of other tools.

There are a variety of structurally-disordered models displaying topological phases, ranging from strong topological states [120, 417, 418, 459–470] to spatial-symmetry-protected topological phases [456, 471–477], as well as topologically ordered states in strongly correlated amorphous systems [478–481]. A variety of topological phases have also been studied in quasicrystals [110, 482–494]. Amorphous strong topological states include 2D Chern insulators in class A [120, 459–466], 2D and 3D time-reversal invariant topological insulators in class AII [417, 418, 459, 465, 467, 468], and 2D time-reversal breaking topological superconductors in class D [469, 470]. Amorphous structures also support phases *a priori* protected by crystalline symmetries, such as 2D reflection-symmetry-protected topological insulators [456], 2D and 3D higher-order topological insulators [472–474, 477], 2D and 3D obstructed insulators [475], and 3D topological metals [471, 476]. While structural disorder is detrimental to some of these states, it can also induce nontrivial phases when starting from a trivial crystalline state [468, 471, 473], and it can give rise to new phenomenology intrinsically associated with amorphous topological matter and phase transitions [456, 465, 466, 471, 475–477].

A common starting point to study these models is a crystalline tight-binding Hamiltonian known to host a topologically nontrivial phase. The hopping terms are generalized to account for arbitrary angles and distances between sites. For example the angular dependence can be modelled using the Slater-Koster parametrization [495], and the radial dependence can be accounted for by an exponential [456, 459, 465, 466, 470–473, 496] or polynomial [468] decay with the distance. There are several ways to introduce structural disorder, including lattices with uncorrelated random sites [456, 459, 465, 466, 469–473, 496], more realistic random network models which preserve the local coordination number [120, 462, 463, 475], and lattices with controllable deviations from the crystalline limit [460, 461, 468, 473]. Alternatively, DFT and *ab initio* molecular dynamics are also applied to generate realistic atomic structures [416–418]. In these methods, the noncrystalline structures are modelled as periodic supercells, but only the zero momentum eigenstates are needed for sufficiently large systems.

On the experimental side, amorphous topological matter has been mainly realized in synthetic platforms, such as mechanical systems of coupled gyroscopes [462], and photonic lattices [497–499]. The only direct evidence for an amorphous topological solid state system was reported in amorphous Bi_2Se_3, grown by physical vapor deposition in Refs. [4, 410]. The crystalline phase

of the van der Waals material Bi_2Se_3 is a textbook strong topological insulator. The amorphous samples of Ref. [4] are characterized by a local environment similar to the crystal, but with no van der Waals gap. ARPES shows surface states crossing the bulk electronic gap with a spin-momentum locking in agreement with the spin-resolved spectral function of an amorphous topological model. While Ref. [416] has studied an amorphous Bi_2Se_3 structure generated by *ab initio* molecular dynamics and determined it to be topologically trivial, the obtained structure is different from the experimental one. This indicates that the short- and medium-range structural orders are crucial for the topological properties.

Characterizing topology without translational symmetry

Predicting which solids host nontrivial topological phases is a central problem in the field of topological matter. As explained above, crystal symmetries are extremely useful to define computationally efficient symmetry indicators to identify topological materials [102, 104–107]. However, symmetry-based methods cannot be generically applied to diagnose nontrivial topology in materials that lack translational invariance such as amorphous, polycrystalline, and quasicrystalline materials. We now review different topological indicators applicable far from the translationally invariant limit.

For calculations modelling the noncrystalline structures as periodic supercells, Refs. [500, 501] have derived single $\boldsymbol{k}$-point formulas to determine the Chern and spin Chern numbers. Another wide-spread tool to characterize noncrystalline topological phases are topological markers, which allow to determine the topological invariants from a real-space description of the system. Topological markers can be local, i.e., defined for each real-space position, or nonlocal, i.e., globally defined for the whole real-space system.

The most studied local topological marker is the local Chern marker [502, 503], which measures the Chern number in even dimensions. The local Chern marker $\mathcal{C}(\boldsymbol{r})$ is a gauge invariant quantity essentially given by the diagonal elements of the Fourier transform of the Berry curvature, traced over the internal degrees of freedom:

$$\mathcal{C}(\boldsymbol{r}) = -2\pi i \sum_{\alpha} \langle \boldsymbol{r}\alpha | \left[P\mathcal{X}P, P\mathcal{Y}P \right] | \boldsymbol{r}\alpha \rangle, \tag{3.5}$$

where P is the projector onto occupied states, $\mathcal{X}$, $\mathcal{Y}$ are the x, y components of the position operator, and the operator multiplication is defined as $A = BC \Rightarrow \langle \boldsymbol{r}_1\alpha|A|\boldsymbol{r}_2\beta\rangle = \sum_\gamma \int d^d\boldsymbol{r}_3 \langle \boldsymbol{r}_1\alpha|B|\boldsymbol{r}_3\gamma\rangle\langle \boldsymbol{r}_3\gamma|C|\boldsymbol{r}_2\beta\rangle$, with the integral over the whole real space, and α, β, γ the internal degrees of freedom. If $|\psi_N\rangle$ are the eigenstates of the system, the projector onto occupied

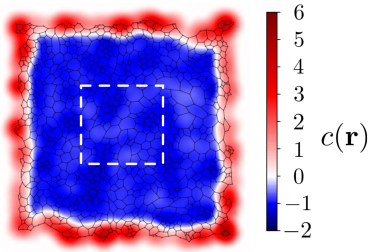

FIGURE 3: Local Chern marker for a finite amorphous sample in a Chern insulating state. The bulk of the system, indicated by a white dashed square, displays a relatively smooth local Chern marker, whose integral over the bulk is quantized to -1, signaling the topological phase. The boundary has a large contribution of opposite sign, so that the integral of the local Chern marker over the whole open system vanishes, as required. Extracted from Ref. [120].

states P is defined as the sum over occupied states of the density operators:

$$P = \sum_{N}^{\text{occ}} |\psi_N\rangle\langle\psi_N|, \tag{3.6}$$

so that $P^2 = P$, and the trace of P is the number of occupied states. The local Chern marker $\mathcal{C}(\boldsymbol{r})$ might spatially fluctuate, but, for a crystalline supercell with periodic boundary conditions, its average over a unit cell is quantized to the Chern number, $C = \frac{1}{V_{\text{cell}}} \int_{\text{cell}} d^d\boldsymbol{r}\mathcal{C}(\boldsymbol{r})$. In the case of noncrystalline lattices, obtaining the quantized Chern number requires averaging over a large enough region far from the edges of the system, with the size of the region being model dependent [503, 504]. The average has to be performed in the bulk far from the edges, or alternatively for a supercell with periodic boundary conditions, since, in a finite sample with open boundary conditions, the integral of $\mathcal{C}(\boldsymbol{r})$ over the whole system vanishes (see Fig. 3). Extending to real space the derivation of the spin Chern number [505–507], which measures the $\mathbb{Z}_2$ invariant in 2D time-reversal invariant systems, Ref. [508] has derived the local spin Chern marker. The local markers of Refs. [509, 510] are similar to the local Chern marker, but they are directly derived from and give the local Hall conductivity in the bulk of the system. Local topological markers have also been extended to other symmetry classes by Ref. [504], which introduced the chiral marker indicating the $\mathbb{Z}$ invariant of odd-dimensional phases with chiral symmetry, as well as the Chern-Simons marker characterizing the $\mathbb{Z}_2$ invariant of phases with either time-reversal or particle-hole symmetry in odd dimensions. Other local markers have also been developed for systems with chiral symmetry [511, 512], for Dirac Hamiltonians [513], and for topological crystalline insulators [514].

A different type of marker which is also locally defined is the spectral localizer [515–526]. It is an operator that quantifies the extent to which the Hamiltonian and the position operator can be continuously transformed to commute by an adiabatic process respecting the symmetries of the

system. The spectrum of the spectral localizer can signal strong [515, 516, 519–522, 524], weak [110] and crystalline [526] topological insulators, as well as topological gapless systems [476, 525–527].

Another class of markers are nonlocal topological markers, which indicate the topological indices globally. For instance, the Bott index [471, 518, 528–533], which is related to the spectral localizer since it also measures the obstruction to make the projected position operators commute, indicates the Chern number [534]. Analogously, the spin Chern number is signaled by the spin Bott index [416, 491, 492]. Generalizations to all strong topological invariants have also been developed [535]. Similar generalizations to determine the winding of the quadrupole and octupole moments have also been proposed [472, 473]. Finally, the scattering matrix can also determine topological invariants of d-dimensional noncrystalline systems attached to leads in one direction and with (anti-)periodic boundary conditions in the other $d-1$ dimensions [399].

The quantized response of topological phases is another useful tool in the absence of translational symmetry, such as the longitudinal conductance of 2D quantum Hall and quantum spin Hall insulators [459], and the Witten effect [496]. The presence of anomalous boundary states is signaled by the flow of the entanglement spectrum in noncrystalline topological insulators too, which can be learned by neural networks [536]. Neural networks can also learn features associated to topology directly from the wavefunctions [467].

Another efficient approach to determine topological transitions in noncrystalline matter is based on the effective Hamiltonian [111, 120, 456]. The effective Hamiltonian H_{eff} of a noninteracting tight-binding model is defined as the inverse of the Green's function G of the system projected into plane waves:

$$H_{\text{eff}}(\boldsymbol{p}) = E_F - G_{\text{eff}}^{-1}(\boldsymbol{p}, \omega = E_F), \tag{3.7}$$

$$G_{\text{eff}}^{\alpha,\beta}(\boldsymbol{p}, \omega) = \langle \boldsymbol{p}\alpha | G(\omega) | \boldsymbol{p}\beta \rangle, \tag{3.8}$$

$$G(\omega) = \lim_{\eta \to 0^+} \left[\omega - H + i\eta\right]^{-1}, \tag{3.9}$$

where H is the full Hamiltonian of the system, E_F is the Fermi energy, $\boldsymbol{p}$ is the linear momentum, α, β are the internal degrees of freedom (orbitals, spins...) of each site, and $|\boldsymbol{p}\alpha\rangle$ is the plane-wave state with momentum $\boldsymbol{p}$ and internal degree of freedom α:

$$|\boldsymbol{p}\alpha\rangle = \frac{1}{\sqrt{N_{\text{sites}}}} \sum_{\boldsymbol{r} \in \text{sites}} e^{i\boldsymbol{p}\cdot\boldsymbol{r}} |\boldsymbol{r}\alpha\rangle. \tag{3.10}$$

If the spectral gap of the total Hamiltonian closes, so does the spectral gap of H_{eff}, allowing the detection of topological phase transitions between gapped phases. Therefore, one can construct

topological invariants defined in terms of H_{eff}, which only change when its gap closes.

Finally, Ref. [120] has introduced average symmetry indicators for amorphous models displaying average local symmetries. For instance, in a certain limit where the system is topologically trivial, the model considered in Ref. [120] is symmetric under a local symmetry consisting of a threefold rotation in orbital space. Away from this particular limit, this symmetry is only respected on average, but the eigenstates can still be decomposed in the eigenbasis of the symmetry, and a symmetry-resolved spectral function can be computed. A topological transition is signaled by a crossing of states labelled by a different symmetry eigenvalue. Then, Ref. [120] has proposed a symmetry indicator that determines the Chern number modulo three by summing the symmetry eigenvalues of the occupied states. Moreover, at the momenta invariant under the symmetry, which are $\boldsymbol{p} = 0, \infty$, the eigenstates of the effective Hamiltonian can also be labelled by the symmetry, which allows to construct symmetry indicators analogous to the crystalline ones.

3.2 Structural spillage

In this Chapter, we focus on the problem of predicting topologically nontrivial phases in noncrystalline solids. As explained in previous sections, this task can be efficiently carried out in crystals using symmetry indicators [102–107], which have allowed high-throughput topological classifications based on DFT calculations [385, 537–542]. However, the lack of translational invariance and crystalline symmetries prevents a generic definition of symmetry indicators in amorphous, polycrystalline, and quasicrystalline materials. Real-space topological markers [462, 502, 504, 509–511, 513, 520, 522, 525, 526, 532, 543, 544] can be computationally costly and require the system to be treated on a case-by-case basis. Efficient approaches based on the effective Hamiltonian and average symmetry indicators have been applied in simple tight-binding models [120, 456, 475, 536, 545]. However, these do not include the full chemical and structural specificity found in real matter. Refs. [416–418] have modelled realistic amorphous materials using *ab initio* methods, but the topological characterization required extracting a Wannier-based tight-binding Hamiltonian, which is computationally demanding and system specific. Single-point formulas for the Chern and $\mathbb{Z}_2$ numbers constitute powerful tools for given symmetry classes [500, 501], but general and efficient formulas are still lacking.

To overcome this methodological problem, we introduce the "structural spillage", which is inherently compatible with first-principles approaches. The structural spillage is a method to calculate the overlap between wavefunctions with different structural configurations. The structural spillage is inspired by the spin-orbit spillage of Liu and Vanderbilt [117], which can identify topological band inversions in insulating crystals by comparing the wavefunction overlap of the same structure with and without spin-orbit coupling. In our case, we compare the wavefunctions

of a noncrystalline target system with those of a crystalline reference state, whose topological state can be efficiently determined by standard symmetry-based methods [102–107]. Based on arguments concerning its connections with the SOC spillage [117], the strange correlators [118, 119], and the average symmetry indicators [120], we propose that the structural spillage can signal the topological phase of noncrystalline materials. Indeed, we numerically demonstrate that the structural spillage reproduces the topological phase diagrams determined by the longitudinal conductance in amorphous tight-binding models inspired by bismuthene and a Bismuth bilayer. By construction, the structural spillage is applicable to generic noncrystalline materials in any symmetry class, and can be directly implemented in currently available DFT codes. Therefore, it is suitable to establish a high-throughput catalogue of potential noncrystalline topological materials.

The rest of the chapter is organized as follows. First, we review the SOC spillage of Ref. [117]. Then, we introduce the structural spillage, in a formulation which is directly compatible with first-principles calculations. We also comment the link between strange correlators and spillages. Afterwards, we comment the subtleties that arise when trying to apply the structural spillage to phenomenological tight-binding models, and adapt its formulation. In the following sections, we introduce simple amorphous tight-binding models inspired by bismuthene and bilayer Bismuth. We numerically determine their topological phase diagram using the structural spillage, benchmarking its predictions against the longitudinal conductance results. Finally, we review the structural spillage predictions for the DFT calculations of amorphous bilayer Bismuth performed by our collaborators Paul Corbae et al. in Ref. [3]. The Appendices describe the explicit connection between the structural spillage and the average symmetry indicators in the bismuthene tight-binding model, as well as further details regarding the application of the structural spillage in the tight-binding approximation.

3.2.1 Spin-orbit spillage

In Ref. [117], Liu and Vanderbilt introduced the spin-orbit (SOC) spillage for crystalline insulators. The SOC spillage measures the mismatch between the occupied projectors of a given crystalline structure with and without SOC as a function of the crystal momentum. Therefore, it shows the band inversions induced by SOC in the Brillouin zone. Based on the Wannier obstruction to find a smooth symmetric gauge for topological insulators, they showed that the SOC spillage can indicate the topological transitions induced by SOC.

Consider the two projection operators P and $\tilde{P}$ onto the occupied states of a target and a reference system, respectively (see Eq. (3.6) for the definition of the projector). Throughout this Chapter, we will add a tilde to the quantities belonging to the reference system $\tilde{P}$, while the quantities associated to the target system P will carry no tilde. Assume that both projectors have

the same rank, i.e., that both systems have the same number of occupied states or filling N_{occ}:

$$\text{Tr}\left[P\right] = \text{Tr}\left[\tilde{P}\right] = N_{\text{occ}}, \tag{3.11}$$

where Tr is the trace over the whole Hilbert space. Liu and Vanderbilt [117] defined the total spillage γ between the two systems as

$$\gamma = N_{\text{occ}} - \text{Tr}\left[P\tilde{P}\right] = \text{Tr}\left[P(1-\tilde{P})\right]. \tag{3.12}$$

When $P = \tilde{P}$, the spillage vanishes. However, when the overlap between the two projectors is zero, it equals the total number of occupied states N_{occ}. Therefore, γ acts as an indicator of band inversions caused by the parameters that differ in P and $\tilde{P}$ [117]. In particular, Liu and Vanderbilt took the target system P to be a crystalline insulator with SOC, and the reference system $\tilde{P}$ to be the same crystalline structure but without SOC. Taking advantage of the translational invariance, the projectors can be decomposed as a function of the crystal momentum $\boldsymbol{k}$ in the Brillouin zone:

$$P = \sum_{\boldsymbol{k}} P(\boldsymbol{k}), \tag{3.13}$$

$$P(\boldsymbol{k}) = \sum_{n=1}^{n_{\text{occ}}} P_n(\boldsymbol{k}) = \sum_{n=1}^{n_{\text{occ}}} |\psi_{n\boldsymbol{k}}\rangle\langle\psi_{n\boldsymbol{k}}|, \tag{3.14}$$

where $|\psi_{n\boldsymbol{k}}\rangle$ is the Bloch eigenstate of band n at Bloch momentum $\boldsymbol{k}$. n_{occ} is the number of occupied bands, which is independent of $\boldsymbol{k}$ for band insulators, and coincides in both target and reference systems. We remark that $P(\boldsymbol{k})$ is itself a projector, meaning that $P(\boldsymbol{k})P(\boldsymbol{k}') = P(\boldsymbol{k})\delta_{\boldsymbol{k}\boldsymbol{k}'}$. The total spillage can therefore be decomposed as a sum of $\boldsymbol{k}$-resolved SOC "Bloch" spillages $\gamma_{\text{B}}(\boldsymbol{k})$:

$$\gamma = \sum_{\boldsymbol{k}} \gamma_{\text{B}}(\boldsymbol{k}), \tag{3.15}$$

$$\gamma_{\text{B}}(\boldsymbol{k}) = n_{\text{occ}} - \text{tr}\left[P(\boldsymbol{k})\tilde{P}(\boldsymbol{k})\right] = n_{\text{occ}} - \sum_{n,m=1}^{n_{\text{occ}}} |M_{nm}(\boldsymbol{k})|^2, \tag{3.16}$$

where now the trace tr is taken over the bands at $\boldsymbol{k}$, and we have defined the overlap matrix $M_{nm}(\boldsymbol{k}) = \langle\psi_{n\boldsymbol{k}}|\tilde{\psi}_{m\boldsymbol{k}}\rangle$. With the goal to determine the SOC spillage with plane-wave based DFT, Liu and Vanderbilt [117] provided the particular expression of the overlap matrix $M_{nm}(\boldsymbol{k})$ in the plane-wave basis. Plane-wave states $|\boldsymbol{p}\alpha\rangle$ have a definite plane-wave continuum momentum $\boldsymbol{p}$ not necessarily restricted to the first BZ, and a internal spin degree of freedom α, and form an orthonormal basis of the Hilbert space, $\langle\boldsymbol{p}\alpha|\boldsymbol{p}'\beta\rangle = \delta_{\boldsymbol{p}\boldsymbol{p}'}\delta_{\alpha\beta}$. Bloch eigenstates are expressed in this basis as:

$$|\psi_{n\boldsymbol{k}}\rangle = \sum_{\boldsymbol{G}\alpha} \langle\boldsymbol{k}+\boldsymbol{G}\alpha|\psi_{n\boldsymbol{k}}\rangle|\boldsymbol{k}+\boldsymbol{G}\alpha\rangle, \tag{3.17}$$

where $\boldsymbol{G}$ are the reciprocal lattice vectors, and therefore the overlap matrix is:

$$M_{nm}(\boldsymbol{k}) = \langle \psi_{n\boldsymbol{k}} | \tilde{\psi}_{m\boldsymbol{k}} \rangle = \sum_{\boldsymbol{G}\alpha} \langle \psi_{n\boldsymbol{k}} | \boldsymbol{k}+\boldsymbol{G}\alpha \rangle \langle \boldsymbol{k}+\boldsymbol{G}\alpha | \tilde{\psi}_{m\boldsymbol{k}} \rangle \tag{3.18}$$

It is also useful for our purposes to express the SOC Bloch spillage in terms of projector matrix elements in the plane-wave basis $P^{\alpha\beta}_{\boldsymbol{p},\boldsymbol{p}'} = \langle \boldsymbol{p}\alpha | \, P \, | \boldsymbol{p}'\beta \rangle$:

$$\gamma_{\mathrm{B}}(\boldsymbol{k}) = n_{\mathrm{occ}} - \sum_{\boldsymbol{G}\alpha} \sum_{\boldsymbol{G}'\beta} P^{\alpha\beta}_{\boldsymbol{k}+\boldsymbol{G},\boldsymbol{k}+\boldsymbol{G}'} \tilde{P}^{\beta\alpha}_{\boldsymbol{k}+\boldsymbol{G}',\boldsymbol{k}+\boldsymbol{G}} \tag{3.19}$$

We note that the SOC Bloch spillage can be also determined with local-basis DFT as well as with Wannier and phenomenological tight-binding models; only the particular evaluation of the overlap matrix will differ.

Liu and Vanderbilt [117] also unveiled the link between the SOC Bloch spillage and the topological character of the target P and reference $\tilde{P}$ systems. They showed that if P and $\tilde{P}$ are in a different topological phase, the SOC Bloch spillage has to be larger than 1 at least at one crystal momentum $\boldsymbol{k}$ in the Brillouin zone, where the topological band inversion occurs. The proof is by contradiction and is based on the Wannier obstruction. We assume that P is topological and $\tilde{P}$ is trivial, so that a smooth symmetric gauge can be found for $|\tilde{\psi}_{m\boldsymbol{k}}\rangle$. If we assume that $\gamma_{\mathrm{B}}(\boldsymbol{k}) < 1, \forall \boldsymbol{k}$, then the overlap matrix is nonsingular, $\det[M(\boldsymbol{k})] > 0$. This would allow constructing a smooth symmetric gauge for $|\psi_{n\boldsymbol{k}}\rangle$, which contradicts the assumption of P being topological. Therefore, $\gamma_{\mathrm{B}}(\boldsymbol{k}_0) > 1$ at least at one $\boldsymbol{k}_0$ in the Brillouin zone. If there is TRS, then a band inversion will also occur at $-\boldsymbol{k}_0$, $\gamma_{\mathrm{B}}(-\boldsymbol{k}_0) > 1$. In this case, if $\boldsymbol{k}_0$ is a time-reversal invariant momentum, $\boldsymbol{k}_0 = -\boldsymbol{k}_0 + \boldsymbol{G}$, then the band inversions add up, $\gamma_{\mathrm{B}}(\boldsymbol{k}_0) > 2$. Moreover, Ref. [117] found numerically that when comparing a trivial state with a Chern insulator, the SOC Bloch spillage is larger that the absolute value of the Chern number.

The previous argument can be generalized, so that if P and $\tilde{P}$ are in a different topological state and thus not adiabatically connected, then necessarily $\gamma_{\mathrm{B}}(\boldsymbol{k}) > 1$ at least at one $\boldsymbol{k}$ in the Brillouin zone. The SOC Bloch spillage can therefore act as an efficient topological indicator for strong and crystalline topological insulators induced by the SOC. Indeed, Refs. [546, 547] have successfully applied the SOC spillage as a screening method in high-throughput searches for topological crystals. Due to the sizable band inversion close to the nodes of several topological semimetals, they observed that the SOC spillage can also signal them.

However, $\gamma_{\mathrm{B}}(\boldsymbol{k}) > 1$ is only a necessary but not sufficient condition for topology. For instance, two band inversions can make the target system to have the same topology as the reference. Another example relevant to the topic of this Thesis is when the periodic real-space unit cell is large and complex, as an amorphous supercell. In this case, there can be many bands close to the Fermi

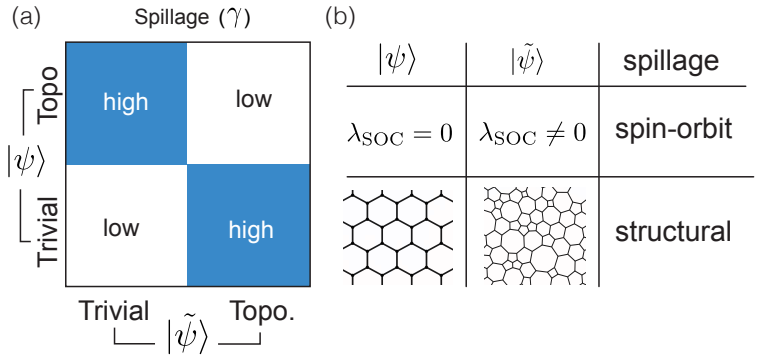

FIGURE 4: (a) The spillage γ is high or low depending on whether the target wavefunction $|\psi\rangle$ is in the same or different topological state compared to a known reference wavefunction $|\tilde{\psi}\rangle$. (b) The spin-orbit spillage [117] compares crystalline wavefunctions with and without SOC. The structural spillage takes advantage of the knowledge of the topological state of a crystalline solid to find the topological state of an amorphous solid.

level. Each of them can be slightly mixed by SOC, giving rise to a high SOC Bloch spillage even if there is no topological band inversion. In this case of a big supercell, in order to identify the bands that have been possibly inverted by SOC, Liu and Vanderbilt [117] proposed to use a band-resolved spillage. However, this quantity is not gauge invariant under a unitary transformation of the occupied or unoccupied subspaces, and its connection with the topological character is not clear. Here, we propose a different path to tackle this situation. We introduce the structural spillage, which is applicable to noncrystalline structures. We show that, by applying it to compare the noncrystalline material with its corresponding crystal, the structural spillage can detect topological band inversions.

3.2.2 Structural spillage: general formulation

In this section we introduce the structural spillage as an efficient method to screen noncrystalline topological materials, from amorphous and disordered systems to quasicrystals and nanocrystals. We propose to compare the noncrystalline target system with its crystalline counterpart closest in local structure. The topological state of the latter can be readily characterized with the well-developed methods for crystals, such as the symmetry indicators [104]. With this information, the band inversions measured by the structural spillage can indicate the topological state of the target noncrystalline material (see Fig. 4). The structural spillage can also be applied to compare two crystalline systems with a different lattice structure, which allows to study the topological transitions as a function of pressure or strain. Moreover, it is well defined even in the absence of a spectral gap.

We start by rewriting the expression for the total spillage between the target P and reference $\tilde{P}$ systems of Eq. (3.12):

$$\gamma = \frac{1}{2}\mathrm{Tr}\left[\left(P-\tilde{P}\right)^2\right] = \frac{1}{2}\left(N_{\mathrm{occ}} + \tilde{N}_{\mathrm{occ}} - \mathrm{Tr}\left[P\tilde{P}+\tilde{P}P\right]\right), \tag{3.20}$$

where the trace Tr acts on the entire Hilbert space. If both systems have the same total number of occupied states $N_{\mathrm{occ}} = \mathrm{Tr}[P] = \mathrm{Tr}[\tilde{P}] = \tilde{N}_{\mathrm{occ}}$, Eq. (3.20) simplifies to Eq. (3.12). Even if this is not the case and $N_{\mathrm{occ}} \neq \tilde{N}_{\mathrm{occ}}$, the formulation (3.20) has the advantage that $\gamma \geq 0$ by definition. Actually, Eq. (3.20) allows the spillage to be interpreted as the variance between two distributions with the same average. In what follows, we propose a spillage that compares a noncrystalline system P with its crystalline counterpart $\tilde{P}$, defined as the crystalline phase of the same composition which has the more similar local structural environment.

Here we formulate the structural spillage in a plane-wave basis, which enables its direct incorporation into standard plane-wave-based DFT codes. Note that plane-wave states are well-defined for crystalline and noncrystalline systems. By substituting the closure relation in the plane-wave basis into Eq. (3.20), we can rewrite the full spillage γ in terms of the projector matrix elements $P^{\alpha\beta}_{\boldsymbol{p},\boldsymbol{p}'} = \langle \boldsymbol{p}\alpha | \, P \, | \boldsymbol{p}'\beta \rangle$:

$$\gamma = \frac{1}{2}\sum_{\boldsymbol{p}\alpha}\sum_{\boldsymbol{p}'\beta}\left[P^{\alpha\beta}_{\boldsymbol{p},\boldsymbol{p}'}P^{\beta\alpha}_{\boldsymbol{p}',\boldsymbol{p}} + \tilde{P}^{\alpha\beta}_{\boldsymbol{p},\boldsymbol{p}'}\tilde{P}^{\beta\alpha}_{\boldsymbol{p}',\boldsymbol{p}} - P^{\alpha\beta}_{\boldsymbol{p},\boldsymbol{p}'}\tilde{P}^{\beta\alpha}_{\boldsymbol{p}',\boldsymbol{p}} - \tilde{P}^{\alpha\beta}_{\boldsymbol{p},\boldsymbol{p}'}P^{\beta\alpha}_{\boldsymbol{p}',\boldsymbol{p}}\right]. \tag{3.21}$$

Any plane-wave momentum $\boldsymbol{p}$ can be uniquely decomposed as $\boldsymbol{p} = \boldsymbol{k} + \boldsymbol{G}$, the sum of a crystal momentum $\boldsymbol{k}$ in the first BZ of the reference crystal plus a reciprocal lattice vector $\boldsymbol{G}$ of the reference crystal. We can therefore split the summations of Eq. (3.21) as $\sum_{\boldsymbol{p}} = \sum_{\boldsymbol{k}}\sum_{\boldsymbol{G}}$. Then, we rewrite the total spillage as:

$$\gamma = \sum_{\boldsymbol{k}} \gamma_{\mathrm{qB}}(\boldsymbol{k}), \tag{3.22}$$

where we have defined the structural quasi-Bloch spillage $\gamma_{\mathrm{qB}}(\boldsymbol{k})$:

$$\gamma_{\mathrm{qB}}(\boldsymbol{k}) = \frac{1}{2}\sum_{\boldsymbol{k}'}\sum_{\boldsymbol{G}\boldsymbol{G}'}\sum_{\alpha\beta}\left[P^{\alpha\beta}_{\boldsymbol{k}+\boldsymbol{G},\boldsymbol{k}'+\boldsymbol{G}'}P^{\beta\alpha}_{\boldsymbol{k}'+\boldsymbol{G}',\boldsymbol{k}+\boldsymbol{G}} - P^{\alpha\beta}_{\boldsymbol{k}+\boldsymbol{G},\boldsymbol{k}'+\boldsymbol{G}'}\tilde{P}^{\beta\alpha}_{\boldsymbol{k}'+\boldsymbol{G}',\boldsymbol{k}+\boldsymbol{G}}\right] + \left[P \leftrightarrow \tilde{P}\right] = \tag{3.23a}$$

$$= \frac{1}{2}\left\{\left[\sum_{\boldsymbol{G}\alpha}P^{\alpha\alpha}_{\boldsymbol{k}+\boldsymbol{G},\boldsymbol{k}+\boldsymbol{G}}\right] + \tilde{n}_{\mathrm{occ}}(\boldsymbol{k}) - \sum_{\boldsymbol{G}\alpha}\sum_{\boldsymbol{G}'\beta}\left[P^{\alpha\beta}_{\boldsymbol{k}+\boldsymbol{G},\boldsymbol{k}+\boldsymbol{G}'}\tilde{P}^{\beta\alpha}_{\boldsymbol{k}+\boldsymbol{G}',\boldsymbol{k}+\boldsymbol{G}} + \tilde{P}^{\alpha\beta}_{\boldsymbol{k}+\boldsymbol{G},\boldsymbol{k}+\boldsymbol{G}'}P^{\beta\alpha}_{\boldsymbol{k}+\boldsymbol{G}',\boldsymbol{k}+\boldsymbol{G}}\right]\right\}, \tag{3.23b}$$

To arrive at Eq. (3.23b), we have used the fact that the reference projector $\tilde{P}$ corresponds to a crystal, which allows us to set $\boldsymbol{k}' = \boldsymbol{k}$ in terms involving at least one $\tilde{P}$, since there are no finite

matrix elements (hereafter referred as scattering) between different crystal momenta $\boldsymbol{k}$ and $\boldsymbol{k}'$ due to the discrete translational symmetry. In Eq. (3.23b), $\tilde{n}_{\mathrm{occ}}(\boldsymbol{k})$ is the number of occupied bands of the reference crystal at crystal momentum $\boldsymbol{k}$:

$$\tilde{n}_{\mathrm{occ}}(\boldsymbol{k}) = \sum_{\boldsymbol{k}'} \sum_{\boldsymbol{G}\boldsymbol{G}'} \sum_{\alpha\beta} \tilde{P}^{\alpha\beta}_{\boldsymbol{k}+\boldsymbol{G},\boldsymbol{k}'+\boldsymbol{G}'} \tilde{P}^{\beta\alpha}_{\boldsymbol{k}'+\boldsymbol{G}',\boldsymbol{k}+\boldsymbol{G}} = \sum_{\boldsymbol{G}\alpha} \tilde{P}^{\alpha\alpha}_{\boldsymbol{k}+\boldsymbol{G},\boldsymbol{k}+\boldsymbol{G}} = \mathrm{tr}\left[\tilde{P}(\boldsymbol{k})\right] \tag{3.24}$$

Note that $\gamma_{\mathrm{qB}}(\boldsymbol{k})$ fulfills the same sum rule (3.22) as the Bloch spillage in Eq. (3.15). Therefore, when applied to two insulating crystals, $\gamma_{\mathrm{qB}}(\boldsymbol{k})$ recovers the Bloch spillage $\gamma_{\mathrm{B}}(\boldsymbol{k})$ of Eqs. (3.16) and (3.19). The quasi-Bloch spillage is well-defined in the absence of a spectral gap. For instance, when applied to semimetallic crystals, it simplifies to:

$$\gamma_{\mathrm{qB}}^{\mathrm{crystals}}(\boldsymbol{k}) = \frac{1}{2}\left[n_{\mathrm{occ}}(\boldsymbol{k}) + \tilde{n}_{\mathrm{occ}}(\boldsymbol{k})\right] - \mathrm{tr}\left[P(\boldsymbol{k})\tilde{P}(\boldsymbol{k})\right], \tag{3.25}$$

which is similar to the Bloch spillage $\gamma_{\mathrm{B}}(\boldsymbol{k})$ of Eq. (3.16), but with n_{occ} replaced by $\frac{1}{2}[n_{\mathrm{occ}}(\boldsymbol{k}) + \tilde{n}_{\mathrm{occ}}(\boldsymbol{k})]$, which accounts for the possibly different fillings at different $\boldsymbol{k}$ for the two systems P and $\tilde{P}$. By construction, our quasi-Bloch spillage particularized to semimetallic crystals $\gamma_{\mathrm{qB}}^{\mathrm{crystals}}(\boldsymbol{k})$ of Eq. (3.25) is bounded by zero, in contrast to recent extensions of the Bloch spillage semimetallic crystals [546, 547].

Our key result is that the structural quasi-Bloch spillage, defined by Eq. (3.23), can be used as an efficient topological indicator in noncrystalline systems. Crucially, it can be efficiently computed with plane-wave-based DFT methods, since the projector matrix elements are an output of the calculation. Consequently, this method is suitable for high-throughput identification of noncrystalline topological materials. Eq. (3.23) can also be computed using localized-basis DFT or Wannier-based tight-binding modelling, by determining the plane-wave coefficients using a Fourier transform. However, as we will discuss in Section 3.2.3, Eq. (3.23) requires certain recasting in order to be applicable within the tight-binding approximation to compare two systems with different lattice structures. By tight-binding approximation, we refer to lattice models where the only information about the wavefunctions is the position of their Wannier charge centers and their transformation properties under symmetries, but their spatial structure is unknown and therefore considered to be a Dirac delta. In the next section, we explain the approximations required to adapt the structural quasi-Bloch spillage of Eq. (3.23) to the tight-binding approximation. The connection between the average symmetry indicators and the structural spillage, explained in Appendix 3.B, allows to justify these approximations and describes an alternative path to arrive at the tight-binding formulation of the structural spillage.

Rationale for the spillage: non-Wannierizability and strange correlators

Before concluding this section, we comment several arguments that support the application of the structural spillage as a topological indicator. While we provide no formal mathematical proof of the rigorous validity of the structural spillage, we give a qualitative discussion based on general features that strongly support its applicability.

First, the structural spillage is an extension of Liu and Vanderbilt's SOC spillage [117] that, in the limit of vanishing disorder, recovers the latter. This justifies the validity of the structural spillage in the weak-disorder case. We highlight that weak disorder here means that there is a significant degree of short-range order, while the lack of long-range order does not have much effect. This feature is usually displayed by covalently-bonded amorphous solids [401].

More generally, the main justification for the structural spillage comes from the obstruction to Wannierization, which is also the reason why Liu and Vanderbilt's SOC spillage works. This Wannier obstruction has been shown to occur in strong topological phases irrespective of their lattice structure, and therefore applies to noncrystalline systems as well. Mathematically, this has been proven using the spectral localizer [515–526]. In particular, the Wannier obstruction emerges as an obstruction to close the gap of the spectrum of the spectral localizer. While this does not mathematically prove the validity of the structural spillage, the non-Wannierizability of noncrystalline topological insulators suggests that there is no reason to believe why it should not work. Accordingly, our numerical benchmarks in amorphous tight-binding models indicate this is indeed the case.

Another argument justifying the validity of the structural spillage is the general relationship between the spillage in noninteracting systems and the so-called strange correlators [118, 119]. Strange correlators are real-space quantities that diagnose the topology of symmetry protected topological phases, based on the non-Wannierizability of short-range entangled topologically non-trivial phases. Strange correlators compute the overlap of a given operator between the ground state wavefunctions of a target and a trivial reference systems. For translationally-invariant noninteracting systems, the operator can be chosen to be the identity, which then coincides with the Liu and Vanderbilt's SOC spillage when resolved in crystal momentum. However, the strange correlator is not restricted to translationally-invariant systems. In this latter case, the strange correlator would be related to our structural spillage by choosing the appropriate operator and Fourier transforming to momentum space[5].

[5]More precisely, what would be directly related to a strange correlator is the structural plane-wave spillage defined in Eqs. (3.49) and (3.51) of Appendix 3.B.3, which indeed correctly works in tight-binding models. The additional resummations of the structural quasi-Bloch spillage of Eq. (3.23) are added so that the structural spillage recovers Liu and Vanderbilt's spillage in the crystalline limit.

A final argument justifying the validity of our structural spillage in noncrystalline systems is its relation with average symmetry indicators, which were introduced by Ref. [120] in simple amorphous tight-binding models. Amorphous average symmetry indicators evaluate the topology by measuring the number of occupied states characterized by a given eigenvalue of an average symmetry. Furthermore, these can be resolved in momentum by projecting to plane waves. In a topological phase transition, these numbers change at a given momentum. The structural spillage indeed measures band inversions. So when the band inversion changes the occupied symmetry eigenvalues, the structural spillage is equivalent to the symmetry indicator[6]. With our amorphous bismuthene model as an example, we will discuss their particular connection in Appendix 3.B.

In summary, the non-Wannierizability of noncrystalline topological states as well as the connections to SOC spillage, strange correlators and average symmetry indicators, all suggest that the structural spillage can signal the topology of noncrystalline solids, at least when there is a certain degree of short-range order, as demonstrated by our numerical tight-binding benchmarks in Sections 3.3 and 3.4.

3.2.3 Structural spillage in the tight-binding approximation

In this section, we explain why the structural quasi-Bloch spillage $\gamma_{\mathrm{qB}}(\boldsymbol{k})$ of Eq. (3.23) cannot be directly applied within the tight-binding approximation, and we propose several approximations to adapt it. The full details of the steps sketched here can be found in Appendix 3.C.

We mention again that the ingredients of the tight-binding approximation are the Wannier centers of the orbitals, as well as the hopping values and their dependence on relative positions, but not the real-space wavefunctions of the orbitals. It is the lack of this information that prevents the direct application of Eq. (3.23) to compare two systems with different lattice structure. This same lack of spatial information, together with the requirement of gauge invariance, forces the position operator to be diagonal, with vanishing matrix elements connecting neighbouring orbitals. In other words, orbitals wavefunctions in real space are considered to be Dirac deltas located at the Wannier centers. This approximation not only affects the structural spillage, but also other quantities, such as optical responses, which depend on the position operator matrix elements.

An implicit assumption in the general derivation of Eq. (3.23) is that the Hilbert space of the system is the whole real space (with spin), in which the plane waves constitute an orthonormal basis. While this is applicable in DFT (see Appendix 3.A), it is not true in the tight-binding approximation, where the Hilbert space is just spanned by the positions of the Wannier charge centers with the internal degrees of freedom of spin and orbital type. The fundamental problem for comparing two

[6] As with strange correlators, it is the plane-wave spillage (3.49) that exactly coincides with the symmetry indicator (see Appendix 3.B).

tight-binding systems with different lattice structures, as done by the structural spillage, stems from the fact that their Hilbert spaces are different, and therefore, strictly, their overlap is ill-defined. Nevertheless, we can derive a physically motivated expression for the structural spillage in the tight-binding approximation. In Appendix 3.B, we show that this expression is directly linked to the average symmetry indicators. In subsequent sections we will show numerically that this approximation correctly captures the topological phase diagrams of tight-binding models.

Target and reference with the same lattice structure: non-orthogonal formalism

For pedagogical reasons, we first study the problem of applying the structural spillage to compare target and reference systems with the same lattice structure, i.e., we compare two amorphous or two crystalline systems. This case is exactly solvable, since the Hilbert spaces spanned by the target and reference systems are the same. Moreover, it can be useful beyond its pedagogical value, for example to study the effect of Anderson disorder in the onsite and hopping energies. Afterwards, we will consider the general case of comparing two different lattice structures, which requires several approximations.

With this in mind, we consider a tight-binding model with N_{sites} sites, each with N_{orb} internal degrees of freedom (spin and orbital). The Hilbert space of the tight-binding model is spanned by the Dirac delta-like states $|\boldsymbol{r}\alpha\rangle$, where $\boldsymbol{r}$ labels the position of each site and α labels the internal quantum numbers. Plane-wave states with continuum momentum $\boldsymbol{p}$ in the tight-binding are defined as in Eq. (3.10):

$$|\boldsymbol{p}\alpha\rangle = \frac{1}{\sqrt{N_{\text{sites}}}} \sum_{\boldsymbol{r}} e^{i\boldsymbol{p}\cdot\boldsymbol{r}} |\boldsymbol{r}\alpha\rangle. \tag{3.26}$$

These plane waves have two important properties.

First, while the set of plane-wave states is a basis of the real space, it constitutes an overcomplete set when projected to the tight-binding Hilbert space. Therefore, we have to choose a subset of them to form a basis. Consider the Hilbert space of a tight-binding model of a crystal with N_{cell} unit cells, $N_{\text{s/c}}$ sites per unit cell, and N_{orb} orbitals, which has dimension $N_{\text{cell}} \times N_{\text{s/c}} \times N_{\text{orb}} = N_{\text{sites}} \times N_{\text{orb}}$, where $N_{\text{sites}} = N_{\text{cell}} \times N_{\text{s/c}}$ is the total number of sites. Before proposing a well-defined plane wave basis, we note that Brillouin zones are labelled by the reciprocal lattice vectors $\boldsymbol{G}$: the momentum $\boldsymbol{p} = \boldsymbol{k} + \boldsymbol{G}$ belongs to the Brillouin zone $\boldsymbol{G}$, with the first Brillouin zone corresponding to $\boldsymbol{G} = 0$. We can classify Brillouin zones $\boldsymbol{G}$ in different types depending on the phase factors $\{e^{i\boldsymbol{G}\cdot\boldsymbol{t}}\}$ which enter in the observables projected to a plane-wave momentum $\boldsymbol{p} = \boldsymbol{k} + \boldsymbol{G}$, where $\boldsymbol{t}$ are the relative positions of the sites inside the unit cell (see Appendix 3.C.2). Such classification is known in ARPES [548], since the intensities of photoelectrons with momentum $\boldsymbol{k}$ and $\boldsymbol{k} + \boldsymbol{G}$ are different in general. This is not just an effect of the ARPES matrix elements [548], but it comes from the overlap between Bloch states and plane waves (see

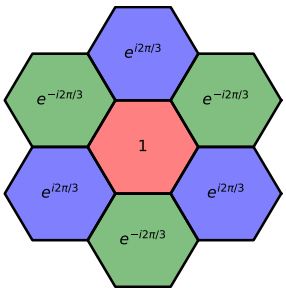

FIGURE 5: Types of Brillouin zones for the honeycomb lattice labelled by the phase factor $e^{-i\boldsymbol{G}\cdot\boldsymbol{t}}$, with $\boldsymbol{t} = -a(0, 1/\sqrt{3})$. The first Brillouin zone (red) is labelled by $\boldsymbol{G} = 0$ and therefore a phase factor 1. The nearest neighbour Brillouin zones have phase factors $e^{\pm i2\pi/3}$.

also Eq. (3.29)). For instance, in the honeycomb lattice there are $N_{\text{BZs}} = 3$ types of BZ, since $e^{-i\boldsymbol{G}\cdot\boldsymbol{t}} = e^{ia2\pi/3}$, with $a \in \mathbb{Z}_3$ (see Fig. 5). With this in mind, a well-defined plane-wave basis $\{|\boldsymbol{k}+\boldsymbol{G}\rangle\}_{\boldsymbol{G}\in N_{\text{s/c}}\text{ BZs}}$ consists of a subset with N_{cell} momenta per Brillouin zone, in $N_{\text{s/c}}$ Brillouin zones labelled by an inequivalent $\boldsymbol{G}$. For instance, in the honeycomb lattice with $N_{\text{s/c}} = 2$, we can choose a basis with momenta in the first Brillouin zone $\boldsymbol{G} = 0$ and one of the second Brillouin zones, e.g. $\boldsymbol{G} = \frac{4\pi}{\sqrt{3}a}(0, 1)$: $\{|\boldsymbol{k}+\boldsymbol{G}_0\rangle, |\boldsymbol{k}+\boldsymbol{G}_1\rangle\}$.

Second, the plane waves projected to the tight binding are non-orthogonal in general. Moreover, their overlap for a given system depends on the atomic positions. Indeed, for a given system, their overlap reads:

$$\langle \boldsymbol{p}'\beta|\boldsymbol{p}\alpha\rangle = \frac{1}{N_{\text{sites}}}\delta_{\alpha\beta}\sum_{\boldsymbol{r}} e^{i(\boldsymbol{p}-\boldsymbol{p}')\cdot\boldsymbol{r}}. \tag{3.27}$$

For a sufficiently large amorphous system, where the size depends on the amount of structural disorder, the large sum of random phases implies that plane waves are approximately orthogonal (unless $e^{i\boldsymbol{p}\cdot\boldsymbol{r}} = e^{i\boldsymbol{p}'\cdot\boldsymbol{r}}$ for all sites):

$$\langle \boldsymbol{p}'\beta|\boldsymbol{p}\alpha\rangle_{\text{amorphous}} \simeq \delta_{\alpha\beta}\delta_{\boldsymbol{p}\boldsymbol{p}'}. \tag{3.28}$$

On the other hand, for a crystal with $N_{\text{s/c}}$ sites per unit cell at positions $\boldsymbol{t}$ with respect to the center of the unit cell, the overlap is nonzero if the momenta are separated by a reciprocal lattice vector,

$$\langle \tilde{\boldsymbol{p}}'\beta|\tilde{\boldsymbol{p}}\alpha\rangle_{\text{crystal}} \simeq \delta_{\alpha\beta}\delta_{\tilde{\boldsymbol{p}}',\tilde{\boldsymbol{p}}+\boldsymbol{G}}\frac{1}{N_{\text{s/c}}}\sum_{\boldsymbol{t}} e^{-i\boldsymbol{G}\cdot\boldsymbol{t}}. \tag{3.29}$$

To apply the structural quasi-Bloch spillage to compare two systems with the same lattice structure, we therefore have to generalize Eq. (3.23) using the formalism of non-orthogonal bases (see e.g. [549]). Using the previous choice of basis within this formalism, the closure relation

reads:

$$\mathbb{1} = \sum_{k} \sum_{GG'}^{\text{basis}} |k+G\rangle \left(S^{-1}\right)_{G,G'} \langle k+G'|, \tag{3.30}$$

where $\mathbb{1}$ is the identity operator, the sums over reciprocal lattice vectors run over the Brillouin zones chosen in the basis, and the overlap matrix is defined as $S_{G,G'} = \langle k+G\alpha | k+G'\alpha \rangle$, which depends only on the difference $G'-G$. We thus arrive at the following expression for the quasi-Bloch spillage:

$$\begin{aligned}\gamma_{\text{qB}}^{\text{non-orth}}(k) = \frac{1}{2}\sum_{k'} \sum_{G_1G_2G_3G_4}^{\text{basis}} \sum_{\alpha\beta} \Big[& P^{\alpha\beta}_{k+G_1,k'+G_2} \left(S^{-1}\right)_{G_2,G_3} P^{\beta\alpha}_{k'+G_3,k+G_4} \left(S^{-1}\right)_{G_4,G_1} - \\ & - P^{\alpha\beta}_{k+G_1,k'+G_2} \left(S^{-1}\right)_{G_2,G_3} \tilde{P}^{\beta\alpha}_{k'+G_3,k+G_4} \left(S^{-1}\right)_{G_4,G_1} \Big] + \left[P \leftrightarrow \tilde{P}\right].\end{aligned} \tag{3.31}$$

This expression is directly applicable within the tight-binding approximation, irrespective of whether the target system had additional Anderson disorder in the onsite and hopping energies. In particular, when comparing two insulting crystals, Eq. (3.31) exactly recovers the Bloch spillage.

Target and reference with different lattice structures: no-scattering approximation

We now focus on the general case where the target and reference systems have different atomic structure. We recall that in this case their Hilbert spaces are different in the tight-binding approximation, and therefore their overlap is ill-defined. This is reflected in the fact that the overlap between plane waves projected to the noncrystalline target and plane waves projected to the reference crystal is ill-defined:

$${}_{\text{crystal}}\langle \tilde{p}'\beta | p\alpha \rangle_{\text{noncryst}} = \frac{1}{N_{\text{sites}}} \sum_{r} \sum_{\tilde{r}} e^{ip\cdot r - \tilde{p}'\cdot\tilde{r}} \, {}_{\text{crystal}}\langle \tilde{r}\beta | r\alpha \rangle_{\text{noncryst}}, \tag{3.32}$$

since the overlap $\langle \tilde{r}\beta | r\alpha \rangle$ would require the knowledge of the real-space wavefunctions. Moreover, the overlap between plane-waves projected to a given system depends on its atomic positions (see Eqs. (3.27)-(3.29)). Therefore, the usual formalism for non-orthogonal bases [549] cannot be applied.

The structural quasi-Bloch spillage of Eq.(3.23) contains the matrix elements of the products of two projectors in the plane wave basis. By neglecting the momentum scattering, and thus assuming that the projectors are diagonal in momentum space, $P^{\alpha\beta}_{p,p'} \propto \delta_{p,p'}$, we avoid the problem of the disorder-dependent plane-wave overlaps. This approximation is justified for amorphous and disordered systems, since we expect continuous translational symmetry to be recovered after averaging over different disorder realizations [550]. This assumption has been successfully used to determine the topology of noncrystalline systems, including amorphous and quasicrystalline

models, using the effective Hamiltonian approach (see Eq. (3.7)) and the amorphous average symmetry indicators [120, 456, 475, 493].

However, the no-scattering approximation introduces a new issue: the values of observables depend on the choice of basis. For instance, the $\boldsymbol{k}$-resolved number of occupied bands $\tilde{n}_{\mathrm{occ}}(\boldsymbol{k}) = \mathrm{tr}[\tilde{P}(\boldsymbol{k})]$ in a crystal would read as

$$\mathrm{tr}\left[\tilde{P}(\boldsymbol{k})\right] = \sum_{\alpha}\sum_{\boldsymbol{G}}^{\text{basis}}\sum_{\boldsymbol{G}'}^{\text{basis}} \tilde{P}^{\alpha\alpha}_{\boldsymbol{k}+\boldsymbol{G},\boldsymbol{k}+\boldsymbol{G}'} \underset{\text{no-scatt}}{\simeq} \sum_{\alpha}\sum_{\boldsymbol{G}}^{\text{basis}} \tilde{P}^{\alpha\alpha}_{\boldsymbol{k}+\boldsymbol{G}}, \tag{3.33}$$

where we have defined the single plane-wave momentum projector $\tilde{P}^{\alpha\beta}_{\boldsymbol{p}} = \tilde{P}^{\alpha\beta}_{\boldsymbol{p},\boldsymbol{p}}$. In particular, $\mathrm{tr}\left[\tilde{P}(\boldsymbol{k})\right]_{\text{no-scatt}}$ depends on the types of Brillouin zones $\boldsymbol{G}$ chosen in the basis (see Appendix 3.C.2). This issue can be handled by replacing the sum over the $N_{\mathrm{s/c}}$ reciprocal lattice vectors $\boldsymbol{G}$ in a basis by an average over the different types of Brillouin zone $\boldsymbol{G}$, and multiplying by $N_{\mathrm{s/c}}$. This prescription gives exact results for the quantities containing matrix elements of just one projector in the crystalline limit. For example, in Appendix 3.C we show that

$$\mathrm{tr}\left[\tilde{P}(\boldsymbol{k})\right]^{\text{BZ-av}}_{\text{no-scatt}} = \frac{N_{\mathrm{s/c}}}{N_{\mathrm{BZs}}}\sum_{\boldsymbol{G}\in\mathrm{BZs}}\sum_{\alpha}\tilde{P}^{\alpha\alpha}_{\boldsymbol{k}+\boldsymbol{G}} = \tilde{n}_{\mathrm{occ}}(\boldsymbol{k}), \tag{3.34}$$

where the sum over $\boldsymbol{G}$ runs over one BZ of each of the N_{BZs} types, and the key factor for the last equality is that the average $\frac{1}{N_{\mathrm{BZs}}}\sum_{\boldsymbol{G}}^{\mathrm{BZs}} e^{-i\boldsymbol{G}\cdot(\boldsymbol{t}-\boldsymbol{t}')} = \delta_{\boldsymbol{t}\boldsymbol{t}'}$.

With these modifications, the structural quasi-Bloch spillage (3.23) can be defined in the tight-binding approximation as

$$\gamma^{\mathrm{TB}}_{\mathrm{qB}}(\boldsymbol{k}) = \left[\gamma^{\mathrm{TB}}_{\mathrm{qB}}(\boldsymbol{k})\right]^{\text{BZ-av}}_{\text{no-scatt}} = \frac{N_{\mathrm{s/c}}}{N_{\mathrm{BZs}}}\sum_{\boldsymbol{G}}^{\mathrm{BZs}}\frac{1}{2}\mathrm{tr}\left[\left(P_{\boldsymbol{k}+\boldsymbol{G}} - \tilde{P}_{\boldsymbol{k}+\boldsymbol{G}}\right)^2\right], \tag{3.35}$$

where the sum over $\boldsymbol{G}$ runs over one BZ of each of the N_{BZs} types, and the trace tr acts over the internal degrees of freedom α. For later convenience, we define each term in the sum for a momentum $\boldsymbol{p} = \boldsymbol{k} + \boldsymbol{G}$ as a plane-wave-momentum resolved spillage $\gamma^{\mathrm{TB}}_{\mathrm{pw}}(\boldsymbol{p}) = \frac{1}{2}\mathrm{tr}[(P_{\boldsymbol{p}} - \tilde{P}_{\boldsymbol{p}})^2]$, so that $\gamma^{\mathrm{TB}}_{\mathrm{qB}}(\boldsymbol{k}) = \frac{N_{\mathrm{s/c}}}{N_{\mathrm{BZs}}}\sum_{\boldsymbol{G}}^{\mathrm{BZs}}\gamma^{\mathrm{TB}}_{\mathrm{pw}}(\boldsymbol{k}+\boldsymbol{G})$. In particular, if the reference crystal has a single atom per cell, $N_{\mathrm{s/c}} = N_{\mathrm{BZs}} = 1$ and $\gamma^{\mathrm{TB}}_{\mathrm{qB}}(\boldsymbol{k}) = \gamma^{\mathrm{TB}}_{\mathrm{pw}}(\boldsymbol{k})$. Eq. (3.35) defines the structural spillage to be used in the tight-binding approximation.

While our prescription gives the exact results for the quantities containing matrix elements of just one projector in the crystalline limit, in the case of quantities containing matrix elements of the product of two projectors, such as the structural spillage (3.35), our results in the crystalline limit are not exact. However, we will numerically show for selected amorphous models that the

results are similar in absolute value, and more importantly that the sharp changes in the spillage that signal topological transitions still show up.

Phase transition criterion in the tight-binding approximation

In order to define our criterion for the topological transition in the structural spillage in the tight-binding approximation, it is important to note that Eq. (3.35) does not exactly recover the values of the Bloch spillage when applied to two crystals with and without SOC, because we neglected scattering. However, we have numerically verified that it results in similar values. In particular, we will show that the maximum spillage without scattering is $\max\left[\gamma_{\mathrm{qB}}^{\mathrm{TB}}(\boldsymbol{k}=0)\right]=1.5$ in the two models we have studied, which is a factor of $4/3$ smaller than the exact spillage $\max\left[\gamma_{\mathrm{qB}}(\boldsymbol{k}=0)\right]=2$ that would be recovered after considering the scattering. There is no reason to believe that this factor is universal, and thus we consider it model dependent.

With this in mind, in order to identify the topological phases in a tight-binding phase diagram, we take the criterion that the topological transition occurs when the quasi-Bloch spillage of Eq. (3.35) equals to half the maximum value of the spillage between two topologically different crystals when scattering is neglected. In both our models, this critical value equals 0.75. However, in general, this critical value of the tight-binding structural spillage will be model-dependent, and must be determined in a case-to-case basis.

In summary, Eqs. (3.35) and (3.23) define the structural spillage to be used in the tight-binding approximation and first-principles calculations, respectively. In the remainder of the Chapter, we demonstrate how they capture topological phase transitions of amorphous systems, using low-dimensional Bismuth as an example.

3.3 Amorphous tight-binding model: bismuthene on a substrate

In this section, we describe the method for generating the amorphous tight-binding models based on the Voronoi tessellation [120, 462, 551]. In particular, we construct a 2D amorphous tight-binding network inspired by amorphous bismuthene supported on a substrate [417, 418]. We will show that its topological phase diagram can be correctly captured by the structural spillage. In Appendix 3.B, we will use this model as an example to establish the connection between the structural spillage and the average symmetry indicators.

3.3.1 Bismuthene model Hamiltonian

Crystalline bismuthene consists of a 2D honeycomb monolayer of Bismuth atoms. Experiments suggest it to be a quantum spin Hall insulator with topological helical edge states when

grown on SiC(0001) [552] or Ag(111) [553] substrates. The effect of the substrate is crucial: it filters the p_z orbitals away from the Fermi level leaving the $p_{x,y}$ orbitals, resulting in a large gap (~ 0.67eV) and a non-zero strong $\mathbb{Z}_2$ topological index. Moreover, amorphous bismuthene on a substrate is predicted to remain topological via first-principles calculations [417, 418], making it a convenient system to benchmark our proposed structural spillage.

The low-energy physics of bismuthene is captured by a tight-binding model with $p_{x,y}$ orbitals in the honeycomb lattice [552], coupled by nearest-neighbour σ and π hoppings, a large onsite SOC, and a substrate-induced Rashba SOC. In real space and in the basis $\left\{p_{x\uparrow}, p_{x\downarrow}, p_{y\uparrow}, p_{y\downarrow}\right\}$, the Hamiltonian reads:

$$H = -\frac{1}{2}\sum_{\langle ij\rangle} p_i^\dagger \cdot \left[(t_\sigma - t_\pi)\,\tau_0 + (t_\sigma + t_\pi)\left(c_{ij}^{(2)}\tau_z + s_{ij}^{(2)}\tau_x\right)\right]\sigma_0 \cdot p_j + \sum_i p_i^\dagger \cdot \left[\lambda\tau_y\sigma_z\right]\cdot p_i + \\ + \sum_{\langle ij\rangle} i p_i^\dagger \cdot \left\{\lambda_R^A\tau_0\left[s_{ij}\sigma_x - c_{ij}\sigma_y\right] + \lambda_R^E\left[\left(c_{ij}\tau_x - s_{ij}\tau_z\right)\sigma_x - \left(c_{ij}\tau_z + s_{ij}\tau_x\right)\sigma_y\right]\right\}\cdot p_j, \tag{3.36}$$

where we have defined $c_{ij} = \cos(\theta_{ij})$, $s_{ij} = \sin(\theta_{ij})$, $c_{ij}^{(2)} = \cos(2\theta_{ij})$, and $s_{ij}^{(2)} = \sin(2\theta_{ij})$, with θ_{ij} the angle between the bond joining site i to site j and the x axis. τ_μ and σ_μ are the Pauli matrices acting on the orbital $\left\{p_x, p_y\right\}$ and spin $\{\uparrow,\downarrow\}$ degrees of freedom, respectively. t_σ and t_π are the σ and π nearest-neighbour hoppings, λ is the onsite SOC, and λ_R^A and λ_R^E are the orbital-independent and orbital-dependent Rashba SOC, respectively. As in Ref. [552], here we will assume that $\lambda_R^A = \lambda_R^E = \lambda_R$. The values used in Ref. [552] are $t_\sigma \simeq 2.0$eV, $t_\pi \simeq 0.21\text{eV} \simeq 0.11 t_\sigma$, $\lambda \simeq 0.44\text{eV} \simeq 0.22 t_\sigma$, and $\lambda_R \simeq 0.032\text{eV} \simeq 0.074\lambda$. In our calculations, we will take t_σ as the unit of energy, we will use the same value for $t_\pi = 0.11 t_\sigma$, and we will vary both the onsite SOC λ as well as the Rashba SOC proportionally to the former, $\lambda_R = 0.074\lambda$.

The bismuthene Hamiltonian (3.36) can be readily applied to an amorphous structure once we define which sites are nearest neighbours of each other. In principle, it could be generalized to include a dependence on the distance in the hoppings, such as the Harrison law [554]. However, we will consider fixed values for the hoppings, which can be a good approximation for covalently-bonded amorphous solids, which usually display a rather narrow distribution of bond distances [401]. Moreover, this approximation enables us to isolate the effect of structural disorder.

3.3.2 Construction of amorphous structures: Voronoi method

Covalently-bonded amorphous materials usually preserve local environments similar to the ones in the corresponding crystals, since they are set by the strong covalent bonds. Therefore, numerous amorphous materials have average coordination numbers, bond distances, bond angles,

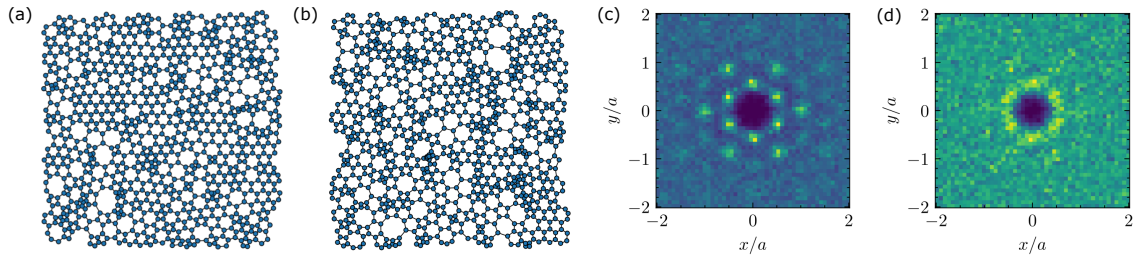

FIGURE 6: (a,b) Examples of amorphous bismuthene structures obtained by the Voronoi method. The structural disorder strengths are (a) $r = 0.3$ with a density of non-hexagonal plaquettes $\rho_{\text{non-hex}} \simeq 0.53$, and (b) $r = 0.5$ with $\rho_{\text{non-hex}} \simeq 0.65$. (c,d) Histograms of the relative positions of atoms for the two amorphous structures of (a,b), respectively.

etc., which are centered around those of the crystal [401]. With this in mind, our bismuthene amorphous models preserve, for every site, the threefold coordination of the honeycomb lattice. This is achieved by applying the Voronoi method similar to Refs. [120, 462, 551], but with a modification that enables us to control the degree of amorphization.

Voronoi method.— We first construct a pointset forming a triangular lattice with lattice constant a, whose points will be called seeds. If we performed the voronization of this triangular pointset, it would produce its dual honeycomb lattice. To generate amorphous networks, however, we randomly displace the seeds from their initial triangular positions. We sample their displacements from an exponential distribution with characteristic distance $r \cdot a$ in the radial direction, and from an uniform distribution in the angular direction. We then compute their corresponding Voronoi diagram, which is defined by the Voronoi cells, i.e., the regions consisting of all points closer to one seed point than to any other. The vertices of such cells, called Voronoi vertices, form a threefold coordinated network with the edges of the Voronoi cells corresponding to the nearest-neighbour bonds; only the vertices at the boundaries of the system have fewer than three neighbours. The resulting amorphous network has threefold coordination, as the crystalline honeycomb lattice, but with a finite density of non-hexagonal plaquettes (see Figs. 6(a,b)) [551].

Relaxation procedure.— The networks obtained in this way have large variances in the bond angle and bond length distributions, which might not be very realistic due to the expected short-range order. To reduce this artifact, we apply an iterative relaxation procedure. We select the threefold coordinated sites one by one and displace them to the barycenter formed by their three nearest neighbours. We iterate this process until convergence is reached, i.e., until the displacements are smaller than a given small cutoff. This relaxation procedure tends to set the bond angles as close as possible to the crystalline angle, 120°. Finally, once the network is relaxed, we rescale the distances so that the average nearest-neighbour distance is $a/\sqrt{3}$, which is the corresponding value in the crystalline honeycomb lattice.

Figs. 6(a,b) shows two example amorphous structures obtained by this procedure with structural disorders parametrized by $r = 0.3$ and $r = 0.5$, respectively. Although the amorphousness is reflected in the presence of plaquettes with different number of sides, every site in the bulk has threefold coordination. The relaxation procedure, which favours angles close to 120°, induces a correlation between the size of a plaquette and its number of sides. Figs. 6(c,d) show the resulting histograms of the relative positions of atoms for the two amorphous structures of Figs. 6(a,b), respectively. They reveal that both structures are isotropic at long distances, although for small disorder the nanocrystalline domains in Fig. 6(a) give rise to broad nearest neighbour peaks around the crystalline positions in Fig 6(c). For strong disorder, the correlation hole for distances under $a/\sqrt{3}$ and an annular peak are visible [4].

Structural disorder control.— The parameter r, characterizing the exponential distribution by which the seeds are displaced from the regular triangular lattice, continuously controls the amorphousness of the resulting Voronoi network. Indeed, since the Voronoi diagram of a triangular lattice is a honeycomb lattice, we recover the crystal in the $r \to 0$ limit. Increasing r introduces non-hexagonal plaquettes in the Voronoi network, at least until $r \gtrsim 1$, when the seed becomes completely random, since all the information from the initial triangular seed is lost. This can be observed in Fig. 7(a), which shows that the configuration-averaged standard deviations of the distributions of bond angles, bond distances, and plaquettes start to saturate at about $r \gtrsim 0.6$.

Structural disorder can be quantified by several physical properties of the network. These include the standard deviations of the distributions of nearest-neighbour distances, angles and plaquettes normalized by the corresponding average values, as well as the density of noncrystalline plaquettes. In our models, where the crystalline limit consists of a honeycomb lattice, the noncrystalline plaquettes correspond to the non-hexagonal ones. In order to take into account the finite-size effects, for each parameter r, we consider the configuration-average of these quantities over 100 disorder realizations. As shown in Fig. 7(a), all these configuration-averaged quantities have the same qualitative dependence with the parameter r. In particular, there exists a one-to-one monotonous correspondence between our control parameter r and any of these configuration-averaged quantities. However, for particular disorder realizations in a finite system, there are fluctuations that make their relation to r not one-to-one before performing the configuration average. This is illustrated by the distribution of ratios of non-hexagonal plaquettes $\rho_{\text{non-hex}}$ shown in Fig. 7(b) for different disorder realizations with fixed $r = 0.3$. Therefore, we have chosen to physically characterize the amorphousness of a system by the configuration-averaged density of non-hexagonal plaquettes formed by the nearest neighbour sites $\rho_{\text{non-hex}}$. This measure could be generalized to other models whose crystalline limit consisted of lattices other than the honeycomb. Finally, Fig. 7(c) shows an example distribution of plaquettes obtained for a particular disorder realization with $r = 0.3$, which corresponds to $\rho_{\text{non-hex}} \simeq 0.55$, while the configuration-average for this r corresponds to

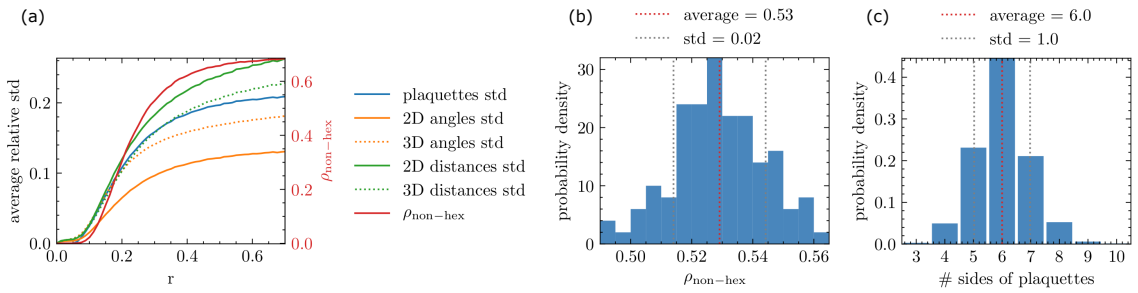

FIGURE 7: (a) Configuration-averaged structural quantities as a function of the parameter r controlling the amorphousness: standard deviations (std) of the distributions of nearest neighbour bond angles, bond distances (both for the planar bismuthene as well as for the buckled Bi bilayer), and plaquettes, as well as density of non-hexagonal plaquettes. For each disorder intensity r, the results have been averaged over 100 different realizations. (b) Distribution of the ratios of non-hexagonal plaquettes $\rho_{\text{non-hex}}$ obtained with 100 disorder realizations with fixed disorder $r = 0.3$. (c) Distribution of plaquettes for a given disorder realization with $r = 0.3$ (corresponding to $\rho_{\text{non-hex}} \simeq 0.55$).

$\rho_{\text{non-hex}} \simeq 0.53$.

Periodic boundary conditions.— The above procedure generates structures with open boundary conditions, which is useful to compute e.g. the local density of states at the edges or the longitudinal conductance once leads have been attached. However, for spectral quantities such as the spillage, we can reduce the possible finite-size effects by imposing periodic boundary conditions, or equivalently by putting the system on a torus. An amorphous system might have a different number of atoms at opposite edges, so the periodic boundary conditions cannot be imposed directly, but rather before computing the Voronoi tessellation, as described below.

Before explaining the procedure to impose the periodic boundary conditions, we note that our periodic systems consist of a rectangular supercell with sides L_x and L_y. In order for the periodic boundary conditions to be applicable to systems with an arbitrary amount of structural disorder, including the crystalline limit, L_x and L_y are restricted to the values such that the supercell is commensurate with the initial crystalline unit cell. In our models, where the crystalline limit is a honeycomb lattice, the previous condition imposes that $L_x = n_x a$ and $L_y = n_y\sqrt{3}a$, where a is the lattice constant, and n_x, n_y are integer numbers.

Taking this into account, we now describe the procedure to impose periodic boundary conditions on a system with an arbitrary amount of disorder. First, we generate a triangular seed within the supercell $x \in [0, L_x)$, $y \in [0, L_y)$, and we disorder it choosing a finite value of r. Then, we repeat this initial seed in the eight nearest-neighbour supercells, i.e., we copy the seed points displaced from their initial positions $\boldsymbol{x}$ to $\boldsymbol{x} + \boldsymbol{L} = \boldsymbol{x} + (n_x L_x, n_y L_y)$, with $n_x, n_y \in \{1, 0, -1\}$. Then, the Voronoi tessellation of the whole system composed by the nine supercells is determined.

This gives rise to a threefold coordinated network with the following convenient feature: the supercell defined by the sites inside the region $x \in [0, L_x)$, $y \in [0, L_y)$ has the same number of sites in opposite sides. Therefore, the periodic boundary conditions can be now applied to this supercell, discarding all the sites outside this supercell. Finally, we carry out the relaxation procedure of this supercell, being careful to preserve the periodic boundary conditions.

To conclude this section, we mention that we generate the systems with open boundary conditions starting from a system with periodic boundary conditions, by first removing the bonds at the edges of the supercell and then removing the dangling sites. This way, the bulk of the periodic structure where the spillage is computed is the same as the bulk of the open system where the conductance is determined, which allows us to safely compare their predictions of the topological phase.

3.3.3 Calculation details

We use the Kwant software package [555] to generate the tight-binding Hamiltonians and perform the calculations. To be able to treat larger system sizes, we apply the kernel polynomial method (KPM) [556] to estimate the density of states (DOS) and the projector onto the occupied states. The projector is computed following the procedure of Ref. [557] and using plane waves as initial KPM vectors, which allows us to calculate the projector matrix elements $\langle \boldsymbol{p}\alpha | P | \boldsymbol{p}\beta \rangle$. We use a KPM energy resolution of $0.01 t_\sigma$ (645 moments) for the bismuthene structures. The DOS is computed by performing a KPM stochastic trace with 50 random vectors. The system sizes considered are $21a \times 12\sqrt{3}a$.

The structural quasi-Bloch spillage is computed in the systems with periodic boundary conditions using Eq. (3.35), which reduces to Eq. (3.76) of Appendix 3.C in our models, since the crystalline phase has a honeycomb lattice. On the other hand, the conductance is determined with the Kwant software in the systems with open boundary conditions. In order to avoid possible artifacts arising from trivial edge states in a particular termination, the conductance is calculated using leads in both x and y directions, such that in the crystalline case the edges are zigzag and armchair, respectively. Since the aim of the conductance is to identify the insulating and topological insulating regions, which have a quantized conductance of 0 and $2e^2/h$, respectively, regardless of the shape of the leads, we use leads consisting of a 2D planar square lattice with nearest-neighbour hoppings such that their bandwidth is larger than that of the system. These leads are attached to all the atoms on the corresponding edge of the system. Fig. 8 shows two example configurations with the leads in the y (armchair) and x (zigzag) directions.

Lastly, to compute the phase diagrams we only need a single disorder realization for each r. The reason is twofold. First, we noticed that for sufficiently large systems sizes, as the ones

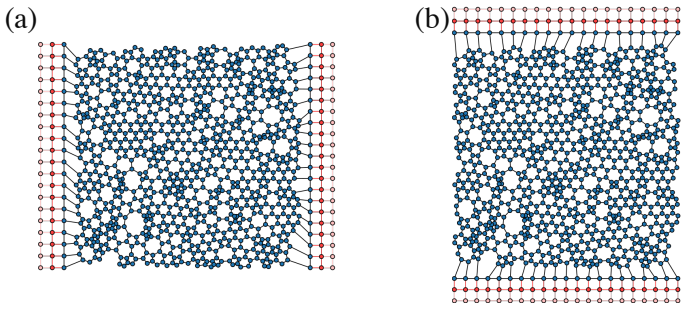

FIGURE 8: Example amorphous bismuthene structure ($r = 0.3$, $\rho_{\text{non-hex}} \simeq 0.53$) where leads have been attached to calculate the conductance. (a) System with leads in the x axis, which would correspond to a zigzag ribbon in the crystalline case. (b) System with leads in the y axis, which would correspond to an armchair ribbon in the crystalline case.

considered in this work, the fluctuations of the structural spillage for different disorder realizations are rather small. Indeed, they are smaller than the fluctuations in the conductance, which is another convenient feature for the use of the structural spillage in high-throughput searches for topological amorphous materials. Second, while extracting a precise topological phase diagram from the conductance would require a configuration average, it is not strictly necessary if we just aim to use it as a benchmark for the structural spillage.

3.3.4 Topological phase diagram

In Fig. 9 we present the topological phase diagram of amorphous bismuthene as a function of SOC λ and structural disorder, parametrized by the density of non-hexagonal plaquettes $\rho_{\text{non-hex}}$. We benchmark the structural spillage $\gamma^{\text{TB}}_{\text{qB}}(\boldsymbol{k})$ against the two-terminal conductance results. In the crystalline limit ($\rho_{\text{non-hex}} = 0$), the system starts as a Dirac semimetal for vanishing vanishing SOC, $\lambda = \lambda_R = 0$. The point nodes occur at the K points in the Brillouin zone, similar to graphene, but with $p_{x,y}$ orbitals instead of p_z. Finite λ opens a topological gap, rendering the system to a quantum spin Hall state. The onsite SOC λ here acts as the Kane-Mele SOC in graphene [558]. Increasing λ widens the topological gap at K, while it shrinks the gap at Γ. Above a critical λ, where the gap closes at the Γ point, the system becomes a topologically trivial insulator, adiabatically connected to the atomic limit in which only the onsite SOC is non-zero.

Both the conductance (Figs. 9(b,c)) and the structural quasi-Bloch spillage (Fig. 9(d-f)) capture the topological transition, even at finite structural disorder ($\rho_{\text{non-hex}} \neq 0$). The zero-temperature conductance in the topological insulator phase is equal to $2e^2/h$, originating from the helical edge states in the absence of inelastic scattering, while it reduces to zero after the phase transition to the trivial insulator at a critical SOC. The fact that the conductances along the two perpendicular "armchair" and "zigzag" directions coincide demonstrates that the quantized conductance does

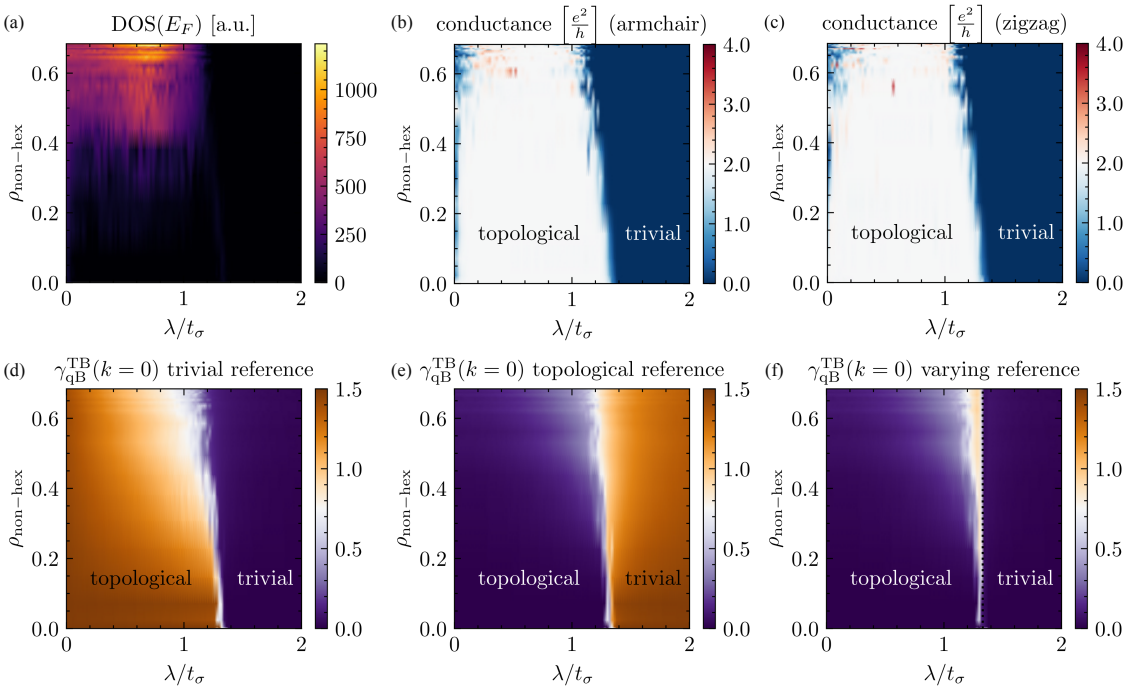

FIGURE 9: Bismuthene model phase diagrams of different quantities as a function of SOC λ and amorphousness, parametrized by the density of non-hexagonal plaquettes $\rho_{\text{non-hex}}$. (a) Density of states at the Fermi level of the system with periodic boundary conditions. (b, c) Two-terminal longitudinal conductance in the "armchair" and "zigzag" ribbon configurations, respectively. (d-f) Structural quasi-Bloch spillage $\gamma_{\text{qB}}^{\text{TB}}(\boldsymbol{k}=0)$ comparing the amorphous system with SOC λ to a different reference crystal. (d) The reference is a trivial bismuthene crystal with $\lambda/t_\sigma = \infty$. (e) The reference is a topological bismuthene crystal with $\lambda = 0.1t_\sigma$. (d) The reference is the bismuthene crystal with the same SOC λ as the amorphous target at each point. The vertical dotted line indicated the critical SOC in the crystalline limit, which is needed for the topological characterization of the amorphous structures.

indeed arise from topological helical edge states, and not from potential disorder-robust trivial edge states present in one particular crystalline direction. In agreement with the DFT results of Refs. [417, 418], we find that increasing disorder decreases the gap and hence the critical λ. Nevertheless, the realistic value of $\lambda \simeq 0.22t_\sigma$ [552] lies in the topological phase also in the amorphous case. Fig. 9(a) shows that the density of states at the Fermi level increases with $\rho_{\text{non-hex}}$ when the SOC is such that the crystal is in the topological phase ($\lambda \lesssim 1.3t_\sigma$). This arises from the band broadening due to the disorder, and also from the appearance of low-energy states induced by a sublattice imbalance in a bipartite lattice [559]. This induces the band inversion that drives the system from topological to trivial at a smaller critical SOC than in the crystal.

The topological transition at high SOC driven by a band inversion at Γ is also reproduced by the structural quasi-Bloch spillage $\gamma_{\text{qB}}^{\text{TB}}(\boldsymbol{k})$ at $\boldsymbol{k} = 0$ with different reference sates in Figs. 9(d-f).

In Fig. 9(d), we choose the reference system to be a trivial crystal, only with non-zero onsite λ. Therefore, $\gamma_{\mathrm{qB}}^{\mathrm{TB}}(\boldsymbol{k}=0)$ is large in the topological phase (~ 1.5 as advanced in Section 3.2.3) and drops to zero in the trivial phase. The critical λ at the transition for the crystal is correctly predicted by $\gamma_{\mathrm{qB}}^{\mathrm{TB}}(\boldsymbol{k}=0)$. To explore how the structural spillage changes when we choose a different reference system, in Fig. 9(e) we choose a reference crystal with $\lambda = 0.1t_\sigma$, which lies in the topological phase. Contrary to the trivial reference case of Fig. 9(d), now the spillage is small in the topological phase and large in the trivial one, as expected. Importantly, the transition is predicted at approximately the same SOC irrespective of the reference system, which shows the robustness of the spillage.

Finally, in order to isolate the effect of the structural disorder on the topological band inversion from the effect of SOC, we have also computed the structural quasi-Bloch spillage comparing each amorphous system with amorphousness $\rho_{\text{non-hex}}$ and SOC λ to a reference crystal with the same SOC λ, shown in Fig. 9(f). This choice highlights the regions where disorder induces a topological band inversion. For example, if the reference crystal is topological for a given λ, this spillage will have a large value if the disorder induces a trivial state. Therefore, interpreting Fig. 9(f) requires knowledge of the topological phase of the crystal at each λ. For $\lambda \lesssim 1.3t_\sigma$, the reference crystal is topological. At small structural disorder, the spillage is small until $\lambda \lesssim 1.3t_\sigma$, indicating that the amorphous system is topological too. However, at strong disorder, the spillage becomes large between $\lambda \simeq 1.1t_\sigma$ and $\lambda \simeq 1.3t_\sigma$, which signals that the disorder induces a band inversion to the trivial phase. Lastly, for $\lambda \gtrsim 1.3t_\sigma$, the reference crystal is trivial, and the spillage is low, indicating that the amorphous system is also trivial.

Besides the renormalization of the critical λ by disorder, the topological transition becomes smoother with increasing disorder, as signaled by the conductance fluctuations close to the transition and the more gradual jump of the spillage. This is probably caused by finite-size effects. However, we mention that it could also be related to the appearance of a metallic region in the presence of both disorder and non-spin-conserving Rashba spin-orbit coupling [560]. Nevertheless, while this metallic region appears in topological transitions in the presence of non-structural Anderson disorder [561], it has not been observed in structurally disordered models yet [465]. In order to discern the origin of the broadened transition in our models, one should perform a finite-size scaling analysis, but this lies beyond the scope of this Chapter.

In conclusion, all phase diagrams Fig. 9(d-f) agree qualitatively. The spillage is able to predict the topological phase transition regardless of the reference system. We also notice that, in the absence of Rashba SOC, the model would reduce to two time-reversed copies of Chern insulators. Each copy would contribute equally to the structural spillage, demonstrating that the structural spillage works also for other symmetry classes.

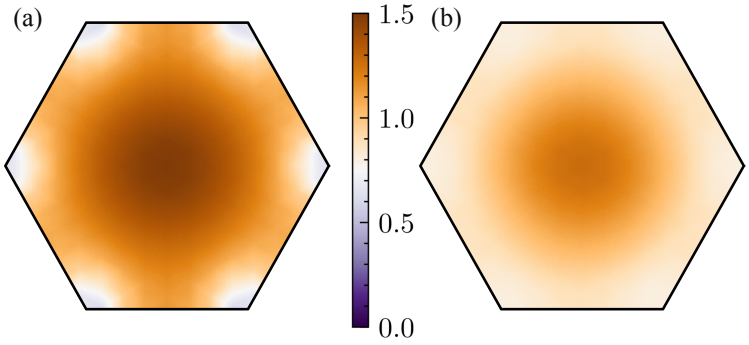

FIGURE 10: Structural quasi-Bloch spillage $\gamma^{\mathrm{TB}}_{\mathrm{qB}}(\boldsymbol{k})$ in the Brillouin zone for the bismuthene model. The reference system is a trivial crystal with $\lambda/t_\sigma = \infty$ in both cases. The target system is (a) crystalline topological bismuthene with $\rho_{\text{non-hex}} = 0$ and $\lambda = 0.22t_\sigma$, and (b) amorphous topological bismuthene with $\rho_{\text{non-hex}} \simeq 0.53$ and $\lambda = 0.22t_\sigma$.

We point out that at small SOC, where the topological gap at K is small, strong disorder closes the mobility gap, as indicated by the insulating conductance, rendering the system topologically trivial. This transition is not captured by $\gamma^{\mathrm{TB}}_{\mathrm{qB}}(\boldsymbol{k} = 0)$. Since the band inversion occurs at K, $\gamma^{\mathrm{TB}}_{\mathrm{qB}}(\boldsymbol{k} = K)$ should be studied instead.

Before concluding this section, we also show the spillage distribution as a function of the Bloch momentum $\boldsymbol{k}$ in Fig. 10. In particular, Fig. 10(a) represents $\gamma^{\mathrm{TB}}_{\mathrm{qB}}(\boldsymbol{k})$ for a target topological crystal with fixed $\lambda = 0.22t_\sigma$, comparing it to the trivial crystal with infinite onsite SOC (as in Fig. 9(d)). The topological band inversion at Γ is reflected in $\gamma^{\mathrm{TB}}_{\mathrm{qB}}(\boldsymbol{k})$ being peaked around $\boldsymbol{k} = 0$ with a value ~ 1.5. The same feature, but broadened and direction-averaged, survives with structural disorder in Fig. 10(b), where the target system is a topological amorphous structure with the same SOC $\lambda = 0.22t_\sigma$ and $\rho_{\text{non-hex}} = 0.53$.

3.4 Amorphous bilayer Bismuth: spillage in DFT vs. tight binding

In this section, we introduce other amorphous tight-binding model inspired by the free-standing Bismuth (111) bilayer, and we show that the structural spillage also acts as a topological indicator in this case. Moreover, we will also present the *ab initio* calculations of this material performed by our collaborators Paul Corbae et al. in Ref. [3]. Both methods predict amorphous bilayer Bismuth to be topological. Comparing the tight-binding and DFT results, we conclude that, while both qualitatively agree, the structural spillage method works even better in DFT.

3.4.1 Bi bilayer tight-binding Hamiltonian

Crystalline Bismuth (111) bilayer consists of a buckled honeycomb lattice of Bismuth atoms, where each sublattice has a different height [562]. The free-standing crystal is predicted to be a strong topological insulator crystal with $\mathbb{Z}_2 = 1$ driven by the strong SOC [562–565]. An effective tight-binding of crystalline Bi bilayer was introduced by Ref. [566], where the three p orbitals are relevant due to the absence of the substrate in this case. Their model consists of spinful p_x, p_y and p_z orbitals in the buckled honeycomb lattice with up to third nearest-neighbour hoppings. For simplicity, we will restrict ourselves to nearest-neighbour hoppings and onsite SOC. In real space and in the basis $\{p_{x\uparrow}, p_{x\downarrow}, p_{y\uparrow}, p_{y\downarrow}, p_{z\uparrow}, p_{z\downarrow}\}$, the Hamiltonian reads:

$$\begin{aligned} H = &\sum_{\langle ij\rangle} p_i^\dagger \cdot \left[t_\pi \mathbb{1} - (t_\sigma + t_\pi)\left(\hat{\boldsymbol{r}}_{ij} \otimes \hat{\boldsymbol{r}}_{ij}\right)\sigma_0\right] \cdot p_j + \\ &+ \sum_i p_i^\dagger \cdot \left[E_{0z}\frac{1}{2}\left(L_x^2 + L_y^2 - L_z^2\right)\sigma_0 + \lambda \boldsymbol{L}\cdot\boldsymbol{\sigma}\right] \cdot p_i, \end{aligned} \tag{3.37}$$

where $\mathbb{1}$ is the 6×6 identity matrix, t_σ and t_π are the nearest neighbour σ and π hoppings, E_{0z} is the difference between the onsite energy of the p_z and $p_{x,y}$ orbitals, λ is the onsite isotropic SOC, and $\hat{\boldsymbol{r}}_{ij}$ is the unit vector along the bond from site i to site j, with its tensor product defined as

$$\hat{\boldsymbol{r}}_{ij} \otimes \hat{\boldsymbol{r}}_{ij} = \begin{pmatrix} (\hat{r}_{ij}^x)^2 & \hat{r}_{ij}^x \hat{r}_{ij}^y & \hat{r}_{ij}^x \hat{r}_{ij}^z \\ \hat{r}_{ij}^y \hat{r}_{ij}^x & (\hat{r}_{ij}^y)^2 & \hat{r}_{ij}^y \hat{r}_{ij}^z \\ \hat{r}_{ij}^z \hat{r}_{ij}^x & \hat{r}_{ij}^z \hat{r}_{ij}^y & (\hat{r}_{ij}^z)^2 \end{pmatrix}, \tag{3.38}$$

where $\hat{r}_{ij}^a$ are the components along the cartesian axes. We have also defined the angular momentum matrices L_a, which act on the orbital subspace $\{p_x, p_y, p_z\}$:

$$L_x = \begin{pmatrix} 0 & 0 & 0 \\ 0 & 0 & -i \\ 0 & i & 0 \end{pmatrix} \quad ; \quad L_y = \begin{pmatrix} 0 & 0 & i \\ 0 & 0 & 0 \\ -i & 0 & 0 \end{pmatrix} \quad ; \quad L_z = \begin{pmatrix} 0 & -i & 0 \\ i & 0 & 0 \\ 0 & 0 & 0 \end{pmatrix}, \tag{3.39}$$

and therefore

$$L_x^2 + L_y^2 - L_z^2 = \begin{pmatrix} 0 & 0 & 0 \\ 0 & 0 & 0 \\ 0 & 0 & 2 \end{pmatrix} \tag{3.40}$$

In our calculations, we will take t_σ as the unit of energy, and fix the value of $t_\pi = 0.25 t_\sigma$ and $E_{0z} = -0.4 t_\sigma$. We vary the onsite SOC λ. From the DFT-derived tight-binding model of Ref. [566], we can estimate that the actual SOC for the Bi bilayer is $\lambda \sim 0.7 t_\sigma$. The height of the bilayer enters via the vectors $\hat{\boldsymbol{r}}_{ij}$. Different DFT calculations have predicted heights ranging from

$d_z = 0.35a$ to $d_z = 0.40a$ [562, 565–567]. In this work, we will use $d_z = 0.9a/\sqrt{6} \simeq 0.37a$.

3.4.2 Construction of amorphous Bi bilayer structures

Our structures of amorphous Bi bilayers are constructed in a similar way to monolayer bismuthene. Indeed, the first step is generating an amorphous bismuthene network following the Voronoi procedure outlined in Section 3.3.2. We then have to assign different heights to the sites. In the crystalline limit, each sublattice has a different fixed height because of the buckling. Sublattices are no longer well-defined in an amorphous network, but we can still define effective sublattices. One differentiating property between the two sublattices in a crystalline honeycomb lattice is the direction of their nearest-neighbour bonds: if the bonds from sublattice A point at polar angles $\theta_1^A = \pi/2, \theta_2^A = -11\pi/12$ and $\theta_3^A = -\pi/12$, then the ones from sublattice B point at $\theta_1^B = -\pi/2, \theta_2^B = \pi/12$ and $\theta_3^B = 11\pi/12$. Therefore, $\eta(S) = \text{sign}\left[\left(\sum_l \theta_l^S \bmod 2\pi\right) - \pi\right]$ is equal to $+1$ for sublattice $S = A$ and -1 for $S = B$. Using $\eta(S) = \pm 1$ to define the effective sublattices in the amorphous structures, we then assign a height $\pm d_z/2$. Finally, we add a random disorder to the height of each site sampled from a Gaussian distribution with standard deviation $r_z \cdot a$. In particular, we choose the height disorder r_z proportional to r, the parameter that controls the in-plane amorphousness. In the calculations presented in this work, we take $r_z = rd_z/(4a) \simeq 0.09r$. Fig. 11(a) shows the top and side views of a representative structure. Figs. 11(b,c) show how the 2D square-lattice leads are attached along the two perpendicular directions.

3.4.3 Calculation details

As in the bismuthene model, we apply the KPM method [556] within the Kwant software package [555]. The KPM energy resolution for the projector calculation ($0.005t_\sigma \equiv 887$ moments), the number of vectors in the KPM stochastic traces for the DOS calculation (100 random vectors), and the system size ($21a \times 12\sqrt{3}a$) are all twice as big as the values considered for the bismuthene model. We choose them larger since the gap in Bi bilayer is smaller, and therefore finite-size effects are larger. Additionally, our Bi bilayer model displays, at weak structural disorder, trivial edge states close to the Fermi level over a wide range of values of SOC, which appear in both zigzag and armchair edges. These alter the Fermi level of a finite system with open boundary conditions E_F^{open} with respect to the one computed with periodic boundary conditions E_F^{periodic}. For the system sizes we are able to treat numerically, the change in the Fermi level E_F^{open} is enough for it to lie outside of the bulk gap, since the thermodynamic gap in the crystal is rather small ($\sim 0.1t_\sigma$). Therefore, the conductance computed at E_F^{open} in the crystal would show metallic regions even in the insulating and topological insulating phases due to this artifact. In order to avoid this issue, in the Bi bilayer systems we compute the conductance at E_F^{periodic} determined with periodic boundary conditions.

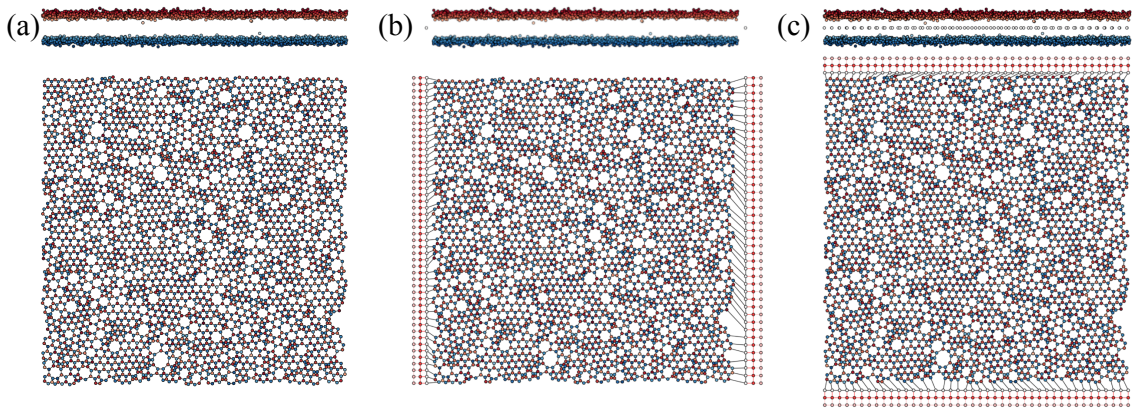

FIGURE 11: Side and top views of an example of amorphous Bi bilayer structure with $\rho_{\text{non-hex}} = 0.53$ ($r = 0.3$) used in the tight-binding calculations. Sites are colored according to their out-of-plane positions: red/blue indicates the effective sublattice, and the color intensity scales with the actual out-of-plane position. The positions in the out-of-plane direction have been rescaled by a factor 10 for visualization purposes. (a) Structure without leads. (b) Structure with leads attached in the x axis, which would correspond to a zigzag ribbon in the crystalline case. (c) Structure with leads attached in the y axis, which would correspond to an armchair ribbon in the crystalline case.

We note that this problem does not appear in the bismuthene models. At large SOC and disorder, these trivial edge states merge into bulk states and therefore $E_F^{\text{periodic}} \simeq E_F^{\text{open}}$.

3.4.4 Tight-binding results

In this section, we study the topological phase diagram of the amorphous Bi bilayer tight-binding model (3.37), and show that, as for bismuthene, the structural spillage correctly predicts the topological band inversion in this model. Unlike for its crystalline phase, no topological study has been carried out for amorphous bilayer Bismuth. Our results indicate that, if amorphous structures are stable and can be synthesized, they will also be topologically nontrivial.

Before analyzing the results, we briefly review the current status regarding the topological characterization of crystalline Bi (111) bilayer. In the crystalline case with SOC, the Bi bilayer has been predicted to be a strong topological insulator [562–565]. Our model can also describe other materials with the same lattice, such as the antimony (111) bilayer. Due to the smaller SOC, the Sb bilayer becomes a strong topological insulator only when strained [568]. Therefore, our model in the crystalline case starts as a $\mathbb{Z}_2 = 0$ insulator for vanishing λ. A band inversion occurs at a finite value of λ, driving the system to a $\mathbb{Z}_2 = 1$ topological insulating phase. For the parameters used in this work (see Appendix 3.4.1), this band inversion in the crystal occurs at Γ for $\lambda \simeq 0.27 t_\sigma$.

The topological character of each phase is also confirmed by the longitudinal conductance along two perpendicular directions, shown in Figs. 12(b,c). In the crystalline limit with $\rho_{\text{non-hex}} = 0$,

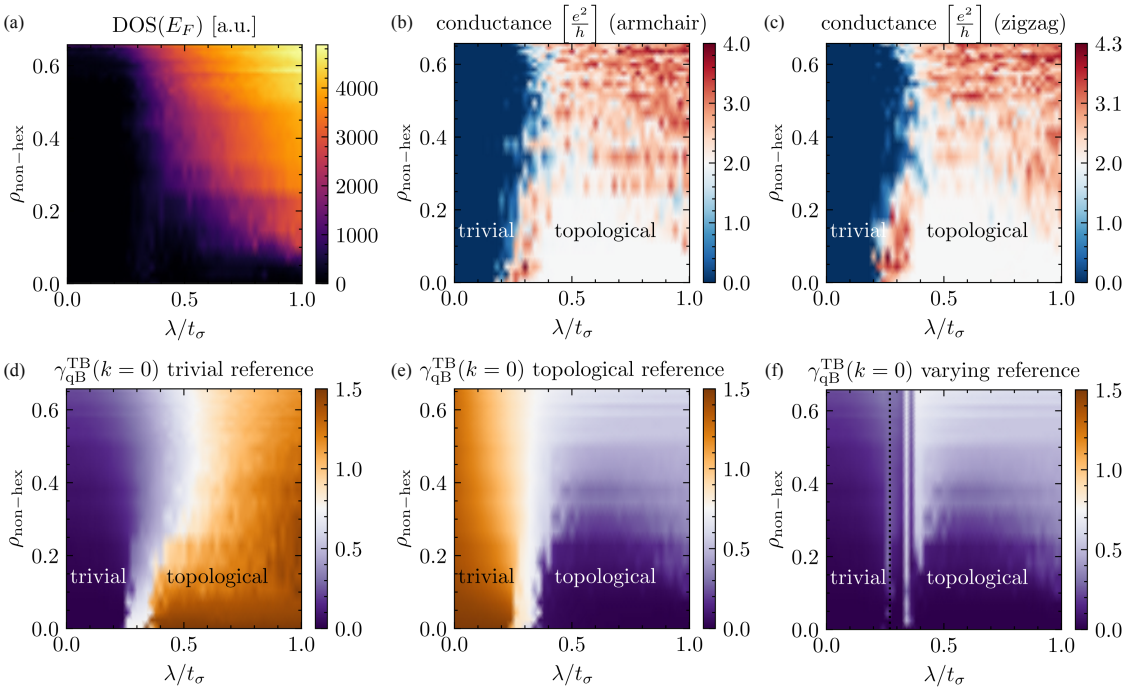

FIGURE 12: Bi bilayer model phase diagrams of different quantities as a function of SOC λ and amorphousness, parametrized by the density of non-hexagonal plaquettes $\rho_{\text{non-hex}}$. (a) Density of states at the Fermi level of the system with periodic boundary conditions. (b, c) Two-terminal longitudinal conductance in the "armchair" and "zigzag" ribbon configurations, respectively. (d-f) Structural quasi-Bloch spillage $\gamma_{\mathrm{qB}}^{\mathrm{TB}}(\boldsymbol{k}=0)$ comparing the amorphous system with SOC λ to a different reference crystal. (d) The reference is a trivial Bi bilayer crystal with $\lambda = 0$. (e) The reference is a topological Bi bilayer crystal with $\lambda = t_\sigma$. (f) The reference is the Bi bilayer crystal with the same SOC λ as the amorphous target at each point. The vertical dotted line indicated the critical SOC in the crystalline limit, which is needed for the topological characterization of the amorphous structures.

the conductance vanishes for small SOC, $\lambda \lesssim 0.2t_\sigma$, corresponding to the trivial phase. Above $\lambda \gtrsim 0.3t_\sigma$, the conductance becomes quantized to $2e^2/h$, indicating the topological phase. Around the transition, for $0.2t_\sigma \lesssim \lambda \lesssim 0.3t_\sigma$, even in this crystalline case, the conductance shows a metallic region. This is an artifact of the finite precision in computing the Fermi level with the kernel polynomial method, compounded with finite-size effects and the presence of trivial edge states (see section 3.4.3). We have checked that this transition region is reduced upon increasing the kernel polynomial method precision and the system size. Note that these issues only appear as one approaches the transition, where the gap is increasingly small. The finite KPM precision manifests itself in the fact that the trace of the crystalline projector $\mathrm{tr}[P]$, which should be equal to N_{occ}, is slightly larger over a region close to the transition (see the discussion of Fig. 3.C.1 in Appendix 3.C).

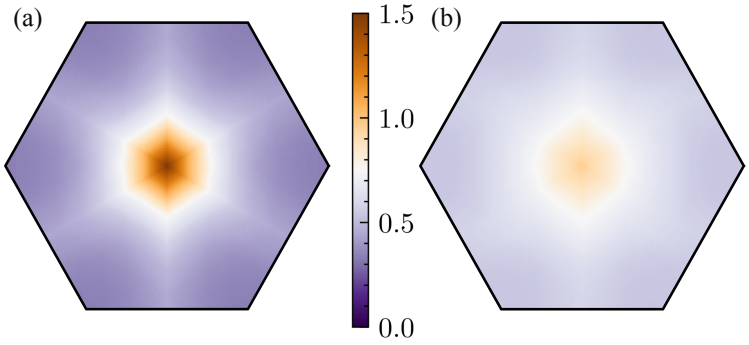

FIGURE 13: Structural quasi-Bloch spillage $\gamma^{\mathrm{TB}}_{\mathrm{qB}}(\boldsymbol{k})$ in the Brillouin zone for the Bi bilayer model. The reference system is a trivial crystal with $\lambda = 0$ in both cases. The target system is (a) crystalline topological Bi bilayer with $\rho_{\text{non-hex}} = 0$ and $\lambda = 0.7t_\sigma$, and (b) amorphous topological Bi bilayer with $\rho_{\text{non-hex}} \simeq 0.53$ and $\lambda = 0.7t_\sigma$.

The topologically trivial phase and the broadened transition to the topological phase also appear for weak structural disorder, $\rho_{\text{non-hex}} \lesssim 0.3$. The critical SOC seems to slightly increase with disorder, although a scaling analysis of the conductance would be required to discern the precise dependence. While the trivial phase survives and remains gapped for stronger structural disorder, the spectral gap closes in the range of SOC corresponding to the topological phase in the crystal (see Fig. 12(a)). The conductance also suggests that the mobility gap closes there and the system becomes metallic. Despite the absence of Rashba SOC in this model, the onsite λ is already spin-non-conserving, and therefore a metallic phase can survive against weak localization [560]. Nevertheless, we cannot discard the possibility that the metallic conductance is arising from finite-size effects with an Anderson localized bulk but with a localization length longer than the system sizes considered. A scaling study would be needed to discern the nature of this metallic conductance, but this lies beyond the scope of this Chapter.

We now examine the predictions of the structural spillage. Figs. 13(a,b) show the distribution of the structural spillage $\gamma^{\mathrm{TB}}_{\mathrm{qB}}(\boldsymbol{k})$ as a function of the crystal momentum $\boldsymbol{k}$ in the Brillouin zone. The reference system is a trivial Bi bilayer crystal with vanishing SOC in both cases. The target systems have a SOC $\lambda = 0.7t_\sigma$, corresponding to the topological region. Indeed, the spillage in Fig. 13(a), whose target system is crystalline, is peaked around Γ, reflecting the band inversion there. Although smoothed, the band inversion survives with moderate structural disorder, as shown in in Fig. 13(b) for a target amorphous system with $\rho_{\text{non-hex}} \simeq 0.53$, where $\gamma^{\mathrm{TB}}_{\mathrm{qB}}(\boldsymbol{k}) > \frac{1}{2}\max[\gamma^{\mathrm{TB}}_{\mathrm{qB}}]_{\text{crystal}} = 0.75$ fulfills our topological criterion explained in Section 3.2.3. Notice that the spillage for the Bi bilayer model (Fig. 13) is sharper than for the bismuthene model (Fig. 10) for both crystalline and amorphous target systems.

With this in mind, we study the phase diagram of the structural spillage $\gamma^{\mathrm{TB}}_{\mathrm{qB}}(\boldsymbol{k})$ at $\boldsymbol{k} = 0$ to

indicate the topological transition. Fig. 12(d) shows such phase diagram for a reference crystal with vanishing SOC, corresponding to the trivial phase. 12(e) displays the corresponding phase diagram for a topologically nontrivial reference crystal with $\lambda = t_\sigma$. For moderate structural disorder, $\rho_{\text{non-hex}} \lesssim 0.3$, both correctly reproduce the topological transition. The same limited precision and finite size effects that affected the conductance also broaden the otherwise sharp transition in the structural spillage. At higher structural disorder, where the system becomes metallic in the range of SOCs previously corresponding to the topological phase, the two structural spillages of Figs. 12(d,e) quantitatively differ due to the band mixing in the gapless region. The structural spillages are not specifically designed to capture metallic phases, but they still capture a partial band inversion.

The same features are reflected in the structural spillage of Fig. 12(f), whose amorphous target and crystalline reference have the same SOC λ in each point of the phase diagram. As in the bismuthene case, this phase diagram has to be interpreted as the effect of disorder in the band inversion. For a given λ, the topology of the amorphous target is the same as the one of the corresponding crystal if $\gamma^{\text{TB}}_{\text{qB}}(\boldsymbol{k} = 0)$ is small.

In summary, both conductance and spillage phase diagrams agree qualitatively and predict the topological phase transition as long as the mobility gap remains closed. Quantitative differences only arise in the metallic regions, where the band inversion is just partial. We also note that the realistic SOC $\lambda = 0.7 t_\sigma$ lies in the topological region.

3.4.5 DFT results

In this section, we present the DFT calculations of the structural spillage in amorphous bilayer Bismuth performed by our collaborators Paul Corbae et al. in Ref. [3]. By comparing them to our tight-binding results, we point out that the structural spillage is more convenient for first-principles calculations. This suggests that the structural spillage of Eq. (3.23) is well suited for high-throughput screening of amorphous topological materials.

The structurally disordered systems studied in these DFT calculations consisted of $5 \times 5 \times 1$ supercells comprising 50 Bi atoms. Starting from a crystalline supercell, the structures were disordered by adding random displacements in the $x, y,$ and z directions, sampled from a Gaussian distribution. Two amorphous structures with different degree of structural disorder were studied. Fig. 14 shows their structures and their corresponding radial distribution functions. We remark that these structures are not relaxed and not necessarily realistic, since our aim in Ref. [3] was to benchmark the structural spillage method in a structurally disordered system.

The electronic structure was calculated with plane-wave-based DFT for a single supercell momentum, the center of the supercell Brillouin zone. While the weak-disorder structure remains

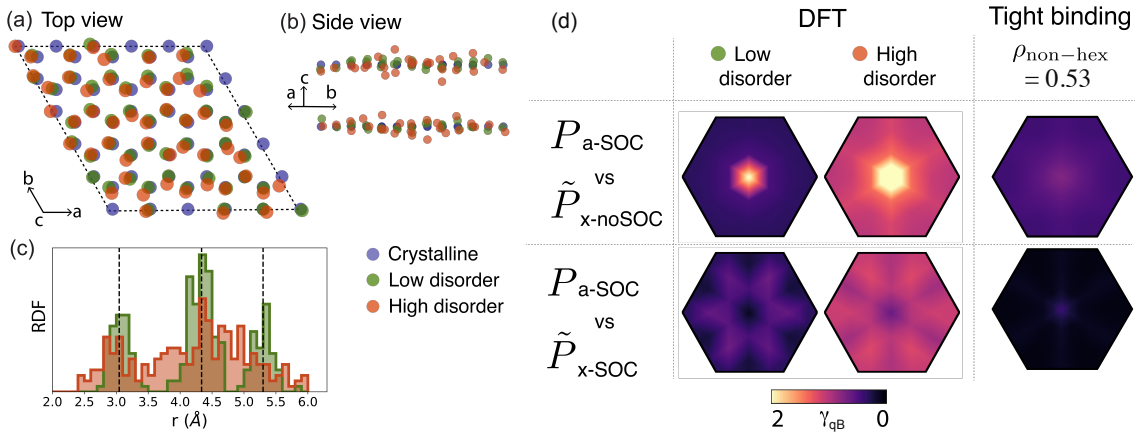

FIGURE 14: Structure and structural spillage of the disordered Bismuth bilayer systems studied in DFT calculations performed by our collaborators Paul Corbae et al. Extracted from Ref. [3]. (a) and (b) show the in-plane and out-of-plane views of the supercell, respectively. The colors indicate different degrees of disorder: crystal (blue), weak disorder (green) and strong disorder (orange). The disorder is sampled from a Gaussian distribution with a standard deviation of 0.15 Å for the weak disorder and 0.30 Å for the strong disorder. (c) Radial distribution function (RDF) showing the statistics of the bond lengths in the disordered Bismuth bilayer and their deviations from the perfect crystal (vertical dashed lines). (d) Structural quasi-Bloch spillage $\gamma_{\mathrm{qB}}(\boldsymbol{k})$ as a function of $\boldsymbol{k}$ in the Brillouin zone. First row: comparison between an amorphous system with SOC (a-SOC) and a crystalline system without SOC (x-noSOC). Comparing an amorphous system without SOC with a crystalline sample with SOC leads to similar results. Second row: comparison between the amorphous and crystalline systems with SOC (a-SOC and x-SOC, respectively). $\gamma_{\mathrm{qB}}(\boldsymbol{k})$ is high at $\boldsymbol{k} = 0$ for the first row while small for the second row, indicating that amorphous Bismuth bilayer is a topological insulator. The last column shows a comparison with the tight-binding quasi-Bloch spillage $\gamma^{\mathrm{TB}}_{\mathrm{qB}}(\boldsymbol{k})$ of Eq. (3.35) for the Bi bilayer model studied in section 3.4.4 with $\rho_{\text{non-hex}} \simeq 0.53$ and $\lambda = 0.7t_\sigma$. Note that the top plot is the same as in Fig. 13(b), but with a different scale and color map.

insulating, the strong-disorder one becomes metallic, as in our tight-binding model studied in the previous section. The structural quasi-Bloch spillage of Eq. (3.23) was determined using the output wavefunctions of the first-principles calculations. The amorphous target systems with SOC were compared to crystalline reference systems without and with SOC, which are topologically trivial and nontrivial, respectively. For a topologically trivial reference with vanishing SOC, the first row of Fig. 14 shows that $\gamma_{\mathrm{qB}}(\boldsymbol{k})$ is peaked at $\boldsymbol{k} = 0$, with $\gamma_{\mathrm{qB}}(\boldsymbol{k} = 0) > 2$. Increasing disorder smoothens $\gamma_{\mathrm{qB}}(\boldsymbol{k})$, yet it remains peaked at Γ with a value greater than 2. In contrast, the second row of Fig. 14 shows that the spillage is always small when the reference crystal is topological. Both rows together show that amorphous Bismuth bilayer with SOC is in the same topological state as the crystal with SOC, a strong topological insulator crystal with $\mathbb{Z}_2 = 1$.

Qualitatively, these results match our tight-binding predictions. For a better quantitative comparison, in the last column of Fig. 14 we have included the structural spillage $\gamma^{\mathrm{TB}}_{\mathrm{qB}}(\boldsymbol{k})$ of

Eq. (3.35) computed in the tight-binding approximation for an amorphous Bi bilayer with an structural disorder $\rho_{\text{non-hex}} \simeq 0.53$. While the structural disorders in the tight-binding and DFT structures are different, the width of the nearest-neighbour peak in the radial distribution function of this tight-binding structure is similar to the one of the weak-disorder system studied in DFT. Contrasting the first and last columns of Fig. 14, we conclude that for comparable disorder strengths $\gamma_{\text{qB}}^{\text{TB}}(\boldsymbol{k})$ is broader and its maximum value is smaller than $\gamma_{\text{qB}}(\boldsymbol{k})$ in DFT. In conclusion, due to the approximations in the tight-binding calculation of the spillage, which lacks information of the real space extension of the orbitals, the spillage method is more suitable for DFT, an advantageous feature compared to other topological indicators available for noncrystalline systems.

3.5 Discussion and conclusions

We have introduced the structural spillage as an efficient method to signal noncrystalline topological phases, compatible with *ab initio* simulations. We have also adapted it to the tight-binding approximation. We have applied the structural spillage to reproduce amorphous monolayer bismuthene as topologically nontrivial and to predict amorphous bilayer Bismuth as a novel topological insulator.

As with the spin-orbit spillage in crystals [117], we expect the structural spillage to signal a large fraction of promising materials, but not to be infallible: if multiple band inversions are introduced upon amorphization, the spillage might also be artificially large. While it can signal these false positive cases, we expect the number of false negatives to be considerably small: if no band inversion occurs, the topology is generally the same. Moreover, unlike for crystals, the spillage is currently the only systematic, model-independent method that is compatible with *ab initio* calculations of noncrystalline systems. Additionally, it can be applied to systems without a spectral gap, where the effective Hamiltonian approach [493] can fail [120]. All these features suggest the structural spillage as a candidate for a first screening in high-throughput searches to identify potential candidates for topological insulators in noncrystalline materials.

An important requirement for the application of the structural spillage involves finding an appropriate crystalline reference. The general recipe is finding the crystal whose local environments, defined by the coordination numbers, bond lengths and bond angles, are closer to a given amorphous structure. In practice, several methods to generate amorphous materials start from a crystalline system, and then distort it using a given procedure. In these cases, a generally good crystalline reference would be this initial system. For example, this is clear in our tight-binding models, where the starting point is a crystalline honeycomb lattice, which is then made amorphous by adding a controlled amount of structural disorder via the described Voronoi procedure. The same idea applies to the bond-flipping amorphization method, which has been employed to

generate realistic ab-initio amorphous materials [417, 418]. In the case of the widely extended *ab initio* molecular dynamics methods [416, 569, 570], amorphous structures are generated by a melt-and-quench procedure, whereby a seed crystal is heated above the melting temperature, with certain annealing time, and then quenched to low temperatures again.

In a few cases, however, there might not be an appropriate crystalline reference, either because no crystal of the desired composition exists, or because the local environments of the existing crystals are significantly different from those of the noncrystalline system. In such cases, one may define a plane-wave-resolved spillage by using Eq. (3.23a) without the sum over $\boldsymbol{G}$ (see Appendix 3.B.3 and the paragraph below Eq. (3.35)). In Appendix 3.B.3 we demonstrate that also this plane-wave-resolved spillage works within our bismuthene and Bi bilayer tight-binding models. Its usefulness in DFT calculations is worth studying in the future.

In summary, the structural spillage constitutes a promising step in the roadmap to systematically construct a high-throughput catalogue of noncrystalline topological materials. In the current stage, it could be readily applied to screen existing databases of amorphous solids, as well as known quasicystalline and polycrystalline materials.

3.5.1 Outlook

An important open problem in the field is experimentally manufacturing an amorphous solid state system that is unambiguously topological. Amorphous Bi_2Se_3 is an auspicious candidate thanks to its spin-momentum locked surface states observed by ARPES [410, 545], but other experiments are desirable for a definite proof. The establishment of a high-throughput catalogue of noncrystalline topological materials with the structural spillage could aid this search by finding a *textbook* amorphous topological material feasible to be synthesized. Nevertheless, interesting subsets of materials where to look for include those with high spin-orbit coupling or those which undergo topological transitions under pressure or strain, since the amorphization could mimic the local environments of these situations. Material candidates include amorphous pnictogen trichalcogenides, such as amorphous Sb_2Se_3 [571].

Besides a catalogue of noncrystalline topological materials, several other avenues are open in the field of noncrystalline topological matter. First, a complete classification of the possible topological phases in noncrystalline systems is lacking. A first step in this direction was taken by Refs. [113, 452–457] with the introduction and characterization of gapped statistical topological insulators. In particular, Ref. [456] classified 2D amorphous statistical topological insulators protected by average reflection symmetry based on the effective Hamiltonian approach. A different approach which might also be useful for this classification is that of real space invariants [385, 514, 572–574], which are quantities defined in real space based on the number of occupied Wannier

states in the high-symmetry Wyckoff positions. For their application in noncrystalline system, the calculation of the Wannier centers should be generalized to non-translationally invariant systems. Ref. [475] carried out the first step in this direction. The authors considered an amorphous tight-binding model, and differentiated whether the charge centers of the filled states were located in the sites or in the bonds, allowing to identify amorphous obstructed insulators. Once this is generalized to all noncrystalline materials, real space invariants would allow the topological classification of, for instance, quasicrystals with a well-defined point group.

Several questions remain unsettled in the field of noncrystalline topological superconductors at different levels of their description. For instance, while topological superconductivity has been self-consistently determined in attractive Hubbard models in quasicrystals [575], it remains to be demonstrated in amorphous systems, where topological superconductivity has only been studied by imposing a finite pairing [469, 470]. Although Anderson's theorem [423–425], which states that the superconductivity is unaffected by dilute disorder, only applies to isotropic superconductivity pairing time-reversal partners, it is not the end of the story. Indeed, theories treating the disorder exactly predict that unconventional superconductivity can be robust and even enhanced by disorder due to the multifractal properties of the spectrum and related enhancement of the local DOS in certain regions [426–428]. This enables the possibility of self-consistently finding amorphous topological superconductivity, especially in multiorbital models with a local superconducting pairing. A related problem consists of studying the difference between the impact of structural and Anderson disorders in superconductivity, which might display a markedly distinct spatial distribution of the order parameter. In a further level of description, tools beyond mean-field theory would be needed to discern what features are not artifacts of mean-field theory, which suffers from rare region effects [427]. At the same time, another frontier in noncrystalline superconductivity consists of developing more elaborate models with realistic interactions beyond attractive Hubbard models. For instance, vibrational properties of amorphous solids are different than those of crystals, showing an excess of low-frequency vibrational modes which can affect superconductivity [576–578].

In summary, we believe that our theory provides a meaningful advance in the field of noncrystalline topological matter. We also hope that the near future will see significant contributions to several of the far-reaching open questions in the field.

Appendices

3.A Structural spillage in DFT calculations

Unlike in the tight-binding approximation, the structural spillage of Eq. (3.23) can be directly implemented in DFT. Here, the overlap between two systems is well-defined irrespective of whether they have atoms at different positions. However, strictly speaking, the continuous set of plane waves is always overcomplete in any numerical scheme. Nevertheless, the structural spillage of Eq. (3.23) is still well-defined in DFT implemented with both a plane-wave or a localized basis. On the one hand, plane-wave-based DFT codes feature discretized momenta imposed by the periodic boundary conditions of the supercell, as well as a high-momentum cutoff. These features do not constitute any fundamental problem for comparing two systems with different atomic structures, as long as one has access to, or can interpolate, the information at the same momenta in both target and reference systems. On the other hand, implementations of DFT with a localized basis, such as Gaussian or atomic orbitals, do not directly output the information in plane-wave momentum space. However, knowing the shape of the orbitals, a Fourier transform gives access to it, and no problem appears regardless of the atomic structure.

3.B Structural spillage and average symmetry indicators in amorphous systems

Symmetry indicators are a powerful tool to identify topological phases in crystalline systems [102, 104–107]. Average-symmetry indicators have been extended to simple amorphous tight-binding models [120]. In particular, Ref. [120] studied Weaire-Thorpe models [406, 412, 413] with a well-defined atomic limit with an exact local threefold symmetry C_3 which acts on the internal degrees of freedom. While for other parameters this local symmetry is only present on average, the spectral density can still be projected to the eigenvectors of C_3. If the spectral density is also momentum-resolved by projecting to plane-wave states, the topological transitions of this model are characterized by a band inversion of two bands with different average C_3 symmetry at a given momentum $\boldsymbol{p}$, which in their models is $\boldsymbol{p} = 0$.

3.B.1 Amorphous average symmetry indicators in the bismuthene tight-binding model

The same concept can be applied to our bismuthene model. The trivial atomic limit with infinite onsite SOC λ or, analogously, vanishing hoppings, has a local rotational $O(2) \simeq U(1)$ symmetry in the space of internal orbital and spin degrees of freedom, which can therefore be labelled by their angular momentum J_z. In our model with $|L_z| = 1$ $p_{x,y}$ orbitals with spin $|S_z| = \frac{1}{2}$, the local $O(2)$ symmetry has eigenvalues, $|J_z| = \frac{1}{2}, \frac{3}{2}$. Due to time-reversal symmetry, the Hamiltonian eigenvectors with equal $|J_z|$ are degenerate, with eigenvalue $+\lambda$ for the $|J_z| = \frac{1}{2}$ states $\{p_{+\downarrow}, p_{-\uparrow}\}$, and eigenvalue $-\lambda$ for the $|J_z| = \frac{3}{2}$ states $\{p_{+\uparrow}, p_{-\downarrow}\}$. Therefore, at half-filling, only $|J_z| = \frac{3}{2}$ are occupied.

Away from this atomic limit, the local $O(2)$ symmetry is broken, but a local C_3 symmetry is recovered on average. We note that the crystalline lattice has exact C_3 symmetry. The local C_3 symmetry can also be labelled by $|J_z|$. Therefore, it makes sense to resolve the spectral function in $|J_z|$. Following Ref. [120], we project onto plane waves with momentum $\boldsymbol{p}$, keeping only the diagonal elements, i.e., we neglect momentum scattering. The resulting momentum and C_3-resolved spectral densities are $\rho_{|J_z|}(\omega, \boldsymbol{p})$. The total spectral density is $\rho(\omega, \boldsymbol{p}) = \rho_{1/2}(\omega, \boldsymbol{p}) + \rho_{3/2}(\omega, \boldsymbol{p})$.

Recall that, in the crystalline case, bismuthene starts in a topological phase for small SOC, and increasing SOC drives a band inversion at Γ that renders the system trivial. This band inversion occurs between states with different $|J_z|$. At high structural disorder, the inversion between states survives at plane-wave momentum $\boldsymbol{p} = 0$. As seen from the C_3-resolved spectral densities are $\rho_{|J_z|}(\omega, \boldsymbol{p})$, the inversion is between states with a state with mainly $|J_z| = \frac{3}{2}$ and another with mainly $|J_z| = \frac{1}{2}$. In particular, two unoccupied $|J_z| = \frac{1}{2}$ states at $\boldsymbol{p} = 0$ in the trivial phase become occupied in the topological state. This can be captured by the symmetry indicator that counts the difference between the occupied states with distinct C_3 projection:

$$\nu(\boldsymbol{p}) = \int_{-\infty}^{E_F} d\omega \left[\rho_{3/2}(\omega, \boldsymbol{p}) - \rho_{1/2}(\omega, \boldsymbol{p})\right], \tag{3.41}$$

Indeed, $\nu(0)$ jumps from $\simeq 2$ at high SOC in the trivial phase, to $\simeq 0$ after the transition to the topological state.

3.B.2 Relationship to the structural spillage

A change in the amorphous average symmetry indicators signals a band inversion, which can also be detected with an spillage comparing two appropriate systems. We now discern the particular relationship between them in our amorphous bismuthene model. Note that the trace of

the plane-wave resolved projector onto occupied states equals the integral of the spectral function:

$$\mathrm{tr}\left[P_{\boldsymbol{p}}\right] = \int_{-\infty}^{E_F} d\omega \rho(\omega, \boldsymbol{p}). \tag{3.42}$$

Projecting onto the eigenstates of the average local C_3 symmetry, we can also write

$$\mathrm{tr}\left[P_{|J_z|,\boldsymbol{p}}\right] = \int_{-\infty}^{E_F} d\omega \rho_{|J_z|}(\omega, \boldsymbol{p}), \tag{3.43}$$

with $\mathrm{tr}[P_{\boldsymbol{p}}] = \mathrm{tr}[P_{3/2,\boldsymbol{p}}] + \mathrm{tr}[P_{1/2,\boldsymbol{p}}]$. Therefore, we can rewrite the symmetry indicator as

$$\nu(\boldsymbol{p}) = \mathrm{tr}\left[P_{3/2,\boldsymbol{p}} - P_{1/2,\boldsymbol{p}}\right] \tag{3.44}$$

In our particular case, $\mathrm{tr}[P_{3/2,\boldsymbol{p}=0}] \simeq 2$ for all SOCs, so we can simplify

$$\nu(\boldsymbol{p}=0) \simeq 2 - \mathrm{tr}\left[P_{1/2,\boldsymbol{p}=0}\right]. \tag{3.45}$$

For the spillage, we consider a reference trivial crystal with infinite onsite SOC $\tilde{P}$, which has $\mathrm{tr}[\tilde{P}_{3/2,\boldsymbol{p}}] = 2$ and $\tilde{P}_{1/2,\boldsymbol{p}} = 0$. Consider the $\boldsymbol{G} = 0$ term of the summation in the structural quasi-Bloch spillage $\gamma^{\mathrm{TB}}_{\mathrm{qB}}(\boldsymbol{k}=0)$ of (3.35). In section 3.2.3, we called this quantity plane-wave-momentum resolved spillage $\gamma^{\mathrm{TB}}_{\mathrm{pw}}(\boldsymbol{p})$:

$$\gamma^{\mathrm{TB}}_{\mathrm{pw}}(\boldsymbol{p}=0) = \frac{1}{2}\mathrm{tr}\left[\left(P_{\boldsymbol{p}=0} - \tilde{P}_{\boldsymbol{p}=0}\right)^2\right] = \frac{1}{2}\left(\mathrm{tr}\left[P^2_{\boldsymbol{p}=0}\right] + \mathrm{tr}\left[\tilde{P}^2_{\boldsymbol{p}=0}\right]\right) - \mathrm{tr}\left[P_{\boldsymbol{p}=0}\tilde{P}_{\boldsymbol{p}=0}\right]. \tag{3.46}$$

In Appendix 3.C, we will show that $\mathrm{tr}[P^2_{\boldsymbol{p}}] \simeq \mathrm{tr}[P_{\boldsymbol{p}}]$, so

$$\gamma^{\mathrm{TB}}_{\mathrm{pw}}(\boldsymbol{p}=0) \simeq \frac{1}{2}\left(\mathrm{tr}\left[P_{\boldsymbol{p}=0}\right] + \mathrm{tr}\left[\tilde{P}_{\boldsymbol{p}=0}\right]\right) - \mathrm{tr}\left[P_{\boldsymbol{p}=0}\tilde{P}_{\boldsymbol{p}=0}\right]. \tag{3.47}$$

Now, resolving the projectors in $|J_z|$, and using that $\mathrm{tr}[P_{3/2,\boldsymbol{p}=0}] \simeq 2 = \mathrm{tr}[\tilde{P}_{3/2,\boldsymbol{p}}]$, $\tilde{P}_{1/2,\boldsymbol{p}} = 0$, $\mathrm{tr}[P_{\boldsymbol{p}=0}\tilde{P}_{\boldsymbol{p}=0}] = \mathrm{tr}[P_{3/2,\boldsymbol{p}=0}\tilde{P}_{3/2,\boldsymbol{p}=0}] = \mathrm{tr}[P_{3/2,\boldsymbol{p}=0}]$, we can write

$$\begin{aligned}\gamma^{\mathrm{TB}}_{\mathrm{pw}}(\boldsymbol{p}=0) &\simeq \frac{1}{2}\left(\mathrm{tr}\left[P_{3/2,\boldsymbol{p}=0}\right] + \mathrm{tr}\left[P_{1/2,\boldsymbol{p}=0}\right] + \mathrm{tr}\left[\tilde{P}_{3/2,\boldsymbol{p}=0}\right]\right) - \mathrm{tr}\left[P_{3/2,\boldsymbol{p}=0}\right] \simeq \\ &\simeq \frac{1}{2}\mathrm{tr}\left[P_{1/2,\boldsymbol{p}=0}\right] \simeq 1 - \frac{1}{2}\nu(\boldsymbol{p}=0).\end{aligned} \tag{3.48}$$

Therefore, the plane-wave spillage $\gamma^{\mathrm{TB}}_{\mathrm{pw}}(\boldsymbol{p})$ comparing the target amorphous system to a trivial crystalline atomic limit is just the symmetry indicator $\nu(\boldsymbol{p})$ rescaled. Indeed, $\gamma^{\mathrm{TB}}_{\mathrm{pw}}(\boldsymbol{p}=0)$ jumps from 0 in the trivial phase to 1 in the topological phase. This relationship further justifies the validity of our structural spillage.

3.B.3 Structural plane-wave spillage

Eq. (3.48) demonstrates the direct link between the plane-wave-momentum resolved spillage $\gamma^{\mathrm{TB}}_{\mathrm{pw}}(\boldsymbol{p})$ and the amorphous average symmetry indicators. The structural quasi-Bloch spillage $\gamma^{\mathrm{TB}}_{\mathrm{qB}}(\boldsymbol{k})$ is related to this structural plane-wave spillage $\gamma^{\mathrm{TB}}_{\mathrm{pw}}(\boldsymbol{p})$ via the average over Brillouin zone types (see Section 3.2.3):

$$\gamma^{\mathrm{TB}}_{\mathrm{pw}}(\boldsymbol{p}) = \frac{1}{2}\mathrm{tr}\left[\left(P_{\boldsymbol{p}} - \tilde{P}_{\boldsymbol{p}}\right)^2\right], \tag{3.49}$$

$$\gamma^{\mathrm{TB}}_{\mathrm{qB}}(\boldsymbol{k}) = \frac{N_{\mathrm{s/c}}}{N_{\mathrm{BZs}}}\sum_{\boldsymbol{G}}^{\mathrm{BZs}} \gamma^{\mathrm{TB}}_{\mathrm{pw}}(\boldsymbol{k}+\boldsymbol{G}). \tag{3.50}$$

The additional sums over the different types of Brillouin zones are kept in our formulation to recover, in the crystalline limit, the results as similar as possible to Liu and Vanderbilt's spillage[7]. However, we remark that the structural plane-wave spillage $\gamma^{\mathrm{TB}}_{\mathrm{pw}}(\boldsymbol{p})$ should also act as a topological indicator in the tight-binding approximation. Besides its explicit connection to average symmetry indicators, the structural plane-wave spillage $\gamma^{\mathrm{TB}}_{\mathrm{pw}}(\boldsymbol{p})$ is also more directly related to the Fourier transform of an appropriately chosen strange correlator [118, 119] (see Section 3.2.2). The topological transition criterion in this case should be taken as $\gamma^{\mathrm{TB}}_{\mathrm{pw}}(\boldsymbol{p})_{\mathrm{crit}} \sim \frac{1}{N_{\mathrm{s/c}}}$.

This observation allows to expand the applicability of the structural spillage. One of the key points for the structural quasi-Bloch spillage of Eqs. (3.23), (3.35) to work as a topological indicator is that there exists a crystalline structure with similar local environments to the noncrystalline one. While this is a quite generic feature [401], there are also a few amorphous and quasicrystalline structures whose local environment is different to any crystalline phase of the same material. In this case, while the structural quasi-Bloch spillage could still be calculated, it would probably not be very indicative of the topology, since many trivial band inversions could occur. It is for such cases without a crystalline counterpart, where we propose the plane-wave spillage $\gamma^{\mathrm{TB}}_{\mathrm{pw}}(\boldsymbol{p})$, but now comparing the noncrystalline target to a reference system with the same structure but another differing parameter, such as SOC. While this poses the challenge of identifying the topology of the reference in the first place, it can indicate the topological band inversions between them. In particular, strong topological phases could be indicated by such a SOC plane-wave spillage, since the reference with vanishing SOC would not be strong topological. Indeed, Fig. 3.B.1 shows $\gamma^{\mathrm{TB}}_{\mathrm{pw}}(\boldsymbol{p}=0)$ for the bismuthene and Bi bilayer amorphous tight-binding models using a trivial amorphous reference system. As the full quasi-Bloch structural spillage, the plane-wave spillage comparing two amorphous structures does also predict the topological phase transition in both models. We highlight that this SOC plane-wave spillage is different from Liu and Vanderbilt's

[7]They are also kept so that the structural spillage works in DFT, where plane wave states do not have the orbital degree of freedom.

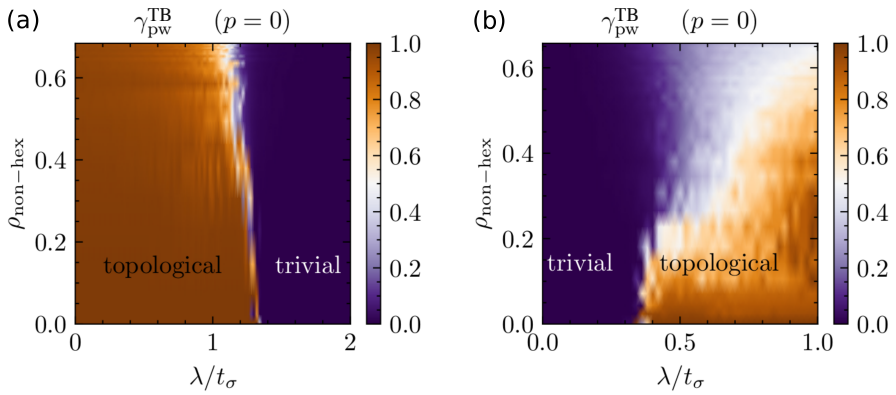

FIGURE 3.B.1: Phase diagram of the plane-wave spillage $\gamma_{\mathrm{pw}}^{\mathrm{TB}}(\boldsymbol{p})$ at $\boldsymbol{p}=0$. (a) Amorphous bismuthene, where the reference system is the trivial amorphous phase with $t_\sigma = 0$. (b) Amorphous Bi bilayer, where the reference system is the trivial amorphous phase with $\lambda = 0$.

SOC Bloch spillage, which is resolved in the Bloch momentum of the supercell, and is always larger for a large supercell regardless of the topology.

This plane-wave spillage can be generalized to DFT calculations by reincorporating the momentum scattering in the tight-binding plane-wave spillage of Eq. (3.49), or equivalently by neglecting the sum over crystalline reciprocal lattice vectors $\boldsymbol{G}$ in the quasi-Bloch spillage of Eq. (3.23):

$$\gamma_{\mathrm{pw}}(\boldsymbol{p}) = \frac{1}{2}\sum_{\boldsymbol{p}'}\sum_{\alpha\beta}\left[P^{\alpha\beta}_{\boldsymbol{p},\boldsymbol{p}'}P^{\beta\alpha}_{\boldsymbol{p}',\boldsymbol{p}} - P^{\alpha\beta}_{\boldsymbol{p},\boldsymbol{p}'}\tilde{P}^{\beta\alpha}_{\boldsymbol{p}',\boldsymbol{p}}\right] + \left[P \leftrightarrow \tilde{P}\right] \tag{3.51}$$

where $\boldsymbol{p}$ and $\boldsymbol{p}'$ are plane-wave momenta. For a supercell Gamma calculation in DFT, $\boldsymbol{p}$ and $\boldsymbol{p}'$ would be the supercell reciprocal lattice vectors. While this is a promising avenue, we acknowledge that further studies should be carried out to apply the plane-wave spillage within DFT, since it is not clear the topological transition criterion yet. The crucial difference with the tight-binding, where this criterion is easily extracted, is that plane waves projected to the tight binding are not pure plane waves, but are are also orbital resolved. That $\gamma_{\mathrm{pw}}^{\mathrm{TB}}(\boldsymbol{p}) = 1$ means therefore that one orbital per atom has been inverted in the band inversion at momentum $\boldsymbol{p}$.

Finally, we mention that, since both systems that are being compared have the same structure, momentum scattering could also be included within a tight-binding approximation:

$$\begin{aligned}\gamma_{\mathrm{pw}}^{\text{non-orth}}(\boldsymbol{p}) = \frac{1}{2}\sum_{\boldsymbol{p}_1,\boldsymbol{p}_2,\boldsymbol{p}_3}\sum_{\alpha\beta}\Big[&P^{\alpha\beta}_{\boldsymbol{p},\boldsymbol{p}_1}\left(S^{-1}\right)_{\boldsymbol{p}_1,\boldsymbol{p}_2}P^{\beta\alpha}_{\boldsymbol{p}_2,\boldsymbol{p}_3}\left(S^{-1}\right)_{\boldsymbol{p}_3,\boldsymbol{p}} - \\ &-P^{\alpha\beta}_{\boldsymbol{p},\boldsymbol{p}_1}\left(S^{-1}\right)_{\boldsymbol{p}_1,\boldsymbol{p}_2}\tilde{P}^{\beta\alpha}_{\boldsymbol{p}_2,\boldsymbol{p}_3}\left(S^{-1}\right)_{\boldsymbol{p}_3,\boldsymbol{p}}\Big] + \left[P \leftrightarrow \tilde{P}\right].\end{aligned} \tag{3.52}$$

where the overlap matrix is defined as $S_{\boldsymbol{p},\boldsymbol{p}'} = \langle \boldsymbol{p}\alpha | \boldsymbol{p}'\alpha \rangle$, which depends only on the difference $\boldsymbol{p}' - \boldsymbol{p}$. However, the no-scattering approximation of the plane-wave spillage $\gamma^{\mathrm{TB}}_{\mathrm{pw}}(\boldsymbol{p})$ of Eq. (3.49) is much more efficient to compute, and it already indicates topology. (3.23)

3.C Structural spillage in the tight-binding approximation

In this Appendix, we give a pedagogical justification of Eq. (3.35) for computing the structural quasi-Bloch spillage in the tight-binding approximation, where only the Wannier charge centers are known. We recall that plane wave states projected to the tight-binding Hilbert space are non-orthogonal and overcomplete. When trying to compare a target and a reference system with different atomic structure, their overlap is ill-defined since their Hilbert spaces are different. As explained in Section 3.2.3, this issue can be circumvented by neglecting the matrix elements of the projectors that are off-diagonal in momentum, which we call the no-scattering approximation. However, this approximation, together with the non-orthogonal and overcomplete character of the plane waves, causes new issues. Here we thoroughly explain these and our approach to bypass them, which aims to obtain the results as close as possible to the exact ones in the crystalline limit.

In order to separately understand the different issues that appear in the tight binding, we first consider the simple case of a system whose corresponding crystalline limit has a single site per unit cell, where only a part of the problems appear. Then, we will analyze the general multi-site case.

3.C.1 Reference crystal with a single site per unit cell

Setting the stage: crystalline system

Consider a crystalline tight-binding system with N_{cell} unit cells and one site per unit cell, i.e., only one Wyckoff position with multiplicity one is occupied by an atom, $N_{\mathrm{s/c}} = 1$. Therefore, the number of sites is the same as the number of cells, $N_{\mathrm{sites}} = N_{\mathrm{cell}}$. The number of internal degrees of freedom (orbitals and spins) at each site does not influence the discussion below, so we omit this internal index for simplicity in the notation. In the tight-binding approximation, Wannier functions $|\phi_{\boldsymbol{R}}\rangle$ at different lattice sites $\boldsymbol{R}$ are orthogonal

$$\langle \phi_{\boldsymbol{R}'} | \phi_{\boldsymbol{R}} \rangle = \delta_{\boldsymbol{R},\boldsymbol{R}'}. \tag{3.53}$$

Since their real-space wavefunction is unknown, gauge invariance requires the position operator to be diagonal in the Wannier function basis

$$\langle \phi_{\boldsymbol{R}'} | \boldsymbol{\mathcal{R}} | \phi_{\boldsymbol{R}} \rangle = \delta_{\boldsymbol{R},\boldsymbol{R}'}, \tag{3.54}$$

Therefore, Wannier functions are considered to be Dirac delta distributions:

$$\phi_{\boldsymbol{R}}(\boldsymbol{r}) = \langle \boldsymbol{r}|\phi_{\boldsymbol{R}}\rangle = \delta(\boldsymbol{r}-\boldsymbol{R}). \tag{3.55}$$

The plane wave with momentum $\boldsymbol{p}$ projected to the tight-binding Hilbert space is a state with a phase $\boldsymbol{p}\cdot\boldsymbol{R}$ at the site $\boldsymbol{R}$, and normalized in the total volume of the system (see Eq. (3.26)). Then, the overlap between Wannier functions and plane wave reads:

$$\phi_{\boldsymbol{R}}(\boldsymbol{p}) = \langle \boldsymbol{p}|\phi_{\boldsymbol{R}}\rangle = \frac{1}{\sqrt{N_{\text{sites}}}} e^{-i\boldsymbol{p}\cdot\boldsymbol{R}}. \tag{3.56}$$

Moreover, the Bloch states defined at crystal momentum $\boldsymbol{k}$ in the first BZ are:

$$|\phi_{\boldsymbol{k}}\rangle = \frac{1}{\sqrt{N_{\text{cell}}}} \sum_{\boldsymbol{R}} e^{i\boldsymbol{k}\cdot\boldsymbol{R}} |\phi_{\boldsymbol{R}}\rangle, \tag{3.57}$$

Since $N_{\text{sites}} = N_{\text{cell}}$, the overlap between the Bloch states and the plane waves is thus:

$$\langle \boldsymbol{p}|\phi_{\boldsymbol{k}}\rangle = \frac{1}{N_{\text{sites}}} \sum_{\boldsymbol{R}} e^{i(\boldsymbol{k}-\boldsymbol{p})\cdot\boldsymbol{R}} = \sum_{\boldsymbol{G}} \delta_{\boldsymbol{p},\boldsymbol{k}+\boldsymbol{G}}, \tag{3.58}$$

where $\boldsymbol{G}$ are the reciprocal lattice vectors, i.e., $\boldsymbol{G}\cdot\boldsymbol{R}/2\pi \in \mathbb{Z}$. Therefore, all the BZs are exactly equivalent in a crystalline one-atom tight-binding, since

$$\langle \boldsymbol{k}+\boldsymbol{G}|\phi_{\boldsymbol{k}}\rangle = 1 \tag{3.59}$$

does not depend on $\boldsymbol{G}$. In other words, $\langle \boldsymbol{p}|\boldsymbol{p}+\boldsymbol{G}\rangle = 1$ for the crystal, i.e., both plane waves are projected to the same state, which is exactly the Bloch state at $\boldsymbol{k}$ too.

Finally, as a side remark, it is worth mentioning that even if there is a single site per unit cell, the BZs of a crystal are no longer equivalent if the orbitals have a finite spread in real space. Indeed, in this case, the overlap between the Bloch state and the plane waves is:

$$\langle \boldsymbol{k}+\boldsymbol{G}|\phi_{\boldsymbol{k}}\rangle = \frac{1}{N_{\text{cell}}} \sum_{\boldsymbol{R}} e^{i\boldsymbol{k}\cdot\boldsymbol{R}} \langle \boldsymbol{k}+\boldsymbol{G}|\phi_{\boldsymbol{R}}\rangle = \frac{1}{N_{\text{cell}}} \sum_{\boldsymbol{R}} e^{-i\boldsymbol{G}\cdot\boldsymbol{R}} \langle \boldsymbol{k}+\boldsymbol{G}|\phi_0\rangle = \phi_0(\boldsymbol{k}+\boldsymbol{G}), \tag{3.60}$$

where $\phi_0(\boldsymbol{k}+\boldsymbol{G})$ is the Fourier transform of the orbital located at the origin, which is generically not constant.

Spillage comparing two crystals

Remember that plane waves are an overcomplete set in the tight-binding Hilbert space. In this single-site case, the Hilbert space dimension is N_{sites}, which is the number of linearly independent plane waves needed for a basis. One possible choice is selecting all the $N_{\text{cell}} = N_{\text{sites}}$ momenta in one BZ $\{|\boldsymbol{k}+\boldsymbol{G}\rangle\}_{\text{fixed }\boldsymbol{G}}$, e.g. the first BZ, with $\boldsymbol{G} = 0$. These are linearly independent and orthogonal in the crystalline case, $\langle \boldsymbol{k}'+\boldsymbol{G}|\boldsymbol{k}+\boldsymbol{G}\rangle = \delta_{\boldsymbol{k}\boldsymbol{k}'}$. Therefore, this choice constitutes an orthonormal basis. Therefore, in this basis we can compute the spillage comparing a target and a reference with the same crystalline lattice by directly applying Eq. (3.23), with the particularity that the sums over reciprocal lattice vectors $\boldsymbol{G}$ disappear since there is only one in the basis.

The key difference from the general multi-site case is that observables are the same irrespective of the BZ where the momenta for the basis are chosen, i.e., irrespective of the $\boldsymbol{G}$ chosen in the basis. Moreover, thanks to the equivalence between plane waves $|\boldsymbol{k}+\boldsymbol{G}\rangle$ and Bloch states $|\phi_{\boldsymbol{k}}\rangle$ in this single-site case, observables projected to a plane wave $\boldsymbol{p}$ are equal to the crystalline quantities computed at Bloch momentum $\boldsymbol{k} = \boldsymbol{p} \bmod \boldsymbol{G}$. In particular, the quasi-Bloch spillage (3.23), which is equal to the Bloch spillage because we are comparing two crystals, is also equal to the quasi-Bloch spillage without scattering (3.35) in this crystalline one-site case.

Structural spillage comparing an amorphous system to a reference crystal

The previous basis choice $\{|\boldsymbol{k}+\boldsymbol{G}\rangle\}_{\text{fixed }\boldsymbol{G}}$ is also orthonormal for an amorphous system in the infinite-size limit, $\langle \boldsymbol{k}'+\boldsymbol{G}|\boldsymbol{k}+\boldsymbol{G}\rangle \simeq \delta_{\boldsymbol{k}\boldsymbol{k}'}$ (see Eq. (3.28)). Consequently, unlike in the multi-site case that will be analyzed in the next section, the issue of the overlap between plane waves being different for the amorphous and crystalline systems does not appear. This makes the single-site case anomalous in the following sense. Strictly, the Hilbert spaces of amorphous target and crystalline reference are different and therefore their overlap not well-defined. Nevertheless, the exact structural spillage including scattering of Eq. (3.31) can be applied if we impose that the ill-defined overlap between plane waves projected to the tight binding ${}_{\text{crystal}}\langle \tilde{\boldsymbol{k}}'+\boldsymbol{G}|\boldsymbol{k}+\boldsymbol{G}\rangle_{\text{noncryst}}$ coincides with the true overlap for plane waves defined in the whole real space $\langle \tilde{\boldsymbol{k}}'+\boldsymbol{G}|\boldsymbol{k}+\boldsymbol{G}\rangle = \delta_{\boldsymbol{k}\tilde{\boldsymbol{k}}'}$. With this assumption, the exact structural spillage including scattering can also be applied for comparing the amorphous structure with a crystalline reference in this single-site tight-binding case, and it reduces to Eq. (3.23) with only the $\boldsymbol{G}$ chosen in the basis.

It is worth pointing out the following difference between comparing two crystals and comparing an amorphous system to a crystal, within this single-site case. As mentioned in the previous section, when comparing two crystals with a single site per unit cell, the quasi-Bloch spillage including scattering of Eq. (3.23) coincides with the one without scattering of Eq. (3.35). This is no longer

true when comparing an amorphous structure to a crystal, since the scattering resummation over $\boldsymbol{k}'$ in the amorphous projector, which is carried out in Eq. (3.23), is neglected in Eq. (3.35).

Now, although the structural quasi-Bloch spillage including scattering of Eq. (3.23) could in principle be applied, this would entail a high computational cost. Indeed, other methods to indicate the topology in the tight-binding would be equally (in)efficient (such as the local topological markers [502, 504, 532, 543] or single-point topological invariants [500, 501]), questioning the usefulness of the structural spillage applied to a tight-binding model. Therefore, to implement efficiently the structural spillage, we assume the no-scattering approximation of Eq. (3.35). Because we neglect the scattering resummation over $\boldsymbol{k}'$, the structural spillage of Eq. (3.35) becomes much more computationally efficient.

However, an important inconvenience arising from neglecting the scattering is that the spillage depends on the BZ where the momenta for the plane wave basis are chosen. This is because momenta from different crystalline BZs will no longer lead to equivalent results in the amorphous system, unlike in the single-site crystal. In fact, $|\boldsymbol{p}+\boldsymbol{G}\rangle$ and $|\boldsymbol{p}\rangle$ no longer project to the same state ($\langle\boldsymbol{p}|\boldsymbol{p}+\boldsymbol{G}\rangle = 0$ for the amorphous case in the infinite size limit), and the quantities projected in $|\boldsymbol{p}+\boldsymbol{G}\rangle$ differ from those projected onto $|\boldsymbol{p}\rangle$.

This problem raises the question of how to compute correctly the structural spillage in the no-scattering approximation between an amorphous material and a crystal, even in this single-site case. Although there is no unique answer, we now provide a justification for using momenta just in the first BZ, i.e., choosing $\boldsymbol{G} = 0$. The tight binding has no information about the spatial extent of the orbitals, although we know that they are exponentially localized around the atom. Therefore, the tight-binding approximation captures well long-distance physics, but there is a short-distance-cutoff below which the tight-binding results are no longer reliable. It is reasonable to assume that this cutoff is of the order of the nearest-neighbour distance r_{nn}, which coincides with the lattice constant a in the crystalline single-site tight-binding. Therefore, only plane-wave momenta below $\sim 2\pi/a$ are reliable. Consequently, the quasi-Bloch spillage computed just with plane-wave momenta in the first BZ is a sensible option (optionally, one could average over the first BZ and second BZs). Considering just the first BZ, the structural quasi-Bloch spillage without scattering reads

$$\gamma_{\mathrm{qB}}^{\text{single-site-TB}}(\boldsymbol{k}) = \frac{1}{2}\mathrm{tr}\left[\left(P_{\boldsymbol{k}} - \tilde{P}_{\boldsymbol{k}}\right)^2\right], \tag{3.61}$$

which is just Eq. (3.35) in the single-site case because, as mentioned before, all BZs are equivalent in the crystal, and therefore there is a single type of BZ, $N_{\mathrm{BZs}} = 1$.

3.C.2 Reference crystal with several sites per unit cell

In this section, we will first show that for crystals with more than one site in the unit cell, a phase factor depending on the relative positions of the sites appears in the observables, which allows classifying different types of BZs. We recapitulate how the formalism for non-orthogonal bases has to be applied in the spillage comparing two crystals. Afterwards, we explain why the no-scattering approximation is required to compare an amorphous target to a crystalline reference. We finally give a recipe to deal with the presence of different types of BZs in the no-scattering approximation, which recovers the results as close as possible to the exact ones in the crystalline limit.

Crystal: definitions and types of Brillouin zones

Consider a crystal with N_{cell} unit cells at positions $\boldsymbol{R}$ and $N_{\text{s/c}}$ sites per unit cell at positions $\boldsymbol{t}_A$ with respect to the center of the cell $\boldsymbol{R}$, so that the total number of sites is $N_{\text{sites}} = N_{\text{cell}} \cdot N_{\text{s/c}}$. We will show that i) not all inequivalent plane wave states are orthogonal, and ii) plane wave states are no longer equivalent to Bloch states. We will also illustrate that the inequivalent recriprocal lattice vectors $\boldsymbol{G}$ define different types of Brillouin zones.

We start with the overlap between the Wannier functions and the plane waves, which now reads:

$$\phi^A_{\boldsymbol{R}}(\boldsymbol{p}) = \langle \boldsymbol{p} | \phi^A_{\boldsymbol{R}} \rangle = \frac{1}{\sqrt{N_{\text{sites}}}} e^{-i\boldsymbol{p}\cdot(\boldsymbol{R}+\boldsymbol{t}_A)}. \tag{3.62}$$

This leads to the overlap between plane waves projected to the tight binding given by Eq. (3.29) in the infinite-size limit:

$$\langle \boldsymbol{p} | \boldsymbol{p} \rangle \simeq \delta_{\boldsymbol{p}',\boldsymbol{p}+\boldsymbol{G}} \frac{1}{N_{\text{s/c}}} \sum_A e^{-i\boldsymbol{G}\cdot\boldsymbol{t}_A}. \tag{3.63}$$

This shows that certain $\big|\boldsymbol{p}+\boldsymbol{G}\big\rangle$ are different states from $\big|\boldsymbol{p}\big\rangle$, yet their overlap is non-zero, $\langle \boldsymbol{p} \big| \boldsymbol{p}+\boldsymbol{G} \rangle \neq 0$.

We now show that, contrary to the single-site case, plane wave states are different from Bloch states. The Bloch states with a definite sublattice are, therefore:

$$|\phi^A_{\boldsymbol{k}}\rangle = \frac{1}{\sqrt{N_{\text{cell}}}} \sum_{\boldsymbol{R}} e^{i\boldsymbol{k}\cdot(\boldsymbol{R}+\boldsymbol{t}_A)} |\phi^A_{\boldsymbol{R}}\rangle. \tag{3.64}$$

The overlap between the Bloch states and the plane waves is:

$$\langle \boldsymbol{k}+\boldsymbol{G} | \phi^A_{\boldsymbol{k}} \rangle = \frac{1}{\sqrt{N_{\text{s/c}}}} e^{-i\boldsymbol{G}\cdot\boldsymbol{t}_A}. \tag{3.65}$$

However, the band eigenvectors are combinations of these Bloch states in different sublattices:

$$|\psi_{\boldsymbol{k}}^n\rangle = \sum_A c_{\boldsymbol{k}}^{nA} |\phi_{\boldsymbol{k}}^A\rangle, \tag{3.66}$$

and, therefore, their overlap with the plane waves reads:

$$\langle \boldsymbol{k}+\boldsymbol{G}|\psi_{\boldsymbol{k}}^n\rangle = \frac{1}{\sqrt{N_{\mathrm{s/c}}}} \sum_A c_{\boldsymbol{k}}^{nA} e^{-i\boldsymbol{G}\cdot\boldsymbol{t}_A}, \tag{3.67}$$

which demonstrates that, in the multi-site case, plane wave states are no longer equivalent to Bloch states.

We now show that observables projected to a plane wave with momentum $\boldsymbol{p} = \boldsymbol{k}+\boldsymbol{G}$ depend on the phase factors $e^{-i\boldsymbol{G}\cdot\boldsymbol{t}_{AB}}$, where $\boldsymbol{t}_{AB} = \boldsymbol{t}_A - \boldsymbol{t}_B$ are the relative positions of the different sublattices. For concreteness, we start considering the simplest observable, that will be a building block for e.g. the spillage: the projector onto band n at crystal momentum $\boldsymbol{k}$, $P_n(\boldsymbol{k}) = \left|\psi_{\boldsymbol{k}}^n\right\rangle\left\langle\psi_{\boldsymbol{k}}^n\right|$. Its projection to a plane wave reads:

$$\begin{aligned}\left\langle \boldsymbol{k}+\boldsymbol{G}\middle|P_n(\boldsymbol{k})\middle|\boldsymbol{k}+\boldsymbol{G}\right\rangle =& \left|\left\langle \boldsymbol{k}+\boldsymbol{G}\middle|\psi_{\boldsymbol{k}}^n\right\rangle\right|^2 = \frac{1}{N_{\mathrm{s/c}}} \sum_{A,B} c_{\boldsymbol{k}}^{nA} \left(c_{t\boldsymbol{k}}^{nB}\right)^* e^{-i\boldsymbol{G}\cdot\boldsymbol{t}_{AB}} = \\ =& \frac{1}{N_{\mathrm{s/c}}} \left[1 + \sum_{A\neq B} c_{\boldsymbol{k}}^{nA} \left(c_{\boldsymbol{k}}^{nB}\right)^* e^{-i\boldsymbol{G}\cdot\boldsymbol{t}_{AB}}\right],\end{aligned} \tag{3.68}$$

which is different from $\mathrm{tr}\left[P_n(\boldsymbol{k})\right] = 1$ in general. These phase factors, which depend on $\boldsymbol{G}$, lead to certain BZs being inequivalent even if the orbitals are still Dirac deltas. Therefore, the types of BZs in the multi-site crystal can be classified by the set of phase factors $\left\{e^{-i\boldsymbol{G}\cdot\boldsymbol{t}_{AB}}\right\}$. In general, certain BZs become inequivalent whenever there is structure inside the unit cell, irrespective of whether it comes from spatially-extended orbitals or from several sites.

As an example, consider the honeycomb lattice, where there are $N_{\mathrm{s/c}} = 2$ sublattices A and B such that $\boldsymbol{t}_{AB} = -a\left[0, 1/\sqrt{3}\right]$. The reciprocal lattice basis vectors are $\boldsymbol{G}_1 = 4\pi/\sqrt{3}a\left[\frac{\sqrt{3}}{2}, \frac{1}{2}\right]$, and $\boldsymbol{G}_2 = 4\pi/\sqrt{3}a\,[0,1]$. A general reciprocal lattice vector $\boldsymbol{G} = n_1\boldsymbol{G}_1 + n_2\boldsymbol{G}_2$, with $n_1, n_2 \in \mathbb{Z}$, satisfies $\boldsymbol{G}\cdot\boldsymbol{t}_{AB} = -2\pi/3(n_1+2n_2)$. Therefore, $e^{-i\boldsymbol{G}\cdot\boldsymbol{t}_{AB}} = e^{ia2\pi/3}$, with $a \in \mathbb{Z}_3$, so there are $N_{\mathrm{BZs}} = 3$ different types of BZs depending on the value of this phase factor. If we consider all possible momenta, from zero to infinity, then the multiplicity in momentum space of each type of BZ is the same. On the other hand, if we only consider momenta up to a cutoff $p_{\max}$, then the multiplicity in momentum space of each type of BZ can be different. Fig. 5 shows the type of the first BZ and the six nearest-neighbour second BZs. Note that the first BZ has $\boldsymbol{G} = 0$, and therefore it is always characterized by $a = 0$, i.e., by a phase $e^{-i\boldsymbol{G}\cdot\boldsymbol{t}_{AB}} = e^{ia2\pi/3} = 1$.

Exact spillage comparing two crystals: non-orthogonal basis

In section 3.2.3 we described how to compute exactly the spillage comparing a target and reference with the same crystalline lattice, using a non-orthogonal basis of plane waves $\{|\boldsymbol{k}+\boldsymbol{G}\rangle\}_{\boldsymbol{G}\in N_{\mathrm{s/c}}\ \mathrm{BZs}}$ consisting of N_{cell} plane waves in $N_{\mathrm{s/c}}$ inequivalent BZs. The closure relation and the quasi-Bloch spillage in this formalism are given in Eqs. (3.30) and (3.31), respectively. For completeness, here we write down the trace of the projector onto band n at crystal momentum $\boldsymbol{k}$, $\mathrm{tr}\,[P_n(\boldsymbol{k})]$:

$$\mathrm{tr}\,[P_n(\boldsymbol{k})]_{\text{non-orth}} = \sum_{\boldsymbol{G}\boldsymbol{G}'}^{\text{basis}} \langle \boldsymbol{k}+\boldsymbol{G}|P_n(\boldsymbol{k})|\boldsymbol{k}+\boldsymbol{G}'\rangle \left(S^{-1}\right)_{\boldsymbol{G}',\boldsymbol{G}}, \tag{3.69}$$

Importantly, Eq. (3.69) recovers the expected crystalline value $\mathrm{tr}\,[P_n(\boldsymbol{k})] = 1$, irrespective of the chosen plane-wave basis.

Structural spillage comparing an amorphous system to a crystal: no-scattering approximation

Now, we focus on computing the structural spillage between a crystalline and an amorphous structure. Aside from the issues already discussed for the single-site case, here is where comparing two tight bindings with sites at different positions becomes problematic. The reason is that overlap between the plane waves is different in the crystal (Eq. (3.29)) and in the amorphous (Eq. (3.28)) cases. In the structural spillage of Eq. (3.31), the crystalline and the amorphous projector appear sandwiched between the overlap matrices, but this overlap depends on the system. Therefore, we cannot apply the previous non-orthogonal formalism.

As explained in the main text, this issue can be avoided by neglecting the momentum scattering, i.e., by setting $\boldsymbol{k}' = \boldsymbol{k}$ and $\boldsymbol{G}' = \boldsymbol{G}$ in Eq. (3.23). Such approximation has been used previously to determine the topology of an amorphous system using other methods such as the effective Hamiltonian approach [120, 493]. It is also inspired by the fact that continuous translational symmetry is recovered after averaging over different disorder realizations. The resulting expressions for the trace of a band projector and the spillage are

$$\mathrm{tr}\,[P_n(\boldsymbol{k})]_{\text{no-scatt}} = \sum_{\boldsymbol{G}}^{\text{basis}} \langle \boldsymbol{k}+\boldsymbol{G}|P_n(\boldsymbol{k})|\boldsymbol{k}+\boldsymbol{G}\rangle, \tag{3.70}$$

$$\gamma_{\mathrm{qB}}^{\text{no-scatt}}(\boldsymbol{k}) = \frac{1}{2}\sum_{\boldsymbol{G}}^{\text{basis}} \mathrm{tr}\left[\left(P_{\boldsymbol{k}+\boldsymbol{G}} - \tilde{P}_{\boldsymbol{k}+\boldsymbol{G}}\right)^2\right], \tag{3.71}$$

where the sums over the reciprocal lattice vectors $\boldsymbol{G}$ again run over the $N_{\mathrm{s/c}}$ BZs chosen in the plane wave basis. The trace acts over the internal degrees of freedom α (which are otherwise not explicitly written in this Appendix), and, as in the main text, $P_{\boldsymbol{p}}^{\alpha\beta} = \langle \boldsymbol{p}|P|\boldsymbol{p}\rangle$. Eq. (3.71) is not yet

the definite expression of Eq. (3.35) for the structural spillage in the tight-binding approximation, since it still has the problem of depending on the $\boldsymbol{G}$ chosen in the basis. Below we detail how to solve this issue.

Taking into account different types of Brillouin zones

In contrast to the single-site case, the values of the observables computed within this no-scattering approximation depend on the types of BZs chosen in the basis even in the crystal. In this section, we provide a method to circumvent this issue based on the condition that, when applied to crystals, it leads to values as close as possible to the exact ones, where rigorous proofs exist [117].

Our solution consists of computing a observable without scattering, performing an average over the N_{BZs} different types of BZs, and then multiplying by the number of sites per unit cell $N_{\text{s/c}}$ in the crystal. First, we show that our proposal recovers the correct crystalline result for the observables that depend only on one projector. Indeed, the BZ-averaged Eq. (3.70) representing the trace of the projector into the band n at crystal momentum $\boldsymbol{k}$ becomes:

$$\begin{aligned}\text{tr}\left[P_n(\boldsymbol{k})\right]^{\text{BZ-av}}_{\text{no-scatt}} =& \frac{N_{\text{s/c}}}{N_{\text{BZs}}}\sum_{\boldsymbol{G}}^{\text{BZs}}\langle\boldsymbol{k}+\boldsymbol{G}|P_n(\boldsymbol{k})|\boldsymbol{k}+\boldsymbol{G}\rangle = \\ =& 1+\sum_{A\neq B} c^{nA}_{\boldsymbol{k}}\left(c^{nB}_{\boldsymbol{k}}\right)^*\left[\frac{1}{N_{\text{BZs}}}\sum_{\boldsymbol{G}}^{\text{BZs}} e^{-i\boldsymbol{G}\cdot\boldsymbol{t}_{AB}}\right] = 1,\end{aligned} \tag{3.72}$$

where the sum over $\boldsymbol{G}$ runs over a representative BZ of each type, and we have used Eq. (3.68) and the fact that the term inside the square brackets vanishes identically for $A \neq B$. If there is a finite number N_{BZs} of BZ types, this term vanishes because the N_{BZs} phases $e^{-i\boldsymbol{G}_a\cdot\boldsymbol{t}_{AB}}$ are the $1/N_{\text{BZs}}$ roots of unity. If there are infinite BZ types, which might occur, e.g., if the sites are located at a generic nonsymmetric Wyckoff position incommensurate with the reciprocal lattice vectors, then this term vanishes due to the infinite sum of a continuum of phases. In the example of the honeycomb lattice, where $N_{\text{BZs}} = 3$ and $e^{-i\boldsymbol{G}_a\cdot\boldsymbol{t}_{AB}} = e^{ia2\pi/3}$ with $a \in \mathbb{Z}_3$ if $A \neq B$, and $e^{-i\boldsymbol{G}_a\cdot\boldsymbol{t}_{AB}} = 1$ if $A = B$, we obtain, as expected:

$$\frac{1}{3}\sum_{a=0,1,2} e^{-i\boldsymbol{G}_a\cdot\boldsymbol{t}_{AB}} = \delta_{AB}. \tag{3.73}$$

We have also numerically verified that the correct crystalline results are obtained in our bismuthene and Bi bilayer tight-binding models. Indeed, the blue lines in Figs. 3.C.1(a,b) show the number of occupied states per unit cell $\sum_{n\in\text{occ}}\text{tr}\left[P_n(\boldsymbol{k})\right]^{\text{BZ-av}}_{\text{no-scatt}}$ at $\boldsymbol{k} = 0$ as a function of the onsite SOC for crystalline bismuthene and Bi bilayer, respectively. In both models, this number of occupied states (or filling) is constant and equal to 4 and 6, as expected, since they correspond to

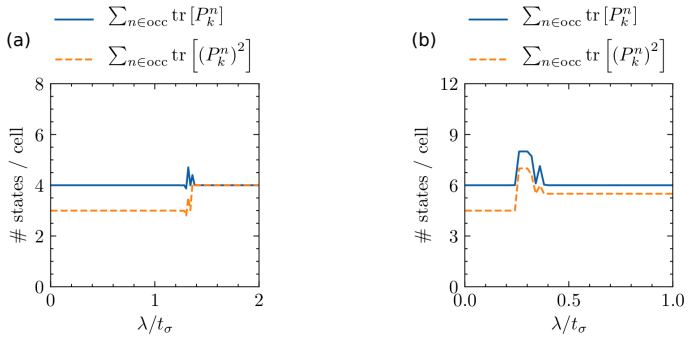

FIGURE 3.C.1: Sum over occupied bands of the trace of one and two projectors, $\sum_{n\in\mathrm{occ}} \mathrm{tr}\,[P_n(\boldsymbol{k})]^{\text{BZ-av}}_{\text{no-scatt}}$ and $\sum_{n\in\mathrm{occ}} \mathrm{tr}\left[(P_n(\boldsymbol{k}))^2\right]^{\text{BZ-av}}_{\text{no-scatt}}$, as a function of onsite SOC, computed using the formalism of Eqs. (3.72) and (3.75) at $\boldsymbol{k} = 0$. (a) Bismuthene crystal. (b) Bi bilayer crystal. On the one hand, the filling $\sum_{n\in\mathrm{occ}} \mathrm{tr}\,[P_n(\boldsymbol{k})]^{\text{BZ-av}}_{\text{no-scatt}}$ recovers the exact crystalline result, except close to the transition due to finite precision effects. On the other hand, the trace of the projector square $\sum_{n\in\mathrm{occ}} \mathrm{tr}\left[(P_n(\boldsymbol{k}))^2\right]^{\text{BZ-av}}_{\text{no-scatt}}$, which should be equal to the filling, is just slightly ($\sim 8-25\%$) smaller due to neglecting the momentum scattering.

half-filling in bismuthene and Bi bilayer, respectively. Note that the filling artificially deviates from these values close to the topological transition (around $\lambda \simeq 1.2t_\sigma$ for bismuthene and $\lambda \simeq 0.3t_\sigma$ for bilayer Bi). However, this is an artifact stemming from the finite KPM resolution. Indeed, this artifact only appears close to the transition, which is where the bulk gap is smaller, and therefore is where the required precision to obtain the correct results is higher. We have checked that the deviations from the exact filling shrink when increasing the KPM precision and the system size.

In summary, we have shown that, by averaging over the BZ types and multiplying by $N_{\mathrm{s/c}}$, we recover the correct values in the crystal for the quantities that involve the trace of one projector. This exact result is recovered despite neglecting both the scattering by different reciprocal lattice vectors and the non-orthogonality of the plane waves. This means that the scattering does not play a crucial role in the quantities that involve the trace of only one projector.

Structural spillage without scattering in the tight-binding approximation

Now, we consider quantities that involve the trace of two projectors, such as the spillage. Unlike in the quantities involving just one projector, here scattering plays an important role. Indeed, we will show that scattering should be included to obtain the exact result in the crystalline limit (see, e.g., Eq. (3.23b), where the sum over $\boldsymbol{G}'$ represents the scattering). However, as explained in Appendix 3.C.2, the scattering has to be neglected in order to be able to use the structural spillage to compare amorphous and crystalline systems. Nevertheless, we will also show that, even if the

crystalline results are not exactly recovered, our method gives reasonably good results, which allows the structural spillage to work as a topological indicator also in the tight-binding approximation.

Consider the trace of $[P_n(\boldsymbol{k})]^2$, which should be equal to one if $P_n(\boldsymbol{k})$ is a projector. If we include scattering and average over Brillouin zones this exact condition is fulfilled for the crystal, as can be checked explicitly:

$$\begin{aligned}
&\mathrm{tr}\left[\left(P_n(\boldsymbol{k})\right)^2\right]_{\text{scatt}}^{\text{BZ-av}} = \\
&= \frac{N_{\text{s/c}}}{N_{\text{BZs}}}\sum_{\boldsymbol{G}}^{\text{BZs}}\frac{N_{\text{s/c}}}{N_{\text{BZs}}}\sum_{\boldsymbol{G}'}^{\text{BZs}}\left[\langle\boldsymbol{k}+\boldsymbol{G}|P_n(\boldsymbol{k})|\boldsymbol{k}+\boldsymbol{G}+\boldsymbol{G}'\rangle\langle\boldsymbol{k}+\boldsymbol{G}+\boldsymbol{G}'|P_n(\boldsymbol{k})|\boldsymbol{k}+\boldsymbol{G}\rangle\right] = \\
&= \sum_{A,B,C,D} c_{\boldsymbol{k}}^{nA}\left(c_{\boldsymbol{k}}^{nB}\right)^* c_{\boldsymbol{k}}^{nC}\left(c_{\boldsymbol{k}}^{nD}\right)^* \frac{1}{N_{\text{BZs}}}\sum_{\boldsymbol{G}}^{\text{BZs}} e^{-i\boldsymbol{G}\cdot(\boldsymbol{t}_{AB}+\boldsymbol{t}_{CD})}\frac{1}{N_{\text{BZs}}}\sum_{\boldsymbol{G}'}^{\text{BZs}} e^{-i\boldsymbol{G}'\cdot\boldsymbol{t}_{CB}} = \\
&= \sum_{A,B,D} c_{\boldsymbol{k}}^{nA}\left|c_{\boldsymbol{k}}^{nB}\right|^2\left(c_{\boldsymbol{k}}^{nD}\right)^*\frac{1}{N_{\text{BZs}}}\sum_{\boldsymbol{G}}^{\text{BZs}} e^{-i\boldsymbol{G}\cdot\boldsymbol{t}_{AD}} = \sum_{A,B}\left|c_{\boldsymbol{k}}^{nA}\right|^2\left|c_{\boldsymbol{k}}^{nB}\right|^2 = 1.
\end{aligned} \tag{3.74}$$

However, including scattering is not possible in general, unlike BZ averaging. As explained above, the scattering cannot be taken into account when the two projectors belong to systems with a different lattice structure. Therefore, when computing two-projector quantities we still perform the BZ average on the external sum over $\boldsymbol{G}_a$, but are forced to neglect the scattering resummation over $\boldsymbol{G}'$:

$$\begin{aligned}
\mathrm{tr}\left[\left(P_n(\boldsymbol{k})\right)^2\right]_{\text{no-scatt}}^{\text{BZ-av}} &= \frac{N_{\text{s/c}}}{N_{\text{BZs}}}\sum_{\boldsymbol{G}}^{\text{BZs}}\left[\langle\boldsymbol{k}+\boldsymbol{G}|P_n(\boldsymbol{k})|\boldsymbol{k}+\boldsymbol{G}\rangle\langle\boldsymbol{k}+\boldsymbol{G}|P_n(\boldsymbol{k})|\boldsymbol{k}+\boldsymbol{G}\rangle\right] = \\
&= \frac{1}{N_{\text{s/c}}}\sum_{A,B,C,D} c_{\boldsymbol{k}}^{nA}\left(c_{\boldsymbol{k}}^{nB}\right)^* c_{\boldsymbol{k}}^{nC}\left(c_{\boldsymbol{k}}^{nD}\right)^*\frac{1}{N_{\text{BZs}}}\sum_{\boldsymbol{G}}^{\text{BZs}} e^{-i\boldsymbol{G}\cdot(\boldsymbol{t}_{AB}+\boldsymbol{t}_{CD})} = \\
&= \frac{1}{N_{\text{s/c}}}\sum_{A,B,C,D} c_{\boldsymbol{k}}^{nA}\left(c_{\boldsymbol{k}}^{nB}\right)^* c_{\boldsymbol{k}}^{nC}\left(c_{\boldsymbol{k}}^{nD}\right)^*\delta_{\boldsymbol{t}_{AB}+\boldsymbol{t}_{CD},0}.
\end{aligned} \tag{3.75}$$

Although this equation does not exactly recover the crystalline value, we have numerically verified that the sum over occupied bands of this Eq. (3.75), $\sum_{n\in\text{occ}}\mathrm{tr}[(P_n(\boldsymbol{k}))^2]_{\text{no-scatt}}^{\text{BZ-av}}$, gives values just $\sim 8-25\%$ smaller than $\sum_{n\in\text{occ}}\mathrm{tr}[P_n(\boldsymbol{k})]_{\text{no-scatt}}^{\text{BZ-av}}$ in the crystal, as shown by the orange lines in Fig. 3.C.1. Therefore, we take this as a reasonable approximation, especially taking into account that this quantity can also be computed when one of the projectors corresponds to an amorphous structure. Applying this method to the structural quasi-Bloch spillage, we arrive at Eq. (3.35).

In order to implement the tight-binding spillage of Eq. (3.35) we need to account for a final detail: the choice of a representative BZ of each type. This is a requirement because we introduced the average over BZ types in Eqs. (3.72)-(3.75). To perform this average, one has to select one

representative for each type of BZ. To this end, we consider the example of the honeycomb lattice relevant to our Bi models, which has $N_{\mathrm{BZs}} = 3$ types of BZ, as sketched in Fig. 5. Due to the argument which lead us to Eq. (3.61) in Appendix 3.C.1, the optimal criterion for choosing the BZ representatives is to consider the ones whose reciprocal lattice vector is smaller in modulus. For example, the first BZ will always be chosen as the representative of the BZs characterized by a phase $e^{i\boldsymbol{G}\cdot\boldsymbol{t}_{AB}} = 1$. There can still be several options, such as the three possibilities for the BZs with phases $e^{i\boldsymbol{G}\cdot\boldsymbol{t}_{AB}} = e^{\pm i2\pi/3}$ (see Fig. 5). In this case, one can choose any of them. A better choice however is to perform an angular average over them. Indeed, while the crystal is anisotropic, the amorphous structure is effectively isotropic. In particular, although the total traces in the crystal are exactly the same in all equivalent BZs, certain orbital-resolved quantities might vary. For instance, in the honeycomb lattice, if the occupied eigenstate at $\boldsymbol{G} = \frac{4\pi}{\sqrt{3}}(0,1)$ is of p_y character, the eigenstate at the threefold rotated $\hat{C}_3\boldsymbol{G} = \frac{4\pi}{\sqrt{3}}(-\frac{\sqrt{3}}{2},-\frac{1}{2})$ is of the threefold rotated $-\frac{\sqrt{3}}{2}p_x - \frac{1}{2}p_y$ character. On the other hand, for sufficiently large samples, amorphous structures are expected to be isotropic in momentum space. Therefore, one would ideally perform an angular average over the $\boldsymbol{G}$ corresponding to equivalent BZs with the same modulus, but pointing in a different direction. In the honeycomb lattice, the quantity corresponding to the BZs with phase $e^{i\boldsymbol{G}\cdot\boldsymbol{t}_{AB}} = e^{+i2\pi/3}$ would be an average over the three BZs shown in blue in Fig. 5. Consequently, when the corresponding crystal displays a honeycomb lattice, the angle-averaged Eq. (3.35) for the structural quasi-Bloch spillage in the tight-binding approximation reads:

$$\begin{aligned}\gamma_{\mathrm{qB}}^{\mathrm{TB}}(\boldsymbol{k}) = \frac{2}{3}\Bigg\{&\frac{1}{2}\mathrm{tr}\left[\left(P_{\boldsymbol{k}+\boldsymbol{G}_0} - \tilde{P}_{\boldsymbol{k}+\boldsymbol{G}_0}\right)^2\right] + \\ &+\frac{1}{3}\sum_{\boldsymbol{G}_1^m}\frac{1}{2}\mathrm{tr}\left[\left(P_{\boldsymbol{k}+\boldsymbol{G}_1^m} - \tilde{P}_{\boldsymbol{k}+\boldsymbol{G}_1^m}\right)^2\right] + \\ &+\frac{1}{3}\sum_{\boldsymbol{G}_2^m}\frac{1}{2}\mathrm{tr}\left[\left(P_{\boldsymbol{k}+\boldsymbol{G}_2^m} - \tilde{P}_{\boldsymbol{k}+\boldsymbol{G}_2^m}\right)^2\right]\Bigg\},\end{aligned} \tag{3.76}$$

where:

$$\boldsymbol{G}_0 = 0 \qquad \Rightarrow e^{-i\boldsymbol{G}_0\cdot\boldsymbol{t}_{AB}} = 1, \tag{3.77}$$

$$\left.\begin{aligned}\boldsymbol{G}_1^0 &= \tfrac{4\pi}{\sqrt{3}}(0,1)\\ \boldsymbol{G}_1^1 &= \hat{C}_3\boldsymbol{G}_1^0 = \tfrac{4\pi}{\sqrt{3}}(-\tfrac{\sqrt{3}}{2},-\tfrac{1}{2})\\ \boldsymbol{G}_1^2 &= (\hat{C}_3)^2\boldsymbol{G}_1^0 = \tfrac{4\pi}{\sqrt{3}}(\tfrac{\sqrt{3}}{2},-\tfrac{1}{2})\end{aligned}\right\} \Rightarrow e^{-i\boldsymbol{G}_1^m\cdot\boldsymbol{t}_{AB}} = e^{i2\pi/3}, \tag{3.78}$$

$$\left.\begin{aligned}\boldsymbol{G}_2^0 &= \tfrac{4\pi}{\sqrt{3}}(0,-1)\\ \boldsymbol{G}_2^1 &= \hat{C}_3\boldsymbol{G}_2^0 = \tfrac{4\pi}{\sqrt{3}}(\tfrac{\sqrt{3}}{2},\tfrac{1}{2})\\ \boldsymbol{G}_2^2 &= (\hat{C}_3)^2\boldsymbol{G}_2^0 = \tfrac{4\pi}{\sqrt{3}}(-\tfrac{\sqrt{3}}{2},\tfrac{1}{2})\end{aligned}\right\} \Rightarrow e^{-i\boldsymbol{G}_2^m\cdot\boldsymbol{t}_{AB}} = e^{-i2\pi/3}. \tag{3.79}$$

Eq. (3.76) is a specific instance of the general Eq. (3.35) that we used for computing the spillage in our bismuthene and Bi bilayer tight-binding models. However, we have also checked that in these models, for the system sizes considered, performing the angular average or not does not noticeably change the results.

In summary, our proposed method for computing two-projector quantities, such as the structural spillage, consists of neglecting the momentum scattering, performing an average over the different types of BZs, and multiplying by the number of sites per unit cell in the corresponding crystal. Applying this method to the structural quasi-Bloch spillage, we arrive at the final expression for the structural spillage in the tight-binding approximation, Eq. (3.35) of the main text. To conclude, we highlight that, in the specific case when the number of types of BZs is infinite or very large, Eq. (3.35) would involve reciprocal lattice vectors $|\boldsymbol{G}| \gg 2\pi/a$, with a the crystalline lattice constant. In this case, as in the single-site case, we may introduce a momentum cutoff and consider only the reciprocal lattice vectors $\boldsymbol{G}$ smaller than this cutoff.

Conclusions and perspectives

In this thesis, we have studied three problems that highlight the role of symmetry and topology in classifying and understanding quantum matter, from correlated systems to amorphous materials. We have studied charge density wave (CDW) and superconducting phases in transition metal dichalcogenides, and we have proposed a topological indicator for amorphous and noncrystalline materials.

In Chapter 1, we have analyzed the transition metal dichalcogenide 1T-$TiSe_2$, which undergoes a 2×2 CDW instability in the monolayer. We have first performed the symmetry analysis of the CDW, and constructed a low-energy $\boldsymbol{k} \cdot \boldsymbol{p}$ model for the monolayer. Using general arguments based on this $\boldsymbol{k} \cdot \boldsymbol{p}$ model, we have predicted two transitions to broken threefold rotational symmetry phases within the CDW upon electron doping the system [1]. At low doping, the system starts in a threefold symmetric CDW, represented by a three-component order parameter $\vec{\Delta} = (\Delta, \Delta, \Delta)$, where each component indicates the charge modulation in one of the three ΓM directions. This is the state obtained by most *ab initio* calculations at stoichiometry [141, 177]. When the chemical potential crosses a peak in the DOS originated from an incipient van Hove singularity, the system is driven to a nematic CDW, with a preferred direction $\vec{\Delta} = (\Delta_1, \Delta_2, \Delta_2)$. Further increasing the doping, the total electronic energy induces a different broken-rotational-symmetry phase, a stripe CDW, where the charge is only modulated in one direction, $\vec{\Delta} = (\Delta, 0, 0)$. We have confirmed these general predictions on an interacting tight-binding model, solving it within the self-consistent mean-field approximation. Our predictions are robust against different interactions and the presence of additional order parameters. We have also discussed our results in the context of STM experiments, where observations of both a symmetric CDW [114] and a nematic CDW [52–54] have been reported. Our theory might rationalize these findings based on the usual electron doping induced in the synthesis process. On the other hand, the signatures of a stripe CDW only in short-range domains in doped samples [56] might be related to the phase separation in a first order transition, and to additional contributions to the total energy by the lattice, which might suppress this stripe order.

Further work is required to prove our predictions. A monolayer sample with gating electrodes would be an ideal platform to probe doping effects. Nonlinear transport and elastoresistance

measurements could provide hints about the symmetry and nematic susceptibility of the system, respectively. Optical probes, such as Raman spectroscopy, circular photogalvanic effect, and second harmonic generation, can also indicate the broken symmetries in the CDW. The situation is further complicated since doping also drives a crossover to an incommensurate CDW. Theoretically studying how the threefold symmetry breaking CDWs are affected by the discommensurations and disorder is an interesting open problem. A different challenge posed by $TiSe_2$ is the understanding of the light-induced chiral phase [186, 187], which might require invoking metastable chiral CDW states. A detailed understanding of the CDW phase of $TiSe_2$ might also shed light onto the coexisting superconducting phase that appears under doping or pressure. Thanks to the analogies with kagome AV_3Sb_5 metals [48–51], the study of $TiSe_2$ might also be helpful for understanding these correlated systems.

In Chapter 2, we have studied the superconductivity of monolayer 1H-$NbSe_2$. Motivated by the STM evidence for a bosonic mode linked to the superconducting state [2], we have analyzed the superconducting collective modes in this material. We have considered a $\boldsymbol{k} \cdot \boldsymbol{p}$ model for the main bands involved in the superconductivity, whose essential ingredient is the Ising spin-orbit coupling, which splits the spin degeneracy of the bands thanks to the absence of inversion symmetry. We have added the static local interactions allowed by symmetry [306], which decouple into two superconducting pairings, namely an s-wave spin-singlet and an f-wave spin-triplet. While the ground state is the conventional s-wave pairing [30–33], the twofold-anisotropic in-plane critical magnetic field [115, 116] and the enhanced spin fluctuations in the monolayer [298–301] suggest that the f-wave channel is subleading. As long as the interaction in the f-wave channel remains attractive, we have found that a Leggett mode is well-defined, with energy smaller than the superconducting gap, $\Omega_L < 2\Delta$. This Leggett mode consists of the fluctuation of the relative phase of the superconducting pairings in the spin-split bands of $NbSe_2$, and it is related to the fluctuation towards the subleading f-wave channel. Considering elastic scattering via a low-energy effective action coupling the Leggett mode to the electrons in the superconductor, we have shown that the Leggett mode renormalizes the electron spectral function, producing peaks at the energies $\Delta + \Omega_L$. The Leggett mode should therefore be observable in tunneling experiments, as well as ARPES. Together with the suppression of the STM bosonic resonances with temperature and magnetic field within the superconducting state, and the anticorrelation between the resonance energy and the superconducting gap, this puts forward the Leggett mode as a possible interpretation of the STM experiment [2].

While further work is needed to confirm whether the resonances are actually caused by the Leggett mode, one of our main messages is that collective modes in the particle-particle channel should also be taken into account when interpreting tunneling experiments. It would be desirable to further characterize the bosonic modes with techniques sensitive to their symmetry, such as Raman

spectroscopy and nonlinear optics, which have already been applied to detect Leggett modes in MgB_2 [258, 259, 261, 262, 267]. On the theory side, it is interesting to determine the actual microscopic interactions to analyze whether there is indeed a subleading pairing that could give rise to a superconducting collective mode. Along these lines, the Migdal-Eliashberg calculations of Ref. [33] including *ab initio* electron-phonon coupling and effective spin fluctuations also predict a Leggett mode, but related to the relative phase fluctuation between different bands than in our case. The effect of the CDW on the superconductivity and its collective modes remains an open problem, although it has been suggested to suppress both electron-phonon coupling [31] and spin-fluctuations [297]. Furthermore, an appropriate treatment of the CDW is also needed to properly discard other candidate bosonic modes from the interpretation of the STM resonances [2]. These alternative candidates might be spin fluctuations, and phonons, whose energies can be significantly modified when accounting for the incommensurate nature of the CDW. The insights acquired in 1H-$NbSe_2$ might be translated to the isostructural compounds 1H-TaS_2 and 1H-NbS_2, where STM dip-hump features have also been observed [339, 340], although outside of the superconducting phase. Moreover, the understanding of the superconducting phase of the 1H compounds is essential to rationalize the unconventional observations in the $4H_b$ polytype of TaS_2 [341–350].

Finally, in Chapter 3, we have dealt with topological insulators in noncrystalline systems, ranging from amorphous and disordered materials to quasicrystals and nanocrystals. Noncrystalline materials can accommodate the known topological phases studied in crystals, as well as novel phases [4]. However, the tools to diagnose topology are not as well developed in the absence of exact translational and point group symmetries, since traditional symmetry indicators [102–107] cannot be applied. The available methods, such as the local topological markers, are usually either not generic, computationally expensive, or difficult to directly implement in DFT calculations. Here, inspired by the spin-orbit spillage [117] and the strange correlators [118, 119], we have introduced the structural spillage, which can act as a generic and efficient topological indicator, and is directly applicable within first-principles calculations [3]. The structural spillage determines the overlap between the projectors onto occupied states of the noncrystalline target and its reference crystalline counterpart, thus indicating the band inversions between them. Since the link between band inversions and the Wannier obstruction permeates to the noncrystalline case, the structural spillage can predict whether the topological phase of the noncrystalline target is the same or not as that of the crystalline reference. After adapting its formulation to tight-binding calculations, we have confirmed its predictive power in amorphous tight-binding models of bismuthene and bilayer Bismuth, where the structural spillage correctly reproduces the topological transition indicated by the longitudinal conductance. Finally, we have discussed the results of the structural spillage within the DFT calculations of amorphous bilayer Bismuth performed by our collaborators [3]. Based on both the tight-binding and the DFT results, we have predicted the amorphous Bismuth

bilayer to be a topological insulator.

Thanks to its efficiency and its DFT implementation, the structural spillage constitutes a first step towards a high-throughput catalogue of topological noncrystalline materials. In this regard, the structural spillage can be applied as a first screening method to discard all the materials with a low spillage. A more detailed topological characterization of the reduced number of cases with a high spillage should then be carried out with other methods. For this high-throughput screening, an appropriate choice of the reference system is advantageous. In the few cases where there is no crystalline system with the same local structure as the noncrystalline target, it would be interesting to further analyze the proposed plane-wave structural spillage as a potential topological indicator in these cases.

The combination of all three topics considered in this Thesis motivates exciting future research directions. Electron-phonon interactions are crucial in the CDW of both $TiSe_2$ and $NbSe_2$, as well as in the superconductivity of the latter. Electron-phonon interactions are also central for the superconductivity in amorphous systems [576]. Considering their frequency-dependence in a Migdal-Eliashberg theory is even more important than in $NbSe_2$. Indeed, depending on their energy, vibrational modes in amorphous systems might become overdamped [577], similar to phase modes in incommensurate CDWs and moiré systems [578–580]. Therefore, the knowledge of superconductivity in amorphous systems [576] might be useful for understanding, for instance, the superconducting dome in $TiSe_2$ at high doping or pressure and its interplay with the CDW discommensurations [26], and vice versa [578]. These links open up an interesting research avenue for the future.

Bibliography

1. Muñoz Segovia, D., Venderbos, J. W. F., Grushin, A. G. & de Juan, F. *Nematic and stripe orders within the charge density wave state of doped $TiSe_2$* arXiv:2308.15541. 2023. http://arxiv.org/abs/2308.15541.
2. Wan, W., Dreher, P., Muñoz Segovia, D., Harsh, R., Guo, H., Martínez-Galera, A. J., Guinea, F., de Juan, F. & Ugeda, M. M. Observation of Superconducting Collective Modes from Competing Pairing Instabilities in Single-Layer $NbSe_2$. *Adv Mater* **34,** 2206078. https://onlinelibrary.wiley.com/doi/abs/10.1002/adma.202206078 (2022).
3. Muñoz Segovia, D., Corbae, P., Varjas, D., Hellman, F., Griffin, S. M. & Grushin, A. G. Structural spillage: An efficient method to identify noncrystalline topological materials. *Phys. Rev. Res.* **5,** L042011. https://link.aps.org/doi/10.1103/PhysRevResearch.5.L042011 (2023).
4. Corbae, P., Hannukainen, J. D., Marsal, Q., Muñoz Segovia, D. & Grushin, A. G. Amorphous topological matter: Theory and experiment. *EPL* **142,** 16001. https://dx.doi.org/10.1209/0295-5075/acc2e2 (2023).
5. Landau, L. D. On the theory of phase transitions. I. *Phys. Z. Sowjet.* **11,** 26. https://cds.cern.ch/record/480039 (1937).
6. Beekman, A., Rademaker, L. & van Wezel, J. An introduction to spontaneous symmetry breaking. *SciPost Physics Lecture Notes,* 011. https://scipost.org/10.21468/SciPostPhysLectNotes.11 (2019).
7. Goldstone, J. Field theories with « Superconductor » solutions. *Nuovo Cim* **19,** 154–164. https://doi.org/10.1007/BF02812722 (1961).
8. McMillan, W. L. in *Electron-Phonon Interactions and Phase Transitions* (ed Riste, T.) 137–141 (Springer US, Boston, MA, 1977). ISBN: 978-1-4615-8921-1. https://doi.org/10.1007/978-1-4615-8921-1_6.
9. Gruner, G. *Density Waves In Solids* ISBN: 978-0-429-50101-2 (CRC Press, Boca Raton, 1994).
10. Keimer, B., Kivelson, S. A., Norman, M. R., Uchida, S. & Zaanen, J. From quantum matter to high-temperature superconductivity in copper oxides. *Nature* **518,** 179–186. https://www.nature.com/articles/nature14165 (2015).

11. Frano, A., Blanco-Canosa, S., Keimer, B. & Birgeneau, R. J. Charge ordering in superconducting copper oxides. *J. Phys.: Condens. Matter* **32,** 374005. https://doi.org/10.1088/1361-648x/ab6140 (2020).
12. Wilson, J., Di Salvo, F. & Mahajan, S. Charge-density waves and superlattices in the metallic layered transition metal dichalcogenides. *Advances in Physics* **24,** 117–201. https://doi.org/10.1080/00018737500101391 (1975).
13. McMillan, W. L. Landau theory of charge-density waves in transition-metal dichalcogenides. *Phys. Rev. B* **12,** 1187–1196. https://link.aps.org/doi/10.1103/PhysRevB.12.1187 (1975).
14. Di Salvo, F. J. & Rice, T. M. Charge-density waves in transition-metal compounds. *Physics Today* **32,** 32–38. https://physicstoday.scitation.org/doi/10.1063/1.2995488 (1979).
15. Kolobov, A. V. & Tominaga, J. *Two-Dimensional Transition-Metal Dichalcogenides* ISBN: 978-3-319-31449-5 978-3-319-31450-1. http://link.springer.com/10.1007/978-3-319-31450-1 (Springer International Publishing, Cham, 2016).
16. Manzeli, S., Ovchinnikov, D., Pasquier, D., Yazyev, O. V. & Kis, A. 2D transition metal dichalcogenides. *Nature Reviews Materials* **2,** 1–15. https://www.nature.com/articles/natrevmats201733 (2017).
17. Kohn, W. Image of the Fermi Surface in the Vibration Spectrum of a Metal. *Phys. Rev. Lett.* **2,** 393–394. https://link.aps.org/doi/10.1103/PhysRevLett.2.393 (1959).
18. McMillan, W. L. Theory of discommensurations and the commensurate-incommensurate charge-density-wave phase transition. *Phys. Rev. B* **14,** 1496–1502. https://link.aps.org/doi/10.1103/PhysRevB.14.1496 (1976).
19. Chen, C.-W., Choe, J. & Morosan, E. Charge density waves in strongly correlated electron systems. *Rep. Prog. Phys.* **79,** 084505. https://doi.org/10.1088%2F0034-4885%2F79%2F8%2F084505 (2016).
20. Yu, Y. & Kivelson, S. A. Fragile superconductivity in the presence of weakly disordered charge density waves. *Phys. Rev. B* **99,** 144513. https://link.aps.org/doi/10.1103/PhysRevB.99.144513 (2019).
21. Morosan, E., Zandbergen, H. W., Dennis, B., Bos, J., Onose, Y, Klimczuk, T., Ramirez, A., Ong, N. & Cava, R. J. Superconductivity in Cu_xTiSe_2. *Nat. Phys.* **2,** 544–550 (2006).
22. Kusmartseva, A. F., Sipos, B., Berger, H., Forró, L. & Tutiš, E. Pressure Induced Superconductivity in Pristine 1T-$TiSe_2$. *Phys. Rev. Lett.* **103,** 236401. https://link.aps.org/doi/10.1103/PhysRevLett.103.236401 (2009).
23. Joe, Y. I., Chen, X., Ghaemi, P, Finkelstein, K., de La Peña, G., Gan, Y, Lee, J., Yuan, S, Geck, J, MacDougall, G., *et al.* Emergence of charge density wave domain walls above the superconducting dome in 1T-$TiSe_2$. *Nat. Phys.* **10,** 421–425 (2014).
24. Li, L., O'Farrell, E., Loh, K., Eda, G., Özyilmaz, B & Neto, A. C. Controlling many-body states by the electric-field effect in a two-dimensional material. *Nature* **529,** 185 (2015).

25. Kogar, A., de la Pena, G. A., Lee, S., Fang, Y., Sun, S. X.-L., Lioi, D. B., Karapetrov, G., Finkelstein, K. D., Ruff, J. P. C., Abbamonte, P. & Rosenkranz, S. Observation of a Charge Density Wave Incommensuration Near the Superconducting Dome in Cu_xTiSe_2. *Phys. Rev. Lett.* **118,** 027002. https://link.aps.org/doi/10.1103/PhysRevLett.118.027002 (2 2017).
26. Chen, C., Su, L., Castro Neto, A. H. & Pereira, V. M. Discommensuration-driven superconductivity in the charge density wave phases of transition-metal dichalcogenides. *Phys. Rev. B* **99,** 121108. https://link.aps.org/doi/10.1103/PhysRevB.99.121108 (12 2019).
27. Park, T.-H., Uzoh, O. P. & Choi, H.-Y. Maximal superconductivity in proximity to the charge density wave quantum critical point in Cu_xTiSe_2. *Phys. Rev. B* **104,** 184506. https://link.aps.org/doi/10.1103/PhysRevB.104.184506 (2021).
28. Hinlopen, R. D. H., Moulding, O., Broad, W., Buhot, J., Bangma, F., McCollam, A., Ayres, J., Sayers, C., Da Como, E., Flicker, F., van Wezel, J. & Friedemann, S. *Lifshitz transition enabling superconducting dome around the quantum critical point in $TiSe_2$* arXiv:2308.02475. 2023. http://arxiv.org/abs/2308.02475.
29. Foner, S. & McNiff, E. J. Upper critical fields of layered superconducting $NbSe_2$ at low temperature. *Physics Letters A* **45,** 429–430. https://www.sciencedirect.com/science/article/pii/0375960173906932 (1973).
30. Leroux, M., Errea, I., Le Tacon, M., Souliou, S.-M., Garbarino, G., Cario, L., Bosak, A., Mauri, F., Calandra, M. & Rodière, P. Strong anharmonicity induces quantum melting of charge density wave in 2H-$NbSe_2$ under pressure. *Phys. Rev. B* **92,** 140303. https://link.aps.org/doi/10.1103/PhysRevB.92.140303 (2015).
31. Zheng, F. & Feng, J. Electron-phonon coupling and the coexistence of superconductivity and charge-density wave in monolayer $NbSe_2$. *Phys. Rev. B* **99,** 161119. https://link.aps.org/doi/10.1103/PhysRevB.99.161119 (2019).
32. Sanna, A., Pellegrini, C., Liebhaber, E., Rossnagel, K., Franke, K. J. & Gross, E. K. U. Real-space anisotropy of the superconducting gap in the charge-density wave material 2H-NbSe2. *npj Quantum Mater.* **7,** 1–7. https://www.nature.com/articles/s41535-021-00412-8 (2022).
33. Das, S., Paudyal, H., Margine, E. R., Agterberg, D. F. & Mazin, I. I. Electron-phonon coupling and spin fluctuations in the Ising superconductor $NbSe_2$. *npj Comput Mater* **9,** 1–9. https://www.nature.com/articles/s41524-023-01017-4 (2023).
34. Johannes, M. D. & Mazin, I. I. Fermi surface nesting and the origin of charge density waves in metals. *Phys. Rev. B* **77,** 165135. https://link.aps.org/doi/10.1103/PhysRevB.77.165135 (2008).
35. Rossnagel, K. On the origin of charge-density waves in select layered transition-metal dichalcogenides. *J. Phys.: Cond. Matt.* **23,** 213001 (2011).

36. Feng, Y., van Wezel, J., Wang, J., Flicker, F., Silevitch, D. M., Littlewood, P. B. & Rosenbaum, T. F. Itinerant density wave instabilities at classical and quantum critical points. *Nature Phys* **11,** 865–871. https://www.nature.com/articles/nphys3416 (2015).
37. Zhu, X., Cao, Y., Zhang, J., Plummer, E. W. & Guo, J. Classification of charge density waves based on their nature. *Proceedings of the National Academy of Sciences* **112,** 2367–2371. https://www.pnas.org/doi/full/10.1073/pnas.1424791112 (2015).
38. Zhu, X., Guo, J., Zhang, J. & Plummer, E. W. Misconceptions associated with the origin of charge density waves. *Advances in Physics: X* **2,** 622–640. https://doi.org/10.1080/23746149.2017.1343098 (2017).
39. Fröhlich, H. On the theory of superconductivity: the one-dimensional case. *Proc. R. Soc. Lond. A* **223,** 296–305. https://royalsocietypublishing.org/doi/10.1098/rspa.1954.0116 (1954).
40. Peierls, R. E. *Quantum Theory of Solids* ISBN: 978-0-19-850781-9 (Oxford University Press, Oxford, New York, 2001).
41. Wigner, E. On the Interaction of Electrons in Metals. *Phys. Rev.* **46,** 1002–1011. https://link.aps.org/doi/10.1103/PhysRev.46.1002 (1934).
42. Mott, N. F. The transition to the metallic state. *The Philosophical Magazine: A Journal of Theoretical Experimental and Applied Physics* **6,** 287–309. https://doi.org/10.1080/14786436108243318 (1961).
43. Keldysh, L & Kopaev, Y. V. Possible instability of semimetallic state toward Coulomb interaction. *Fiz. Tverd. Tela* **6,** 2791 (1964) (Sov. Phys. Solid State 6, 2219 (1965)).
44. Jérome, D., Rice, T. M. & Kohn, W. Excitonic Insulator. *Phys. Rev.* **158,** 462–475. https://link.aps.org/doi/10.1103/PhysRev.158.462 (1967).
45. Halperin, B. I. & Rice, T. M. in *Solid State Physics* (eds Seitz, F., Turnbull, D. & Ehrenreich, H.) 115–192 (Academic Press, 1968). http://www.sciencedirect.com/science/article/pii/S0081194708607407.
46. Nayak, C. Density-wave states of nonzero angular momentum. *Phys. Rev. B* **62,** 4880–4889. https://link.aps.org/doi/10.1103/PhysRevB.62.4880 (2000).
47. Maharaj, A. V., Thomale, R. & Raghu, S. Particle-hole condensates of higher angular momentum in hexagonal systems. *Phys. Rev. B* **88,** 205121. https://link.aps.org/doi/10.1103/PhysRevB.88.205121 (2013).
48. Jiang, Y.-X., Yin, J.-X., Denner, M. M., Shumiya, N., Ortiz, B. R., Xu, G., Guguchia, Z., He, J., Hossain, M. S., Liu, X., *et al.* Unconventional chiral charge order in kagome superconductor KV_3Sb_5. *Nature Materials* **20,** 1353–1357 (2021).
49. Li, H., Zhao, H., Ortiz, B. R., Park, T., Ye, M., Balents, L., Wang, Z., Wilson, S. D. & Zeljkovic, I. Rotation symmetry breaking in the normal state of a kagome superconductor KV_3Sb_5. *Nature Physics* **18,** 265–270 (2022).

50. Nie, L., Sun, K., Ma, W., Song, D., Zheng, L., Liang, Z., Wu, P., Yu, F., Li, J., Shan, M., *et al.* Charge-density-wave-driven electronic nematicity in a kagome superconductor. *Nature* **604,** 59–64 (2022).
51. Christensen, M. H., Birol, T., Andersen, B. M. & Fernandes, R. M. Theory of the charge density wave in AV_3Sb_5 kagome metals. *Phys. Rev. B* **104,** 214513. https://link.aps.org/doi/10.1103/PhysRevB.104.214513 (21 2021).
52. Ishioka, J, Liu, Y. H., Shimatake, K, Kurosawa, T, Ichimura, K, Toda, Y, Oda, M & Tanda, S. Chiral charge-density waves. *Phys. Rev. Lett.* **105,** 176401 (2010).
53. Ishioka, J., Fujii, T., Katono, K., Ichimura, K., Kurosawa, T., Oda, M. & Tanda, S. Charge-parity symmetry observed through Friedel oscillations in chiral charge-density waves. *Phys. Rev. B* **84,** 245125. https://link.aps.org/doi/10.1103/PhysRevB.84.245125 (24 2011).
54. Iavarone, M., Di Capua, R., Zhang, X., Golalikhani, M., Moore, S. A. & Karapetrov, G. Evolution of the charge density wave state in Cu_xTiSe_2. *Phys. Rev. B* **85,** 155103. https://link.aps.org/doi/10.1103/PhysRevB.85.155103 (2012).
55. Castellan, J.-P., Rosenkranz, S., Osborn, R., Li, Q., Gray, K. E., Luo, X, Welp, U, Karapetrov, G., Ruff, J. P. C. & van Wezel, J. Chiral Phase Transition in Charge Ordered 1T-$TiSe_2$. *Physical Review Letters* **110,** 196404 (2013).
56. Novello, A. M., Spera, M., Scarfato, A., Ubaldini, A., Giannini, E., Bowler, D. R. & Renner, C. Stripe and Short Range Order in the Charge Density Wave of 1T-Cu_xTiSe_2. *Phys. Rev. Lett.* **118,** 017002 (2017).
57. Coleman, P. *Introduction to Many-Body Physics* ISBN: 978-1-139-02091-6. http://ebooks.cambridge.org/ref/id/CBO9781139020916 (Cambridge University Press, Cambridge, 2015).
58. Meissner, W. & Ochsenfeld, R. Ein neuer Effekt bei Eintritt der Supraleitfähigkeit. *Naturwissenschaften* **21,** 787–788. ISSN: 1432-1904. https://doi.org/10.1007/BF01504252 (Nov. 1933).
59. Cooper, L. N. Bound Electron Pairs in a Degenerate Fermi Gas. *Phys. Rev.* **104,** 1189–1190. https://link.aps.org/doi/10.1103/PhysRev.104.1189 (1956).
60. Elitzur, S. Impossibility of spontaneously breaking local symmetries. *Phys. Rev. D* **12,** 3978–3982. https://link.aps.org/doi/10.1103/PhysRevD.12.3978 (1975).
61. Kivelson, S. A. & Rokhsar, D. S. Bogoliubov quasiparticles, spinons, and spin-charge decoupling in superconductors. *Phys. Rev. B* **41,** 11693–11696. https://link.aps.org/doi/10.1103/PhysRevB.41.11693 (1990).
62. Hansson, T. H., Oganesyan, V. & Sondhi, S. L. Superconductors are topologically ordered. *Annals of Physics* **313,** 497–538. https://www.sciencedirect.com/science/article/pii/S0003491604001046 (2004).

63. Girvin, S. M. & Yang, K. *Modern Condensed Matter Physics* 1st ed. ISBN: 978-1-316-48064-9 978-1-107-13739-4. https://www.cambridge.org/highereducation/books/modern-condensed-matter-physics/F0A27AC5DEA8A40EA6EA5D727ED8B14E#contents (Cambridge University Press, 2019).
64. Bardeen, J., Cooper, L. N. & Schrieffer, J. R. Theory of Superconductivity. *Phys. Rev.* **108,** 1175–1204. https://link.aps.org/doi/10.1103/PhysRev.108.1175 (1957).
65. Migdal, A. Interaction between electrons and lattice vibrations in a normal metal. *Sov. Phys. JETP* **7,** 996–1001 (1958).
66. Eliashberg, G. Interactions between electrons and lattice vibrations in a superconductor. *Sov. Phys. JETP* **11,** 696–702 (1960).
67. Kohn, W. & Luttinger, J. M. New Mechanism for Superconductivity. *Phys. Rev. Lett.* **15,** 524–526. https://link.aps.org/doi/10.1103/PhysRevLett.15.524 (1965).
68. Scalapino, D. Superconductivity and Spin Fluctuations. *J. Low Temp. Phys.* **117,** 179–188. https://doi.org/10.1023/A:1022559920049 (1999).
69. Khalaf, E., Chatterjee, S., Bultinck, N., Zaletel, M. P. & Vishwanath, A. Charged skyrmions and topological origin of superconductivity in magic-angle graphene. *Sci. Adv.* **7,** eabf5299. https://www.science.org/doi/10.1126/sciadv.abf5299 (2021).
70. Takada, Y. Plasmon Mechanism of Superconductivity in Two- and Three-Dimensional Electron Systems. *J. Phys. Soc. Jpn.* **45,** 786–794. https://journals.jps.jp/doi/10.1143/JPSJ.45.786 (1978).
71. Sigrist, M. & Ueda, K. Phenomenological theory of unconventional superconductivity. *Rev. Mod. Phys.* **63,** 239–311. https://link.aps.org/doi/10.1103/RevModPhys.63.239 (1991).
72. Sigrist, M. Introduction to Unconventional Superconductivity. *AIP Conference Proceedings* **789,** 165–243. https://aip.scitation.org/doi/abs/10.1063/1.2080350 (2005).
73. Tsuei, C. C. & Kirtley, J. R. Pairing symmetry in cuprate superconductors. *Rev. Mod. Phys.* **72,** 969–1016. https://link.aps.org/doi/10.1103/RevModPhys.72.969 (2000).
74. Hirschfeld, P. J., Korshunov, M. M. & Mazin, I. I. Gap symmetry and structure of Fe-based superconductors. *Rep. Prog. Phys.* **74,** 124508. https://doi.org/10.1088/0034-4885/74/12/124508 (2011).
75. White, B. D., Thompson, J. D. & Maple, M. B. Unconventional superconductivity in heavy-fermion compounds. *Physica C: Superconductivity and its Applications. Superconducting Materials: Conventional, Unconventional and Undetermined* **514,** 246–278. https://www.sciencedirect.com/science/article/pii/S0921453415000714 (2015).
76. McMillan, W. L. & Rowell, J. M. Lead Phonon Spectrum Calculated from Superconducting Density of States. *Phys. Rev. Lett.* **14,** 108–112. https://link.aps.org/doi/10.1103/PhysRevLett.14.108 (1965).

77. Anderson, P. W. Random-Phase Approximation in the Theory of Superconductivity. *Phys. Rev.* **112,** 1900–1916. https://link.aps.org/doi/10.1103/PhysRev.112.1900 (1958).
78. Anderson, P. W. Plasmons, Gauge Invariance, and Mass. *Phys. Rev.* **130,** 439–442. https://link.aps.org/doi/10.1103/PhysRev.130.439 (1963).
79. Higgs, P. W. Broken Symmetries and the Masses of Gauge Bosons. *Phys. Rev. Lett.* **13,** 508–509. https://link.aps.org/doi/10.1103/PhysRevLett.13.508 (1964).
80. Bardasis, A. & Schrieffer, J. R. Excitons and Plasmons in Superconductors. *Phys. Rev.* **121,** 1050–1062. https://link.aps.org/doi/10.1103/PhysRev.121.1050 (1961).
81. Leggett, A. J. Number-Phase Fluctuations in Two-Band Superconductors. *Progress of Theoretical Physics* **36,** 901–930. https://doi.org/10.1143/PTP.36.901 (1966).
82. Lee, W.-C., Zhang, S.-C. & Wu, C. Pairing State with a Time-Reversal Symmetry Breaking in FeAs-Based Superconductors. *Phys. Rev. Lett.* **102,** 217002. https://link.aps.org/doi/10.1103/PhysRevLett.102.217002 (2009).
83. Kretzschmar, F., Muschler, B., Böhm, T., Baum, A., Hackl, R., Wen, H.-H., Tsurkan, V., Deisenhofer, J. & Loidl, A. Raman-Scattering Detection of Nearly Degenerate s-Wave and d-Wave Pairing Channels in Iron-Based $Ba_{0.6}K_{0.4}Fe_2As_2$ and $Rb_{0.8}Fe_{1.6}Se_2$ Superconductors. *Phys. Rev. Lett.* **110,** 187002. https://link.aps.org/doi/10.1103/PhysRevLett.110.187002 (2013).
84. Klitzing, K. V., Dorda, G. & Pepper, M. New Method for High-Accuracy Determination of the Fine-Structure Constant Based on Quantized Hall Resistance. *Physical Review Letters* **45,** 494–497 (1980).
85. Hofstadter, D. R. Energy levels and wave functions of Bloch electrons in rational and irrational magnetic fields. *Phys. Rev. B* **14,** 2239–2249. https://link.aps.org/doi/10.1103/PhysRevB.14.2239 (6 1976).
86. Laughlin, R. B. Quantized Hall conductivity in two dimensions. *Physical Review B* **23,** 5632–5633. https://link.aps.org/doi/10.1103/PhysRevB.23.5632 (1981).
87. Thouless, D. J., Kohmoto, M., Nightingale, M. P. & den Nijs, M. Quantized Hall Conductance in a Two-Dimensional Periodic Potential. *Physical Review Letters* **49,** 405–408. https://link.aps.org/doi/10.1103/PhysRevLett.49.405 (1982).
88. Thouless, D. J. Wannier functions for magnetic sub-bands. *Journal of Physics C: Solid State Physics* **17,** L325–L327. https://iopscience.iop.org/article/10.1088/0022-3719/17/12/003 (1984).
89. Niu, Q., Thouless, D. J. & Wu, Y.-S. Quantized Hall conductance as a topological invariant. *Physical Review B* **31,** 3372–3377. https://link.aps.org/doi/10.1103/PhysRevB.31.3372 (1985).

90. Haldane, F. D. M. Model for a Quantum Hall Effect without Landau Levels: Condensed-Matter Realization of the "Parity Anomaly". *Phys. Rev. Lett.* **61,** 2015–2018. https://link.aps.org/doi/10.1103/PhysRevLett.61.2015 (1988).
91. Qi, X. L., Hughes, T. L. & Zhang, S.-C. Topological field theory of time-reversal invariant insulators. *Physical Review B* **78,** 195424 (2008).
92. Essin, A. M., Moore, J. E. & Vanderbilt, D. Magnetoelectric Polarizability and Axion Electrodynamics in Crystalline Insulators. *Physical Review Letters* **102,** 146805 (2009).
93. Wu, L., Salehi, M., Koirala, N., Moon, J., Oh, S. & Armitage, N. P. Quantized Faraday and Kerr rotation and axion electrodynamics of a 3D topological insulator. *Science* **354,** 1124–1127. https://www.science.org/doi/10.1126/science.aaf5541 (2016).
94. Altland, A. & Zirnbauer, M. R. Nonstandard symmetry classes in mesoscopic normal-superconducting hybrid structures. *Phys. Rev. B* **55,** 1142–1161. https://link.aps.org/doi/10.1103/PhysRevB.55.1142 (1997).
95. Schnyder, A. P., Ryu, S., Furusaki, A. & Ludwig, A. W. W. Classification of topological insulators and superconductors in three spatial dimensions. *Phys. Rev. B* **78,** 195125. https://link.aps.org/doi/10.1103/PhysRevB.78.195125 (2008).
96. Kitaev, A. Periodic table for topological insulators and superconductors. *AIP Conference Proceedings* **1134,** 22–30. https://aip.scitation.org/doi/abs/10.1063/1.3149495 (2009).
97. Ryu, S., Schnyder, A. P., Furusaki, A. & Ludwig, A. W. W. Topological insulators and superconductors: tenfold way and dimensional hierarchy. *New J. Phys.* **12,** 065010. https://doi.org/10.1088/1367-2630/12/6/065010 (2010).
98. Chiu, C.-K., Teo, J. C. Y., Schnyder, A. P. & Ryu, S. Classification of topological quantum matter with symmetries. *Reviews of Modern Physics* **88,** 035005 (2016).
99. Fu, L. Topological Crystalline Insulators. *Phys. Rev. Lett.* **106,** 106802. https://link.aps.org/doi/10.1103/PhysRevLett.106.106802 (10 2011).
100. Ando, Y. & Fu, L. Topological Crystalline Insulators and Topological Superconductors: From Concepts to Materials. *Annu. Rev. Condens. Matter Phys.* **6,** 361–381. https://www.annualreviews.org/doi/10.1146/annurev-conmatphys-031214-014501 (2015).
101. Fu, L. & Kane, C. L. Topological insulators with inversion symmetry. *Physical Review B* **76,** 45302 (2007).
102. Kruthoff, J., de Boer, J., van Wezel, J., Kane, C. L. & Slager, R.-J. Topological Classification of Crystalline Insulators through Band Structure Combinatorics. *Phys. Rev. X* **7,** 041069. https://link.aps.org/doi/10.1103/PhysRevX.7.041069 (4 2017).
103. Bradlyn, B., Elcoro, L., Cano, J., Vergniory, M. G., Wang, Z., Felser, C., Aroyo, M. I. & Bernevig, B. A. Topological quantum chemistry. *Nature* **547,** 298–305. https://www.nature.com/articles/nature23268 (2017).

104. Po, H. C., Vishwanath, A. & Watanabe, H. Symmetry-based indicators of band topology in the 230 space groups. *Nature Communications* **8,** 1–9. https://www.nature.com/articles/s41467-017-00133-2 (2017).

105. Song, Z., Zhang, T., Fang, Z. & Fang, C. Quantitative mappings between symmetry and topology in solids. *Nature Communications* **9,** 3530. https://doi.org/10.1038/s41467-018-06010-w (2018).

106. Po, H. C. Symmetry indicators of band topology. *Journal of Physics: Condensed Matter* **32,** 263001. https://doi.org/10.1088%2F1361-648x%2Fab7adb (2020).

107. Wieder, B. J., Bradlyn, B., Cano, J., Wang, Z., Vergniory, M. G., Elcoro, L., Soluyanov, A. A., Felser, C., Neupert, T., Regnault, N. & Bernevig, B. A. Topological materials discovery from crystal symmetry. *Nature Reviews Materials* **7,** 196–216. https://doi.org/10.1038/s41578-021-00380-2 (2022).

108. Li, J., Chu, R.-L., Jain, J. K. & Shen, S.-Q. Topological Anderson Insulator. *Phys. Rev. Lett.* **102,** 136806. https://link.aps.org/doi/10.1103/PhysRevLett.102.136806 (13 2009).

109. Groth, C. W., Wimmer, M., Akhmerov, A. R., Tworzydło, J. & Beenakker, C. W. J. Theory of the Topological Anderson Insulator. *Phys. Rev. Lett.* **103,** 196805. https://link.aps.org/doi/10.1103/PhysRevLett.103.196805 (19 2009).

110. Fulga, I. C., Pikulin, D. I. & Loring, T. A. Aperiodic Weak Topological Superconductors. *Physical Review Letters* **116,** 257002. https://link.aps.org/doi/10.1103/PhysRevLett.116.257002 (2016).

111. Varjas, D., Lau, A., Pöyhönen, K., Akhmerov, A. R., Pikulin, D. I. & Fulga, I. C. Topological Phases without Crystalline Counterparts. *Physical Review Letters* **123,** 196401. https://link.aps.org/doi/10.1103/PhysRevLett.123.196401 (2019).

112. Huang, H., Wu, Y.-S. & Liu, F. Aperiodic topological crystalline insulators. *Physical Review B* **101,** 145. https://link.aps.org/doi/10.1103/PhysRevB.101.041103 (2020).

113. Fulga, I. C., van Heck, B., Edge, J. M. & Akhmerov, A. R. Statistical topological insulators. *Physical Review B* **89,** 155424. https://link.aps.org/doi/10.1103/PhysRevB.89.155424 (2014).

114. Hildebrand, B., Jaouen, T., Mottas, M.-L., Monney, G., Barreteau, C., Giannini, E., Bowler, D. R. & Aebi, P. Local Real-Space View of the Achiral 1T-$TiSe_2$ $2 \times 2 \times 2$ Charge Density Wave. *Phys. Rev. Lett.* **120,** 136404. https://link.aps.org/doi/10.1103/PhysRevLett.120.136404 (13 2018).

115. Hamill, A., Heischmidt, B., Sohn, E., Shaffer, D., Tsai, K.-T., Zhang, X., Xi, X., Suslov, A., Berger, H., Forró, L., Burnell, F. J., Shan, J., Mak, K. F., Fernandes, R. M., Wang, K. & Pribiag, V. S. Two-fold symmetric superconductivity in few-layer $NbSe_2$. *Nat. Phys.,* 1–6. https://www.nature.com/articles/s41567-021-01219-x (2021).

116. Cho, C.-w., Lyu, J., An, L., Han, T., Lo, K. T., Ng, C. Y., Hu, J., Gao, Y., Li, G., Huang, M., Wang, N., Schmalian, J. & Lortz, R. Nodal and Nematic Superconducting Phases in $NbSe_2$ Monolayers from Competing Superconducting Channels. *Phys. Rev. Lett.* **129,** 087002. https://link.aps.org/doi/10.1103/PhysRevLett.129.087002 (2022).

117. Liu, J. & Vanderbilt, D. Spin-orbit spillage as a measure of band inversion in insulators. *Physical Review B* **90,** 125133. https://link.aps.org/doi/10.1103/PhysRevB.90.125133 (2014).

118. You, Y.-Z., Bi, Z., Rasmussen, A., Slagle, K. & Xu, C. Wave Function and Strange Correlator of Short-Range Entangled States. *Phys. Rev. Lett.* **112,** 247202. https://link.aps.org/doi/10.1103/PhysRevLett.112.247202 (2014).

119. Lee, J. Y., You, Y.-Z. & Xu, C. *Symmetry protected topological phases under decoherence* arXiv:2210.16323. 2022. http://arxiv.org/abs/2210.16323.

120. Marsal, Q., Varjas, D. & Grushin, A. G. Topological Weaire–Thorpe models of amorphous matter. *Proceedings of the National Academy of Sciences.* https://www.pnas.org/content/early/2020/11/17/2007384117 (2020).

121. Overhauser, A. W. Observability of Charge-Density Waves by Neutron Diffraction. *Phys. Rev. B* **3,** 3173–3182. https://link.aps.org/doi/10.1103/PhysRevB.3.3173 (1971).

122. Cercellier, H., Monney, C., Clerc, F., Battaglia, C., Despont, L., Garnier, M. G., Beck, H., Aebi, P., Patthey, L., Berger, H. & Forr/'o, L. Evidence for an Excitonic Insulator Phase in 1T-$TiSe_2$. *Phys. Rev. Lett.* **99,** 146403. https://link.aps.org/doi/10.1103/PhysRevLett.99.146403 (2007).

123. Monney, C., Cercellier, H., Clerc, F., Battaglia, C., Schwier, E. F., Didiot, C., Garnier, M. G., Beck, H., Aebi, P., Berger, H., Forr/'o, L. & Patthey, L. Spontaneous exciton condensation in 1T-$TiSe_2$: BCS-like approach. *Phys. Rev. B* **79,** 045116. https://link.aps.org/doi/10.1103/PhysRevB.79.045116 (2009).

124. Monney, C., Schwier, E. F., Garnier, M. G., Battaglia, C., Mariotti, N., Didiot, C., Cercellier, H., Marcus, J., Berger, H., Titov, A. N., Beck, H. & Aebi, P. Dramatic effective mass reduction driven by strong electronic correlations. *arXiv:0912.5283.* http://arxiv.org/abs/0912.5283 (2009).

125. Kolekar, S., Bonilla, M., Diaz, H. C., Hashimoto, M., Lu, D. & Batzill, M. Controlling the Charge Density Wave Transition in Monolayer $TiSe_2$: Substrate and Doping Effects. *Advanced Quantum Technologies* **1,** 1800070. https://onlinelibrary.wiley.com/doi/abs/10.1002/qute.201800070 (2018).

126. Watson, M. D., Clark, O. J., Mazzola, F., Marković, I., Sunko, V., Kim, T. K., Rossnagel, K. & King, P. D. C. Orbital- and k_z-Selective Hybridization of Se $4p$ and Ti $3d$ States in the Charge Density Wave Phase of $TiSe_2$. *Phys. Rev. Lett.* **122,** 076404. https://link.aps.org/doi/10.1103/PhysRevLett.122.076404 (7 2019).

127. Watson, M. D., Rajan, A., Antonelli, T., Underwood, K., Marković, I., Mazzola, F., Clark, O. J., Siemann, G.-R., Biswas, D., Hunter, A., *et al.* Strong-coupling charge density wave in monolayer $TiSe_2$. *2D Materials* **8,** 015004 (2020).

128. Weber, F, Rosenkranz, S, Castellan, J.-P., Osborn, R, Karapetrov, G, Hott, R, Heid, R, Bohnen, K.-P. & Alatas, A. Electron-phonon coupling and the soft phonon mode in $TiSe_2$. *Phys. Rev. Lett.* **107,** 266401 (2011).

129. Duong, D. L., Ryu, G., Hoyer, A., Lin, C., Burghard, M. & Kern, K. Raman Characterization of the Charge Density Wave Phase of 1T-$TiSe_2$: From Bulk to Atomically Thin Layers. *ACS Nano* **11,** 1034–1040. https://doi.org/10.1021/acsnano.6b07737 (2017).

130. Lee, P. A., Rice, T. M. & Anderson, P. W. Conductivity from charge or spin density waves. *Solid State Communications. Special Issue A Celebratory Issue to Commemorate 30 Years of Solid State Communications* **88,** 1001–1007. http://www.sciencedirect.com/science/article/pii/003810989390284T (1993).

131. Watson, M. D., Beales, A. M. & King, P. D. C. On the origin of the anomalous peak in the resistivity of $TiSe_2$. *Phys. Rev. B* **99,** 195142. https://link.aps.org/doi/10.1103/PhysRevB.99.195142 (2019).

132. Varma, C. M. & Simons, A. L. Strong-Coupling Theory of Charge-Density-Wave Transitions. *Phys. Rev. Lett.* **51,** 138–141. https://link.aps.org/doi/10.1103/PhysRevLett.51.138 (1983).

133. Kogar, A., Rak, M. S., Vig, S., Husain, A. A., Flicker, F., Joe, Y. I., Venema, L., MacDougall, G. J., Chiang, T. C., Fradkin, E., *et al.* Signatures of exciton condensation in a transition metal dichalcogenide. *Science* **358,** 1314–1317 (2017).

134. Lian, C., Ali, Z. A. & Wong, B. M. Charge density wave hampers exciton condensation in 1T-$TiSe_2$. *Phys. Rev. B* **100,** 205423. https://link.aps.org/doi/10.1103/PhysRevB.100.205423 (2019).

135. Lin, Z., Wang, C., Balassis, A., Echeverry, J. P., Vasenko, A. S., Silkin, V. M., Chulkov, E. V., Shi, Y., Zhang, J., Guo, J. & Zhu, X. Dramatic Plasmon Response to the Charge-Density-Wave Gap Development in 1T-$TiSe_2$. *Phys. Rev. Lett.* **129,** 187601. https://link.aps.org/doi/10.1103/PhysRevLett.129.187601 (2022).

136. Monarkha, Y. P. & Syvokon, V. E. A two-dimensional Wigner crystal (Review Article). *Low Temperature Physics* **38,** 1067–1095. https://doi.org/10.1063/1.4770504 (2012).

137. Rice, T. M. & Scott, G. K. New Mechanism for a Charge-Density-Wave Instability. *Phys. Rev. Lett.* **35,** 120–123. https://link.aps.org/doi/10.1103/PhysRevLett.35.120 (1975).

138. Valenzuela, B. & Vozmediano, M. A. Pomeranchuk instability in doped graphene. *New Journal of Physics* **10,** 113009 (2008).

139. Kiesel, M. L., Platt, C. & Thomale, R. Unconventional Fermi Surface Instabilities in the Kagome Hubbard Model. *Phys. Rev. Lett.* **110,** 126405. https://link.aps.org/doi/10.1103/PhysRevLett.110.126405 (12 2013).

140. Katzke, H., Tolédano, P. & Depmeier, W. Phase transitions between polytypes and intralayer superstructures in transition metal dichalcogenides. *Phys. Rev. B* **69,** 134111. https://link.aps.org/doi/10.1103/PhysRevB.69.134111 (2004).

141. Guster, B., Canadell, E., Pruneda, M. & Ordejón, P. First principles analysis of the CDW instability of single-layer 1T-$TiSe_2$ and its evolution with charge carrier density. *2D Mater.* **5,** 025024. https://doi.org/10.1088%2F2053-1583%2Faab568 (2018).

142. Rasch, J. C. E., Stemmler, T., Müller, B., Dudy, L. & Manzke, R. 1T-$TiSe_2$: Semimetal or Semiconductor? *Phys. Rev. Lett.* **101,** 237602. https://link.aps.org/doi/10.1103/PhysRevLett.101.237602 (2008).

143. Mottas, M.-L., Jaouen, T., Hildebrand, B., Rumo, M., Vanini, F., Razzoli, E., Giannini, E., Barreteau, C., Bowler, D. R., Monney, C., Beck, H. & Aebi, P. Semimetal-to-semiconductor transition and charge-density-wave suppression in 1T-$TiSe_{2-x}S_x$ single crystals. *Phys. Rev. B* **99,** 155103. https://link.aps.org/doi/10.1103/PhysRevB.99.155103 (2019).

144. Jaouen, T., Hildebrand, B., Mottas, M.-L., Di Giovannantonio, M., Ruffieux, P., Rumo, M., Nicholson, C. W., Razzoli, E., Barreteau, C., Ubaldini, A., Giannini, E., Vanini, F., Beck, H., Monney, C. & Aebi, P. Phase separation in the vicinity of Fermi surface hot spots. *Phys. Rev. B* **100,** 075152. https://link.aps.org/doi/10.1103/PhysRevB.100.075152 (2019).

145. Zunger, A. & Freeman, A. J. Band structure and lattice instability of $TiSe_2$. *Phys. Rev. B* **17,** 1839–1842. https://link.aps.org/doi/10.1103/PhysRevB.17.1839 (1978).

146. Hellgren, M., Baima, J., Bianco, R., Calandra, M., Mauri, F. & Wirtz, L. Critical Role of the Exchange Interaction for the Electronic Structure and Charge-Density-Wave Formation in $TiSe_2$. *Phys. Rev. Lett.* **119,** 176401. https://link.aps.org/doi/10.1103/PhysRevLett.119.176401 (2017).

147. Campbell, D. J., Eckberg, C., Zavalij, P. Y., Kung, H.-H., Razzoli, E., Michiardi, M., Jozwiak, C., Bostwick, A., Rotenberg, E., Damascelli, A. & Paglione, J. Intrinsic insulating ground state in transition metal dichalcogenide $TiSe_2$. *Phys. Rev. Materials* **3,** 053402. https://link.aps.org/doi/10.1103/PhysRevMaterials.3.053402 (5 2019).

148. Moya, J. M., Huang, C.-L., Choe, J., Costin, G., Foster, M. S. & Morosan, E. Effect of synthesis conditions on the electrical resistivity of $TiSe_2$. *Phys. Rev. Materials* **3,** 084005. https://link.aps.org/doi/10.1103/PhysRevMaterials.3.084005 (2019).

149. Monney, G., Monney, C., Hildebrand, B., Aebi, P. & Beck, H. Impact of Electron-Hole Correlations on the 1T-$TiSe_2$ Electronic Structure. *Phys. Rev. Lett.* **114,** 086402. https://link.aps.org/doi/10.1103/PhysRevLett.114.086402 (2015).

150. Zhao, J., Lee, K., Li, J., Lioi, D. B., Karapetrov, G., Trivedi, N. & Chatterjee, U. Spectroscopic fingerprints of many-body renormalization in 1T-$TiSe_2$. *Phys. Rev. B* **100,** 045106. https://link.aps.org/doi/10.1103/PhysRevB.100.045106 (2019).

151. Cazzaniga, M., Cercellier, H., Holzmann, M., Monney, C., Aebi, P., Onida, G. & Olevano, V. Ab initio many-body effects in $TiSe_2$: A possible excitonic insulator scenario from GW band-shape renormalization. *Phys. Rev. B* **85,** 195111. https://link.aps.org/doi/10.1103/PhysRevB.85.195111 (2012).

152. Hellgren, M., Baguet, L., Calandra, M., Mauri, F. & Wirtz, L. Electronic structure of $TiSe_2$ from a quasi-self-consistent G_0W_0 approach. *Phys. Rev. B* **103,** 075101. https://link.aps.org/doi/10.1103/PhysRevB.103.075101 (2021).

153. Acharya, S., Pashov, D., Rudenko, A. N., Rösner, M., van Schilfgaarde, M. & Katsnelson, M. I. Importance of charge self-consistency in first-principles description of strongly correlated systems. *npj Comput Mater* **7,** 1–8. https://www.nature.com/articles/s41524-021-00676-5 (2021).

154. Di Salvo, F. J., Moncton, D. & Waszczak, J. Electronic properties and superlattice formation in the semimetal $TiSe_2$. *Phys. Rev. B* **14,** 4321 (1976).

155. Kolekar, S., Bonilla, M., Ma, Y., Diaz, H. C. & Batzill, M. Layer- and substrate-dependent charge density wave criticality in 1T-$TiSe_2$. *2D Mater.* **5,** 015006. https://doi.org/10.1088/2053-1583/aa8e6f (2017).

156. Novko, D., Torbatian, Z. & Lončarić, I. Electron correlations rule the phonon-driven instability in single-layer $TiSe_2$. *Phys. Rev. B* **106,** 245108. https://link.aps.org/doi/10.1103/PhysRevB.106.245108 (2022).

157. Yan, S., Iaia, D., Morosan, E., Fradkin, E., Abbamonte, P. & Madhavan, V. Influence of Domain Walls in the Incommensurate Charge Density Wave State of Cu Intercalated 1T-$TiSe_2$. *Phys. Rev. Lett.* **118,** 106405. https://doi.org/10.1103/PhysRevLett.118.106405 (2017).

158. Wei, M. J., Lu, W. J., Xiao, R. C., Lv, H. Y., Tong, P., Song, W. H. & Sun, Y. P. Manipulating charge density wave order in monolayer 1T-$TiSe_2$ by strain and charge doping: A first-principles investigation. *Phys. Rev. B* **96,** 165404. https://link.aps.org/doi/10.1103/PhysRevB.96.165404 (16 2017).

159. Chen, C., Singh, B., Lin, H. & Pereira, V. M. Reproduction of the Charge Density Wave Phase Diagram in 1T-$TiSe_2$ Exposes its Excitonic Character. *Phys. Rev. Lett.* **121,** 226602. https://link.aps.org/doi/10.1103/PhysRevLett.121.226602 (2018).

160. Spera, M., Scarfato, A., Giannini, E. & Renner, C. Energy-dependent spatial texturing of charge order in 1T-Cu_xTiSe_2. *Phys. Rev. B* **99,** 155133. https://link.aps.org/doi/10.1103/PhysRevB.99.155133 (2019).

161. Calandra, M. & Mauri, F. Charge-Density Wave and Superconducting Dome in $TiSe_2$ from Electron-Phonon Interaction. *Phys. Rev. Lett.* **106,** 196406. https://link.aps.org/doi/10.1103/PhysRevLett.106.196406 (2011).
162. Hughes, H. P. Structural distortion in $TiSe_2$ and related materials-a possible Jahn-Teller effect? *Journal of Physics C: Solid State Physics* **10,** L319 (1977).
163. Whangbo, M. H. & Canadell, E. Analogies between the concepts of molecular chemistry and solid-state physics concerning structural instabilities. Electronic origin of the structural modulations in layered transition metal dichalcogenides. *Journal of the American Chemical Society* **114,** 9587–9600 (1992).
164. Calandra, M. & Mauri, F. Charge-Density Wave and Superconducting Dome in $TiSe_2$ from Electron-Phonon Interaction. *Phys. Rev. Lett.* **106,** 196406 (2011).
165. Wilson, J. A. Concerning the semimetallic characters of TiS_2 and $TiSe_2$. *Solid State Communications* **22,** 551–553. http://www.sciencedirect.com/science/article/pii/0038109877901338 (1977).
166. Van Wezel, J., Nahai-Williamson, P. & Saxena, S. S. An alternative interpretation of recent ARPES measurements on $TiSe_2$. *Europhys. Lett.* **89,** 47004 (2010).
167. Van Wezel, J., Nahai-Williamson, P. & Saxena, S. S. Exciton-phonon-driven charge density wave in $TiSe_2$. *Phys. Rev. B* **81,** 165109. https://link.aps.org/doi/10.1103/PhysRevB.81.165109 (16 2010).
168. Porer, M., Leierseder, U., Ménard, J.-M., Dachraoui, H., Mouchliadis, L., Perakis, I. E., Heinzmann, U., Demsar, J., Rossnagel, K. & Huber, R. Non-thermal separation of electronic and structural orders in a persisting charge density wave. *Nature Materials* **13,** 857–861. https://www.nature.com/articles/nmat4042 (2014).
169. Monney, C., Puppin, M., Nicholson, C. W., Hoesch, M., Chapman, R. T., Springate, E., Berger, H., Magrez, A., Cacho, C., Ernstorfer, R. & Wolf, M. Revealing the role of electrons and phonons in the ultrafast recovery of charge density wave correlations in 1T-$TiSe_2$. *Phys. Rev. B* **94,** 165165. https://link.aps.org/doi/10.1103/PhysRevB.94.165165 (2016).
170. Hedayat, H., Sayers, C. J., Bugini, D., Dallera, C., Wolverson, D., Batten, T., Karbassi, S., Friedemann, S., Cerullo, G., van Wezel, J., Clark, S. R., Carpene, E. & Da Como, E. Excitonic and lattice contributions to the charge density wave in 1T-$TiSe_2$ revealed by a phonon bottleneck. *Phys. Rev. Research* **1,** 023029. https://link.aps.org/doi/10.1103/PhysRevResearch.1.023029 (2019).
171. Cheng, Y., Zong, A., Li, J., Xia, W., Duan, S., Zhao, W., Li, Y., Qi, F., Wu, J., Zhao, L., Zhu, P., Zou, X., Jiang, T., Guo, Y., Yang, L., Qian, D., Zhang, W., Kogar, A., Zuerch, M. W., Xiang, D. & Zhang, J. Light-induced dimension crossover dictated by excitonic correlations. *Nat Commun* **13,** 963. https://www.nature.com/articles/s41467-022-28309-5 (2022).

172. Huber, M., Lin, Y., Dale, N., Sailus, R., Tongay, S., Kaindl, R. A. & Lanzara, A. Revealing the order parameter dynamics of 1T-$TiSe_2$ following optical excitation. *Sci Rep* **12,** 15860. https://www.nature.com/articles/s41598-022-19319-w (2022).

173. Chen, P, Chan, Y.-H., Fang, X.-Y., Mo, S.-K., Hussain, Z, Fedorov, A.-V., Chou, M. & Chiang, T.-C. Hidden Order and Dimensional Crossover of the Charge Density Waves in $TiSe_2$. *Sci. Rep.* **6,** 37910 (2016).

174. Knowles, P., Yang, B., Muramatsu, T., Moulding, O., Buhot, J., Sayers, C. J., Da Como, E. & Friedemann, S. Fermi Surface Reconstruction and Electron Dynamics at the Charge-Density-Wave Transition in $TiSe_2$. *Phys. Rev. Lett.* **124,** 167602. https://link.aps.org/doi/10.1103/PhysRevLett.124.167602 (2020).

175. Holt, M., Zschack, P., Hong, H., Chou, M. Y. & Chiang, T.-C. X-Ray Studies of Phonon Softening in $TiSe_2$. *Phys. Rev. Lett.* **86,** 3799–3802. https://link.aps.org/doi/10.1103/PhysRevLett.86.3799 (17 2001).

176. Fang, X.-Y., Hong, H., Chen, P. & Chiang, T.-C. X-ray study of the charge-density-wave transition in single-layer $TiSe_2$. *Phys. Rev. B* **95,** 201409. https://link.aps.org/doi/10.1103/PhysRevB.95.201409 (2017).

177. Bianco, R., Calandra, M. & Mauri, F. Electronic and vibrational properties of $TiSe_2$ in the charge-density-wave phase from first principles. *Phys. Rev. B* **92,** 094107. http://link.aps.org/doi/10.1103/PhysRevB.92.094107 (9 2015).

178. Van Wezel, J. Chirality and orbital order in charge density waves. *Europhysics Letters* **96,** 67011 (2011).

179. Van Wezel, J. *The chiral charge density wave transition in 1T-$TiSe_2$* in *J. Phys.: Conf. Ser.* **391** (2012), 012167.

180. Zenker, B., Fehske, H., Beck, H., Monney, C. & Bishop, A. R. Chiral charge order in 1T-$TiSe_2$: Importance of lattice degrees of freedom. *Phys. Rev. B* **88,** 075138. https://link.aps.org/doi/10.1103/PhysRevB.88.075138 (7 2013).

181. Gradhand, M. & van Wezel, J. Optical gyrotropy and the nonlocal Hall effect in chiral charge-ordered $TiSe_2$. *Phys. Rev. B* **92,** 041111. https://link.aps.org/doi/10.1103/PhysRevB.92.041111 (4 2015).

182. Peng, Y., Guo, X., Xiao, Q., Li, Q., Strempfer, J., Choi, Y., Yan, D., Luo, H., Huang, Y., Jia, S., Janson, O., Abbamonte, P., van den Brink, J. & van Wezel, J. Observation of orbital order in the van der Waals material 1T-$TiSe_2$. *Phys. Rev. Res.* **4,** 033053. https://link.aps.org/doi/10.1103/PhysRevResearch.4.033053 (3 2022).

183. Lin, M.-K., Hlevyack, J. A., Chen, P., Liu, R.-Y. & Chiang, T.-C. Comment on "Chiral Phase Transition in Charge Ordered 1T-$TiSe_2$". *Phys. Rev. Lett.* **122,** 229701. https://link.aps.org/doi/10.1103/PhysRevLett.122.229701 (22 2019).

184. Ueda, H., Porer, M., Mardegan, J. R. L., Parchenko, S., Gurung, N., Fabrizi, F., Ramakrishnan, M., Boie, L., Neugebauer, M. J., Burganov, B., Burian, M., Johnson, S. L., Rossnagel, K. & Staub, U. Correlation between electronic and structural orders in 1T-$TiSe_2$. *Phys. Rev. Research* **3,** L022003. https://link.aps.org/doi/10.1103/PhysRevResearch.3.L022003 (2 2021).

185. Subedi, A. Trigonal-to-monoclinic structural transition in $TiSe_2$ due to a combined condensation of $q = (\frac{1}{2}, 0, 0)$ and $(\frac{1}{2}, 0, \frac{1}{2})$ phonon instabilities. *Phys. Rev. Mater.* **6,** 014602. https://link.aps.org/doi/10.1103/PhysRevMaterials.6.014602 (1 2022).

186. Xu, S.-Y., Ma, Q., Gao, Y., Kogar, A., Zong, A., Valdivia, A. M. M., Dinh, T. H., Huang, S.-M., Singh, B., Hsu, C.-H., *et al.* Spontaneous gyrotropic electronic order in a transition-metal dichalcogenide. *Nature* **578,** 545–549 (2020).

187. Jog, H., Harnagea, L., Rout, D., Taniguchi, T., Watanabe, K., Mele, E. J. & Agarwal, R. Optically Induced Symmetry Breaking Due to Nonequilibrium Steady State Formation in Charge Density Wave Material 1T-$TiSe_2$. *Nano Lett.* **23,** 9634–9640. https://doi.org/10.1021/acs.nanolett.3c03736 (2023).

188. Jiang, Y., Lai, X., Watanabe, K., Taniguchi, T., Haule, K., Mao, J. & Andrei, E. Y. Charge order and broken rotational symmetry in magic-angle twisted bilayer graphene. *Nature* **573,** 91–95 (2019).

189. Rubio-Verdú, C., Turkel, S., Song, Y., Klebl, L., Samajdar, R., Scheurer, M. S., Venderbos, J. W., Watanabe, K., Taniguchi, T., Ochoa, H., *et al.* Moiré nematic phase in twisted double bilayer graphene. *Nature Physics* **18,** 196–202 (2022).

190. Basko, D. M. Theory of resonant multiphonon Raman scattering in graphene. *Phys. Rev. B* **78,** 125418. https://link.aps.org/doi/10.1103/PhysRevB.78.125418 (2008).

191. Venderbos, J. W. F. Symmetry analysis of translational symmetry broken density waves: Application to hexagonal lattices in two dimensions. *Phys. Rev. B* **93,** 115107. https://link.aps.org/doi/10.1103/PhysRevB.93.115107 (2016).

192. Venderbos, J. W. F. Multi-Q hexagonal spin density waves and dynamically generated spin-orbit coupling: Time-reversal invariant analog of the chiral spin density wave. *Phys. Rev. B* **93,** 115108. https://link.aps.org/doi/10.1103/PhysRevB.93.115108 (2016).

193. Ganesh, R., Baskaran, G., van den Brink, J. & Efremov, D. V. Theoretical Prediction of a Time-Reversal Broken Chiral Superconducting Phase Driven by Electronic Correlations in a Single $TiSe_2$ Layer. *Phys. Rev. Lett.* **113,** 177001. https://link.aps.org/doi/10.1103/PhysRevLett.113.177001 (2014).

194. Wickramaratne, D., Subedi, S., Torchinsky, D. H., Karapetrov, G. & Mazin, I. I. Photoinduced chiral charge density wave in $TiSe_2$. *Phys. Rev. B* **105,** 054102. https://link.aps.org/doi/10.1103/PhysRevB.105.054102 (5 2022).

195. *SpringerMaterials – properties of materials* https://materials.springer.com/.

196. Kaneko, T., Ohta, Y. & Yunoki, S. Exciton-phonon cooperative mechanism of the triple-q charge-density-wave and antiferroelectric electron polarization in $TiSe_2$. *Phys. Rev. B* **97,** 155131. https://link.aps.org/doi/10.1103/PhysRevB.97.155131 (15 2018).

197. Wu, G., Yang, H. X., Zhao, L., Luo, X. G., Wu, T., Wang, G. Y. & Chen, X. H. Transport properties of single-crystalline Cu_xTiSe_2 $(0.015 \leq x \leq 0.110)$. *Phys. Rev. B* **76,** 024513. https://link.aps.org/doi/10.1103/PhysRevB.76.024513 (2007).

198. Zhou, J. S., Monacelli, L., Bianco, R., Errea, I., Mauri, F. & Calandra, M. Anharmonicity and Doping Melt the Charge Density Wave in Single-Layer $TiSe_2$. *Nano Lett.* **20,** 4809–4815. https://doi.org/10.1021/acs.nanolett.0c00597 (2020).

199. Li, L. J., Zhao, W. J., Liu, B., Ren, T. H., Eda, G. & Loh, K. P. Enhancing charge-density-wave order in 1T-$TiSe_2$ nanosheet by encapsulation with hexagonal boron nitride. *Appl. Phys. Lett.* **109,** 141902. https://aip.scitation.org/doi/10.1063/1.4963885 (2016).

200. Kos, S., Millis, A. J. & Larkin, A. I. Gaussian fluctuation corrections to the BCS mean-field gap amplitude at zero temperature. *Phys. Rev. B* **70,** 214531. https://link.aps.org/doi/10.1103/PhysRevB.70.214531 (2004).

201. Nuñez-Regueiro, M. Uniaxial stress-induced resistivity anisotropy in $TiSe_2$ below 200K. *J. Phys. C: Solid State Phys.* **16,** L1061 (1983).

202. Scott, G. K., Bardhan, K. K. & Irwin, J. C. Raman Scattering from the Orthorhombic Charge-Density-Wave State of 2H-$TaSe_2$. *Phys. Rev. Lett.* **50,** 771–774. https://link.aps.org/doi/10.1103/PhysRevLett.50.771 (10 1983).

203. Sodemann, I. & Fu, L. Quantum Nonlinear Hall Effect Induced by Berry Curvature Dipole in Time-Reversal Invariant Materials. *Phys. Rev. Lett.* **115,** 216806. https://link.aps.org/doi/10.1103/PhysRevLett.115.216806 (21 2015).

204. Song, Y., Jia, C., Xiong, H., Wang, B., Jiang, Z., Huang, K., Hwang, J., Li, Z., Hwang, C., Liu, Z., Shen, D., Sobota, J. A., Kirchmann, P., Xue, J., Devereaux, T. P., Mo, S.-K., Shen, Z.-X. & Tang, S. Signatures of the exciton gas phase and its condensation in monolayer 1T-$ZrTe_2$. *Nat Commun* **14,** 1116. https://www.nature.com/articles/s41467-023-36857-7 (2023).

205. Gao, Q., Chan, Y.-h., Wang, Y., Zhang, H., Jinxu, P., Cui, S., Yang, Y., Liu, Z., Shen, D., Sun, Z., Jiang, J., Chiang, T. C. & Chen, P. Evidence of high-temperature exciton condensation in a two-dimensional semimetal. *Nat Commun* **14,** 994. https://www.nature.com/articles/s41467-023-36667-x (2023).

206. Aroyo, M. I., Perez-Mato, J. M., Orobengoa, D & Tasci, E. Crystallography online: Bilbao Crystallographic Server. *Bulg. Chem. Commun.* **43,** 183–197. http://www.bgcryst.com/symp10/proceeding/02_Aroyo_183-197.pdf (2011).

207. Berg, E., Fradkin, E. & Kivelson, S. A. Charge-4e superconductivity from pair-density-wave order in certain high-temperature superconductors. *Nature Phys* **5,** 830–833. https://www.nature.com/articles/nphys1389 (2009).

208. Yang, C. N. Concept of Off-Diagonal Long-Range Order and the Quantum Phases of Liquid He and of Superconductors. *Rev. Mod. Phys.* **34,** 694–704. https://link.aps.org/doi/10.1103/RevModPhys.34.694 (1962).

209. Erten, O., Chang, P.-Y., Coleman, P. & Tsvelik, A. M. Skyrme Insulators: Insulators at the Brink of Superconductivity. *Phys. Rev. Lett.* **119,** 057603. https://link.aps.org/doi/10.1103/PhysRevLett.119.057603 (2017).

210. London, F. A New Conception of Supraconductivity. *Nature* **140,** 793–796. https://www.nature.com/articles/140793a0 (1937).

211. Mermin, N. D. & Wagner, H. Absence of Ferromagnetism or Antiferromagnetism in One- or Two-Dimensional Isotropic Heisenberg Models. *Phys. Rev. Lett.* **17,** 1133–1136. https://link.aps.org/doi/10.1103/PhysRevLett.17.1133 (1966).

212. Hohenberg, P. C. Existence of Long-Range Order in One and Two Dimensions. *Phys. Rev.* **158,** 383–386. https://link.aps.org/doi/10.1103/PhysRev.158.383 (1967).

213. Wegner, F. Spin-ordering in a planar classical Heisenberg model. *Z. Physik* **206,** 465–470. https://doi.org/10.1007/BF01325702 (1967).

214. Mermin, N. D. Crystalline Order in Two Dimensions. *Phys. Rev.* **176,** 250–254. https://link.aps.org/doi/10.1103/PhysRev.176.250 (1968).

215. Leggett, A. J. *Lecture Notes: Physics in Two Dimensions.* 2013. https://courses.physics.illinois.edu/phys598PTD/fa2013/.

216. Palle, G. & Sunko, D. K. Physical limitations of the Hohenberg-Mermin-Wagner theorem. https://doi.org/10.1088/1751-8121/ac0a9d (2021).

217. Jenkins, S., Rózsa, L., Atxitia, U., Evans, R. F. L., Novoselov, K. S. & Santos, E. J. G. Breaking through the Mermin-Wagner limit in 2D van der Waals magnets. *Nat. Commun* **13,** 6917. https://www.nature.com/articles/s41467-022-34389-0 (2022).

218. Berezinskii, V. L. Destruction of long-range order in one-dimensional and two-dimensional systems having a continuous symmetry group I. Classical systems. *Zh. Eksp. Teor. Fiz.* **59.** [Sov. Phys. JETP 32, 493-500 (1971)], 907–920 (1971).

219. Kosterlitz, J. M. & Thouless, D. J. Long range order and metastability in two dimensional solids and superfluids. (Application of dislocation theory). *J. Phys. C: Solid State Phys.* **5,** L124. https://dx.doi.org/10.1088/0022-3719/5/11/002 (1972).

220. Berezinskii, V. L. Destruction of Long-range Order in One-dimensional and Two-dimensional Systems Possessing a Continuous Symmetry Group. II. Quantum Systems. *Zh. Eksp. Teor. Fiz.* **61.** [Sov. Phys. JETP 34, 3, 610 (1972)], 1144–1156 (1972).

221. Kosterlitz, J. M. & Thouless, D. J. Ordering, metastability and phase transitions in two-dimensional systems. *J. Phys. C: Solid State Phys.* **6,** 1181. https://dx.doi.org/10.1088/0022-3719/6/7/010 (1973).

222. Kosterlitz, J. M. Kosterlitz–Thouless physics: a review of key issues. *Rep. Prog. Phys.* **79,** 026001. https://doi.org/10.1088/0034-4885/79/2/026001 (2016).

223. Beasley, M. R., Mooij, J. E. & Orlando, T. P. Possibility of Vortex-Antivortex Pair Dissociation in Two-Dimensional Superconductors. *Phys. Rev. Lett.* **42,** 1165–1168. https://link.aps.org/doi/10.1103/PhysRevLett.42.1165 (1979).

224. Halperin, B. I. & Nelson, D. R. Resistive transition in superconducting films. *J Low Temp Phys* **36,** 599–616. https://doi.org/10.1007/BF00116988 (1979).

225. Fulde, P. & Ferrell, R. A. Superconductivity in a Strong Spin-Exchange Field. *Phys. Rev.* **135,** A550–A563. https://link.aps.org/doi/10.1103/PhysRev.135.A550 (1964).

226. Larkin, A. I. & Ovchinnikov, Y. N. Nonuniform state of superconductors. *Zh. Eksp. Teor. Fiz.* **47.** [Sov. Phys. JETP 20, 762 (1965)], 1136–1146 (1964).

227. Agterberg, D. F., Davis, J. S., Edkins, S. D., Fradkin, E., Van Harlingen, D. J., Kivelson, S. A., Lee, P. A., Radzihovsky, L., Tranquada, J. M. & Wang, Y. The Physics of Pair-Density Waves: Cuprate Superconductors and Beyond. *Annu. Rev. Condens. Matter Phys.* **11,** 231–270. https://www.annualreviews.org/doi/10.1146/annurev-conmatphys-031119-050711 (2020).

228. Maiti, S. & Hirschfeld, P. J. Collective modes in superconductors with competing s- and d-wave interactions. *Phys. Rev. B* **92,** 094506. https://link.aps.org/doi/10.1103/PhysRevB.92.094506 (2015).

229. Chubukov, A. V., Abanov, A., Esterlis, I. & Kivelson, S. A. Eliashberg theory of phonon-mediated superconductivity - When it is valid and how it breaks down. *Annals of Physics. Eliashberg theory at 60: Strong-coupling superconductivity and beyond* **417,** 168190. https://www.sciencedirect.com/science/article/pii/S0003491620301238 (2020).

230. Dai, P., Mook, H. A., Aeppli, G., Hayden, S. M. & Doğan, F. Resonance as a measure of pairing correlations in the high-Tc superconductor $YBa_2Cu_3O_{6.6}$. *Nature* **406,** 965–968. https://www.nature.com/articles/35023094 (2000).

231. Chen, T., Chen, Y., Tam, D. W., Gao, B., Qiu, Y., Schneidewind, A., Radelytskyi, I., Prokes, K., Chi, S., Matsuda, M., Broholm, C. & Dai, P. Anisotropic effect of a magnetic field on the neutron spin resonance in FeSe. *Phys. Rev. B* **101,** 140504. https://link.aps.org/doi/10.1103/PhysRevB.101.140504 (2020).

232. Thorsmolle, V. K., Khodas, M., Yin, Z. P., Zhang, C., Carr, S. V., Dai, P. & Blumberg, G. Critical quadrupole fluctuations and collective modes in iron pnictide superconductors. *Phys. Rev. B* **93,** 054515. https://link.aps.org/doi/10.1103/PhysRevB.93.054515 (2016).

233. Sun, Z., Fogler, M. M., Basov, D. N. & Millis, A. J. Collective modes and terahertz near-field response of superconductors. *Phys. Rev. Research* **2,** 023413. https://link.aps.org/doi/10.1103/PhysRevResearch.2.023413 (2020).

234. Pekker, D. & Varma, C. Amplitude/Higgs Modes in Condensed Matter Physics. *Annual Review of Condensed Matter Physics* **6,** 269–297. https://doi.org/10.1146/annurev-conmatphys-031214-014350 (2015).

235. Littlewood, P. B. & Varma, C. M. Gauge-Invariant Theory of the Dynamical Interaction of Charge Density Waves and Superconductivity. *Phys. Rev. Lett.* **47,** 811–814. https://link.aps.org/doi/10.1103/PhysRevLett.47.811 (1981).

236. Littlewood, P. B. & Varma, C. M. Amplitude collective modes in superconductors and their coupling to charge-density waves. *Phys. Rev. B* **26,** 4883–4893. https://link.aps.org/doi/10.1103/PhysRevB.26.4883 (1982).

237. Cea, T. & Benfatto, L. Nature and Raman signatures of the Higgs amplitude mode in the coexisting superconducting and charge-density-wave state. *Phys. Rev. B* **90,** 224515. https://link.aps.org/doi/10.1103/PhysRevB.90.224515 (2014).

238. Méasson, M.-A., Gallais, Y., Cazayous, M., Clair, B., Rodière, P., Cario, L. & Sacuto, A. Amplitude Higgs mode in the 2H-$NbSe_2$ superconductor. *Phys. Rev. B* **89,** 060503. https://link.aps.org/doi/10.1103/PhysRevB.89.060503 (2014).

239. Grasset, R., Cea, T., Gallais, Y., Cazayous, M., Sacuto, A., Cario, L., Benfatto, L. & Méasson, M.-A. Higgs-mode radiance and charge-density-wave order in 2H-$NbSe_2$. *Phys. Rev. B* **97,** 094502. https://link.aps.org/doi/10.1103/PhysRevB.97.094502 (2018).

240. Wu, W.-C. & Griffin, A. Condensate pair fluctuations in a two-dimensional d-wave superconductor and Raman scattering. *Phys. Rev. B* **51,** 1190–1205. https://link.aps.org/doi/10.1103/PhysRevB.51.1190 (1995).

241. Scalapino, D. J. & Devereaux, T. P. Collective d-wave exciton modes in the calculated Raman spectrum of Fe-based superconductors. *Phys. Rev. B* **80,** 140512. https://link.aps.org/doi/10.1103/PhysRevB.80.140512 (2009).

242. Khodas, M., Chubukov, A. V. & Blumberg, G. Collective modes in multiband superconductors: Raman scattering in iron selenides. *Phys. Rev. B* **89,** 245134. https://link.aps.org/doi/10.1103/PhysRevB.89.245134 (2014).

243. Böhm, T., Kemper, A. F., Moritz, B., Kretzschmar, F., Muschler, B., Eiter, H.-M., Hackl, R., Devereaux, T. P., Scalapino, D. J. & Wen, H.-H. Balancing Act: Evidence for a Strong Subdominant d-Wave Pairing Channel in $Ba_0.6K_0.4Fe_2As_2$. *Phys. Rev. X* **4,** 041046. https://link.aps.org/doi/10.1103/PhysRevX.4.041046 (2014).

244. Maiti, S., Maier, T. A., Böhm, T., Hackl, R. & Hirschfeld, P. J. Probing the Pairing Interaction and Multiple Bardasis-Schrieffer Modes Using Raman Spectroscopy. *Phys. Rev. Lett.* **117,** 257001. https://link.aps.org/doi/10.1103/PhysRevLett.117.257001 (2016).

245. Jost, D., Scholz, J.-R., Zweck, U., Meier, W. R., Böhmer, A. E., Canfield, P. C., Lazarević, N. & Hackl, R. Indication of subdominant d-wave interaction in superconducting $CaKFe_4As_4$. *Phys. Rev. B* **98,** 020504. https://link.aps.org/doi/10.1103/PhysRevB.98.020504 (2018).

246. Müller, M. A. & Eremin, I. M. Signatures of Bardasis-Schrieffer mode excitation in third-harmonic generated currents. *Phys. Rev. B* **104,** 144508. https://link.aps.org/doi/10.1103/PhysRevB.104.144508 (2021).

247. Müller, M. A., Volkov, P. A., Paul, I. & Eremin, I. M. Interplay between nematicity and Bardasis-Schrieffer modes in the short-time dynamics of unconventional superconductors. *Phys. Rev. B* **103,** 024519. https://link.aps.org/doi/10.1103/PhysRevB.103.024519 (2021).

248. Fertig, H. A. & Das Sarma, S. Collective modes in layered superconductors. *Phys. Rev. Lett.* **65,** 1482–1485. https://link.aps.org/doi/10.1103/PhysRevLett.65.1482 (1990).

249. Fertig, H. A. & Das Sarma, S. Collective excitations and mode coupling in layered superconductors. *Phys. Rev. B* **44,** 4480–4494. https://link.aps.org/doi/10.1103/PhysRevB.44.4480 (1991).

250. Côté, R. & Griffin, A. Cooper-pair-condensate fluctuations and plasmons in layered superconductors. *Phys. Rev. B* **48,** 10404–10425. https://link.aps.org/doi/10.1103/PhysRevB.48.10404 (1993).

251. Wu, W.-C. & Griffin, A. Phase and Amplitude Modes in a Superconductor with Interlayer Pair Tunneling. *Phys. Rev. Lett.* **74,** 158–161. https://link.aps.org/doi/10.1103/PhysRevLett.74.158 (1995).

252. Bittner, N., Einzel, D., Klam, L. & Manske, D. Leggett Modes and the Anderson-Higgs Mechanism in Superconductors without Inversion Symmetry. *Phys. Rev. Lett.* **115,** 227002. https://link.aps.org/doi/10.1103/PhysRevLett.115.227002 (2015).

253. Huang, W., Sigrist, M. & Weng, Z.-Y. Identifying the dominant pairing interaction in high-T_c FeSe superconductors through Leggett modes. *Phys. Rev. B* **97,** 144507. https://link.aps.org/doi/10.1103/PhysRevB.97.144507 (14 2018).

254. Ota, Y., Machida, M., Koyama, T. & Aoki, H. Collective modes in multiband superfluids and superconductors: Multiple dynamical classes. *Phys. Rev. B* **83,** 060507. https://link.aps.org/doi/10.1103/PhysRevB.83.060507 (2011).

255. Carlström, J., Garaud, J. & Babaev, E. Length scales, collective modes, and type-1.5 regimes in three-band superconductors. *Phys. Rev. B* **84,** 134518. https://link.aps.org/doi/10.1103/PhysRevB.84.134518 (2011).

256. Lin, S.-Z. & Hu, X. Massless Leggett Mode in Three-Band Superconductors with Time-Reversal-Symmetry Breaking. *Phys. Rev. Lett.* **108,** 177005. https://link.aps.org/doi/10.1103/PhysRevLett.108.177005 (2012).

257. Stanev, V. Model of collective modes in three-band superconductors with repulsive interband interactions. *Phys. Rev. B* **85,** 174520. https://link.aps.org/doi/10.1103/PhysRevB.85.174520 (2012).

258. Klein, M. V. Theory of Raman scattering from Leggett's collective mode in a multiband superconductor: Application to MgB_2. *Phys. Rev. B* **82,** 014507. https://link.aps.org/doi/10.1103/PhysRevB.82.014507 (2010).

259. Cea, T. & Benfatto, L. Signature of the Leggett mode in the A_{1g} Raman response: From MgB_2 to iron-based superconductors. *Phys. Rev. B* **94,** 064512. https://link.aps.org/doi/10.1103/PhysRevB.94.064512 (2016).

260. Kamatani, T., Kitamura, S., Tsuji, N., Shimano, R. & Morimoto, T. Optical response of the Leggett mode in multiband superconductors in the linear response regime. *Phys. Rev. B* **105,** 094520. https://link.aps.org/doi/10.1103/PhysRevB.105.094520 (2022).

261. Murotani, Y., Tsuji, N. & Aoki, H. Theory of light-induced resonances with collective Higgs and Leggett modes in multiband superconductors. *Phys. Rev. B* **95,** 104503. https://link.aps.org/doi/10.1103/PhysRevB.95.104503 (2017).

262. Fiore, J., Udina, M., Marciani, M., Seibold, G. & Benfatto, L. Contribution of collective excitations to third harmonic generation in two-band superconductors: The case of MgB_2. *Phys. Rev. B* **106,** 094515. https://link.aps.org/doi/10.1103/PhysRevB.106.094515 (2022).

263. Mou, D., Jiang, R., Taufour, V., Flint, R., Bud'ko, S. L., Canfield, P. C., Wen, J. S., Xu, Z. J., Gu, G. & Kaminski, A. Strong interaction between electrons and collective excitations in the multiband superconductor MgB_2. *Phys. Rev. B* **91,** 140502. https://link.aps.org/doi/10.1103/PhysRevB.91.140502 (2015).

264. Ota, Y., Machida, M. & Koyama, T. Macroscopic quantum tunneling in multigap superconducting Josephson junctions: Enhancement of escape rate via quantum fluctuations of the Josephson-Leggett mode. *Phys. Rev. B* **83,** 060503. https://link.aps.org/doi/10.1103/PhysRevB.83.060503 (2011).

265. Cuozzo, J. J., Yu, W., Davids, P., Nenoff, T. M., Soh, D. B., Pan, W. & Rossi, E. *Leggett Modes in Dirac Semimetals* arXiv:2205.15995. 2022. http://arxiv.org/abs/2205.15995.

266. Blumberg, G., Mialitsin, A., Dennis, B. S., Klein, M. V., Zhigadlo, N. D. & Karpinski, J. Observation of Leggett's Collective Mode in a Multiband MgB_2. *Phys. Rev. Lett.* **99,** 227002. https://link.aps.org/doi/10.1103/PhysRevLett.99.227002 (2007).

267. Giorgianni, F., Cea, T., Vicario, C., Hauri, C. P., Withanage, W. K., Xi, X. & Benfatto, L. Leggett mode controlled by light pulses. *Nat. Phys.* **15,** 341–346. https://www.nature.com/articles/s41567-018-0385-4 (2019).

268. Burnell, F. J., Hu, J., Parish, M. M. & Bernevig, B. A. Leggett mode in a strong-coupling model of iron arsenide superconductors. *Phys. Rev. B* **82,** 144506. https://link.aps.org/doi/10.1103/PhysRevB.82.144506 (2010).

269. Zhao, S. Z., Song, H.-Y., Hu, L. L., Xie, T., Liu, C., Luo, H. Q., Jiang, C.-Y., Zhang, X., Nie, X. C., Meng, J.-Q., Duan, Y.-X., Liu, S.-B., Xie, H.-Y. & Liu, H. Y. Observation of soft Leggett mode in superconducting $CaKFe_4As_4$. *Phys. Rev. B* **102,** 144519. https://link.aps.org/doi/10.1103/PhysRevB.102.144519 (2020).

270. Huang, W., Scaffidi, T., Sigrist, M. & Kallin, C. Leggett modes and multiband superconductivity in Sr_2RuO_4. *Phys. Rev. B* **94,** 064508. https://link.aps.org/doi/10.1103/PhysRevB.94.064508 (2016).

271. Karchev, N. Leggett's modes in magnetic systems with Jahn–Teller distortion. *Annals of Physics* **363,** 371–384. https://www.sciencedirect.com/science/article/pii/S0003491615003796 (2015).

272. Meier, Q. N., Hickox-Young, D., Laurita, G., Spaldin, N. A., Rondinelli, J. M. & Norman, M. R. Leggett Modes Accompanying Crystallographic Phase Transitions. *Phys. Rev. X* **12,** 011024. https://link.aps.org/doi/10.1103/PhysRevX.12.011024 (2022).

273. Balatsky, A. V., Kumar, P. & Schrieffer, J. R. Collective Mode in a Superconductor with Mixed-Symmetry Order Parameter Components. *Phys. Rev. Lett.* **84,** 4445–4448. https://link.aps.org/doi/10.1103/PhysRevLett.84.4445 (2000).

274. Poniatowski, N. R., Curtis, J. B., Yacoby, A. & Narang, P. Spectroscopic signatures of time-reversal symmetry breaking superconductivity. *Commun Phys* **5,** 1–11. https://www.nature.com/articles/s42005-022-00819-0 (2022).

275. Kee, H.-Y., Kim, Y. B. & Maki, K. Spin waves in a two-dimensional p-wave superconductor: Sr_2RuO_4. *Phys. Rev. B* **61,** 3584–3591. https://link.aps.org/doi/10.1103/PhysRevB.61.3584 (2000).

276. Carlson, R. V. & Goldman, A. M. Propagating Order-Parameter Collective Modes in Superconducting Films. *Phys. Rev. Lett.* **34,** 11–15. https://link.aps.org/doi/10.1103/PhysRevLett.34.11 (1975).

277. Rowell, J. M. & McMillan, W. L. Electron Interference in a Normal Metal Induced by Superconducting Contracts. *Phys. Rev. Lett.* **16,** 453–456. https://link.aps.org/doi/10.1103/PhysRevLett.16.453 (1966).

278. Tomasch, W. J. Geometrical Resonance in the Tunneling Characteristics of Superconducting Pb. *Phys. Rev. Lett.* **15,** 672–675. https://link.aps.org/doi/10.1103/PhysRevLett.15.672 (1965).

279. McMillan, W. L. & Anderson, P. W. Theory of Geometrical Resonances in the Tunneling Characteristics of Thick Films of Superconductors. *Phys. Rev. Lett.* **16,** 85–87. https://link.aps.org/doi/10.1103/PhysRevLett.16.85 (1966).

280. Braz, J. a. E. H., Amorim, B. & Castro, E. V. Valley-polarized magnetic state in hole-doped monolayers of transition-metal dichalcogenides. *Phys. Rev. B* **98,** 161406. https://link.aps.org/doi/10.1103/PhysRevB.98.161406 (2018).

281. Hsu, Y.-T., Vaezi, A., Fischer, M. H. & Kim, E.-A. Topological superconductivity in monolayer transition metal dichalcogenides. *Nat Commun* **8,** 14985. https://www.nature.com/articles/ncomms14985 (2017).

282. Ribeiro-Soares, J., Almeida, R. M., Barros, E. B., Araujo, P. T., Dresselhaus, M. S., Cançado, L. G. & Jorio, A. Group theory analysis of phonons in two-dimensional transition metal dichalcogenides. *Phys. Rev. B* **90,** 115438. https://link.aps.org/doi/10.1103/PhysRevB.90.115438 (2014).

283. Yang, Z., Sheng, H., Guo, Z., Zhang, R., Wu, Q., Weng, H., Fang, Z. & Wang, Z. *Superconductivity in unconventional metals* arXiv:2306.08347. 2023. http://arxiv.org/abs/2306.08347.

284. Lian, C.-S., Heil, C., Liu, X., Si, C., Giustino, F. & Duan, W. Intrinsic and doping-enhanced superconductivity in monolayer 1H-TaS_2: Critical role of charge ordering and spin-orbit coupling. *Phys. Rev. B* **105,** L180505. https://link.aps.org/doi/10.1103/PhysRevB.105.L180505 (2022).

285. Hörhold, S., Graf, J., Marganska, M. & Grifoni, M. Two-bands Ising superconductivity from Coulomb interactions in monolayer $NbSe_2$. *2D Mater.* **10,** 025008. https://dx.doi.org/10.1088/2053-1583/acb21d (2023).

286. Heil, C., Poncé, S., Lambert, H., Schlipf, M., Margine, E. R. & Giustino, F. Origin of Superconductivity and Latent Charge Density Wave in NbS_2. *Phys. Rev. Lett.* **119,** 087003. https://link.aps.org/doi/10.1103/PhysRevLett.119.087003 (2017).

287. Moncton, D. E., Axe, J. D. & DiSalvo, F. J. Study of Superlattice Formation in 2H-$NbSe_2$ and 2H-$TaSe_2$ by Neutron Scattering. *Phys. Rev. Lett.* **34,** 734–737. https://link.aps.org/doi/10.1103/PhysRevLett.34.734 (1975).

288. Harper, J. M. E., Geballe, T. H. & Di Salvo, F. J. Heat capacity of 2H-$NbSe_2$ at the charge density wave transition. *Physics Letters A* **54,** 27–28. https://www.sciencedirect.com/science/article/pii/0375960175905927 (1975).

289. Xi, X., Zhao, L., Wang, Z., Berger, H., Forró, L., Shan, J. & Mak, K. F. Strongly enhanced charge-density-wave order in monolayer $NbSe_2$. *Nature Nanotech* **10,** 765–769. https://www.nature.com/articles/nnano.2015.143 (2015).

290. Ugeda, M. M., Bradley, A. J., Zhang, Y., Onishi, S., Chen, Y., Ruan, W., Ojeda-Aristizabal, C., Ryu, H., Edmonds, M. T., Tsai, H.-Z., Riss, A., Mo, S.-K., Lee, D., Zettl, A., Hussain, Z., Shen, Z.-X. & Crommie, M. F. Characterization of collective ground states in single-layer NbSe 2. *Nat. Phys* **12,** 92–97. https://www.nature.com/articles/nphys3527 (2016).

291. Bianco, R., Monacelli, L., Calandra, M., Mauri, F. & Errea, I. Weak Dimensionality Dependence and Dominant Role of Ionic Fluctuations in the Charge-Density-Wave Transition of $NbSe_2$. *Phys. Rev. Lett.* **125,** 106101. https://link.aps.org/doi/10.1103/PhysRevLett.125.106101 (2020).

292. Dreher, P., Wan, W., Chikina, A., Bianchi, M., Guo, H., Harsh, R., Mañas Valero, S., Coronado, E., Martínez-Galera, A. J., Hofmann, P., Miwa, J. A. & Ugeda, M. M. Proximity Effects on the Charge Density Wave Order and Superconductivity in Single-Layer $NbSe_2$. *ACS Nano* **15,** 19430–19438. https://doi.org/10.1021/acsnano.1c06012 (2021).

293. Lin, D., Li, S., Wen, J., Berger, H., Forró, L., Zhou, H., Jia, S., Taniguchi, T., Watanabe, K., Xi, X. & Bahramy, M. S. Patterns and driving forces of dimensionality-dependent charge density waves in 2H-type transition metal dichalcogenides. *Nat Commun* **11,** 2406. https://www.nature.com/articles/s41467-020-15715-w (2020).

294. Guster, B., Rubio-Verdú, C., Robles, R., Zaldívar, J., Dreher, P., Pruneda, M., Silva-Guillén, J. A., Choi, D.-J., Pascual, J. I., Ugeda, M. M., Ordejón, P. & Canadell, E. Coexistence of Elastic Modulations in the Charge Density Wave State of 2H-$NbSe_2$. *Nano Lett.* **19,** 3027–3032. https://doi.org/10.1021/acs.nanolett.9b00268 (2019).

295. Gye, G., Oh, E. & Yeom, H. W. Topological Landscape of Competing Charge Density Waves in 2H-$NbSe_2$. *Phys. Rev. Lett.* **122,** 016403. https://link.aps.org/doi/10.1103/PhysRevLett.122.016403 (2019).

296. Malliakas, C. D. & Kanatzidis, M. G. Nb–Nb Interactions Define the Charge Density Wave Structure of 2H-NbSe2. *J. Am. Chem. Soc.* **135,** 1719–1722. https://doi.org/10.1021/ja3120554 (2013).

297. Zheng, F., Zhou, Z., Liu, X. & Feng, J. First-principles study of charge and magnetic ordering in monolayer $NbSe_2$. *Phys. Rev. B* **97,** 081101. https://link.aps.org/doi/10.1103/PhysRevB.97.081101 (2018).

298. Das, S. & Mazin, I. I. Quantitative assessment of the role of spin fluctuations in 2D Ising superconductor NbSe2. *Computational Materials Science* **200,** 110758. https://www.sciencedirect.com/science/article/pii/S0927025621004857 (2021).

299. Costa, A. T., Costa, M. & Fernández-Rossier, J. Ising and XY paramagnons in two-dimensional 2H-$NbSe_2$. *Phys. Rev. B* **105,** 224412. https://link.aps.org/doi/10.1103/PhysRevB.105.224412 (2022).

300. Wickramaratne, D., Khmelevskyi, S., Agterberg, D. F. & Mazin, I. I. Ising Superconductivity and Magnetism in $NbSe_2$. *Phys. Rev. X* **10,** 041003. https://link.aps.org/doi/10.1103/PhysRevX.10.041003 (2020).

301. Divilov, S., Wan, W., Dreher, P., Bölen, E., Sánchez-Portal, D., Ugeda, M. M. & Ynduráin, F. Magnetic correlations in single-layer $NbSe_2$. *J. Phys.: Condens. Matter* **33,** 295804. https://dx.doi.org/10.1088/1361-648X/ac00da (2021).

302. Suderow, H., Tissen, V. G., Brison, J. P., Martínez, J. L. & Vieira, S. Pressure Induced Effects on the Fermi Surface of Superconducting 2H-$NbSe_2$. *Phys. Rev. Lett.* **95,** 117006. https://link.aps.org/doi/10.1103/PhysRevLett.95.117006 (2005).

303. Moulding, O., Osmond, I., Flicker, F., Muramatsu, T. & Friedemann, S. Absence of superconducting dome at the charge-density-wave quantum phase transition in 2H-$NbSe_2$. *Phys. Rev. Research* **2,** 043392. https://link.aps.org/doi/10.1103/PhysRevResearch.2.043392 (2020).

304. Cho, K., Kończykowski, M., Teknowijoyo, S., Tanatar, M. A., Guss, J., Gartin, P. B., Wilde, J. M., Kreyssig, A., McQueeney, R. J., Goldman, A. I., Mishra, V., Hirschfeld, P. J. & Prozorov, R. Using controlled disorder to probe the interplay between charge order and superconductivity in $NbSe_2$. *Nat Commun* **9,** 2796. https://www.nature.com/articles/s41467-018-05153-0 (2018).

305. Wan, W., Wickramaratne, D., Dreher, P., Harsh, R., Mazin, I. I. & Ugeda, M. M. Nontrivial Doping Evolution of Electronic Properties in Ising-Superconducting Alloys. *Adv Mater* **34,** 2200492. https://onlinelibrary.wiley.com/doi/abs/10.1002/adma.202200492 (2022).

306. Shaffer, D., Kang, J., Burnell, F. J. & Fernandes, R. M. Crystalline nodal topological superconductivity and Bogolyubov Fermi surfaces in monolayer $NbSe_2$. *Physical Review B* **101,** 224503. https://link.aps.org/doi/10.1103/PhysRevB.101.224503 (2020).

307. Khestanova, E., Birkbeck, J., Zhu, M., Cao, Y., Yu, G. L., Ghazaryan, D., Yin, J., Berger, H., Forró, L., Taniguchi, T., Watanabe, K., Gorbachev, R. V., Mishchenko, A., Geim, A. K. & Grigorieva, I. V. Unusual Suppression of the Superconducting Energy Gap and Critical Temperature in Atomically Thin $NbSe_2$. *Nano Lett.* **18,** 2623–2629. https://doi.org/10.1021/acs.nanolett.8b00443 (2018).

308. Noat, Y., Silva-Guillén, J. A., Cren, T., Cherkez, V., Brun, C., Pons, S., Debontridder, F., Roditchev, D., Sacks, W., Cario, L., Ordejón, P., García, A. & Canadell, E. Quasiparticle spectra of 2H-$NbSe_2$: Two-band superconductivity and the role of tunneling selectivity. *Phys. Rev. B* **92,** 134510. https://link.aps.org/doi/10.1103/PhysRevB.92.134510 (2015).

309. Silva-Guill/'en, J. A., Ordej/'on, P., Guinea, F. & Canadell, E. Electronic structure of 2H-$NbSe_2$ single-layers in the CDW state. *2D Mater.* **3,** 035028. https://doi.org/10.1088/2053-1583/3/3/035028 (2016).

310. Xi, X., Wang, Z., Zhao, W., Park, J.-H., Law, K. T., Berger, H., Forró, L., Shan, J. & Mak, K. F. Ising pairing in superconducting $NbSe_2$ atomic layers. *Nature Phys* **12,** 139–143. https://www.nature.com/articles/nphys3538 (2016).

311. Sohn, E., Xi, X., He, W.-Y., Jiang, S., Wang, Z., Kang, K., Park, J.-H., Berger, H., Forró, L., Law, K. T., Shan, J. & Mak, K. F. An unusual continuous paramagnetic-limited superconducting phase transition in 2D NbSe 2. *Nat. Mater* **17,** 504–508. https://www.nature.com/articles/s41563-018-0061-1 (2018).

312. Dvir, T., Massee, F., Attias, L., Khodas, M., Aprili, M., Quay, C. H. L. & Steinberg, H. Spectroscopy of bulk and few-layer superconducting $NbSe_2$ with van der Waals tunnel

junctions. *Nat. Commun* **9,** 598. https://www.nature.com/articles/s41467-018-03000-w (2018).

313. Kuzmanović, M., Dvir, T., LeBoeuf, D., Ilić, S., Haim, M., Möckli, D., Kramer, S., Khodas, M., Houzet, M., Meyer, J. S., Aprili, M., Steinberg, H. & Quay, C. H. L. Tunneling spectroscopy of few-monolayer $NbSe_2$ in high magnetic fields: Triplet superconductivity and Ising protection. *Phys. Rev. B* **106,** 184514. https://link.aps.org/doi/10.1103/PhysRevB.106.184514 (2022).
314. He, W.-Y., Zhou, B. T., He, J. J., Yuan, N. F. Q., Zhang, T. & Law, K. T. Magnetic field driven nodal topological superconductivity in monolayer transition metal dichalcogenides. *Communications Physics* **1,** 1–7. https://www.nature.com/articles/s42005-018-0041-4 (2018).
315. Gor'kov, L. P. & Rashba, E. I. Superconducting 2D System with Lifted Spin Degeneracy: Mixed Singlet-Triplet State. *Phys. Rev. Lett.* **87,** 037004. https://link.aps.org/doi/10.1103/PhysRevLett.87.037004 (2001).
316. Smidman, M., Salamon, M. B., Yuan, H. Q. & Agterberg, D. F. Superconductivity and spin–orbit coupling in non-centrosymmetric materials: a review. *Reports on Progress in Physics* **80,** 036501. https://doi.org/10.1088/1361-6633/80/3/036501 (2017).
317. Möckli, D. & Khodas, M. Robust parity-mixed superconductivity in disordered monolayer transition metal dichalcogenides. *Phys. Rev. B* **98,** 144518. https://link.aps.org/doi/10.1103/PhysRevB.98.144518 (2018).
318. Haim, M., Levchenko, A. & Khodas, M. Mechanisms of in-plane magnetic anisotropy in superconducting $NbSe_2$. *Phys. Rev. B* **105,** 024515. https://link.aps.org/doi/10.1103/PhysRevB.105.024515 (2022).
319. Möckli, D. & Khodas, M. Magnetic-field induced $s + if$ pairing in Ising superconductors. *Phys. Rev. B* **99,** 180505. https://link.aps.org/doi/10.1103/PhysRevB.99.180505 (2019).
320. Möckli, D. & Khodas, M. Ising superconductors: Interplay of magnetic field, triplet channels, and disorder. *Phys. Rev. B* **101,** 014510. https://link.aps.org/doi/10.1103/PhysRevB.101.014510 (2020).
321. Wickramaratne, D., Haim, M., Khodas, M. & Mazin, I. I. Magnetism-driven unconventional effects in Ising superconductors: Role of proximity, tunneling, and nematicity. *Phys. Rev. B* **104,** L060501. https://link.aps.org/doi/10.1103/PhysRevB.104.L060501 (2021).
322. Kang, K., Jiang, S., Berger, H., Watanabe, K., Taniguchi, T., Forró, L., Shan, J. & Mak, K. F. *Giant anisotropic magnetoresistance in Ising superconductor-magnetic insulator tunnel junctions* arXiv:2101.01327. 2021. http://arxiv.org/abs/2101.01327.
323. Lian, C.-S. Interplay of charge ordering and superconductivity in two-dimensional 2H group V transition-metal dichalcogenides. *Phys. Rev. B* **107,** 045431. https://link.aps.org/doi/10.1103/PhysRevB.107.045431 (2023).

324. Eschrig, M. The effect of collective spin-1 excitations on electronic spectra in high- Tc superconductors. *Advances in Physics* **55,** 47–183. https://doi.org/10.1080/00018730600645636 (2006).
325. Crépel, V. & Fu, L. Spin-triplet superconductivity from excitonic effect in doped insulators. *Proceedings of the National Academy of Sciences* **119,** e2117735119. https://www.pnas.org/doi/10.1073/pnas.2117735119 (2022).
326. Georges, A., Medici, L. d. & Mravlje, J. Strong correlations from Hund's coupling. *Annu. Rev. Condens. Matter Phys.* **4,** 137–178 (2013).
327. Lee, P. A. & Wen, X.-G. Spin-triplet *p*-wave pairing in a three-orbital model for iron pnictide superconductors. *Phys. Rev. B* **78,** 144517. https://link.aps.org/doi/10.1103/PhysRevB.78.144517 (14 2008).
328. Hoshino, S. & Werner, P. Superconductivity from Emerging Magnetic Moments. *Phys. Rev. Lett.* **115,** 247001. https://link.aps.org/doi/10.1103/PhysRevLett.115.247001 (24 2015).
329. Vafek, O. & Chubukov, A. V. Hund Interaction, Spin-Orbit Coupling, and the Mechanism of Superconductivity in Strongly Hole-Doped Iron Pnictides. *Phys. Rev. Lett.* **118,** 087003. https://link.aps.org/doi/10.1103/PhysRevLett.118.087003 (8 2017).
330. Cheung, A. K. C. & Agterberg, D. F. Superconductivity in the presence of spin-orbit interactions stabilized by Hund coupling. *Phys. Rev. B* **99,** 024516. https://link.aps.org/doi/10.1103/PhysRevB.99.024516 (2 2019).
331. Böker, J., Volkov, P. A., Efetov, K. B. & Eremin, I. $s+is$ superconductivity with incipient bands: Doping dependence and STM signatures. *Physical Review B* **96,** 014517. https://link.aps.org/doi/10.1103/PhysRevB.96.014517 (2017).
332. Altland, A. & Simons, B. D. *Condensed Matter Field Theory* 2nd ed. ISBN: 978-0-521-76975-4. https://www.cambridge.org/core/books/condensed-matter-field-theory/0A8DE6503ED868D96985D9E7847C63FF (Cambridge University Press, 2010).
333. Eremenko, V., Sirenko, V., Ibulaev, V., Bartolomé, J., Arauzo, A. & Reményi, G. Heat capacity, thermal expansion and pressure derivative of critical temperature at the superconducting and charge density wave (CDW) transitions in $NbSe_2$. *Physica C: Superconductivity* **469,** 259–264. https://www.sciencedirect.com/science/article/pii/S0921453409000392 (2009).
334. Brinkman, A., Van Der Ploeg, S., Golubov, A. A., Rogalla, H., Kim, T. & Moodera, J. Charge transport in normal metal–magnesiumdiboride junctions. *J. Phys. Chem. Sol.* **67,** 407–411 (2006).
335. Abanov, A., Chubukov, A. V. & Schmalian, J. Fingerprints of spin mediated pairing in cuprates. *Journal of Electron Spectroscopy and Related Phenomena* **117,** 129–151 (2001).
336. Jandke, J., Hlobil, P., Schackert, M., Wulfhekel, W. & Schmalian, J. Coupling to real and virtual phonons in tunneling spectroscopy of superconductors. *Phys. Rev. B* **93,** 060505. https://link.aps.org/doi/10.1103/PhysRevB.93.060505 (6 2016).

337. Hlobil, P., Jandke, J., Wulfhekel, W. & Schmalian, J. Tracing the Electronic Pairing Glue in Unconventional Superconductors via Inelastic Scanning Tunneling Spectroscopy. *Phys. Rev. Lett.* **118,** 167001. https://link.aps.org/doi/10.1103/PhysRevLett.118.167001 (16 2017).

338. Abanov, A., Chubukov, A. V. & Schmalian, J. Quantum-critical theory of the spin-fermion model and its application to cuprates: Normal state analysis. *Advances in Physics* **52,** 119–218. https://doi.org/10.1080/00018730210000057123 (2003).

339. Vano, V., Ganguli, S. C., Amini, M., Yan, L., Khosravian, M., Chen, G., Kezilebieke, S., Lado, J. L. & Liljeroth, P. Evidence of Nodal Superconductivity in Monolayer 1H-TaS_2 with Hidden Order Fluctuations. *Adv Mater* **n/a,** 2305409. https://onlinelibrary.wiley.com/doi/abs/10.1002/adma.202305409 (2023).

340. Knispel, T., Berges, J., Schobert, A., van Loon, E. G. C. P., Jolie, W., Wehling, T., Michely, T. & Fischer, J. *Unconventional charge-density-wave gap in monolayer NbS_2* arXiv:2307.13791. 2023. http://arxiv.org/abs/2307.13791.

341. Ribak, A., Skiff, R. M., Mograbi, M., Rout, P. K., Fischer, M. H., Ruhman, J., Chashka, K., Dagan, Y. & Kanigel, A. Chiral superconductivity in the alternate stacking compound 4H_b-TaS_2. *Science Advances* **6,** eaax9480. https://www.science.org/doi/10.1126/sciadv.aax9480 (2020).

342. Nayak, A. K., Steinbok, A., Roet, Y., Koo, J., Margalit, G., Feldman, I., Almoalem, A., Kanigel, A., Fiete, G. A., Yan, B., Oreg, Y., Avraham, N. & Beidenkopf, H. Evidence of topological boundary modes with topological nodal-point superconductivity. *Nat. Phys.* **17,** 1413–1419. https://www.nature.com/articles/s41567-021-01376-z (2021).

343. Margalit, G., Berg, E. & Oreg, Y. Theory of multi-orbital topological superconductivity in transition metal dichalcogenides. *Annals of Physics. Special issue on Philip W. Anderson* **435,** 168561. https://www.sciencedirect.com/science/article/pii/S0003491621001676 (2021).

344. Dentelski, D., Day-Roberts, E., Birol, T., Fernandes, R. M. & Ruhman, J. Robust gapless superconductivity in 4H_b-TaS_2. *Phys. Rev. B* **103,** 224522. https://link.aps.org/doi/10.1103/PhysRevB.103.224522 (2021).

345. Persky, E., Bjorlig, A. V., Feldman, I., Almoalem, A., Altman, E., Berg, E., Kimchi, I., Ruhman, J., Kanigel, A. & Kalisky, B. Magnetic memory and spontaneous vortices in a van der Waals superconductor. *Nature* **607,** 692–696. https://www.nature.com/articles/s41586-022-04855-2 (2022).

346. Silber, I., Mathimalar, S., Mangel, I., Green, O., Avraham, N., Beidenkopf, H., Feldman, I., Kanigel, A., Klein, A., Goldstein, M., Banerjee, A., Sela, E. & Dagan, Y. *Chiral to Nematic Crossover in the Superconducting State of 4H_b-TaS_2* arXiv:2208.14442. 2022. http://arxiv.org/abs/2208.14442.

347. Almoalem, A., Feldman, I., Shlafman, M., Yaish, Y. E., Fischer, M. H., Moshe, M., Ruhman, J. & Kanigel, A. *Evidence of a two-component order parameter in $4H_b$-TaS_2 in the Little-Parks effect* arXiv:2208.13798. 2022. http://arxiv.org/abs/2208.13798.

348. Kumar Nayak, A., Steinbok, A., Roet, Y., Koo, J., Feldman, I., Almoalem, A., Kanigel, A., Yan, B., Rosch, A., Avraham, N. & Beidenkopf, H. First-order quantum phase transition in the hybrid metal–Mott insulator transition metal dichalcogenide $4H_b$-TaS_2. *PNAS* **120,** e2304274120. https://www.pnas.org/doi/10.1073/pnas.2304274120 (2023).

349. Xie, Z., Yang, M., Cheng, Z. G., Ying, T., Guo, J.-g. & Chen, X. A Revisit of Superconductivity in $4H_b$-$TaS_{2-2x}Se_{2x}$ Single Crystals. *J. Phys. Soc. Jpn.* **92,** 054702. https://journals.jps.jp/doi/10.7566/JPSJ.92.054702 (2023).

350. Fischer, M. H., Lee, P. A. & Ruhman, J. *A mechanism for π phase shifts in Little-Parks experiments: application to 2H-TaS_2 intercalated with chiral molecules and to $4H_b$-TaS_2* arXiv:2304.10583. 2023. http://arxiv.org/abs/2304.10583.

351. Habe, T. Three-orbital continuous model for $1H$-type metallic transition metal dichalcogenide monolayers. *Physical Review B* **102,** 195430. https://link.aps.org/doi/10.1103/PhysRevB.102.195430 (2020).

352. Chen, X., Gu, Z.-C. & Wen, X.-G. Local unitary transformation, long-range quantum entanglement, wave function renormalization, and topological order. *Phys. Rev. B* **82,** 155138. https://link.aps.org/doi/10.1103/PhysRevB.82.155138 (2010).

353. Chen, X., Gu, Z.-C., Liu, Z.-X. & Wen, X.-G. Symmetry protected topological orders and the group cohomology of their symmetry group. *Phys. Rev. B* **87,** 155114. https://link.aps.org/doi/10.1103/PhysRevB.87.155114 (2013).

354. Senthil, T. Symmetry-Protected Topological Phases of Quantum Matter. *Annual Review of Condensed Matter Physics* **6,** 299–324. https://doi.org/10.1146/annurev-conmatphys-031214-014740 (2015).

355. Wen, X. G. Topological orders in rigid states. *Int. J. Mod. Phys. B* **04,** 239–271. https://www.worldscientific.com/doi/abs/10.1142/s0217979290000139 (1990).

356. Wen, X. G. & Niu, Q. Ground-state degeneracy of the fractional quantum Hall states in the presence of a random potential and on high-genus Riemann surfaces. *Phys. Rev. B* **41,** 9377–9396. https://link.aps.org/doi/10.1103/PhysRevB.41.9377 (1990).

357. Wen, X.-G. Topological orders and edge excitations in fractional quantum Hall states. *Advances in Physics* **44,** 405–473. https://doi.org/10.1080/00018739500101566 (1995).

358. Wen, X. G. Mean-field theory of spin-liquid states with finite energy gap and topological orders. *Phys. Rev. B* **44,** 2664–2672. https://link.aps.org/doi/10.1103/PhysRevB.44.2664 (1991).

359. Castelnovo, C., Moessner, R. & Sondhi, S. Spin Ice, Fractionalization, and Topological Order. *Annual Review of Condensed Matter Physics* **3,** 35–55. https://doi.org/10.1146/annurev-conmatphys-020911-125058 (2012).

360. Savary, L. & Balents, L. Quantum spin liquids: a review. *Rep. Prog. Phys.* **80,** 016502. https://dx.doi.org/10.1088/0034-4885/80/1/016502 (2016).

361. Broholm, C., Cava, R. J., Kivelson, S. A., Nocera, D. G., Norman, M. R. & Senthil, T. Quantum spin liquids. *Science* **367,** eaay0668. https://www.science.org/doi/full/10.1126/science.aay0668 (2020).

362. Brouwer, P. W. & Dwivedi, V. Homotopic classification of band structures: Stable, fragile, delicate, and stable representation-protected topology. *Phys. Rev. B* **108,** 155137. https://link.aps.org/doi/10.1103/PhysRevB.108.155137 (2023).

363. Altland, A., Brouwer, P. W., Dieplinger, J., Foster, M. S., Moreno-Gonzalez, M. & Trifunovic, L. *Fragility of spectral flow for topological phases in non-Wigner-Dyson classes* arXiv:2308.12931. 2023. http://arxiv.org/abs/2308.12931.

364. Bradley, C. J. & Cracknell, A. P. *The mathematical theory of symmetry in solids: representation theory for point groups and space groups* OCLC: 699521526. ISBN: 978-0-19-958258-7 (Clarendon Press, Oxford, 1972).

365. Elliott, J. P. & Dawber, P. G. *Symmetry in Physics* ISBN: 978-0-333-38270-7 978-1-349-07635-2. http://link.springer.com/10.1007/978-1-349-07635-2 (Macmillan Education UK, London, 1979).

366. Zirnbauer, M. R. in *The Oxford Handbook of Random Matrix Theory* (eds Akemann, G., Baik, J. & Di Francesco, P.) 0 (Oxford University Press, 2015). ISBN: 978-0-19-874419-1. https://doi.org/10.1093/oxfordhb/9780198744191.013.3.

367. Dyson, F. J. The Threefold Way. Algebraic Structure of Symmetry Groups and Ensembles in Quantum Mechanics. *Journal of Mathematical Physics* **3,** 1199–1215. https://doi.org/10.1063/1.1703863 (1962).

368. Wen, X.-G. Symmetry-protected topological phases in noninteracting fermion systems. *Phys. Rev. B* **85,** 085103. https://link.aps.org/doi/10.1103/PhysRevB.85.085103 (2012).

369. Fidkowski, L. & Kitaev, A. Topological phases of fermions in one dimension. *Phys. Rev. B* **83,** 075103. https://link.aps.org/doi/10.1103/PhysRevB.83.075103 (2011).

370. Isobe, H. & Fu, L. Theory of interacting topological crystalline insulators. *Phys. Rev. B* **92,** 081304. https://link.aps.org/doi/10.1103/PhysRevB.92.081304 (2015).

371. Song, H., Huang, S.-J., Fu, L. & Hermele, M. Topological Phases Protected by Point Group Symmetry. *Phys. Rev. X* **7,** 011020. https://link.aps.org/doi/10.1103/PhysRevX.7.011020 (2017).

372. Fu, L., Kane, C. L. & Mele, E. J. Topological Insulators in Three Dimensions. *Phys. Rev. Lett.* **98,** 106803. https://link.aps.org/doi/10.1103/PhysRevLett.98.106803 (2007).

373. Chiu, C.-K., Yao, H. & Ryu, S. Classification of topological insulators and superconductors in the presence of reflection symmetry. *Phys. Rev. B* **88,** 075142. https://link.aps.org/doi/10.1103/PhysRevB.88.075142 (2013).

374. Liu, C.-X., Zhang, R.-X. & VanLeeuwen, B. K. Topological nonsymmorphic crystalline insulators. *Phys. Rev. B* **90,** 085304. https://link.aps.org/doi/10.1103/PhysRevB.90.085304 (2014).

375. Schindler, F., Cook, A. M., Vergniory, M. G., Wang, Z., Parkin, S. S. P., Bernevig, B. A. & Neupert, T. Higher-order topological insulators. *Science Advances* **4,** eaat0346. https://www.science.org/doi/10.1126/sciadv.aat0346 (2018).

376. Watanabe, H., Po, H. C. & Vishwanath, A. Structure and topology of band structures in the 1651 magnetic space groups. *Science Advances* **4,** eaat8685 (2018).

377. Song, Z., Zhang, T. & Fang, C. Diagnosis for Nonmagnetic Topological Semimetals in the Absence of Spin-Orbital Coupling. *Phys. Rev. X* **8,** 031069. https://link.aps.org/doi/10.1103/PhysRevX.8.031069 (2018).

378. Khalaf, E., Po, H. C., Vishwanath, A. & Watanabe, H. Symmetry Indicators and Anomalous Surface States of Topological Crystalline Insulators. *Phys. Rev. X* **8,** 031070. https://link.aps.org/doi/10.1103/PhysRevX.8.031070 (2018).

379. Thouless, D. J. Wannier functions for magnetic sub-bands. *J. Phys. C: Solid State Phys.* **17,** L325. https://dx.doi.org/10.1088/0022-3719/17/12/003 (1984).

380. Thonhauser, T. & Vanderbilt, D. Insulator/Chern-insulator transition in the Haldane model. *Phys. Rev. B* **74,** 235111. https://link.aps.org/doi/10.1103/PhysRevB.74.235111 (2006).

381. Soluyanov, A. A. & Vanderbilt, D. Wannier representation of Z2 topological insulators. *Physical Review B* **83,** 035108. https://link.aps.org/doi/10.1103/PhysRevB.83.035108 (3 2011).

382. Marzari, N., Mostofi, A. A., Yates, J. R., Souza, I. & Vanderbilt, D. Maximally localized Wannier functions: Theory and applications. *Rev. Mod. Phys.* **84,** 1419–1475. https://link.aps.org/doi/10.1103/RevModPhys.84.1419 (2012).

383. Benalcazar, W. A., Bernevig, B. A. & Hughes, T. L. Quantized electric multipole insulators. *Science* **357,** 61–66. https://www.science.org/doi/10.1126/science.aah6442 (2017).

384. Schindler, F., Brzezińska, M., Benalcazar, W. A., Iraola, M., Bouhon, A., Tsirkin, S. S., Vergniory, M. G. & Neupert, T. Fractional corner charges in spin-orbit coupled crystals. *Physical Review Research* **1,** 033074. https://doi.org/10.1103/PhysRevResearch.1.033074 (2019).

385. Xu, Y., Elcoro, L., Song, Z.-D., Vergniory, M. G., Felser, C., Parkin, S. S. P., Regnault, N., Mañes, J. L. & Bernevig, B. A. *Filling-Enforced Obstructed Atomic Insulators* arXiv:2106.10276. 2021. http://arxiv.org/abs/2106.10276.

386. Cano, J., Elcoro, L., Aroyo, M. I., Bernevig, B. A. & Bradlyn, B. Topology invisible to eigenvalues in obstructed atomic insulators. *Physical Review B* **105,** 125115. https://link.aps.org/doi/10.1103/PhysRevB.105.125115 (12 2022).

387. Armitage, N. P., Mele, E. J. & Vishwanath, A. Weyl and Dirac semimetals in three-dimensional solids. *Reviews of Modern Physics* **90,** 1443 (2018).

388. Nielsen, H. B. & Ninomiya, M. Absence of neutrinos on a lattice: (I). Proof by homotopy theory. *Nuclear Physics B* **185,** 20–40. https://www.sciencedirect.com/science/article/pii/0550321381903618 (1981).

389. Nielsen, H. B. & Ninomiya, M. Absence of neutrinos on a lattice: (II). Intuitive topological proof. *Nuclear Physics B* **193,** 173–194. https://www.sciencedirect.com/science/article/pii/0550321381905241 (1981).

390. Nielsen, H. B. & Ninomiya, M. A no-go theorem for regularizing chiral fermions. *Physics Letters B* **105,** 219–223. https://www.sciencedirect.com/science/article/pii/0370269381910261 (1981).

391. Burkov, A. A., Hook, M. D. & Balents, L. Topological nodal semimetals. *Phys. Rev. B* **84,** 235126. https://link.aps.org/doi/10.1103/PhysRevB.84.235126 (2011).

392. Bradlyn, B., Cano, J., Wang, Z., Vergniory, M. G., Felser, C, Cava, R. J. & Bernevig, B. A. Beyond Dirac and Weyl fermions: Unconventional quasiparticles in conventional crystals. *Science* **353,** aaf5037 (2016).

393. Read, N. & Green, D. Paired states of fermions in two dimensions with breaking of parity and time-reversal symmetries and the fractional quantum Hall effect. *Phys. Rev. B* **61,** 10267–10297. https://link.aps.org/doi/10.1103/PhysRevB.61.10267 (2000).

394. Witten, E. Dyons of charge $e\theta/2\pi$. *Physics Letters B* **86,** 283–287. https://www.sciencedirect.com/science/article/pii/0370269379908384 (1979).

395. Wilczek, F. Two applications of axion electrodynamics. *Physical Review Letters* **58,** 1799–1802. https://link.aps.org/doi/10.1103/PhysRevLett.58.1799 (1987).

396. Rosenberg, G. & Franz, M. Witten effect in a crystalline topological insulator. *Physical Review B* **82,** 035105. https://link.aps.org/doi/10.1103/PhysRevB.82.035105 (2010).

397. Büttiker, M. Absence of backscattering in the quantum Hall effect in multiprobe conductors. *Phys. Rev. B* **38,** 9375–9389. https://link.aps.org/doi/10.1103/PhysRevB.38.9375 (1988).

398. Qi, J., Liu, H., Jiang, H. & Xie, X. C. Dephasing effects in topological insulators. *Front. Phys.* **14,** 43403. https://doi.org/10.1007/s11467-019-0907-2 (2019).

399. Fulga, I. C., Hassler, F. & Akhmerov, A. R. Scattering theory of topological insulators and superconductors. *Physical Review B* **85,** 165409. https://link.aps.org/doi/10.1103/PhysRevB.85.165409 (16 2012).

400. Alexandradinata, A., Hughes, T. L. & Bernevig, B. A. Trace index and spectral flow in the entanglement spectrum of topological insulators. *Phys. Rev. B* **84,** 195103. https://link.aps.org/doi/10.1103/PhysRevB.84.195103 (2011).
401. Zallen, R. *The Physics of Amorphous Solids* (Wiley, 1998).
402. Porai-Koshits, E. Structure of glass: The struggle of ideas and prospects. *Journal of Non-Crystalline Solids* **73,** 79–89. https://www.sciencedirect.com/science/article/pii/0022309385903382 (1985).
403. Wright, A. C. & Thorpe, M. F. Eighty years of random networks. *physica status solidi (b)* **250,** 931–936. https://onlinelibrary.wiley.com/doi/abs/10.1002/pssb.201248500 (2013).
404. Wright, A. C. The Great Crystallite Versus Random Network Controversy: A Personal Perspective. *International Journal of Applied Glass Science* **5,** 31–56. https://ceramics.onlinelibrary.wiley.com/doi/abs/10.1111/ijag.12039 (2014).
405. Lewis, L. J. Fifty years of amorphous silicon models : the end of the story? *Journal of Non-Crystalline Solids* **580,** 121383. https://www.sciencedirect.com/science/article/pii/S0022309321007444 (2022).
406. Weaire, D. & Thorpe, M. F. Electronic Properties of an Amorphous Solid. I. A Simple Tight-Binding Theory. *Physical Review B* **4,** 2508–2520. https://link.aps.org/doi/10.1103/PhysRevB.4.2508 (8 1971).
407. Zachariasen, W. H. The atomic arrangement in glass. *J. Am. Chem. Soc.* **54,** 3841. http://dx.doi.org/10.1021/ja01349a006 (1932).
408. Warren, B. E. Summary of Work on Atomic Arrangement in Glass. *Journal of the American Ceramic Society* **24,** 256–261. https://ceramics.onlinelibrary.wiley.com/doi/abs/10.1111/j.1151-2916.1941.tb14858.x (1941).
409. Valenkov, N. & Poray-Koshitz, E. X-ray Investigation of the Glassy State. *Zeitschrift für Kristallographie - Crystalline Materials* **95,** 195–229. https://doi.org/10.1524/zkri.1936.95.1.195 (1936).
410. Ciocys, S. T., Marsal, Q., Corbae, P., Varjas, D., Kennedy, E., Scott, M., Hellman, F., Grushin, A. G. & Lanzara, A. *Establishing Coherent Momentum-Space Electronic States in Locally Ordered Materials* arXiv:2302.05945. 2023. http://arxiv.org/abs/2302.05945.
411. Toh, C.-T., Zhang, H., Lin, J., Mayorov, A. S., Wang, Y.-P., Orofeo, C. M., Ferry, D. B., Andersen, H., Kakenov, N., Guo, Z., Abidi, I. H., Sims, H., Suenaga, K., Pantelides, S. T. & Özyilmaz, B. Synthesis and properties of free-standing monolayer amorphous carbon. *Nature* **577,** 199–203. https://www.nature.com/articles/s41586-019-1871-2 (2020).
412. Thorpe, M. F. & Weaire, D. Electronic Properties of an Amorphous Solid. II. Further Aspects of the Theory. *Phys. Rev. B* **4,** 3518–3527. https://link.aps.org/doi/10.1103/PhysRevB.4.3518 (1971).

413. Thorpe, M. F., Weaire, D & Alben, R. Electronic Properties of an Amorphous Solid. III. The Cohesive Energy and the Density of States. *Physical Review B* **7,** 3777–3788. https://link.aps.org/doi/10.1103/PhysRevB.7.3777 (1973).

414. Car, R. & Parrinello, M. Unified Approach for Molecular Dynamics and Density-Functional Theory. *Phys. Rev. Lett.* **55,** 2471–2474. https://link.aps.org/doi/10.1103/PhysRevLett.55.2471 (1985).

415. Car, R. & Parrinello, M. Structural, Dymanical, and Electronic Properties of Amorphous Silicon: An ab initio Molecular-Dynamics Study. *Phys. Rev. Lett.* **60,** 204–207. https://link.aps.org/doi/10.1103/PhysRevLett.60.204 (1988).

416. Focassio, B., Schleder, G. R., Crasto de Lima, F., Lewenkopf, C. & Fazzio, A. Amorphous Bi_2Se_3 structural, electronic, and topological nature from first principles. *Phys. Rev. B* **104,** 214206. https://link.aps.org/doi/10.1103/PhysRevB.104.214206 (2021).

417. Costa, M., Schleder, G. R., Buongiorno Nardelli, M., Lewenkopf, C. & Fazzio, A. Toward Realistic Amorphous Topological Insulators. *Nano Letters* **19,** 8941–8946. https://doi.org/10.1021/acs.nanolett.9b03881 (2019).

418. Focassio, B., Schleder, G. R., Costa, M., Fazzio, A. & Lewenkopf, C. Structural and electronic properties of realistic two-dimensional amorphous topological insulators. *2D Materials* **8,** 025032. https://doi.org/10.1088/2053-1583/abdb97 (2021).

419. Weaire, D. Existence of a Gap in the Electronic Density of States of a Tetrahedrally Bonded Solid of Arbitrary Structure. *Physical Review Letters* **26,** 1541–1543. https://link.aps.org/doi/10.1103/PhysRevLett.26.1541 (1971).

420. Streubel, R., Bouma, D. S., Bruni, F., Chen, X., Ercius, P., Ciston, J., N'Diaye, A. T., Roy, S., Kevan, S. D., Fischer, P. & Hellman, F. Chiral Spin Textures in Amorphous Iron–Germanium Thick Films. *Advanced Materials* **33,** 2004830. https://onlinelibrary.wiley.com/doi/abs/10.1002/adma.202004830 (2021).

421. Chen, J. T., Chen, T. T., Leslie, J. D. & Smith, H. J. T. Strong-coupling superconductivity in amorphous bismuth. *Physics Letters A* **25,** 679–680. https://www.sciencedirect.com/science/article/pii/0375960167904719 (1967).

422. Bergmann, G. Amorphous metals and their superconductivity. *Physics Reports* **27,** 159–185. https://www.sciencedirect.com/science/article/pii/0370157376900405 (1976).

423. Anderson, P. Theory of dirty superconductors. *Journal of Physics and Chemistry of Solids* **11,** 26–30. https://www.sciencedirect.com/science/article/pii/0022369759900368 (1959).

424. Tsuneto, T. On Dirty Superconductors. *Progress of Theoretical Physics* **28,** 857–869. https://doi.org/10.1143/PTP.28.857 (1962).

425. Moradian, R. & Mousavi, H. The validity of Anderson's theorem for binary alloy s-wave superconductors in the Bardeen–Cooper–Schrieffer regime. *Supercond. Sci. Technol.* **19,** 449–453. https://doi.org/10.1088/0953-2048/19/6/005 (2006).

426. Feigel'man, M. V., Ioffe, L. B., Kravtsov, V. E. & Cuevas, E. Fractal superconductivity near localization threshold. *Annals of Physics. July 2010 Special Issue* **325,** 1390–1478. https://www.sciencedirect.com/science/article/pii/S000349161000062X (2010).
427. Dodaro, J. F. & Kivelson, S. A. Generalization of Anderson's theorem for disordered superconductors. *Phys. Rev. B* **98,** 174503. https://link.aps.org/doi/10.1103/PhysRevB.98.174503 (2018).
428. Gastiasoro, M. N. & Andersen, B. M. Enhancing superconductivity by disorder. *Phys. Rev. B* **98,** 184510. https://link.aps.org/doi/10.1103/PhysRevB.98.184510 (2018).
429. Tsuei, C. C. in *Superconductor Materials Science: Metallurgy, Fabrication, and Applications* (eds Foner, S. & Schwartz, B. B.) 735–756 (Springer US, Boston, MA, 1981). ISBN: 978-1-4757-0037-4. https://doi.org/10.1007/978-1-4757-0037-4_12.
430. Prakash, O., Kumar, A., Thamizhavel, A. & Ramakrishnan, S. Evidence for bulk superconductivity in pure bismuth single crystals at ambient pressure. *Science* **355,** 52–55. https://science.sciencemag.org/content/355/6320/52 (2017).
431. Le Gallo, M. & Sebastian, A. An overview of phase-change memory device physics. *Journal of Physics D: Applied Physics* **53,** 213002. https://iopscience.iop.org/article/10.1088/1361-6463/ab7794 (2020).
432. Gaspard, J.-P. Structure of covalently bonded materials: From the Peierls distortion to Phase-Change Materials. *Comptes Rendus Physique* **17,** 389–405. https://www.sciencedirect.com/science/article/pii/S1631070515002558 (2016).
433. Matsunaga, T. & Yamada, N. Structural investigation of $GeSb_2Te_4$: A high-speed phase-change material. *Phys. Rev. B* **69,** 104111. https://link.aps.org/doi/10.1103/PhysRevB.69.104111 (10 2004).
434. Senechal, M. *Quasicrystals and Geometry* https://books.google.es/books?id=Ojh5zQEACAAJ (Cambridge University Press, 1995).
435. Lifshitz, R. Quasicrystals: A Matter of Definition. *Foundations of Physics* **33,** 1703–1711. https://doi.org/10.1023/A:1026247120031 (2003).
436. Senechal, M. & Taylor, J. E. Quasicrystals: The View from Stockholm. *Math Intelligencer* **35,** 1–9. https://doi.org/10.1007/s00283-013-9381-9 (2013).
437. Smith, D., Myers, J. S., Kaplan, C. S. & Goodman-Strauss, C. *A chiral aperiodic monotile* arXiv:2305.17743. 2023. http://arxiv.org/abs/2305.17743.
438. Shechtman, D., Blech, I., Gratias, D. & Cahn, J. W. Metallic Phase with Long-Range Orientational Order and No Translational Symmetry. *Phys. Rev. Lett.* **53,** 1951–1953. https://link.aps.org/doi/10.1103/PhysRevLett.53.1951 (1984).
439. Levine, D. & Steinhardt, P. J. Quasicrystals: A New Class of Ordered Structures. *Phys. Rev. Lett.* **53,** 2477–2480. https://link.aps.org/doi/10.1103/PhysRevLett.53.2477 (1984).

440. Levine, D. & Steinhardt, P. J. Quasicrystals. I. Definition and structure. *Phys. Rev. B* **34,** 596–616. https://link.aps.org/doi/10.1103/PhysRevB.34.596 (1986).
441. Yamamoto, A. Crystallography of Quasiperiodic Crystals. *Acta Cryst A* **52,** 509–560. //scripts.iucr.org/cgi-bin/paper?au0059 (1996).
442. Aubry, S. & André, G. Analyticity breaking and Anderson localization in incommensurate lattices. *Proceedings, VIII International Colloquium on Group-Theoretical Methods in Physics* **3** (1980).
443. Flicker, F. & van Wezel, J. One-Dimensional Quasicrystals from Incommensurate Charge Order. *Phys. Rev. Lett.* **115,** 236401. https://link.aps.org/doi/10.1103/PhysRevLett.115.236401 (2015).
444. Grünbaum, B. & Shephard, G. *Tilings and Patterns* ISBN: 978-0-486-46981-2. https://books.google.es/books?id=0x0vDAAAQBAJ (W. H. Freeman & Co., New York, 1986).
445. Levine, H., Libby, S. B. & Pruisken, A. M. M. Electron Delocalization by a Magnetic Field in Two Dimensions. *Phys. Rev. Lett.* **51,** 1915–1918. https://link.aps.org/doi/10.1103/PhysRevLett.51.1915 (1983).
446. Chalker, J. T. & Coddington, P. D. Percolation, quantum tunnelling and the integer Hall effect. *J. Phys. C: Solid State Phys.* **21,** 2665. https://dx.doi.org/10.1088/0022-3719/21/14/008 (1988).
447. Evers, F. & Mirlin, A. D. Anderson transitions. *Rev. Mod. Phys.* **80,** 1355–1417. https://link.aps.org/doi/10.1103/RevModPhys.80.1355 (4 2008).
448. Kim, K.-S. & Kivelson, S. A. The quantum Hall effect in the absence of disorder. *npj Quantum Mater.* **6,** 1–3. https://www.nature.com/articles/s41535-021-00321-w (2021).
449. Hikami, S., Larkin, A. I. & Nagaoka, Y. Spin-Orbit Interaction and Magnetoresistance in the Two Dimensional Random System. *Progress of Theoretical Physics* **63,** 707–710. https://doi.org/10.1143/PTP.63.707 (1980).
450. Anderson, P. W. Absence of Diffusion in Certain Random Lattices. *Phys. Rev.* **109,** 1492–1505. https://link.aps.org/doi/10.1103/PhysRev.109.1492 (5 1958).
451. Borchmann, J., Farrell, A. & Pereg-Barnea, T. Anderson topological superconductor. *Phys. Rev. B* **93,** 125133. https://link.aps.org/doi/10.1103/PhysRevB.93.125133 (2016).
452. Fu, L. & Kane, C. L. Topology, Delocalization via Average Symmetry and the Symplectic Anderson Transition. *Phys. Rev. Lett.* **109,** 246605. https://link.aps.org/doi/10.1103/PhysRevLett.109.246605 (2012).
453. Diez, M., Pikulin, D. I., Fulga, I. C. & Tworzyd\lo, J. Extended topological group structure due to average reflection symmetry. *New J. Phys.* **17,** 043014. https://doi.org/10.1088/1367-2630/17/4/043014 (2015).

454. Milsted, A., Seabra, L., Fulga, I. C., Beenakker, C. W. J. & Cobanera, E. Statistical translation invariance protects a topological insulator from interactions. *Phys. Rev. B* **92,** 085139. https://link.aps.org/doi/10.1103/PhysRevB.92.085139 (2015).

455. Song, J. & Prodan, E. Quantization of topological invariants under symmetry-breaking disorder. *Phys. Rev. B* **92,** 195119. https://link.aps.org/doi/10.1103/PhysRevB.92.195119 (2015).

456. Spring, H., Akhmerov, A. & Varjas, D. Amorphous topological phases protected by continuous rotation symmetry. *SciPost Physics* **11,** 022. https://scipost.org/10.21468/SciPostPhys.11.2.022 (2021).

457. Ma, R. & Wang, C. Average Symmetry-Protected Topological Phases. *Phys. Rev. X* **13,** 031016. https://link.aps.org/doi/10.1103/PhysRevX.13.031016 (2023).

458. Gruzberg, I. A., Klümper, A., Nuding, W. & Sedrakyan, A. Geometrically disordered network models, quenched quantum gravity, and critical behavior at quantum Hall plateau transitions. *Phys. Rev. B* **95,** 125414. https://link.aps.org/doi/10.1103/PhysRevB.95.125414 (2017).

459. Agarwala, A. & Shenoy, V. B. Topological Insulators in Amorphous Systems. *Phys. Rev. Lett.* **118,** 236402. https://link.aps.org/doi/10.1103/PhysRevLett.118.236402 (23 2017).

460. Xiao, M. & Fan, S. Photonic Chern insulator through homogenization of an array of particles. *Physical Review B* **96,** 100202. https://link.aps.org/doi/10.1103/PhysRevB.96.100202 (2017).

461. Mansha, S. & Chong, Y. D. Robust edge states in amorphous gyromagnetic photonic lattices. *Physical Review B* **96,** 121405. https://link.aps.org/doi/10.1103/PhysRevB.96.121405 (2017).

462. Mitchell, N. P., Nash, L. M., Hexner, D., Turner, A. M. & Irvine, W. T. M. Amorphous topological insulators constructed from random point sets. *Nature Physics* **14,** 380–385. https://www.nature.com/articles/s41567-017-0024-5 (2018).

463. Minarelli, E. L., Pöyhönen, K., van Dalum, G. A. R., Ojanen, T. & Fritz, L. Engineering of Chern insulators and circuits of topological edge states. *Physical Review B* **99,** 165413. https://link.aps.org/doi/10.1103/PhysRevB.99.165413 (2019).

464. Chern, G.-W. Topological insulator in an atomic liquid. *Europhysics Letters* **126,** 37002. https://dx.doi.org/10.1209/0295-5075/126/37002 (2019).

465. Sahlberg, I., Weststrom, A., Pöyhönen, K. & Ojanen, T. Topological phase transitions in glassy quantum matter. *Physical Review Research* **2,** 013053. https://link.aps.org/doi/10.1103/PhysRevResearch.2.013053 (2020).

466. Ivaki, M. N., Sahlberg, I. & Ojanen, T. Criticality in amorphous topological matter: Beyond the universal scaling paradigm. *Physical Review Research* **2,** 043301. https://link.aps.org/doi/10.1103/PhysRevResearch.2.043301 (2020).

467. Mano, T. & Ohtsuki, T. Application of Convolutional Neural Network to Quantum Percolation in Topological Insulators. *Journal of the Physical Society of Japan* **88,** 123704. https://journals.jps.jp/doi/10.7566/JPSJ.88.123704 (2019).

468. Wang, C., Cheng, T., Liu, Z., Liu, F. & Huang, H. Structural Amorphization-Induced Topological Order. *Physical Review Letters* **128,** 056401. https://link.aps.org/doi/10.1103/PhysRevLett.128.056401 (2022).

469. Pöyhönen, K., Sahlberg, I., Weststrom, A. & Ojanen, T. Amorphous topological superconductivity in a Shiba glass. *Nature Communications* **9,** 2103. https://www.nature.com/articles/s41467-018-04532-x (2018).

470. Manna, S., Das, S. K. & Roy, B. *Noncrystalline topological superconductors* arXiv:2207.02203. 2022. http://arxiv.org/abs/2207.02203.

471. Yang, Y.-B., Qin, T., Deng, D.-L., Duan, L.-M. & Xu, Y. Topological Amorphous Metals. *Physical Review Letters* **123,** 076401. https://link.aps.org/doi/10.1103/PhysRevLett.123.076401 (2019).

472. Agarwala, A., Juričić, V. & Roy, B. Higher-order topological insulators in amorphous solids. *Physical Review Research* **2,** 012067. https://link.aps.org/doi/10.1103/PhysRevResearch.2.012067 (2020).

473. Wang, J.-H., Yang, Y.-B., Dai, N. & Xu, Y. Structural-Disorder-Induced Second-Order Topological Insulators in Three Dimensions. *Physical Review Letters* **126,** 206404. https://link.aps.org/doi/10.1103/PhysRevLett.126.206404 (2021).

474. Peng, T., Hua, C.-B., Chen, R., Liu, Z.-R., Huang, H.-M. & Zhou, B. Density-driven higher-order topological phase transitions in amorphous solids. *Phys. Rev. B* **106,** 125310. https://link.aps.org/doi/10.1103/PhysRevB.106.125310 (2022).

475. Marsal, Q., Varjas, D. & Grushin, A. G. Obstructed insulators and flat bands in topological phase-change materials. *Physical Review B* **107,** 045119. https://link.aps.org/doi/10.1103/PhysRevB.107.045119 (4 2023).

476. Franca, S. & Grushin, A. G. *Topological diffusive metal in amorphous transition metal mono-silicides* arXiv:2306.17117. 2023. http://arxiv.org/abs/2306.17117.

477. Tao, Y.-L., Wang, J.-H. & Xu, Y. *Average Symmetry Protected Higher-order Topological Amorphous Insulators* arXiv:2306.02246. 2023. http://arxiv.org/abs/2306.02246.

478. Prodan, E. Fermionic Topological Order on Generic Triangulations. *Ann. Henri Poincaré* **22,** 1133–1161. https://doi.org/10.1007/s00023-020-00999-x (2021).

479. Kim, S., Agarwala, A. & Chowdhury, D. Fractionalization and Topology in Amorphous Electronic Solids. *Phys. Rev. Lett.* **130,** 026202. https://link.aps.org/doi/10.1103/PhysRevLett.130.026202 (2023).

480. Cassella, G., D'Ornellas, P., Hodson, T., Natori, W. M. H. & Knolle, J. *An Exact Chiral Amorphous Spin Liquid* arXiv:2208.08246. 2023. http://arxiv.org/abs/2208.08246.

481. Grushin, A. G. & Repellin, C. Amorphous and Polycrystalline Routes toward a Chiral Spin Liquid. *Phys. Rev. Lett.* **130,** 186702. https://link.aps.org/doi/10.1103/PhysRevLett.130.186702 (2023).

482. Kraus, Y. E., Lahini, Y., Ringel, Z., Verbin, M. & Zilberberg, O. Topological States and Adiabatic Pumping in Quasicrystals. *Physical Review Letters* **109,** 106402. https://link.aps.org/doi/10.1103/PhysRevLett.109.106402 (2012).

483. Mei, F., Zhu, S.-L., Zhang, Z.-M., Oh, C. H. & Goldman, N. Simulating Z_2 topological insulators with cold atoms in a one-dimensional optical lattice. *Physical Review A* **85,** 013638. https://link.aps.org/doi/10.1103/PhysRevA.85.013638 (2012).

484. Kraus, Y. E., Ringel, Z. & Zilberberg, O. Four-Dimensional Quantum Hall Effect in a Two-Dimensional Quasicrystal. *Physical Review Letters* **111,** 226401. https://link.aps.org/doi/10.1103/PhysRevLett.111.226401 (2013).

485. Madsen, K. A., Bergholtz, E. J. & Brouwer, P. W. Topological equivalence of crystal and quasicrystal band structures. *Physical Review B* **88,** 125118. https://link.aps.org/doi/10.1103/PhysRevB.88.125118 (2013).

486. Verbin, M., Zilberberg, O., Kraus, Y. E., Lahini, Y. & Silberberg, Y. Observation of Topological Phase Transitions in Photonic Quasicrystals. *Physical Review Letters* **110,** 076403. https://link.aps.org/doi/10.1103/PhysRevLett.110.076403 (2013).

487. Deng, X. & Santos, L. Topological transitions of interacting bosons in one-dimensional bichromatic optical lattices. *Physical Review A* **89,** 033632. https://link.aps.org/doi/10.1103/PhysRevA.89.033632 (2014).

488. Tran, D.-T., Dauphin, A., Goldman, N. & Gaspard, P. Topological Hofstadter insulators in a two-dimensional quasicrystal. *Physical Review B* **91,** 085125. https://link.aps.org/doi/10.1103/PhysRevB.91.085125 (2015).

489. Bandres, M. A., Rechtsman, M. C. & Segev, M. Topological Photonic Quasicrystals: Fractal Topological Spectrum and Protected Transport. *Physical Review X* **6,** 011016. https://link.aps.org/doi/10.1103/PhysRevX.6.011016 (2016).

490. Lau, A., van den Brink, J. & Ortix, C. Topological mirror insulators in one dimension. *Physical Review B* **94,** 165164. https://link.aps.org/doi/10.1103/PhysRevB.94.165164 (2016).

491. Huang, H. & Liu, F. Quantum Spin Hall Effect and Spin Bott Index in a Quasicrystal Lattice. *Phys. Rev. Lett.* **121,** 126401. https://link.aps.org/doi/10.1103/PhysRevLett.121.126401 (12 2018).

492. Huang, H. & Liu, F. Theory of spin Bott index for quantum spin Hall states in nonperiodic systems. *Phys. Rev. B* **98,** 125130 (12 2018).

493. Varjas, D., Lau, A., Pöyhönen, K., Akhmerov, A. R., Pikulin, D. I. & Fulga, I. C. Topological Phases without Crystalline Counterparts. *Phys. Rev. Lett.* **123,** 196401. https://link.aps.org/doi/10.1103/PhysRevLett.123.196401 (19 2019).

494. Zilberberg, O. Topology in quasicrystals [Invited]. *Opt. Mater. Express, OME* **11,** 1143–1157. https://opg.optica.org/ome/abstract.cfm?uri=ome-11-4-1143 (2021).

495. Slater, J. C. & Koster, G. F. Simplified LCAO Method for the Periodic Potential Problem. *Physical Review* **94,** 1498–1524. https://link.aps.org/doi/10.1103/PhysRev.94.1498 (1954).

496. Mukati, P., Agarwala, A. & Bhattacharjee, S. Topological and conventional phases of a three-dimensional electronic glass. *Physical Review B* **101,** 035142. https://link.aps.org/doi/10.1103/PhysRevB.101.035142 (2020).

497. Liu, G.-G., Yang, Y., Ren, X., Xue, H., Lin, X., Hu, Y.-H., Sun, H.-x., Peng, B., Zhou, P., Chong, Y. & Zhang, B. Topological Anderson Insulator in Disordered Photonic Crystals. *Phys. Rev. Lett.* **125,** 133603. https://link.aps.org/doi/10.1103/PhysRevLett.125.133603 (13 2020).

498. Zhou, P., Liu, G.-G., Ren, X., Yang, Y., Xue, H., Bi, L., Deng, L., Chong, Y. & Zhang, B. Photonic amorphous topological insulator. *Light: Science & Applications* **9,** 133. https://doi.org/10.1038/s41377-020-00368-7 (2020).

499. Jia, Z., Seclì, M., Avdoshkin, A., Redjem, W., Dresselhaus, E., Moore, J. & Kanté, B. Disordered topological graphs enhancing nonlinear phenomena. *Science Advances* **9,** eadf9330. https://doi.org/10.1126/sciadv.adf9330 (2023).

500. Ceresoli, D. & Resta, R. Orbital magnetization and Chern number in a supercell framework: Single **k**-point formula. *Physical Review B* **76,** 012405. https://link.aps.org/doi/10.1103/PhysRevB.76.012405 (2007).

501. Favata, R. & Marrazzo, A. Single-point spin Chern number in a supercell framework. *Electron. Struct.* **5,** 014005. https://dx.doi.org/10.1088/2516-1075/acba6f (2023).

502. Kitaev, A. Anyons in an exactly solved model and beyond. *Annals of Physics. January Special Issue* **321,** 2–111. https://www.sciencedirect.com/science/article/pii/S0003491605002381 (2006).

503. Bianco, R. & Resta, R. Mapping topological order in coordinate space. *Phys. Rev. B* **84,** 241106 (24 2011).

504. Hannukainen, J. D., Martínez, M. F., Bardarson, J. H. & Kvorning, T. K. Local Topological Markers in Odd Spatial Dimensions and Their Application to Amorphous Topological Matter. *Phys. Rev. Lett.* **129,** 277601. https://link.aps.org/doi/10.1103/PhysRevLett.129.277601 (27 2022).

505. Sheng, D. N., Weng, Z. Y., Sheng, L. & Haldane, F. D. M. Quantum Spin-Hall Effect and Topologically Invariant Chern Numbers. *Phys. Rev. Lett.* **97,** 036808. https://link.aps.org/doi/10.1103/PhysRevLett.97.036808 (2006).

506. Prodan, E. Robustness of the spin-Chern number. *Phys. Rev. B* **80,** 125327. https://link.aps.org/doi/10.1103/PhysRevB.80.125327 (2009).
507. Sheng, L., Li, H.-C., Yang, Y.-Y., Sheng, D.-N. & Xing, D.-Y. Spin Chern numbers and time-reversal-symmetry-broken quantum spin Hall effect. *Chinese Phys. B* **22,** 067201. https://doi.org/10.1088/1674-1056/22/6/067201 (2013).
508. Chen, W. Optical absorption measurement of spin Berry curvature and spin Chern marker. *J. Phys.: Condens. Matter* **35,** 155601. https://dx.doi.org/10.1088/1361-648X/acba72 (2023).
509. Marrazzo, A. & Resta, R. Locality of the anomalous Hall conductivity. *Physical Review B* **95,** 121114. https://link.aps.org/doi/10.1103/PhysRevB.95.121114 (2017).
510. d'Ornellas, P., Barnett, R. & Lee, D. K. K. Quantized bulk conductivity as a local Chern marker. *Phys. Rev. B* **106,** 155124. https://link.aps.org/doi/10.1103/PhysRevB.106.155124 (2022).
511. Guzmán, M., Bartolo, D. & Carpentier, D. Geometry and topology tango in ordered and amorphous chiral matter. *SciPost Physics* **12,** 038. https://scipost.org/SciPostPhys.12.1.038 (2022).
512. Jezequel, L., Tauber, C. & Delplace, P. Estimating bulk and edge topological indices in finite open chiral chains. *Journal of Mathematical Physics* **63,** 121901. https://doi.org/10.1063/5.0096720 (2022).
513. Chen, W. Universal topological marker. *Phys. Rev. B* **107,** 045111. https://link.aps.org/doi/10.1103/PhysRevB.107.045111 (2023).
514. Mondragon-Shem, I. & Hughes, T. L. Robust topological invariants of topological crystalline phases in the presence of impurities. arXiv:1906.11847. http://arxiv.org/abs/1906.11847 (2019).
515. Loring, T. A. K-theory and pseudospectra for topological insulators. *Annals of Physics* **356,** 383–416 (2015).
516. Loring, T. & Schulz-Baldes, H. *Finite volume calculation of K-theory invariants* arXiv:1701.07455. 2017. http://arxiv.org/abs/1701.07455.
517. Liu, D. T., Shabani, J. & Mitra, A. Long-range Kitaev chains via planar Josephson junctions. *Phys. Rev. B* **97,** 235114. https://link.aps.org/doi/10.1103/PhysRevB.97.235114 (2018).
518. Loring, T. A. A guide to the Bott index and localizer index. *arXiv:1907.11791*. https://arxiv.org/abs/1907.11791 (2019).
519. Lozano Viesca, E., Schober, J. & Schulz-Baldes, H. Chern numbers as half-signature of the spectral localizer. *Journal of Mathematical Physics* **60,** 072101. https://doi.org/10.1063/1.5094300 (2019).

520. Loring, T. A. & Schulz-Baldes, H. The spectral localizer for even index pairings. *Journal of Noncommutative Geometry* **14,** 1–23. https://ems.press/journals/jncg/articles/16731 (2020).

521. Doll, N. & Schulz-Baldes, H. Approximate symmetries and conservation laws in topological insulators and associated Z-invariants. *Annals of Physics* **419,** 168238. https://www.sciencedirect.com/science/article/pii/S000349162030172X (2020).

522. Schulz-Baldes, H. & Stoiber, T. The spectral localizer for semifinite spectral triples. *Proc. Amer. Math. Soc.* **149,** 121–134. https://www.ams.org/proc/2021-149-01/S0002-9939-2020-15230-6/ (2021).

523. Michala, J., Pierson, A., Loring, T. A. & Watson, A. B. Wave-packet propagation in a finite topological insulator and the spectral localizer index. *Involve, a Journal of Mathematics* **14,** 209–239. https://msp.org/involve/2021/14-2/p03.xhtml (2021).

524. Doll, N. & Schulz-Baldes, H. Skew localizer and Z2-flows for real index pairings. *Advances in Mathematics* **392,** 108038. https://www.sciencedirect.com/science/article/pii/S0001870821004771 (2021).

525. Cerjan, A. & Loring, T. A. Local invariants identify topology in metals and gapless systems. *Phys. Rev. B* **106,** 064109. https://link.aps.org/doi/10.1103/PhysRevB.106.064109 (2022).

526. Cerjan, A. & Loring, T. A. An operator-based approach to topological photonics. *Nanophotonics* **11,** 4765–4780. https://www.degruyter.com/document/doi/10.1515/nanoph-2022-0547/html (2022).

527. Franca, S. & Grushin, A. G. *Obstructions in trivial metals as topological insulator zero-modes* arXiv:2304.01983. 2023. http://arxiv.org/abs/2304.01983.

528. Bellissard, J., van Elst, A. & Schulz- Baldes, H. The noncommutative geometry of the quantum Hall effect. *Journal of Mathematical Physics* **35,** 5373–5451. https://doi.org/10.1063/1.530758 (1994).

529. Hastings, M. B. & Loring, T. A. Almost commuting matrices, localized Wannier functions, and the quantum Hall effect. *J. Math. Phys.* **51,** 015214. https://aip.scitation.org/doi/10.1063/1.3274817 (2010).

530. Loring, T. A. & Hastings, M. B. Disordered topological insulators via C∗-algebras. *EPL (Europhysics Letters)* **92,** 67004. https://iopscience.iop.org/article/10.1209/0295-5075/92/67004 (2010).

531. Hastings, M. B. & Loring, T. A. Topological insulators and C∗-algebras: Theory and numerical practice. *Annals of Physics. July 2011 Special Issue* **326,** 1699–1759. https://www.sciencedirect.com/science/article/pii/S0003491610002277 (2011).

532. Prodan, E. Non-commutative tools for topological insulators. *New Journal of Physics* **12,** 065003. https://dx.doi.org/10.1088/1367-2630/12/6/065003 (2010).

533. Prodan, E. Disordered topological insulators: a non-commutative geometry perspective. *J. Phys. A* **44,** 113001 (2011).
534. Toniolo, D. On the Bott index of unitary matrices on a finite torus. *Lett Math Phys* **112,** 126. https://doi.org/10.1007/s11005-022-01602-6 (2022).
535. Katsura, H. & Koma, T. The noncommutative index theorem and the periodic table for disordered topological insulators and superconductors. *Journal of Mathematical Physics* **59,** 031903. https://doi.org/10.1063/1.5026964 (2018).
536. Uría-Álvarez, A. J., Molpeceres-Mingo, D. & Palacios, J. J. *Deep learning for disordered topological insulators through entanglement spectrum* arXiv:2201.13306. 2022. http://arxiv.org/abs/2201.13306.
537. Vergniory, M. G., Elcoro, L., Felser, C., Regnault, N., Bernevig, B. A. & Wang, Z. A complete catalogue of high-quality topological materials. *Nature* **566,** 480–485. https://www.nature.com/articles/s41586-019-0954-4 (2019).
538. Xu, Y., Elcoro, L., Song, Z.-D., Wieder, B. J., Vergniory, M. G., Regnault, N., Chen, Y., Felser, C. & Bernevig, B. A. High-throughput calculations of magnetic topological materials. *Nature* **586,** 702–707. https://www.nature.com/articles/s41586-020-2837-0 (2020).
539. Frey, N. C., Horton, M. K., Munro, J. M., Griffin, S. M., Persson, K. A. & Shenoy, V. B. High-throughput search for magnetic and topological order in transition metal oxides. *Science Advances* **6,** eabd1076 (2020).
540. Vergniory, M. G., Wieder, B. J., Elcoro, L., Parkin, S. S. P., Felser, C., Bernevig, B. A. & Regnault, N. All topological bands of all nonmagnetic stoichiometric materials. *Science* **376,** eabg9094. https://www.science.org/doi/10.1126/science.abg9094 (2022).
541. Tang, F., Ono, S., Wan, X. & Watanabe, H. High-Throughput Investigations of Topological and Nodal Superconductors. *Phys. Rev. Lett.* **129,** 027001. https://link.aps.org/doi/10.1103/PhysRevLett.129.027001 (2022).
542. Su, Y., Hu, J., Cai, X., Shi, W., Xia, Y., Xu, Y., Xu, X., Chen, Y. & Li, G. High-throughput first-principle prediction of collinear magnetic topological materials. *npj Comput Mater* **8,** 1–8. https://www.nature.com/articles/s41524-022-00954-w (2022).
543. Bianco, R. & Resta, R. Mapping topological order in coordinate space. *Physical Review B* **84,** 241106. https://link.aps.org/doi/10.1103/PhysRevB.84.241106 (2011).
544. Li, Z. & Mong, R. S. K. Local formula for the $\mathbb{Z}_2$ invariant of topological insulators. *Phys. Rev. B* **100,** 205101. https://link.aps.org/doi/10.1103/PhysRevB.100.205101 (2019).
545. Corbae, P., Ciocys, S., Varjas, D., Kennedy, E., Zeltmann, S., Molina-Ruiz, M., Griffin, S. M., Jozwiak, C., Chen, Z., Wang, L.-W., Minor, A. M., Scott, M., Grushin, A. G., Lanzara, A. & Hellman, F. Observation of spin-momentum locked surface states in amorphous Bi_2Se_3. *Nature Materials.* https://doi.org/10.1038/s41563-022-01458-0 (2023).

546. Choudhary, K., Garrity, K. F. & Tavazza, F. High-throughput Discovery of Topologically Non-trivial Materials using Spin-orbit Spillage. *Scientific Reports* **9,** 8534. https://www.nature.com/articles/s41598-019-45028-y (2019).

547. Choudhary, K., Garrity, K. F., Ghimire, N. J., Anand, N. & Tavazza, F. High-throughput search for magnetic topological materials using spin-orbit spillage, machine learning, and experiments. *Physical Review B* **103,** 155131. https://link.aps.org/doi/10.1103/PhysRevB.103.155131 (2021).

548. Jung, W. S., Leem, C. S., Kim, C., Park, S. R., Park, S. Y., Kim, B. J., Rotenberg, E. & Kim, C. Imaging the electron density in solids by using multi-Brillouin-zone angle resolved photoelectron spectroscopy. *Physical Review B* **82,** 235105. https://link.aps.org/doi/10.1103/PhysRevB.82.235105 (2010).

549. Soriano, M. & Palacios, J. J. Theory of projections with nonorthogonal basis sets: Partitioning techniques and effective Hamiltonians. *Physical Review B* **90,** 075128. https://link.aps.org/doi/10.1103/PhysRevB.90.075128 (2014).

550. Bruus, H., Flensberg, K., Bruus, H. & Flensberg, K. *Many-Body Quantum Theory in Condensed Matter Physics: An Introduction* ISBN: 978-0-19-856633-5 (Oxford University Press, Oxford, New York, 2004).

551. Grushin, A. G. & Repellin, C. Amorphous and Polycrystalline Routes toward a Chiral Spin Liquid. *Phys. Rev. Lett.* **130,** 186702. https://link.aps.org/doi/10.1103/PhysRevLett.130.186702 (2023).

552. Reis, F., Li, G., Dudy, L., Bauernfeind, M., Glass, S., Hanke, W., Thomale, R., Schäfer, J. & Claessen, R. Bismuthene on a SiC substrate: A candidate for a high-temperature quantum spin Hall material. *Science* **357,** 287–290. https://science.sciencemag.org/content/357/6348/287 (2017).

553. Sun, S., You, J.-Y., Duan, S., Gou, J., Luo, Y. Z., Lin, W., Lian, X., Jin, T., Liu, J., Huang, Y., Wang, Y., Wee, A. T. S., Feng, Y. P., Shen, L., Zhang, J. L., Chen, J. & Chen, W. Epitaxial Growth of Ultraflat Bismuthene with Large Topological Band Inversion Enabled by Substrate-Orbital-Filtering Effect. *ACS Nano* **16,** 1436–1443. https://doi.org/10.1021/acsnano.1c09592 (2022).

554. Harrison, W. A. *Electronic Structure and the Properties of Solids: The Physics of the Chemical Bond* (Dover Publications, 1989).

555. Groth, C. W., Wimmer, M., Akhmerov, A. R. & Waintal, X. Kwant: a software package for quantum transport. *New Journal of Physics* **16,** 063065. https://doi.org/10.1088/1367-2630/16/6/063065 (2014).

556. Weisse, A., Wellein, G., Alvermann, A. & Fehske, H. The kernel polynomial method. *Reviews of Modern Physics* **78,** 275–306. https://link.aps.org/doi/10.1103/RevModPhys.78.275 (2006).

557. Varjas, D., Fruchart, M., Akhmerov, A. R. & Perez-Piskunow, P. M. Computation of topological phase diagram of disordered $Pb_{1-x}Sn_xTe$ using the kernel polynomial method. *Phys. Rev. Research* **2,** 013229. https://link.aps.org/doi/10.1103/PhysRevResearch.2.013229 (1 2020).

558. Kane, C. L. & Mele, E. J. Z_2 Topological Order and the Quantum Spin Hall Effect. *Physical Review Letters* **95,** 146802. https://link.aps.org/doi/10.1103/PhysRevLett.95.146802 (2005).

559. Lieb, E. H. Two theorems on the Hubbard model. *Physical Review Letters* **62,** 1201–1204. https://link.aps.org/doi/10.1103/PhysRevLett.62.1201 (1989).

560. Hikami, S., Larkin, A. I. & Nagaoka, Y. Spin-Orbit Interaction and Magnetoresistance in the Two Dimensional Random System. *Progress of Theoretical Physics* **63,** 707–710. https://doi.org/10.1143/PTP.63.707 (1980).

561. Yamakage, A., Nomura, K., Imura, K.-I. & Kuramoto, Y. Disorder-Induced Multiple Transition Involving Z2 Topological Insulator. *Journal of the Physical Society of Japan* **80,** 053703. https://journals.jps.jp/doi/10.1143/JPSJ.80.053703 (2011).

562. Liu, Z., Liu, C.-X., Wu, Y.-S., Duan, W.-H., Liu, F. & Wu, J. Stable Nontrivial Z_2 Topology in Ultrathin Bi (111) Films: A First-Principles Study. *Physical Review Letters* **107,** 136805. https://link.aps.org/doi/10.1103/PhysRevLett.107.136805 (2011).

563. Murakami, S. Quantum Spin Hall Effect and Enhanced Magnetic Response by Spin-Orbit Coupling. *Physical Review Letters* **97,** 236805. https://link.aps.org/doi/10.1103/PhysRevLett.97.236805 (2006).

564. Wada, M., Murakami, S., Freimuth, F. & Bihlmayer, G. Localized edge states in two-dimensional topological insulators: Ultrathin Bi films. *Physical Review B* **83,** 121310. https://link.aps.org/doi/10.1103/PhysRevB.83.121310 (2011).

565. Huang, Z.-Q., Chuang, F.-C., Hsu, C.-H., Liu, Y.-T., Chang, H.-R., Lin, H. & Bansil, A. Nontrivial topological electronic structures in a single Bi(111) bilayer on different substrates: A first-principles study. *Physical Review B* **88,** 165301. https://link.aps.org/doi/10.1103/PhysRevB.88.165301 (2013).

566. Li, Q., Smith, J. S., Yin, Y., Wang, C., Klymenko, M. V., Cole, J. H. & Medhekar, N. V. Localized Wannier function based tight-binding models for two-dimensional allotropes of bismuth. *New Journal of Physics* **23,** 063042. https://doi.org/10.1088/1367-2630/ac04c9 (2021).

567. Singh, S., Zanolli, Z., Amsler, M., Belhadji, B., Sofo, J. O., Verstraete, M. J. & Romero, A. H. Low-Energy Phases of Bi Monolayer Predicted by Structure Search in Two Dimensions. *The Journal of Physical Chemistry Letters* **10,** 7324–7332. https://doi.org/10.1021/acs.jpclett.9b03043 (2019).

568. Ares, P., Palacios, J. J., Abellán, G., Gómez-Herrero, J. & Zamora, F. Recent Progress on Antimonene: A New Bidimensional Material. *Advanced Materials* **30,** 1703771. https://onlinelibrary.wiley.com/doi/abs/10.1002/adma.201703771 (2018).

569. Kühne, T. D. *et al.* CP2K: An electronic structure and molecular dynamics software package - Quickstep: Efficient and accurate electronic structure calculations. *The Journal of Chemical Physics* **152,** 194103. https://doi.org/10.1063/5.0007045 (2020).

570. Harrelson, T. F., Sheridan, E., Kennedy, E., Vinson, J., N'Diaye, A. T., Altoé, M. V. P., Schwartzberg, A., Siddiqi, I., Ogletree, D. F., Scott, M. C., *et al.* Elucidating the local atomic and electronic structure of amorphous oxidized superconducting niobium films. *Applied Physics Letters* **119,** 244004 (2021).

571. Zhang, K., Xu, M., Li, N., Xu, M., Zhang, Q., Greenberg, E., Prakapenka, V. B., Chen, Y.-S., Wuttig, M., Mao, H.-K. & Yang, W. Superconducting Phase Induced by a Local Structure Transition in Amorphous Sb_2Se_3 under High Pressure. *Phys. Rev. Lett.* **127,** 127002. https://link.aps.org/doi/10.1103/PhysRevLett.127.127002 (12 2021).

572. Van Miert, G. & Ortix, C. Higher-order topological insulators protected by inversion and rotoinversion symmetries. *Phys. Rev. B* **98,** 081110. https://link.aps.org/doi/10.1103/PhysRevB.98.081110 (2018).

573. Song, Z.-D., Elcoro, L. & Bernevig, B. A. Twisted bulk-boundary correspondence of fragile topology. *Science* **367,** 794–797. https://www.science.org/doi/10.1126/science.aaz7650 (2020).

574. Xu, Y., Elcoro, L., Li, G., Song, Z.-D., Regnault, N., Yang, Q., Sun, Y., Parkin, S., Felser, C. & Bernevig, B. A. *Three-Dimensional Real Space Invariants, Obstructed Atomic Insulators and A New Principle for Active Catalytic Sites* arXiv: 2111.02433. 2021. http://arxiv.org/abs/2111.02433.

575. Hori, M., Ghadimi, R., Sugimoto, T., Tohyama, T. & Tanaka, K. in *Proceedings of the 29th International Conference on Low Temperature Physics (LT29) JPS Conference Proceedings* 38 (2023). https://journals.jps.jp/doi/abs/10.7566/JPSCP.38.011065.

576. Baggioli, M., Setty, C. & Zaccone, A. Effective theory of superconductivity in strongly coupled amorphous materials. *Phys. Rev. B* **101,** 214502. https://link.aps.org/doi/10.1103/PhysRevB.101.214502 (2020).

577. Wang, L., Szamel, G. & Flenner, E. Low-Frequency Excess Vibrational Modes in Two-Dimensional Glasses. *Phys. Rev. Lett.* **127,** 248001. https://link.aps.org/doi/10.1103/PhysRevLett.127.248001 (2021).

578. Jiang, C., Zaccone, A., Setty, C. & Baggioli, M. *Glassy heat capacity from overdamped phasons and a hypothetical phason-induced superconductivity in incommensurate structures* arXiv:2305.05407. 2023. http://arxiv.org/abs/2305.05407.

579. Finger, W. & Rice, T. M. Theory of the Crossover in the Low-Frequency Dynamics of an Incommensurate System, $Hg_{3-\delta}AsF_6$. *Phys. Rev. Lett.* **49,** 468–470. https://link.aps.org/doi/10.1103/PhysRevLett.49.468 (1982).

580. Ochoa, H. & Fernandes, R. M. Degradation of Phonons in Disordered Moirè Superlattices. *Phys. Rev. Lett.* **128,** 065901. https://link.aps.org/doi/10.1103/PhysRevLett.128.065901 (2022).